The University of Nottingham
UNITED KINGDOM · CHINA · MALAYSIA

FACULTY OF ENGINEERING
NOTTINGHAM GEOSPATIAL INSTITUTE

PhD THESIS

Engineering Surveying and Space Geodesy – Satellite Navigation

ACADEMIC YEAR 2016-2017

ROBERTO SABATINI

A NOVEL AVIONICS BASED GNSS INTEGRITY AUGMENTATION SYSTEM FOR MANNED AND UNMANNED AIRCRAFT

Supervisor: **Prof TERRY MOORE**

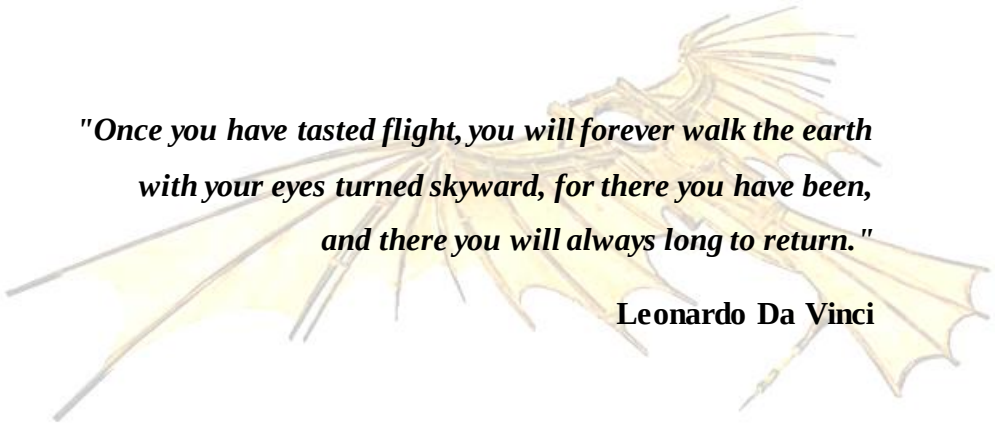
Co-Supervisor: **Dr CHRIS HILL**

June 2017

This Thesis is submitted to the University of Nottingham in fulfilment of the requirements for the degree of Doctor of Philosophy

© 2017 Roberto Sabatini. All rights reserved.

No part of this publication may be reproduced without the written permission of the copyright owner.



"Once you have tasted flight, you will forever walk the earth with your eyes turned skyward, for there you have been, and there you will always long to return."

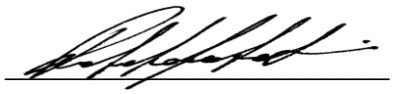
Leonardo Da Vinci

(This page is left black for the purpose of typesetting)

DECLARATION OF ORIGINALITY

I hereby certify that I am the sole author of this thesis and that the intellectual content of this document is the product of my own work. I declare that any ideas, techniques, quotations, or any other material from the work of other people are fully acknowledged in accordance with standard referencing practices. I declare that this is a true copy of my thesis, including any final revisions, as approved by the thesis examination committee.

Date: 30th June 2017



Roberto Sabatini

(This page is left black for the purpose of typesetting)

SUMMARY OF THESIS

The aviation community has to implement very stringent navigation integrity requirements in a variety of manned and unmanned aircraft applications. This thesis presents the results of the research activities carried out by the Italian Air Force Research and Flight Test Centre (CSV-RSV) in collaboration with the Nottingham Geospatial Institute (NGI) and RMIT University in the area of Avionics Based Integrity Augmentation (ABIA) for mission-essential and safety-critical Global Navigation Satellite Systems (GNSS) applications in the civil/military aviation context.

Space and Ground Based Augmentation Systems (SBAS/GBAS) have been developed in recent years to improve GNSS integrity, accuracy and availability for aircraft navigation and particularly for landing applications. SBAS satellites broadcast correction messages back to the earth, where suitably enabled receivers use the information to improve accuracy and integrity. The US, Europe and other nations have developed their own SBAS systems. In the US, the Wide Area Augmentation System (WAAS) exists and is operational. In Europe, SBAS coverage is provided by the European Geostationary Navigation Overlay Service (EGNOS), in Japan by the Multi-functional Satellite Augmentation System (MSAS) and India is developing the GNSS Aided Geo Augmented Navigation (GAGAN) system. An alternative approach to GNSS augmentation is to transmit integrity and correction messages from ground-based systems. An example is the American Local Area Augmentation System (LAAS), which allows a suitably equipped receiver to derive enhanced accuracy and integrity information in a local area. The combination of WAAS and LAAS is targeted to provide the Required Navigation Performance (RNP) in all phases of aircraft navigation, including en-route, terminal, approach/landing and surface operations.

Along with SBAS and GBAS, GNSS augmentation may take the form of additional information being provided by other avionics systems. In most cases, the additional avionics systems operate via separate principles than GNSS and, therefore, are not subject to the same sources of error or interference. A system such as this is referred

to as an Aircraft Based Augmentation System (ABAS). The additional sensors used in ABAS may include Inertial Navigation Systems (INS), TACAN/VOR-DME, Radar, Vision Based Sensors, etc. Unlike SBAS and GBAS technology, research on ABAS is limited and mainly concentrates on additional information being blended into the position calculation to increase accuracy and/or continuity of the integrated navigation solutions. Additionally, no significant attempts have been made of developing ABAS architectures capable of generating integrity signals suitable for safety-critical GNSS applications (e.g., aircraft precision approach and landing) and no flight certified ABAS products are available at present.

During flight test activities with GNSS and Differential GNSS (DGNSS) systems, it was observed that one or more of the following conditions was prone to cause navigation data outages or severe performance degradations:

- Antenna obscuration due to aircraft manoeuvring;
- Bad satellite geometries and low carrier-to-noise ratios (C/N_0);
- Doppler shifts caused by aircraft-satellites relative motion;
- Interference, at the airborne GNSS antenna, caused by non-GNSS RF signals;
- Multipath caused by GNSS signals reflected by the earth surface or the aircraft body.

The last two problems can be mitigated by existing technology solutions (i.e., choosing a VHF/UHF Data Link, filtering the radio frequency signals reaching the GNSS antenna, identifying suitable locations for the GNSS antenna and providing adequate shielded of the antenna itself, either by physical devices or via dedicated software masks, etc.). However, there is little one can do in order to prevent critical events during realistic test/training manoeuvres and particular approach procedures (e.g., curved and segmented approaches) performed with high performance military aircraft. Furthermore, although in some cases a careful mission planning may significantly reduce the number of GNSS outages, the adoption of specific aircraft piloting strategies (using the information currently available in the cockpit) cannot effectively avoid the occurrence of these events.

ABIA is a new concept that progressively evolved based on research with GNSS-based Time and Space Position Information (TSPI) systems. TSPI research activities included design, integration and ground/flight testing carried out on MB-339CD, TORNADO and TYPHOON military aircraft. As soon as the validity of the TSPI-ABIA (T-ABIA) concept was established, a prototype system was developed for use in flight test applications. This system is capable of alerting the pilot when the critical conditions for GNSS signal loss are likely to occur (within a specified maximum time-to-alert). In this T-ABIA prototype, the aircraft on-board sensors provide information on the aircraft relevant flight parameters (navigation data, engine settings, etc.) to an Integrity Flag Generator (IFG), which is also connected to the on-board GNSS receiver. The IFG can be incorporated into one of the existing airborne computers or can be a dedicated processing unit. Using the available data on GNSS and the aircraft flight parameters, integrity signals are generated which are displayed on one of the cockpit displays and sent to an Aural Warning Generator. At the same time, an alternate flight path is computed taking into account the geometry and the tracking status of the available GNSS satellites, together with the current mission requirements and the information provided by the aircraft Flight Test Instrumentation (FTI) and standard on-board sensors.

Based on the results of T-ABIA research a more advanced ABIA system was developed suitable for manned and unmanned aircraft applications. Detailed mathematical algorithms were developed to cope with the main causes of GNSS signal outages and degradation in flight, namely: obscuration, multipath, interference, fading due to adverse geometry and Doppler shift. Adopting these algorithms, the ABIA system is able to provide steering information to the pilot and electronic commands to the aircraft flight control system, allowing real-time avoidance of safety-critical flight conditions and fast recovery of the required navigation performance in case of GNSS data losses. This is achieved by implementing both caution (predictive) and warning (reactive) integrity flags, as well as 4-Dimensional Trajectory (4DT) optimisation models suitable for all phases of flight.

The detailed design of the ABIA IFG module was completed and validation activities were performed on TORNADO-IDS, A-320 and AEROSONDE UAV simulated platforms to determine the Time-to-Alert (TTA) performances of the ABIA system in various flight phases from departure to final approach. The results of these activities were encouraging, showing that the system TTA performance is in line with current ICAO, FAA and CAA requirements for the different flight phases, with a potential synergy with SBAS and GBAS systems to support departure, enroute and TMA operations, including CAT-I/III precision approach. Further research concentrated on the 4DT computation module and extended the scope of ABIA applications to Unmanned Aircraft Systems (UAS). In particular, an initial investigation was accomplished to identify the potential synergies of ABIA with UAS Sense-and-Avoid (SAA) architectures for mid-air collision avoidance tasks.

In conclusion, although current and likely future SBAS/GBAS augmentation systems can provide significant improvement of GNSS navigation performance, it is shown that the novel ABIA system developed in this research can play a key role in GNSS integrity augmentation for mission-essential and safety-critical applications such as aircraft precision approach/auto-landing and UAS sense-and-avoid. Furthermore, using suitable data link and data processing technologies, a certified ABIA system could play a key role as part of a future GNSS Space-Ground-Aircraft Augmentation Network (SGAAN).

ACKNOWLEDGEMENTS

First of all, I would like to express my deepest gratitude to my supervisors Professor Terry Moore and Dr Chris Hill for their precious guidance throughout this research project. I am also in debt with the many staff and friends of the Italian Air Force Research and Flight Test Centre (DASRS/CSV and RSV), the MIDS International Program Office (MIDS IPO), the US Space and Naval Warfare Systems Command (SPAWAR), the US Program Executive Office for C4I&SPACE, the Italian Ministry of Defence General Directorate for Aeronautics & Airworthiness (ARMAEREO) and the General Directorate for Telecommunications, IT & Advanced Technologies (TELEDIFE), which directly or indirectly contributed to the success of this research project. Special thanks go to my colleagues from RMIT University and Cranfield University for many stimulating conversations and for their genuine interest in my GNSS research. Last, but not least, I wish to thank my wife Janete and my three children Christian, Jacqueline and Jennifer. I will be forever indebted to them for understanding my unstoppable passion for research and for sharing with me the challenges and strains of constantly living and working outside the comfort zone. With their love, patience and courage while moving across three continents and changing six houses over a period of only three years, they gave me the motivation and support required to achieve very ambitious goals.

(This page is left black for the purpose of typesetting)

TABLE OF CONTENTS

SUMMARY OF THESIS VII

ACKNOWLEDGEMENTS XI

LIST OF FIGURES XIX

LIST OF TABLES XXV

LIST OF ABBREVIATIONS XXIX

1. INTRODUCTION

1.1 Research Context and Motivation 1

1.2 Research Aim and Objectives 5

1.3 Research Methodology 6

2. GNSS AVIATION APPLICATIONS

2.1 Introduction 9

2.2 GNSS Segments 10

2.3 GNSS Observables 12

2.3.1 Pseudorange Observable 13

2.3.2 Carrier Phase Observable 16

2.3.3 Doppler Observable 18

2.4 GPS Error Sources 19

2.4.1 Receiver Dependent Errors 19

2.4.2 Ephemeris Prediction Errors 20

2.4.3 Satellite Dependent Errors 21
2.4.4 Propagation Errors 22
2.4.5 Multipath Errors 26
2.4.6 User Dynamics Error 27
2.5 UERE Vector 27
2.6 DOP Factors 31
2.7 GNSS Performance Requirements in Aviation 37
2.8 GNSS Accuracy Augmentation 42
2.8.1 Ranging-Code DGNSS 46
2.8.2 Carrier-phase DGNSS 49
2.8.3 DGNSS Data Link Implementations 52
2.8.4 DGNSS Accuracy 54
2.8.5 RTK Evolution and Precise Point Positioning 58
2.9 GNSS Integrity Augmentation 60
2.10 Space Based Augmentation 66
2.11 Ground Based Augmentation 78
2.12 Conclusion 87
2.13 References 88

3. GNSS PERFORMANCE IN AVIONICS TSPI APPLICATIONS

3.1 Introduction 97
3.2 Flight Test Activities 98
3.3 Aircraft Installations 99
3.4 TSPI Systems Setup 102
3.5 Ground Test Activities 103

3.6 MB-339CD Flight Test Activities 104

3.7 TORNADO-IDS and TYPHOON Flight Trials 119

3.7.1 TSPI Accuracy and Continuity Evaluation 119

3.7.2 GNSS Masking Investigation 128

3.7.3 Signal-to-Noise Ratio Investigation 139

3.7.4 Doppler Investigation 142

3.7.5 Data Link/GNSS Electromagnetic Compatibility 144

3.7.6 Flight Test Mission Planning and Optimisation 144

3.8 TSPI ABIA System Development 147

3.9 Conclusion 150

3.10 References 152

4. ADVANCED ABIA SYSTEM ARCHITECTURE

4.1 Introduction 153

4.2 ABIA Concept Evolution 154

4.3 ABIA IFG DEVELOPMENT 158

4.3.1 IFG Module Architecture 159

4.3.2 Antenna Obscuration 161

4.3.3 GNSS Signal and Interference 164

4.3.4 Doppler Shift 174

4.3.5 Multipath 174

4.4 Conclusion 181

4.5 References 182

5. ABIA INTEGRITY FLAGS

5.1 Introduction 185

5.2 IFG Module Simulator 185

5.3 Integrity Flag Criteria 187

5.3.1 Relative Geometry and Obscuration 188

5.3.2 Radio Frequency Link Errors 189

5.3.3 Receiver Tracking Errors 194

5.3.4 EHE and EVE Integrity Flags 200

5.4 Simulation Case Studies 202

5.4.1 TORNADO-IDS Simulation 204

5.4.2 A320 Simulation 209

5.4.3 AEROSONDE UAV Simulation 214

5.4.4 EHE and EVE Integrity Flags 221

5.5 Discussion 225

5.5 Conclusion 227

5.6 References 228

6. ABIA FLIGHT PATH GUIDANCE MODULE

6.1 Introduction 231

6.2 Trajectory Optimisation 231

6.3 Flight Dynamics Models 233

6.4 FPG Module Dynamics Model Implementation 238

6.5 Path Constraints AND Boundary Conditions 242

6.6 Cost Functions 247

6.7 Trajectory Optimisation Algorithms 248

6.7.1 Mission Planning and ATM Applications 252

6.7.2 Real-time Applications 252

6.7.3 Optimisation Criteria 254

6.8 Simulation Case Studies 255

6.9 Conclusions 260

6.10 References 261

7. ABIA SYNERGY WITH SBAS AND GBAS

7.1 Introduction 265

7.2 SBAS and GBAS Integrity Models 265

7.3 Simulation Case Studies 285

7.4 Discussion 302

7.5 Conclusion 304

7.6 References 304

8. ABIA SYNERGY WITH UAS SENSE-AND-AVOID

8.1 Introduction 307

8.2 ABIA System for UAS 308

8.3 Sense-and-Avoid 309

8.4 ABIA/SAA Systems Integration 311

8.5 Simulation 313

8.6 Conclusion 319

8.7 References 320

9. CONCLUSIONS AND FUTURE RESEARCH

9.1 Conclusions 321

9.2 Future Research 327

APPENDIXES

A – TORNADO-IDS EMC/EMI Investigation

B – 3DOF ADM Practical Implementation

LIST OF FIGURES

Figure 1-1. WAAS and LAAS services

Figure 2-1 GNSS segments

Figure 2-2 Navigation solution in the ECEF co-ordinate system

Figure 2-3 Error components in ephemeris estimation

Figure 2-4 Multipath Error

Figure 2-5 UERE variation with time in normal and extended operations

Figure 2-6 PDOP tetrahedron construction

Figure 2-7 "Cut and fold" tetrahedron for PDOP determination

Figure 2-8 Navigation accuracy in aviation applications

Figure 2-9 Typical DGNSS system architecture

Figure 2-10 Pseudorange differencing

Figure 2-11 GBAS and SBAS services

Figure 2-12 FDE events

Figure 2-13 Protection levels and alert limits

Figure 2-14 Protection levels and alert limits

Figure 2-15 Current and possible future SBAS systems coverage

Figure 2-16 WAAS architecture and operational environment

Figure 2-17 WAAS IGPs for bands 0-8

Figure 2-18 Ionospheric pierce point geometry

Figure 2-19 Principle of Interpolation of the IPPs

Figure 2-20 GBAS architecture

Figure 2-21 Minimum category I, II and APV service volume

Figure 3-1 MB-339CD aircraft DGNSS/FTI installation

Figure 3-2 MB-339CD FTI and ASHTECH receiver

Figure 3-3 TORNADO-IDS GNSS/Telemetry antennae installation

Figure 3-4 EF-2000 GNSS/Telemetry installation

Figure 3-5 Aerodrome chart with reference station and trolley track

Figure 3-6 INS data recorded by the FTI

Figure 3-7 SNR of the GNSS satellites

Figure 3-8 Relative geometry of the aircraft and satellites

Figure 3-9 GNSS data loss periods (manoeuvres)

Figure 3-10 GNSS data loss periods (SNRs)

Figure 3-11 Aircraft-satellites relative geometry during data loss

Figure 3-12 TANS data loss periods (manoeuvres)

Figure 3-13 SNRs during TANS data loss periods

Figure 3-14 Aircraft-satellites relative geometry during TANS data loss

Figure 3-15 Aircraft-satellites relative geometry (no data losses)

Figure 3-16 Manoeuvres without GNSS data losses

Figure 3-17 PDOP increase with loss of 1 satellite

Figure 3-18 Stick-jerk manoeuvres

Figure 3-19 Pull-up manoeuvres

Figure 3-20 Comparison between DGNSS and R/A data

Figure 3-21 CLDP TV and IR configurations

Figure 3-22 TORNADO-IDS CLDP installation

Figure 3-23 Differences between DGNSS and CLDP laser range

Figure 3-24 Differences between optical tracker and DGNSS data

Figure 3-25 TYPHOON GNSS (FTI) satellites tracking and aircraft dynamics

Figure 3-26 Satellite visibility from receiver almanac data

Figure 3-27 Example of antenna masking matrix

Figure 3-28 Simplified aircraft model (TORNADO-IDS)

Figure 3-29 Example of global masking matrix

Figure 3-30 Example of VIEWSAT output and relevant flight conditions

Figure 3-31 Relative geometry of the aircraft and satellites

Figure 3-32 Altitude variations without satellite losses

Figure 3-33 Critical manoeuvres (loss of satellite signals)

Figure 3-34 Satellite masking (SV's 17, 20, 23 and 25)

Figure 3-35 Critical conditions (CBA, heading change) without loss of GNSS data

Figure 3-36 Approach manoeuvres with high bank and no loss of GNSS data

Figure 3-37 GPS sky-plot example

Figure 3-38 VIEWSAT diagram corresponding to GNSS data loos and reacquisition

Figure 3-39 B-file in ASCII format

Figure 3-40 B-file for GNSS data loss

Figure 3-41 B-file for signal reacquisition

Figure 3-42 Signal loss shown in a B-file with no GNSS data interruption in the C-file

Figure 3-43 B-file corresponding to data loss in the C-file with four satellites tracked

Figure 3-44 Doppler shift and signal acquisition in an avionics receiver

Figure 3-45 Optimised manoeuvres for DGNSS data gathering

Figure 3-46 Measured aircraft trajectory with mission optimisation criteria

Figure 3-47 Masking/performance analysis results (example)

Figure 3-48 T-ABIA systems for flight test applications

Figure 3-49 T-ABIA cockpit integration scheme

Figure 4-1 ABIA evolution for manned and unmanned aerial vehicles

Figure 4-2 ABIA PA and RC functions representation

Figure 4-3 ABIA PC function representation

Figure 4-4 IFG module architecture

Figure 4-5 GNSS satellite obscuration analysis

Figure 4-6 TORNADO-IDS upper antenna AOM (Right Roll=50^{o})

Figure 4-7 Avionics antenna gain pattern (L1 frequency)

Figure 4-8 Turning descent manoeuvre

Figure 4-9 Satellite Visibility (TDM)

Figure 4-10 GPS Satellite Antenna Coverage

Figure 4-11 Depth of scintillation fading at 1.5 GHz during solar max. and min. years

Figure 4-12 Calculated C/N_0 for PRN-14

Figure 4-13 Phase of GNSS signal

Figure 4-14 Variation of A_c as function of the angle β

Figure 4-15 Multipath channel model

Figure 4-16 Geometric reflection model

Figure 5-1 ABIA IFG module simulator

Figure 5-2 Integrity flag thresholds criteria

Figure 5-3 TORNADO-IDS global masking profile

Figure 5-4 Probability of detecting multipath for varying ELP thresholds

Figure 5-5 PFA for varying ELP threshold

Figure 5-6 Doppler shift and signal acquisition in avionics GPS receivers

Figure 5-7 Simplified GPS antenna gain pattern

Figure 5-8 GPS satellites ground traces

Figure 5-9 TORNADO-IDS 3-D CATIA model

Figure 5-10 TORNADO-IDS antennae locations

Figure 5-11 TORNADO-IDS flight profile

Figure 5-12 Detailed causes of CIFs and WIFs (TORNADO-IDS)

Figure 5-13 A320 dimensions and GPS antenna location

Figure 5-14 CATIA models of A320

Figure 5-15 A320 flight profiles

Figure 5-16 Detailed causes of CIFs and WIFs (A320)

Figure 5-17 AEROSONDE 3-D CATIA model

Figure 5-18 AEROSONDE UAV antenna location

Figure 5-19 AMPC logic diagram

Figure 5-20 AEROSONDE mesh in MATLAB™

Figure 5-21 AEROSONDE masking profile simulation

Figure 5-22 AEROSONDE UAV simulated trajectory

Figure 5-23 Detailed causes of CIFs and WIFs (AEROSONDE)

Figure 5-24 CIFs and WIFs with EHE/EVE flags (TORNADO-IDS)

Figure 5-25 CIFs and WIFs with EHE/EVE flags (A320).

Figure 5-26 CIFs and WIFs with EHE/EVE flags (AEROSONDE)

Figure 6-1 Trajectory optimization problem

Figure 6-2 Thrust coefficient as a function of advance ratio

Figure 6-3 AEROSONDE fuel flow map

Figure 6-4 Elevation and azimuth in body frame

Figure 6-5 Reference geometry for Doppler shift analysis

Figure 6-6 Reference geometry for Doppler shift manoeuvre corrections

Figure 6-7 DCO implementation scheme

Figure 6-8 Reference AEROSONDE flight profile

Figure 6-9 CIFs and WIFs generated by the IFG module

Figure 6-10 CIFs and WIFs generated during level turn

Figure 6-11 CIFs and WIFs generated during turning descent

Figure 6-12 Turning descent segment with CIF and WIF

Figure 6-13 Turning descent segment optimised with MPO

Figure 6-14 Turning descent segment optimised with CGO

Figure 7-1 SBAS integrity algorithm

Figure 7-2 Residual tropospheric error from the WAAS MOPS

Figure 7-3 GBAS integrity algorithm

Figure 7-4 Flight test data analysis procedure

Figure 7-5 Multipath error for AMD type A

Figure 7-6 TORNADO-IDS flight trajectory and GCA

Figure 7-7 A320 flight trajectory and GCA

Figure 7-8 AEROSONDE UAV simulated trajectory

Figure 8-1 ABIA system architecture for UAS applications

Figure 8-2 SAA system architecture

Figure 8-3 ABIA/SAA integrated architecture

Figure 8-4 2 UAV 90º collision cooperative SAA scenario

Figure 8-5 Achieved horizontal separation

Figure 8-6 Predicted conflict probability

Figure 8-7 UAV 90º collision non-cooperative SAA scenario

Figure 8-8 Horizontal and vertical separation

Figure 8-9 3 UAV collision cooperative SAA scenario

Figure 8-10 Horizontal and vertical separation of intruder 1

Figure 8-11 Horizontal and vertical separation of intruder 2

Figure 8-12 Avoidance trajectory in the presence of an omnidirectional jammer

Figure 8-13 Avoidance trajectory in the presence of a directional jammer

LIST OF TABLES

Table 2-1 Tropospheric delay for varying elevation angle

Table 2-2 GPS single frequency C/A code UERE budget

Table 2-3 Typical UEE error buidget (95%)

Table 2-4 SPS SIS URE accuracy standards

Table 2-5 DOP Expressions

Table 2-6 GNSS figure of merit

Table 2-7 Aviation GNSS signal-in-space performance requirements

Table 2-8 Possible DGNSS data link frequencies

Table 2-9 Possible classification scheme of DGNSS techniques

Table 2-10 Error sources in DGPS

Table 2-11 DGNSS L1 pseudorange rrrors with increasing distance from RS

Table 2-12 Evaluation of GIVEIi

Table 2-13 $\delta UDRE$ Indicators and values in MT 27

Table 2-14 GBAS service levels

Table 2-15 GBAS service level performance

Table 3-1 Identification of aircraft parameters

Table 3-2 DGNSS-TSPI data accuracy

Table 4-1 Nominal Receiver GPS Signal Power and Received C/N_0

Table 4.2 Empirical conversion table for scintillation indices

Table 4-3 J/S calculations for 25 dB-Hz tracking threshold

Table 5-1 TORNADO-IDS dimensions

Table 5-2 Integrity flag time for TORNADO-IDS

Table 5-3 Integrity flag time for A320

Table 5-4 Integrity flags for AEROSONDE

Table 7-1 SBAS vertical alert limit and horizontal alert limit.

Table 7-2 UDREIi and UDREi.

Table 7-3 GAD and accuracy requirements.

Table 7-4 Vertical missed detection multipliers.

Table 7-5 Lateral missed detection multipliers.

Table 7-6 Fault-free detection multipliers.

Table 7-7 Vertical alert limit.

Table 7-8 Lateral alert limit.

Table 7-9 FASVAL and FASLAL.

Table 7-10 WIFs for SBAS (TORNADO-IDS).

Table 7-11 SBAS CIFs and WIFs causes (TORNADO-IDS).

Table 7-12 CIFs and WIFs for GBAS (TORNADO-IDS).

Table 7-13 Causes of CIFs and WIFs for GBAS (TORNADO-IDS).

Table 7-14 CIFs and WIFs for ABIA/SBAS/GBAS (TORNADO-IDS) from climb to descent.

Table 7-15 CIFs and WIFs for ABIA/SBAS/GBAS (TORNADO-IDS) in descent/approach.

Table 7-16 CIFs and WIFs for SBAS obscuration (TORNADO-IDS).

Table 7-17 CIFs and WIFs for GBAS obscuration (TORNADO-IDS).

Table 7-18 CIFs and WIFs for ABIA/SBAS/GBAS (TORNADO-IDS) from climb to descent.

Table 7-19 SBAS CIF and WIF causes (A320).

Table 7-20 CIFs and WIFs for GBAS (A320).

Table 7-21 GBAS CIF and WIF causes (A320).

Table 7-22 Combined CIFs and WIFs for ABIA/SBAS/GBAS (A320).

Table 7-23 CIF and WIF for SBAS (AEROSONDE).

Table 7-24 SBAS CIF and WIF causes (AEROSONDE).

Table 7-25 CIF and WIF for GBAS (AEROSONDE)

Table 7-26 GBAS CIF and WIF causes (AEROSONDE)

Table 7-27 Combined CIF and WIF flags for ABIA/SBAS/GBAS (AEROSONDE)

(This page is left black for the purpose of typesetting)

LIST OF ABBREVIATIONS

A

A/C	Aircraft
A3DM	Aircraft 3-Dimensional Model
AAD	Airborne Accuracy Designator
A-B	After Buner
ABAS	Aircraft Based Augmentation System
ABIA	Avionics Based Integrity Augmentation
ACAS	Airborne Collision Avoidance System
ADC	Aircraft Dynamic Constraints
ADM	Aircraft Dynamics Model
ADN	Aircraft Data Network
ADS	Aircraft Dynamics Simulator
ADS-B	Automatic Dependent Surveillance Broadcast
AFCS	Automatic Flight Control System
AGL	Above Ground Level
AL	Alert Limit
AltBOC	Alternative Binary Offset Carrier (modulation)
AMD	Airframe Multipath Designator
AMM	Aircraft Masking Matrix
AMPC	Automatic Masking Profile Computation
ANSP	Air Navigation Service Provider
AOM	Antenna Obscuration Matrix

APP	Approach
APV	Approach with Vertical Guidance (procedure)
ATCo	Air Traffic Controller
ATK	Along Track (error)
ATM	Air Traffic Management
AWG	Aural Warning Generator

B

BADA	Base of Aircraft Data (Eurocontrol)
BOC	Binary Offset Carrier
BPSK	Binary Phase Shift Keying (modulation)

C

C/A	Coarse/Acquisition (code)
C/N_0	Carrier-to-Noise Ratio
CA	Collision Avoidance
CAA	Civil Aviation Authority
CAA	Critical Attitude Angle
CAD	Computer Assisted Design
CAS	Calibrated Airspeed
CAT	Category (landing)
CATIA	Computer aided three-dimensional interactive application
CBA	Critical Bank Angle
CDMA	Code Division Multiple Access

CG	Centre of Gravity
CIF	Caution Integrity Flag
CJM	Carrier-to-Noise Ratio and Jamming-to-Signal Models
CNS	Communication, Navigation and Surveillance
CNS/ATM	Communication, Navigation & Surveillance/Air Traffic Management
CNS+A	CNS/ATM and Avionics
CPA	Critical Pitch Angle
CPDLC	Controller to Pilot Data Link Communications
CPS	Control and Processing Station
CS	Commercial Service
C-SAA	Cooperative Sense-and-Avoid
CSG	Critical Satellite Geometry

D

3DOF	3-Degree of Freedom
6DOF	6-Degree of Freedom
D8FSK	Differential Eight Phase Shift Keying
DAE	Differential Algebraic Equations
DCC	Doppler Critical Condition
DCO	Direct Constrained Optimisation
DF	Automatic Direction Finder
DGNSS	Differential Global Navigation Satellite System
DGPS	Differential Global Positioning System
DH	Decision Height
DLL	Delay Locked Loop

DME	Distance Measurement Equipment
DoD	Department of Defence (US)
DoHS	Department of Homeland Security
DOP	Dilution of Precision
DoT	Department of Transport
DR	Detection Rate
DSM	Doppler Shift Model
DSSS	Direct Sequence Spread Spectrum
DTED	Digital Terrain Elevation Database

E

ECEF	Earth-Centred Earth-Fixed
EGNOS	European Geostationary Navigation Overlay Service
EHE	Estimated Horizontal Error
EKF	Extended Kalman Filter
ELP	Early-Late Phase
EM	Electro-Magnetic
EMC	Electro-Magnetic Compatibility
EMI	Electro-Magnetic Interference
ENU	East-North-Up
EPE	Estimated Position Error
EPE	Estimated Position Error
eRAIM	Enhanced Receiver Autonomous Integrity Monitoring
ETE	Estimated Time Error
EVE	Estimated Vertical Error

F

FAA	Federal Aviation Administration
FAR	False Alarm Rate
FCS	Flight Control System
FDE	Failure Detection and Exclusion
FDIR	Fault Detection, Isolation and Recovery
FDMA	Frequency Division Multiple Access
FLL	Frequency Locked Loop
FLOT	Forward Line of Own Troops
FMS	Flight Management System
FOC	Full Operational Capability
FOM	Figure of Merit
FOR	Field-of-Regard
FOV	Filed-of-View
FPAP	Flight Path Alignment Point
FPO	Flight Path Optimization
FPOM	FPO Module
FTE	Flight Technical Error
FTI	Flight Test Instrumentation
FTP	Fictitious Threshold Point

G

GAD	Ground Accuracy Designator
GAGAN	GPS and GEO Augmented Navigation System

GBAS	Ground Based Augmentation System
GBAS/E	Elliptically Polarised GBAS VHF Data Broadcast
GBAS/H	Horizontally Polarised GBAS VHF Data Broadcast
GCOS	Ground Control Station
GCS	GNSS Constellation Simulator
GDOP	Geometric Dilution of Precision
GEO	Geostationary Orbit (satellite)
GIVE	Grid Ionospheric Vertical Error
GIVEI	Grid Ionospheric Vertical Error Indicator
GLONASS	Globalnaya Navigatsionnaya Sputnikovaya Sistema (Russia)
GLS	GNSS Based Landing System
GMP	Global Masking Profile
GMS	Ground Monitoring Station
GNC	Guidance Navigation and Control
GNSS	Global Navigation Satellite System
GO	Ground Operations
GPA	Glide Path Angle
GPIP	Glide Path Intercept Point
GPOPS	Generalised Pseudospectral Optimal Control (software)
GPS	Global Positioning System
GS	Ground Speed
GSL	GBAS Service Level

H

HA	Horizontal Accuracy

HAL	Horizontal Alert Limit
HDOP	Horizontal Dilution of Precision
HMI	Hazardously Misleading Information
HPL	Horizontal Protection Level

I

IAS	Integrity-Augmented Sense-and-Avoid (for UAS)
ICAO	International Civil Aviation Organisation
ICO	Intermediate Circular Orbit (satellite)
IDs	Interdiction and Strike(TORNADO aircraft version)
IFG	Integrity Flight Generator
IGP	Ionospheric Grid Point
IGSO	Inclined Geosynchronous Orbit
ILS	Instrument Landing System
INS	Inertial Navigation System
IOC	Initial Operational Capability
IR	Integrity Risk
IRNSS	Indian Radionavigation Satellite System
ITD	Ionospheric and Tropospheric Delay
IVD	Ionospheric Vertical Delay

J

J/S	Jamming-to-Signal Ratio
JPO	Joint Program Office (US DoD)

K

KGNSS	Kinematic GNSS

L

L1	1575.42 MHz (frequency)
L2	1227.60 MHz (frequency)
L5	1176.45 MHz (frequency)
LAAS	Local Area Augmentation System
LAD	Local Area DGNSS
LAL	Lateral Alert Level
LIDAR	Light Detection and Ranging
LNAV	Lateral Navigation
LOS	Line of Sight
LP	Localizer Performance
LPL	Lateral Protection Level
LPV	Localizer Performance with Vertical Guidance
LT	Level Turn
LTP	Landing Threshold Point

M

MAM	Multipath Analysis Module
MAP	Manifold Pressure
MAS	Malaysian Augmentation System
MBOC	Multiplexed Binary Offset Carrier

MCC	Mission Control Centre (EGNOS)
MCC	Multipath Critical Condition
MEO	Medium Earth Orbit
MI	Misleading Information
MIA	Manoeuvre Identification Algorithm
MLS	Microwave Landing System
MMW	Millimetric Wave (radar)
MOPS	Minimum Operational Performance Standard
MPCM	Masking Profile Computation Module
MSAS	MTSAT Space Based Augmentation System
MSM	Multipath Signal Model
MT	Message Type
MTSAT	Multifunctional Transport Satellite (Japan)

N

NATO	North Atlantic Treaty Organisation
NC-SAA	Non Cooperative Sense-and-Avoid
NED	North East Down (reference frame)
NEU	North East Down (reference frame)
NextGen	Next Generation Air Transportation System (USA)
NFC	Navigation Data and Flight Parameters at CIF
NLES	Navigation Land Earth Station (EGNOS)
NOTAM	Notice to Airmen
NSE	Navigation System Error

O

OCP	Optimal Control Problem
OS	Open Service
OTF	On-The-Fly (ambiguity resolution)

P

PBN	Performance Based Navigation
PDG	Precise Differential GNSS
PDOP	Position Dilution of Precision
PFA	Probability of False Alarm
PFT	Planned Flight Trajectory
PL	Protection Level
PLL	Phase Locked Loop
PLPL	Predicted Lateral Protection Level
PMO	Pseudospectral Multi-Objective (trajectory optimisation)
PPP	Precise Point Positioning
PPS	Precise Positioning Service
pRAIM	Predictive Receiver Autonomous Integrity Monitoring
PRN	Pseudorandom Noise
PRS	Public Regulated Service
PVPL	Predicted Vertical Protection Level
PVT	Position, Velocity and Time
RNP	Required Navigation Performance

Q

QZSS	Quasi-Zenith Satellite System

R

RAD	Radial (error)
RAIM	Receiver Autonomous Integrity Monitoring
RAM	Random Access Memory
RF	Radio Frequency
RIMS	Ranging and Integrity Monitoring Station
RNP	Required Navigation Performance
RPM	Revolutions per Minute
RR	Reference Receiver
RS	Reference Station
RTCA	Radio Technical Commission for Aeronautics
RTCM	Radio Technical Committee for Maritime Services
RTE	Residual Tropospheric Error
RTK	Real-Time Kinematic
RTO	Real Time Operations
Rx	Receiver

S

SAA	Sense-and-Avoid (for UAS)
SAM	SNR Analysis Module
SAR	Search and Rescue

SARPS	Standards and Recommended Practices (ICAO)
SBAS	Satellite Based Augmentation System
SC	Straight Climb
SCAT-I	Special Category I (precision approach)
SD	Straight Descent
SESAR	Single European Sky ATM Research
SIS	Signal-in-Space
SL	Straight and Level
SM	Separation Maintenance
SNAS	Satellite Navigation Augmentation System
SNR	Signal-to-Noise Ratio
SoL	Safety of Life
SPS	Standard Positioning Service
STANAG	Standardised Agreement (NATO)
STL	Stereo Lithography (file format)
SV	Satellite Vehicle
SLSF	Straight, Level and Steady Flight
SLUF	Straight, Level and Unsteady Flight

T

T-ABIA	TSPI ABIA
TAC	Telemetry Antenna Coverage
TACAN	Tactical Air Navigation
TC	Turning Climb
TCAS	Traffic Collision Avoidance System

TD	Turning Descent
TDA	Tracking, Deciding and Avoiding
TDM	Turning Descent Manoeuvre
TDOP	Time Dilution of Precision
TEC	Total Electron Content
TID	Total Ionospheric Delay
TMA	Terminal Manoeuvring Area
TOD	Terrain and Objects Data
TRD	Turn Radius Diagram
TSE	Total System Error
TSPI	Time-and-Space Position Information
TT&C	Telemetry, Tracking and Command
TTA	Time-to-Alert
TTC	Time-to-Caution
TTFF	Time-to-First-Fix
TTR	Time-to-Recovery
TTSF	Time-to-Subsequent-Fix
TTW	Time-to-Warning
TVD	Thrust-Velocity Diagram

U

UAS	Unmanned Aircraft Systems
UAV	Unmanned Aerial Vehicles
UDRE	User Differential Range Error
UDREI	User Differential Range Error Indicator

UEE	User Equipment Error
UERE	User-Equivalent Range Error
UHF	Ultra High Frequency
UIRE	User Ionospheric Range Error
UIVE	User Ionospheric Vertical Error
UPDG	Ultra Precise Differential GNSS
UR	User Receiver
URA	User Range Accuracy
URE	User Range Error

V

VA	Vertical Accuracy
VAL	Vertical Alert Limit
VDOP	Vertical Dilution of Precision
VHF	Very High Frequency
VNAV	Vertical Navigation
VOR	VHF Omnidirectional Radio Range
VPDG0	Very Precise Differential GNSS
VPL	Vertical Protection Level

W

WAAS	Wide Area Augmentation System
WAD	Wide Area DGNSS
WGS-84	World Geodetic System 1984

WIF	Warning Integrity Flag
WMS	Wide Area Master Station
WOW	Weight on Wheels
WRS	Wide Area Reference Station

X

XTK	Across Track Eerror

(This page is left black for the purpose of typesetting)

1

INTRODUCTION

1.1 RESEARCH CONTEXT AND MOTIVATION

In an era of significant civil/military air traffic expansion characterised by a widespread introduction of Unmanned Aerial Systems (UAS) and by a rising congestion of the radiofrequency spectrum, GNSS and other aeronautical telecommunication systems are being exposed to a variety of integrity threats including signal interferences, adverse propagation effects and challenging platform-satellite relative dynamics. GNSS systems typically use signals 20 dB below the ambient noise floor and, despite several research efforts devoted to interference detection and mitigation strategies at receiver and platform level (mostly for military applications), no effective solution has been implemented so far in the civil aviation context. Thus, there is a need to characterize GNSS signal degradations and assess the effects of interfering sources on the performance of avionics GNSS receivers and Differential GNSS (DGNSS) systems used for an increasing number of mission-essential and safety-critical aviation tasks (e.g., experimental flight testing, flight inspection/certification of ground-based radio navigation aids, wide area navigation and precision approach). GNSS signal deteriorations typically occur due to antenna obscuration caused by natural and man-made obstructions present in the environment (e.g., elevated terrain and tall buildings when flying at low altitude) or by the aircraft itself during manoeuvring (e.g., aircraft wings and empennage masking the on-board GNSS antenna), ionospheric scintillation, Doppler shift, multipath, jamming and spurious satellite transmissions. Anyone of these phenomena can result in partial to

total loss of tracking and possible tracking errors, depending on the severity of the effect and the receiver characteristics. Tracking errors, especially if undetected by the receiver software, can result in large position errors. Partial loss of tracking results in geometry degradation, which in turn affects position accuracy. Consequently, GNSS alone does not always provide adequate performance in mission-essential and safety-critical aviation applications where high levels of integrity are required (CAA, 2003). For an avionics navigation system, integrity directly relates to the level of confidence that can be placed in the information provided by the on-board system. It includes the ability of the navigation system to provide timely and valid warnings to users when the system must not be used for the intended operation or phase of flight. Specifically, an avionics navigation system is required to deliver an alert of any malfunction (as a result of a set alert threshold being exceeded) to users within a given period of time. Time-to-alert (TTA) is defined as the maximum time allowed from the moment a fault resulting in an unsafe condition is detected to the moment that the user is made aware of it (Ochieng et al., 2003). Integrity risk is defined as the probability that the navigation positioning error exceeds the alert limit and that the event is not detected. Loss of integrity can happen in one of two ways. Either an unsafe condition is not detected or it is detected, but the alert is not received by the user within the required TTA. The alert limit defines the largest position error, which results in a safe operation. This is specified such that the error can degrade to a level larger than the 95th percentile accuracy requirement but still within a safe limit. GNSS augmentation can take many forms but all share the same fundamental principle of providing supplementary information whose objective is improving the performance and/or trustworthiness of the system. GNSS augmentation benefits in the aviation domain can be summarized as follows:

- Increased runway access, more direct en-route flight paths and new precision approach services;
- Reduced and simplified avionics equipment;
- Potential elimination of some ground-based navigation aids (VOR, ILS, etc.) with cost saving to Air Navigation Service Providers (ANSPs).

Space Based Augmentation Systems (SBAS) are designed to improve GNSS system integrity and accuracy for aircraft navigation and landing. SBAS satellites broadcast correction messages back to Earth, where suitably enabled receivers use the information to improve accuracy and integrity. The USA, Europe and Asia are developing their own SBAS systems. In Europe, the European Geostationary Navigation Overlay Service (EGNOS) system exists and is now operational. In the USA there is the Wide Area Augmentation System (WAAS), in Japan the Multi-functional Satellite Augmentation System (MSAS) and India is developing the GNSS Aided Geo Augmented Navigation (GAGAN) system. An alternative approach to GNSS augmentation is to transmit integrity and the correction messages from ground-based augmentation systems. An example is the American Local Area Augmentation Systems (LAAS), which allows a suitably equipped receiver to derive enhanced accuracy and integrity information in a local area. The combination of WAAS and LAAS is targeted to provide the required navigation performance in all phases of aircraft navigation, including en-route, terminal, approach/landing and surface operations (Fig. 1-1).



Figure 1-1. WAAS and LAAS services (Eldredge, 2009).

In addition to the existing Space and Ground Based Augmentation Systems (SBAS and GBAS), GNSS augmentation may take the form of additional information being provided by other on-board avionics systems. As these systems normally operate via separate principles than the GNSS, they are not subject to the same sources of error or interference. A system such as this is referred to as an Aircraft Based Augmentation System or ABAS (ICAO, 2005). ABAS is different from RAIM (Receiver Autonomous Integrity Monitoring), in which the aircraft characteristics (flight dynamics, body shape, antenna location, EMC/EMI, etc.) are typically not considered and various kinds of consistency check are accomplished using the GNSS signals to detect and exclude faulty/unreliable satellites.

The additional sensors used in ABAS may include Inertial Navigation Systems (INS), VOR-DME/TACAN, Radar, Vision Based Sensors, etc. Unlike SBAS and GBAS technology, published research on ABAS is limited and mainly concentrates on additional information being blended into the position calculation to increase accuracy and/or continuity of the integrated navigation solutions. Additionally, no significant attempts have been made of developing ABAS architectures capable of generating integrity signals suitable for safety-critical GNSS applications (e.g., aircraft precision approach and landing) and no certified Avionics Based Integrity Augmentation (ABIA) products are available at present.

Although current and likely future SBAS/GBAS augmentation systems can provide significant improvement of GNSS navigation performance, a properly designed and flight-certified ABAS could play a key role in GNSS integrity augmentation for mission-essential and safety-critical applications such as aircraft precision approach, automatic landing and UAS Sense-and-Avoid (SAA). Furthermore, using suitable data link and data processing technologies on the ground, a certified ABAS capability could be a core element of a future GNSS Space-Ground-Avionics Augmentation Network (SGAAN).

1.2 RESEARCH AIM AND OBJECTIVES

The aim of this research is to develop a novel avionics system for mission-essential and safety-critical navigation and guidance applications, specifically targeting GNSS integrity monitoring and augmentation requirements for manned and unmanned aircraft operations. In line with this overall aim, the following objectives were set and achieved during this research:

- Perform a detailed review on GNSS aviation applications with a focus on integrity augmentation systems.
- Investigate GNSS and DGNSS performance in TSPI applications.
- Develop a TSPI ABIA system suitable for flight test, flight inspection and training applications.
- Define the functional architecture of an ABIA system suitable for manned and unmanned aircraft applications.
- Develop suitable models and algorithms to generate ABIA alerts, including caution (predictive) and warning (reactive) integrity flags.
- Perform simulation case studies to verify the technical suitability of the models and algorithms developed for the ABIA caution and warning integrity flags.
- Develop suitable mathematical models for flight path guidance, allowing avoidance of (or fast recovery from) mission/safety-critical conditions.
- Start investigating the potential of ABIA techniques to supplement SBAS/GBAS technology for en-route, terminal and approach operations.
- Start investigating the potential of ABIA techniques to enhance the performance of cooperative and non-cooperative UAS Sense-and-Avoid (SSA) in the Communication, Navigation and Surveillance/Air Traffic Management (CNS/ATM) and Avionics (CNS+A) context.

1.3 RESEARCH METHODOLOGY

A combination of experimental and analytical methods was implemented in the ABIA research project. This included aircraft ground/flight test activities with GNSS systems, as well as mathematical model development (i.e., purely analytical, empirical and semi-empirical models) and various simulation activities performed to properly plan experiments and to support the development of the ABIA functionalities, including a verification of the ABIA system performance (and comparison with GBAS/SBAS) in a limited but representative portion of the considered manned/unmanned aircraft operational flight envelopes.

Flight test activities were performed with GNSS-based TSPI systems to identify and study the main causes of unacceptable accuracy degradations or data losses in mission-essential and safety-critical tasks. These included:

- The aircraft reaching the Critical Attitude Angles (CAA) associated with a particular antenna installation and aircraft-satellites relative geometry;
- Bad satellite geometries and low satellite Carrier-to-Noise (C/N_0) values;
- Aircraft DGNSS Data Link antennae coverage limitations;
- Interference caused by the DGNSS Data Link or other RF signals;
- Multipath caused by GNSS signals reflected by the earth or the aircraft body surfaces.

The last two problems could be mitigated by existing technology solutions (i.e., choosing a VHF/UHF Data Link, filtering the radio frequency signals reaching the GNSS antenna, identifying suitable locations for the GNSS antenna and providing adequate shielded of the antenna itself, either by physical devices or via dedicated software masks, etc.). However, there was little to nothing one could do in order to prevent critical GNSS data losses during realistic test/training manoeuvres and particular approach procedures (e.g., curved and segmented approaches) performed with high performance military aircraft. Furthermore, although in some cases a careful mission planning could significantly reduce the number of DGNSS outages, the adoption of specific aircraft piloting strategies (using the information currently

available in the aircraft cockpits) cannot effectively avoid the occurrence of these events.

A case study was therefore undertaken in order to identify an integrity augmentation method suitable for DGNSS-TSPI and other aircraft GNSS applications. As a first step, a dedicated analysis (based on mathematical algorithms and experimental data) of the aircraft flight dynamics/performance was required in order to determine the actual flight envelope limitations associated with the use of GNSS during test/training missions. Such a method was intended for adoption in a dedicated ground-based simulation tool, as well as for a successive incorporation into the aircraft avionics systems.

Extensive simulation activities were performed to corroborate the validity of the mathematical algorithms for ABIA and a GNSS integrity augmentation system called TSPI ABIA (T-ABIA was developed for integration in a TORNADO test-bed aircraft to generate pilot alerts (within the specified maximum TTA) when the critical conditions for GNSS signal losses were likely to occur.

The next step was to extend the results obtained from flight test to the development of a more advanced GNSS ABIA system suitable for manned and unmanned aircraft applications. This advanced ABIA system was designed to provide steering information to the pilot (as the T-ABIA system) and electronic commands to the aircraft/UAV Flight Control System (FCS), allowing for a continuous aircraft-based integrity augmentation, avoidance of mission/safety-critical flight conditions and fast recovery of the required navigation performance in case of GNSS data losses. The performance of the ABIA system key modules (i.e., Integrity Flag Generator and Flight Pat Guidance) were tested by performing a number of representative simulation case studies. In addition to detailed mathematical models for Doppler shift, antenna masking, multipath, C/N_0, Jamming-to-Signal (J/S) and other factors, appropriate trajectory optimisation models, aircraft dynamics models and CAD/CATIA models were used to investigate the ABIA performance on different civil/military aircraft and UAV platforms (i.e., A-320, TORNADO-IDS, B-747 and AEROSONDE).

Successively, the synergies of ABIA with GBAS and SBAS systems were investigated by comparing the performances attainable from the three systems on the same simulated test platform listed above and in representative mission tasks, with a special focus on en-route and Terminal Manoeuvring Area (TMA) operations including GNSS assisted precision approach down to CAT-III.

Only the Required Navigation Performance (RNP) applicable to civil aviation applications are specified and addressed in the thesis and data from state-of-the-art avionics C/A code GPS receivers are used in the simulation case studies. No simulations are included for P(Y) code GPS receivers. Intentionally, military RNP is omitted without loss in generality.

Finally, additional modelling and simulation activities were performed to investigate the synergies of ABIA with state-of-the-art solutions for cooperative and non-cooperative UAS SAA and the concept of an integrity-augmented SAA system was proposed to support UAS trusted autonomy in the future CNS+A context.

2

GNSS AVIATION APPLICATIONS

2.1 INTRODUCTION

Various GNSS systems are currently in service or under development. The US Navigation Signal Time and Range (NAVSTAR) Global Positioning System (GPS) and the Russian GLONASS ("GLObalnaya NAvigazionnaya Sputnikovaya Sistema") have achieved their Full Operational Capability (FOC) back in the 90's. Other GNSS systems that are currently at the advanced development or deployment stages, include the European GALILEO and the People's Republic of China "Beidou" Navigation Satellite System (BDS). Although these systems operate at different frequencies, employ various signal processing techniques and adopt different multiple access schemes, most of them employ or are planned to progressively transition to Code Division Multiple Access (CDMA) for operations at the L-band frequency of 1575.42 MHz (L1). This signal, originally introduced by GPS for Standard Positioning Service (SPS) users, will guarantee interoperability between the various GNSS constellations with substantial benefits to the existing vast community of GPS users, including aviation[1]. Signal-in-Space (SIS) interoperability is also being actively pursued on other frequencies, with a focus on those that are currently allocated to Safety-of-Life (SOL) services. From a user's perspective, the advantage to having access to multiple GNSS systems is increased

[1] The acronyms GNSS and GPS are not used interchangeably in this thesis. GNSS is the standard acronym for satellite navigation systems that provide global-coverable geospatial positioning. Where appropriate, GNSS is used to describe GPS and other systems referring to SPS interoperability, which is currently either achieved or planned.

accuracy, continuity, availability and integrity. Having access to multiple satellite constellations is very beneficial in aviation applications, where the aircraft-satellite relative dynamics can lead to signal tracking issues and/or line-of-sight obstructions. Even when interoperability at SIS level cannot be guaranteed, the introduction of multi-constellation receivers can bring significant improvements in GNSS performance. The literature on this subject is vast and it is beyond the scope of this thesis to address in details the various signal and data processing techniques implemented in GNSS systems. Instead, an introduction to the GNSS principles relevant to aviation users is presented in this chapter. Later sections address in more details the accuracy and integrity augmentation strategies adopted in the aviation CNS+A context.

2.2 GNSS SEGMENTS

Although different GNSS systems employ different hardware and software features, all systems are composed by a space segment, a control segment and a user segment (Fig. 2-1).

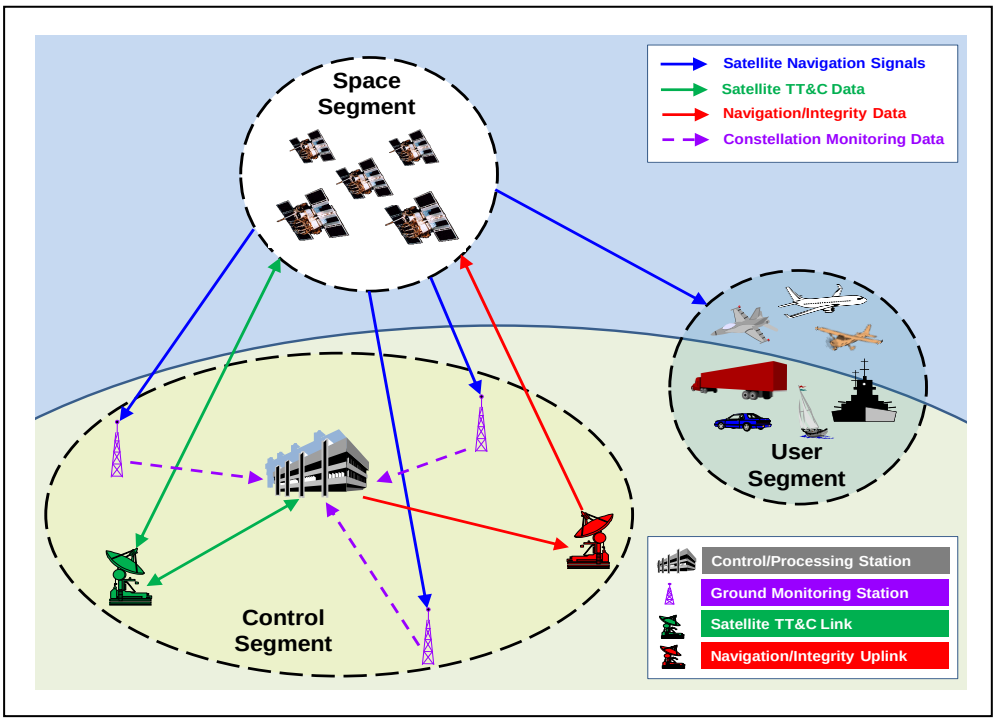


Figure 2-1. GNSS segments.

The space segment includes the satellites required for global coverage. These satellites are predominantly in Intermediate Circular Orbit (ICO), at nominal altitudes of 19,100 km (GLONASS), 20,184 km (GPS) and 23,222 km (GALILEO) km from the Earth's surface. BDS also employs satellites in Geostationary Orbit (GEO) and Inclined Geosynchronous Orbit (IGSO). The user segment includes the large variety of GNSS receivers developed for air, ground and marine navigation and positioning applications. The control segment includes one or more Control and Processing Stations (CPSs) connected to a number of Ground Monitoring Stations (GMSs) and antennae located around the globe for Telemetry, Tracking and Command (TT&C) signals down/uplink and navigation/integrity signals uplink to the satellites.

The GMS antennae passively track all GNSS satellites in view collecting ranging signals from each satellite. This information is passed on to the CPS where the satellite ephemeris and clock parameters are estimated and predicted. Additionally, satellite integrity data are analysed and appropriate integrity flags are generated for faulty/unreliable satellites. The ephemeris/clock and integrity data are then up-linked to the satellite for retransmission in the navigation message. The satellite clock drift is corrected so that all transmitted data are synchronised with GNSS time. The fundamental equation is the following:

$$t_{GPS} = t_s - \Delta t_s \tag{2.1}$$

where :

t_{GPS} = GNSS time;

t_s = satellite time;

Δt_s = difference between satellite and GNSS time.

The corrections are applied to the last term of equation (2.1), typically using polynomial coefficients and a relativistic correction term. The correction equation can be written as:

$$\Delta t_s = a_0 + a_1\left(t_{GPS} - t_{0c}\right) + a_2\left(t_{GPS} - t_{0c}\right)^2 + \Delta t_r \tag{2.2}$$

where :

a_0, a_1, a_2 = polynomial coefficients for phase, frequency and age offset;

Δt_r = relativistic correction term;

t_{0c} = time of transmission of the corrections.

Typically, the ephemeris corrections are obtained through the estimation of the Cartesian co-ordinates of the satellites along the orbits by integrating there equations of motion. For integrity purposes, suitable Fault Detection, Isolation and Recovery (FDIR) techniques are employed. In particular, the health status of the satellite subsystems is continuously monitored (satellite payload, bus, solar arrays, battery power and the level of propellant used for manoeuvres) and any anomaly must be promptly detected and resolved. When needed, spare satellites can be activated. The Signal-in-Space (SIS) is also constantly monitored to guarantee the required performance standards. Despite the significant technological enhancements recently introduced in control segment integrity features, current GNSS systems have limited FDIR capability. In most cases, several minutes or even hours are required to provide the required integrity information (i.e., use/do not use signals) to GNSS users. Obviously, this is not acceptable for mission-essential and safety-critical aviation applications.

2.3 GNSS OBSERVABLES

There are basically three types of GNSS observables that can be used in aviation GNSS receivers: pseudorange, carrier phase, and Doppler observable. Pseudoranges are commonly used in real-time aircraft navigation and can provide an accuracy ranging from about 20 m (stand-alone L1 code positioning) to about 2 m in Differential GNSS (DGNSS) positioning. The carrier phases are traditionally used in high precision trajectory determination applications (e.g., TSPI systems for flight test and flight inspection) and can achieve sub-centimetre accuracy. However, it is also quite common to use combinations of pseudoranges and carrier phase measurements both in real-time and post mission applications. Moreover, it has become common practice to take advantage of various combinations of the original phase observation, such as double differences and triple differences.

2.3.1 Pseudorange Observable

The concept of pseudoranging is based on measuring difference between the time of transmission of the code from the satellite and the epoch of reception of the same signal at the receiver antenna. This is achieved by correlating identical pseudorandom noise (PRN) codes generated by the satellite's clock, with those generated internally by the receiver's own clock. If this time difference is multiplied by the speed of propagation of the radio wave, a range value is obtained which is the distance between the satellite and the receiver's antenna referring to the epoch of observation. Both receiver and satellite clock errors affect the pseudoranges. Therefore, they differ from the actual geometric distance corresponding to the epochs of emission and reception. The general pseudorange equation is:

$$P_k^p(t_k) = (t_A - t^p) \cdot c \tag{2.3}$$

where P_k^p represents the actual measurement, t_k denotes the nominal time of the receiver clock ***k*** at reception, t^p denotes the nominal time of the satellite clock ***p*** at emission and ***c*** denotes the speed of light. Equation (2.3) would correspond to the actual distance between the satellite and receiver's antenna, if there were no clock biases, the signal travelled through vacuum and there was no multipath effect. The clock drifts can be represented by the following expressions:

$$t_{r,k} = t_k + dt_k \tag{2.4}$$

$$t_k^p = t^p + dt^p \tag{2.5}$$

where the symbol ***r*** denotes the true time and the terms dt_k and dt^p are the receiver and satellite clock errors respectively. Taking these errors and biases into account, the complete expression for the pseudorange becomes:

$$\begin{aligned} P_k^p(t_k) &= (t_{r,k} - t_r^p)c - (dt_k - dt^p)c + I_{k,p}^p(t_k) + T_k^p(t_k) \\ &\quad + d_{k,P}(t_k) + d_{k,P}^p(t_k) + d_P^p(t_k) + \varepsilon_p \\ &= \rho_k^p(t_{r,k}) - (dt_k - dt^p)c + I_{k,p}^p(t_k) + T_k^p(t_k) \\ &\quad + d_{k,P}(t_k) + d_{k,P}^p(t_k) + d_P^p(t_k) + \varepsilon_P \end{aligned} \tag{2.6}$$

where $I_{k,P}^{p}(t_k)$ and $T_k^p(t_k)$ are the ionospheric and tropospheric delays, depending on varying conditions along the path of the signal. The symbols $d_{k,P}(t_k)$ and $d_P^p(t_k)$ denote the receiver and satellite hardware code delays respectively. The symbol $d_{k,P}^{p}(t_k)$ denotes the multipath of the codes, which depends on the geometry of the antenna and satellite with respect to surrounding reflective surfaces. The term ε_p denotes the random measurement noise. The term $\rho_k^p(t_{r,k})$ is the actual geometric distance between the receiver's antenna and the satellite at a specific epoch and therefore:

$$\rho_k^p(t_k) = \sqrt{(u^p - u_k)^2 + (v^p - v_k)^2 + (w^p - w_k)^2} \tag{2.7}$$

The terms (u_k, v_k, w_k) are the Cartesian co-ordinates of the receiver and (u^p, v^p, w^p) denote the position of the satellite at the epoch of transmission. With reference to Fig. 2-2, assuming a constant receiver clock error dt_k for measurements to any satellite and omitting all other error terms in Eq. (2.6), the following system of equations is formed:

$$\begin{cases} P_k^1(t) = \sqrt{(u^1 - u_k)^2 + (v^1 - v_k)^2 + (w^1 - w_k)^2} - cdt_k \\ P_k^2(t) = \sqrt{(u^2 - u_k)^2 + (v^2 - v_k)^2 + (w^2 - w_k)^2} - cdt_k \\ P_k^3(t) = \sqrt{(u^3 - u_k)^2 + (v^3 - v_k)^2 + (w^3 - w_k)^2} - cdt_k \\ P_k^4(t) = \sqrt{(u^4 - u_k)^2 + (v^4 - v_k)^2 + (w^4 - w_k)^2} - cdt_k \end{cases} \tag{2.8}$$

Therefore, the co-ordinates of the user receiver (and GNSS time) can be derived from the simultaneous observation of four (or more) satellites. If more than four satellites are visible, a least-square solution can be determined. The GNSS receiver calculates its position in an Earth-Centred Earth Fixed (ECEF) Cartesian co-ordinate system (typically using WGS84). These co-ordinates may be expressed to some other system such as latitude, longitude and altitude if desired. Solution of the

system (2.8) requires the measurement of the pseudoranges to four different satellites. The GNSS receiver's computer may be programmed to solve directly the navigation equations in the form given above. However, the computation time required in order to solve them may be too long for many applications.

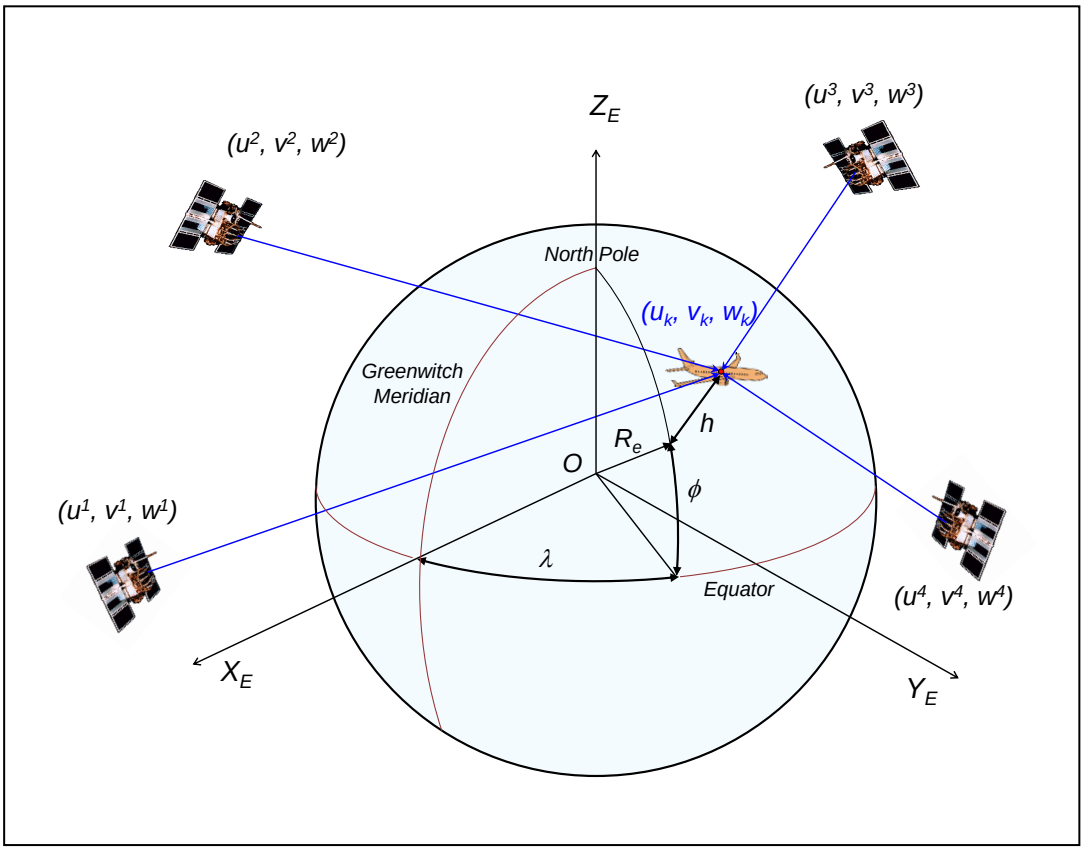


Figure 2-2. Navigation solution in the ECEF co-ordinate system (at time zero, the XE axis passes through the North Pole, and the YE. axis completes the right-handed orthogonal system.

As an alternate way, these equations may be approximated by a set of four linear equations that the GPS receiver can solve using a much faster and simpler algorithm. The system of equations (2.6) can be rewritten in the form:

$$P_k^i = \sqrt{\left(u^i - u_k\right)^2 + \left(v^i - v_k\right)^2 + \left(w^i - w_k\right)^2} + T \qquad (\text{i} = 1, 2, 3, 4) \qquad (2.9)$$

where u^i, v^i and w^i represent the co-ordinates of the i^{th} satellite, $T = cdt_k$ and the units have been chosen so that the speed of light is unity.

Linearization of equation (2.9) can proceed as described in Thomis (1984) and Siouris (1993). The resulting set of linearized equations relates the pseudorange measurements to the desired user navigation information as well as the user's clock bias. This can be written as:

$$\left(\frac{u_n - u^i}{P_{ni} - T_n}\right)\Delta u_k + \left(\frac{v_n - v^i}{P_{nii} - T_n}\right)\Delta v_k + \left(\frac{w_n - w^i}{P_{ni} - T_n}\right)\Delta w_k + \Delta T = \Delta P_i \qquad \text{(i = 1, 2, 3, 4)} \quad (2.10)$$

where :

u_n, v_n, w_n, T_n = nominal (a priori best-estimate) values of u_k, v_k, w_k and T;

$\Delta u_k, \Delta v_k, \Delta w_k, \Delta T$ = corrections to the nominal values;

P_{ni} = nominal pseudorange measurement to the i^{th} satellite;

ΔP_i = difference between actual and nominal range measurements.

The quantities on the right-hand side are simply the differences between the actual measured pseudoranges and the predicted measurements, which are supplied by the user's computer, based on knowledge of the satellite position and current estimate of the user's position and clock bias. Therefore, the quantities to be computed ($\Delta u_k, \Delta v_k, \Delta w_k, \Delta T$) are the corrections that the user will make to the current estimate of position and clock bias. The coefficients of the quantities on the left-hand side represent the direction cosines of the LOS vector from the user to the satellite as projected along the Cartesian co-ordinate system.

2.3.2 Carrier Phase Observable

The carrier phase observable is the difference between the received satellite carrier phase and the phase of the carrier generated by the receiver oscillator. The error sources that affect pseudoranges also affect carrier phases (Leick, 2003). However, the mathematical formulation of any specific error component is different from the pseudorange case (i.e., phase measurement errors instead of range measurement errors).

Since the antenna cannot sense the number of whole carrier waves between the satellite and the receiver (called the integer ambiguity), an extra parameter is inserted in the carrier phase equation:

$$\Phi_k^p = \Phi_k(t) - \Phi^p(t) + N_k^p + I_{k,\Phi}^p(t) - \frac{f}{c}T_k^p(t) + d_{k,\Phi}(t) + d_{k,\Phi}^p(t) + d_\Phi^p(t) + \varepsilon_\Phi \quad (2.11)$$

The symbols $\Phi_k(t)$ and $\Phi^p(t)$ denote the phase of the receiver generated signal and the phase of the satellite signal respectively, at the epoch t of satellite signal reception. The symbol N_k^p is the integer ambiguity. The terms $I_{k,\Phi}^p(t)$ and $T_k^p(t)$ are the ionospheric and tropospheric delays. The ionospheric delay factor has a negative value because the carrier phase progresses when travelling through the ionosphere. Furthermore, the tropospheric factor is converted in cycles multiplying by f/c, where f is the nominal frequency and c is the speed of light in vacuum. The symbols $d_{k,\Phi}(t)$ and $d_k^p(t)$ refer to the receiver and satellite hardware delays respectively. The symbol $d_{k,\Phi}^p$ denotes the multipath effect and ε_Φ denotes the carrier phase measurement noise. Assuming synchronisation of the satellite and receiver clocks, omitting other error sources (receiver phase tracking circuits, local oscillator, multipath and measurement noise), and taking into account both the time of transmission and reception of the signal, the equation for the phase observation between a satellite *i* and a receiver *A*, can be written as (Ashkenazi, 1995):

$$\Phi_A^i(\tau) = \Phi^i(t) - \Phi_A(\tau) \quad (2.12)$$

where:

$\Phi_A^i(\tau)$ = phase reading (phase at receiver *A* of the signal from satellite *i* at time τ);

$\Phi^i(t)$ = received signal (phase of the signal as it left the satellite at time t);

$\Phi_A(\tau)$ = generated signal phase (phase of the receiver's signal at time τ).

If $\rho_A^i(t)$ is the range between receiver and satellite, we have:

$$t = \tau - \frac{\rho_A^i(t)}{c} \tag{2.13}$$

Therefore:

$$\Phi^j(t) = \Phi^j\left(\tau - \frac{\rho_A^i(t)}{c}\right) = \Phi^i(\tau) - \underbrace{\frac{\partial\Phi^i(t)}{dt}}_{f} \times \frac{\rho_A^i(t)}{c} + \ldots = \Phi^j(\tau) - f\frac{\rho_A^i(t)}{c} + \ldots \tag{2.14}$$

and finally:

$$\Phi_A^j(\tau) = \Phi^j(\tau) - \frac{f}{c}\rho_A^i(t) - \Phi_A(\tau) + N_A^i \tag{2.15}$$

where:

$\Phi_A^j(\tau)$ = phase reading (degree or cycles);

$\Phi^j(\tau)$ = emitted signal;

$\frac{f}{c}\rho_A^i(t)$ = total number of wavelengths;

$\Phi_A(\tau)$ = generated signal;

N_A^i = integer ambiguity.

The carrier phase measurement technique typically uses the difference between the carrier phases measured at a reference receiver and a user receiver. This is therefore an inherently differential technique.

2.3.3 Doppler Observable

The equation that associates the transmitted frequency from the satellite with the received frequency is:

$$f_k = \frac{f^p}{1 + \frac{r'}{c}} \tag{2.16}$$

where f_k is the received frequency, f^p denotes the emitted frequency from the satellite, *r'* denotes the radial velocity in the satellite-receiver direction and *c* denotes the speed of light in vacuum. The Doppler frequency shift is given by the difference $f^p - f_k$. The radial velocity *r'* is the actual rate of change in the satellite-receiver distance and it is given by:

$$r' = -\frac{f_k - f^p}{f_k} \cdot c \tag{2.17}$$

The integrated Doppler count between two epochs t_1 and t_2 is given by:

$$N_{(t_1,t_2)} = \int_{t_1}^{t_2} \left(f^p - f_k \right) dt \tag{2.18}$$

More information about the Doppler observable and on some of its practical uses can be found in the literature (Seeber, 2003), (Gleason et al., 2009)..

2.4 GPS ERROR SOURCES

The main errors affecting pseudorange and carrier phase measurements can be classified into the four broad categories listed below:

- ***Receiver Dependent Errors:*** Clock Error; Noise and Resolution.
- ***Ephemeris Prediction Errors.***
- ***Satellite Dependent Errors:*** Clock Offset; Group Delays.
- ***Propagation Errors:*** Ionospheric Delay; Tropospheric Delay; Multipath.
- ***User Dynamics Errors.***

2.4.1 Receiver Dependent Errors

Most receivers have quartz clocks to measure the GNSS time, which are not as accurate as the atomic clocks of the satellites. Therefore, there is an offset between the receiver and satellite clocks called Receiver Clock Error. This error

affects both the measurement of the signal flight time and the calculation of the satellite's position at time of transmission.

Measurement Noise is a random error, which depends entirely on the electronic components of the receiver. Receivers for very precise measurements are designed to minimise this error component. Both noise and resolution errors can be reduced by using appropriate filtering techniques. Theoretically, receiver noise can be removed by averaging the measurements, but only over fairly long periods of observation time.

2.4.2 Ephemeris Prediction Errors

The ephemeris data are required for both pseudorange and phase computations. These errors are due to incorrect estimation of the satellites ephemeris at the CPS. A model for evaluating these errors (Fig. 2-3) is obtained by considering the three components of the vector representing the difference between estimated and true distance: Along Track (ATK), Across Track (XTK) and Radial (RAD).

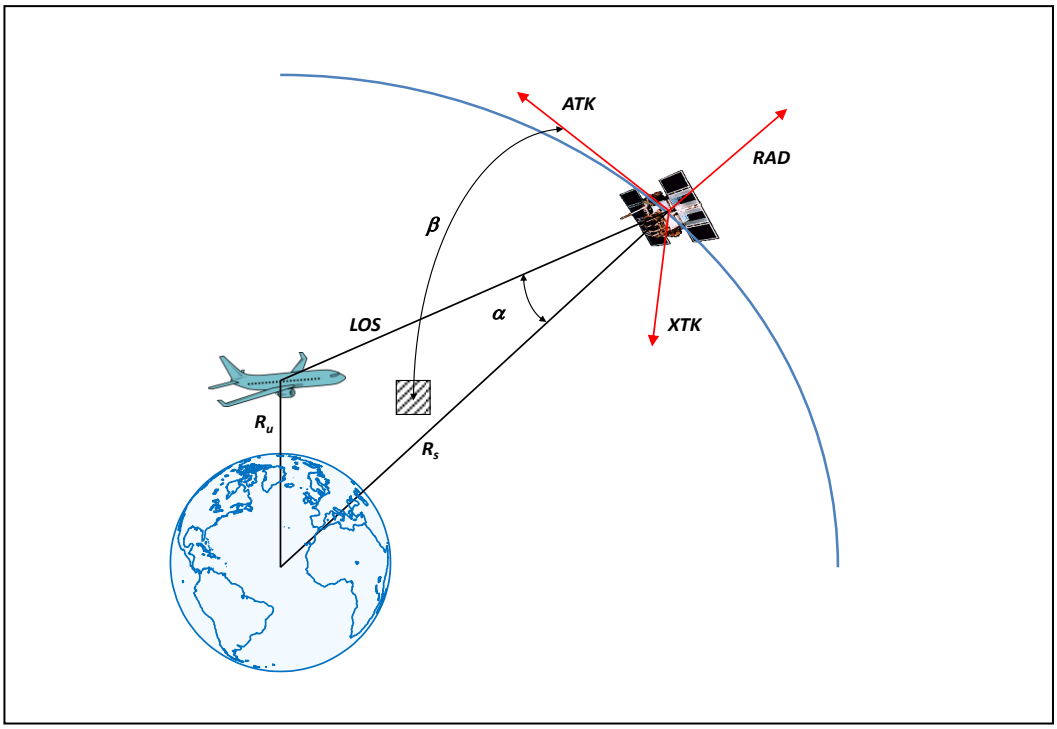


Figure 2-3. Error Components in Ephemeris Estimation.

The maximum error is experienced when the satellite has an elevation of 0° on the receiver horizon and the line-of-sight (LOS) user-satellite lies on the geometric plane containing ATK. In general, the error can be expressed as a function of the three components, in the form:

$$ERR = RAD\cos\alpha + ATK\sin\alpha\cos\beta + XTK\sin\alpha\sin\beta \qquad (2.19)$$

where:

α = angle between the LOS user-satellite and the satellite vertical

β = angle between the ATK direction and the plane containing the LOS and the satellite vertical.

The US DoD Precise Ephemeris is calculated from actual observation to the satellites from a ground network of 20 stations distributed around the world. It is produced a few days after the observation period and is available only to authorised users. Other non-DoD organisations produce precise ephemeris, both globally and locally, by suitable modelling of all forces and moments acting on the satellites. Orbit relaxation techniques can be developed within GNSS software. These techniques solve for orbital errors in the broadcast ephemeris and produce improved relative positioning (Ashkenazi et al., 1990), (Moore, 1996-b), (Ashkenazi et al., 1990), (Monico et al., 1997).

2.4.3 Satellite Dependent Errors

As discussed above, corrections to the drift of the satellite atomic clocks are computed by the CPS and then broadcasted to the users in the navigation message. The effect of Satellite Clock Offset is negligible in most positioning applications (using the polynomial coefficients corrections computed at the CPS it is possible to reduce this error down to 1 part per 10^{12}). The residual error is due to the fact that corrections from the CPS are periodic and not continuous. Group Delays are the delays typical of the satellite electronic circuits. They are estimated on the ground before the satellites are launched and corrections are included in the navigation message.

2.4.4 Propagation Errors

As discussed, propagation errors include both inospheric and tropospheric delays. As the satellite signal passes through the ionosphere, it is delayed for two reasons (Dodson, 1995). Firstly, because it travels through a non-vacuum material (propagation delay); thus the Pseudo Random Noise (PRN) codes are delayed, while the carrier phase is advanced when passing through the ionosphere layers. Secondly, because it bends due to refraction; for many applications, the error caused by the bending effect can be considered negligible if the signals are transmitted by satellites with an elevation of 15° or more.

The ionospheric delay is dependent primarily on the number of electrons that the signal encounters along its propagation path. It is therefore dependent both on the ionosphere characteristics (variable during the day and with seasons), and the path angle (elevation angle of the satellite). It is possible to approximately evaluate the ionospheric delay using the following equation (Dodson, 1995):

$$\Delta\tau = 40.31\frac{TEC}{cf^2} \tag{2.20}$$

where TEC is the total electron content integrated along the LOS to the satellite in units of electrons/m^2 and f is the frequency in Hz and c is the speed of light. TEC varies with time and depends on the location of the ionosphere 'pierced' by the LOS to the satellite. At the L1 frequency (1575.42 MHz), Eq. (2.20) can be written for a satellite that is not at the zenith (Giffard, 1999):

$$\Delta\tau = 0.162\frac{F \cdot TEC_v}{c} \tag{2.21}$$

where TEC_v is the TEC value for a vertical column located at the pierce point, in units of 10^{16} electrons per m^2 and F is the obliquity factor. Assuming that the active region of the ionosphere can be represented by a thin shell at an elevation of 350 km, the obliquity can be approximately expressed as a simple function of the elevation angle in degrees (E) of the satellite at the receiver's antenna (Giffard, 1999):

$$F = 1 + 2.74 \cdot 10^{-6}(96 - E)^3 \tag{2.22}$$

Depending on the receiver design, different models can be adopted to calculate the correction terms to be applied to the pseudorange before solving the navigation

equations. Particularly, L1 code-range receivers use a sinusoidal model of the ionosphere (called Klobuchar model), which take into account the variations of the ionospheric layers (low over night, rapidly getting higher after dawn, getting slightly higher during the afternoon and rapidly getting lower after sunset). The sinusoidal parameters (amplitude and period) are transmitted in the navigation message. The relevant equations are the following (Klobuchar, 1986):

$$IDV = DC + A\cos\left[\frac{2\pi(t-\Phi)}{P}\right] \quad \text{(day)} \tag{2.23}$$

$$IDV = DC \quad \text{(night)} \tag{2.24}$$

where *IDV* (Ionospheric Vertical Delay) is expressed in nsec, DC is the constant night-day offset (5 nsec), *A* is the amplitude (whose value is between 10 and 100 nsec), Φ is the constant phase offset (14.00 hours), *t* is the local time, and *P* is the period. The two factors *A* and *P* are transmitted as coefficients of a cubic equation representing a model of the ionosphere with varying latitude. As the delay also depends on obliquity of the path, elevation is included as an additional factor in the equation:

$$TID = \left[1 + 16(0.53 - E_h)^3\right] IDV \tag{2.25}$$

where *TID* is the Total Ionospheric Delay (nsec) and E_h is the elevation angle of the satellites over the horizon. As the ionosphere is dispersive at radio frequencies, two signals at frequencies the L1 and L2 signals will be delayed by different amounts. Therefore, double frequency GNSS receivers (e.g., GPS P-code receivers) can measure the difference (Δt) between the time of reception of L1 and L2, and evaluate the delay associated with both of them. For L1 we have:

$$\Delta\tau_{L1} = \Delta T\left[\left(\frac{f_{L1}}{f_{L2}}\right)^2 - 1\right]^{-1} \tag{2.26}$$

where :

$$\Delta T = \frac{40.31 \cdot TEC}{cf^2}\left(\frac{1}{f_{L2}^2} - \frac{1}{f_{L1}^2}\right) \tag{2.27}$$

The troposphere is the lower part of the atmosphere (up to about 50 km) and its characteristics depend on local humidity, temperature and altitude. The tropospheric

delay for a given slant range can be described as a product of the delay at the zenith and a mapping function, which models the elevation dependence of the propagation delay. In general, the total Slant Tropospheric Delay (STD) is given by the sum of a Slant Hydrostatic Delay (SHD) and a Slant Wet Delay (SWD), and both of them can be expressed by a relevant Zenith Tropospheric Delay (ZTD) and a Mapping Function (MF). The SHD (or "dry component") account for about 90% of the total tropospheric delay and accurate estimations are normally available. On the other hand, the "wet component" (SWD) estimations are generally less accurate and there is a significant variability depending on the actual models implemented. Table 2-1 shows some typical values of the tropospheric delay for various elevation angles (Dodson, 1997).

Table 2-1. Tropospheric delay for varying elevation angle.

Elevation Angle (°)	Dry Component (m)	Wet Component (m)
90	2.3	0.2
30	4.6	0.4
10	13.0	1.2
5	26.0	2.3

The total STD can be expressed as:

$$STD = SHD + SWD = ZHD \times MF_H + ZWD \times MF_W \qquad (2.28)$$

where ZHD and ZWD are the zenith hydrostatic delay and zenith wet delay, respectively (ZTD = ZHD + ZWD); MF_H and MF_W are their corresponding MFs. There are many ZTD models and MFs currently used in GNSS positioning applications. Popular models include the ZTD empirical models developed by Saastamoinen (1972 and 1973), Hopfield (1969 and 1971) and by the University of New Brunswick (Leandro et al., 2006). The Saastamoinen model can be written as (Saastamoinen, 1973):

$$\mathrm{ZTD} = \frac{0.00227668}{1 - 0.00266\cos(2\varphi) - 0.00000028H}\left[P + \left(\frac{1255}{T} + 0.05\right)e\right] \quad (2.29)$$

where P, T and e are the atmospheric pressure in hPa, temperature in Kelvin, and partial water vapor pressure in hPa, respectively; φ and H are the latitude and height of the station in radians and meter, respectively.

The Hopfield model reads:

$$\mathrm{ZTD} = 10^{-6}\left\{k_1\frac{P}{T}\frac{40136 + 148.72(T - 273.16) - H}{5} + [273(k_2 - k_1) + k_3]\frac{e}{T^2}\frac{11000 - H}{5}\right\} \quad (2.30)$$

where the constants are k_1 = 77.604 K/hPa, k_2 = 64.79 K/hPa, and $k3$ = 3.776×10^5 K^2/hPa.

The University of New Brunswick (UNB) developed various models, with the most popular being the so-called UNB Model 3 (UNB3). This model reads:

$$\mathrm{ZTD} = \mathrm{ZHD} + \mathrm{ZWD} = \tau_h^z \cdot \kappa_h \cdot P + \tau_w^z \cdot \kappa_w \cdot \frac{e}{T} \quad (2.31)$$

with

$$\kappa_h = \left(1 - \frac{\beta H}{T}\right)^{\frac{g}{R_d\beta}}, \quad \kappa_w = \left(1 - \frac{\beta H}{T}\right)^{\frac{\lambda/g}{R_d\beta}}, \quad \tau_h^z = \frac{10^{-6}k_1R_d}{g_m}, \quad \tau_w^z = \frac{10^{-6}k_3'R_d}{g_m\lambda' - \beta R_d}$$

where g = 9.80665m/s^2; R_d = 287.054 J/kg/K; k_3' = 382,000 K^2/hpa; g_m = 9.784[1 – 2.66 × 10^{-3}cos(2φ) – 2.8× 10^{-7} H) m/s^2; λ' = λ + 1. For a certain day of the year (*doy*), the parameters P, T, e, β and λ can be calculated by the expression:

$$\xi(\varphi,\ doy) = \xi_{avg}(\varphi) - \xi_{amp}(\varphi)\cos\left(2\pi\frac{doy - 28}{365.25}\right) \quad (2.32)$$

where ξ denotes the respective parameters to be computed, and $\xi_{avg}(\varphi)$ and $\xi_{amp}(\varphi)$ are linearly interpolated considering the specific latitude of a station as described in Leandro et al. (2006). Popular MFs include the ones described by Chao (1972), Ifadis (1986), Herring (1992), Niell (1996), and Boehm (Boehm et al., 2006).

2.4.5 Multipath Errors

GNSS signals may arrive at the receiver antenna via different paths, due to reflections by objects along the path. Such effect is known as multipath. The reflected signal will have a different path length compared to the direct signal; therefore, it will give a biased distance measurement (Fig. 2-4). Multipath depends on the environment surrounding the receiver and the satellite geometry. In general, multipath errors are greater for low elevation satellites and code multipath is two orders of magnitude larger than carrier phase multipath (Seeber, 2003). For code measurements, the multipath error can reach a theoretical value of 1.5 times the chip rate. So, for instance, the GPS C/A code chip rate is 293.1 metre and the maximum multipath error is about 439.65 metres. However, values of less than 2-3 metres are the norm and upper values of 15 metres are rarely observed. For carrier phase, the maximum theoretical multipath error is a quarter of the wavelength. This equates to about 5 centimetres for the GPS L1 and L2 frequencies, although typical values are less than 1 centimetre (Sanz Subirana et al., 2011)

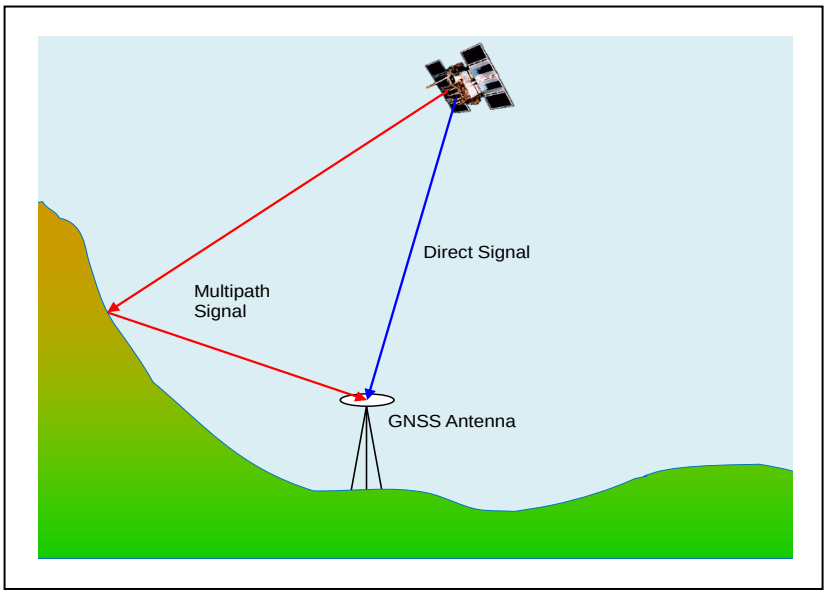


Figure 2-4. Multipath Error.

Multipath can be accurately modelled and removed only at static points, by taking observations at the same points and at the same hour on consecutive days. This, however, is not practical or even impossible in a dynamic environment. Other

techniques use Signal-to-Noise Ratio (SNR) and signal phase/frequency information to detect and quantify multipath. Despite several research efforts addressing multipath detection and mitigation techniques, this is still a major error source in GNSS applications. Techniques such as the Narrow Correlator (Van Dierendonck et al., 1992), the Double Delta/Strobe Correlator (McGraw et al., 1999), or the Vision Correlator by Fenton and Jones (Fenton et al., 2005), are not capable to eliminate multipath-related errors completely.

2.4.6 User Dynamics Errors

There are various errors associated with a dynamic GNSS platform. These errors range from the physical masking of the GNSS antenna to the accuracy degradation caused by sudden acceleration of the antenna. If carrier phase is used, the resulting effect of "cycle slips" is the need for re-initialisation (i.e., re-determination of the integer ambiguities). In general, a distinction is made between medium-low and high dynamic platforms. The effects of high dynamic aircraft manoeuvres on GNSS performance have been investigated in this research and the key results of this investigation are discussed in Chapter 3 and Chapter 5.

2.5 UERE VECTOR

The User Equivalent Range Error (UERE) is an error vector along the line-of-sight user-satellite given by the projection of all system errors. The value of this vector can be reduced only by careful design of the receiver, since there is nothing the users of non-augmented GNSS receivers can do to reduce other error sources. The UERE is generally measured in metres and is given as eithr a 1-sigma error (often denoted σ_r) or a 2-sigma error (95%). The portion of the UERE allocated to the space and control segments is called the User Range Error (URE) and is defined at the phase centre of the satellite antenna. The portion of the UERE allocated to the User Equipment is called the UE Error (UEE). Specifically, the UERE is the root-sum-square of the URE and UEE. When SA was on, typical values of the UERE

vector for GPS were below 10 m (95%) for P(Y) code receivers and about 33 m (95%) for C/A code receivers. With SA turned off, the UERE of C/A code receivers is typically less than 20 metres, with the actual value dominated by ionospheric and multipath effects. Dual-frequency receivers (with the capability of removing almost entirely the ionospheric errors), typically experience smaller UEREs. Users of the new modernised GPS civilian signals, as well as future users of GALILEO and BDS, will be able to use multiple frequencies to compensate for the ionospheric errors and thereby to achieve lower UEREs. In GNSS systems the UERE values are strongly dependent on the time elapsed since the last upload from the control segment. As an example, Fig. 2-5 shows the GPS SPS UERE variation with time (US DOD, 2008). In GPS normal operations, the time since last upload is limited to no more than one day. The smallest UERE and best SIS accuracy will generally occur immediately after an upload of fresh NAV message data to a satellite, while the largest UERE and worst SIS accuracy will usually be with the stalest NAV message data just prior to the next upload to that satellite.

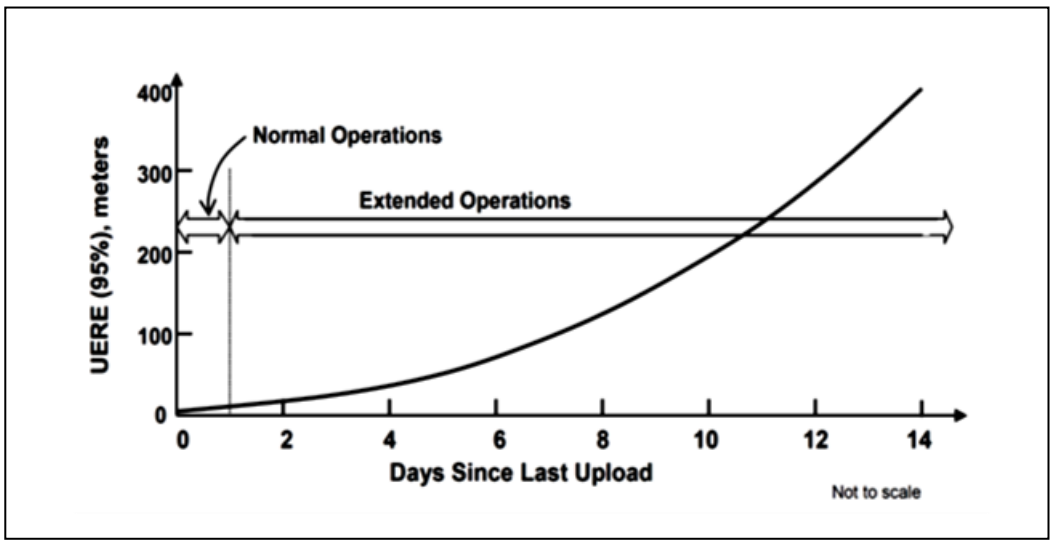


Figure 2-5. UERE variation with time in normal and extended operations (US DOD, 2008).

The metric used to characterize whether the NAV message data being transmitted by a satellite is fresh or stale is the age of data (AOD), where the AOD is the elapsed time since the control segment generated the satellite clock/ephemeris prediction used to create the NAV message data upload. The AOD is approximately equal to

the time since last upload plus the time it took the Control Segment to create the NAV message data and upload it to the satellite. For Normal Operations (NOP), the GPS UERE budget and the traditional SPS SIS accuracy specifications apply at each AOD. Because the largest UERE and worst SIS accuracy usually occur with the oldest NAV message data, the UERE budget and traditional SPS SIS accuracy specifications are taken as applying at the maximum AOD. For reference, the GPS UERE budgets for SPS receivers at zero AOD, at maximum AOD in normal operations, and at 14.5 day AOD in extended operations, are shown in Table 2-2.

Table 2-2. GPS single frequency C/A code UERE budget. Adapted from US DOD (2008).

Segment	Error Source	UERE Contribution (95%) [m]		
		Zero AOD	Max AOD in NOP	14.5 Day AOD
Space	Clock Stability	0.0	8.9	257
	Group Delay Stability	3.1	3.1	3.1
	Differential Group Delay Stability	0.0	0.0	0.0
	Satellite Acceleration Uncertainty	0.0	2.0	204
	Other Space Segment Errors	1.0	1.0	1.0
Control	Clock/Ephemeris Estimation	2.0	2.0	2.0
	Clock/Ephemeris Prediction	0.0	6.7	206
	Clock/Ephemeris Curve Fit	0.8	0.8	1.2
	Ionospheric Delay Model Terms	9.8-19.6	9.8-19.6	9.8-19.6
	Group Delay Time Correction	4.5	4.5	4.5
	Other Control Segment Errors	1.0	1.0	1.0
User*	Ionospheric Delay Compensation	N/A	N/A	N/A
	Tropospheric Delay Compensation	3.9	3.9	3.9
	Receiver Noise and Resolution	2.9	2.9	2.9
	Multipath	2.4	2.4	2.4
	Other User Segment Errors	1.0	1.0	1.0
95% System UERE (SPS)		**12.7-21.2**	**17.0-24.1**	**388**

* For illusdtration only (see Table 2.4 for detailes).

The breakout of the individual segment components of the UERE budgets shown in this table is given for illustration purposes only assuming average receiver characteristics. The actual GPS SPS ranging accuracy standards are better specified in terms of the UEE and URE components and the overall error budget is dependent on a number of assumptions, conditions and constraints. For reference, Tables 2-3

lists the error budgets and typical UEE values applicable to airborne C/A-code GPS receivers in normal operating conditions. Table 2-4 lists the condition and criteria that apply to the URE budgeting.

Table 2-3. Typical UEE error buidget (95%). Adapted from US DOD (2008).

Error Source	Traditional Spec., Single Freq. Receiver	Improved Spec., Single Freq. Receiver	Modern Single Freq. Receiver	Moderm Dual Freq. Receiver*
Ionospheric Delay Compensation	N/A	N/A	N/A	0.8
Tropospheric Delay Compensation	3.9	4.0	3.9	1.0
Receiver Noise and Resolution	2.9	2.0	2.0	0.4
Multipath	2.4	0.5	0.2	0.2
Other Errors	1.0	1.0	1.0	0.8
UEE (m), 95%	**5.5**	**4.6**	**4.5**	**1.6**

*Assuming benign conditions (US DOD, 2008)

Table 2-4. SPS SIS URE accuracy standards. Adapted from US DOD (2008).

SIS Accuracy Standard	Conditions and Constraints
Single-Frequency C/A-Code: • ≤ 7.8 m 95% Global Average URE during Normal Operations over all AODs • ≤ 6.0 m 95% Global Average URE during Normal Operations at Zero AOD • ≤ 12.8 m 95% Global Average URE during Normal Operations at Any AOD	• For any healthy SPS SIS • Neglecting single-frequency ionospheric delay model errors • Including group delay time correction errors at L1 • Including inter-signal bias (P(Y)-code to C/A-code) errors at L1
Single-Frequency C/A-Code: • ≤ 30 m 99.94% Global Average URE during Normal Operations • ≤ 30 m 99.79% Worst Case Single Point Average URE during Normal Operations	• For any healthy SPS SIS • Neglecting single-frequency ionospheric delay model errors • Including group delay time correction errors at L1 • Including inter-signal bias (P(Y)-code to C/A-code) errors at L1 • Standard based on measurement interval of one year; average of daily values within the service volume • Standard based on 3 service failures per year, lasting no more than 6 hours each
Single-Frequency C/A-Code: • ≤ 388 m 95% Global Average URE during Extended Operations after 14 Days without Upload	• For any healthy SPS SIS

2.6 DOP FACTORS

Ranging errors alone do not determine GNSS positioning accuracy. The accuracy of the navigation solution is also affected by the relative geometry of the satellites and the user. This is described by the Dilution of Precision (DOP) factors. The four linearized equations represented by Eq. (2.10) can be expressed in matrix notation as:

$$\begin{bmatrix} \Delta P_1 \\ \Delta P_2 \\ \Delta P_3 \\ \Delta P_4 \end{bmatrix} = \begin{bmatrix} \beta_{11} & \beta_{12} & \beta_{13} & 1 \\ \beta_{21} & \beta_{22} & \beta_{23} & 1 \\ \beta_{31} & \beta_{32} & \beta_{33} & 1 \\ \beta_{41} & \beta_{42} & \beta_{43} & 1 \end{bmatrix} \times \begin{bmatrix} \Delta u_k \\ \Delta v_k \\ \Delta w_k \\ \Delta T \end{bmatrix} + \begin{bmatrix} \varepsilon_1 \\ \varepsilon_2 \\ \varepsilon_3 \\ \varepsilon_4 \end{bmatrix} \tag{2.33}$$

where an error vector has been added to account for pseudorange measurement noise plus model errors and any non-modelled effects (e.g., SA when present), and β_{ij} is the direction cosine of the angle between the LOS to the i^{th} satellite and the j^{th} co-ordinate. This can be written more compactly as:

$$r = B\bar{x} + \varepsilon \tag{2.34}$$

where:

B = 4×4 solution matrix (i.e., matrix of coefficients of the linear equation);

$\bar{x}$ = user position and time correction vector ($\bar{x} \equiv [\Delta u_k \quad \Delta v_k \quad \Delta w_k \quad \Delta T]^T$);

r = pseudorange measurement difference vector ($r \equiv [\Delta P_1 \quad \Delta P_2 \quad \Delta P_3 \quad \Delta P_4]^T$);

ε = vector of measurement and other errors ($\varepsilon \equiv [\varepsilon_1 \quad \varepsilon_2 \quad \varepsilon_3 \quad \varepsilon_4]^T$);

The GNSS receiver (or post-processing software) solves the matrix equation using least squares or a Kalman filter. The solution is:

$$\bar{x} = -\left(B^T W B\right)^{-1} B^T W r \tag{2.35}$$

The new term in Eq. (2.35) is the weight matrix (W) that characterizes the differences in the errors of the simultaneous measurements as well as any correlations that may exist among them. The weight matrix is given by:

$$W = \sigma_0^2 C_r \tag{2.36}$$

where C_r is the covariance matrix of the pseudorange errors and σ_0^2 is a scale factor known as the a priori variance of unit weight. Applying the law of propagation of error (also known as the covariance law), we obtain:

$$C_{\bar{x}} = \left[\left(B^T W B\right)^{-1} B^T W\right] C_r \left[\left(B^T W B\right)^{-1} B^T W\right]^T = \left(B^T C_r^{-1} B\right)^{-1} \tag{2.37}$$

in which $C_{\bar{x}}$ is the covariance matrix of the parameter estimates.

If we assume that the measurement and model errors are the same for all observations with a particular standard deviation (σ) and that they are uncorrelated, we can write:

$$C_r = I\sigma^2 \tag{2.38}$$

where I is the identity matrix. Therefore, the expression for $C_{\bar{x}}$ simplifies to:

$$C_{\bar{x}} = \left(B^T B\right)^{-1} \sigma_r^2 = D\sigma_r^2 \tag{2.39}$$

The term σ_r represents the standard deviation of the pseudorange measurement error plus the residual model error, which is assumed to be equal for all simultaneous observations. If we further assume that the measurement error and the model error components are all independent, then we can simply root-sum-square these errors to obtain the value of σ_r. Based on the definition of UERE given above, we can use the 1-sigma UERE for σ_r. The elements of matrix D are a function of receiver-satellite geometry only. The explicit form of this matrix is:

$$D = \begin{bmatrix} D_{11} & D_{12} & D_{13} & D_{14} \\ D_{21} & D_{22} & D_{23} & D_{24} \\ D_{31} & D_{32} & D_{33} & D_{34} \\ D_{41} & D_{42} & D_{43} & D_{44} \end{bmatrix} \tag{2.40}$$

The DOP factor can be defined as follows:

$$DOP_d = \sqrt{Trace_d D} \qquad d = 1,2,3,4 \tag{2.41}$$

where d is the dimension of the DOP factor.

The diagonal elements of $C_{\bar{x}}$ are the estimated receiver coordinate and clock-offset variances, and the off-diagonal elements (i.e., covariances) indicate the degree to which these estimates are correlated. The explicit form of the $C_{\bar{x}}$ matrix is:

$$C_{\bar{x}} = \begin{bmatrix} \sigma_u^2 & \sigma_{uv} & \sigma_{uw} & \sigma_{uT} \\ \sigma_{vu} & \sigma_v^2 & \sigma_{vw} & \sigma_{vT} \\ \sigma_{wu} & \sigma_{wv} & \sigma_w^2 & \sigma_{wT} \\ \sigma_{Tu} & \sigma_{Tv} & \sigma_{Tw} & \sigma_T^2 \end{bmatrix} \tag{2.42}$$

The various DOP values can be expressed as functions of the diagonal elements of the $C_{\bar{x}}$ matrix or of the D matrix. Converting the Cartesian co-ordinates in matrix (2.42) to more convenient local geodetic coordinates, we have:

$$C_{\overline{LG}} = \begin{bmatrix} \sigma_N^2 & \sigma_{NE} & \sigma_{NH} & \sigma_{NT} \\ \sigma_{EN} & \sigma_E^2 & \sigma_{EH} & \sigma_{ET} \\ \sigma_{HN} & \sigma_{HE} & \sigma_H^2 & \sigma_{HT} \\ \sigma_{TN} & \sigma_{TE} & \sigma_{TH} & \sigma_T^2 \end{bmatrix} \tag{2.43}$$

Table 2-5 shows the relationship between the DOP factors and the diagonal elements of the $C_{\overline{LG}}$ matrix and of the D matrix in Eq. (2.40).

Table 2-5. DOP Expressions.

DOP Factor	D Matrix Formulation	C Matrix Formulation
Geometric DOP (GDOP)	$GDOP = \sqrt{D_{11} + D_{22} + D_{33} + D_{44}}$	$GDOP = \frac{1}{\sigma_r}\sqrt{\sigma_N^2 + \sigma_E^2 + \sigma_H^2 + \sigma_T^2}$
Position DOP (PDOP)	$PDOP = \sqrt{D_{11} + D_{22} + D_{33}}$	$PDOP = \frac{1}{\sigma_r}\sqrt{\sigma_N^2 + \sigma_E^2 + \sigma_H^2}$
Horizontal DOP (HDOP)	$HDOP = \sqrt{D_{11} + D_{22}}$	$HDOP = \frac{1}{\sigma_r}\sqrt{\sigma_N^2 + \sigma_E^2}$
Vertical DOP (VDOP)	$VDOP = \sqrt{D_{33}}$	$VDOP = \frac{1}{\sigma_r}\sqrt{\sigma_H^2} = \frac{\sigma_H}{\sigma_r}$
Time DOP (TDOP)	$TDOP = \sqrt{D_{44}}$	$TDOP = \frac{1}{\sigma_r}\sqrt{\sigma_T^2} = \frac{\sigma_T}{\sigma_r}$

It is also evident that:

$$PDOP = \sqrt{HDOP^2 + VDOP^2} \tag{2.44}$$

$$GDOP = \sqrt{PDOP^2 + TDOP^2} \tag{2.45}$$

The PDOP is very frequently used in navigation. This is because it directly relates error in GNSS position to errors in pseudo-range measurements to the satellites. According to the definitions given above, the 1-sigma Estimated Position and Time Errors (EPE and ETE) of a GNSS receiver can be calculated using the PDOP (EPE in 3D), the HDOP (EPE in 2D) or the TDOP. In general, we have:

$$EPE_{3D} = \sigma_P = \sigma_r PDOP \tag{2.46}$$

$$EPE_{2D} = \sigma_H = \sigma_r HDOP \tag{2.47}$$

$$ETE = \sigma_T = \sigma_r TDOP \tag{2.48}$$

Table 2-6 shows the relationship between the EPE_{3D} and the Figure of Merit (FOM). This parameter is frequently used in avionics GNSS receivers to provide an indication of the quality of information provided by GNSS.

Table 2-6. GNSS Figure of Merit.

FOM	Est. Position Error 3-D (m)	Est. Time Error
1	< 25	< 1ns
2	25-50	1ns-10ns
3	50-75	10ns-100ns
4	75-100	100ns-1ms
5	100-200	1ms-10ms
6	200-500	10ms-100ms
7	500-1000	100ms-1ms
8	1000-5000	1ms-10ms
9	> 5000	>10ms

There is a proportionality between the PDOP and the reciprocal value of the volume V of a particular tetrahedron formed by the satellites and the user position (Fig. 2-6).

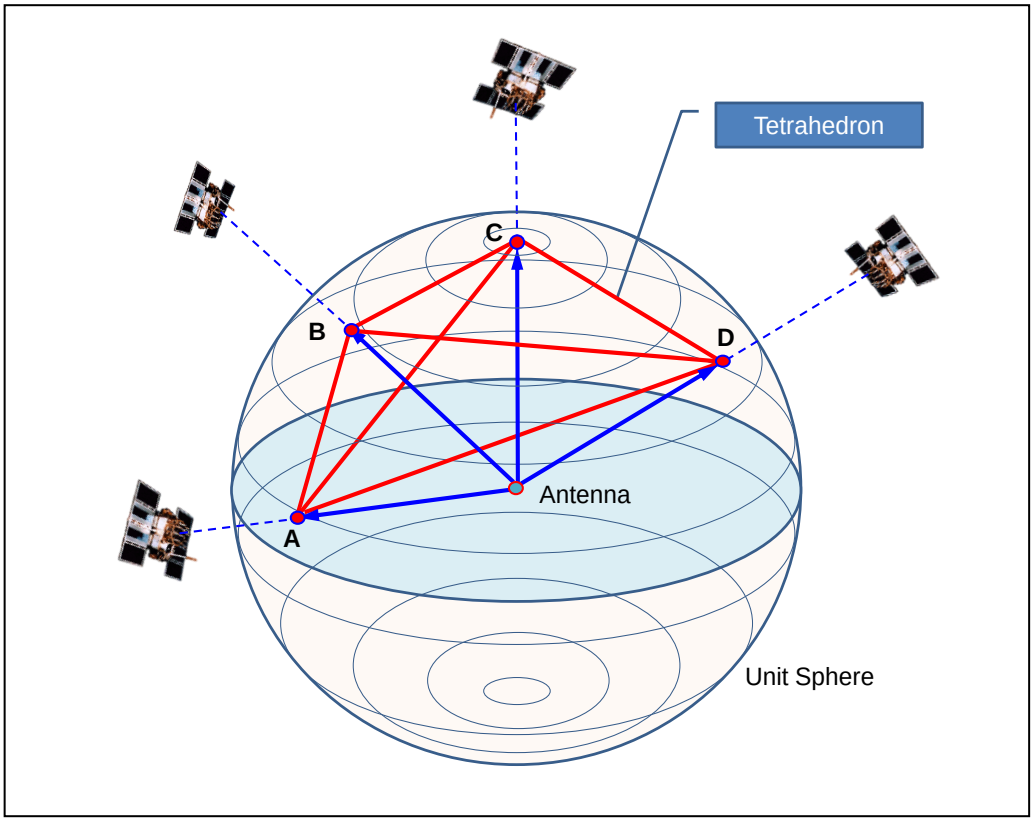


Figure 2-6. PDOP tetrahedron construction. Four unit-vectors point toward the satellites and the ends of these vectors are connected with 6 line segments.

It can in fact be demonstrated (Phillips, 1990) that the PDOP is the RSS (i.e., square root of the sum of the squares) of the areas of the 4 faces of the tetrahedron, divided by its volume (i.e., the RSS of the reciprocals of the 4 altitudes of the tetrahedron). Therefore, we can write:

$$PDOP = \sqrt{\frac{1}{h_A^{\,2}} + \frac{1}{h_B^{\,2}} + \frac{1}{h_C^{\,2}} + \frac{1}{h_D^{\,2}}} \tag{2.49}$$

At a particular time and location, the four satellites shown in Fig. 2-6 have determined elevations and azimuths with respect to the receiver. From these satellite positions the components *(x, y, z)* of the unit vectors to the satellites can be determined. Using the Pythagorean theorem, the distances between the ends of the

unit vectors can be determined. Knowing these distances, a tetrahedron can be constructed (Fig. 2-7) and the four altitudes of the tetrahedron can be measured. Finally, using equation (2.41), the PDOP can be determined.

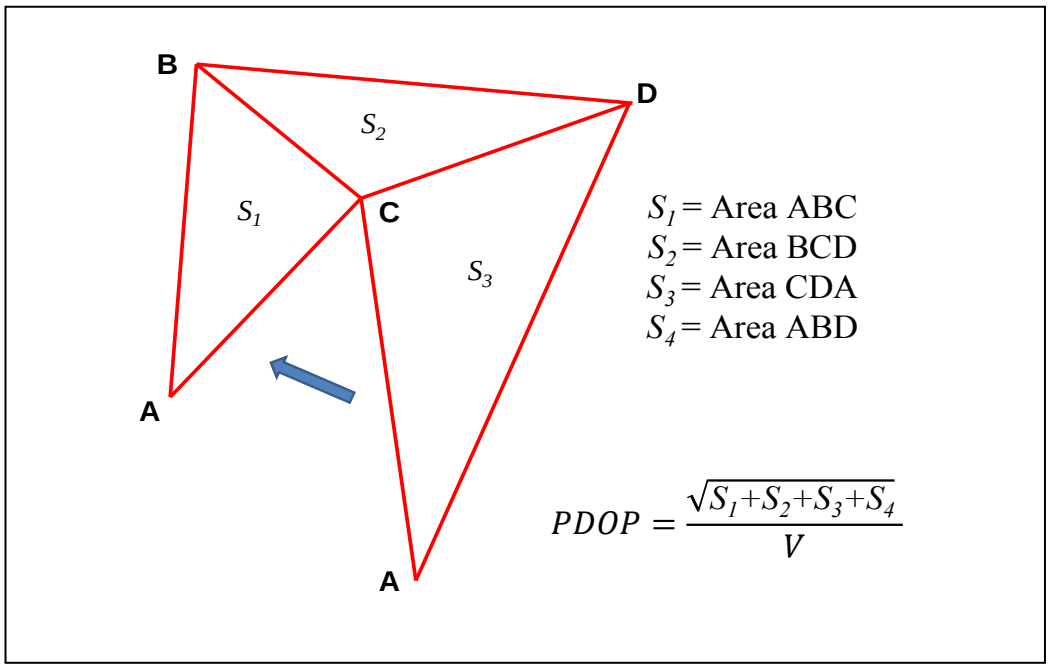


Figure 2-7. "Cut and fold" tetrahedron for PDOP determination.

There is no approximation associated with the geometric expression. Any residual error in PDOP determination is only due to construction of the tetrahedron and measurement of the altitudes. If the angle $A\hat{C}A$ in Fig. 2-6 is small, one can recognise that the PDOP will be large (poor) even without measuring the altitudes, since this leads to a tetrahedron having a small volume. From the geometric definition of PDOP we deduce that it is optimal from the user's point of view (i.e., low PDOP) to select the four satellites giving a large volume of the tetrahedron (and a small RSS of the areas of the 4 faces of the tetrahedron). This can be obtained primarily by selecting a combination of satellites far from each other and uniformly distributed around the receiver. The condition for the maximum volume is with a satellite at the zenith and the other three separated by 120° (azimuth) and low over the horizon. This condition, however, would degrade the signal quality, due to the

longer propagation paths (i.e., a compromise between signal quality and accuracy of the solution is therefore necessary).

A further consequence of the above construction is that if the ends of the unit vectors are coplanar (a not unusual circumstance) the PDOP becomes infinite, and a position is not obtainable. This is the reason why the various GNSS constellations have been designed so that there are almost always 6-7 satellites in view anywhere on Earth, giving an alternate choice of the 4 satellites to be utilised. If *m* satellites are in view, the number of possible combinations is:

$$N = \frac{m!}{4!(m-4)!} \tag{2.50}$$

In most GNSS receivers the number of combinations *N* also corresponds to the number of PDOP/GDOP computations necessary for selection of the best satellite geometry. Some systems can automatically reject, prior performing positioning calculations, subsets of satellites with associated DOP factors below pre-set thresholds.

2.7 GNSS PERFORMANCE REQUIREMENTS IN AVIATION

The aviation community has devoted great efforts to the rationalization and standardization of the navigation performance parameters and requirements, thus specifying the so-called Required Navigation Performance (RNP) that an airborne navigation system must achieve (ICAO, 1995), (ICAO, 2008). Accuracy, integrity, availability and continuity are used to describe the RNP for operations in various flight phases and within specified classes of airspace. The four parameters used to characterize the navigation systems performance are accuracy, integrity, contunity and availability. Appropriate definitions are provided hereafter (US DoT/DoD/DoHS, 2008):

- ***Accuracy*** of an estimated or measured position of a craft (vehicle, aircraft, or vessel) at a given time is the degree of conformance of that position with the true position, velocity and/or time of the craft. Since accuracy is a statistical measure of performance, a statement of navigation system accuracy is meaningless unless it includes a statement of the uncertainty (e.g., confidence

level) in position that applies.

- ***Integrity*** is the measure of the trust that can be placed in the correctness of the information supplied by a navigation system. Integrity includes the ability of the system to provide timely warnings to users when the system should not be used for navigation.
- ***Continuity*** of a system is the ability of the total system (comprising all elements necessary to maintain craft position within the defined area) to perform its function without interruption during the intended operation. More specifically, continuity is the probability that the specified system performance will be maintained for the duration of a phase of operation, presuming that the system was available at the beginning of that phase of operation.
- ***Availability*** of a navigation system is the percentage of time that the services of the system are usable by the navigator. Availability is an indication of the ability of the system to provide usable service within the specified coverage area. Signal availability is the percentage of time that navigation signals transmitted from external sources are available for use. It is a function of both the physical characteristics of the environment and the technical capabilities of the transmitter facilities.

In aviation applications, accuracy is a measure of the difference between the estimated and the true or desired aircraft position under nominal fault-free conditions. It is normally expressed as 95% bounds on Horizontal and Vertical position errors (ICAO, 2008). In the avionics context, there are two distinguished types of accuracy that must be considered: the accuracy relative to the navigation system alone and the accuracy achieved by the combination of navigation and flight control systems. This second type of accuracy is called Total System Error (TSE) and is measured as deviation from the required flight trajectory. In large commercial aircraft and several military aircraft, the required flight trajectory and associated guidance information is computed by a Flight Management System (FMS) and constantly updated based on ATM and weather information. The navigation system

estimates the aircraft state vector (i.e., position, velocity, attitude and associated rates), determines the deviation from the required flight trajectory and sends these information either to the cockpit displays or to an Automatic Flight Control System (AFCS).

The error in the estimation of the aircraft's position is referred to as Navigation System Error (NSE), which is the difference between the aircraft's true position and its displayed position. The difference between the desired flight path and the displayed position of the aircraft is called Flight Technical Error (FTE) and accounts for aircraft dynamics, turbulence effects, human-machine interface, etc. As illustrated in Fig. 2-8, the TSE is obtained as the vector sum of the NSE and the FTE.

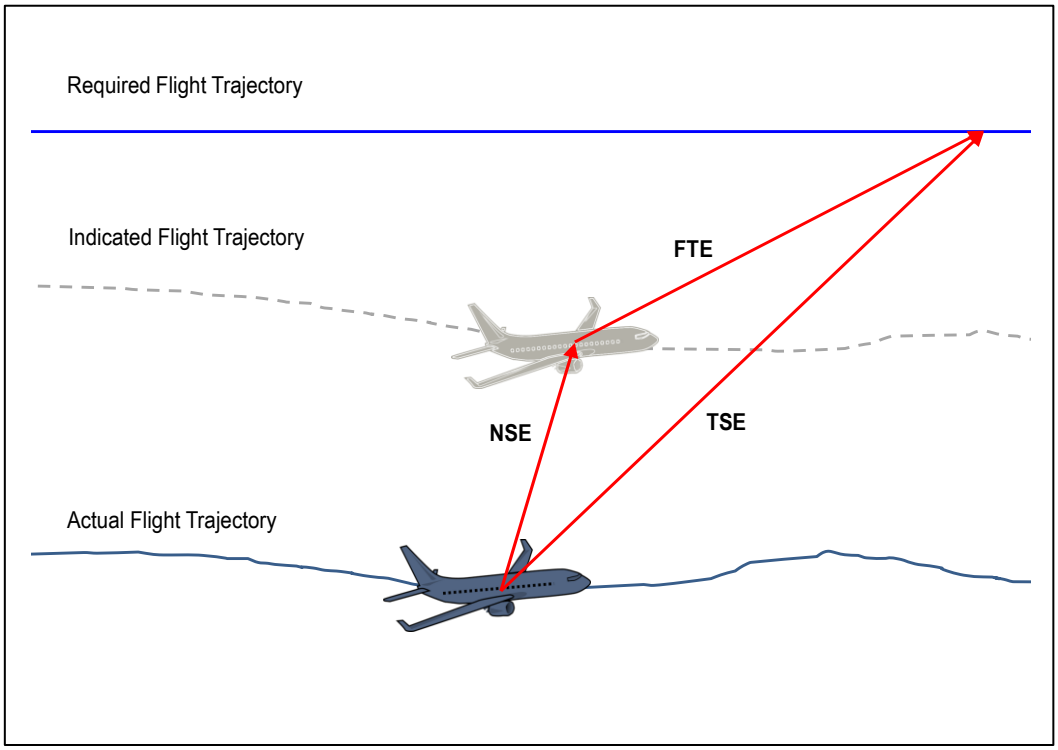


Figure 2-8. Navigation accuracy in aviation applications.

The integrity risk can be conveniently defined as the probability of providing a signal that is out of tolerance without warning the user in a given period of time. It is typically derived from the high-level Target Level of Safety (TLS) which is an index, generally determined through historic accident data, against which the calculated risk

can be compared to judge whether the operation of the system is safe or not. The navigation integrity requirements in various flight phases/operational tasks have been specified by ICAO in terms of three key performance indicators: the probability of failure over time (or per single approach), the Time-To-Alert (TTA) and the Horizontal/Vertical Alert Limits. The TTA is the maximum allowable time elapsed from the onset of the system being out of tolerance until the equipment enunciates the alert. The alert limits represent the largest horizontal and vertical position errors allowable for safe operations. They are defined as follows (RTCA, 2008-a):

- ***Horizontal Alert Limit (HAL):*** the HAL is the radius of a circle in the horizontal plane (the local plane tangent to the WGS-84 ellipsoid), with its centre being at the true position, that describes the region that is required to contain the indicated horizontal position with the required probability for a particular navigation mode.
- ***Vertical Alert Limit (VAL):*** the VAL is half the length of a segment on the vertical axis (perpendicular to the horizontal plane of the WGS-84 ellipsoid), with its centre being at the true position, that describes the region that is required to contain the indicated vertical position with the required probability for a particular navigation mode.

According to these definitions, in order to assess the navigation system integrity, the NSE must be determined first and checked against the Alert Limits (ALs) applicable to the current flight operational phase. However, since the NSE is not observable by the pilot or by the avionics on board the aircraft, another approach to evaluate the system integrity has to be adopted. The standard approach consists in estimating the worst-case NSE and confronting this value with the corresponding AL. These limits for NSE are known as Protection Levels (PLs) and represent high-confidence bounds for the NSE. Similarly to the positioning errors, the PLs are stated in terms of Horizontal and Vertical components (HPL and VPL).

Table 2-7 lists the required level of accuracy, integrity, continuity and availability defined by ICAO for the different aircraft flight phases. Various applicable national and international standards have been used in this compilation (CAA, 2003), (ICAO,

2006), (ICAO, 2010), (RTCA, 2004), (RTCA, 2006-a). An additional performance indicator that is often used to characterise avionics GNSS receivers is the Time-To-First-Fix (TTFF). The TTFF accounts for the time elapsed from the GNSS receiver switch-on until the output of a navigation solution is provided to the user within the required performance boundaries (typically in terms of 2D/3D accuracy).

Table 2-7. Aviation GNSS signal-in-space performance requirements (CAA, 2003), (ICAO, 2006), (ICAO, 2010), (RTCA, 2004), (RTCA, 2006-a).

TYPE OF OPERATION	HOR./VERT. ACCURACY (95%)	CONTINUITY	AVAILABILITY	INTEGRITY	TTA	HAL / VAL
En Route Oceanic	3700m/NA	$1\text{-}10^{-4}$/hr to $1\text{-}10^{-8}$/hr	0.99 to 0.99999	$1\text{-}10^{-7}$/hr	5 min	7408m/NA
En Route Continental	3700m/NA	$1\text{-}10^{-4}$/hr to $1\text{-}10^{-8}$/hr	0.99 to 0.99999	$1\text{-}10^{-7}$/hr	5 min	3704m/NA
En Route Terminal	740m/NA	$1\text{-}10^{-4}$/hr to $1\text{-}10^{-8}$/hr	0.99 to 0.99999	$1\text{-}10^{-7}$/hr	15 s	1852m/NA
APV-I	16m/20 m	$1\text{-}8\text{x}10^{-6}$/15 s	0.99 to 0.999	$1\text{-}2\text{x}10^{-7}$/ Approach	10 s	40m/50 m
APV-II	16m/8 m	$1\text{-}8\text{x}10^{-6}$/15 s	0.99 to 0.999	$1\text{-}2\text{x}10^{-7}$/ Approach	6 s	40m/20m
Category I	16m/4m	$1\text{-}8\text{x}10^{-6}$/15 s	0.99 to 0.99999	$1\text{-}2\text{x}10^{-7}$/ Approach	6 s	40m/10m
Category II	6.9m/2m	$1\text{-}4\text{x}10^{-6}$/15 s	0.99 to 0.99999	$1\text{-}10^{-9}$/15 s	1 s	17.3m/5.3m
Category III	6.2 m/2 m	$1\text{-}2\text{x-}10^{-6}$/30 s (lateral) $1\text{-}2\text{x}10^{-6}$/15 s (vertical)	0.99 to 0.99999	$1\text{-}10^{-9}$/30 s (lateral) $1\text{-}10^{-9}$/15 s (vertical)	1 s	15.5m/5.3m

The TTFF is commonly broken down into three more specific scenarios, as defined in the GPS equipment guide:

- ***Cold Start:*** the receiver has no recent Position, Velocity and Time (PVT) data estimates and no valid almanac data. Therefore, it must systematically search for all possible satellites in the sky. After acquiring a satellite signal, the receiver can obtain the almanac data (approximate information relative to satellites), based on which the process of PVT estimation can start. For instance, in the case of GPS receivers, manufacturers typically claim the factory TTFF to be in the order of 15 minutes.
- ***Warm Start:*** the receiver has estimates of the current time within 20 seconds, the current position within 100 km, and its velocity within 25 m/s, and it has valid almanac data. Therefore, it must acquire each satellite signal and obtain the satellite's detailed ephemeris data.
- ***Hot Start:*** the receiver has valid PVT, almanac and ephemeris data, enabling a rapid acquisition of satellite signals. The time required by a receiver in this state to calculate a position fix is also called Time-to-Subsequent-Fix (TTSF). TTSF is particularly important in aviation applications due to frequent satellite data losses caused by high dynamics aircraft manoeuvres.

In aviation applications, GNSS alone does not guarantee the level of performance required in several flight phases and operational tasks. In particular, GNSS fails to deliver sufficient accuracy and integrity levels for mission-essential and safety-critical operations such as precision approach/auto-landing, avionics flight test and flight inspection. Therefore, appropriate augmentation strategies must be implemented to accomplish these challenging tasks using GNSS as the primary source of navigation data.

2.8 GNSS ACCURACY AUGMENTATION

Differential GNSS (DGNSS) techniques can be used to address accuracy requirements. Specifically, in the case of GPS, differential techniques have been developed which can provide accuracies comparable with current landing systems.

A variety of Local Area DGNSS (LAD) and Wide Area DGNSS (WAD) networks have been proposed over the past twenty years and some LAD/WAD systems have achieved the levels of maturity required to enter the market. Due to the existence of a copious literature on GPS/GNSS basic principles and applications, these will not be covered in this thesis. DGNSS was developed to meet the needs of positioning and distance-measuring applications that required higher accuracies than stand-alone GNSS could deliver. DGNSS involves the use of a control or reference receiver at a known location to measure the systematic GNSS errors; and, by taking advantage of the spatial correlation of the errors, the errors can then be removed from the measurement taken by moving or remote receivers located in the same general vicinity. There have been a wide variety of implementations described for affecting such a DGNSS system. Our intent is to characterise various DGNSS systems and to compare their strengths and weaknesses. Two general categories of DGNSS systems can be identified: those that rely primarily upon the code measurements and those that rely primarily upon the carrier phase measurements. Using carrier phase, high accuracy can be obtained (centimetre level), but the solution suffers from integer ambiguity and cycle slips. Whenever a cycle slip occurs, it must be corrected for, and the integer ambiguity must be re-calculated. The pseudorange solution is more robust but less accurate (2 to 5 m). As it is not affected by cycle slips, there is no need for re-initialisation.

A typical DGNSS architecture is shown in Fig. 2-9. The system consists of a Reference Receiver (RR) located at a known location that has been previously surveyed, and one or more DGNSS User Receivers (URs). The RR antenna, differential correction processing system, and data link equipment (if used) are collectively called the Reference Station (RS). Both the UR and the RR data can be collected and stored for later processing, or sent to the desired location in real time via the data link. DGNSS is based on the principle that receivers in the same vicinity will simultaneously experience common errors on a particular satellite ranging signal. In general, the UR (mobile receiver) use measurements from the RR to remove the common errors. In order to accomplish this, the UR must simultaneously use a subset or the same set of satellites as the reference station. The DGNSS

positioning equations are formulated so that the common errors cancel. The common errors include signal path delays through the atmosphere, and satellite clock and ephemeris errors. For PPS users, the common satellite errors are residual system errors that are normally present in the PVT solution. For SPS users, the common satellite errors also include the intentionally added errors from SA. Errors that are unique to each receiver, such as receiver measurement noise and multipath, cannot be removed without additional recursive processing (by the reference receiver, user receiver, or both) to provide an averaged, smoothed, or filtered solution.

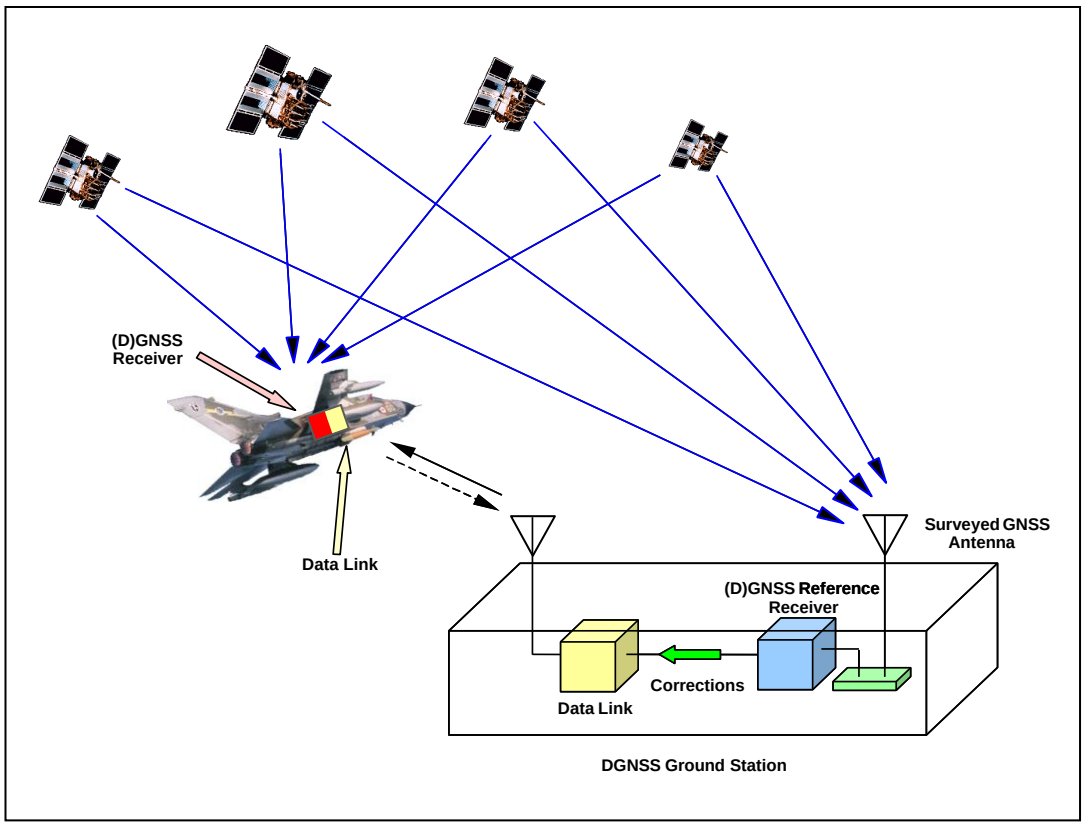


Figure 2-9. Typical DGNSS system architecture.

Various DGNSS techniques are employed depending on the accuracy desired, where the data processing is to be performed, and whether real-time results are required. If real-time results are required then a data link is also required. For applications without a real-time requirement, the data can be collected and processed later. The accuracy requirements usually dictate which measurements are used and what algorithms are employed. In the case of Differential GPS (DGPS), accuracy is

independent of whether SPS or PPS is being used, although real-time PPS DGPS can have a lower data rate than SPS DGPS because the rate of change of the nominal system errors is slower than the rate of change of SA. However, the user and the Reference Station must be using the same service (either PPS or SPS). The clock and frequency biases for a particular satellite will appear the same to all users since these parameters are unaffected by signal propagation or distance from the satellite. The pseudorange and delta-range (Doppler) measurements will be different for different users because they will be at different locations and have different relative velocities with respect to the satellite, but the satellite clock and frequency bias will be common error components of those measurements. The signal propagation delay is truly a common error for receivers in the same location, but as the distance between receivers increases, this error gradually de-correlates and becomes independent. The satellite ephemeris has errors in all three dimensions. Therefore, part of the error will appear as a common range error and part will remain a residual ephemeris error. The residual portion is normally small and its impact remains small for similar observation angles to the satellite. The first accepted standard for SPS DGPS was developed by the Radio Technical Commission for Maritime Services (RTCM) Special Committee-104 (RTCM, 2001). The data interchange format for NATO users of DGPS is documented in STANAG 4392 (NATO, 1998). The SPS reversionary mode specified in STANAG 4392 is compatible with the RCTM SC-104 standards. The standards are primarily intended for real-time operational use and cover a wide range of DGPS measurement types. Most SPS DGPS receivers are compatible with the RCTM SC-104 differential message formats. DGPS standards for aeronautical use were originally developed by the Radio Technical Commission for Aeronautics (RTCA) to allow Special Category-I (SCAT-I) precision approach using range-code differential. These standards were contained in RCTA document DO-217 and intended only for limited use until an international standard could be developed for precision approach (RTCA, 1993). More recently, the two separate standards were developed by RTCA for GPS Wide Area and Local Area Augmentation Systems (WAAS/LAAS). These standards define the minimum operational performance requirements for different WAAS/LAAS implementation types allowing WAAS operations down to CAT-I (RTCA, 2006-a) and LAAS

operations down to CAT-IIIb (RTCA, 2008-a), (RTCA, 2008-b). There are two primary variations of the differential measurements and equations. One is based on ranging-code measurements and the other is based on carrier-phase measurements. There are also several ways to implement the data link function. DGNSS systems can be designed to serve a limited area from a single reference station, or can use a network of reference stations and special algorithms to extend the validity of the DGNSS technique over a wide area. The result is that there is a large variety of possible DGNSS system implementations using combinations of these design features.

2.8.1 Ranging-Code DGNSS

The ranging-code differential technique uses the pseudorange measurements of the RS to calculate pseudorange or position corrections for the UR. The RS calculates pseudorange corrections for each visible satellite by subtracting the "true" range determined by the surveyed position and the known orbit parameters from the measured pseudorange. The UR receiver then selects the appropriate correction for each satellite that it is tracking, and subtracts the correction from the pseudorange that it has measured. The mobile receiver must only use those satellites for which corrections have been received. If the RS provides position corrections rather than pseudorange corrections, the corrections are simply determined by subtracting the measured position from the surveyed position. The advantage of using position corrections is obviously the simplicity of the calculations. The disadvantage is that the reference receiver and the user receiver must use the exact same set of satellites. This can be accomplished by coordinating the choice of satellite between the RR and the UR, or by having the RS compute a position correction for each possible combination of satellites. For these reasons, it is usually more flexible and efficient to provide pseudorange corrections rather than position corrections. RTCA, NATO STANAG and RCTM standards are all based on pseudorange rather than position corrections. The pseudorange or position corrections are time tagged with the time that the measurements were taken. In real-time systems, the rate of change of the corrections is also calculated. This allows the user to propagate the corrections to the

time that they are actually applied to the user position solution. This reduces the impact of data latency on the accuracy of the system but does not eliminate it entirely. SPS corrections become fully uncorrelated with the user measurements after about 2 minutes. Corrections used after two minutes may produce solutions which are less accurate than stand-alone SPS GPS. PPS corrections can remain correlated with the user measurements for 10 minutes or more under benign (slowly changing) ionospheric conditions. There are two ways of pseudorange data processing: post-mission and real-time processing. The advantage of the post-mission solution over the real-time one, is that it is more accurate, because the user can easily detect blunders and analyse the residuals of the solution. On the other hand the main disadvantage of the post-mission solution is that the results are not available immediately for navigation. The typical algorithm of the ranging-code DGNSS post-processed solution used in flight test and inspection tasks is the double difference pseudorange.

Fig. 2-10 shows the possible pseudorange measurements between two receivers (*k*. *l*) and two satellites (*p*, *q*).

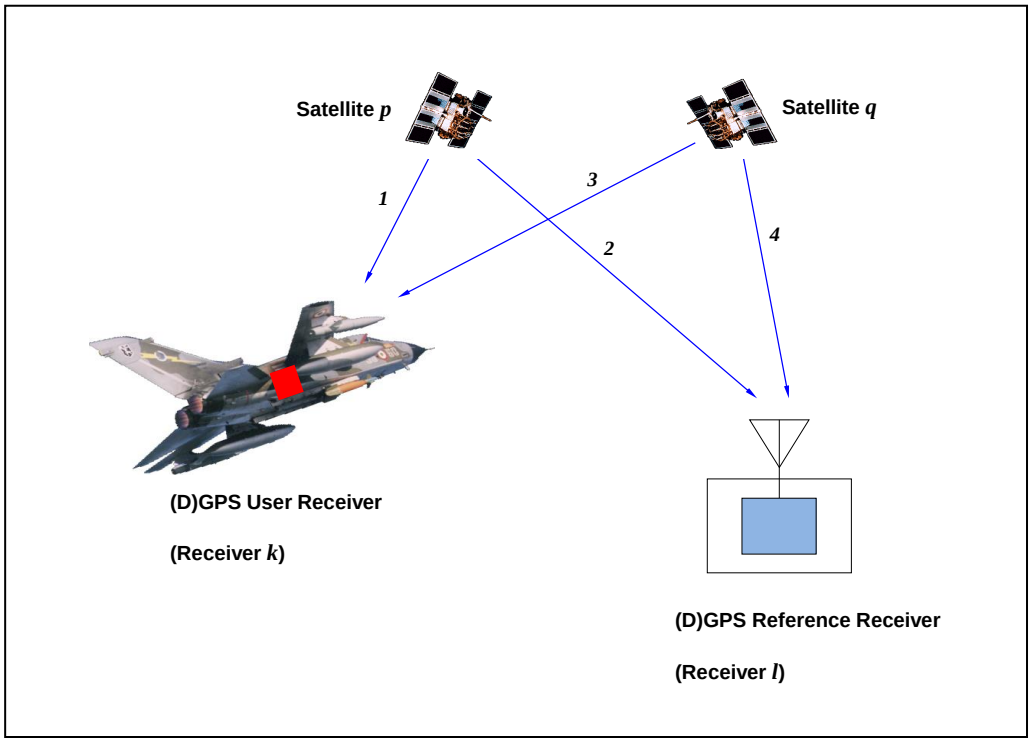


Figure 2-10. Pseudorange differencing.

If pseudoranges 1 and 2 from Figure 2-10 are differenced, then the satellite clock error and satellite orbit errors will be removed. If SA is active (not the present case), it will be removed completely only if the signals utilised in each receiver are transmitted exactly at the same time. The residual error from SA is not a problem for post-processed positioning, where it is easy to ensure that the differencing is done between pseudoranges observed at the same time. Any atmospheric errors will also be reduced significantly with single differencing.

The basic mathematical model for single difference pseudorange observation is the following:

$$P_k^p - P_l^p = \rho_k^p - \rho_l^p - \left(dt_k - dt_l\right)c + d_{k,p} - d_{l,p} + d_{k,p}^p - d_{l,p}^p + \Delta\varepsilon_p \qquad (2.51)$$

where P_i^p is the pseudorange measurement, ρ_i^p denotes the geometric distance between the stations and satellite, dt_i denotes the receiver's clock offsets, $d_{i,p}$ denotes the receiver's hardware code delays, $d_{i,p}^p$ denotes the multipath of the codes, $\Delta\varepsilon_p$ denotes the measurement noise and c is the velocity of light. Equation (2.51) represents the single difference pseudorange observable between receivers. Based on the geometry in Fig. 2-10, another possible type of single difference is between-satellite single difference.

There are four unknowns in equation (2.51) assuming that the co-ordinates of station k are known and that the difference in clock drifts is one unknown. Hence, four satellites are required to provide four single difference equations in order to solve for the unknowns. Single differences with code observations are frequently used in relative (differential) navigation.

Double differences are constructed by taking two between-receiver single differences and differencing these between two satellites. This procedure removes all satellite dependent, receiver dependent and most of the atmospheric errors (if the distance between the two receivers is not too large). The derived equation is:

$$P_k^p - P_k^q - P_l^p - P_l^q = \rho_k^p - \rho_k^q - \rho_l^p - \rho_l^q + d_{i,p}^j \qquad (2.52)$$

where $d_{i,p}^{j}$ denotes the total effect of multipath.

There are three unknowns in Eq. (2.52); the co-ordinates of station *l*. A minimum of four satellites is required to form a minimum of three double difference equations in order to solve for the unknowns. Using the propagation of errors law, it is shown that the double difference observables are twice as noisy as the pure pseudoranges:

$$\sigma_{DD} = \sqrt{\sigma_P^2 + \sigma_P^2 + \sigma_P^2 + \sigma_P^2} = 2\sigma_P \tag{2.53}$$

but they are more accurate, because most of the errors are removed. Note that multipath remains, because it cannot be modelled and it is independent for each receiver.

2.8.2 Carrier-phase DGNSS

The carrier-phase measurement technique uses the difference between the carrier phases measured at the RR and UR. A double-differencing technique is used to remove the satellite and receiver clock errors. The first difference is the difference between the phase measurement at the UR and the RR for a single satellite. This eliminates the satellite clock error which is common to both measurements. This process is then repeated for a second satellite. A second difference is then formed by subtracting the first difference for the first satellite from the first difference for the second satellite. This eliminates both receiver clock errors which are common to the first difference equations. This process is repeated for two pairs of satellites resulting in three double-differenced measurements that can be solved for the difference between the reference station and user receiver locations. This is inherently a relative positioning technique; therefore, the user receiver must know the reference station location to determine its absolute position.

The single difference observable is the instantaneous phase difference between two receivers and one satellite. It is also possible to define single differences between two satellites and one receiver. Using the basic definition of carrier-phase

observable presented above, the phase difference between the two receivers *A* and *B*, and satellite *i* is given by:

$$\Phi^{i}_{AB}(\tau) = \Phi^{i}_{B}(\tau) - \Phi^{i}_{A}(\tau) \tag{2.54}$$

and can be expressed as:

$$\Phi^{i}_{AB}(\tau) = \left(\frac{f}{c}\right) \cdot \rho^{i}_{AB}(t) + \Phi_{AB}(\tau) - N^{i}_{AB} \tag{2.55}$$

where:

$$\Phi_{AB}(\tau) = \Phi_{A}(\tau) - \Phi_{B}(\tau), \quad N^{i}_{AB} = N^{i}_{B} - N^{i}_{A}, \quad \rho^{i}_{AB}(t) = \rho^{i}_{A}(t) - \rho^{i}_{B}(t)$$

Hence, with four satellites *i*, *j*, *k* and *l*:

$$\Phi^{i}_{AB}(\tau) = \left(\frac{f}{c}\right) \cdot \rho^{i}_{AB}(t) + \Phi_{AB}(\tau) - N^{i}_{AB}; \qquad \Phi^{k}_{AB}(\tau) = \left(\frac{f}{c}\right) \cdot \rho^{k}_{AB}(t) + \Phi_{AB}(\tau) - N^{k}_{AB};$$

$$\Phi^{j}_{AB}(\tau) = \left(\frac{f}{c}\right) \cdot \rho^{j}_{AB}(t) + \Phi_{AB}(\tau) - N^{j}_{AB}; \qquad \Phi^{l}_{AB}(\tau) = \left(\frac{f}{c}\right) \cdot \rho^{l}_{AB}(t) + \Phi_{AB}(\tau) - N^{l}_{AB}.$$

The double difference is formed from subtracting two single differences measured to two satellites *i* and *j*. The basic double difference equation is:

$$\Phi^{ij}_{AB}(\tau) = \Phi^{i}_{AB}(\tau) - \Phi^{j}_{AB}(\tau) \tag{2.56}$$

which simplifies to:

$$\Phi^{ij}_{AB}(\tau) = \left(\frac{f}{c}\right) \rho^{ij}_{AB}(t) - N^{ij}_{AB} \tag{2.57}$$

where $N^{ij}_{AB} = N^{j}_{AB} - N^{i}_{AB}$, and the only unknowns being the double-difference phase ambiguity N^{ij}_{AB} and the receiver co-ordinates. The local clock error is differenced out. Two receivers and four satellites *i*, *j*, *k*, and *l*, will give 3 double difference equations containing the co-ordinates of the receivers A (X_A, Y_A, Z_A) and B (X_B, Y_B, Z_B), and the unknown integer ambiguities N^{ij}_{AB}, N^{ik}_{AB}, and N^{il}_{AB}:

$$\Phi^{ij}_{AB}(\tau) = \left(\frac{f}{c}\right) \rho^{ij}_{AB}(t) - N^{ij}_{AB}; \quad \Phi^{jk}_{AB}(\tau) = \left(\frac{f}{c}\right) \rho^{ik}_{AB}(t) - N^{ik}_{AB}; \quad \Phi^{il}_{AB}(\tau) = \left(\frac{f}{c}\right) \rho^{il}_{AB}(t) - N^{il}_{AB}.$$

Therefore, the double difference observation equation can be written as (Ashkenazi, 1995):

$$\begin{aligned}&\frac{\partial\Phi}{\partial X_A}dX_A+\frac{\partial\Phi}{\partial Y_A}dY_A+\frac{\partial\Phi}{\partial Z_A}dZ_A+\frac{\partial\Phi}{\partial X_B}dX_B+\frac{\partial\Phi}{\partial Y_B}dY_B+\frac{\partial\Phi}{\partial Z_B}dZ_B\\&+\frac{\partial\Phi}{\partial N_1}dN_1+\frac{\partial\Phi}{\partial N_2}dN_2+\frac{\partial\Phi}{\partial N_3}dN_3+\frac{\partial\Phi}{\partial C}dC+\ldots=\left(\Phi^O-\Phi^C\right)+v\end{aligned} \tag{2.58}$$

where:

X_A, Y_A, Z_A = Co-ordinates of receiver A;

X_B, Y_B, Z_B = Co-ordinates of receiver B;

N_1, N_2, N_3 = Integer ambiguities;

C = Correction term;

$\left(\Phi^O-\Phi^C\right)$ = Observed minus computed observable;

ν = Residual.

From equation (2.54) the unknown receiver co-ordinates can be computed. It is necessary, however, to determine the carrier phase integer ambiguities (i.e. the integer number of complete wavelengths between the receiver and satellites). In surveying applications, this integer ambiguity can be resolved by starting with the mobile receiver antenna within a wavelength of the reference receiver antenna. Both receivers start with the same integer ambiguity, so the difference is zero and drops out of the double-difference equations. Thereafter, the phase shift that the mobile receiver observes (whole cycles) is the integer phase difference between the two receivers. An alternative is to place the mobile receiver at a surveyed location. In this case the initial difference is not necessarily zero but it is readily calculated.

For aviation applications where it is not possible to bring the reference/mobile antennas together or to position the aircraft at a surveyed location, the reference and mobile receivers must solve for the ambiguities independently as part of an initialisation process. For these applications, it is essential to be able to solve for integer ambiguity at an unknown location and while in motion. In this case, solving for the integer ambiguity usually consists of eliminating incorrect solutions until the

correct solution is found. A good initial estimate of position (such as from ranging-code differential) helps to keep the initial number of candidate solutions small. Redundant measurements over time and/or from extra satellite signals are used to isolate the correct solution. This version of the carrier-phase DGNSS technique is typically called Real-Time Kinematic (RTK) GNSS. If carrier track or phase lock on a satellite is interrupted (cycle slip) and the integer count is lost, then the initialisation process must be repeated for that satellite. Causes of cycle slips can range from physical obstruction of the antenna to sudden accelerations of the aircraft. Output data flow may also be interrupted if the receiver is not collecting redundant measurements form extra satellites to maintain the position solution. If a precise position solution is maintained, re-initialisation for the lost satellite can be very rapid. Developing a robust and rapid method of initialisation and re-initialisation is the primary challenge facing designers of RTK systems that have to deal with safety critical applications such as aircraft precision approach. A description of various techniques for solving ambiguities both in real-time and post-processing applications, together with information about cycle slips repair techniques can be found in the literature (Hatch, 1991), (Euler et al., 1992), (Hansen, 1994), (Euler, 1994), (Walsh, 1994), (Tiberius et al., 1995), (Teunissen, 2003-a), (Teunissen, 2003-b), (Leick, 2003), (Teunissen, 2005), (Verhagen, 2006), (Liu et al., 2014).

2.8.3 DGNSS Data Link Implementations

DGNSS can also be implemented in several different ways depending on the type of data link used. The simplest way is no data link at all. For non-real-time applications, the measurements can be stored in the receiver or on suitable media and processed at a later time. In most cases to achieve surveying accuracies, the data must be post-processed using precise ephemeris data that is only available after the survey data has been collected. Similarly, for some test applications the cost and effort to maintain a real-time data link may be unnecessary. Nevertheless, low-precision real-time outputs can be useful to confirm that a test is progressing properly even if the accuracy of the results will be enhanced later. Differential corrections or measurements can be uplinked in real-time from the reference station to the users.

This is the most common technique where a large number of users must be served in real-time. For military purposes and proprietary commercial services, the uplink can be encrypted to restrict the use of the DGNSS signals to a selected group of users. Differential corrections can be transmitted to the user at different frequencies. With the exception of satellite data links there is generally a trade-off between the range of the system and the update rate of the corrections. As an example Table 2-8 lists a number of frequency bands, the range, and the rate at which the corrections could be updated using the standard RTCM SC-104 format (RTCM, 1990-a), (RTCM, 1990-b), (RTCM, 2011).

Table 2-8. Possible DGNSS data link frequencies.

FREQUENCY	RANGE (KM)	UPDATE RATE (SEC)
LF (30 - 300 kHz)	> 700	< 20
MF (300 kHz - 3 MHz)	< 500	5 – 10
HF (3 MHz - 25 MHz)	< 200	5
VHF (30 MHz - 300 MHz)	< 100	< 5
L Band (1 GHz - 2 GHz)	Line of Sight	Few Seconds

An uplink can be a separate transmitter/receiver system or the DGNSS signals can be superimposed on a GPS-link L-band ranging signal. The uplink acts as a pseudo-satellite or “pseudolite” and delivers the ranging signal and DGNSS data via the RF section of the user receiver, much in the same way the GPS navigation message is transmitted. The advantages are that the additional ranging signal(s) can increase the availability of the position solution and decrease carrier-phase initialisation time. However, the RS and UR’s become more complex, and the system has a very short range (a few kilometres at the most). This is not only because of the line of sight restriction, but also the power must be kept low in order to avoid interference with

the real satellite signals (i.e., the pseudolite can become a GPS jammer if it overpowers the GPS satellite signals).

A downlink option is also possible from the users to the RS or other central collection point. In this case the differential solutions are all calculated at a central location. This is often the case for test range applications where precise vehicle tracking is desired but the information is not used aboard the vehicle. The downlink data can be position data plus the satellite tracked, or pseudorange and deltarange measurements, or it can be the raw GPS signals translated to an intermediate frequency. The translator method can often be the least expensive with respect to user equipment, and therefore is often used in munitions testing where the user equipment may be expendable (Sabatini et al., 2008).

2.8.4 DGNSS Accuracy

Controlled tests and extensive operational use of DGNSS, have repeatedly demonstrated that DGNSS (pseudorange) provides accuracies in the order of 3 to 10 metres. This figure is largely irrespective of receiver type, whether or not SA is in use, and over distances of up to 100 NM from the Reference Station (Sabatini et al. 2008), (Keith, 2000). With RTK positioning systems, requiring the resolution of the carrier phase integer ambiguities whilst on the move, centimetre level accuracy can be achieved (Ashkenazi, 1995), (Moore, 1996-a, b).

Most current applications of DGNSS use L1 C/A code pseudorange as the only observable, with achieved accuracies of 1 to 5 m in real-time. Other applications use dual frequency pseudoranges (e.g., C/A and P code from GPS) or combinations of pseudorange and carrier phase observables. Various techniques have been developed that achieve increased accuracy at the expense of increased complexity. A possible classification scheme of these techniques is presented in Table 2-9. Precise DGNSS (PDG) can achieve accuracies below 1 m using dual-frequency pseudorange measurements and Very Precise DGNSS (VPDG), taking advantage of both dual frequency code and carrier phase observables, is capable of On-The-Fly (OTF) ambiguity resolution (Walsh, 1994), (Euler, 1994). At the moment, Ultra-Precise

DGNSS (UPDG) using carrier phase observables with integer ambiguities resolved is only utilised in flight testing, flight inspection and other non-real-time aviation applications.

Table 2-9. Possible classification scheme of DGNSS techniques.

NAME	DESCRIPTION	RMS
DGNSS	Single frequency pseudorange (e.g., GPS C/A code)	1 - 5 m
PDG	Dual frequency pseudorange (e.g., GPS P code)	0.1 - 1 m
VPDG	Addition of dual band carrier phase	5 - 30 cm
UPDG	Above with integer ambiguities resolved	< 2 cm

In the absence of Selective Availability (SA), the major sources of error for stand-alone ranging-code GNSS are:

- Ephemeris Error;
- Ionospheric Propagation Delay;
- Tropospheric Propagation Delay;
- Satellite Clock Drift;
- Receiver Noise and clock drift;
- Multipath.

Table 2-10 lists the error budgets from the above sources giving an estimation of the possible improvements provided by L1 ranging-code DGNSS (Moore, 1996). The error from multipath is site dependent and the value in Table 2-10 is only an example. The receiver clock drift is not mentioned in Table 2-10, because it is usually treated as an extra parameter and corrected in the standard solution. Furthermore, it does not significantly add to differential errors. Multipath and receiver noise errors cannot be corrected by DGNSS. It is worth to mention that the errors introduced by SA (currently off) would be corrected by DGNSS techniques.

Table 2-10. Error sources in DGNSS.

ERROR SOURCE	STANDALONE GNSS (m)	L1 C/A CODE DGNSS (m)
Ephemeris	5 - 20	0 – 1
Ionosphere	15 - 20	2 – 3
Troposphere	3 - 4	1
Satellite Clock	3	0
Multipath	2	2
Receiver Noise	2	2

For users near the reference station, the respective signal paths to the satellite are close enough together that the compensation of Ionospheric and Tropospheric Delays (ITD) is almost complete. As the user to RS separation is increased, the different ionospheric and tropospheric paths to the satellites can be far enough apart that the ionospheric and tropospheric delays are no longer common errors. Thus, as the distance between the RS and user receiver increases the effectiveness of the atmospheric delay corrections decreases. The ephemeris error is effectively compensated unless it has quite a large out-of-range component (e.g., 1000 metres or more due to an error in a satellite navigation message). Even then, the error will be small if the distance between the reference receiver and user receiver is small. Finally, the satellite clock error is compensated as long as both reference and user receivers employ the same satellite clock correction data.

As already mentioned, the correlation of the errors experienced at the RS and the user location is largely dependent on the distance between them. As the separation of the user from the RS increases, so does the probability of significant differing ionospheric and tropospheric conditions at the two sites. Similarly, the increasing separation also means that a different geometrical component of the ephemeris error is seen by the RR and UR. This is commonly referred to as "spatial decorrelation" of the ephemeris and atmospheric errors. In general, the errors are likely to remain highly correlated for users within 350 km of the RS. However, if the distance is greater than 250 km the user will obtain better results using correction models for

ionospheric and tropospheric delay (Sabatini et al. 2008), (Keith, 2000). Additionally, practical DGNSS systems are typically limited by the data link to an effective range of around 170 km. Table 2-11 shows the error budget determined for a SPS DGNSS system with increasing distances from the RR (Sabatini et al, 2008).

Table 2-11. DGNSS L1 pseudorange errors (ft) with increasing distance from RS.

ERROR SOURCES	0 NM	100 NM	500 NM	1000 NM
Space Segment:				
Clock Errors	0	0	0	0
Control Segment:				
Ephemeris Errors	0	0.3	1.5	3
Propagation Errors:				
Ionosphere	0	7.2	16	21
Troposphere	0	6	6	6
TOTAL (RMS)	**0**	**9.4**	**17**	**22**
User Segment:				
Receiver Noise	3	3	3	3
Multipath	0	0	0	0
UERE (RMS)	**3**	**9.8**	**17.4**	**22.2**

Since the RR noise and multipath errors are included in the differential corrections and become part of the user's error budget (root-sum-squared with the user receiver noise and multipath errors), the receiver noise and multipath error components in the non-differential receiver can be lower than the correspondent error components experienced in the DGNSS implementation. Another type of error introduced in real-time DGNSS positioning systems is the data link's "age of the corrections." This error is introduced due to the latency of the transmitted corrections (i.e., the transmitted corrections of epoch t_0 arrive at the moving receiver at epoch $t_0 + dt$). These corrections are not the correct ones, because they were calculated under different conditions. Hence, the co-ordinates of the UR would be slightly offset.

DGNSS systems that compensate for accuracy degradations over short distances (typically up to the RS-UR Line-of-Sight (LOS) employing V/UHF data links) are referred to as Local Area DGNSS (LAD). DGNSS systems covering large geographic areas are referred to as Wide Area DGNSS (WAD) systems. They usually employ a network of reference receivers that are coordinated to provide DGNSS data over a wide coverage area. Such systems typically are designed to broadcast the DGNSS data via satellite, although a network of ground transmission sites is also feasible. A user receiver typically must employ special algorithms to derive the ionospheric and tropospheric corrections that are appropriate for its location from the observations taken at the various reference sites.

Various countries including the United States, Canada, Europe, Japan, China, India and Australia have developed LAD/WAD systems. Some of these systems transmit DGNSS data from geostationary satellites for use by commercial navigation users, including the aviation community. Some commercial DGNSS services also broadcast data from multiple reference stations via satellite. However, several such systems remain a group of LAD rather than WAD systems. This is because the reference stations are not integrated into a network allowing the user accuracy to degrade with distance from the individual reference sites.

2.8.5 RTK Evolution and Precise Point Positioning

Although centimetre-level GNSS accuracy is increasingly relevant for a number of aviation and other safety-of-life applications, the possible adoption of RTK techniques in the aviation context is still being researched and no RTK systems are contemplated by the current ICAO standards for air navigation use. From an operational perspective, the main inconvenience of the RTK technique is that it requires a reference station relatively close to the user so that the differential ionospheric delay is negligible. High-accuracy single-baseline RTK solutions are generally limited to a distance of about 20 km (Zhang et al., 2006), although test activities have shown that acceptable results can be achieved over up to 50 km in times of low ionospheric activity (Janssen and Haasdyk, 2011).

A way of partially overcoming such inconvenience is the Network RTK (NRTK) technique, which uses a network of ground reference stations to mitigate atmospheric dependent effects over long distances. The NRTK solution is generally based on between three and six of the closest reference stations with respect to the user and allows much greater inter-station distances (up to 70-90 km) while maintaining a comparable level of accuracy (Janssen and Haasdyk, 2011).

The Wide Area RTK (WARTK) concept was introduced in the late 1990s to overcome the need of a very dense network of reference stations. WARTK techniques provide accurate ionospheric corrections that are used as additional information and allow increasing the RTK service area. In this way, the system needs reference stations separated by about 500–900 kilometres (Juan et al., 1997).

Precise Point Positioning (PPP) is a further carrier-phase GNSS technique that departs from the basic RTK implementation and uses differencing between satellites rather than differencing between receivers. Clearly, in order to be implemented, PPP requires the availability of precise reference GNSS orbits and clocks in real-time. Combining the precise satellite positions and clocks with a dual-frequency GNSS receiver (to remove the first order effect of the ionosphere), PPP is able to provide position solutions at centimetre level (Bisnath and Gao, 2009). PPP differs from double-difference RTK/NRTK positioning in the sense that it does not require access to observations from one or more close reference stations accurately-surveyed. PPP just requires data from reference stations from a relatively sparse station network (thousands of kilometres apart would suffice). This makes PPP a very attractive alternative to RTK especially in long-distance aviation applications where RTK/NRTK coverage would be impractical. However, PPP techniques are still not very mature and typically require a longer convergence time (20-30 minutes) to achieve centimetre-level performance (Bisnath and Gao, 2009). Another possibility is to use local ionospheric corrections in PPP. This approach would reduce convergence time to about 30 seconds and contribute to an augmented integrity. However, they would also require a density of reference networks similar to that of NRTK (Jokinen, 2014).

2.9 GNSS INTEGRITY AUGMENTATION

According to the US Federal Radionavigation Plan, "integrity is a measure of the trust that can be placed in the correctness of the information supplied by a navigation system. Integrity includes the ability of the system to provide timely warnings to users when the system should not be used for navigation." This definition is very comprehensive but, unfortunately, it is too generic and this is why many research efforts were undertaken in the past to better specify the GNSS integrity performance metrics. Previous research has effectively developed and applied statistical criteria to inflate the navigation error bounds in specific flight phases. So, while accuracy is typically specified at 95% (2σ) confidence level, integrity requirements normally refer to percentiles of 99.999% (6σ) or higher depending on the particular phase of flight/application (ESA, 2011a). The intention behind this is to keep the probability of hazardous events (that could possibly put at risk human lives) extremely low. From a system performance perspective, integrity is intended as a real-time decision criterion for using or not using the system. For this reason, it has been a common practice to associate integrity with a mechanism, or set of mechanisms (barriers) that is part of the integrity assurance chain but at the same time is completely independent of the other parts of the system for which integrity is to be assured.

Consequently, the concepts of Alert Limit, Integrity Risk, Protection Level and Time to Alert were introduced and are currently reflected in the applicable ICAO SARPs and in the RTCA standards for WAAS and LAAS. These integrity performance metrics are:

- ***Alert Limit (AL):*** The alert limit for a given parameter measurement is the error tolerance not to be exceeded without issuing an alert.
- ***Time to Alert (TTA):*** The maximum allowable time elapsed from the onset of the navigation system being out of tolerance until the equipment enunciates the alert.
- ***Integrity Risk (IR):*** Probability that, at any moment, the position error exceeds the Alert Limit.

- ***Protection Level (PL):*** Statistical bound error computed so as to guarantee that the probability of the absolute position error exceeding said number is smaller than or equal to the target integrity risk.

As discussed above, integrity is the ability of a system to provide timely warnings to users when the system should not be used for navigation (US DoT/DoD, 2001). In general, it is essential to guarantee that, with a specified probability P, either the horizontal/vertical radial position error does not exceed the pre-specified thresholds (HAL/VAL), or an alarm is raised within a specified TTA interval when the horizontal/vertical radial position errors exceed the thresholds. To detect that the error is exceeding a threshold, a monitor function has to be installed within the navigation system. This is also the case within GNSS systems in the form of the ground segment. However, for GNSS systems, TTA is typically in the order of several hours, that is even too long for the cruise where a TTA of 60 seconds is required (an autoland system for zero meter vertical visibility must not exceed a TTA of 2 seconds). Various methods have been proposed and practically implemented for stand-alone GNSS integrity monitoring. A growing family of such implementations, already very popular in aviation applications, includes the so called Receiver Autonomous Integrity Monitoring (RAIM) techniques. Details about RAIM can be found in the literature (Kalafus, 1987), (Walter et al., 1995), (Parkinson et al., 1996), (GPS JPO, 1997), (Brown, 1992), (Kelly, 1998), (Parkinson et al., 1988), (Brown et al., 1998). Regarding DGNSS, it should be underlined that it does more than increasing GNSS positioning accuracy; it also contributes to enhancing GNSS integrity by compensating for anomalies in the satellite ranging signals and navigation data message. The range and range rate corrections provided in the ranging-code DGNSS correction message can compensate for ramp and step type anomalies in the individual satellite signals, until the corrections exceed the maximum values or rates allowed in the correction format. If these limits are exceeded, the user can be warned not to use a particular satellite by placing "do-not-use" bit patterns in the corrections for that satellite (as defined in STANAG 4392 or RTCA/RTCM message formats) or by omitting the corrections for that satellite.

As mentioned before, step anomalies will normally cause carrier-phase DGNSS receivers to lose lock on the carrier phase, causing the reference and user receivers to reinitialise. UR noise, processing anomalies, and multipath at the user GPS antenna cannot be corrected by a DGNSS system. These errors are included in the overall DGNSS error budget. Errors in determining or transmitting the satellite corrections may be passed on to the differential user if integrity checks are not provided within the RS. These errors can include inaccuracies in the RS antenna location that bias the corrections, systematic multipath due to poor antenna sighting (usually in low elevation angle satellites), algorithmic errors, receiver inter-channel bias errors, receiver clock errors and communication errors. For these reasons, typical WAD and LAD RS designs also include integrity checking provisions to guarantee the validity of the corrections before and after broadcast.

In the aviation context, various strategies have been developed for increasing the levels of integrity of DGNSS based navigation/landing systems. These include both Space Based Augmentation Systems (SBAS) and Ground Based Augmentation Systems (GBAS) to assist aircraft operations in all flight phases (Fig. 2-11).

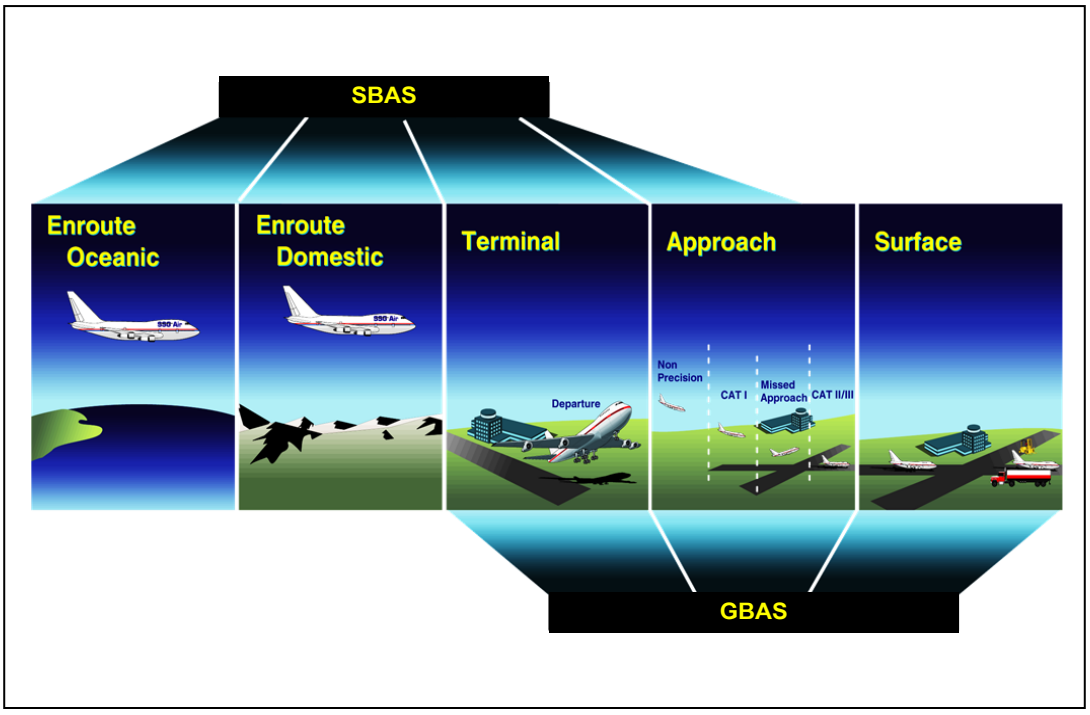


Figure 2-11. GBAS and SBAS services. Adapted from (Skillicorn, 2003).

These systems are effectively WAD and LAD systems that employ, respectively, DGNSS vector correction (SBAS) and scalar (pseudorange) correction techniques (GBAS). Some information about SBAS and GBAS relevant to this thesis are provided in the following sections of this chapter. However, before examining the characteristics of GNSS integrity augmentation systems, it is useful to recall the definitions relative to Failure Detection and Exclusion (FDE).

Fig. 2-12 shows the different conditions associated with FDE.

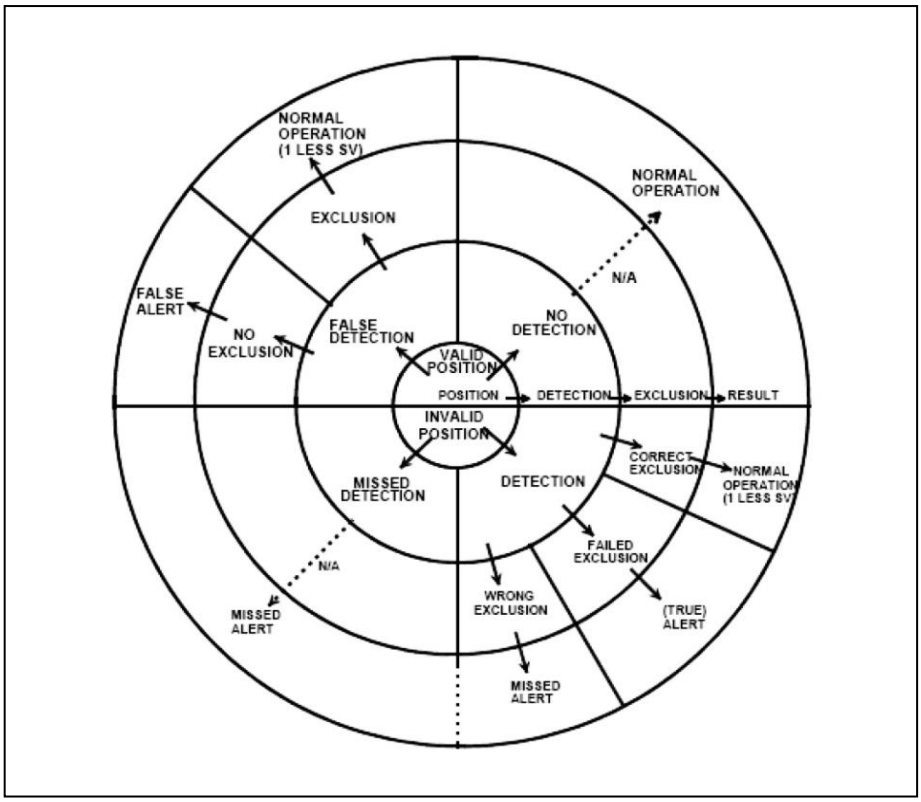


Figure 2-12. FDE Events (RTCA, 2008-a).

The various FDE events are defined as follows (RTCA, 2006-a):

- ***Alert:*** defined to be an indication that is provided by the GNSS equipment when the positioning performance achieved by the equipment does not meet the integrity requirements.
- ***Positioning failure:*** defined to occur whenever the difference between the

true position and the indicated position exceeds the applicable alert limit.

- ***False detection:*** defined as the detection of a positioning failure when a positioning failure has not occurred.
- ***Missed detection:*** defined to occur when a positioning failure is not detected.
- ***Failed exclusion:*** defined to occur when true positioning failure is detected and the detection condition cannot be eliminated within the time-to-alert. A failed exclusion would cause an alert.
- ***Wrong exclusion:*** defined to occur when detection occurs and a positioning failure exists but is undetected after exclusion, resulting in a missed alert.
- ***False alert:*** defined as the indication of a positioning failure when a positioning failure has not occurred. False alerts result from false detections.
- ***Missed alert:*** defined as a positioning failure which is not enunciated as an alert within the time-to-alert. Both missed detection and wrong exclusion can cause missed alerts.

As discussed above, GNSS satisfies the horizontal and vertical integrity requirements for the intended operation when HPL and VPL are below the specified HAL and VAL. This situation is depicted in Fig. 2-13.

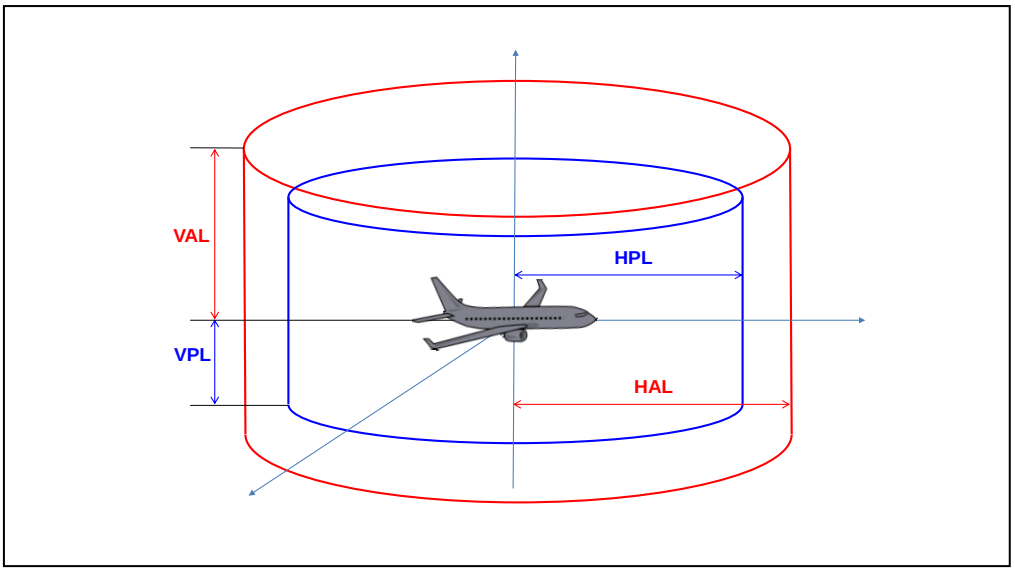


Figure 2-13. Protection levels and alert limits.

The horizontal plane in Fig. 2-13 is locally tangent to the navigation system geodetic reference (e.g., WGS84 ellipsoid in GPS). The vertical axis is locally perpendicular to the same reference. Whenever HPL or VPL exceed HAL or VAL, the integrity required to support the intended operation is not provided and an alert must be issued by the GNSS equipment within the specified TTA. In some unfavourable occasions, the NSE exceeds the HPL/VPL values. In these cases, it is said that an integrity event has occurred and that the system is providing unreliable information, classified as Misleading Information (MI) or Hazardously Misleading Information (HMI).

The difference between MI and HMI is highlighted in Fig. 2-14. As discussed, availability is the probability that the navigation system is operational during a specific flight phase (i.e., the accuracy and integrity provided by the system meet the requirements for the desired operation). Therefore, the navigation system is considered available for use in a specific flight operation if the PLs it is providing are inferior to the corresponding specified ALs for that same operation.

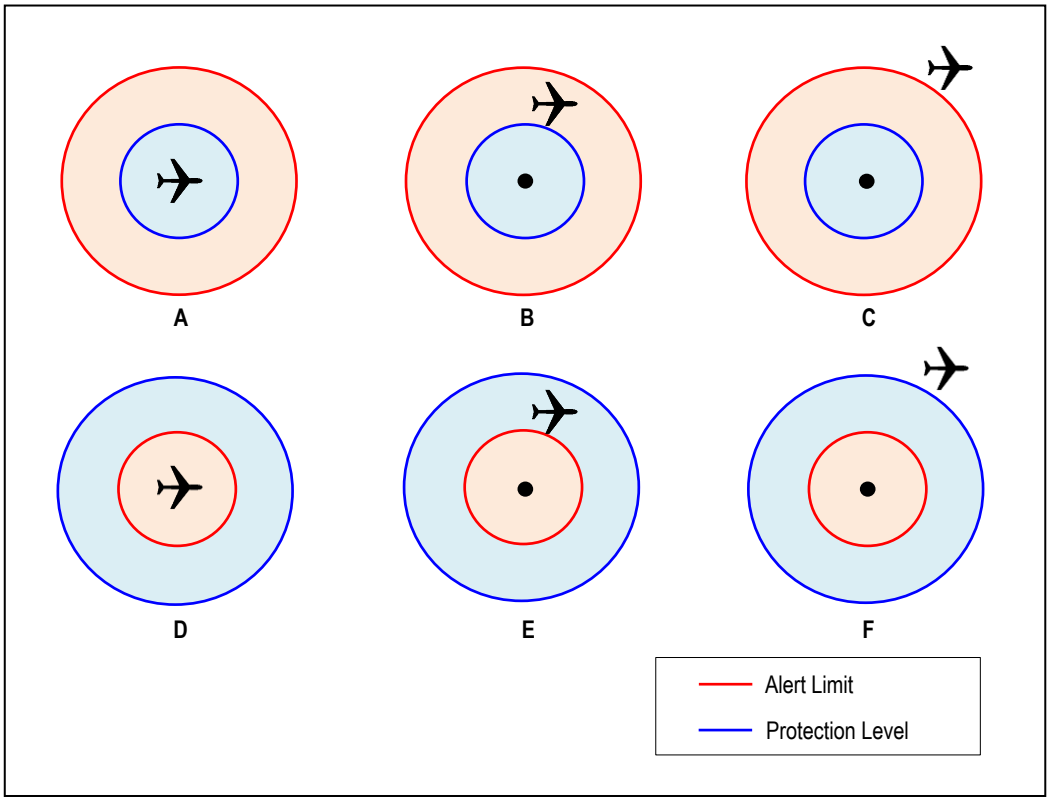


Figure 2-14. Protection levels and alert limits.

The circumferences shown in Fig. 2-14 have their centres at the estimated aircraft position and their radii are the system PLs (blue) and the operation ALs (red). The aircraft shape represents the actual position, so the navigation system error is the distance from the centre of the circumferences to this shape. According to the previous definitions, situations B, C and F represent integrity events. In particular, case B is a MI event and cases C/F are HMI events. The desirable situation is represented by case A. Particular attention should be given to situations B and especially C (which is the most feared situation), as no alert is provided to the user for the unavailability of the system and, depending on the flight operational task, this may lead to a Safety-of-Life (SoL) risk.

2.10 SPACE BASED AUGMENTATION

SBAS is a form of WAD that augments core satellite constellations by providing ranging, integrity and correction information via geostationary satellites.

An SBAS typically comprises (ICAO, 2005):

- a network of ground reference stations that monitor satellite signals;
- master stations that collect and process reference station data and generate SBAS messages;
- uplink stations that send the messages to geostationary satellites;
- transponders on these satellites that broadcast the SBAS messages.

By providing differential corrections, extra ranging signals via geostationary satellites and integrity information for each navigation satellite, SBAS delivers much higher levels of service than the core satellite constellations. In certain configurations, SBAS can support approach procedures with vertical guidance (APV). There are two levels of APV: APV I and APV II. Both use the same lateral obstacle surfaces as localizers; however APV II may have lower minima due to better vertical performance. There will nonetheless be only one APV approach to a runway end, based on the level of service that SBAS can support at an aerodrome. The two APV approach types are identical from the perspective of avionics and pilot

procedures. In many cases, SBAS supports lower minima than that associated with non-precision approaches, resulting in higher airport usability. Almost all SBAS approaches feature vertical guidance, resulting in a significant increase in safety. APV minima (down to a Decision Height (DH) of 75 m (250 ft) approximately) are higher than Category I minima, but APV approaches do not require the same ground infrastructure, so this increase in safety is affordable at most airports. SBAS availability levels allow operators to take advantage of SBAS instrument approach minima when designating an alternate airport. Notably, SBAS approach does not require any SBAS infrastructure at an airport. SBAS can support all en-route and terminal RNAV operations for a wide cross section of users. This will allow a reorganization of the airspace for maximum efficiency and capacity, allowing aircraft to follow the most efficient flight path between airports. High availability of service will permit the decommissioning of traditional radionavigation aids, resulting in lower costs. There are four SBASs currently in service:

- the North American Wide Area Augmentation System (WAAS);
- the European Geostationary Navigation Overlay Service (EGNOS);
- the Indian GPS and Geostationary Earth Orbit (GEO) Augmented Navigation (GAGAN) System;
- the Japanese Multi-functional Transport Satellite (MTSAT) Satellite-based Augmentation System (MSAS).

Other SBAS currently under study or developments include the Russian System for Differential Correction and Monitoring (SDCM), the South/Central American and Caribbean SACCSA (Solución de Aumentación para Caribe, Centro y Sudamérica), the Chinese Satellite Navigation Augmentation System (SNAS), the Malaysian Augmentation System (MAS) and various programs in the African and Indian Ocean (AFI) region. The approximate coverage areas of the various SBAS are shown in Fig. 2-15. Although Australia, Indonesia, New Zealand and various other nations in the southern portion of the Asia-Pacific region have not announced SBAS development programs, the extension of systems such as MSAS, GAGAN and SNAS could provide SBAS coverage in these areas.

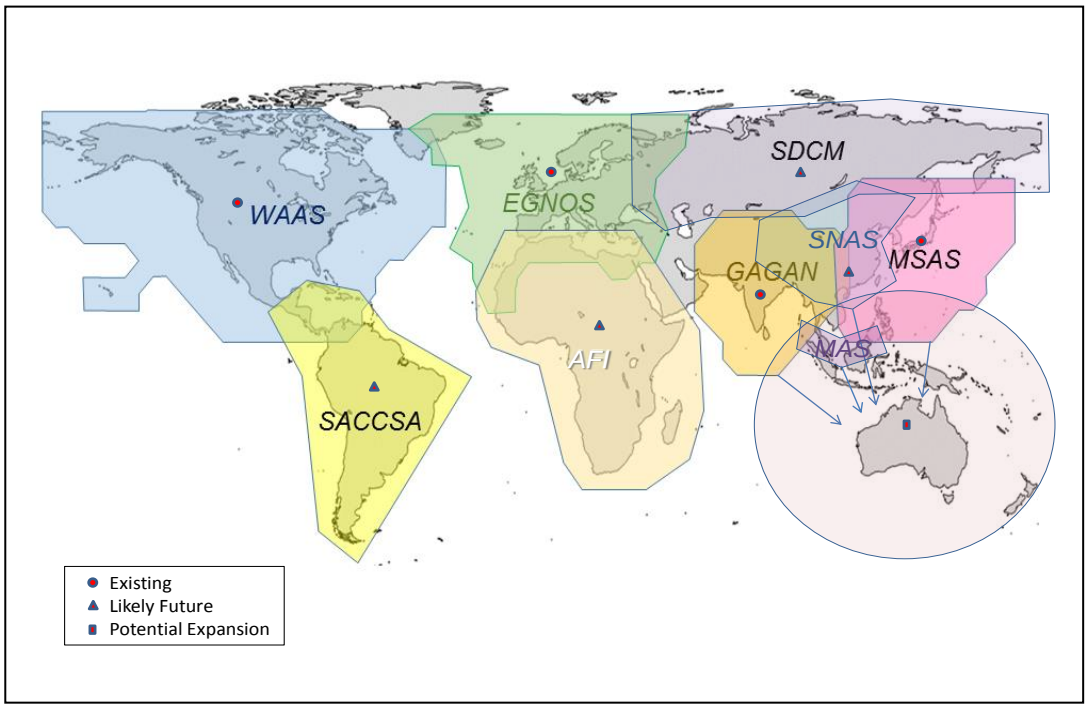


Figure 2-15. Current and possible future SBAS coverage. Adapted from (ESA, 2011b).

Within the coverage area of SBAS, ICAO member states may establish service areas where SBAS supports approved operations. Other States can take advantage of the signals available in the coverage area by fielding SBAS components integrated with an existing SBAS or by authorizing the use of SBAS signals. The first option offers some degree of control and improved performance. The second option lacks any degree of control, and the degree of improved performance depends on the proximity of the host SBAS to the service area. In either case, the nation that has established an SBAS service area, should assume responsibility for the SBAS signals within that service area. This requires the provision of NOTAM information services.

If ABAS-only operations are approved within the coverage area of SBAS, SBAS avionics will also support ABAS operations. Although the architectures of the various existing SBASs are different, they broadcast the standard message format on the same frequency (GPS L1) and so are interoperable from the user's perspective. It is anticipated that these SBAS networks will expand beyond their initial service areas. As discussed, other SBAS networks may also be developed and become operational. When SBAS coverage areas overlap, it is possible for an SBAS operator

to monitor and send integrity and correction messages for the geostationary satellites of another SBAS, thus improving availability by adding ranging sources.

As the American WAAS has been developed in line with ICAO SARPs and RTCA MOPS (ICAO, 2001),. As the GBAS technology considered in this thesis is based on the RTCA WAAS standards (RTCA, 2006-a), which are also aligned with the ICAO SARPs for SBAS (ICAO, 2006). Therefore, GBAS and WAAS will be used interchangeably in the rest of this thesis. The aim of WAAS is to provide augmentation signals to correct some of the main GNSS errors and providing the following services:

- Position correction (ECEF coordinates);
- Ionospheric grid correction;
- Long term ephemeris error correction;
- Short term and long term satellite clock error correction;
- Integrity information.

As illustrated in Fig. 2-16, WAAS consists of four elements:

- ***A ground segment:*** composed by a network of ground reference stations and uplink stations. The reference stations, which are called Wide-area Reference Stations (WRS), are responsible for the analysis of GNSS signals and for producing ranging corrections and integrity signals. The uplink stations are responsible for sending regular corrections/integrity signal updates to the space segment;
- ***A space segment:*** composed by different satellites in geostationary orbits and broadcast the ranging corrections and integrity signals to the WAAS users;
- ***A user segment:*** users equipped with WAAS enabled GNSS receivers, which use the information broadcast from GNSS satellites to compute Position, Velocity and Time (PVT) and WAAS signals broadcast from the space segment to improve position accuracy (applying ionospheric corrections) and integrity of the navigation solution.

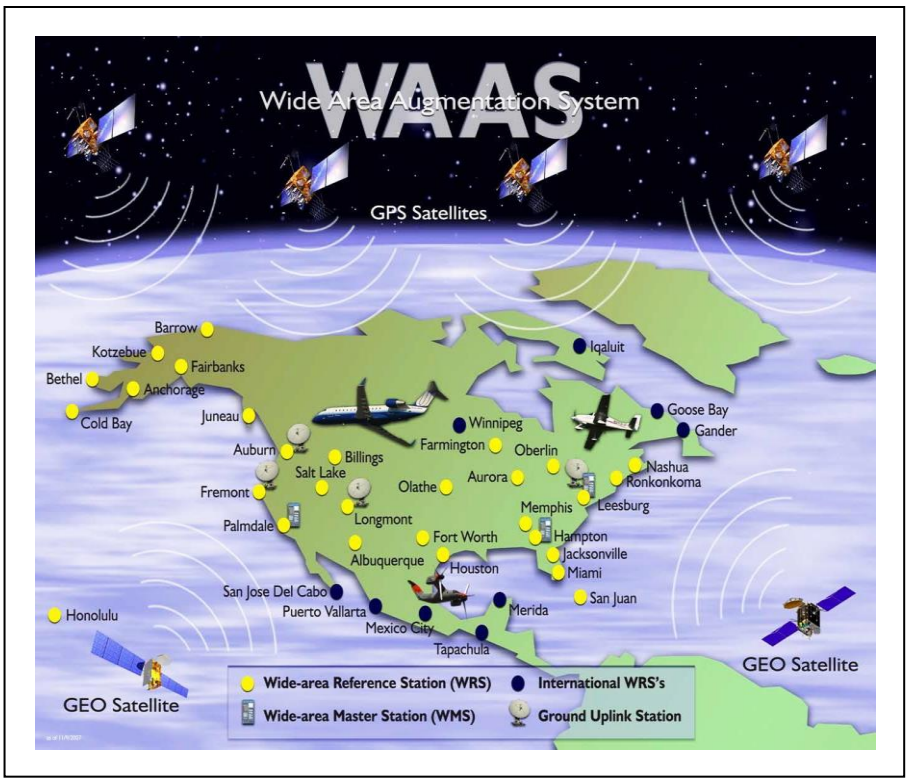


Figure 2-16. WAAS Architecture and Operational Environment (DoT/FAA, 2008).

This correction evaluation, together with the correction of other parameters such as ephemeris error and clock error, allow WAAS to provide to the user a position accuracy of about 7.6 meters (2-D RMS) or better both for lateral and vertical measurements (RTCA, 2006-a). This permits WAAS to achieve, under certain conditions, accuracy levels compatible with CAT-I precision approach requirements. As the CAT-I capability required significant efforts for certification, a new Precision Approach sub-mode was defined called Approach Operations with Vertical Guidance (APV), giving an intermediate precision approach between NPA (Non Precision Approach) and CAT-I. This is further divided in APV-I and APV-II (see Table 2-4 above).

Ionospheric delay is one of the major error sources of pseudorange, as described in this chapter. The WAAS ionospheric delay corrections are broadcast as vertical delay estimates at specified ionospheric grid points (IGPs), applicable to a signal on L1. The WAAS Reference Stations (WRSs) measure the slant ionospheric delays to all satellites in view. These measurements must be translated into a form that can be

applied by the user because the user will have a different line of sight to the satellite than the WRSs.

WAAS uses a two-dimensional grid model to represent the vertical ionospheric delay distribution (RTCA, 2006-a). Ten different bands are used to allow a regular spacing of IGPs. The 1808 possible IGP locations in bands 0-8 are illustrated in Fig. 2-17 (there are 384 additional IGP locations in bands 9-10 not shown). In the bands 0-8, the IGPs are spaced 5° apart from each other both in longitude and latitude for latitudes up to N55° and S55°. Above 55° and up to 75° in latitude the IGPs are spaced 10° from each other both in longitude and in latitude. At S85° and N85° (around the poles), the IGPs are spaced 90°. In the bands 9-10, the IGP grid at 60° has 5° longitudinal spacing, increasing tp 10° spacing at 65°, 70° and 75°, and finally becoming 30° at N85° and S85° round the poles. To accommodate an even distribution of bands, IGPs at 85° are offset by 40° in the 0-8 bands and 10° in the 9-10 bands. The IGPs error data are transmitted in Message 26 and denoted in terms of GIVEI (Grid Ionospheric Vertical Error Indicator), which corresponds to specific values of Grid Ionospheric Vertical Error (GIVE) and GIVE variance ($\sigma^2_{i,GIVE}$). The $GIVEI_i$, $GIVE_i$ and the $\sigma^2_{i,GIVE}$ are listed in Table 2-12.

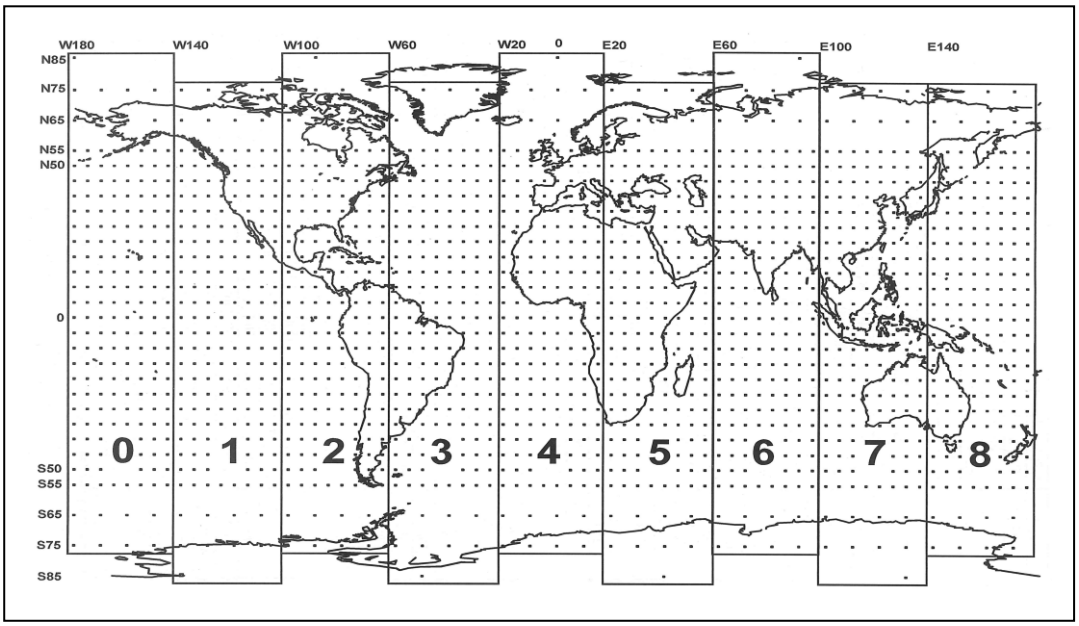


Figure 2-17. WAAS IGPs for bands 0-8 (RTCA, 2006-a).

Table 2-12. Evaluation of GIVEIi (RTCA, 2006-a).

$GIVEI_i$	$GIVE_i$ [m]	$\sigma^2_{i,GIVE}$ [m²]
0	0.3	0.0084
1	0.6	0.0333
2	0.9	0.0749
3	1.20	0.1331
4	1.5	0.2079
5	1.8	0.2994
6	2.1	0.4075
7	2.4	0.5322
8	2.7	0.6735
9	3.0	0.8315
10	3.6	1.1974
11	4.5	1.8709
12	6.0	3.3260
13	15.0	20.7870
14	45.0	187.0826
15	Not Monitored	Not Monitored

The GIVE is used to calculate the User Ionospheric Vertical Error (UIVE) and the User Ionospheric Range Error (UIRE). The UIVE and UIRE are, respectively, the confidence bounds on the user vertical and range errors due to the ionosphere. Both the UIVE and UIRE are referred to the Ionospheric Pierce Point (IPP) location. The IPP is defined as the intersection of the line segment from the receiver to the satellite and an ellipsoid with constant height of 350 km above the WGS-84 ellipsoid. Fig. 2-18 shows the relationship between user location and IPP location (RTCA, 2006-a).

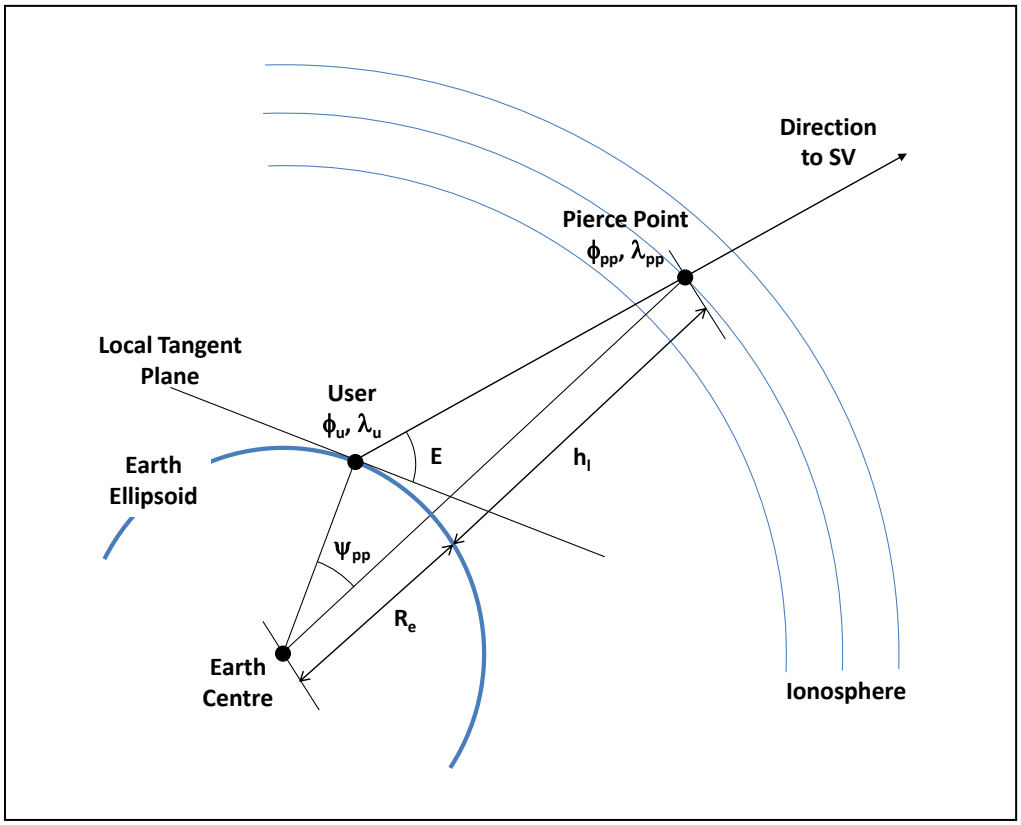


Figure 2-18. Ionospheric Pierce Point Geometry (RTCA, 2006-a).

The latitude of the IPP is given by:

$$\phi_{pp} = \sin^{-1}\left(\sin\phi_u \cos\psi_{pp} + \cos\phi_u \sin\psi_{pp} \cos A\right) \quad \text{[rad]} \qquad (2\text{-}49)$$

where:

ϕ_u = User location latitude;

A = Azimuth angle of the satellite from the user's location (ϕ_u, λ_u) measured clockwise from north.

ψ_{pp} = Earth's central angle between the user position and the projection of the pierce point.

If $\phi_u > 70°$ and $tan\psi_{pp} cosA > tan(\pi/2 - \phi_u)$ or $\phi_u < -70°$ and $tan\psi_{pp}\cos(A + \pi) > tan(\pi/2 + \phi_u)$, the longitude of the IPP is given by:

$$\lambda_{pp} = \lambda_u + sin^{-1}\left(\frac{\sin\psi_{pp}}{\cos\phi_{pp}} \sin A\right) \quad \text{[rad]} \qquad (2\text{-}50)$$

Otherwise:

$$\lambda_{pp} = \lambda_u + sin^{-1}\left(\frac{\sin\psi_{pp}}{\cos\phi_{pp}}\sin A\right) \quad [\text{rad}] \tag{2-50}$$

ψ_{pp} is given by:

$$\psi_{pp} = \frac{\pi}{2} - E - sin^{-1}\left(\frac{R_e}{R_e+h_I}\cos E\right) \quad [\text{rad}] \tag{2-51}$$

where:

E = Elevation angle of the satellite form the user's location measured with respected to the local tangent plane.

R_e = Approximate Earth radius (assumed to be 6378.163 km).

h_I = Height of the maximum electron density (assumed to be 350 km).

Fig. 2-19 shows the principles adopted for interpolation of the IPPs.

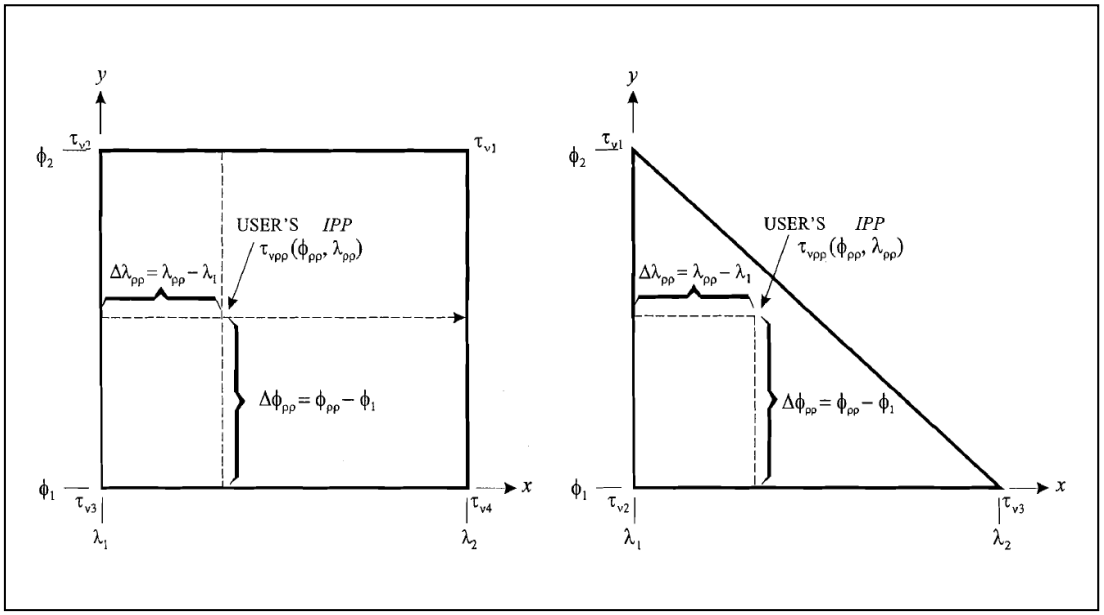


Figure 2-19. Principle of Interpolation of the IPPs (RTCA, 2006-a).

The variance of UIVE can be calculated using one of the following formulas (RTCA, 2006-a):

$$\sigma^2_{UIVE} = \sum_{n=1}^{4} W_n(x_{pp}, y_{pp}) \cdot \sigma^2_{n,ionogrid} \tag{2-52}$$

$$\sigma_{UIVE}^2 = \sum_{n=1}^{3} W_n(x_{pp}, y_{pp}) \cdot \sigma_{n,ionogrid}^2 \quad (2\text{-}53)$$

where $\sigma_{n,ionogrid}^2$ is the model variance of inospheric vertical delays at an IGP. As indicated in the WAAS MOPS (RTCA, 2006-a), a dedicated model can be used to calculate both fast and long-term correction degradation components for inclusion in Message Types (MT) 7 and 10.

If the degradation model is not implemented, the basic WAAS ionospheric model is used by taking $\sigma_{n,ionogrid}^2 = \sigma_{GIVE}^2$. For the i[th] satellite, the variance of UIRE is then calculated as follows:

$$\sigma_{i,UIRE}^2 = F_{pp}^2 \cdot \sigma_{i,UIVE}^2 \quad (2\text{-}54)$$

where F_{pp} is the obliquity factor given by:

$$F_{pp} = \left[1 - \left(\frac{R_e \cos E}{R_e + h_I}\right)^2\right]^{-\frac{1}{2}} \quad (2\text{-}55)$$

In terms of WAAS integrity features, MTs 27 and 28 are particularly important. Type 27 Messages may be transmitted to correct the σ_{UDRE} in selected areas. Each Type 27 Message specifies $\delta UDRE$ correction factors to be applied to integrity monitoring algorithms of users when inside or outside of a set of geographic regions defined in that message. $\delta UDRE$ indicators are associated with the $\delta UDRE$ values listed in Table 2-13 that multiply the model standard deviation defined using the UDREI parameters in the WASS MTs 2-6 and MT 24.

As an alternative to Message 27, a service provider might broadcast MT 28 (not both) to update the correction confidence as a function of user location. MT 28 provides increased availability inside the service volume and increased integrity outside. The covariance matrix is a function of satellite location, reference station observational geometry, and reference station measurement confidence. Consequently it is a slowly changing function of time. Each covariance matrix only needs to be updated on the same order as the long-term corrections. Each message is capable of containing relative covariance matrices for two satellites. This maintains the real-time six-second updates of integrity and scales the matrix to keep it within a reasonable dynamic range.

Table 2-13. $\delta UDRE$ Indicators and values in MT 27.

$\delta UDRE$ Indicator	$\delta UDRE$
0	1
1	1.1
2	1.25
3	1.5
4	2
5	3
6	4
7	5
8	6
9	8
10	10
11	20
12	30
13	40
14	50
15	100

Cholesky factorization is used to reliably compress the information in the covariance matrix (C). This factorization produces 4x4 an upper triangular matrix (R), which can be used to reconstruct the relative covariance matrix as follows:

$$\mathbf{C} = \mathbf{R}^{\mathrm{T}}\mathbf{R} \tag{2.56}$$

Cholesky factorization guarantees that the received covariance matrix remains positive-definite despite quantization errors. Because $\mathbf{R}$ is upper triangular, it contains only 10 non-zero elements for each satellite. These 10 elements are

divided by a scale factor (*SF*) to determine the matrix **E**, which is broadcast in MT 28:

$$\mathbf{E} = \frac{\mathbf{R}}{\psi} = \begin{bmatrix} E_{1,1} & E_{1,2} & E_{1,3} & E_{1,4} \\ 0 & E_{2,2} & E_{2,3} & E_{2,4} \\ 0 & 0 & E_{3,3} & E_{3,4} \\ 0 & 0 & 0 & E_{4,4} \end{bmatrix} \tag{2.57}$$

where $\psi = 2^{(scale\ exponent-5)}$. The covariance matrix is then reconstructed and used to modify the broadcast σ_{UDRE} values as a function of user position. The location-specific modifier is given by:

$$\delta UDRE = \sqrt{(\mathbf{I}^{\mathrm{T}} \cdot \mathbf{C} \cdot \mathbf{I})} + \varepsilon_C \tag{2.58}$$

where **I** is the 4-D line of sight vector from the user to the satellite in the WGS-84 coordinate frame, whose first three components are the unit vector from the user to the satellite and the fourth component is a one. The additional term ε_C is to compensate for the errors introduced by quantization. If degradation data is available, the ε_C value is derived from the covariance data broadcast in a Type 10 message ($\mathrm{C}_{\mathrm{covariance}}$) as follows:

$$\varepsilon_C = C_{covariance} \cdot \psi \tag{2.59}$$

If $\mathrm{C}_{\mathrm{covariance}}$ from MT 10 is not available, ε_C is set to zero, but there is an 8 meter degradation applied as defined in the WAAS MOPS (RTCA, 2006-a).

The WAAS fast corrections and long-term corrections are designed to provide the most recent information to the user (RTCA, 2006-a). However, it is always possible that the user fails to receive one of the messages. In order to guarantee integrity even when some messages are not received, the user performing approach operations (e.g, LNAV/VNAV, LP or LPV) must apply models of the degradation of this information. In other flight phases, the use of these models is optional and a global degradation factor can be used instead as specified in the WAAS MOPS (RTCA, 2006-a).

The residual error associated with the fast and long-term corrections is characterized by the variance (σ_{flt}^2) of a model distribution. This term is computed as:

$$\sigma_{flt}^2 = \begin{cases} (\sigma_{UDRE} \cdot \delta UDRE) + \varepsilon_{fc} + \varepsilon_{rrc} + \varepsilon_{ltc} + \varepsilon_{er}, & if\ RSS_{UDRE} = 0 \\ (\sigma_{UDRE} \cdot \delta UDRE)^2 + \varepsilon_{fc}^2 + \varepsilon_{rrc}^2 + \varepsilon_{ltc}^2 + \varepsilon_{er}^2, & if\ RSS_{UDRE} = 1 \end{cases} \quad (2.60)$$

where:

RSS_{UDRE} = root-sum-square flag in MT 10;

σ_{UDRE} = model parameter from MTs 2-6, 24;

$\delta UDRE$ = user location factor (from MTs 28 or 27, otherwise $\delta UDRE = 1$);

ε_{fc} = degradation parameter for fast correction data;

ε_{rrc} = degradation parameter for range rate correction data;

ε_{ltc} = degradation parameter for long term correction or GEO navigaton message data;

ε_{er} = degradation parameter for en route through NPA operations.

More detailed information about WAAS can be found in the applicable MOPS standard (RTCA, 2006-a).

2.11 GROUND BASED AUGMENTATION

The current GNSS constellations are unable to provide accuracy, availability, continuity and integrity to achieve the stringent accuracy and integrity requirements set by ICAO for precision approach. GBAS employs LADGNSS techniques to augment accuracy and ad-hoc features to augment integrity beyond the levels that can be achieved with SBAS. Employing all provisions included in the current RTCA standards (RTCA, 2008-a), (RTCA, 2008-b), (RTCA, 2004), GBAS could provide augmentation to the core constellations to enable precision approach up to Category IIIb. However, to date, ICAO has only issued Standards and Recommended Practices (SARPs) for GBAS operating over single frequency and single constellation up to CAT I operations (ICAO, 2006). SARPs for CAT II/III have been already developed by the ICAO Navigation System Panel (NSP) but not yet

included in Annex 10, waiting for further developments to take place in the aviation industry.

As shown in Fig. 2-20, GBAS utilises three segments: satellites constellation, ground stations and aircraft receiver.

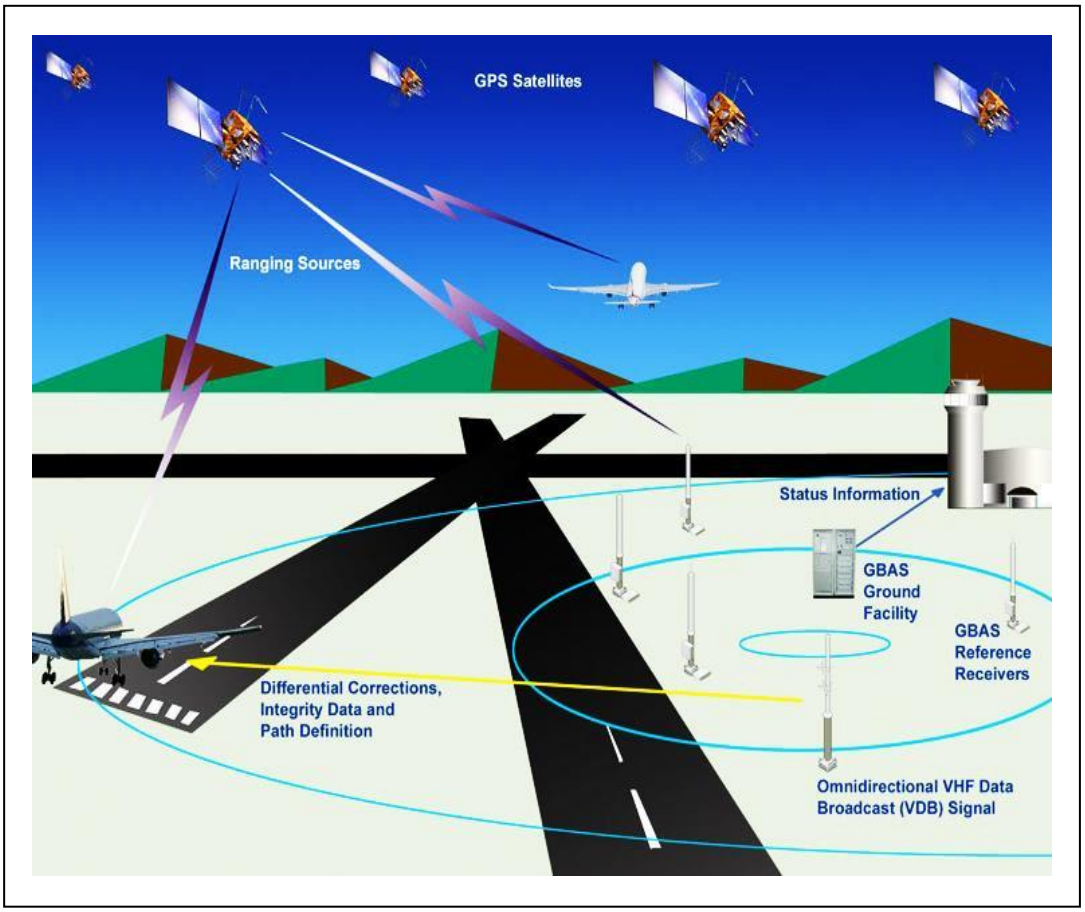


Figure 2-20. GBAS architecture (FAA, 2016).

The GBAS ground station is formed by reference receivers with their antennas installed in precisely surveyed locations. The information generated in the receiver is sent to a processor that computes the corrections for each navigation satellite in view and broadcasts these differential corrections, besides integrity parameters and precision approach path-points data, using a VHF Data Broadcast (VDB). The information broadcast is received by aircraft in VHF coverage that also receive information from the navigation satellites. Then, it uses the differential corrections on the information received directly from the navigation satellites to calculate the

precise position. The precise position is used, along with path-points data, to supply deviation signals to drive appropriate aircraft systems supporting precision approach operations.

Although the operating principle, Signal-in-Space and performance characteristics of GBAS are completely different from ILS, the GBAS approach guidance indications provided to the pilot are similar to the localizer and glide path indications provided by an ILS. However, compared to ILS precision approach systems, GBAS presents several distinct benefits. These include:

- Reduction of critical and sensitive areas typical of ILS;
- Possibility to perform curved approaches;
- Positioning service for RNAV operations in the TMA;
- Provision of service in several runways in the same airport;
- Provision of several approach glide angles and displaced threshold;
- Guided missed approach service;
- Adjacent airports served by a single GBAS (within VDB coverage).

According to Annex 10, vol. 1 (ICAO, 2006), GBAS is intended to support all types of approach, landing, departure and surface operations and may support en-route and terminal operations The SARPs were developed, to date, to support Category I precision approach, approach with vertical guidance and GBAS positioning service. The GBAS ground station performs the following functions:

- Provide locally relevant pseudo-range corrections;
- Provide GBAS-related data;
- Provide final approach segment data when supporting precision approach;
- Provide ranging source availability data; and
- Provide integrity monitoring for GNSS ranging sources.

VDB radio frequencies used in GBAS are selected in the band of 108 to 117.975 (just below the ATM band). The lowest assignable frequency is 108.025 MHz and

the highest assignable frequency is 117.950 MHz, with a channel spacing of 25 kHz. A Time Division Multiple Access (TDMA) technique is used with a fixed frame structure. The data broadcast is assigned one to eight slots. GBAS data is transmitted as 3-bit symbols, modulating the data broadcast carrier by Differential 8 Phase Shift Keying (D8PSK), at a rate of 10 500 symbols per second. GBAS can provide a VHF data broadcast with either horizontal (GBAS/H) or elliptical (GBAS/E) polarization. The navigation data transmitted by GBAS includes the following information:

- Pseudo-range corrections, reference time and integrity data;
- GBAS-related data;
- Final approach segment data when supporting precision approach;
- Predicted ranging source availability data.

Currently, the American LAAS is a system capable to provide local augmentation for the GNSS signals and it is the first candidate to support all types of approach and landing procedures up to Category III, as well as surface operations. All existing GBAS systems refer to the same LAAS standards developed by RTCA (RTCA, 2008-a), (RTCA, 2008-b), (RTCA, 2004). For this reason, the terms GBAS and LAAS are often used interchangeably in the international literature and this will be also the case in the reminder of this thesis.

The typical LAAS facility consists of three elements: the first is the ground segment, usually installed on the airport field, the second is the airborne segment, represented by the data link receiver as well as a system capable of applying the augmentation parameters for landing guidance, the third is the space segment, which is actually made by the GPS/GLONASS constellations and will also include the future GALILEO/BDS constellations when the required levels of maturity will be achieved. WAAS essentially provides two different services: the first is the precision approach service by giving deviation guidance, both lateral and vertical, for the Final Approach Segment (FAS) to the runway; the second is the differentially-corrected positioning service transmitting to the airborne systems the correction message for augmented GNSS accuracy.

The specific data link to be used for communications between aircraft and ground stations is not completely specified by the current standards, while there are constraints in terms of bandwidth, link budget and data rate (RTCA, 2008-b).

For approach and landing services, the LAAS performance is classified in terms of GBAS Service Level (GSL). A GSL defines a specific level of required accuracy, integrity and continuity. The GSL classification and the GSL performance requirements are listed in Tables 2-14 and 2-15. Currently, GBAS/LAAS installations around the world have been certified for GSL-C only. However, several research and development efforts are ongoing towards demonstrating and producing adequate evidence of compliance for GLS-D/E/F installations.

Table 2-14. GBAS Service Levels (adapted from RTCA, 2008-a).

GSL	Operations Supported by GSL
A	Approach operations with vertical guidance (performance of APV-I designation)
B	Approach operations with vertical guidance (performance of APV-II designation)
C	Precision approach to lowest CAT I minima
D	Precision approach to lowest CAT IIIb minima, when augmented with other airborne equipment
E	Precision approach to lowest CAT II/IIIa minima
F	Precision approach to lowest CAT IIIb minima

Table 2-15. GBAS Service Level Performance (adapted from RTCA, 2008-a).

GSL	Accuracy		Integrity				Continuity
	95% Lat. NSE	95% Vert. NSE	Prob. (Loss of Integrity)	Time to Alert	LAL	VAL	Prob. (Loss of Continuity)
A	16 m	20 m	$1\text{-}2\times10^{-7}$/150 sec	10 sec	40 m	50 m	$1\text{-}8\times10^{-6}$/15 sec
B	16 m	8 m	$1\text{-}2\times10^{-7}$/ 150 sec	6 sec	40 m	20 m	$1\text{-}8\times10^{-6}$/15 s
C	16 m	4 m	$1\text{-}2\times10^{-7}$/ 150 sec	6 sec	40 m	10 m	$1\text{-}8\times10^{-6}$/15 s
D	5 m	2.9 m	10^{-9}/15 s (vert.); 30 s (lat.)	2 sec	17 m	10 m	$1\text{-}8\times10^{-6}$/15 s
E	5 m	2.9 m	10^{-9}/15 s (vert.); 30 s (lat.)	2 sec	17 m	10 m	$1\text{-}4\times10^{-6}$/15 s
F	5 m	2.9 m	10^{-9}/15 s (vert.); 30 s (lat.)	2 sec	17 m	10 m	$1\text{-}2\times10^{-6}$/15 s (vert.); 30 s (lat.)

LAAS can also support airport surface operations by enabling several functions associated with the specific aircraft equipment such as an electronic moving map and database:

- ***Enhanced pilot situational awareness of aircraft position:*** the position information will allow the pilot to identify the correct taxi route and to monitor his position along the route; this situational awareness is improved in all visibility conditions, particularly for complex airports. Nowadays to support the low visibility surface movement operations is a very costly task; with LAAS, ADS-B and emerging cockpit displays technologies, these operations could be conducted in the same way of those supported with lights, markings and follow-me operators.
- ***Traffic surveillance:*** this function can support air traffic control and crew with traffic surveillance both in good and low visibility condition.

- ***Runway incursion and conflict detection alerting:*** the availability of accurate LAAS aircraft position information enables automated systems to detect runway incursions and other conflicts providing suitable alerts.

Various error sources affect the system accuracy, integrity and continuity and these are nowadays an active area of research. Some of these errors are:

- Hardware/software faults in ground equipment or satellites;
- Multipath effects occurring on aircraft or ground receiver antennas;
- Errors in the ephemeris information;
- Residual ionospheric and tropospheric errors;
- Degradation of the satellite signal at the source;
- Interference/jamming issues.

The LAAS service volume (Fig. 2-21) is defined as the region where the system is required to meet the accuracy, integrity and continuity requirements for a specific GSL class.

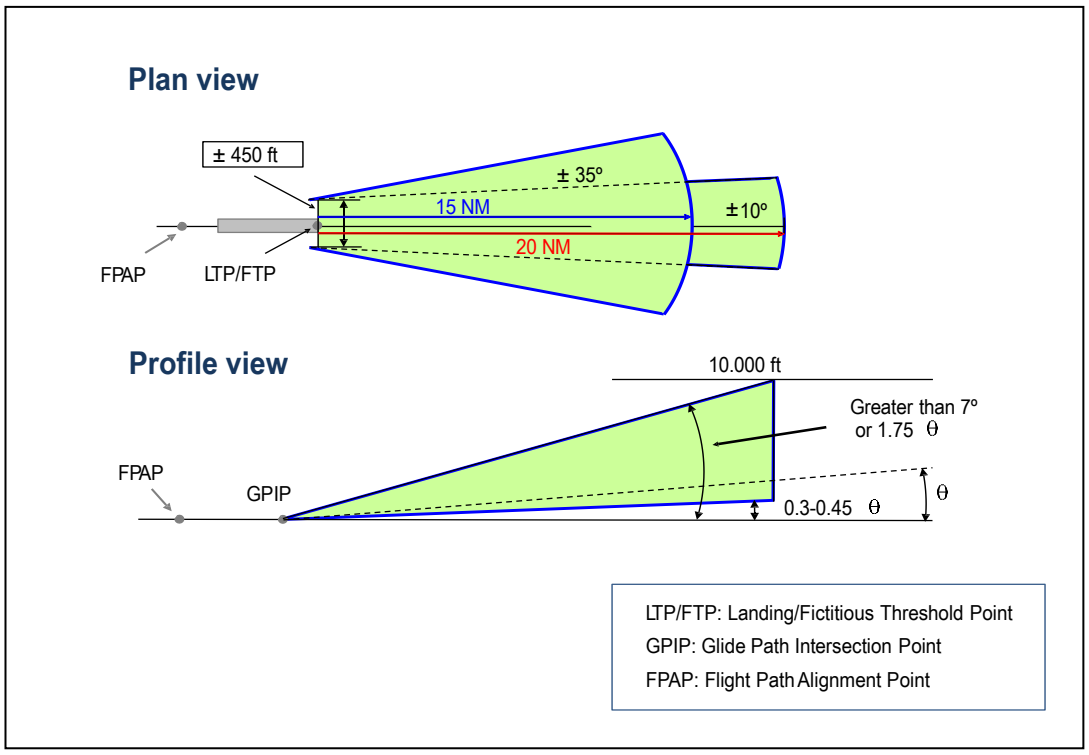


Figure 2-21. Minimum Category I, II and APV Service Volume (adapted from RTCA, 2008-b).

For each runway supported by the system, the minimum service volume to support Category I, Category II or APV (vertical guidance) approaches is defined as follow:

- Laterally: beginning at 450 feet each side of the Landing Threshold Point/Fictitious Threshold Point (LTP/FTP) and projecting out ±35° either side of the final approach path to a distance of 20 NM from the LTP/FTP.
- Vertically: within the lateral region, up to the maximum of 7° or 1.75 times the Glide Path Angle (GPA) above the horizon with the origin at the Glide Path Intercept Point (GPIP), up to a maximum of 10,000 feet AGL and down to 0.9° above the horizon with the origin in the GPIP, to a minimum height of one half the DH.

The minimum service volume to support Category III precision approach or autoland with any minima is the same as the minimum Category II service volume, with the addition of the volume within ±450 feet from the runway centreline extending from the threshold to the runway end, from 8 feet above the surface up to 100 feet. There are different metrics for the GBAS performance; one of these is the Signal-in-Space (SIS) performance. This is defined in terms of accuracy, integrity, continuity and availability of the service (RTCA, 2008-b); this performance refers to the output of the "fault-free" airborne user equipment. The interaction between airborne and ground systems is defined by a separation of responsibilities:

- The ground system is responsible for monitoring the satellites signal quality and availability, computing the differential corrections and detecting and mitigating the faults originated in the ground station or in the space segment.
- The airborne equipment computes the pseudorange values and evaluates the performance level monitoring, detecting and mitigating any fault conditions due to the other avionics equipment. For a precision approach, the avionics GBAS receiver only uses satellites for which corrections are available

Avionics GBAS receivers have to comply with the requirements outlined in ICAO Annex 10, vol. 1 (ICAO, 2006) and the specifications of RTCA/DO-253A (RTCA, 2008-a). GBAS avionics receivers must have the capability to receive navigation satellites signal and the VDB information, with respective antennas, and a way to

select the approach and an indication of course and glide path. Like ILS and Microwave Landing System (MLS), GBAS has to provide lateral and vertical guidance relative to the defined final approach course and glide path. The GBAS receiver employs a channelling scheme that selects the VDB frequency. Approach procedure data are uplinked via the VDB and each separate procedure requires a different channel assignment. In terms of aircraft system integration, GBAS avionics standards have been developed to mimic the ILS in order to minimize the impact of installing GBAS on the existing avionics. Typically, display scaling and deviation outputs are the same utilized for ILS, so that maximum interoperability is achieve at the Human-Machine Interface (HMI) level, allowing the avionics landing systems to provide final approach course and glide path guidance both at airports equipped with ILS and GLS. For TMA area navigation, including segmented and curved approaches, the GBAS avionics receiver provides accurate position, velocity and time data that can be used as an input to an on-board navigation computer. In line with ICAO SARPs and the strategy for the introduction and application of non-visual aids to approach and landing, which permit a mix of systems providing precision approach service, the avation industry has developed multi-mode receivers that support precision approach operations based on ILS, MLS and GNSS (GBAS and SBAS). Also for GBAS, integrity monitoring is accomplished by the avionics continually comparing Horizontal/Lateral and Vertical Protection Levels (HPL/LPL and VPL), derived from the augmentation signal and satellite pseudorange measurements, against the alert limit for the current phase of flight. When either the vertical or the horizontal limit is exceeded, an alert is given to the pilot (ICAO, 2013). Additionally, the LAAS MOPS (RTCA, 2008-a) also contemplate the possibility of introducing avionics-based augmentation functionalities by defining the continuity of protection levels in terms of Predicted Lateral and Vertical Protection Levels (PLPL and PVPL). The standard states that on-board avionics systems could support PLPL and PVPL calculations to generate appropriate caution flags. However, it does not recommend any specific form of ABAS and does not indicate the required performance of such on-board equipment to supplement LAAS operations. Research in this field has concentrated on possible RAIM aiding rather than proper ABAS developments. Some techniques have been developed that

include the possible aiding of barometric altimeter, with a special focus on vertical guidance integrity monitoring and augmentation (Angus, 2006), (Walter et al., 2008), (Ene et al. 2008), (Blanch et al., 2008) and, more recently, the possible inclusion of predictive features has also been studied especially for mission/route planning applications. However, the main limitations of such techniques is in the inability to model GNSS errors due to aircraft dynamics, including antenna obscuration, Doppler shift and multipath contributions due to the aircraft structure and the surrounding environment (the latter being important when the aircraft flies at low altitudes). This is why a new form of ABAS specifically tailored for real-time integrity monitoring and augmentation in mission-essential and safety-critical aviation applications is needed (Sabtini et al., 2013-a), (Sabatini et al. 2013-b).

2.12 CONCLUSION

At the moment, stand-alone satellite navigation systems are not certified to be used as sole means of aircraft navigation and landing. Contrary to Inertial Navigation Systems (INS) and to the various radionavigation aids currently in use, GNSS is only certifiable for aircraft navigation if it is integrated or augmented by systems. The reason is not the accuracy but integrity. While the adoption of RAIM techniques can significantly improve the situation, the inherent reactive nature of traditional RAIM techniques do not allow an immediate implementation of predictive features beyond the extrapolations that can be made from GNSS signals and ephemeris data. The introduction of SBAS and GBAS systems is the US (WAAS and LAAS) and in other regions has allowed for an extended range of integrity monitoring and augmentation features (also providing substantial accuracy and, in some cases, availability improvements), which can be exploited synergically in the various aircraft flight phases. However neither RAIM nor WAAS/LAAS have been successful so far in introducing predictive integrity monitoring and augmentation features suitable for the most demanding flight tasks (i.e., precision approach in CAT-III and autoland certification). Currently, a GNSS Landing System (GLS) can be used o perform precision approach tasks down to CAT-II. GLS exploits WAAS (up to CAT 1) and LAAS (up to CAT IIIb) to achieve the RNP

including Lateral and Vertical Protection Level (LPL and VPL) requirements in line with the Minimum Operational Performance Standards (MOPS) for WAAS and LAAS (RTCA, 2006-a), (RTCA, 2008-a), (RTCA, 2008-b). LAAS MOPS also contemplate the possibility of introducing avionics-based augmentation functionalities by defining the continuity of protection levels in terms of Predicted Lateral and Vertical Protection Levels (PLPL and PVPL). The standard states that on-board avionics systems could support PLPL and PVPL calculations to generate appropriate caution flags. However, it does not recommend any specific form of ABAS and does not indicate the required performance of such on-board equipment to supplement LAAS operations.

2.13 REFERENCES

Angus, J. E. (2006), "RAIM with Multiple Faults", NAVIGATION: Journal of the Institute of Navigation, Vol. 53, No. 4.

Ashkenazi, V. (1995), "Principles of GPS and Observables." Lecture Notes, IESSG, University of Nottingham. 1995.

Ashkenazi, V., Ffoulkes-Jones, G.H., Moore, T., and Walsh, D. (1993), "Real-time Navigation to Centimetre Level." Paper presented at DSNS93, the 2nd International Symposium on Differential Navigation. Amsterdam (The Netherlands).

Ashkenazi, V., Moore, T., and Westrop, J.M. (1990), "Combining Pseudo-range and Phase for Dynamic GPS." Paper presented at the International Symposium on Kinematic Systems in Geodesy, Surveying and Remote Sensing. London (UK).

Ashkenazi, V., Moore, T., Ffoulkes-Jones, G., Whalley, S. and Aquino, M. (1990), "High Precision GPS Positioning by Fiducial Techniques." Global Positioning System: An Overview. Bock Y., Leppard N. Eds. International Association of Geodesy Symposia, Vol. 102. Springer, New York, NY.

Ashkenazi, V., Summerfield P., Westrop J. (1990), "Kinematic Positioning by GPS." Tiré a part des Cahiers du Centre Européen de Géodynamique et de Séismologie, Volume 2.

Bisnath, S. and Gao, Y. (2009), "Precise Point Positioning – A Powerful Techniqe with a Promising Future." GPS World (Algorithms and Methods – Innovation), April 2009, pp. 43-50.

Blanch, J., Ene, A., Walter, T. and Enge, P. (2007), "An Optimized Multiple Hypothesis RAIM Algorithm for Vertical Guidance." In Proceedings of ION GNSS 2007.

Boehm, J., Werl, B. and Schuh, H. (2006), "Troposphere Mapping Functions for GPS and Very Long Baseline Interferometry from European Centre for Medium-Range Weather Forecasts Operational Analysis Data." Journal of Geophysical Research: Solid Earth, Vol. 111, Issue B2.

Brown, R. G. (1992), "A Baseline GPS RAIM Scheme and a Note on the Equivalence of Three RAIM Methods", Journal of the Institute of Navigation, Vol. 39, No. 3.

Brown, R. G. and Chin, G. Y. (1998), "GPS RAIM: Calculation of Thresholds and Protection Radius Using Chi-Square Methods - A Geometric Approach", Journal of the Institute of Navigation, Vol. 5.

CAA (2003). GPS Integrity and Potential Impact on Aviation Safety. CAA Safety Regulation Group Paper 2003/09.

Chao, C. (1972), "A model for tropospheric calibration from daily surface and radiosonde balloon measurements." Technical Memorandum, Jet Propulsion Laboratory (JPL), Pasadena, CA, USA, pp. 350–391.

Cross, P. A. and Roberts, W. D. S. (1990), "Differential Offshore Positioning using Block II GPS Satellites." 7th International Symposium of the Hydrographic Society (Hydro '90). Southampton (UK).

Dodson, A. H. (1997), "Propagation Effects on GPS Measurements." Lecture Notes, IESSG, University of Nottingham (UK).

Ene, A., Blanch, J. and Powell, J. D. (2007), "Fault Detection and Elimination for GALILEO-GPS Vertical Guidance." In Proceedings of the Institute of Navigation National Technical Meeting, San Diego, CA (USA).

ESA (2003), "GALILEO System Requirement Document." European Space Agency Report No. ESA-APPNS-REQ-00011, Issue 3.0.

ESA (2011a), "Integrity." European Space Agency Navipedia website: http://www.navipedia.net/index.php/Integrity. Year of Publication: 2011 (Edited by GMV). Visited on 18th January 2017.

ESA (2011b), "SBAS Systems." European Space Agency Navipedia website: http://www.navipedia.net/index.php/SBAS_Systems. Year of Publication: 2011 (Edited by GMV). Visited on 20th March 2016.

Euler, H. J. (1994), "Achieving high-accuracy relative positioning in real-time: system design, performance and real-time results." In Proceedings of the 4th IEEE Plans Conference. Las Vegas, NV (USA). 1994.

Euler, H. J., and Landau H. (1992), "Fast GPS Ambiguity Resolution On-The-Fly for Real-time Applications." Paper presented at the 6th International Geodetic Symposium on Satellite Positioning. Columbus, Ohio (USA).

EUROCAE ED-114 (2003), "Minimum Operational Performance Standards for a Ground Based Augmentation System (GBAS) ground facility to support CAT I approach and landing." European Organisation for Civil Aviation Equipment, Working Group No. 28.

EUROCAE ED-88 (1997), "MOPS for Multi-Mode Airborne Receiver (MMR) including ILS, MLS and GPS used for Supplemental Means of Navigation." The European Organisation for Civil Aviation Equipment, Working Group No. 28.

EUROCAE ED-95 (1999), "Minimum Aviation System Performance Standards (MASPS) for a Global Navigation Satellite System Ground Based Augmentation System to Support Cat 1 Operations." European Organisation for Civil Aviation Equipment, Working Group No. 28.

FAA (2011), 'Global Positioning System (GPS) Standard Positioning Service (SPS) Performance Analysis Report", US Federal Aviation Administration Report 72.

FAA (2016), "Satellite Navigation - Ground Based Augmentation System (GBAS)." US Federal Aviation Administration Website, Section Dedicated to Navigation Programs/GNSS. Available online at: http://www.faa.gov/about/office_org/ headquarters_offices/ato/service_units/techops/navservices/gnss/laas/. Visted on 24th March 2016.

Fenton, P. C. and Jones, J. (2005), "The Theory and Performance of NovAtel Inc.'s Vision Correlator." In Proceedings of the 2005 ION GNSS Conference. Long Beach, CA (USA).

Giffard, R. (1999), "Estimation of GPS Ionospheric Delay Using Ll Code and Carrier Phase Observables." In Proceedings of the 31st Annual Precise Time and Time Interval (PTTI) Meeting, Dana Point, CA (USA).

Gleason S. and Gebre-Egziabher D., Editors (2009), "GNSS Applications and Methods." GNSS Technology and Application Series, Artech House. Norwood, MA (USA).

GPS JPO (1996), "NAVSTAR GPS User Equipment, Introduction", Public Release Version. US Air Force Space Systems Division, NAVSTAR-GPS Joint Program Office. Los Angeles AFB, California (USA). 1996.

GPS JPO (2007), GPS Precision Positioning Service (PPS) Performance Standard, 1st Edition. NAVSTAR Global Positioning System Joint Program Office.

GPS JPO (2008), GPS Standard Positioning Service (SPS) Performance Standard, 4th Edition. NAVSTAR Global Positioning System Joint Program Office.

Hansen, P. (1994), "Real-time GPS Carrier Phase Navigation." The University of Nottingham, IESSG. Paper presented at the DSNS-94 Conference. London (UK).

Hatch, R. R. (1990), "Instantaneous Ambiguity Resolution." Presented at the KIS Symposium. Banff (Canada).

Sanz Subirana, J., Juan Zornoza, J.M. and Hernández-Pajares M. (2011), "Multipath." European Space Agency (ESA) Navipedia – GNSS Measurements and Data Processing. Available online at: http://www.navipedia.net/index.php/Multipath #cite_ref-1. Accessed on 20/04/2017.

Hatch, R. R. (1991), "Ambiguity Resolution While Moving, Experimental Results." Proc. of ION GPS-91, the 4th International Technical Meeting of the Satellite Division of the US Institute of Navigation. Albuquerque (NM).

Herring, T. (1992), "Modeling atmospheric delays in the analysis of space geodetic data." In Proceedings of Refraction of Transatmospheric Signals in Geodesy, De Munck, J., Spoelstra, T., Eds. Netherlands Geodetic Commission Publications on Geodesy: The Hague, The Netherlands, Volume 36, pp. 157–164.

Hopfield, H. (1969), "Two-quartic tropospheric refractivity profile for correcting satellite data." Journal of Geophysical Research, Vol. 74, Oceans and Atmospheres, pp. 4487–4499.

Hopfield, H. (1971), "Tropospheric effect on electro-magnetically measured range prediction from surface weather data." Radio Science, Vol. 6, Issue 3, pp. 357–367.

ICAO (1995), Report of the Special Communications/Operations Divisional Meeting, ICAO Doc. 9650.

ICAO (2002), "Global Air Navigation Plan for CNS/ATM Systems." International Civil Aviation Organization. Document No. 9750 AN/963. Second Edition, 2002.

ICAO (2005), "Global Navigation Satellite Systems (GNSS) Manual." International Civil Aviation Organization. Document No. 9849 AN/457. First Edition.

ICAO (2006), "Standards and Recommended Practices (SAPRs) Volume 1 – Annex 10", (Including Amendments 1-81), Issue 6.

ICAO (2008), "Performance Based Operations Manual." Document No. 9613 AN/937. Third Edition.

ICAO (2010), "GBAS CAT II/III Development Baseline SARPs." Draft proposed changes to Annex 10, Volume I, as agreed at the 17 – 28 May 2010 meeting of the ICAO Navigation Systems Panel (NSP). Available online at: http://www.icao.int/ safety/airnavigation/documents/gnss_cat_ii_iii.pdf (downloaded 21st May 2013).

ICAO (2013), "Guide for Ground Based Augmentation Systems Implementation." International Civil Aviation Organisation. Available online at: https://www.icao.int/RO_SAM/ eDocuments/GBASGuide.pdf. Accessed on 19/06/2016.

Ifadis, I. (1986), "The Atmospheric Delay of Radio Waves: Modeling the Elevation Dependence on a Global Scale." Technical Report No. 38L, School of Electrical and Computer Engineering, Chalmers University of Technology, Gothenburg (Sweden).

Janssen, V. and Haasdyk, J (2011), "Assessment of Network RTK performance using CORSnet-NSW." Proceeedings of the IGNSS 2011 Symposium, 15-17 November 2011, Sydney, Australia.

Jokinen, A. S. (2014), "Enhanced Ambiguity Resolution and Integrity Monitoring Methods for Precise Point Positioning." PhD Thesis, Centre for Transport Studies, Department of Civil and Environmental Engineering, Imperial College, London.

Juan, J. M., Rius, A., Hernández-Pajares, M. and Sanz, J. (1997), "A Two-layer Model of the Ionosphere using Global Positioning System Data." Geophys. Research Letters, Vol. 24, pp. 393–396.

Kalafus, R. M. (1987), Receiver Autonomous Integrity Monitoring of GPS, DOT-TSC-FAA-FA-736-1, U.S. DOT Transportation Systems Center. Cambridge, MA (USA).

Keith, A. (2000), "Using Wide Area Differential GPS to Improve Total System Error for Precision Flight Operations." PhD Thesis. Stanford University (USA).

Kelly, R. (1998), "Derivation of the RAIM Algorithm from First Principles with Performance Comparisons Between Published Algorithms." Journal of the Institute of Navigation, Vol. 5.

Kleusberg, A. (1986), "Kinematic Relative Positioning Using GPS Code and Carrier Beat Phase Observations." In Proceedings of the 2nd Marine Geodesy Symposium. London (UK).

Klobuchar, J. A. (1986), "Design and Characteristics of the GPS Ionospheric Time Delay Algorithm for Single Frequency Users." In Proceedings of the IEEE Position, Location, and Navigation Symposium, Las Vegas, NV (USA).

Landau, H. (1992), "On-The-Fly Ambiguity Resolution Using Differential P-code Group and Phase Delay Measurements." Proceeedings of the 5th International Technical Meeting of the Satellite Division of the US Institute of Navigation. Orlando, FL (USA).

Leandro, R., Santos, M. and Langley, R (2006), "UNB neutral atmosphere models: Development and performance." In Proceedings of the Institute of Navigation, National Technical Meeting, Monterrey, CA, USA, 18–20 January 2006.

Lee, Y., Van Dyke, K. and De Cleene, B. (1998), "Summary of RTCA SC-159 GPS Integrity Working Group Activities", Journal of the Institute of Navigation, Vol. 5, pp. 195-226.

Leick, A., (2003), "GPS Satellite Surveying." Third Edition. John Wiley and Sons, New York.

Liu H., Chen Z., Ye W., Wang H. (2014), "GNSS carrier phase ambiguity resolution based on integrity restriction in ambiguity domain." Advances in Space Research, Vol. 53, Issue 8, Pages 1207–1218

Mader, G. (1986), "Dynamic Positioning using GPS Carrier Phase Measurements." Manuscripte Geodaetica. Volume 36 (86). 1986.

McGraw, G. A. and Braasch, M. S. (1999), "GNSS Multipath Mitigation Using Gated and High Resolution Correlator Concepts." In Proceedings of the 1999 National Technical Meeting of the Institute of Navigation, San Diego, CA (USA).

Monico, J. F. G., Ashkenazi, V. and Moore, T. (1997), "High Precision GPS Network with Precise Ephemerides and Earth Body Tide Model." Revista Brasileira de Geofisica, Vol. 15, N. 2, pp. 155-160.

Moore, T. (1996). "Other Satellite Navigation Systems." Lecture Notes, IESSG, University of Nottingham (UK).

Moore, T. (1996-a), "An Introduction to Differential GPS." Lecture Notes, IESSG, University of Nottingham (UK).

Moore, T. (1996-b), "GPS Orbit Determination and Fiducial Networks." Lecture Notes, IESSG, University of Nottingham (UK).

NATO (1998), "Data Interchange Format for Navstar Global Positioning System (GPS)", STANAG 4392-1998, Ed. 1.

Niell, A. (1996), "Global mapping functions for the atmosphere delay at radio wavelengths." Journal of Geophysical Research, Vol. 101, pp. 3227–3246. [

Parkinson, B. W. and Axelrad, P. (1988), "Autonomous GPS Integrity Monitoring Using the Pseudorange Residual", Navigation, Vol. 35, No. 2, pp. 255-274.

Parkinson, B. W. and Spilker, J. J. Jr., Editors (1996), "Global Positiong System: Theory and Applications – Volume II." Progress in Astronautics and Aeronautics. Vol. 163. Published by the American Institute of Aeronautics and Astronautics.

Phillips, A. H. (1990), "The Determination of PDOP in GPS." NATO Advisory Group for Aerospace Research and Development (AGARD). Document AGARD-AG-314.

Qin, X., Gourevitch, S. and Kuhl, M. (1992), "Very Precise Differential GPS - Development Status and Test Results." Proceeedings of ION GPS-92, 5th International Technical Meeting of the Satellite Division of the US Institute of Navigation. Albuquerque, NM (USA).

RCTM (1990-a), "RCTM Recommended Standards for Differential NAVSTAR GPS Service." Radio Technical Committee for Maritime Services, Special Committee No. 104. Paper 134-89/SC104-68. Washington DC (USA). 1990 (a).

RCTM (1990-b), "RCTM Recommended Standards for Differential NAVSTAR GPS Service." Radio Technical Committee for Maritime Services, Special Committee No. 104. Paper 194-93/SC104-STD. Washington DC (USA).

RCTM (2011), "RTCM Recommended Standards for Differential GNSS Service." Radio Technical Committee for Maritime Services, Special Committee No. 104. Paper 136-2001/SC104-STD, Vers. 2.3. Washington DC (USA).

RTCA (1993), "Minimum Aviation System Performance Standards DGNSS Instrument Approach System: Special Category 1 (scat-1)." Radio Technical Commission for Aeronautics (RTCA) Inc., Special Committee No. 159. Document RTCA DO-217. Washington DC (USA).

RTCA (2000). "Minimum Operational Performance Standards for GNSS Airborne Antenna Equipment." Radio Technical Commission for Aeronautics (RTCA) Inc., Special Committee No. 159. Document RTCA DO-228. Washington DC (USA).

RTCA (2004), "Minimum Aviation System Performance Standards (MASPS) for the Local Area Augmentation System (LAAS). Radio Technical Commission for Aeronautics (RTCA) Inc., Special Committee No. 159. Document RTCA DO-245A. Washington DC (USA). 2004.

RTCA (2006-a), "Minimum Operational Performance Standards for Global Positioning System/Wide Area Augmentation Systems Airborne Equipmen." Radio Technical Commission for Aeronautics (RTCA) Inc., Special Committee No. 159. Document RTCA DO-229D. Washington DC (USA).

RTCA (2006-b). "Minimum Operational Performance Standards for GNSS Airborne Active Antenna for the L1 Frequency Band." Radio Technical Commission for Aeronautics (RTCA) Inc., Special Committee No. 159. Document RTCA DO-301. Washington DC (USA). 2006-b.

RTCA (2008-a), "Minimum Operational Performance Standards for GPS/GBAS Airborne Equipment." Radio Technical Commission for Aeronautics (RTCA) Inc., Special Committee No. 159. Document RTCA DO-253C. Washington DC (USA).

RTCA (2008-b), "GNSS-Based Precision Approach Local Area Augmentation System (LAAS) Signal-in-Space Interface Control Document (ICD)." Radio Technical Commission for Aeronautics (RTCA) Inc., Special Committee No. 159. Document RTCA DO-246D. Washington DC (USA).

Saastamoinen, J. (1972), "Atmospheric correction for the troposphere and stratosphere in radio ranging satellites." The Use of Artificial Satellites for Geodesy; Henriksen, S., Mancini, A., Chovitz, B., Eds.; American Geophysical Union: Washington, WA, USA, 1972.

Saastamoinen, J. (1973), "Contribution of the theory of atmospheric refraction." Bulletin Géodesique, Vol. 107, pp. 13–34.

Sabatini, R. (2005), "Experimental Investigation of Differential GPS for Flight Test of High Performance Aircraft." University of Rome "La Sapienza", School of Aerospace Engineering. Thesis submitted in partial fulfilment for the degree of Doctor of Engineering in Atronautics.

Sabatini, R. and Palmerini, G. B. (2008), "Differential Global Positioning System (DGPS) for Flight Testing." NATO Research and Technology Organization (RTO) – Systems Concepts and Integration Panel (SCI). AGARDograph Series RTO-AG-160, Vol. 21.

Sabatini, R., Moore, T., Hill, C. (2013-a), "A New Avionics Based GNSS Integrity Augmentation System: Part 1 – Fundamentals." Journal of Navigation, Vol. 66, No. 3, pp. 363-383.

Sabatini, R., Moore, T., Hill, C. (2013-b), "A New Avionics Based GNSS Integrity Augmentation System: Part 2 – Integrity Flags." Journal of Navigation, Vol. 66, No. 4, pp. 511-522.

Seeber, G. (2003), "Satellite Geodesy." Second Edition. Walter de Gruyter Editor. Berlin (Germany), New York (USA).

Siouris, G. M. (1993), "Aerospace Avonics Systems." Academic Press. San Diego, CA (USA).

Skillicorn, G. N. (2003), "The Past, Present, and Future of LAAS." Integrated CNS Technologies Conference and Workshop. Annapolis, MD (USA).

Teunissen, P. J. (2003-a), "Integer aperture GNSS ambiguity resolution." Artificial Satellites, Vol. 38, Issue 3, pp. 79-88.

Teunissen, P. J. (2003-b), "Towards a unified theory of GNSS ambiguity resolution." Journal of Global Positioning Systems, Vol. 2, No. 1: 1-12.

Teunissen, P. J. (2005), "GNSS ambiguity resolution with optimally controlled failure-rate." Artificial Satellites, Vol. 40, Issue 4, pp. 219-227.

Thomis, D. M. (1984), "Global Positioning System – A Modification to the Baseline Satellite Constellation for Improved Geometric Performance." US Air Force Institute of Techonology.

Tiberius, C. C. and De Jonge, P. J. (1995), "Fast positioning using the LAMBDA method." In Proceedings of DSNS'95, Bergen, Norway.

UD DOD (2008), "Global Positioning System Standard Positioning Service Performance Standard." Fourth Edition. Department of Defence, Positioning, Navigation, and Timing Executive Committee. Document GPS SPS PS.

US DOD (2013), "Interface Specification IS-GPS-200 - Navstar GPS Space Segment/Navigation User Interfaces." US Department of Defence, Global Positioning Systems Directorate, Systems Engineering & Integration. Document No. IS-GPS-200H.

US DoD/DoT/DoHS (2012). "Federal Radionavigation Plan – 2012." United States Department of Defence, Department of Transport and Department of Homeland Security - National Technical Information Services. Springfield (VA), 22181. Doc. DOT-VNTSC-RITA-08-02/DoD-4650.05. 2012.

US DoD/FAA (2008), "Global Positioning System Wide Area Augmentation Systems (WAAS) Performance Standard", First Edition. United States Department of Defence and Federal Aviation Administration. Washington DC (USA).

US DoT/DoD (2008), "US Federal Radionavigation Plan." United States Department of Defence, Department of Transport. Doc. DoT-VNTSC-RITA-08-02/DoD-4650.5.

Van Dierendonck, A. J., Fenton, P. and Ford, T. (1992), "Theory and Performance of Narrow Correlator Spacing in GPS Receiver." Navigation: Journal of the Insitute of Navigation, vol. 39, no. 3, pp. 265-284.

Verhagen, S. (2005), "On the reliability of integer ambiguity resolution." NAVIGATION: Journal of the Institute of Navigation. Vol. 52, Issaue 2, pp. 99-110.

Verhagen, S. (2006), "Improved performance of Multi-Carrier Ambiguity Resolution based on the LAMBDA method." In Proceedings of Navitec 2006, ESA-ESTEC, Noordwijk (The Netherlands).

Walsh, D. (1994), "Kinematic GPS Ambiguity Resolution." PhD Thesis, IESSG, University of Nottingham (UK).

Walter, T. and Enge, P. (1995), "Weighted RAIM for Precision Approach", In Proceedings of the 8th International Technical Meeting of the Satellite Division of the Institute of Navigation, Palm Springs, CA (USA).

Walter, T., Enge, P., Blanch, J., and Pervan, B. (2008), "Worldwide Vertical Guidance of Aircraft Based on Modernized GPS and New Integrity Augmentations." In Proceedings of the IEEE, Vol. 96, Issue 12, pp. 1918-1935

3

GNSS PERFORMANCE IN AVIONICS TSPI APPLICATIONS

3.1 INTRODUCTION

The need of the Italian Air Force (ITAF) Research and Flight Test Centre (DASRS/CSV) to develop modern and cost-effective Time-and-Space Position Information (TSPI) solutions for flight test, flight inspection and training applications was the initial motivation behind the experimental research activities carried on GNSS-based TSPI systems (Sabatini et al., 2008). Various GNSS and DGNSS TSPI systems were developed and used on high performance military aircraft (TYPHOON, TORNADO, MB-339CD, AM-X, etc.) for the accomplishment of several experimental and training tasks. However, since the early stages of these activities, it was clear that GNSS performance in terms of data continuity and integrity during high dynamics manoeuvres, even if acceptable for many activities, were not sufficient to fulfil TSPI requirements of modern high performance military aircraft (i.e., fighters, advanced trainers, etc.) and UAV. While carrier-phase DGNSS could provide the required accuracy, some integrity/continuity augmentation strategies had to be adopted. To cope with these issues, further research was performed to develop various methods for post-processing and real-time recovery of DGNSS data losses due to antenna masking, hard manoeuvring or bad satellite configurations, using the data provided by Inertial Navigation Systems (INS) and other on-board sensors (Sabatini et al., 2008). However, it was soon evident that GNSS integrity limitations

were not tolerable for the most demanding tasks of flight-test and flight inspection (e.g., auto-landing, ILS, MLS). In particular, the TTA achievable with standard RAIM techniques exceeded the required safety margins for precision approach/landing applications and the frequent GNSS data losses experienced in high dynamics flight led to unacceptable positioning accuracy degradations even using integrated GNSS/INS Position Reference Systems (PRS). A case study was therefore undertaken in order to identify an integrity augmentation method suitable for GNSS-TSPI and, potentially, other GNSS applications. As a first step, a dedicated analysis (based on mathematical algorithms and experimental data) of the aircraft flight dynamics/performance was required in order to determine the actual flight envelope limitations associated with the use of GNSS during test/training missions. was originally intended for adoption in a dedicated ground-based simulation tool for mission planning and post-mission data analysis purposes. However, the concept successively evolved into a real-time T-ABIA system suitable for integration with the aircraft avionics and Flight Test Instrumentation (FTI) systems; thus effectively providing augmentation of GNSS integrity in flight.

3.2 FLIGHT TEST ACTIVITIES

Experimental investigations were conducted in which GNSS-based TSPI systems were developed and tested. These activities included (Sabatini et al., 2008):

- MB-339CD in-flight evaluation of two GNSS receivers to assess data continuity in high-dynamics manoeuvres;
- TORNADO-IDS DGNSS data continuity and accuracy evaluation;
- EF-2000 DGNSS data continuity, accuracy and overall signal integrity evaluation.

During these activities, GNSS and DGNSS data were analysed with the aim of assessing the performance of the systems and to optimise the design and operations of GNSS-based TSPI systems for various experimental and flight training tasks. Successively, a more detailed analysis was accomplished of the large volume of data

collected in flight and, based on this analysis, the innovative concept of an ABIA system suitable for GNSS-based TSPI applications (T-ABIA) was developed. A brief outline of the various ground and flight test activities performed on GNSS-based TSPI systems is provided below. Further details can be found in (Sabatini, 2005) and (Sabatini et al. 2008).

3.3 AIRCRAFT INSTALLATIONS

The general layout of the MB-339CD installation is shown in Fig. 3-1. In this case, both an ASHTECH Z-12 surveying receiver and a TRIMBLE avionics receiver (TRIMBLE Air Navigation System – TANS) were fitted to the aircraft in order to compare their performances. Using a beam splitter, the same antenna was used for both systems, and a magnetic recorder was used for GNSS and other FTI data gathering.



Figure 3-1. MB-339CD aircraft DGNSS/FTI installation.

The airborne data-recording device used in the MB-339CD flight trials was a magnetic recorder suitable for FTI use. Particularly, all required flight parameters (INS position, velocity, acceleration components, etc.) from the FTI and TSPI data from both GNSS receivers were recorded. A picture of the MB-339CD back-seat FTI rack installation (including the ASHTECH Z-12 GNSS receiver) is shown in Fig. 3-2.

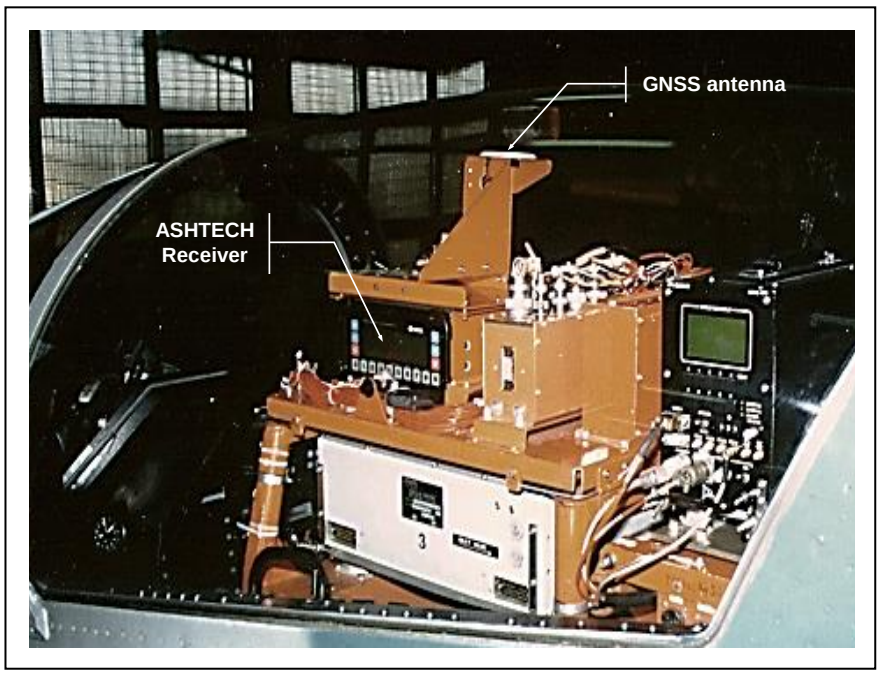


Figure 3-2. MB-339CD FTI and ASHTECH receiver.

Fig. 3-3 shows the GNSS receiver and telemetry antennae installed on the TORNADO-IDS aircraft. The GNSS antenna was located on the aircraft skin at a distance of about 1.5 m from the cockpit and a few decimetres from the telemetry antenna. The ASHTECH Z-12 receiver was installed in the avionics bay. In this case, the Electro-Magnetic Compatibility (EMC) and Interference (EMI) of the GNSS/telemetry equipment (between each other and with the other on-board systems) had to be deeply verified before flight. Airborne GNSS data recording was performed using the ASHTECH Z-12 internal memory, while the other aircraft data (INS position and attitude data, altitude data from radar altimeter and barometric altimeter, etc.) where recorded on a magnetic data recorder and other digital recording equipment available in the FTI.



Figure 3-3. TORNADO-IDS GNSS/Telemetry antennae installation.

The positions of the GNSS and telemetry antennae installed on the EF-2000 DA7 (Development Aircraft No. 7) installation is depicted in Fig. 3-4.



Figure 3-4. EF-2000 GNSS/Telemetry installation.

In this case, due to the greater distance between the GNSS antenna and the telemetry antenna (located in a wing tip pod), there were much less concerns regarding the possible interferences between the telemetry transmitter and GNSS receiver. However, also in this case, the EMC aspects of the installation were investigated before flight.

3.4 TSPI SYSTEMS SETUP

Before performing flight trials, it was important to select the setup parameters of the on-board GNSS receiver. These parameters could be programmed either by using the GNSS receiver control panels (e.g., ASHTECH Z-12 keyboard/display on the receiver front panel) or by using a remote programming unit (e.g., a common PC in the case of TANS). Optimal parameters for flight test TSPI applications are the following:

- Data recording rate: 1-10 samples/sec;
- Mask: 10° (i.e. minimum satellite elevation over the horizon for multipath reduction);
- Minimum number of satellites for position computation: 3 only when using an external accurate altitude input (not with last available GNSS altitude data). 4 in all other cases2;
- PDOP threshold (for position calculation): less than 5;
- Minimum satellite signal Signal-to-Noise Ratio (SNR): 15-30 dB.

GNSS data downloading (from both the on-board and ground reference receivers) and differential processing were performed on the ground (post-flight) for accurate aircraft trajectory reconstruction[3]. In Sabatini et al. (2008), further information is

[2] The TANS GNSS receiver incorporates an option that allows calculation of position using measurements from only 3 satellites (in this case, as tracking to the fourth satellite is lost, the last calculated height data is used to provide a position solution). Obviously, the accuracy may degrade significantly in case of sudden aircraft altitude variations.

[3] In other cases (real-time DGNSS implementations with data link) differentially corrected data are computed on the ground by the reference station (one-way link) or in flight (bi-directional link), and recorded on-board the aircraft. In most practical implementations, however, the post-processing option is preferred both due to simplicity and high accuracy attainable with off-line carrier phase processing.

provided regarding the ground DGNSS reference station, the telemetry data link design and the ASHTECH post-flight data analysis software.

3.5 GROUND TEST ACTIVITIES

A preliminary ground test session was performed with the GNSS receivers in order to test the accuracy of the DGNSS data and to gain confidence with differential techniques (data downloading and processing software tools) before performing actual flight trials. Furthermore, Electro Magnetic Compatibility (EMC) and Interference (EMI) ground tests were performed on the aircraft installations in order to identify possible interferences between the aircraft avionics, the on-board GNSS system and rest of the FTI. The ground trial was performed with two ASHTECH receivers (Fig. 3-5). A roving GNSS receiver was installed on an electrically powered trolley and a second ASHTECH receiver was located in a surveyed site to provide data for differential corrections. The trolley covered a well-known route of about 3 km in the Turin International Airport (Caselle). The track was followed twice (in opposite directions) along a road about 6.2 metres wide. After the trial, data stored into the internal memories of the two receivers were downloaded to a personal computer for differential processing and analysis (i.e., differential pseudorange processing and post-processing noise reduction).

The stand-alone accuracy of the receiver was 22.4 m SEP (SA off) and well within the specifications. The results obtained with C/A code differential processing were also very encouraging with a position data accuracy of 3.1 m SEP. Electro Magnetic Compatibility (EMC) and Interference (EMI) ground trials were also performed with the GNSS system installed on the aircraft, in order to identify possible mutual interferences between the aircraft standard avionics systems (communications, radio-navigation, identification, radar, etc.) and the newly installed GNSS TSPI. Further information on this activity are provided in Sabatini et al. (2008).

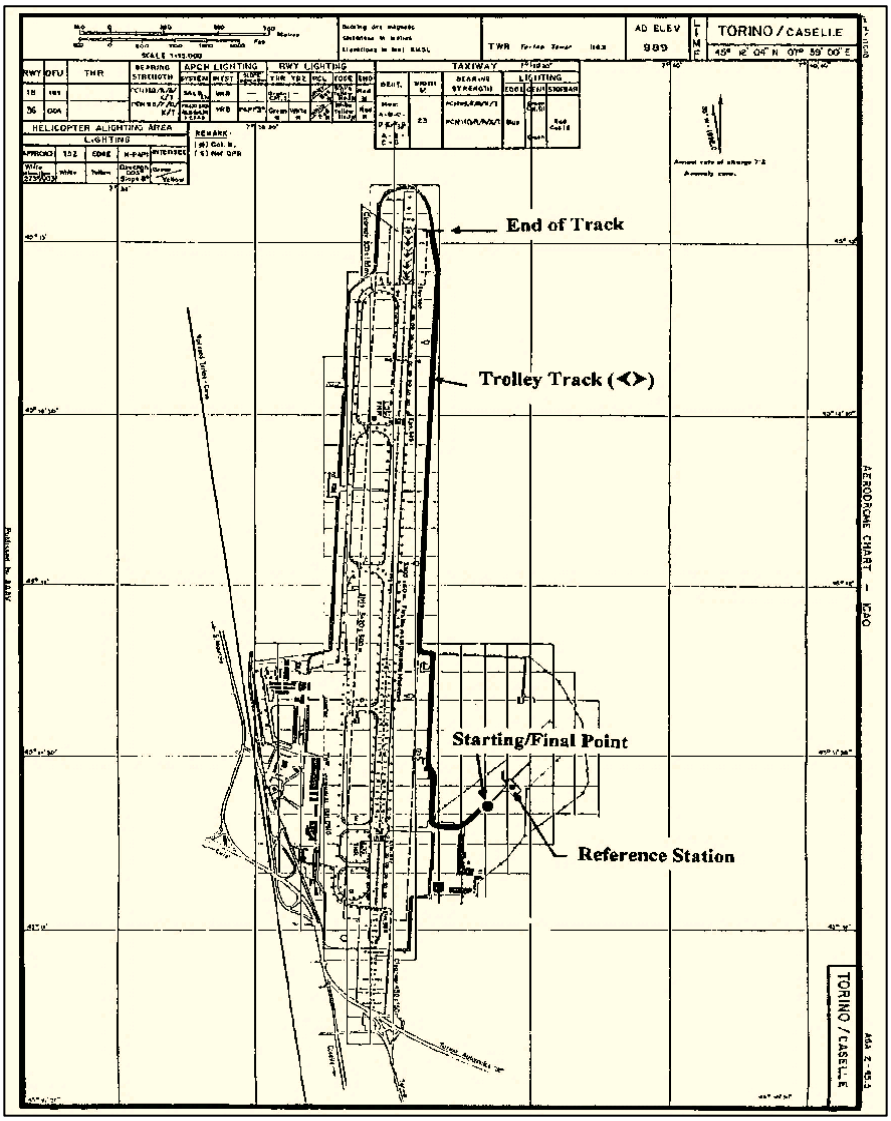


Figure 3-5. Aerodrome chart with reference station and trolley track (Sabatini et al., 2008).

3.6 MB-339CD FLIGHT TEST ACTIVITIES

During the MB-339CD avionics flight trials, an in-flight evaluation of GNSS and DGNSS was carried out. The aim of this assessment was to compare the performance of various GNSS receivers in a dynamic environment, in order to select the system with the best performance for employment in future activities. Particularly, the assessment focused on the data continuity provided by the two GNSS receivers during execution of low, medium, and high dynamics manoeuvres and re-acquisition times after GNSS data losses. Therefore, no dedicated accuracy

tests were performed in this phase, except an initial evaluation of DGNSS altitude data quality. Specific flight test matrixes were defined in order to allow an evaluation of the installed GNSS TSPI receivers (i.e., TRIMBLE-TANS and ASHTECH-Z12) on the MB-339CD aircraft. Particularly, the following manoeuvres, representative of the real dynamic conditions that can be encountered during flight tasks, were performed:

- Turns with constant bank angles;
- Dives followed by a pull up to 4 g's along the four cardinal directions;
- High dynamic manoeuvres as tonneau and stick-jerks.

The first type of manoeuvre was performed in order to evaluate the antenna masking effect. The second is a typical weapon-aiming manoeuvre, while the third type of manoeuvre was performed in order to test the receivers in a high dynamics environment. It must be underlined that a determination of the accuracies provided by two systems was not considered essential in this phase of the program and therefore it was not carried out in the MB-339CD test campaign. This was done for two good reasons:

- The availability of literature concerning previous evaluations conducted of DGNSS systems confirmed the high accuracies declared by TRIMBLE and ASHTECH for the two systems under test. This was particularly through for straight-and-level flight conditions and low dynamic manoeuvres;
- The difficulty of measuring the system accuracy during execution of flight trials. In order to prove that a DGNSS system meets its accuracy requirements, an independent reference system is needed with an accuracy of at least factor 8 (preferably 10). Moreover, the verification should be carried out over the full flight envelope. Systems that could be possibly used were cinetheodolites or laser trackers, with accuracies in the order of 0.2 – 0.5 metre RMS. However, neither cinetheodolites nor laser tracker facilities were available in this phase of the program.

As expected, during straight-and-level flight both receivers under test performed satisfactorily, with no significant data losses recorded. However, during execution of dynamic manoeuvres both systems frequently lost lock to the satellites. Analysing the dynamics of the aircraft it was understood that this phenomenon could be due to shielding of the GNSS antenna by the aircraft body (wings, fuselage and tails).

The INS data (recorder by the FTI) relative to variations of significant flight parameters in a period of a few minutes (heading, altitude, pitch, bank, etc.) are shown in Fig. 3-6. Identification of the aircraft parameters, together with the various associated scales, is given in Table 3-1.

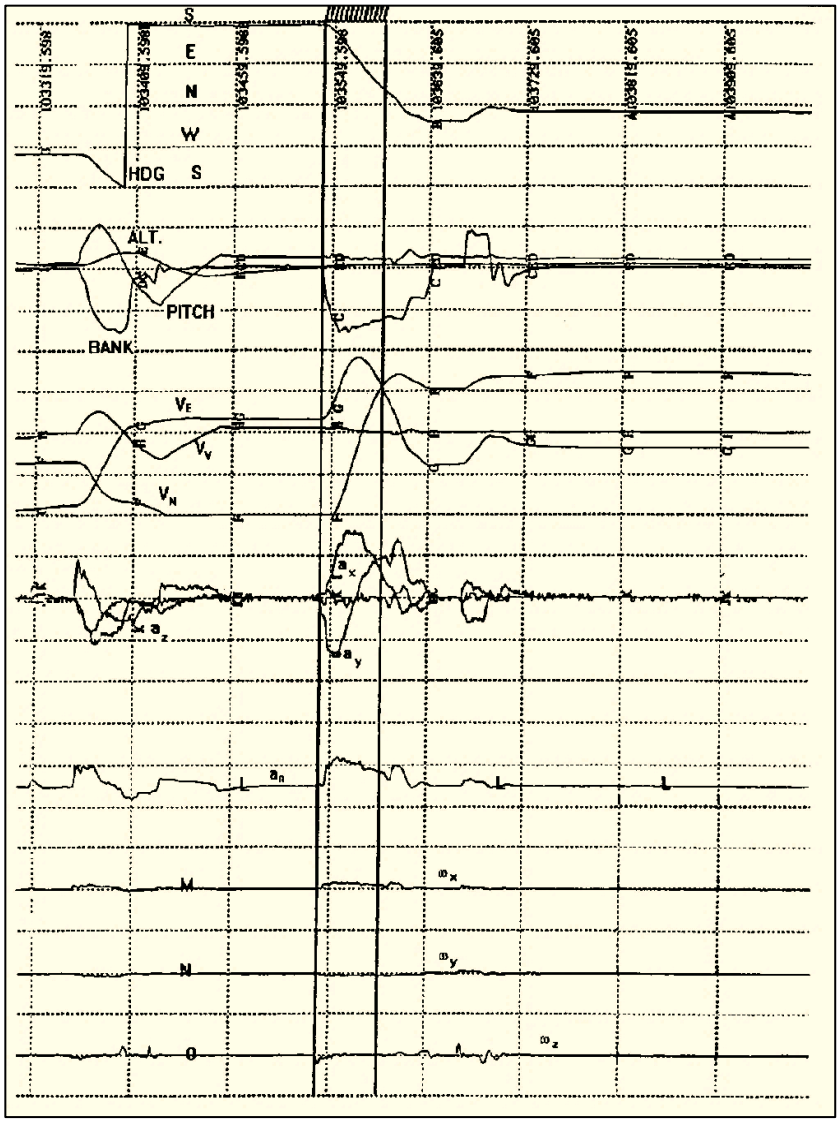


Figure 3-6. INS data recorded by the FTI.

Table 3-1. Identification of aircraft parameters.

- B = Magnetic Heading (-180° ÷ 180°);
- C = Roll Angle (-90 ÷ 90°);
- D = Pitch Angle (-40 ÷ 40°);
- E = Barometric Altitude (0 ÷ 40000 ft);
- F =NORTH Velocity (-800 ÷ 800 ft/s);
- G = EST Velocity (-800 ÷ 800 ft/s);
- H =Vertical Velocity (-800÷800 ft/s);
- I = Along X Acceleration (-80÷80 ft/s^2);
- J = Along Y Acceleration (-80÷80 ft/s^2);
- K = Along Z Acceleration (-80÷80 ft/s^2);
- L = Normal Acceleration (-2 ÷ 6g);
- M = Angular Vel. about X (-40÷ 40 °/s);
- N = Angular Vel. about Y (-40÷ 40 °/s);
- O = Angular Vel. about Z (-100 ÷ 100 °/s).

The manoeuvre presented in Fig. 3-6 is a left turn (about 60° bank angle) corresponding to a GNSS data loss (for both TRIMBLE and ASHTECH receivers). The SNR measured for the satellites in view are shown in Fig. 3-7. It is evident that the signal intensity did not decrease gradually. This confirms that the signal loss, in this case, was due to interposition of an obstacle between the satellites and the antenna and not to receiver tracking problems.

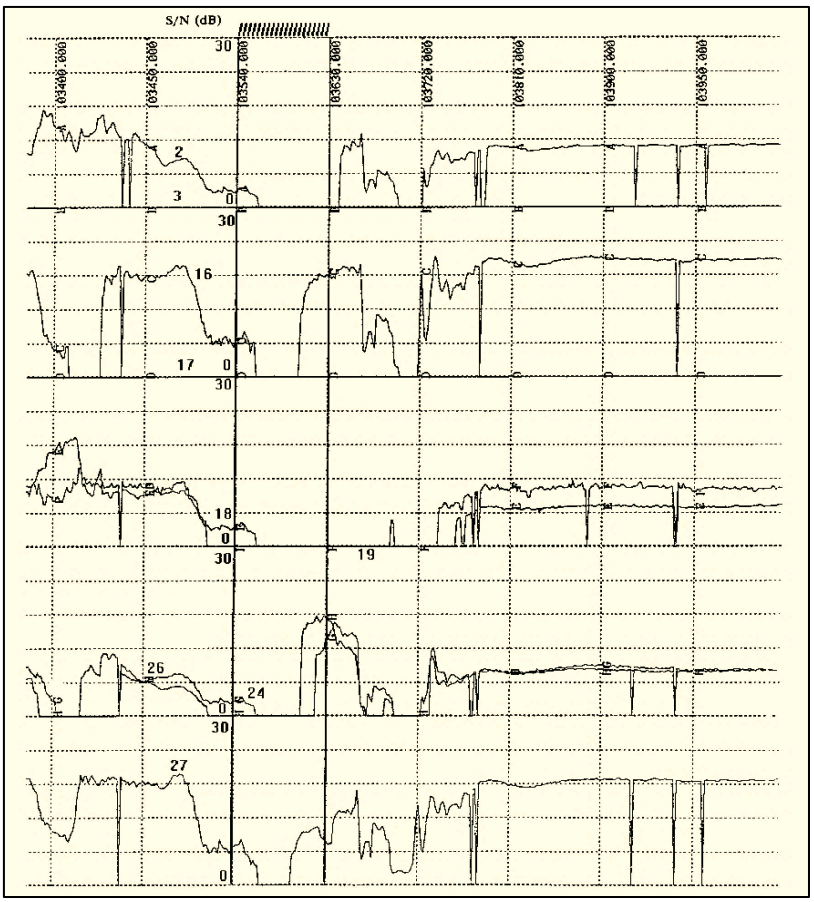


Figure 3-7. SNR of the GNSS satellites.

The relative positions of the aircraft and satellites during the manoeuvre are shown in Fig. 3-8. It can be noticed that the aircraft body masked many of the satellites during the turn (starting from an initial heading of 180°). Signal reacquisition took place when the aircraft progressively reduced the bank angle and the heading variation rate.

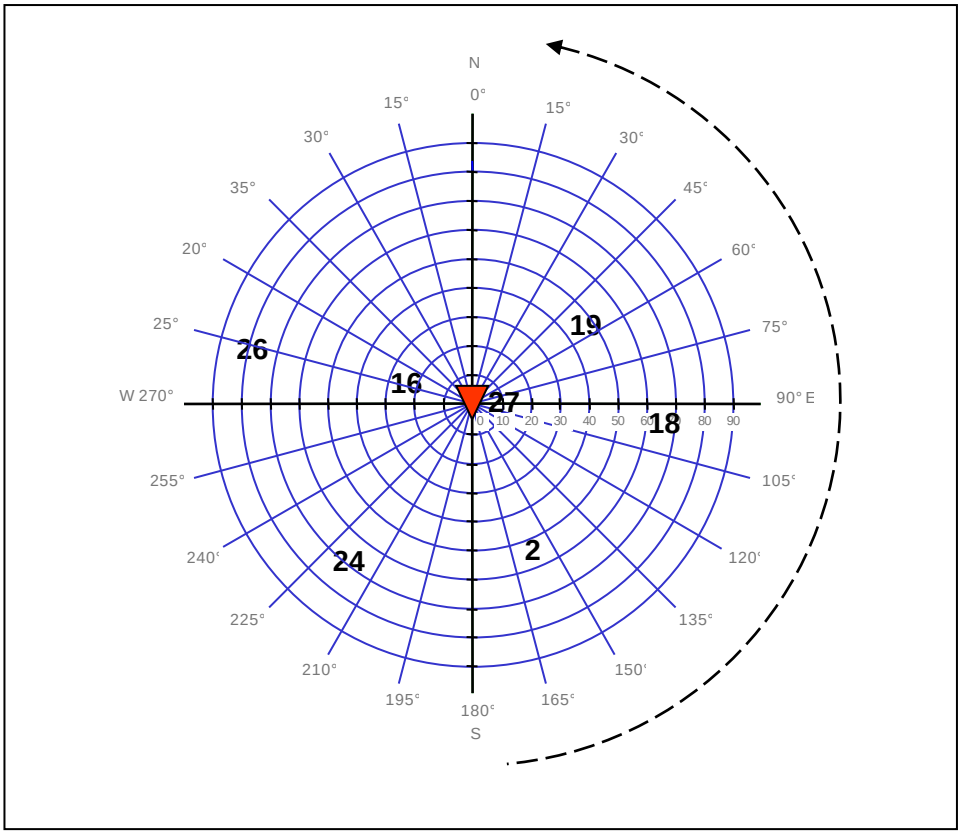


Figure 3-8. Relative geometry of the aircraft and satellites.

Similar considerations can be done looking at the Figures 3-9, 3-10 and 3-11 relative to a left turn with -45° bank angle. However, in this case, a difference was noticed between the two receivers. As the position of the aircraft longitudinal axes during the turn got closer to satellite 2 (in the horizontal plane) the TRIMBLE receiver experienced a loss of track to all satellites, while the satellites 19 and 27 were still tracked by the ASHTECH receiver. This was due to the internal processing of the receiver. In fact, the ASHTECH receiver was able to maintain track to the satellites in view (19 and 27) even when the SNRs were very low (i.e., below 5 dB), while in the same conditions TANS lost track to all satellites. This significantly reduced the

time required by the ASHTECH receiver for a new position fix as soon as four satellites were available again. Other trials, performed in similar conditions, confirmed that with the ASHTECH receiver shorter periods were needed to compute a new positioning solution after loss of satellite signals.

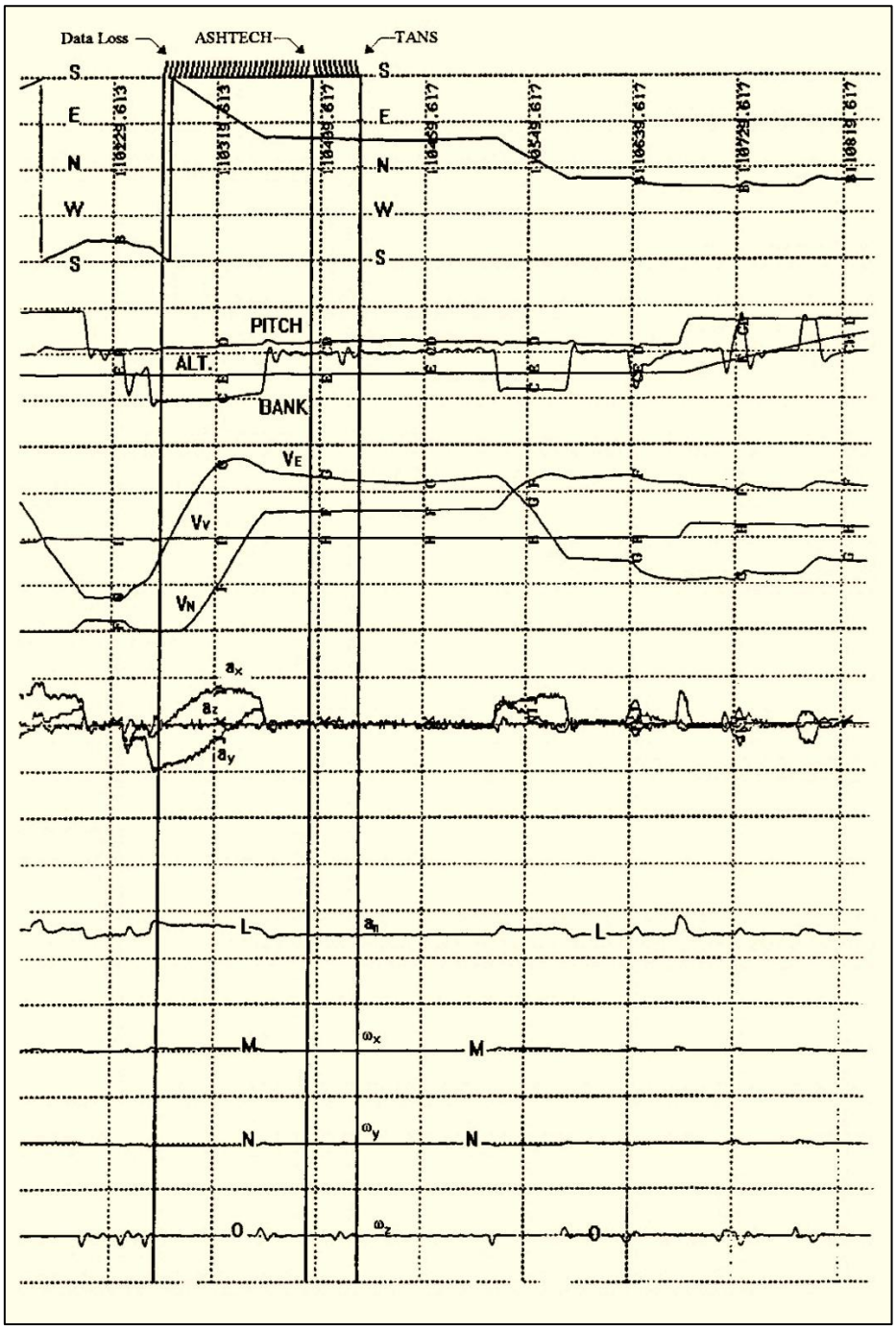


Figure 3-9. GNSS data loss periods (manoeuvres).

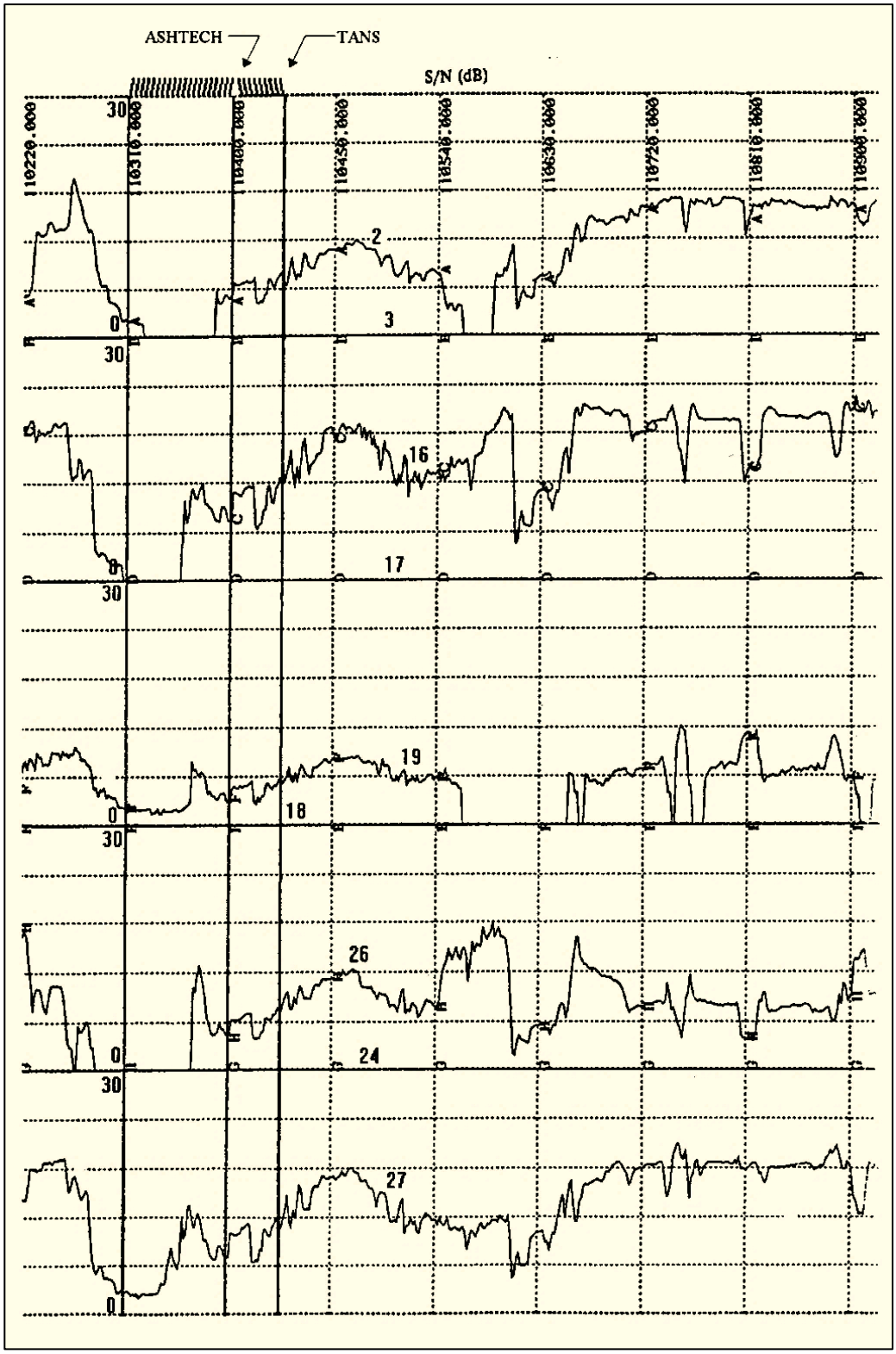


Figure 3-10. GNSS data loss periods (SNRs).

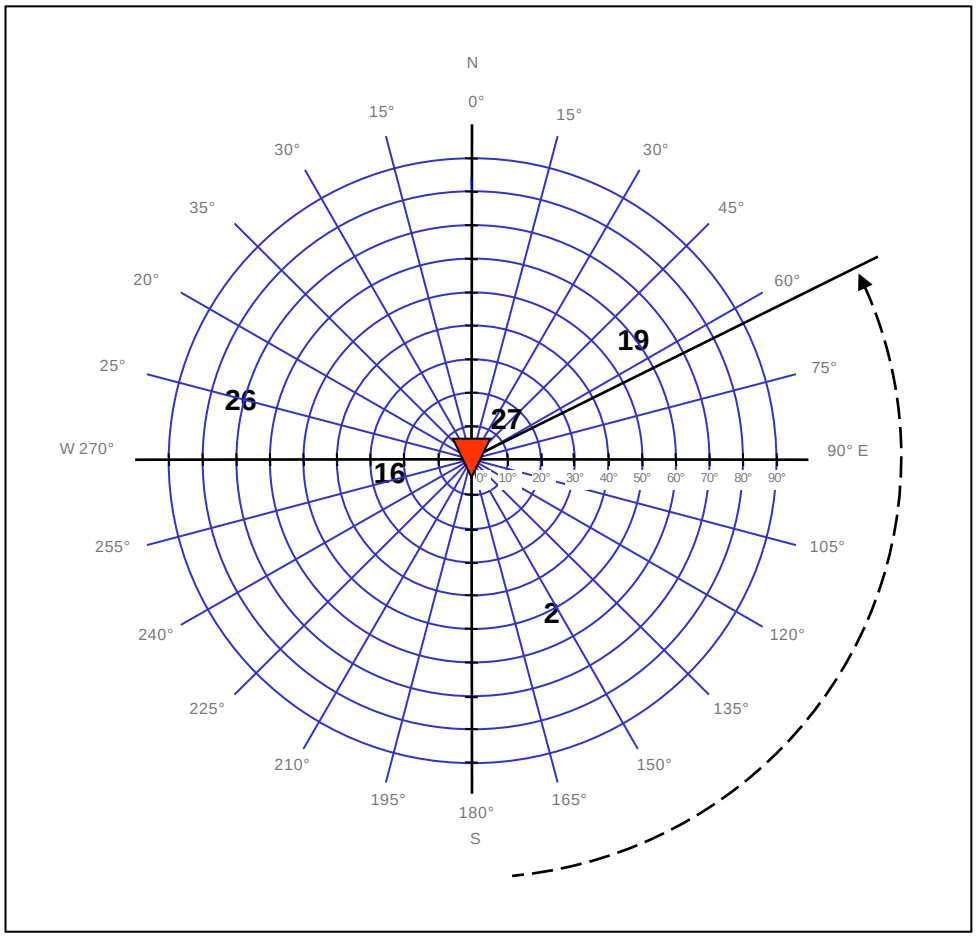


Figure 3-11. Aircraft-satellites relative geometry during data loss.

Figures 3-12, 3-13 and 3-14 confirm that both the increase of PDOP and the reduction of the SNRs due to satellite-receiver geometry degradations were responsible (together with masking of the GNSS antenna), for the GNSS data losses during dynamic manoeuvres. In this case, the TANS navigation data were lost with a small variation of the aircraft-receiver relative geometry, loss occurred with a small variation of the aircraft-receiver relative geometry and no satellites were lost due to masking. The ASHTECH receiver, in the same conditions, did not experience any signal losses.

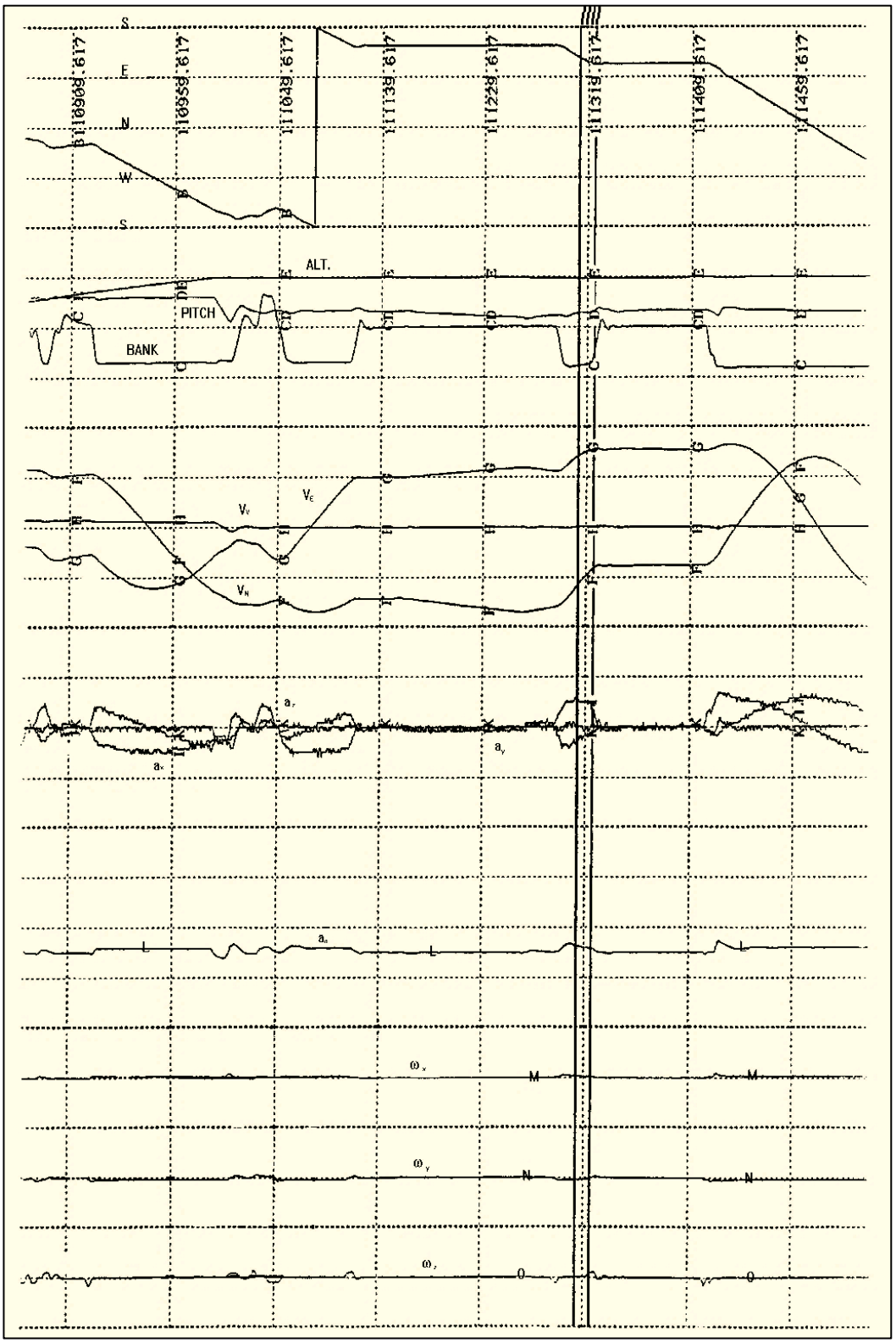


Figure 3-12. TANS data loss periods (manoeuvres).

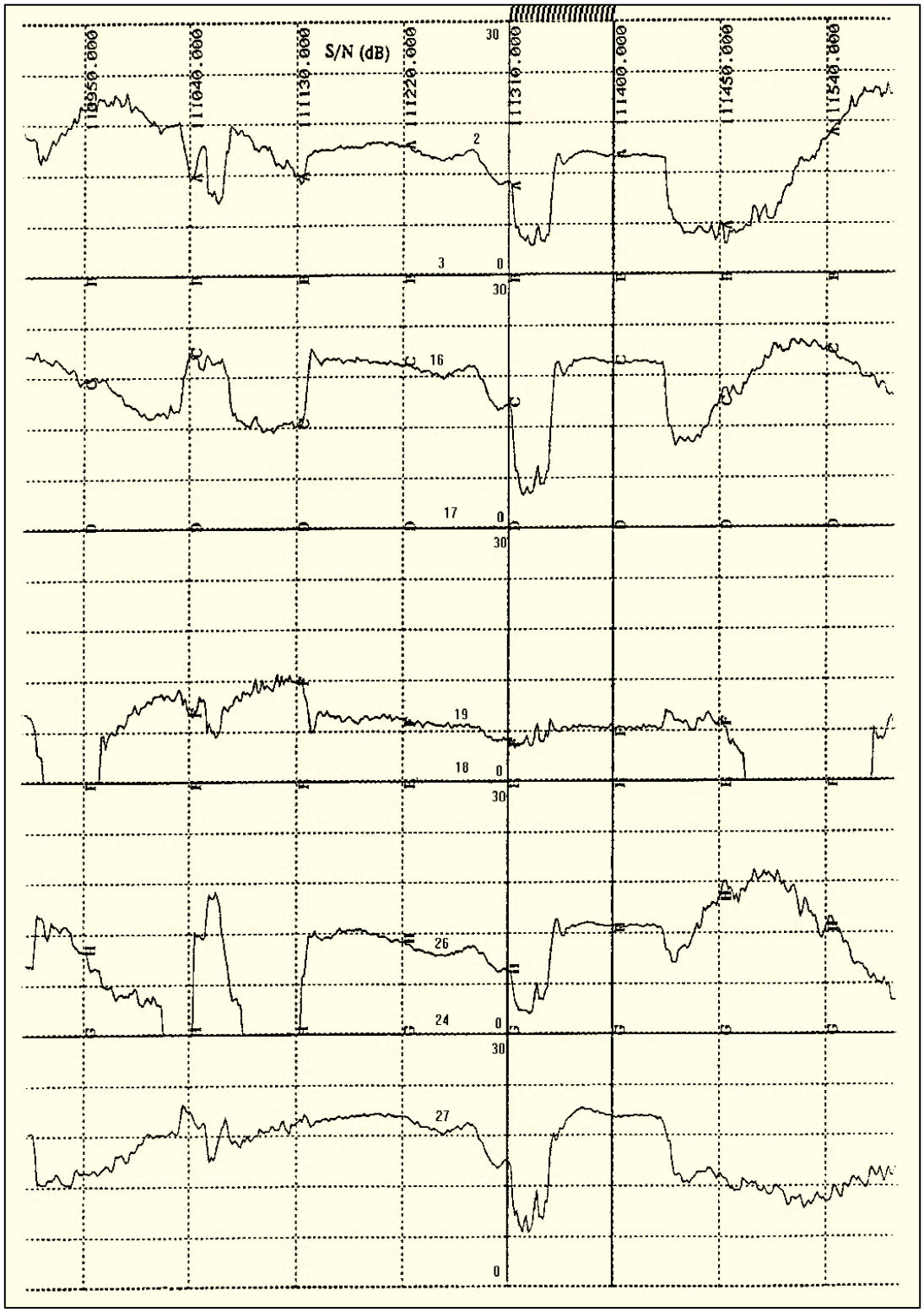


Figure 3-13. SNRs during TANS data loss periods.

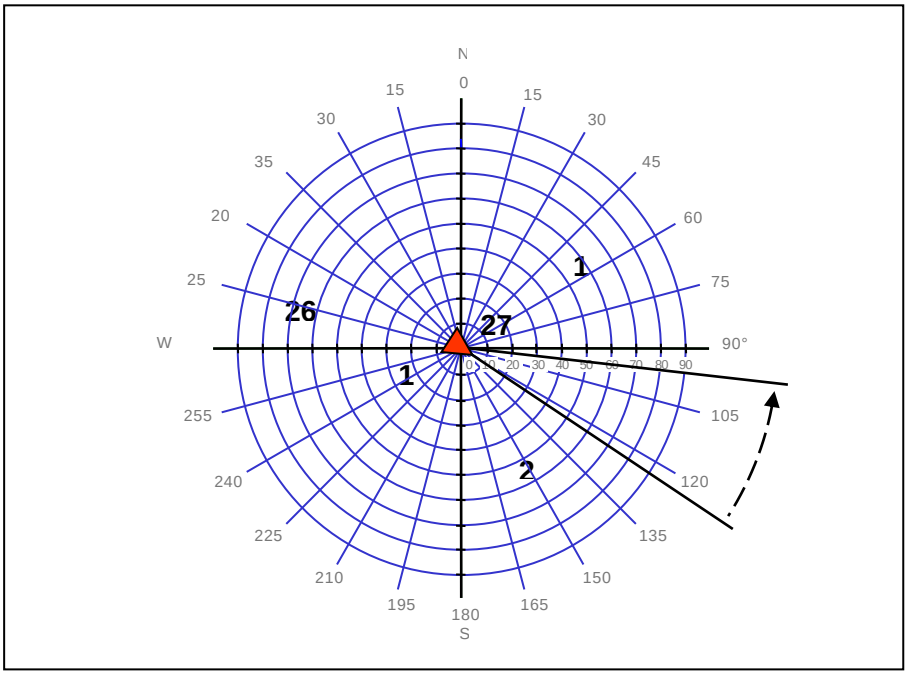


Figure 3-14. Aircraft-satellites relative geometry during TANS data loss.

Similar manoeuvres, performed in other directions, did not cause any problem to the receivers. An example is shown in the Figures 3-15 and 3-16 relative to a right turn with 40° bank, where the satellite configuration changed but without signal losses.

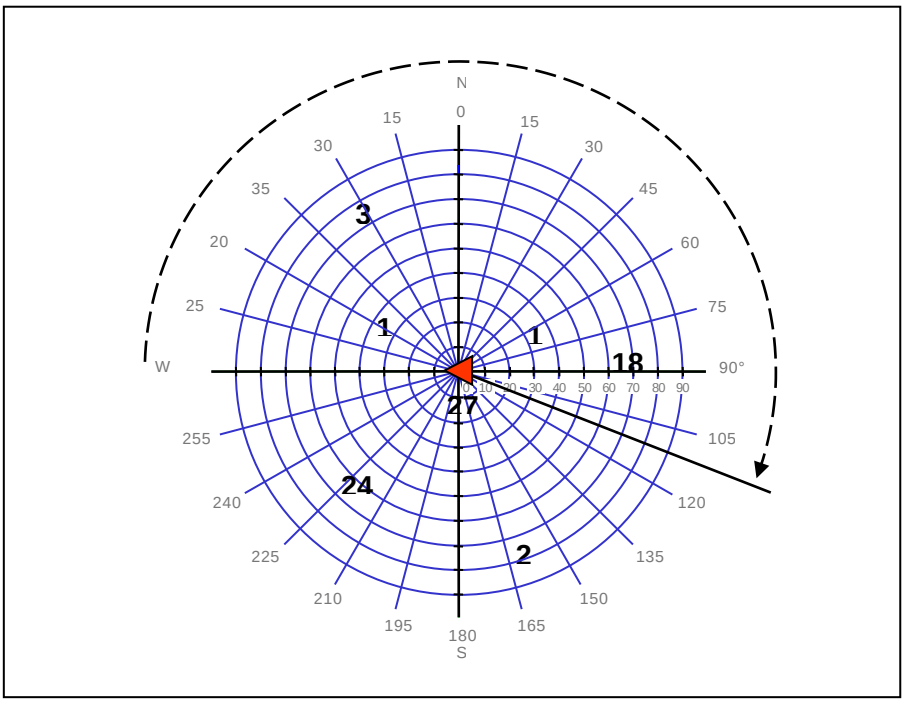


Figure 3-15. Aircraft-satellites relative geometry (no data losses).

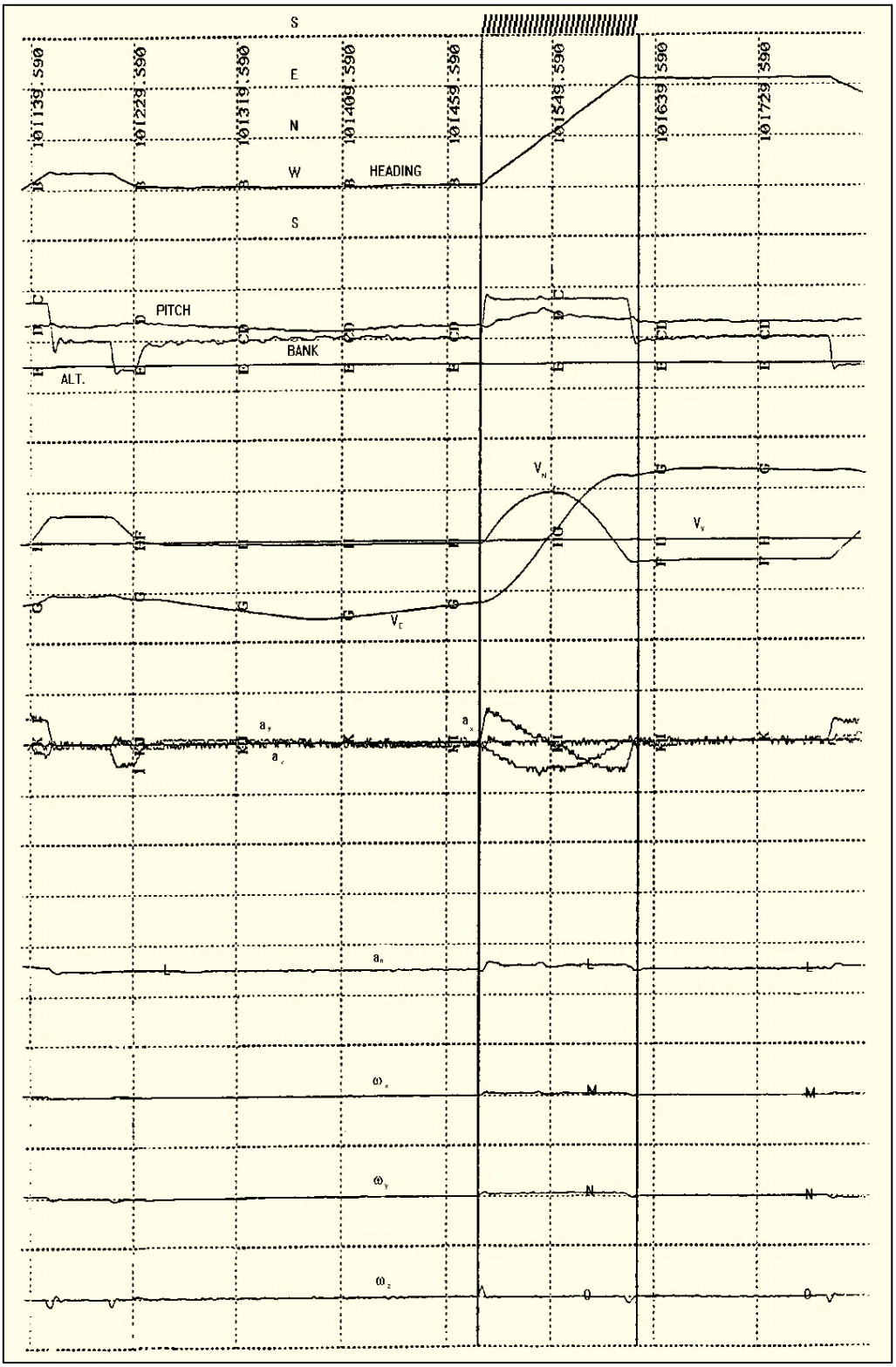


Figure 3-16. Manoeuvres without GNSS data losses.

Fig. 3-17 shows that a change of satellite configuration, even with low dynamics aircraft manoeuvres, may determine a significant accuracy degradation. Particularly, the loss of one satellite (from five to four satellites tracked), determined a considerable increase of the PDOP.

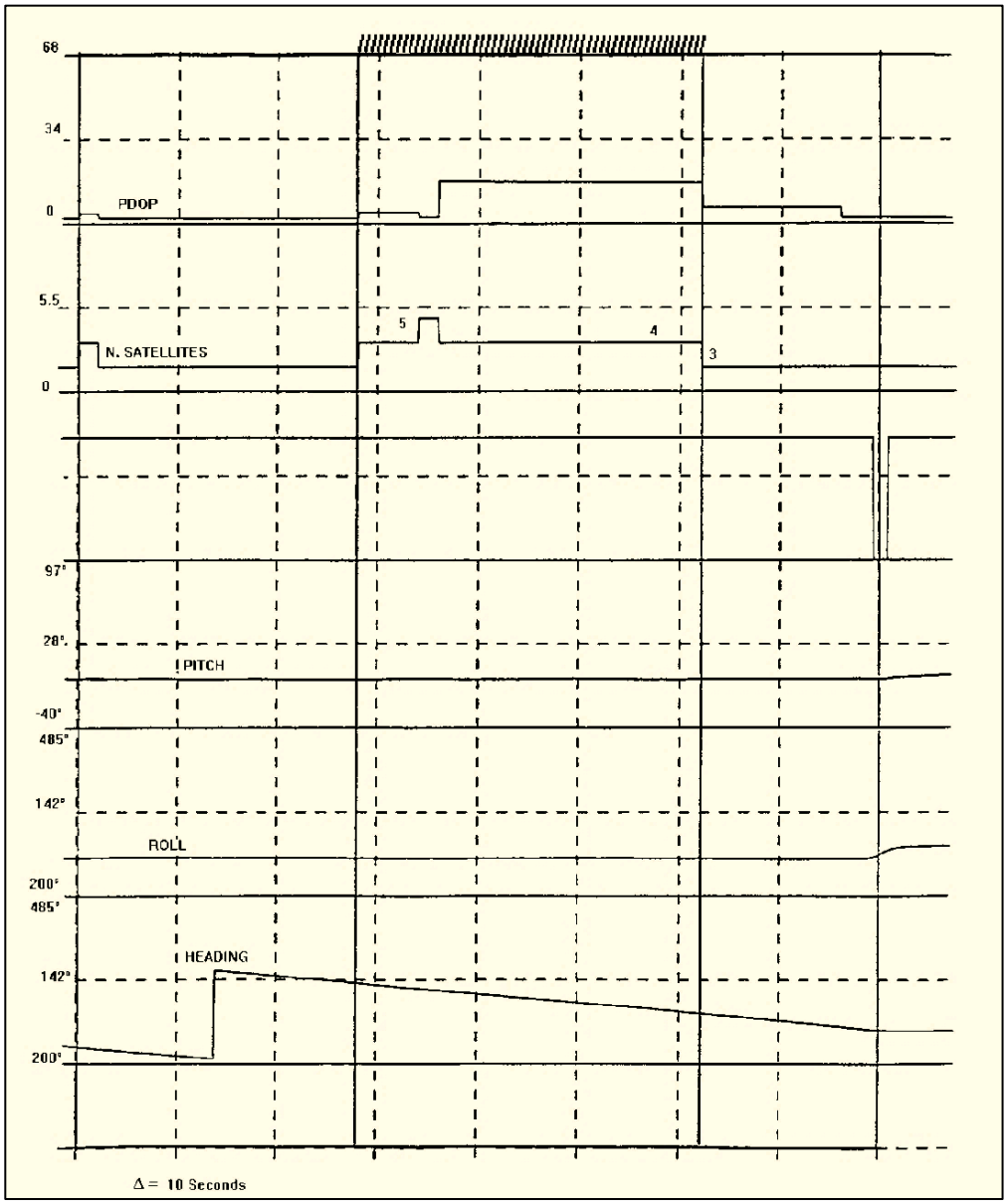


Figure 3-17. PDOP increase with loss of 1 satellite.

We therefore started to investigate if the problem could be significantly amplified by medium/high dynamics aircraft manoeuvres typical of high performance aircraft flight test. The flight parameters relative to a stick-jerk manoeuvre are shown in Fig.

3-7. During this manoeuvre the stick is repetitively pulled and pushed in order to obtain high jerks. This can be a very critical manoeuvre for the GNSS receivers (especially for the code correlation circuits). The jerk limits were not specified for the ASHTECH receiver, while for TANS a jerk limit of 2 g/s was quoted. During the manoeuvre shown in Fig. 3-7, a jerk of about 2.8 g/s was obtained but no data loss occurred in any of the two receivers.

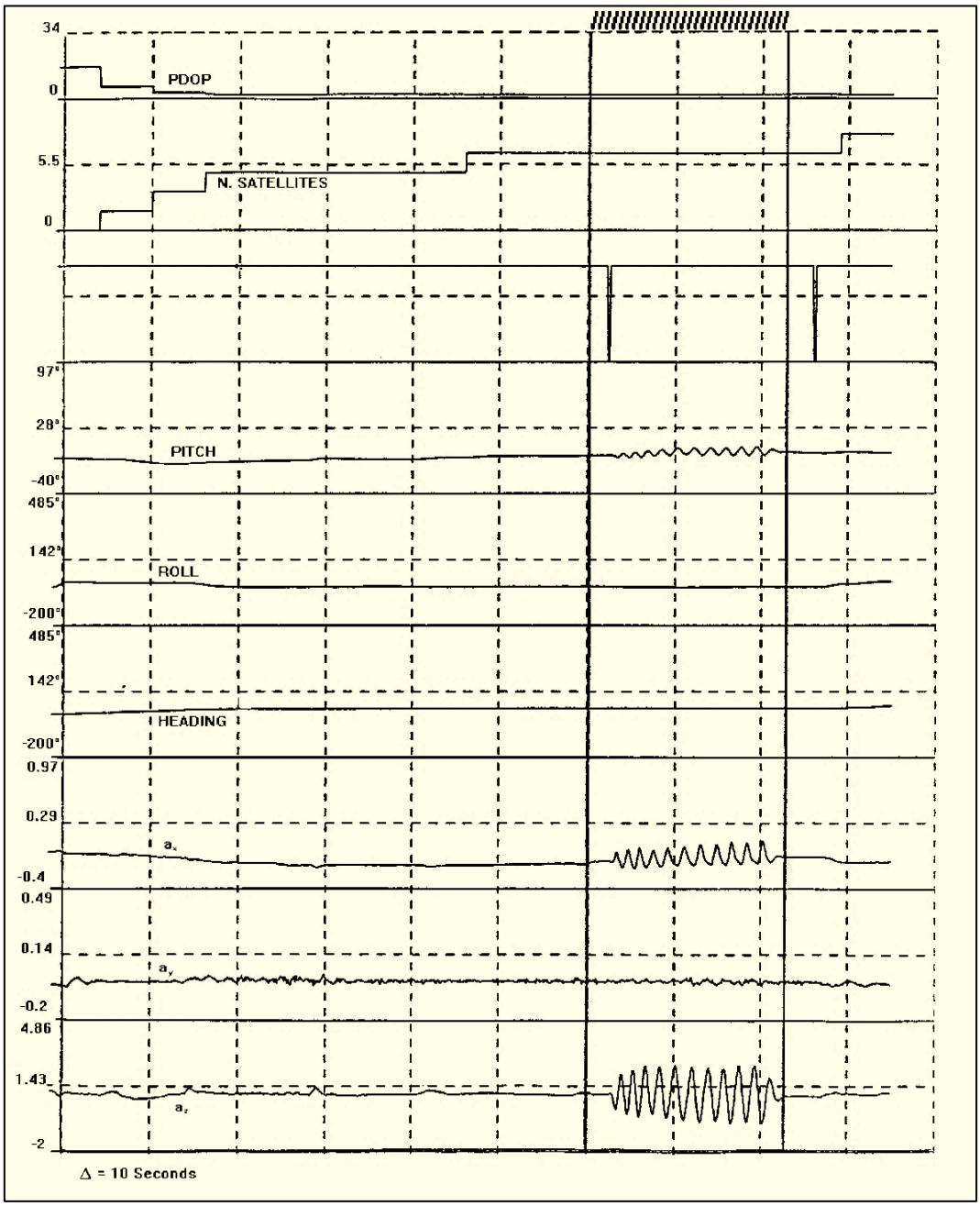


Figure 3-18. Stick-jerk manoeuvre.

The data shown in Fig. 3-19 were recorded during three pull-up manoeuvres at 4 g's (typical in weapon-delivery trials). While during execution of the manoeuvres lock on to the satellites was kept (between four and three satellites tracked), at the end of each manoeuvre total signal losses occurred. The three manoeuvres were always preceded by straight-and-level flight (about 30 seconds) to allow optimal satellite tracking. Again, the reacquisition time after total signal losses was significantly longer for the TANS receiver than for the ASHTECH receiver.

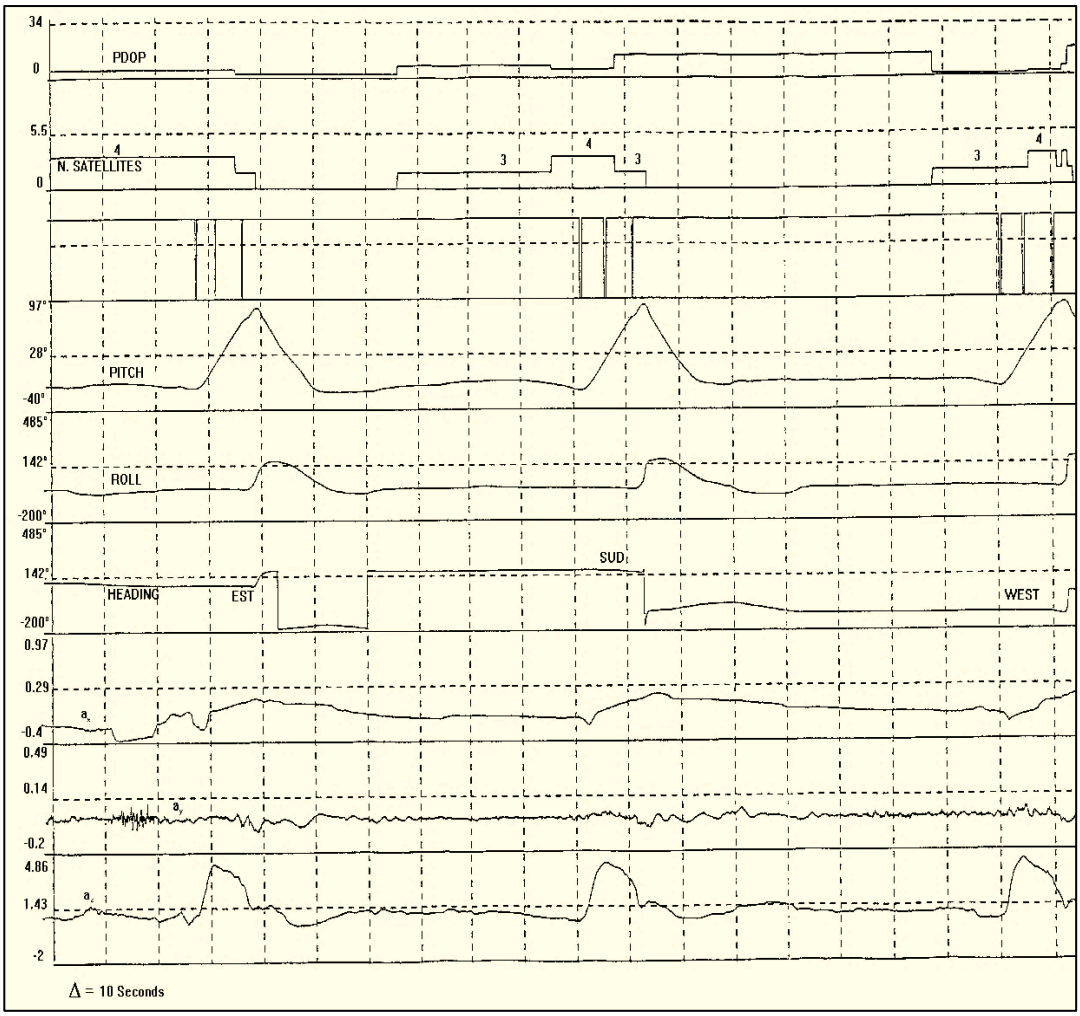


Figure 3-19. Pull-up manoeuvres.

Further tests were also performed with rapid-rolling horizontal manoeuvres (tonneau). In these cases, the lock to the satellites was efficiently maintained by both

receivers, as long as the duration of the manoeuvres did not exceed 5 seconds, which is considered adequate for the majority of flight test tasks. In general, the performances of the receivers during medium/high dynamics manoeuvres without turns were significantly better than the performances during turns with high bank angles. This was mainly due to antenna masking and low SNR of satellites with low elevation angles. Due to the significant differences observed between the two GNSS receivers in terms tracking robustness with degraded SNRs and TTSF in high dynamics manoeuvres, the ASHTECH receiver was selected for the subsequent flight trials. Further details about the MB-339CD flight test campaign are available in Sabatini et al., 2008.

3.7 TORNADO-IDS AND TYPHOON FLIGHT TRIALS

The initial MB-339CD flight test activities demonstrated that GNSS cannot provide the necessary information with regard to data rate and data continuity during high dynamics manoeuvres. In particular, it was observed that the main disadvantage of the GNSS is its vulnerability to signal losses caused by satellites masking and low SNRs. Therefore, further trials were performed on TORNADO-IDS and TYPHOON aircraft to assess DGNSS data accuracy and continuity during high dynamics manoeuvres. Additionally, detailed evaluations of satellite masking, Doppler and SNR variations on GNSS signal acquisition was accomplished on the TORNADO-IDS aircraft equipped with the ASHTECH receiver.

3.7.1 TSPI Accuracy and Continuity Evaluation

A comparison of positioning data provided by the GNSS receiver and by other airborne sensors or ground tracking systems allowed the evaluation of DGNSS data quality and accuracy. It must be underlined that a proper determination of the errors associated with an airborne navigation system would require a reference datum with an accuracy of a list a factor 8 (better 10). This kind of reference is obviously very difficult (if not impossible) to be identified in the case of DGNSS accuracy

testing. The best options available is to use high-accuracy cinetheodolites or laser tracking systems of proven pointing stability, whose quoted accuracy are typically in the order of 0.2 ÷ 0.5 metres. For the accuracy flight trials (TORNADO-IDS), the following position reference systems were used:

- The TORNADO-IDS aircraft Radar Altimeter (R/A);
- Laser range from the THALES Convertible Laser Designation Pod (CLDP) installed on the aircraft;
- Ground based optical cinetheodolites systems.

In the first case, number of over-sea flight legs were performed in order to preliminarily assess the DGNSS altitude data quality. The ASHTECH DGNSS altitude data output was provided both in the form of geodetic altitude or ellipsoidal height. The height above terrain measured by a R/A is obviously different from the geodetic height provided by the GNSS. Moreover, there is not a fixed relationship between the height above Mean Sea Level (MSL) and the geodetic height. This is due to irregularities of the Geoid (i.e., the equipotential surface defined in the Earth's gravity field which can be approximated, for some practical applications, to MSL). Flying over the sea, the R/A height approximates the MSL altitude. As he Geoid-MSL separation was unknown during the trials, a certain degree of uniformity was obtained flying round tracks over limited sea areas (i.e., there was an unknown bias in the comparison).

Various tests were carried out with different satellite numbers and PDOP ranging from 2.4 to 5. The differences between DGNSS and R/A altitudes were measured in the range 3 ÷ 13 metres. Fig. 3-20 shows the GNSS and R/A data recorded in one flight. The R/A data sixth order polynomial fit, shown in the graph, follows quite well the DGNSS data trend. The estimated measurement bias was in the order of 7.5 metres. Considering the R/A quoted error of ± 3% (of the height displayed), the results of the qualitative comparison of DGNSS and R/A data were considered satisfactory.

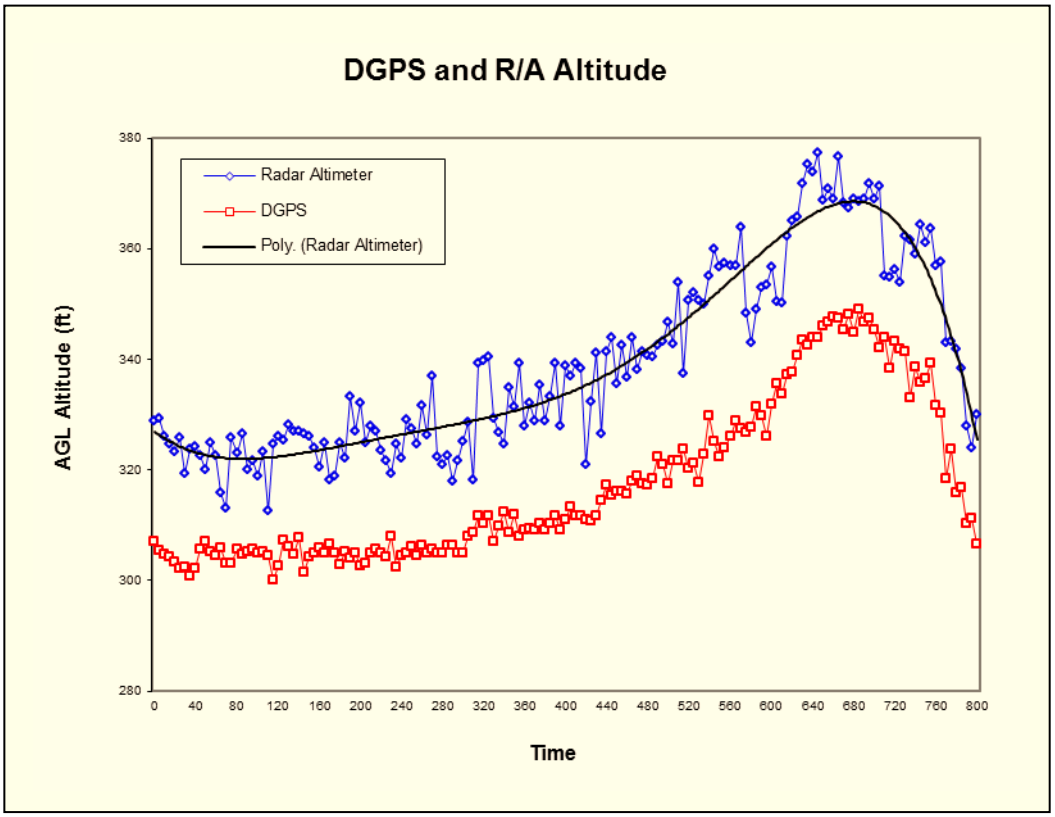


Figure 3-20. Comparison between DGNSS and R/A data.

The DGNSS-Laser Range evaluation was performed with the THALES CLDP during a TORNADO-IDS flight test campaign at the Cazaux range in France. The CLDP system is designed to provide the aircraft with day and night laser designation/ranging capability, for both cooperative and self-designation attacks performed using laser-guided weapons. The pod is equipped with an internal designation laser operating at 1.064 μm (non-eyesafe region of the spectrum) and may be configured for day-time operation by using a television camera (TV) or for day/night operation by using an IR sensor (Fig. 3-21).

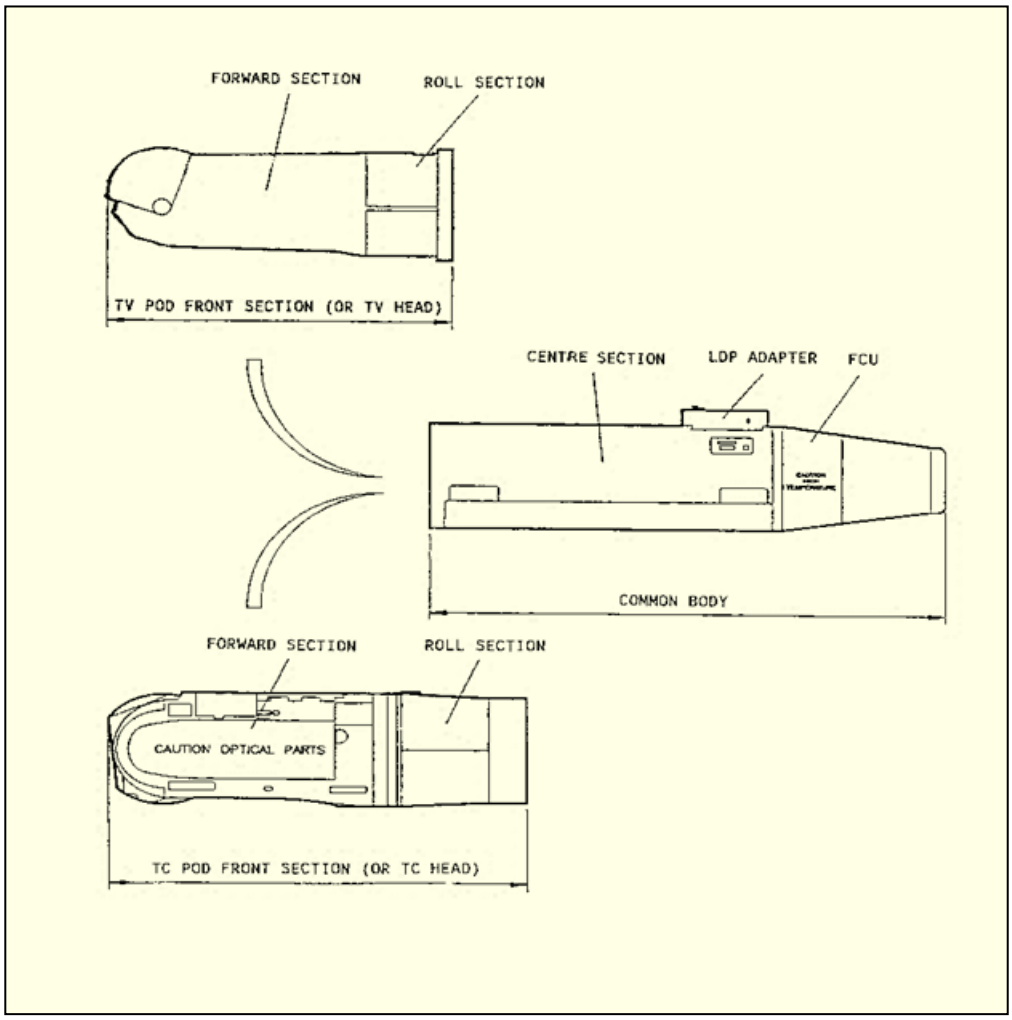


Figure 3-21. CLDP TV and IR configurations.

The TV configuration may also provide daytime advantages in high humidity conditions. In its subsidiary role, the CLDP can also act as a sensor for navigation fixing including altitude fixing. As shown in Fig. 3-21, both CLDP configurations consist primarily of two sections: an interchangeable front section containing a TV sensor head or IR sensor head, and a common body containing a central section and a rear cooling unit. In the TORNADO-IDS integration scheme, the CLDP is a non-jettisonable store and is carried on the forward section of the aircraft left shoulder pylon (Fig. 3-22).



Figure 3-22. TORNADO-IDS CLDP installation.

An electrical adaptor installed on the back of the CLDP centre section provides the electrical interface between the pod and the aircraft. The adaptor interfaces with the aircraft computers via a MIL-STD-1553B data bus. The slant ranges between the aircraft and a fix point obtained by using GNSS latitude, longitude and altitude data have been compared with the laser range provided by the CLDP for the same two test points. The satellite constellation for both tests included 5 satellites with a PDOP value of 4. Fig. 3-23 shows the calculated differences between DGNSS and laser ranges for distances from the fix point up to 8 km. As shown in the graph, these differences were below 25 m up to a distance of about 10 km from the fix point. The error increased with distance mainly due to worsening of the range measurements provided by the CLDP, caused primarily by laser Line-of-Sight (LOS) instability.

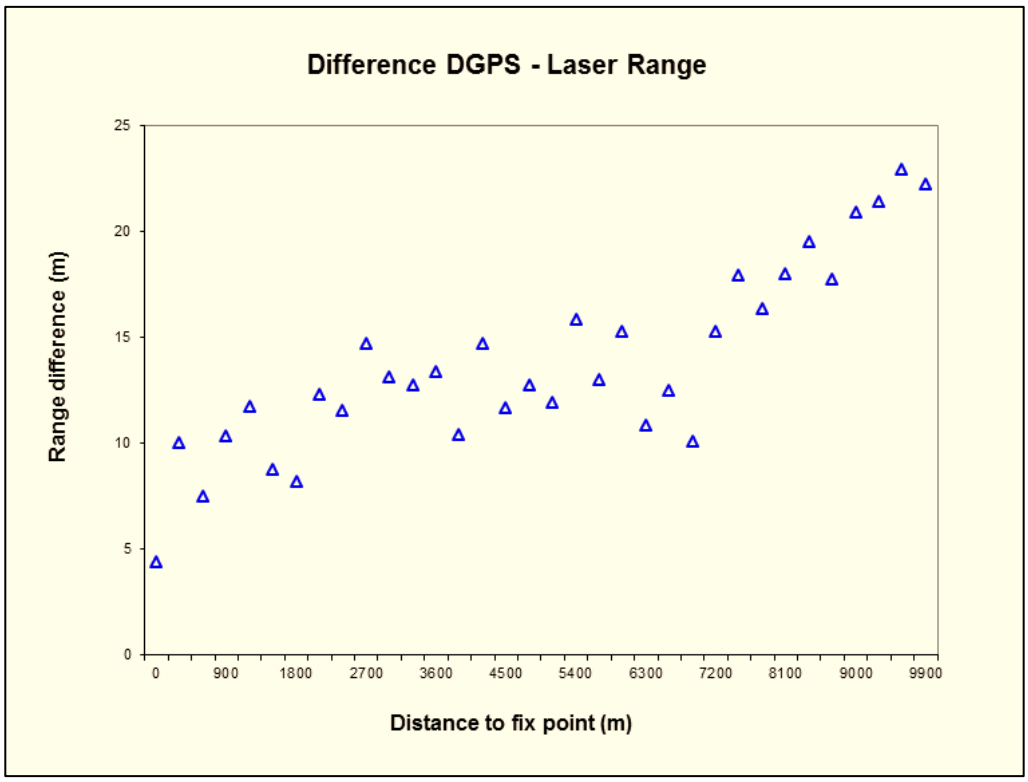


Figure 3-23. Differences between DGNSS and CLDP laser range.

Some flight trials were carried out in the Sardinia test range (Poligono Militare Interforze del Salto di Quirra) in which cinetheodolites (CITE) were available to provide the required datum accuracy (the nominal accuracy provided by the optical trackers was 0.5 metres). One of the difficulties encountered in the data analysis of these trials was the difference of the geodetic reference adopted by the two systems (Gauss-Boaga for CITE and WGS-84 for GNSS), and the time de-correlation of data (CITE provided higher data rate than GNSS). The first problem was solved by using a co-ordinates transformation software, while for the second problem an interpolation was required of the various measurements provided by the CITE in one second (GNSS data-rate was 1 Hz).

Data analysis was carried out with data samples collected in five different TYPHOON flights. The accuracy figures so determined were 23.3 m SEP stand-alone C/A code and 6.3 m SEP C/A code differential. These accuracies were comparable to the values quoted by ASHTECH (i.e., 100 m SEP stand-alone C/A code and 3 m SEP C/A code differential), and well inside the limits stated in the DGNSS technical specification documents (i.e., 100 m SEP stand-alone C/A code and 10 m SEP C/A code differential).

Another DGNSS accuracy evaluation with optical trackers was carried out during the Cazaux activity already mentioned in the previous paragraph. On this occasion, special care was taken to monitoring all factors that could possibly affect the synchronisation between the different sources of data (ground reference station, airborne FTI and cinetheodolites). The calculated spherical errors were in this case 21.7 m SEP for the stand-alone C/A code solution and 5.8 m SEP for the C/A code DGNSS solution (Table 3-2).

Table 3-2. DGNSS-TSPI data accuracy.

Errors	Mean (m)	Standard dev. (m)
Longitude	2.77	3.55
Latitude	2.68	2.28
Altitude	3.56	3.98
SEP	5.8	

Fig. 3-24 shows two sudden variations of the DGNSS errors (latitude, longitude and altitude errors). They both correspond to changes in the configuration of the tracked satellites. However, in the first case (small PDOP increase), the change did not cause a worsening of the overall spherical error, which remained in the order of 6.5 metres. In the second case (greater increase of PDOP), the constellation change caused an evident degradation especially in the altitude and latitude accuracies, giving an overall spherical error of about 14.3 metres.

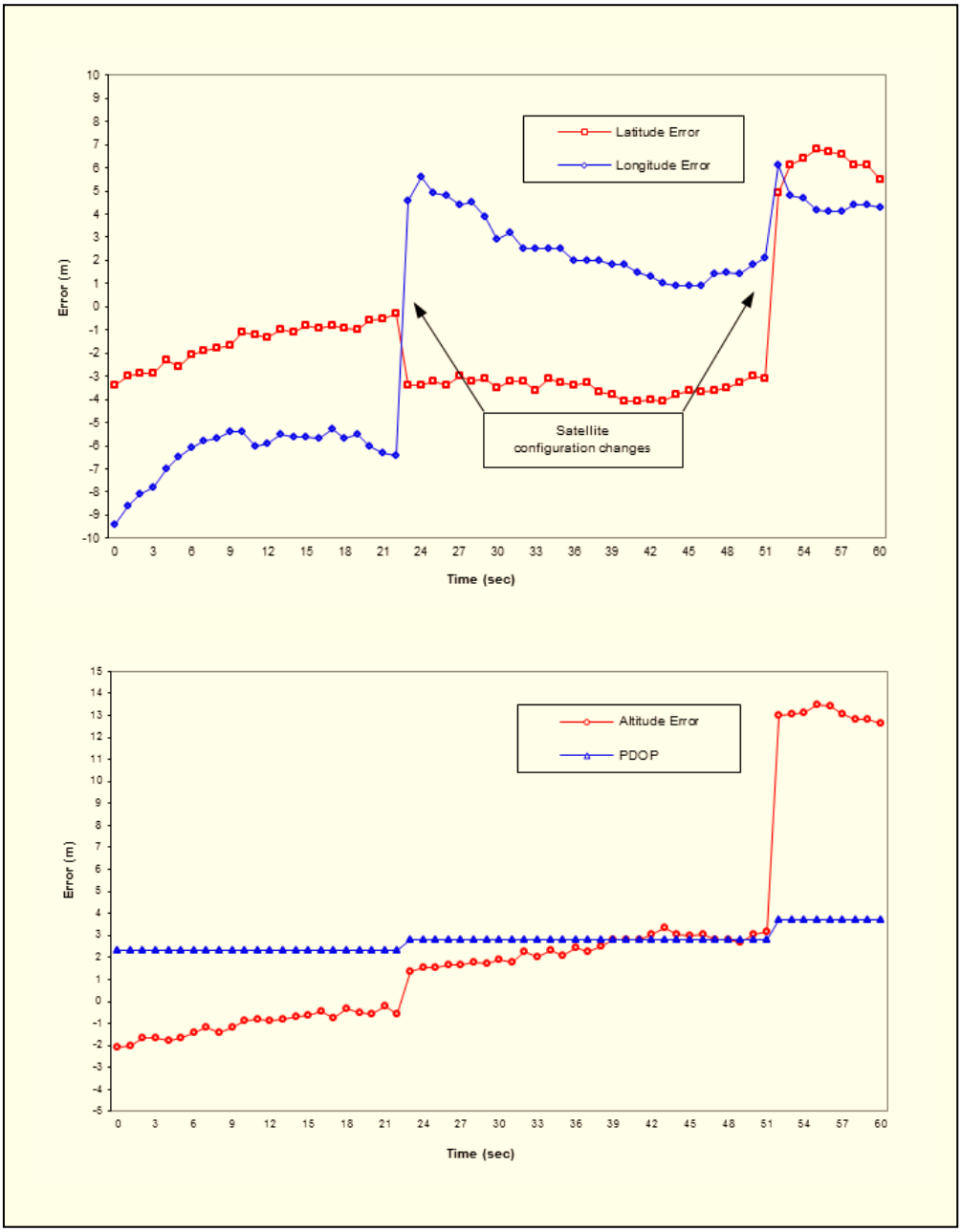


Figure 3-24. Differences between optical tracker and DGNSS data.

Fig. 3-25 shows the data collected during the flight No. 198 of the DA7 prototype aircraft, which was flown by The Italian Flight Test Centre (CSV-RSV) during a dedicated Operational Assessment of the TYPHOON Navigation Sub-system.

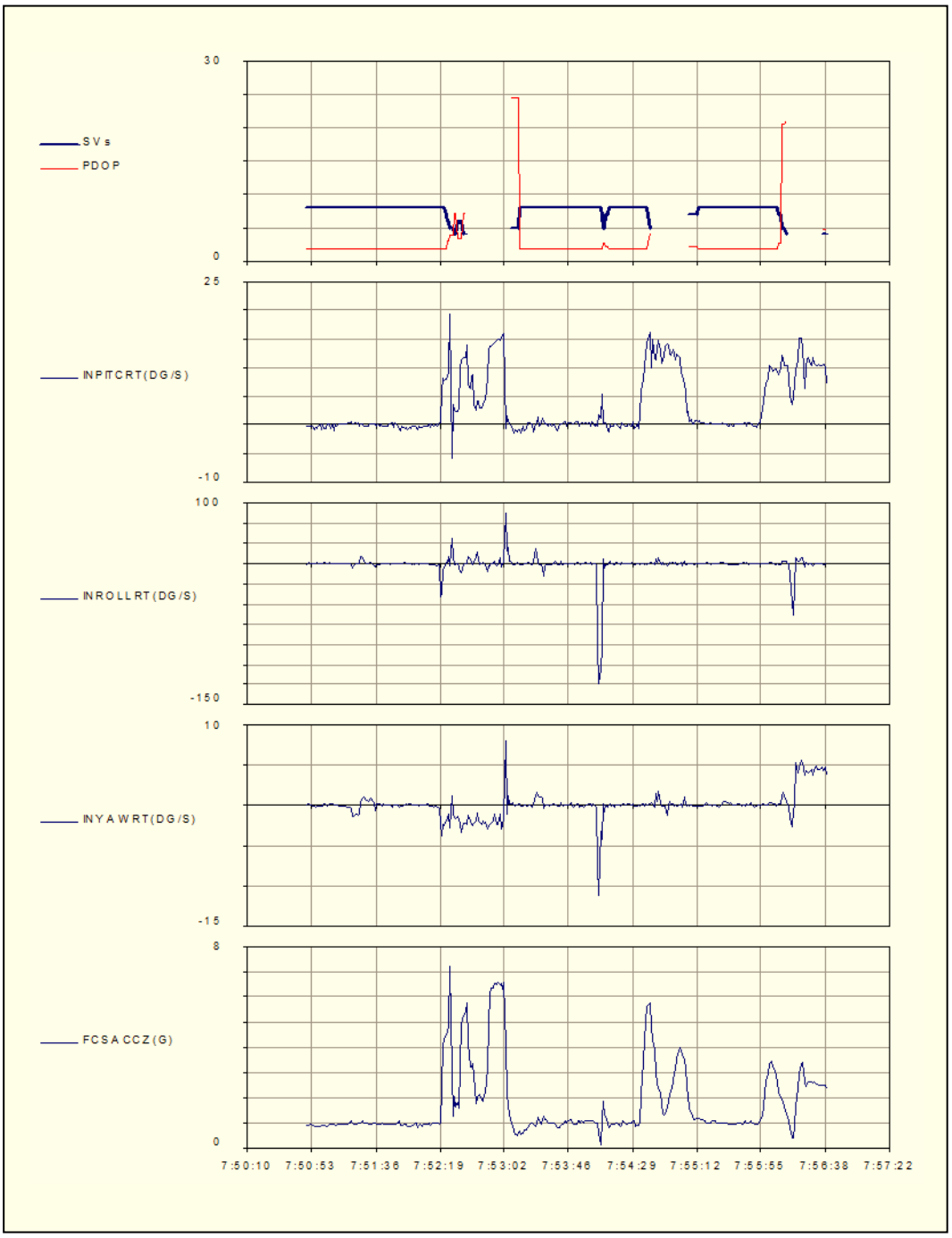


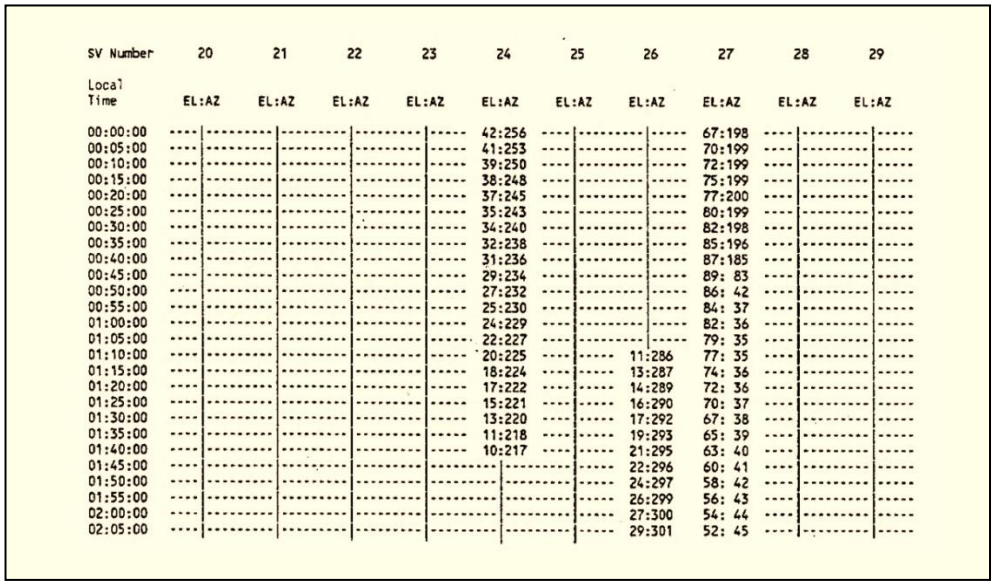
Figure 3-25. TYPHOON GNSS (FTI) satellites tracking and aircraft dynamics.

Such flight was designed as being composed of 3 phases: a first phase of benign en-route navigation, a second phase of manoeuvres representative of close air-to-air engagements and a third phase of benign en-route navigation. Whereas the reference

data continuity[4] during the complete flight was calculated to be in the order of 98%, during the second phase it decreased to 75% with GNSS data loss during all manoeuvres performed.

3.7.2 GNSS Masking Investigation

In order to verify the masking conditions a special simulation software was developed, called VIEWSAT, which modelled the aircraft shape and accepted input data such as the aircraft heading, pitch and bank angles in flight (from the FTI recorders), and positions of the satellites tracked during flight in terms of azimuth and elevation (Fig. 3-26).



SV Number	20	21	22	23	24	25	26	27	28	29
Local Time	EL:AZ	EL:AZ	EL:AZ	EL:AZ	EL:AZ	EL:AZ	EL:AZ	EL:AZ	EL:AZ	EL:AZ
00:00:00	----	---------	---------	---------	-----	42:256	----	---------	-----	67:198	----	---------	-----
00:05:00	----	---------	---------	---------	-----	41:253	----	---------	-----	70:199	----	---------	-----
00:10:00	----	---------	---------	---------	-----	39:250	----	---------	-----	72:199	----	---------	-----
00:15:00	----	---------	---------	---------	-----	38:248	----	---------	-----	75:199	----	---------	-----
00:20:00	----	---------	---------	---------	-----	37:245	----	---------	-----	77:200	----	---------	-----
00:25:00	----	---------	---------	---------	-----	35:243	----	---------	-----	80:199	----	---------	-----
00:30:00	----	---------	---------	---------	-----	34:240	----	---------	-----	82:198	----	---------	-----
00:35:00	----	---------	---------	---------	-----	32:238	----	---------	-----	85:196	----	---------	-----
00:40:00	----	---------	---------	---------	-----	31:236	----	---------	-----	87:185	----	---------	-----
00:45:00	----	---------	---------	---------	-----	29:234	----	---------	-----	89: 83	----	---------	-----
00:50:00	----	---------	---------	---------	-----	27:232	----	---------	-----	86: 42	----	---------	-----
00:55:00	----	---------	---------	---------	-----	25:230	----	---------	-----	84: 37	----	---------	-----
01:00:00	----	---------	---------	---------	-----	24:229	----	---------	-----	82: 36	----	---------	-----
01:05:00	----	---------	---------	---------	-----	22:227	----	---------	-----	79: 35	----	---------	-----
01:10:00	----	---------	---------	---------	-----	20:225	----	-----	11:286	77: 35	----	---------	-----
01:15:00	----	---------	---------	---------	-----	18:224	----	-----	13:287	74: 36	----	---------	-----
01:20:00	----	---------	---------	---------	-----	17:222	----	-----	14:289	72: 36	----	---------	-----
01:25:00	----	---------	---------	---------	-----	15:221	----	-----	16:290	70: 37	----	---------	-----
01:30:00	----	---------	---------	---------	-----	13:220	----	-----	17:292	67: 38	----	---------	-----
01:35:00	----	---------	---------	---------	-----	11:218	----	-----	19:293	65: 39	----	---------	-----
01:40:00	----	---------	---------	---------	-----	10:217	----	-----	21:295	63: 40	----	---------	-----
01:45:00	----	---------	---------	---------	---------	---------	-----	22:296	60: 41	----	---------	-----
01:50:00	----	---------	---------	---------	---------	---------	-----	24:297	58: 42	----	---------	-----
01:55:00	----	---------	---------	---------	---------	---------	-----	26:299	56: 43	----	---------	-----
02:00:00	----	---------	---------	---------	---------	---------	-----	27:300	54: 44	----	---------	-----
02:05:00	----	---------	---------	---------	---------	---------	-----	29:301	52: 45	----	---------	-----

Figure 3-26. Satellite visibility from receiver almanac data.

The VIEWSAT software provided a visibility matrix (one dorsal antenna) for the defined flight conditions (Fig. 3-27), and utilised a simplified aircraft model, as shown in Fig. 3-28. The result was a Global Masking Matrix (GMM), as shown in Fig. 3-29.

[4] Data continuity was calculated as the ratio between the time in which the reference data was recorded and the total time under consideration.

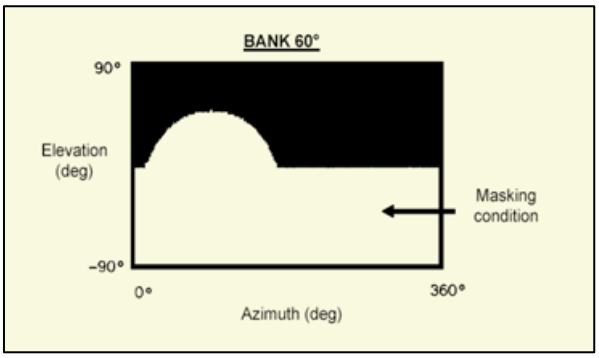


Figure 3-27. Example of antenna masking matrix.

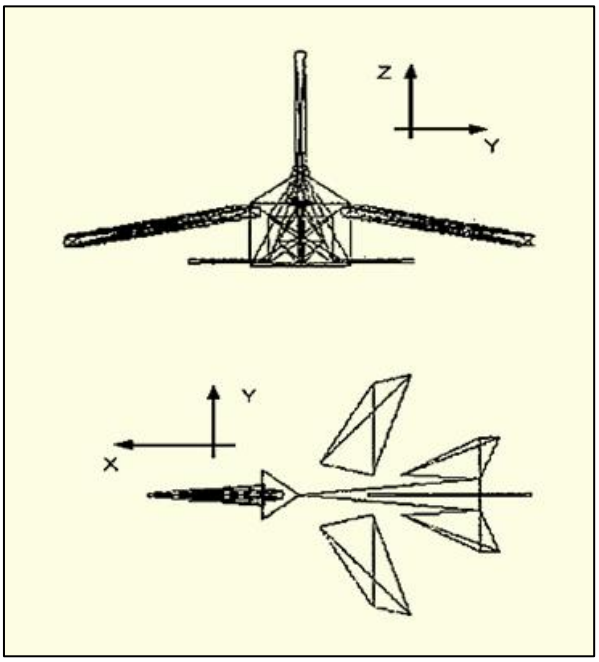


Figure 3-28. Simplified aircraft model (TORNADO-IDS).

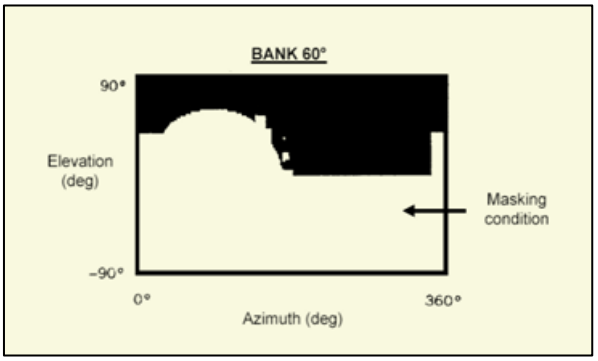


Figure 3-29. Example of global masking matrix.

The program output was a binary diagram in which for every satellite masked a "0" was shown, while unmasked satellites corresponded to the status "1." An example of VIEWSAT output, together with the related flight conditions, is shown in Fig. 3-30.

For every flight segment with loss of GNSS data satellite masking was investigated using VIEWSAT. This was done in the attempt to determine the critical aircraft manoeuvres using the time histories of the recorded flight parameters (i.e., heading, bank and pitch angles, TAS, barometric-altitude and radar-altitude).

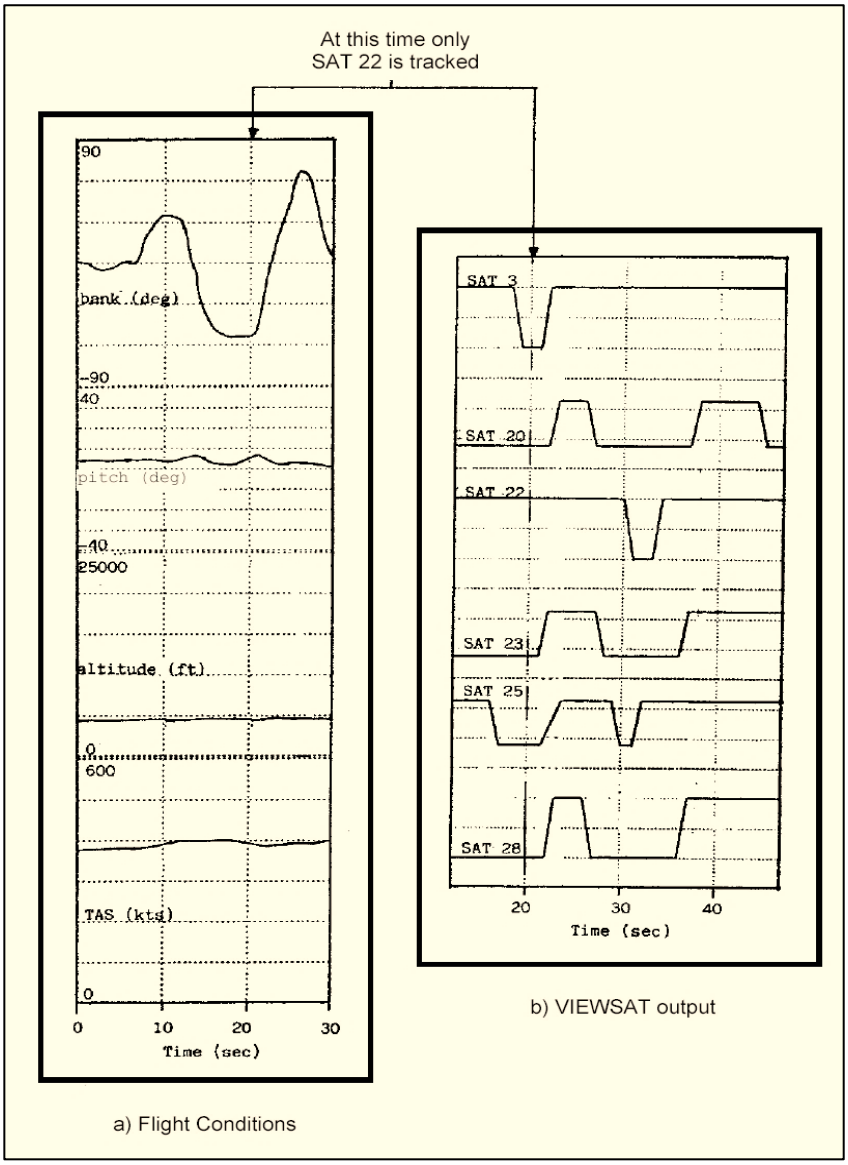


Figure 3-30. Example of VIEWSAT output and relevant flight conditions.

Fig. 3-31 refers to a flight trial carried out with a number of 7 visible satellites. During the trial the maximum variation of the satellite positions was in the order of 30° in azimuth and 20° in elevation. Satellites with low elevations above the horizon (elevation < 10°) were not tracked. During manoeuvres, it was observed that the satellites more likely to be lost were those with an elevation lower than 35°.

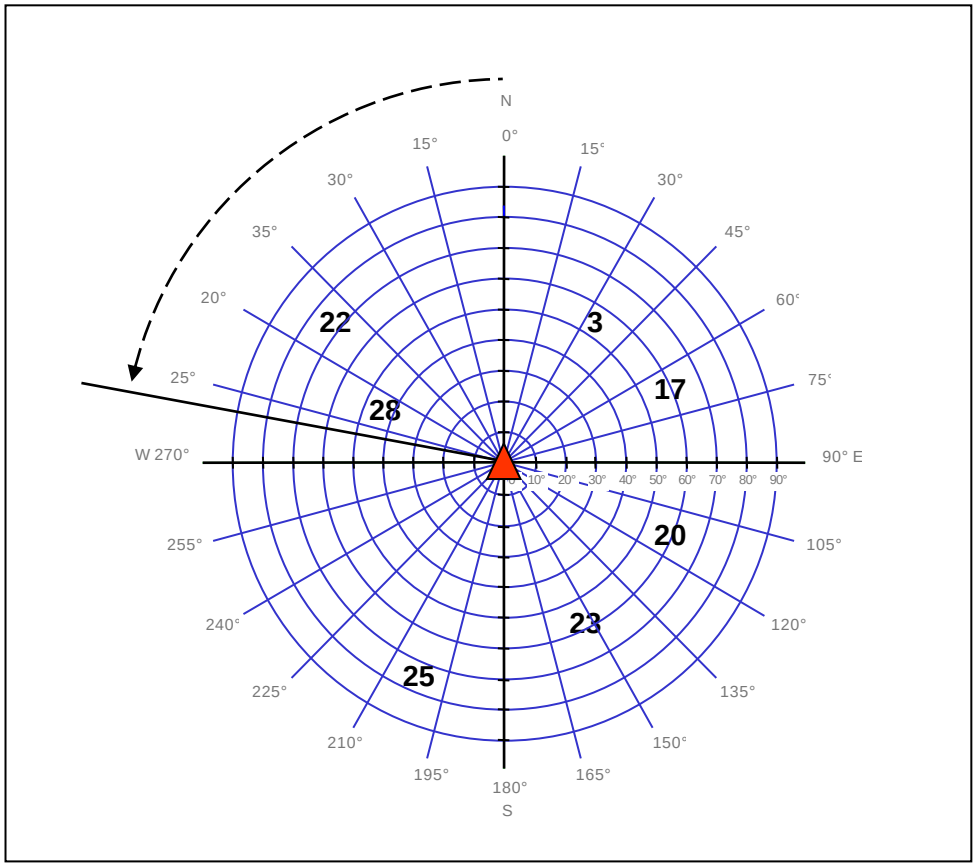


Figure 3-31. Relative geometry of the aircraft and satellites.

Analysis of the aircraft attitude data allowed the identification of some important critical manoeuvres. In general, these manoeuvres were characterized by a simultaneous non-gradual variation of two attitude angles (i.e., pitch, roll and yaw). A very rapid variation of height (if not associated to a considerable variation in pitch and/or roll) was not sufficient alone to determine satellite losses (Fig. 3-32).

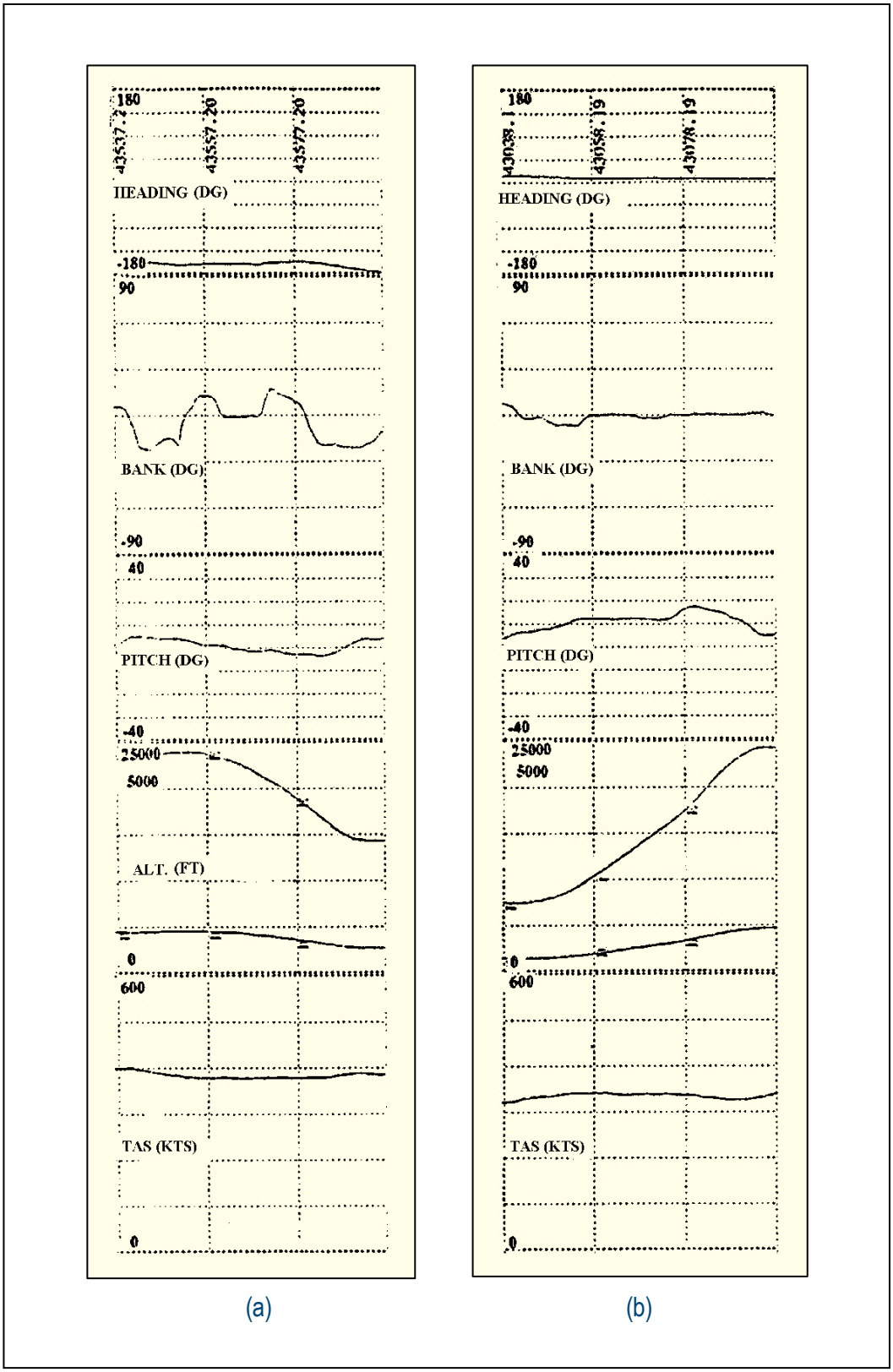


Figure 3-32. Altitude variations without satellite losses observed during low bank manoeuvres (a) and in vertical flight (b).

Manoeuvres that were found to be very critical included turns with bank ≥ 50° and heading change > 90°. Fig. 3-33 shows two flight data slices in which these elements can be identified.

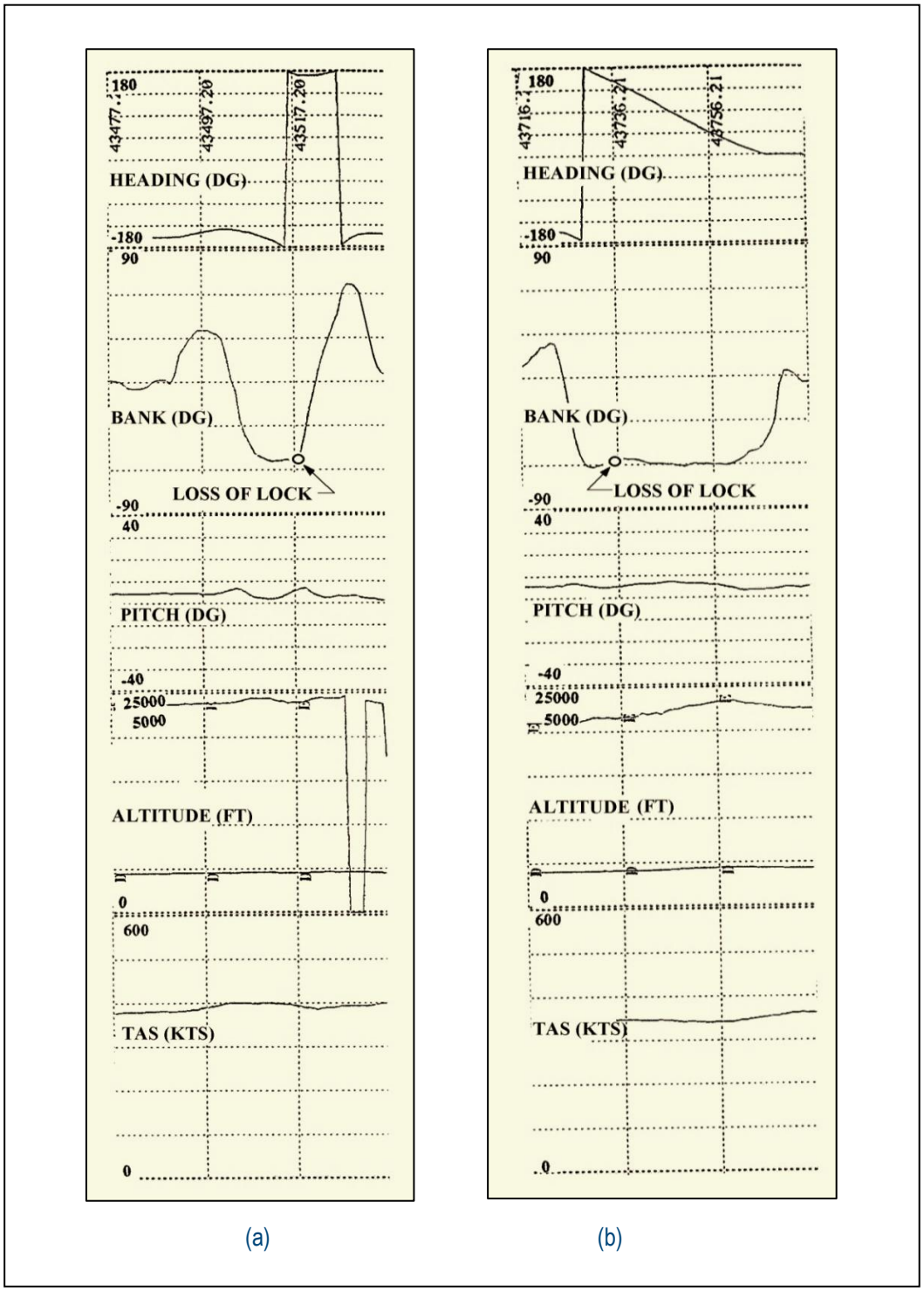


Figure 3-33. Critical manoeuvres (loss of satellite signals).

It was also observed that, after turns with bank ≥ 50° and loss-of-lock to all satellites, the GNSS signals were generally reacquired shortly after the turns were interrupted (a few seconds), but in case of rapid altitude variations the satellite signals reacquisition could be significantly delayed (up to 2 minutes), also during periods of gradual heading variations and low bank (i.e., less than 5°).

There are some important considerations about the Critical Bank Angle (CBA). It is in fact necessary to take into account that, during the turns, the satellites lower on the horizon were likely to be masked; but in most cases the manoeuvre was critical only if the CBA was reached and maintained for a period of time exceeding about 5 seconds and with a large heading change (usually greater than 90°). In these cases, after 5 seconds, the number of satellites lost (n) was greater than (m - 4), being m the initial total number of satellites (Fig. 3-34).

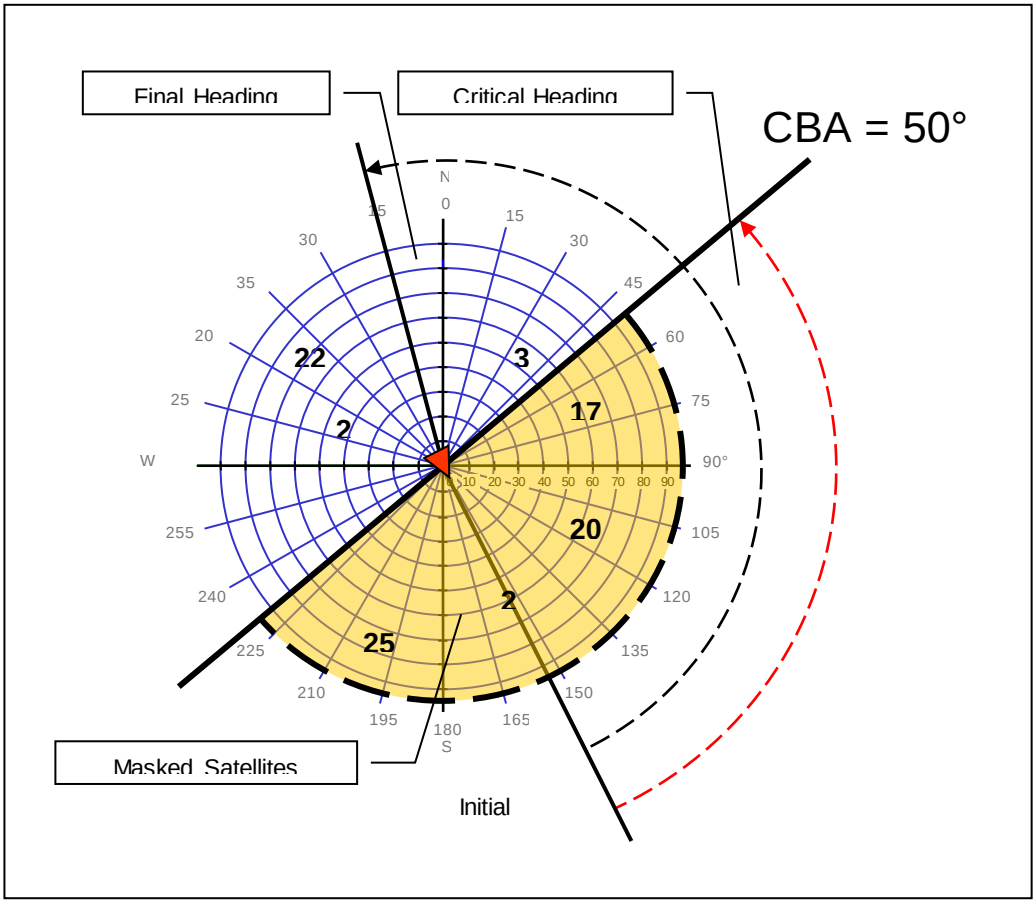


Figure 3-34. Satellite masking (SV's 17, 20, 23 and 25).

In many situations, however, the same manoeuvres did not lead to loss of satellites. The difference between the two cases (loss and no-loss) was represented by the fact that in the no-loss case the turns were following periods of stabilized flight (without significant heading, bank and height variations) of at least 20 seconds. Fig. 3-35 shows a manoeuvre in which both the bank and the heading angles exceeded the critical values but loss of GNSS data did not occur.

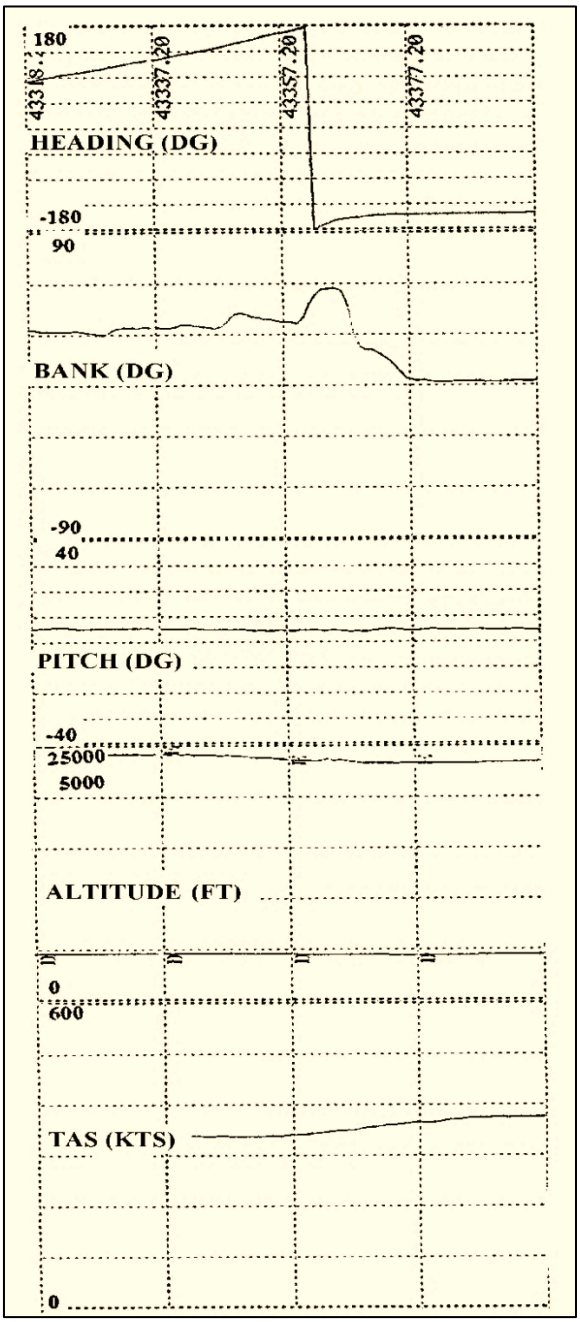


Figure 3-35. Critical conditions (CBA, heading change) without loss of GNSS data.

Similarly, also in the approach phase of the flight, a number of turns with high bank angles, progressively performed at lower altitudes, did not determine the signal loss (Fig. 3-36).

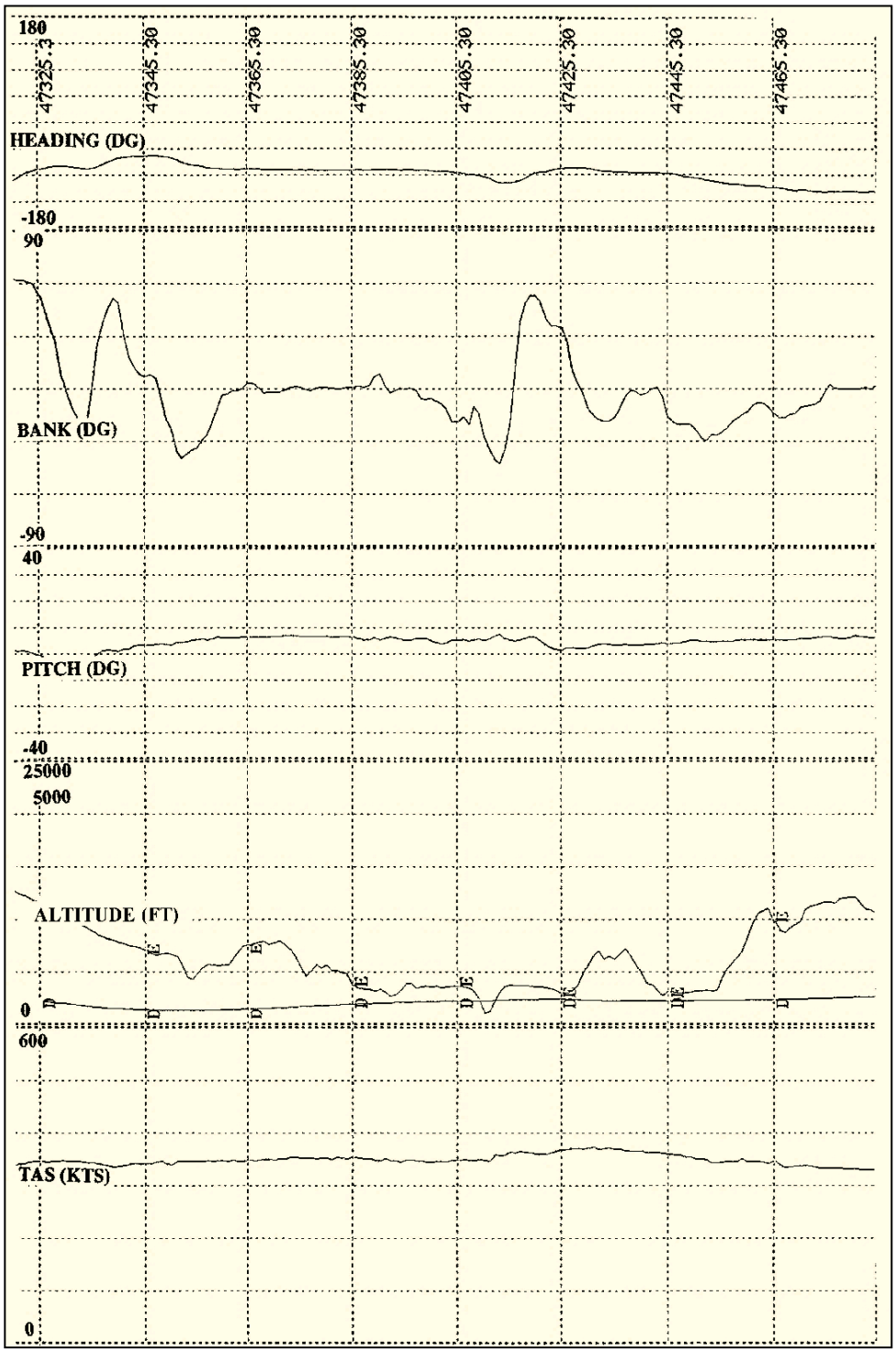


Figure 3-36. Approach manoeuvres with high bank and no loss of GNSS data.

Further analysis of the experimental data showed that the signal losses were maximised if the turns were started with an initial aircraft heading in the sectors from North-East to South-East in case of left turns and from South-West to North-West in case of right turns. In order to assist in the investigation of this behaviour, we started examining the characteristics of typical "sky-plots" (i.e., satellites azimuth and elevations observed from certain locations and for a certain period of time) that can be obtained at our latitudes. Fig. 3-37 shows a GPS sky-plot relative to the city of Rome (date: 25th June 2011; coordinates: North 41° 52', East 12° 37', h = 0; duration: 24 hours).

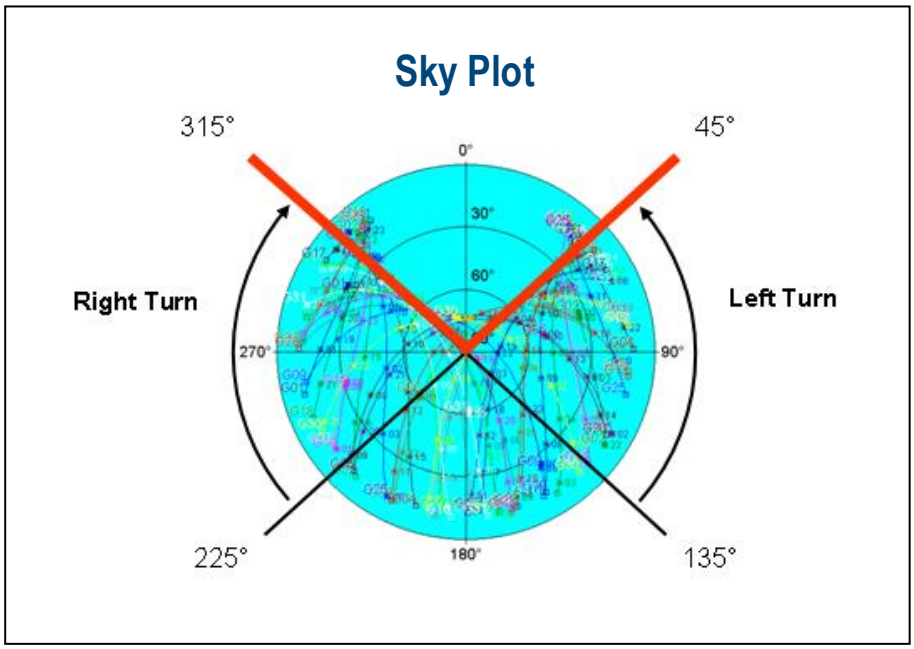


Figure 3-37. GPS sky-plot example.

It is evident that the majority of satellites are available in the azimuth range 45° ÷ 315°, and that a left turn of an aircraft with an Initial Heading (IHG) in the range 45° ÷ 135° (i.e., North-East ÷ South-East) would be prone to data losses, due to the reduced number of satellites available in the direction of the turn. Similar considerations apply for the right turns performed with an IHG in the range 225° ÷ 315° (i.e., South-West ÷ North-West).

On average the ASHTECH receiver was able to give a new position solution within about 20 seconds from restoration of the LOS conditions to the satellites. Therefore,

it was generally sufficient to maintain a low bank angle for about 20 seconds in order to obtain a new solution. However, if the height was kept constant the time required was reduced to about 10 seconds. This can be seen comparing the diagrams in Fig. 3-33(a) with the corresponding VIEWSAT diagram shown in Fig. 3-38.

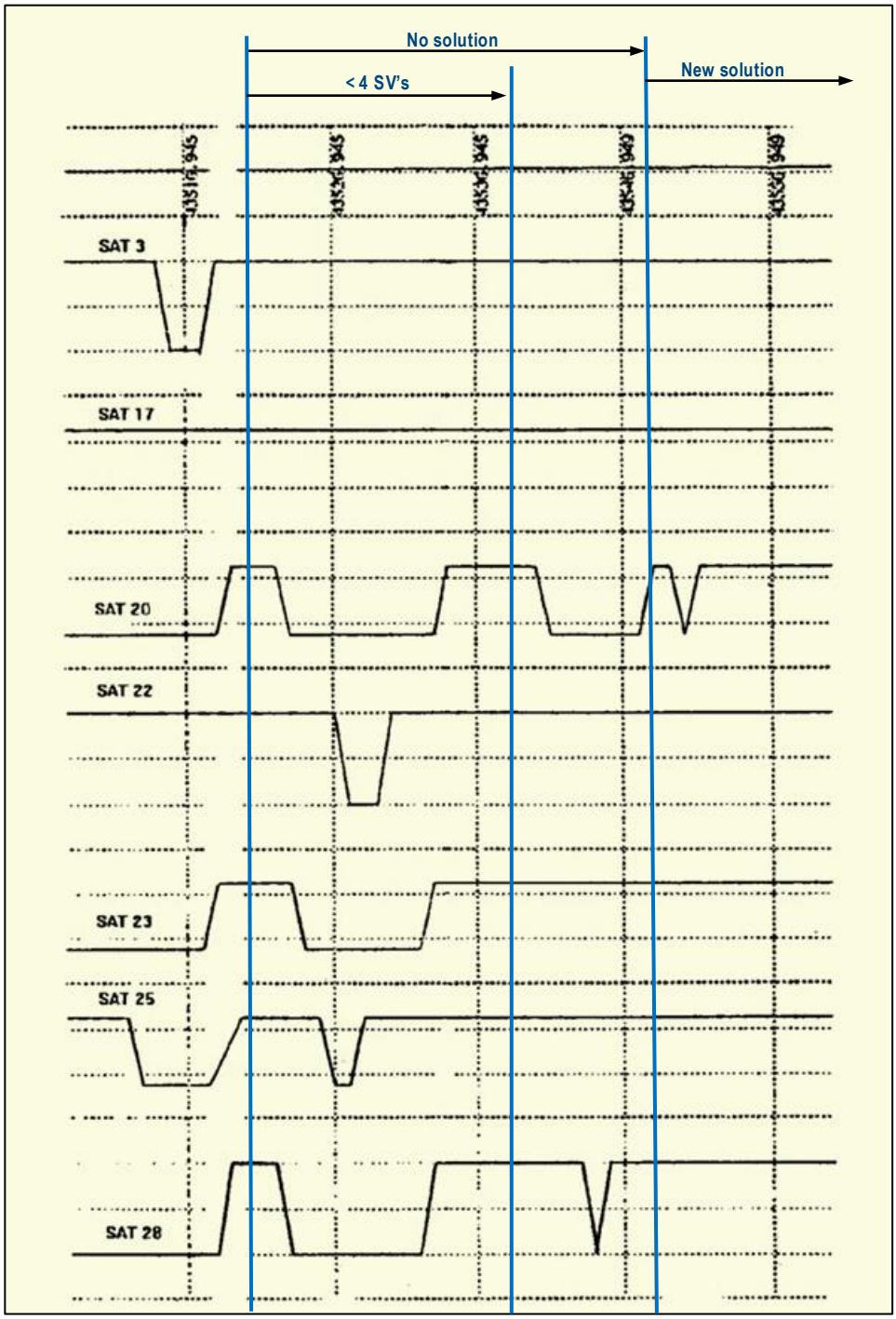


Figure 3-38. VIEWSAT diagram corresponding to GNSS data loos and reacquisition.

3.7.3 Signal-to-Noise Ratio Investigation

Another important aspect to be investigated was the influence of SNR on satellite reacquisition. It was in fact important to verify if the availability at the user location of satellites with high SNR could facilitate the computation of a new positioning solution after data losses. In order to assist in this investigation the ASHTECH receiver B-files (containing the measurements data) were examined. During analysis of the time histories, VIEWSAT diagrams and satellite visibility data, it was not possible to explain all data "holes" in the C-files only in terms of satellite masking. In other cases, masking situations given by the VIEWSAT did not correspond to satellite losses. Reading the B-files it was possible to determine the quality of the signals received from the different satellites especially in terms of SNR. A typical B-file in ASCII format is shown in Fig. 3-39.

```
RECORD = 2675  RECEIVE TIME = 389766.000000
SV CH  WN P G TXMITTIME  CDPHASE     DOPPL     CARRIER_PH  EL  AZ S/N  DT
 3  3   0 5 24 0.9270  21882853  26117310     184380.200  0   0  24   L
22  6   0 5 24 0.9304  20866062 -13418220   -5913972.448  0   0  48   L
23 10   0 5 24 0.9221  23343366 -35951450     -18099.512  0   0  16   L
17 11   0 5 24 0.9319  20408722   9882530    -776080.344  0   0  38   L
SITE        NAVX              NAVY              NAVZ              NAVT
?784   4854639.850000    827511.800000   4041537.260000       56519.87
PDOP      NAVXDOT           NAVYDOT           NAVZDOT           NAVTDOT
   5       129.910           -17.720           -156.700              0.00
```

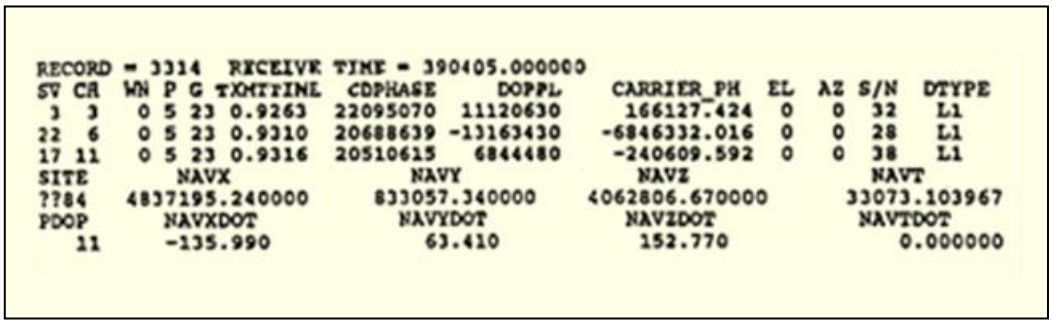
Figure 3-39. B-file in ASCII format.

The B-file contains the following data:

- Record number (RECORD);
- GNSS time (RECEIVE TIME);
- Satellite identifier (SV);
- The channel allocated to each satellite (CH);
- A diagnosis parameter relative to the receiver clock status, the phase of the signal carrier and the loss of signal tracking (WN).;
- A parameter relative to the synchronisation of the received signal (P);

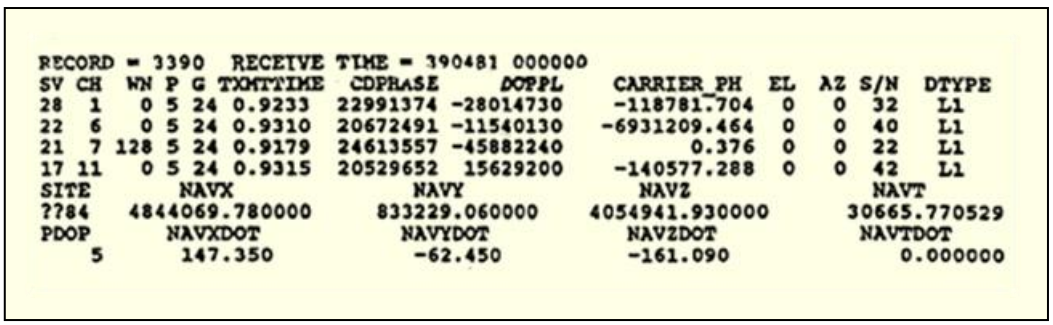
- A parameter for measurement quality for positioning calculation (G);
- The time interval in msec between transmission and reception of the GNSS signal (TXMTIME);
- Doppler frequency measurement in 10^{-4} Hz, positive when the satellite gets farther from the receiving antenna and negative when it gets closer (DOPPL);
- The SNR (S/N).

Analysing the SNR variations, we verified that the loss of satellites often corresponded to bad SNR (SNR < 10), while reacquisition after a signal loss (also with bad geometrical conditions) corresponded to good SNR (SNR > 30). Examples of B-files for loss and reacquisition of GNSS satellites are shown in the Figures 3-40 and 3-41.



```
RECORD = 3314  RECEIVE TIME = 390405.000000
SV CH  WN P G TXMTIME  CDPHASE     DOPPL     CARRIER_PH  EL  AZ S/N  DTYPE
 3  3   0 5 23 0.9263  22095070  11120630    166127.424   0   0  32   L1
22  6   0 5 23 0.9310  20688639 -13163430   -6846332.016  0   0  28   L1
17 11   0 5 23 0.9316  20510615   6844480    -240609.592  0   0  38   L1
SITE       NAVX          NAVY          NAVZ          NAVT
??84   4837195.240000  833057.340000  4062806.670000  33073.103967
PDOP       NAVXDOT       NAVYDOT       NAVZDOT       NAVTDOT
  11      -135.990        63.410        152.770         0.000000
```

Figure 3-40. B-file for GNSS data loss: the quality parameter G = 23 indicates the phase of the code and the carrier have been tracked and the navigation message has been acquired, but the position solution has not been calculated.



```
RECORD = 3390  RECEIVE TIME = 390481.000000
SV CH  WN P G TXMTTIME  CDPHASE     DOPPL     CARRIER_PH  EL  AZ S/N  DTYPE
28  1   0 5 24 0.9233  22991374 -28014730   -118781.704   0   0  32   L1
22  6   0 5 24 0.9310  20672491 -11540130   -6931209.464  0   0  40   L1
21  7 128 5 24 0.9179  24613557 -45882240         0.376   0   0  22   L1
17 11   0 5 24 0.9315  20529652  15629200    -140577.288  0   0  42   L1
SITE       NAVX          NAVY          NAVZ          NAVT
??84   4844069.780000  833229.060000  4054941.930000  30665.770529
PDOP       NAVXDOT       NAVYDOT       NAVZDOT       NAVTDOT
   5       147.350       -62.450       -161.090         0.000000
```

Figure 3-41. B-file for signal reacquisition.

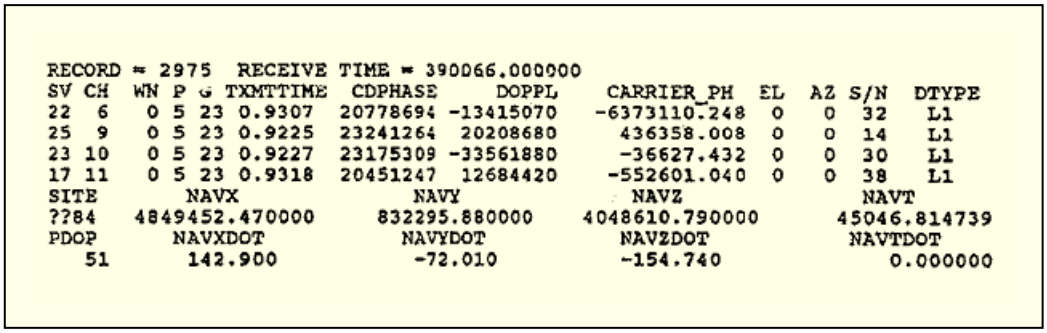
Looking at the various records of B-files it was possible to identify short periods of signal loss, which did not correspond to data "holes" in the C-files. This confirmed that the receiver was able to store positioning data in its memory for short periods, aiding the reacquisition of satellites and reducing the TTSF. An example is shown in Fig. 3-42.

```
RECORD = 2669  RECEIVE TIME = 389760.000000
SV CH  WN P G TXMTTIME  CDPHASE     DOPPL     CARRIER_PH  EL  AZ S/N  DTYPE
 3  3   0 5 23 0.9270  21879892  26164440    168877.046  0   0  40   L1
22  6   0 5 23 0.9304  20867613 -14035390  -5905822.256  0   0  26   L1
17 11   0 5 23 0.9319  20407625   9873000   -781837.576  0   0  28   L1
SITE        NAVX            NAVY            NAVZ            NAVT
??84   4853695.960000  827678.870000  4042789.890000  56912.600227
PDOP       NAVXDOT         NAVYDOT         NAVZDOT         NAVTDOT
   4       128.780          -56.080         -141.360          0.000000

RECORD = 2670  RECEIVE TIME = 389761.000000
SV CH  WN P G TXMTTIME  CDPHASE     DOPPL     CARRIER_PH  EL  AZ S/N  DTYPE
 3  3   0 5 24 0.9270  21880390  25913520    171481.792  0   0  34   L1
22  6   0 5 24 0.9304  20867346 -13758060  -5907210.560  0   0  28   L1
23 10 128 5 24 0.9221  23346821 -35783970        -0.352  0   0  30   L1
17 11   0 5 24 0.9319  20407815   9646100   -780860.712  0   0  34   L1
SITE        NAVX            NAVY            NAVZ            NAVT
??84   4853986.980000  827571.040000  4042311.870000  56705.743431
PDOP       NAVXDOT         NAVYDOT         NAVZDOT         NAVTDOT
   5       131.280          -20.950         -150.090          0.000000
```

Figure 3-42. Signal loss shown in a B-file with no GNSS data interruption in the C-file. Examining the VIEWSAT diagrams, masking was confirmed for SV 23, but the receiver was able to reacquire SV 23 in a short time and to maintain tracking to the satellite for a period sufficient to compute a new positioning solution; the WN parameter at 128 indicates the loss of tracking to the satellite in previous epochs.

The data analysis demonstrated that the receiver was able to provide a positioning solution only if the SNR of at list four satellites was above a pre-defined threshold (between 15 and 30 dB), which was not selectable by the user at the ground programming stage. An example is shown in Fig. 3-43, in which four satellites were in view but no data were recorded in the C-files. As SV 28 was lost (not shown), the receiver was no longer able to compute the position (G = 23) of the aircraft even if four satellites were still available (SV 24 had SNR = 14).



```
RECORD = 2975  RECEIVE TIME = 390066.000000
SV CH   WN P G TXMTTIME  CDPHASE     DOPPL    CARRIER_PH  EL  AZ S/N  DTYPE
22  6    0 5 23 0.9307  20778694 -13415070   -6373110.248  0   0  32   L1
25  9    0 5 23 0.9225  23241264  20208680     436358.008  0   0  14   L1
23 10    0 5 23 0.9227  23175309 -33561880      -36627.432  0   0  30   L1
17 11    0 5 23 0.9318  20451247  12684420     -552601.040  0   0  38   L1
SITE        NAVX            NAVY            NAVZ            NAVT
?784   4849452.470000   832295.880000  4048610.790000   45046.814739
PDOP      NAVXDOT         NAVYDOT         NAVZDOT         NAVTDOT
   51       142.900          -72.010         -154.740        0.000000
```

Figure 3-43. B-file corresponding to data loss in the C-file with four satellites tracked.

3.7.4 Doppler Investigation

During the initial phases of the GPS-TSPI flight test campaign (Sabatini and Palmerini, 2008), it was noted that, even in high dynamics avionics receivers, the reacquisition time after loss of one or more satellite signals could be up to 35 seconds, depending on flight conditions and satellite constellations (Fig. 3-44). Therefore, we investigated how the Doppler shift could affect the receiver capability to track the carrier phase and rapidly reacquire the signal after a loss. Doppler shift directly affects the signal acquisition time of the receiver, both in terms of frequency of the code and frequency of the carrier. In general, acquisition time increases in the presence of Doppler shift.

Considering the case of one satellite tracked, the Doppler shift is due to the relative velocity of the satellite and the receiver (i.e., the difference between the projections of the velocity vectors along the satellite-receiver direction). The worst case is, therefore, that of an aircraft flying along the LOS to the satellite, in which the full velocity vector of the aircraft must be used to determine the relative velocity (e.g., with an aircraft flying along the LOS to the satellite at a velocity of 350 kts, the Doppler shift for L1 is in the order of 10 KHz).

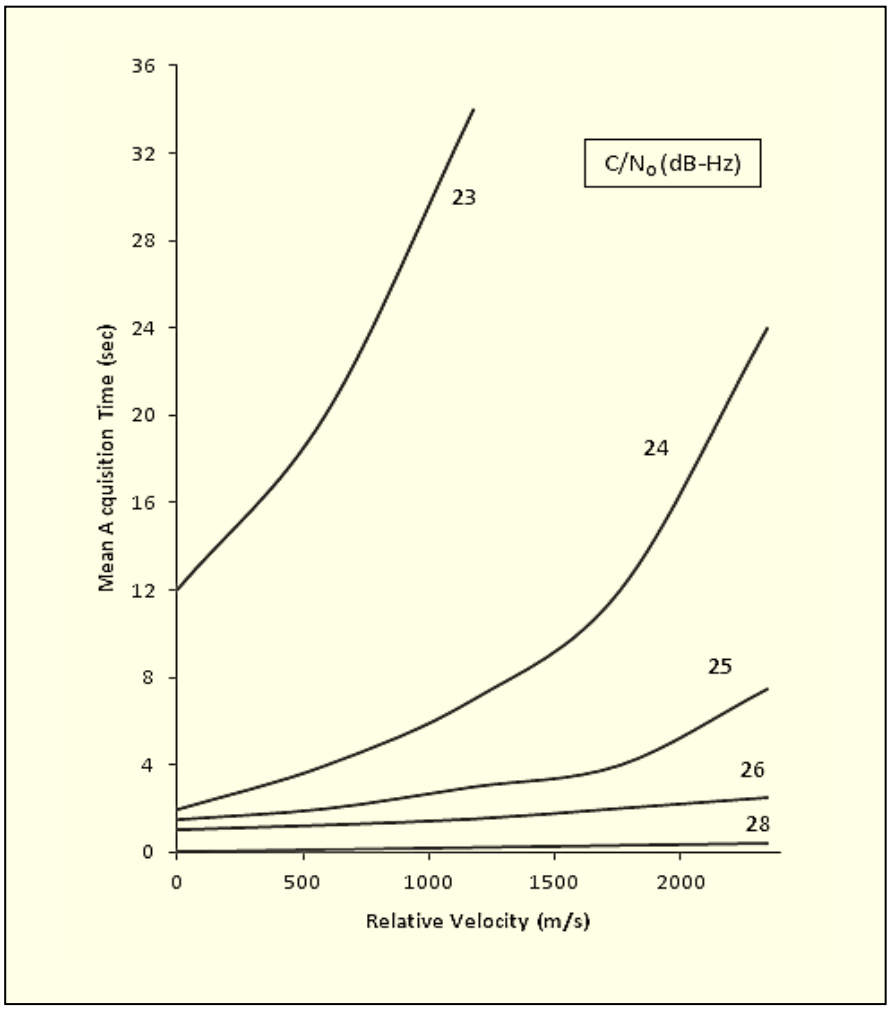


Figure 3-44. Doppler shift and signal acquisition in an avionics receiver.

The analysis of receiver data recorded during several flights and up to speed of 500 kts highlighted that the Doppler effect causes a frequency shift, with respect to the carrier frequency L1, which reaches a maximum value of about 15 KHz. This value is relatively low if compared with the GPS signal bandwidth (i.e., about 30 MHz), and the high dynamic characteristics of the carrier tracking loops internal to the avionics receiver guarantee that neither the data accuracy is degraded nor the carrier phase is lost because of Doppler shift. Nevertheless, the coupling between such frequency shift and the signal reacquisition strategy of the receiver can significantly affects the time necessary to get data after a signal loss, even when a good satellite configuration is available.

3.7.5 Data Link/GNSS Electromagnetic Compatibility

Some dedicated ground tests were performed to investigate Electromagnetic Compatibility and Interference (EMC/EMI) aspects of the GNSS receiver installation on board a TORNADO-IDS experimental aircraft. In fact, due to the need of using a data link for real-time DGNSS applications, the EMC/EMI aspects of the GNSS and data link coexisting installations into the aircraft were deeply analysed. This was necessary because the GNSS and the on board data link typically operate in the same (or contiguous) spectral band and possible interference problems degrading reception/reacquisition of GNSS signals at the airborne antenna location could seriously affect the continuity and integrity of the data. To mitigate the effects of GNSS/data link interferences, various existing technology solutions are possible (i.e., choosing a VHF data link, filtering the radio frequency signals reaching the GNSS antenna, identifying suitable locations for the GNSS antenna and providing adequate shielded of the antenna itself, either by physical devices or via dedicated software masks, etc.). Appendix A provides some additional information on EMC/EMI test activities performed on the TORNADO-IDS aircraft. A more comprehensive discussion can be found in Sabatini et al., 2008.

3.7.6 Flight Test Mission Planning and Optimisation

As a result of the analysis carried out some recommendations were formulated in order to optimise the use of DGNSS as a datum in flight test missions, reducing signal loses and avoiding unacceptable accuracy degradations. In particular, the following practical criteria were identified:

- The visibility of at least four satellites with an elevation near 50° should be guaranteed;
- The maximum bank angle allowed is 50°;
- A stabilisation of at least 20 seconds should precede and follow significant flight phases;
- The heading variations should be as gradual as possible;

- The number of left turns performed with IHG 45° ÷ 135° and or right turns with IHG 225° ÷ 315° should be minimised;
- The distance between aircraft and ground receiver should not exceed 100 km during navigation flight trials and 200 km in other cases.

These restrictions, of course, imply operational limitations that reduce the spread of possible DGNSS applications in the flight test environment. Some flight trials were performed in order to verify the validity of the criteria mentioned above. Fig. 3-45 shows the variations of attitude, altitude and TAS during one of these trials.

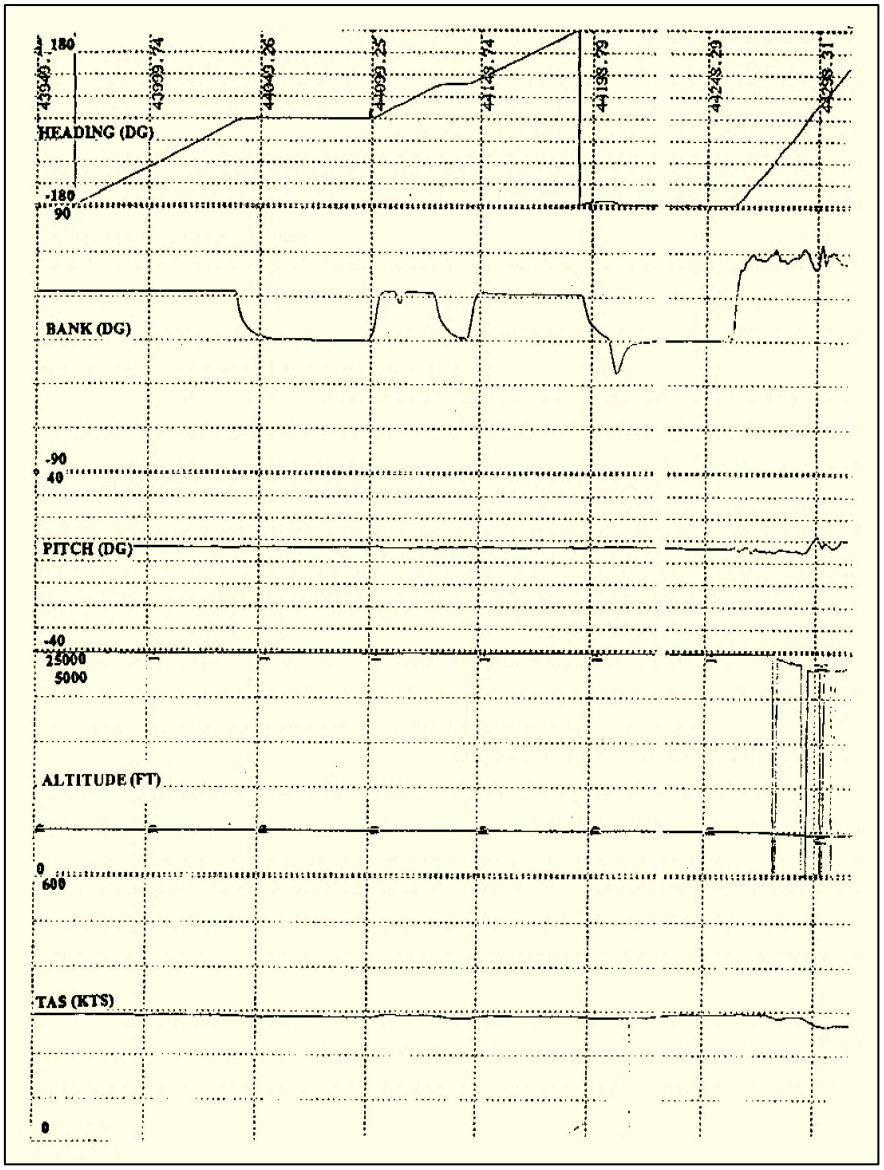


Figure 3-45. Optimised manoeuvres for DGNSS data gathering.

It can be seen that the manoeuvres always followed periods of stabilised flight and the altitude was kept constant. The visible constellation during the flight sortie included a total of eight satellites, with at list four having an average elevation greater than 50° and two with an elevation always greater than 30°. The trajectory diagram shown in Fig. 3-46 is completely free from signal losses.

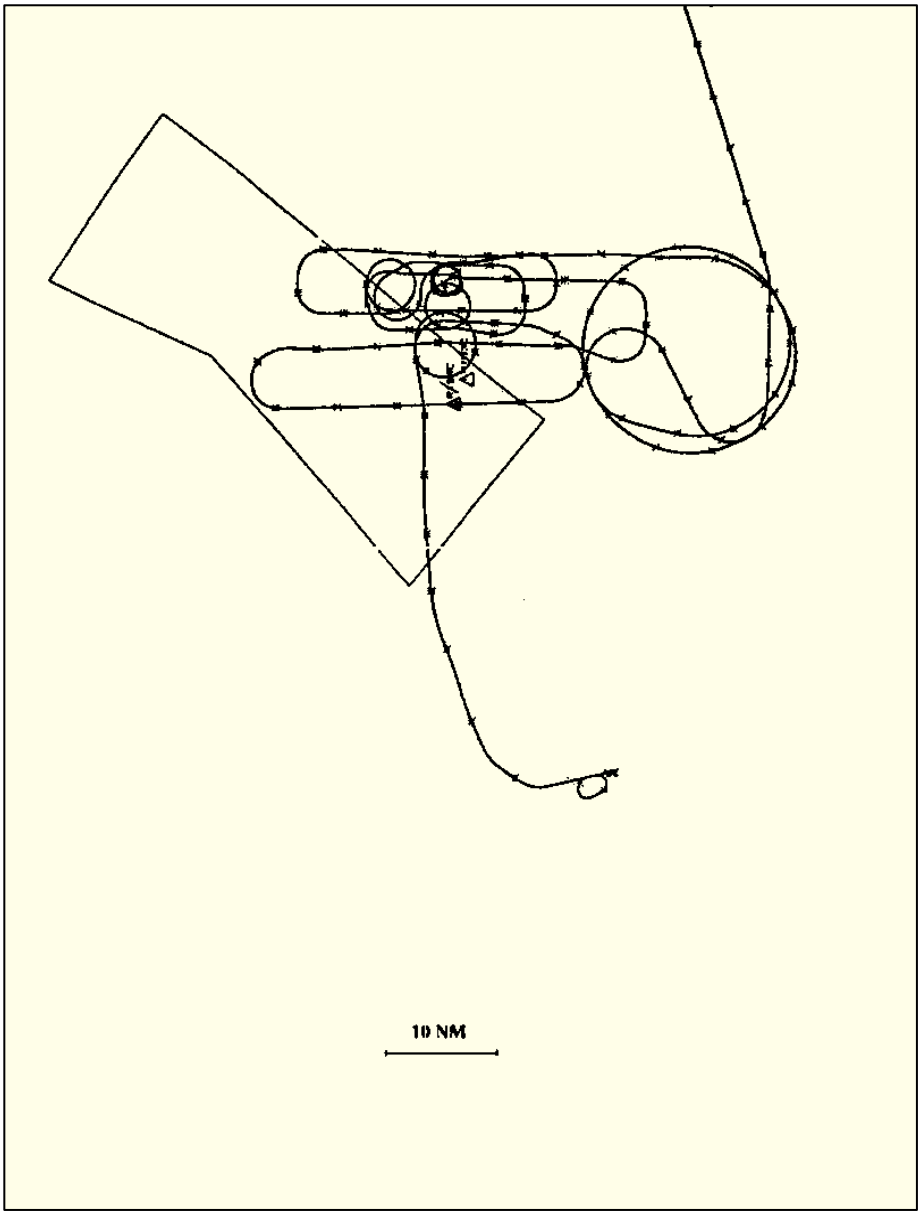


Figure 3-46. Measured aircraft trajectory with mission optimisation criteria.

3.8 TSPI ABIA SYSTEM DEVELOPMENT

In addition to the masking analysis described above, further simulation and experimental data are required in order to determine the whole range of flight envelope limitations associated with the use of GNSS during test/training missions. The TSPI ABIA (T-ABIA) methodology described here was originally intended for adoption in a dedicated ground-based simulation tool for mission planning and post-mission data analysis purposes (Sabatini, 2002). However, the concept successively evolved into a real-time T-ABIA system suitable for integration with the aircraft avionics and FTI systems; thus effectively providing augmentation of GNSS integrity in flight. The steps described below provide further details on the implemented T-ABIA approach.

STEP 1

By simulation and flight testing the following data are obtained:

- The Critical Attitude Angles (CAAs), including the CBA and the Critical Pitch Angles (CPAs) in all relevant aircraft configurations;
- The Critical Satellite Geometries (CSGs) related to adverse configurations of the satellites in view and low C/N_0 values;
- The airborne DGNSS Data Link Antenna Coverage (DAC) limitations (i.e., airborne Data Link antennae masking matrixes and ground/airborne antennae radiation patterns);
- The Telemetry Antenna Coverage (TAC) limitations for test/training missions requiring a real-time telemetry link with a Ground Control Station (GCOS);
- The Multipath Critical Conditions (MCC) causing degraded GNSS performance;
- The Doppler Critical Conditions (DCC) degrading GNSS tracking performance.

STEP 2

Using appropriate aircraft dynamics models, the manoeuvring envelope of the aircraft is determined in all required flight conditions for the planned test/training mission.

STEP 3

Knowing the CAA, CSG, DAC and DCC limits, together with the manoeuvring requirements of specific flight test/training missions, it is possible to identify (by simulation) the aircraft configurations/manoeuvres that are potentially critical for the on-board GNSS system.

STEP 4

Having identified the critical conditions (configurations and manoeuvres), suitable models are developed that describe the critical trends.

STEP 5

Using these models and comparing them with the boundaries set by the required Time-to-Alert (TTA) thresholds, it is possible:

- To determine if a specific manoeuvre required for flight test/training can be performed with/without GNSS and telemetry outages (test/training mission planning stage);
- To generate timely warnings when the aircraft is performing critical manoeuvres prone to induce GNSS/telemetry outages (real-time implementation).

Once the reliability of the mathematical algorithms for T-ABIA is established, a GNSS integrity augmentation function can be integrated in the aircraft or in the ground test/training GCOS to generate alerts when the critical conditions for GNSS/telemetry signal degradations/losses are likely to occur (within a specified maximum TTA). The functional architecture of a the T-ABIA system (ABIA suitable for flight test applications) is shown in Fig. 3-48. The aircraft on-board

sensors provide information on the aircraft relevant flight parameters (navigation data, engine settings, etc.) to an Integrity Flag Generator (IFG), which is also connected to the on-board DGNSS system. The IFG can be incorporated into one of the existing airborne computers or can be a dedicated processing unit. Using the available data on DGNSS and the aircraft flight parameters, integrity signals are generated which can be displayed on one of the cockpit displays and/or sent to an Aural Warning Generator (AWG). At the same time, an alternate flight path is computed taking into account the geometry and the tracking status of the available GNSS satellites, together with the current mission requirements and the information provided by the aircraft sensors.

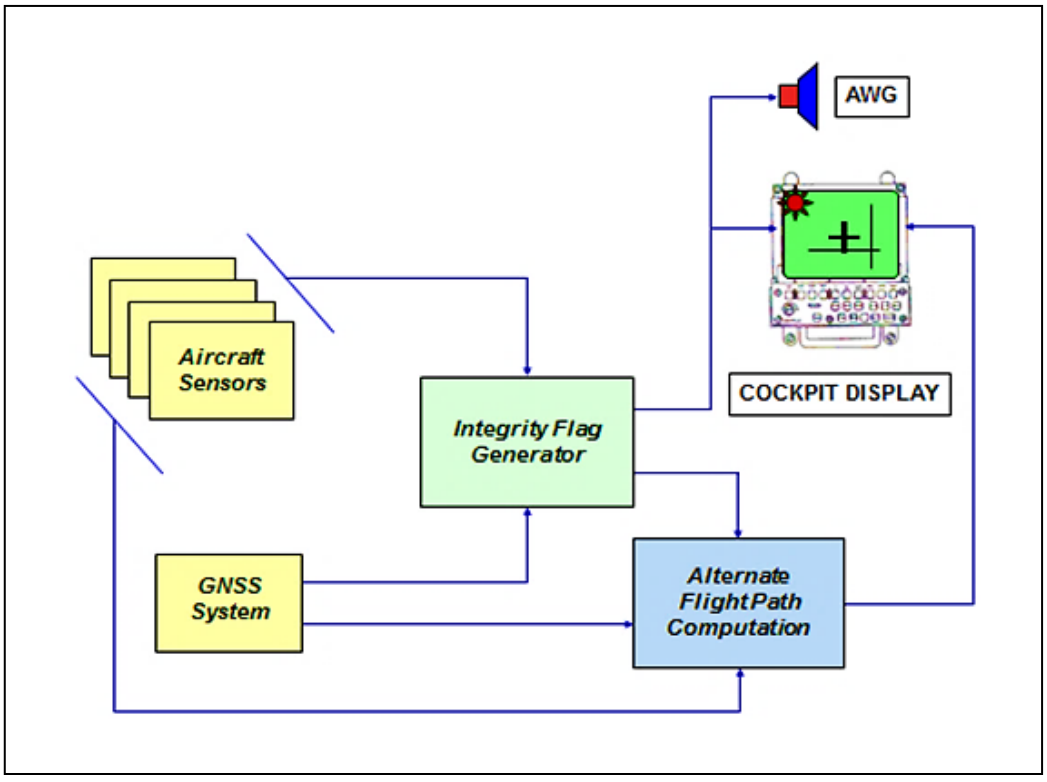


Figure 3-48. T-ABIA systems for flight test applications (Sabatini et al., 2013).

The TORNADO-IDS cockpit integration scheme (rear flight crew) is shown in Fig. 3-49. For monitoring purposes, the pilot is provided with an indication of the CBA in the current aircraft configuration, the vertical acceleration (g) and jerk (g-rate) limits, the satellites (SV) in view, the SNR of each satellite, the PDOP and the

EPE/FOM. If the pre-defined integrity thresholds are exceeded, the navigator is provided with a visual alert (both head-up and head-down) and with some basic guidance information (i.e., reduce rate-of-turn, left/right turn, reduce pitch), thereby allowing the implementation of corrective manoeuvres.

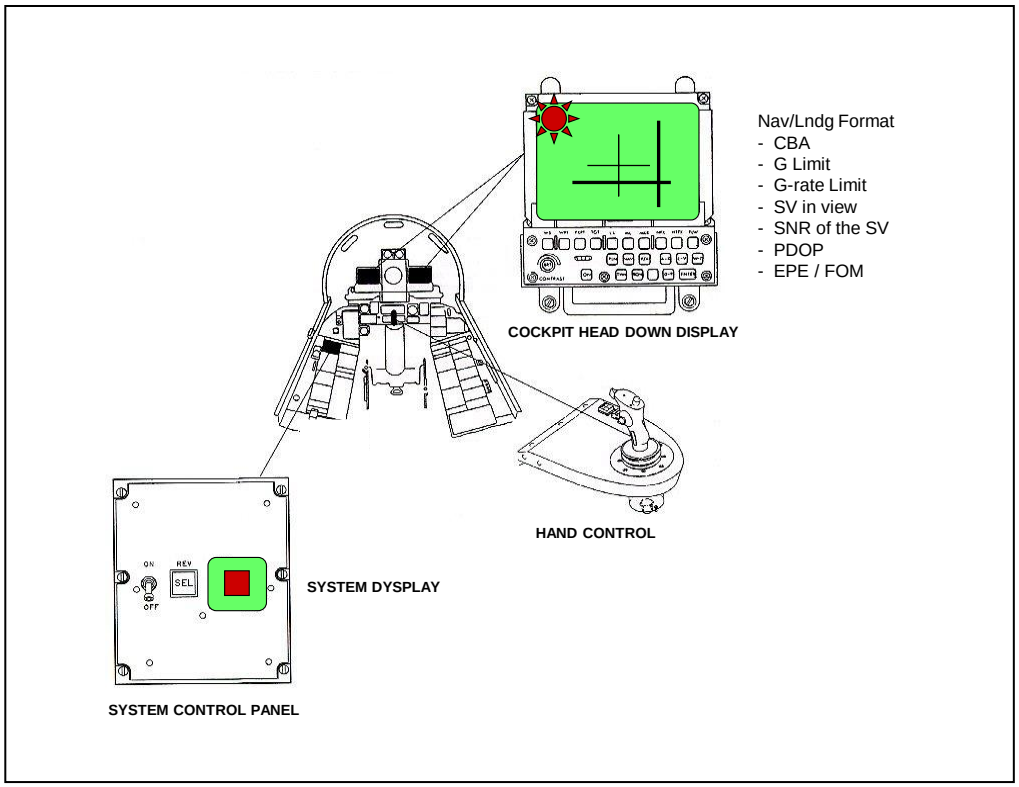


Figure 3-49. T-ABIA cockpit integration scheme (Sabatini et al., 2008).

3.9 CONCLUSION

During flight test activities with DGNSS TSPI systems, it was observed that one or more of the following conditions was prone to cause positioning data degradations or losses:

- The aircraft reaching the CAA associated with a particular aircraft configuration;
- Bad satellite geometries and low satellite C/N_0 values;
- Aircraft DGNSS data link antennae coverage limitations;

- Interference caused by the DGNSS data link or other RF signals;
- Multipath caused by GNSS signals reflected by the earth or the aircraft body surfaces.

The last two problems could be mitigated by existing technology solutions (i.e., choosing a VHF data link, filtering the radio frequency signals reaching the GNSS antenna, identifying suitable locations for the GNSS antenna and providing adequate shielded of the antenna itself, either by physical devices or via dedicated software masks, etc.). However, there was little to nothing one could do in order to prevent critical GNSS data losses during realistic test/training manoeuvres and particular approach procedures (e.g., curved and segmented approaches) performed with high performance military aircraft. Furthermore, although in some cases a careful mission planning could significantly reduce the number of GNSS outages, the adoption of specific aircraft piloting strategies (using the information currently available in the aircraft cockpits) cannot effectively avoid the occurrence of these events. A case study was therefore undertaken in order to identify an integrity augmentation method/technique suitable for GNSS-TSPI. This method was originally intended for adoption in a dedicated ground-based simulation tool for mission planning and post-mission data analysis purposes. However, the concept successively evolved into a real-time T-ABIA system suitable for integration with the aircraft avionics and FTI systems; thus effectively providing augmentation of GNSS integrity in flight. Simulation and flight test activities were performed to corroborate the validity of the mathematical models for T-ABIA and the system was successfully integrated into a TORNADO-IDS test-bed aircraft to generate pilot alerts (within the specified maximum TTA) when the critical conditions for GNSS signal losses were likely to occur. Additionally, the T-ABIA system was able to provide some basic guidance information to prevent the aircraft reaching critical conditions for GNSS data degradations or losses. The next logical step in this research was to extend the results obtained from flight test to the design of a more advanced system suitable for manned/unmanned aircraft applications and beyond flight testing (Sabatini et al., 2013-a), (Sabatini et al., 2013-b). The architecture of this advanced ABIA system is presented in the next chapter.

3.10 REFERENCES

ASHTECH (2001-a), "ASHTECH Z-12 Receiver", Technical Specification Leaflet. 2001-a.

ASHTECH (2001-b), "ASHTECH P-NAV User's Manual", Document Number 756805, Sunnyvale CA (USA).

DMA (1991), "Datums, Ellipsoids, Grids, and Grid Reference Systems." US Defence Mapping Agency. Document No. DMA TM 8358.1. Fairfax, VA (USA). 1991.

Ogonda, G. O. (2003), "Setting-up of GNSS Reference Stations and Investigating the Effects of Antenna Radome." PhD Thesis. University of Stuttgart, Institute of Navigation.

Sabatini, R. (2005), "Experimental Investigation of Differential GPS for Flight Test of High Performance Aircraft." University of Rome "La Sapienza", School of Aerospace Engineering. Thesis submitted in partial fulfilment for the degree of Doctor of Engineering in Atronautics.

Sabatini, R. (2002), "Aircraft Autonomous Integrity Augmentation for High Precision Differential GPS Applications." NATO-RTO Sensors and Electronics Technology Panel (SET) Symposium on "Emerging Military Capabilities Enabled by Advances in Navigation Sensors." Istanbul (Turkey).

Sabatini, R. and Palmerini, G. B. (2008), "Differential Global Positioning System (DGPS) for Flight Testing." NATO Research and Technology Organization (RTO) – Systems Concepts and Integration Panel (SCI). AGARDograph Series RTO-AG-160, Vol. 21.

Sabatini R., Moore T., Hill C. (2013-a), "A New Avionics Based GNSS Integrity Augmentation System: Part 1 – Fundamentals." Journal of Navigation, Vol. 66, No. 3, pp. 363-383.

4

ADVANCED ABIA SYSTEM ARCHITECTURE

4.1 INTRODUCTION

As discussed in Chapter 3, there is a need to avoid GNSS data degradations or losses in flight test applications. This is required to increase flight test mission success rates (i.e., the availability of TPSI data when required), which in turn reduces cost of the overall flight test campaign (avoiding the need to repeat specific flight segment or, in some cases, entire flight sorties). Regarding operational applications beyond flight test, it is also important to be able to predict GNSS data degradations or signal losses experienced by the aircraft during its mission. This concept applies both to civil and military (manned and unmanned) aircraft, although in different flight and operational tasks. Military examples include mission planning and real-time trajectory optimisation to avoid known areas of GNSS jamming (e.g., relying on intelligence information), or the possible loss experienced due to aircraft manoeuvres (e.g., antenna obscuration and dynamic stress errors). An extension of this concept is the use of GNSS in urban canyons, increasingly important within the UAS Traffic Management (UTM) research framework. Other civil/military safety-of-life applications include ATM/ATFM and TMA/airport operations using GNSS systems. It is in fact clear that, due to the possibility of performing GNSS curved/segmented approaches in the TMA as well as autoland/surface operations, both manned and unmanned aircraft would benefit from the predictive integrity features provided by

an ABIA system (e.g., RNAV route planning, separation-assurance and collision-avoidance, auto-go-around, autonomous taxing, etc.).

Based on the experimental research activities described in Chapter 3, further review of the applicable literature and additional analysis of GNSS flight test data, suitable mathematical models were developed to describe the main causes of GNSS signal outages/degradations in a variety of civil/military aviation applications beyond flight testing. These models include Doppler shift, interference/jamming, antenna obscuration, adverse satellite geometries, Carrier-to-Noise ratio (C/N_0) reductions (fading), and multipath (i.e., GNSS signals reflected by the Earth's surface or the aircraft body). Adopting these mathematical models in association with suitable integrity thresholds and guidance algorithms, the ABIA system is able to generate integrity caution (predictive) and warning (reactive) flags, as well as steering information to the pilot and electronic commands to the aircraft/UAV flight control system. These features allow real-time avoidance of safety-critical flight conditions and fast recovery of the required navigation performance in case of GNSS data losses. This chapter presents the ABIA system architecture, ABIA specific integrity flag definitions, and some of the key mathematical models required for the ABIA software modules development.

4.2 ABIA CONCEPT EVOLUTION

Taking the move from the T-ABIA system prototype, the next step in this research was to design a more advanced integrity augmentation system suitable for manned and unmanned aircraft applications. Implementing a Flight Path Guidance (FPG) module, this advanced ABIA system can provide more complete steering information to the pilot and, additionally, electronic commands to the aircraft/UAV Flight Control System (FCS), allowing for real-time and continuous integrity monitoring, avoidance of mission/safety-critical flight conditions and rapid recovery of the RNP in case of GNSS data degradation or loss. The architecture of this advanced ABIA system is depicted in Fig. 4-1.

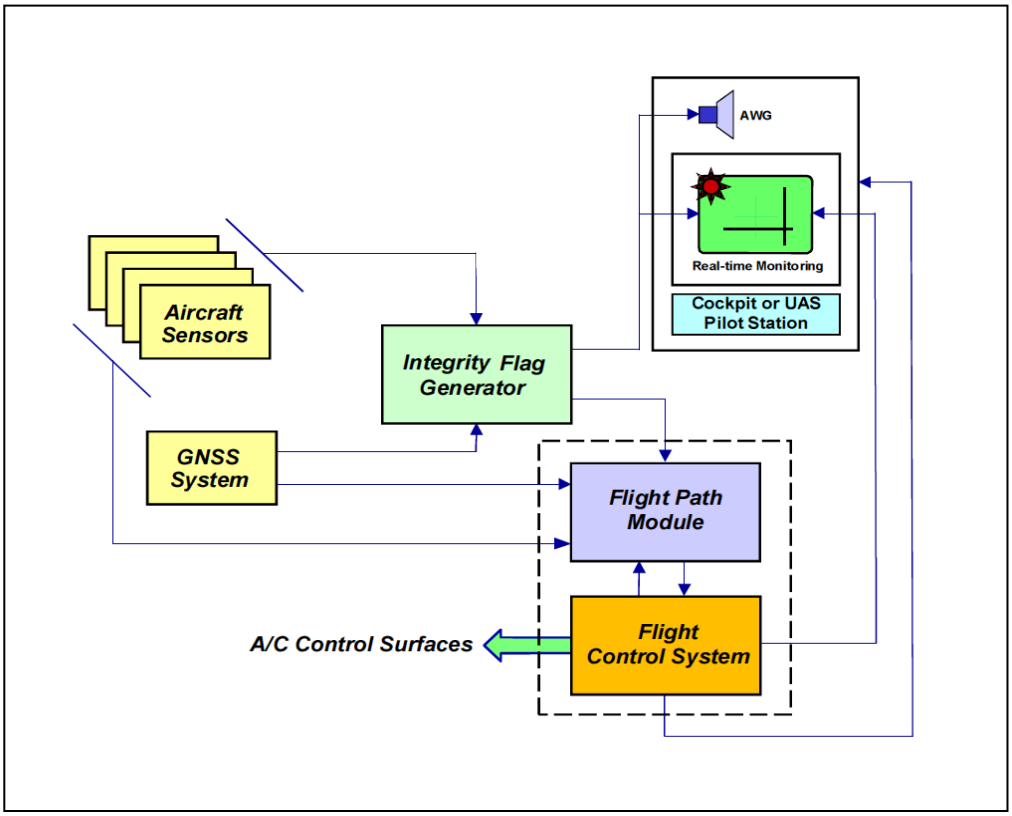


Figure 4-1. ABIA evolution for manned and unmanned aerial vehicles.

This system addresses both the predictive and reactive nature of GNSS integrity augmentation. To understand this concept, let us first introduce some key definitions of alerts and TTAs applicable to the ABIA system.

- ***Alert Limit:*** is the threshold value of a given parameter measurement not to be exceeded without issuing an alert. ABIA alerts are predictive (caution) and reactive (warning) integrity flags.
- ***Caution Integrity Flag (CIF):*** a predictive annunciation that the GNSS data delivered to the avionics system is going to exceed the Required Navigation Performance (RNP) thresholds specified for the current and planned flight operational tasks (GNSS alert status).
- ***Warning Integrity Flag (WIF):*** a reactive annunciation that the GNSS data delivered to the avionics system has exceeded the Required Navigation

Performance (RNP) thresholds specified for the current flight operational task (GNSS fault status).

- ***ABIA Time-to-Caution (TTC):*** the minimum time allowed for the caution flag to be provided to the user before the onset of a GNSS fault resulting in an unsafe condition.
- ***ABIA Time-to-Warning (TTW):*** the maximum time allowed from the onset of a GNSS fault resulting in an unsafe condition to the moment that the ABIA system provides a warning flag to the user.

Based on the above definitions, we can define two separate models for the time responses associated to the Prediction-Avoidance (PA) and Reaction-Correction (RC) functions performed by the ABIA system (Fig. 4-2). The PA time response is given by:

$$\Delta T_{PA} = \Delta T_{Predict} + \Delta T_{C-Report} + \Delta T_{Avoid} \quad (4.1)$$

where:

$\Delta T_{Predict}$ = Time required to predict a critical condition;

$\Delta T_{C-Report}$ = Time required to communicate the failure to the FPG module;

ΔT_{Avoid} = Time required to perform the avoidance manoeuvre.

In this case, we have $\Delta T_{Avoid} \leq$ TTC.

If the available avoidance time ΔT_{Avoid} is not sufficient to perform an adequate avoidance manoeuvre (i.e., $\Delta T_{Avoid} > TTC$), the aircraft will inevitably encroach on critical conditions causing GNSS data losses or unacceptable degradations. In this case, the RC time response applies:

$$\Delta T_{RC} = \Delta T_{Detect} + \Delta T_{W-Report} + \Delta T_{Correct} \quad (4.2)$$

where:

ΔT_{Detect} = Time required to detect a critical condition;

$\Delta T_{W-Report}$ = Time required to communicate the failure to the FPG module;

$\Delta T_{Correct}$ = Time required to perform the correction manoeuvre.

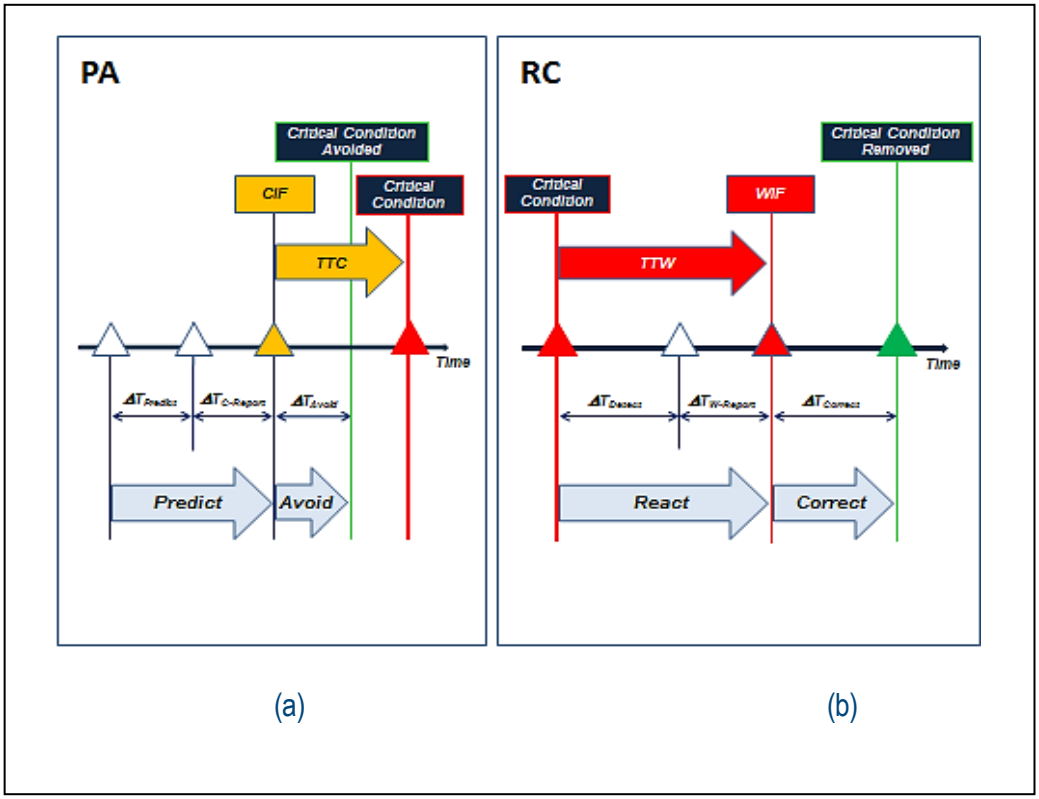


Figure 4-2. ABIA PA and RC functions representation.

In general, we must have $\Delta T_{Detect} + \Delta T_{W-Report} \leq$ TTW. The RC time response is substantially equivalent to what current GBAS and SBAS systems are capable of achieving. A comparison between Fig. 4-2(a) and Fig. 4-2(b) allows to immediately visualise the benefits introduced by the ABIA PA function. Further progress is possible adopting a suitable algorithm in the FPG module capable of initiating an early correction manoeuvre as soon as the condition $\Delta T_{Avoid} \leq$ TTC is violated. In this case, the direct Prediction-Correction (PC) time response would be:

$$\Delta T_{PC} = \Delta T_{Predict} + \Delta T_{C-Report} + \Delta T_{Eraly\ Correct} \tag{4.3}$$

This concept is illustrated in Fig. 4-3. By comparison with Fig. 4-2, it is evident that the ABIA system would be able to reduce the time required to recover from critical conditions if the following inequality is verified:

$$\Delta T_{Eraly\ Correct} < TTC + \Delta T_{Detect} + \Delta T_{C-Report} + \Delta T_{Correct} \tag{4.4}$$

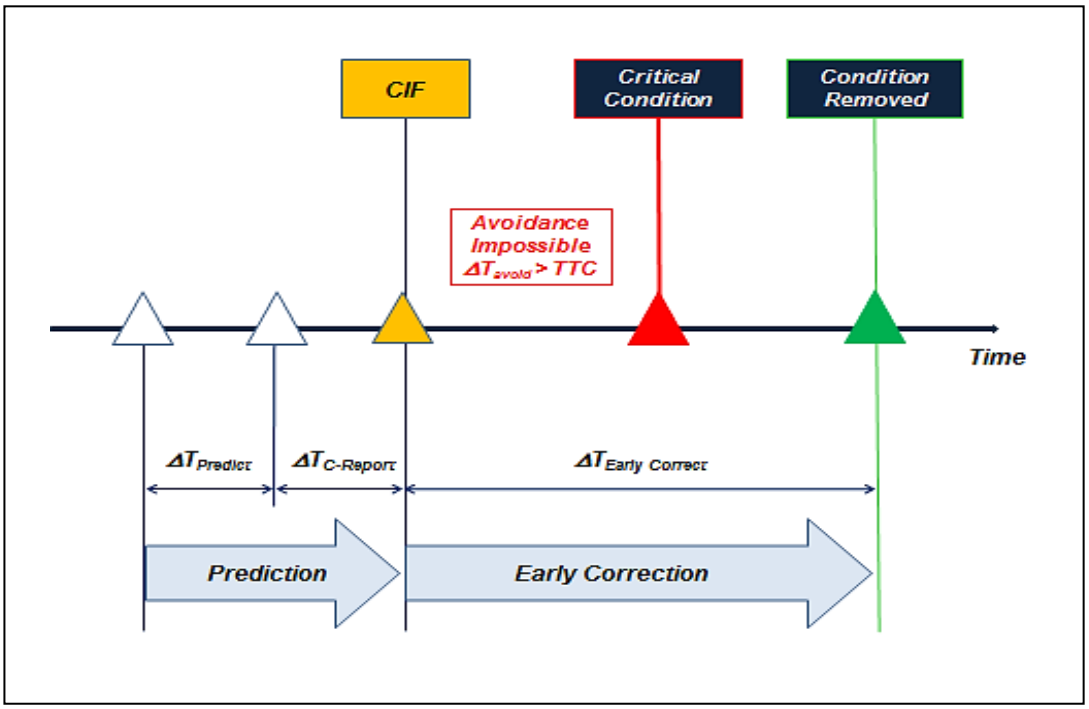


Figure 4-3. ABIA PC function representation.

4.3 ABIA IFG DEVELOPMENT

As in the case of T-ABIA, a dedicated analysis is required in order to determine the flight envelope limitations associated with the use of GNSS. By analysis, simulation and flight test the following models are obtained:

- The Antenna Obscuration Matrixes (AOM) in azimuth and elevation, constructed as a function of attitude (Euler) angles in all relevant aircraft configurations;
- The GNSS Carrier-to-Noise and Jamming-to-Signal Models (CJM), accounting for the relevant transmitter/receiver characteristics, propagation losses and RF interference;
- The Multipath Signal Model (MSM) including fuselage, wing and ground path fading components and the associated range errors;

- The Doppler Shift Model (DSM) and associated critical conditions causing GNSS tracking issues.

Using appropriate aircraft dynamics models, the manoeuvring envelope of the aircraft is determined in all required flight conditions. Using the AOM, CJM, MSM and DSM models, together with the GNSS receiver tracking models and the manoeuvring requirements of specific flight tasks (e.g., test/training missions or standard airport approach procedures), it is possible to identify the conditions that are potentially critical for the on-board GNSS system and set appropriate thresholds for the ABIA CIFs and WIFs, thereby generating timely alerts when the aircraft is performing critical manoeuvres prone to induce GNSS signal outages. Once the reliability of the mathematical algorithms is established, the ABIA IFG module can be implemented in the aircraft for alerting the pilot when the critical conditions for GNSS signal losses are likely to occur. The following sections of this chapter concentrates on the AOM, CJM, MSM and DSM models employed in our research. Next chapter will present CIF and WIF thresholds criteria and the results of a case study performed on the TORNADO-IDS aircraft.

4.3.1 IFG Module Architecture

Fig. 4-4 shows the architecture of ABIA IFG module and its interfaces. This module is designed to provide CIF and WIF alerts in real-time (i.e., in accordance with the specified TTC and TTW requirements in all relevant flight phases). IFG module inputs are from the GNSS Receiver and Flight Dynamics modules. In this research, a dedicated GNSS Constellation Simulator (GCS) was implemented to support GNSS satellite visibility, signal and geometry analysis. Additionally, an Aircraft Dynamics Simulator (ADS) was developed to generate the nominal flight path trajectory and attitude (Euler) angles. Additionally, an Aircraft 3-Dimensional Model (A3DM) in CATIA (Computer Aided Three-dimensional Interactive Application) and a Terrain and Objects Database (TOD) are also required to run the MPS. Using a Digital Terrain Elevation Database (DTED), it is possible to obtain a detailed map of the terrain beneath the aircraft.

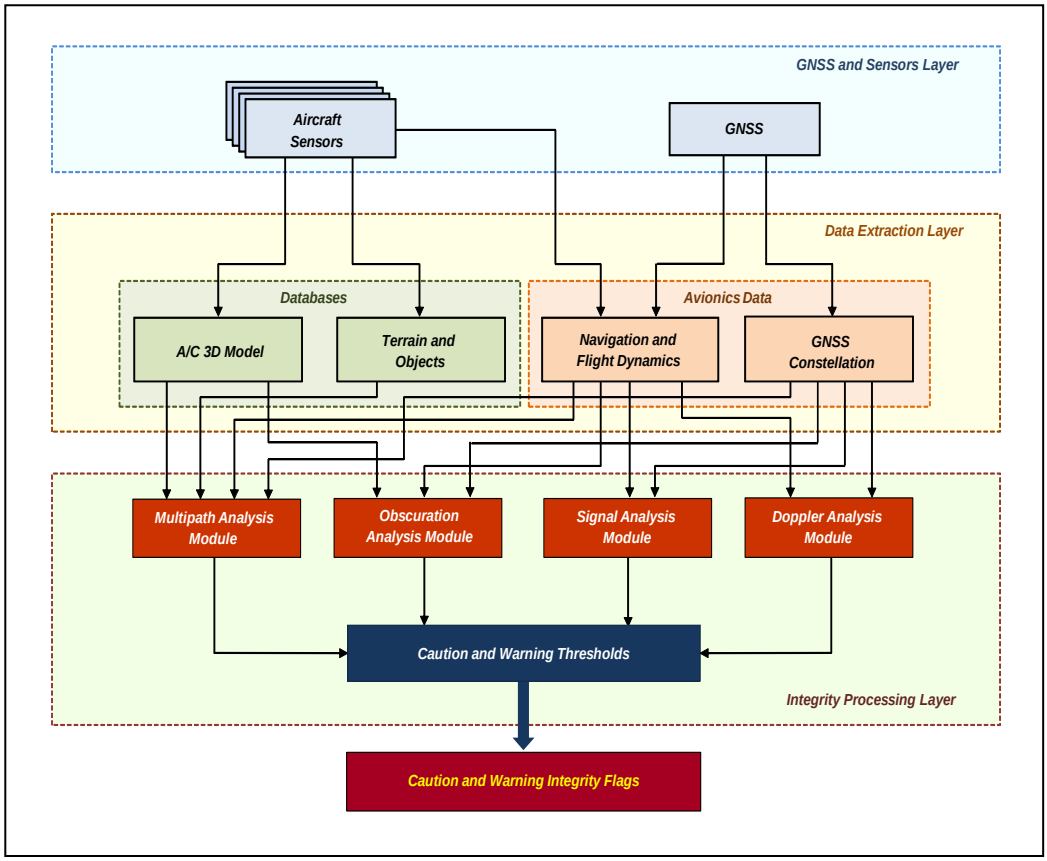


Figure 4-4. IFG module architecture.

Providing the aircraft trajectory inputs from the ADS module, terrain elevation data can be automatically extracted and fed to the TOM module where they are integrated with the database of man-made objects (e.g., buildings). The Doppler Analysis Module (DAM) calculates the Doppler shift by processing ADS and GCS inputs. The Multipath Analysis Module (MAM) processes the A3DM, TEM, GCS and ADS inputs to determine multipath contributions from the aircraft (wings/fuselage) and from the terrain/objects close to the aircraft. The Obscuration Analysis Module (OAM) receives inputs from the A3DM, GCS and ADS, and computes the GNSS antenna(e) obscuration matrixes for all aircraft manoeuvres. The Signal Analysis Module (SAM) calculates the nominal link budget of the direct GNSS signals received by the aircraft in the presence of atmospheric propagation disturbances, as well as the applicable RF interference signal levels. The Integrity Flags Simulator (IFS) uses the set of predefined CIF/WIF threshold parameters to trigger the

generation of both caution and warning flags associated with antenna obscuration, Doppler shift, multipath, S/N, interference and satellite geometry degradations.

4.3.2 Antenna Obscuration

Due to the manoeuvres of the aircraft, the wings, tail and fuselage will obscure some satellites during the flight. Fig. 4-5 shows the structure of the AME analysis algorithm.

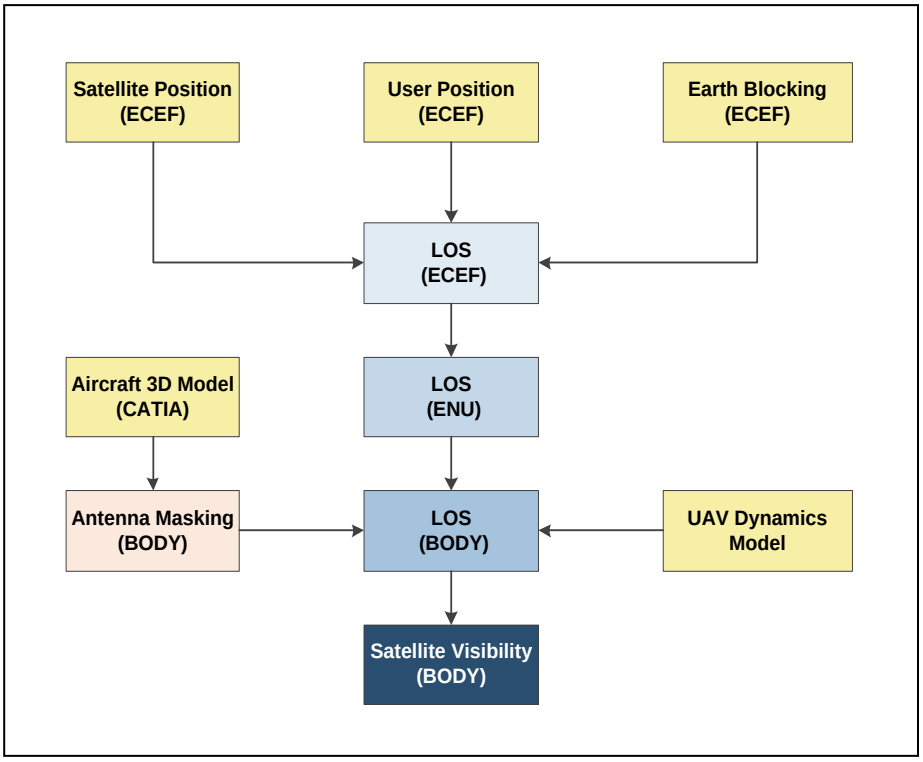


Figure 4-5. GNSS satellite obscuration analysis.

A Three Degrees of Freedom (3DOF) model with variable mass was developed to calculate the trajectory of the aircraft (i.e., position, velocity and attitude angles) during the different flight phases. Taking into account the aircraft shape (CATIA 3-D model), the aircraft flight dynamics (pitch, roll and yaw variations) and the geometric displacement of the GNSS satellites in view, the Antenna Obscuration Matrixes (AOMs) are generated for the different flight conditions. As an example, the TORNADO-IDS AOM obtained with a roll angle of 45° is shown in the Fig. 4-6.

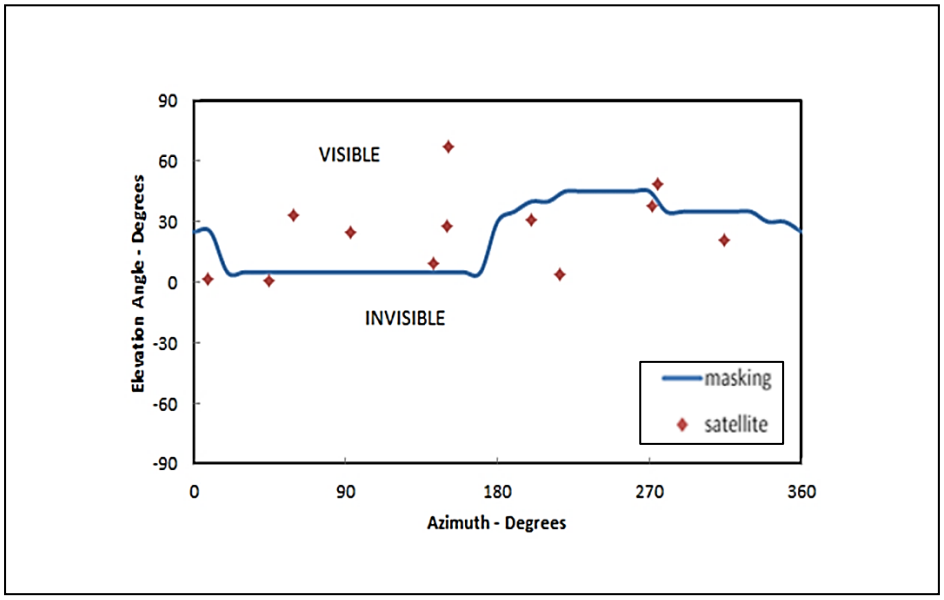


Figure 4-6. TORNADO-IDS upper antenna AOM (Right Roll=50º).

Besides the AOM, other factors influence the satellite visibility. In general, a satellite is geometrically visible to the GNSS receiver only if its elevation in the antenna frame is above the Earth horizon and the antenna elevation mask. It should be noted that even high performance avionics GNSS antennae have gain patterns that are typically below -3dB at about 5 degrees elevation and, as a consequence, their performance become marginal below this limit (Fig. 4-7).

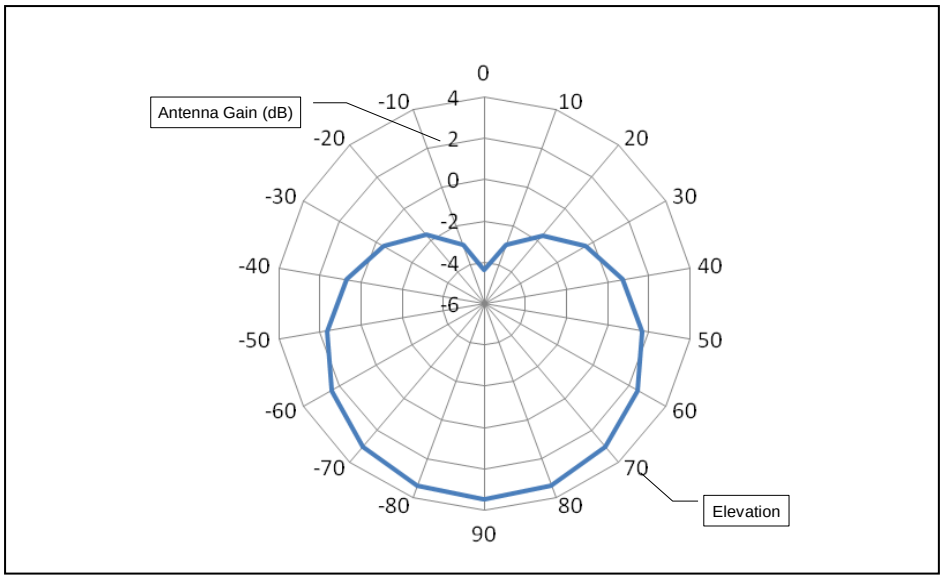


Figure 4-7. Avionics antenna gain pattern (L1 frequency).

In order to determine if a satellite is obscured, the LOS of the satellite with respect to the antenna phase centre has to be determined. To calculate the satellite azimuth and elevation with respect to the antenna transformation matrix between ECEF (Earth Centred Earth Fixed) and antenna frame must be applied. This is obtained from:

$$T_E^a = T_b^a * T_N^b * T_E^N \tag{4.5}$$

where T_b^a is the transformation matrix between the aircraft body frame and the antenna frame, T_N^b is the transformation matrix from ENU (East-North-Up) to body frame, and T_E^N is the ECEF to ENU transformation matrix. As an example, Fig. 9 shows the trajectory of an aircraft during a Turning Descent Manoeuvre (TDM) lasting 300 seconds (spiral flight with a constant turning radius).

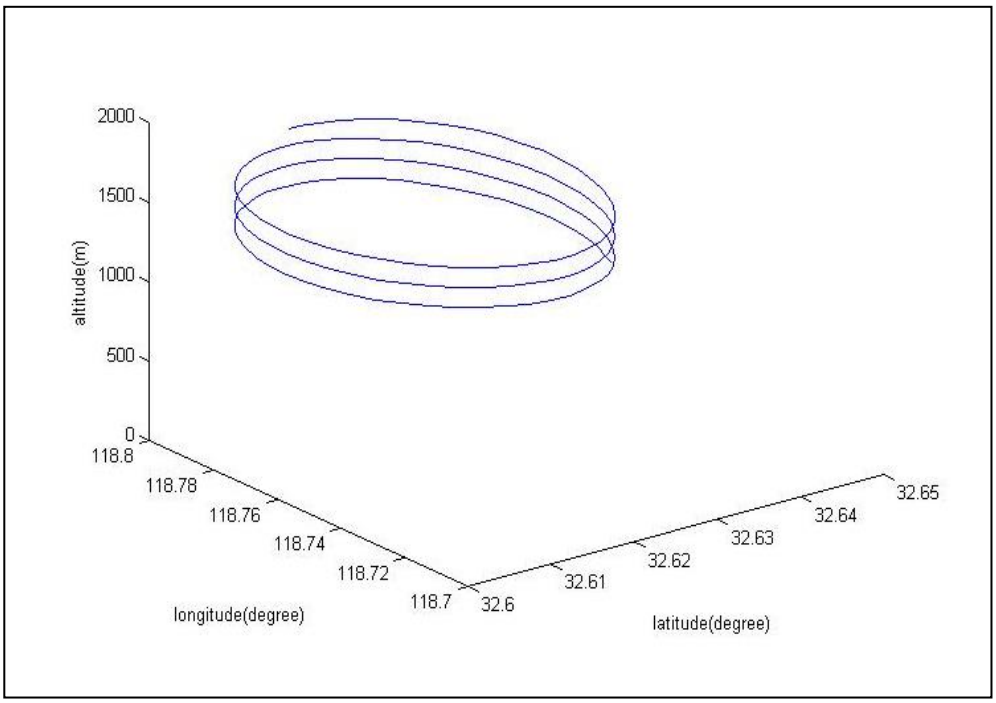


Figure 4-8. Turning descent manoeuvre.

Fig. 4-9 shows the combined GPS/GALILEO satellite visibility during the same flight phase. During the manoeuvre, the number of satellites in view varies from 7 to 16.

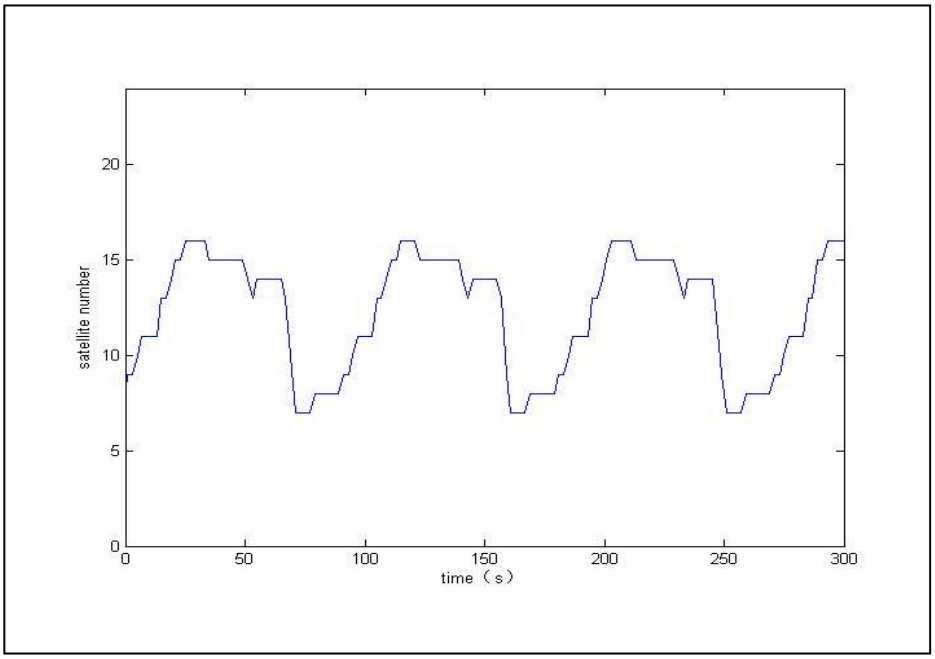


Figure 4-9. Satellite visibility (TDM).

4.3.3 GNSS Signal and Interference

The received signal strength is affected by a number of factors including transmitter and receiver characteristics, propagation losses and interferences. In our case, the SAM combines the various factors contributing to the GNSS link budget and signal degradations due to interference. Multipath induced effects are considered separately. The SAM module takes inputs from the GCS and FDS modules, and computes both C/N_0 and *J/S*. The ratio of total carrier power to noise C/N_0 in dB-Hz is the most generic representation of received signal strength. This is given by:

$$\frac{C}{N_0} = P_t + G_t + G_r + L_s - L_a - L_r - \sigma_m - N_f \ \text{(dB)} \tag{4.6}$$

where:

P_T = Transmitted power level (dBw);

G_t = Satellite antenna gain (dBic);

G_r = Receiver antenna gain toward the satellite;

L_s = Free space loss;

L_a = Atmospheric attenuation (dry-air);

L_r = Rainfall attenuation;

σ_m = Tropospheric fading;

N_f = Receiver noise figure.

As an example, Table 4.1 shows the expected C/N_0 for a receiver tracking a GPS satellite at zenith given a typical noise power density of -205 dBW-Hz (Parkinson et al., 1996).

Table 4-1. Nominal receiver GPS signal power and received C/N_0 (Kintner, 2007).

SV Block IIR-M/IIF	Frequency	P or P(Y)	C/A or L2C
Signal Power	L1	-161.5 dBW	-158.5 dBW
	L2	-161.5 dBW	-160.0 dBW
C/N_0	L1	43.5 dB-Hz	46.5 dB-Hz
	L2	43.5 dB-Hz	45 dB-Hz

The values of C/N_0 listed in Table 1 should be compared against the values required to acquire and track GPS signals. Based on the literature review and previous experimental activities performed on TSPI system, it is clear that these thresholds are heavily dependent on receiver design. For most commercial GNSS receivers they are in the order of 28-33 dB-Hz for acquisition and 25-30 dB-Hz to maintain tracking lock (Parkinson et al., 1996), (Kintner, 2007). Current generation avionics GNSS receivers, which are designed to operate in high dynamics conditions, typically exhibit better C/N_0 thresholds (Sabatini et al., 2008).

The link budget calculated from Eq. (4.6) only refers to the direct GNSS signal received from a satellite. Multipath effects, which are due to the geometric and reflective characteristics of the environment surrounding the GNSS antenna are not included in this calculation and are discussed separately. The L-band antenna on-board GNSS satellites is designed to radiate the composite L-band signals to the

users on and near the Earth. In the case of GPS (Fig. 4-10), the satellite viewing angle from edge-to-edge of the Earth is about 27.7 degrees (Boithias, 1982). The satellite antenna is designed to illuminate the Earth's surface with an almost uniform signal strength. The path loss of the signal is a function of the distance from the antenna phase centre to the surface of the earth. The path loss is minimum when the satellite is directly overhead (90° elevation), and is maximum at the edges of the coverage area (satellite at the horizon).

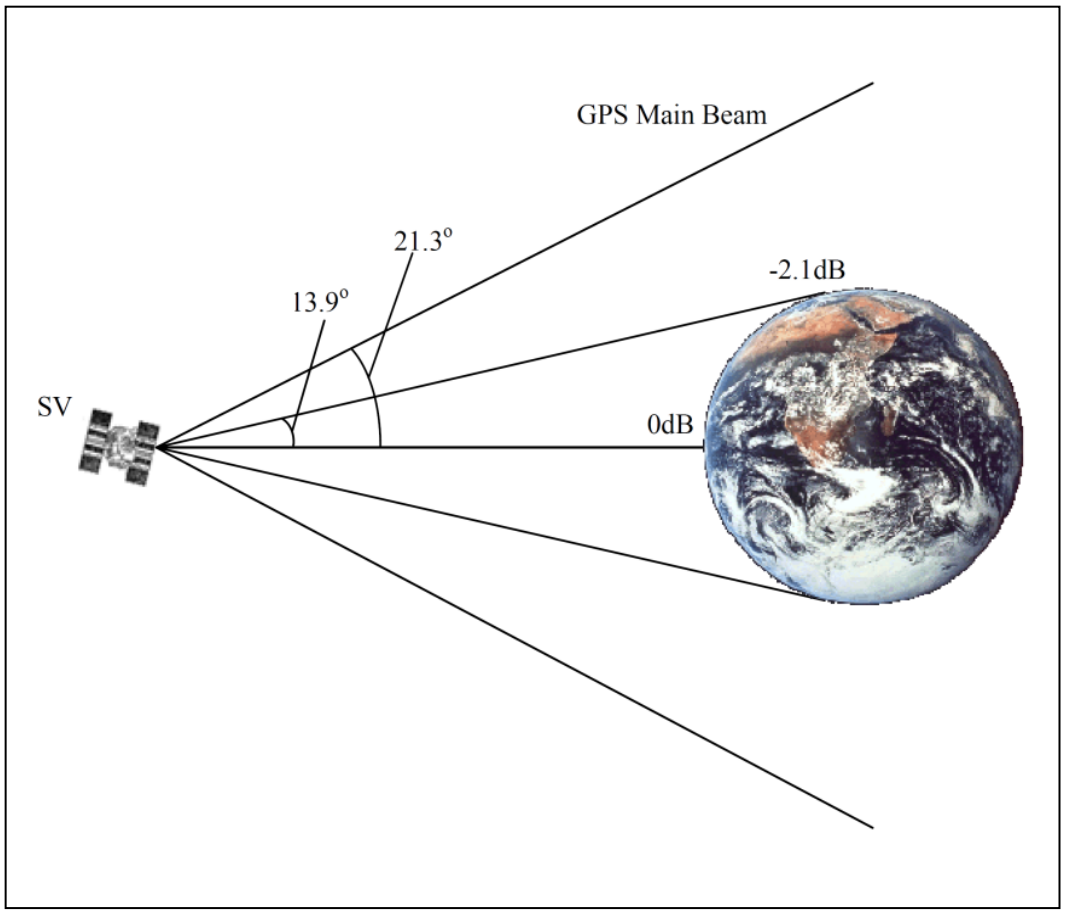


Figure 4-10. GPS satellite antenna coverage.

The difference in signal strength caused by this variation in path length is about 2.1 dB [6] and the satellite antenna gain can be approximated by:

$$G_t(dB) = 2.5413 * sinE - 2.5413 \quad (4.7)$$

where E is the elevation angle. Similarly, the avionics antenna gain pattern shown in Fig. 8 can be approximated by:

$$G_r(dB) = 9.8756 * sinE - 4.7567 \quad (4.8)$$

GNSS signal frequencies (L-band) are sufficiently high to keep the ionospheric delay effects relatively small. On the other hand, they are not so high as to suffer severe propagation losses even in rainy conditions. However, the atmosphere causes small but non-negligible effects that must be taken into account. The major effects that the atmosphere has on GNSS signals include (Parkinson and Spilker, 1996):

- Ionospheric group delay/carrier phase advance;
- Tropospheric group delay;
- Ionospheric scintillation;
- Tropospheric attenuation;
- Tropospheric scintillation.

The first two effects have a significant impact on GNSS data accuracy but do not directly affect the received signal strength (C/N_0). Ionospheric scintillation is due to irregularities in the electron density of Earth's ionosphere (scale size from hundreds of meters to kilometres), producing a variety of local diffraction and refraction effects. These effects cause short-term signal fading, which can severely stress the tracking capabilities of a GNSS receiver. Signal enhancements can also occur for very short periods, but these are not really useful from the GNSS receiver perspective. On the contrary, fading can be so severe that the signal level will drop below the receiver tracking threshold and, as a consequence, the signal must be re-acquired.

Atmospheric scintillation effects are more significant in the equatorial and sub-equatorial regions and tend to be less of a factor at European and North-American latitudes. Signal scintillation is created by fluctuations of the refractive index, which are caused by inhomogeneity in the medium mostly associated to solar activity. At the GNSS receiver location, the signal would exhibit rapid amplitude and phase

fluctuations, as well as modifications to its time coherence properties. The most commonly used parameter characterizing the intensity fluctuations is the scintillation index S_4, defined as (ITU, 2013):

$$S_4 = \sqrt{\left(\frac{\langle I^2 \rangle - \langle I \rangle^2}{\langle I \rangle^2} \right)} \tag{4.9}$$

where I is the intensity of the signal (proportional to the square of the signal amplitude) and $\langle \ \rangle$ denotes averaging. The scintillation index S_4 is related to the peak-to-peak fluctuations of the intensity. The exact relationship depends on the distribution of the intensity. According to ITU (2013), the intensity distribution is best described by the Nakagami distribution for a wide range of S_4 values. The Nakagami density function for the intensity of the signal is given by:

$$p(I) = \frac{m^m}{\Gamma(m)} I^{m-1} \exp(-mI) \tag{4.10}$$

where the Nakagami "m-coefficient" is related to the scintillation index, S_4 by:

$$m = 1/S_4^2 \tag{4.11}$$

In formulating equation (4.10) the average intensity level of I is normalized to be 1. The calculation of the fraction of time that the signal is above or below a given threshold is greatly facilitated by the fact that the distribution function corresponding to the Nakagami density has a closed form expression which is given by:

$$P(I) = \int_0^I p(x)\,dx = \frac{\Gamma(m, mI)}{\Gamma(m)} \tag{4.12}$$

where $\Gamma(m, mI)$ and $\Gamma(m)$ are the incomplete gamma function and gamma function, respectively. Using equation (4.12), it is possible to compute the fraction of time that the signal is above or below a given threshold during ionospheric events. For example, the fraction of time that the signal is more than n dB below the mean is given by $P(10^{-n/10})$ and the fraction of time that the signal is more than m dB above the mean is given by $1 - P(10^{m/10})$.

Scintillation strength may, for convenience, be classified into three regimes: weak, moderate or strong (ITU, 2013). The weak values correspond to $S_4 < 0.3$, the moderate values from 0.3 to 0.6 and the strong case for $S_4 > 0.6$. The relationship between S_4 and the approximate peak-to-peak fluctuations P_{fluc} (dB) can be approximated by:

$$P_{fluc} = 27.5\, S_4^{1.26} \tag{4.13}$$

Table 1 provides a convenient conversion between S_4 and the approximate peak-to-peak fluctuations P_{fluc} (dB).

Table 4.2. Empirical conversion table for scintillation indices. Adapted from ITU (2013).

Scintillation regime	S_4	P_{fluc} [dB]
Weak	0.1	1.5
	0.2	3.5
Moderate	0.3	6
	0.4	8.5
	0.5	11
	0.6	14
Strong	0.7	17
	0.8	20
	0.9	24
	1.0	27.5

Geographically, there are two zones of intense scintillation, one at high latitudes and the other centred within $\pm 20°$ of the magnetic equator as shown in Fig. 4-11. Severe scintillation has been observed in these two sectors, while in the middle latitudes scintillation occurs exceptionally, such as during geomagnetic storms. In the equatorial sector, there is a pronounced night-time maximum of activity. For equatorial scintillation, peak activity around the vernal equinox and high activity at the autumnal equinox have been observed.

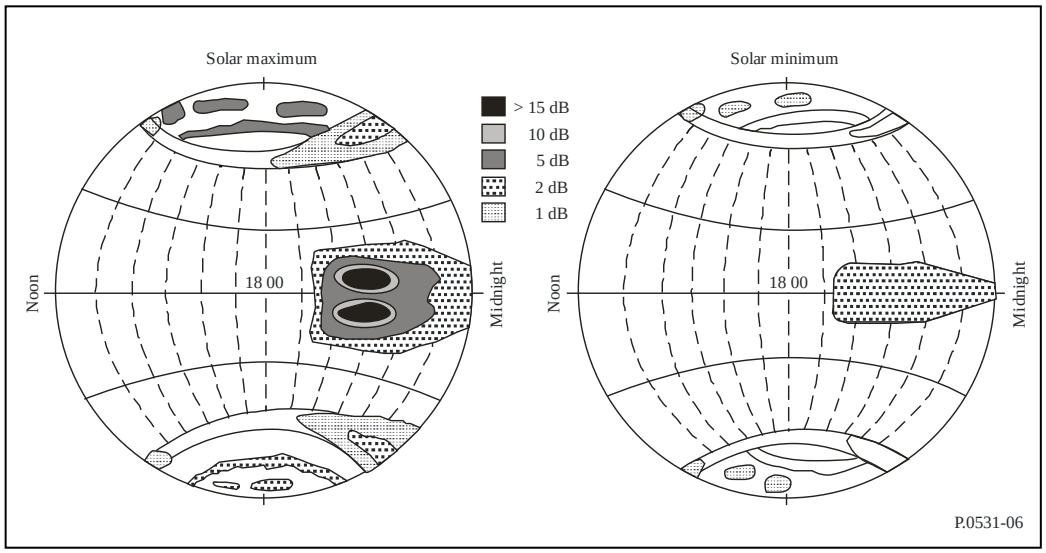


Figure 4.11. Depth of scintillation fading at 1.5 GHz during solar maximum and minimum years (ITU, 2013).

In order to predict the intensity of ionospheric scintillation on Earth-space paths, the International Telecommunication Union (ITU) recommend that the Global Ionospheric Scintillation Model (GISM) be used (ITU, 2013). The GISM permits one to predict the S4 index, the depth of amplitude fading as well as the rms phase and angular deviations due to scintillation as a function of satellite and ground station locations, date, time and working frequency. Unfortunately, at the moment, no adequate algorithms have been identified to account for ionospheric scintillation in the ABIA system implementation. However, as ionospheric propagation effects are a major source of signal disturbances in GNSS applications, future research will focus on possible mission planning implementations useful when flying over regions affected by intense scintillation and/or in times of predicted high scintillation.

Tropospheric attenuation in the GNSS frequency bands is dominated by oxygen, while the effects of water vapour and nitrogen attenuation can be neglected for most applications. Oxygen attenuation (A) is in the order of 0.035dB for a satellite at zenith and its variation with elevation angle (E) can be approximated by (Parkinson et al., 1996):

$$A(E) \cong \frac{0.07}{\sin E + 0.043} \quad \text{(dB)} \quad \text{for } 3 < E < 10 \text{ deg} \tag{4.9}$$

$$A(E) \cong \frac{0.035}{\sin E} \text{ (dB)} \quad \text{for } E > 10 \text{ deg} \tag{4.10}$$

These formulae provide acceptable results only if E > 3 degrees. However, since several other errors affects measurements from satellites with elevation below 5 degrees, a software mask is typically employed in avionics GNSS receivers to exclude these satellites form the navigation computations (Sabatini and Palmerini, 2008). Tropospheric rainfall attenuation has a minor effect in the GNSS frequency bands. For instance, at a frequency of 2 GHz the attenuation even for high rainfall rates (i.e., rates grater then 100 mm/h), is less than 0.01 dB/km (rainfall attenuation below 2 GHz is even less).

Tropospheric scintillation is caused by irregularities (primarily atmospheric turbulence) causing variations of the refractive index, mainly in the first few kilometres above the ground. Tropospheric scintillation effects vary with time and are dependent upon frequency and elevation angle. For small omnidirectional antennas, such as typical avionics GNSS antennas, the CCIR provided the following expression for the long-term RMS amplitude scintillation (Boithias, 1982):

$$\sigma_m = 0.025 f^{0.58} (csc\, E)^{-0.85} \quad \text{(dB)} \tag{4.11}$$

where f is the frequency in GHz. Thus, for low elevation angles tropospheric scintiation can be significant, but otherwise it is quite small. The Noise Figure (in dB) is related to the system noise temperature (T_{sys}) in Kelvin as follows (Davenport, 1987):

$$N_f = 10log\left(1 + \frac{T_{sys}}{T_0}\right) \tag{4.12}$$

where T_0 = 290K = 24.6 dB-K.

The system noise temperature (antenna plus receiver) is computed using the Friis formula (Friis, 1944). Typical noise figures for state-of-the-art GPS receivers are between 2 and 4 dB. Intentional and unintentional RF interference (jamming) can result in degraded navigation accuracy or complete loss of the GNSS receiver tracking. Jammers can be classified into three broad categories: Narrowband

Jammers (NBJ), Spread Spectrum Jammers (SSJ) and Wideband Gaussian Jammers (WGJ).

In mission-essential and safety-critical GNSS applications, both intentional and unintentional jamming must be detected in the GNSS receiver and accounted for in the integrity augmentation architecture. Fortunately, a number of effective jamming detection and anti-jamming (filtering and suppression) techniques have been developed for military GNSS applications and some of them are now available for civil use as well. An overview of these techniques is presented in (Ward, 1994). The J/S performance of a GNSS receiver at its tracking threshold can be evaluated by the following equation (Kaplan and Hegarty, 2006):

$$J/S = 10\,log\,QR_c\left[\frac{1}{10^{0.1(C/N_0)_{MIN}}} - \frac{1}{10^{0.1(C/N_0)}}\right] \tag{4.13}$$

where:

Q = Processing gain adjustment factor (1 for NBJ, 1.5 for SSJ and 2 for WGJ);

R_c = Code chipping rate (chips/sec);

$(C/N_0)_{MIN}$ = Receiver tracking threshold (dB-Hz).

Since the weak limit in an avionics receiver is the carrier tracking loop threshold (typically the PLL), this threshold is usually substituted for $(C/N_0)_{MIN}$. During the GPS-TSPI flight test activities performed on TORNADO-IDS with unaided L1 C/A code avionics receivers, it was found that in all dynamics conditions explored and in the absence of jamming, a C/N_0 of 25 dB-Hz was sufficient to keep tracking to the satellites.

As an example, using this 25 dB-Hz tracking threshold, we can calculate the *J/S* performance of the GPS receiver installed on TORNADO-IDS considering one of the satellites tracked (PRN-14) during the descent manoeuvre illustrated in Fig. 4-8. As shown in Fig. 4-12, during this manoeuvre, the calculated C/N_0 for PRN-14 was approximately 37 dB-Hz.

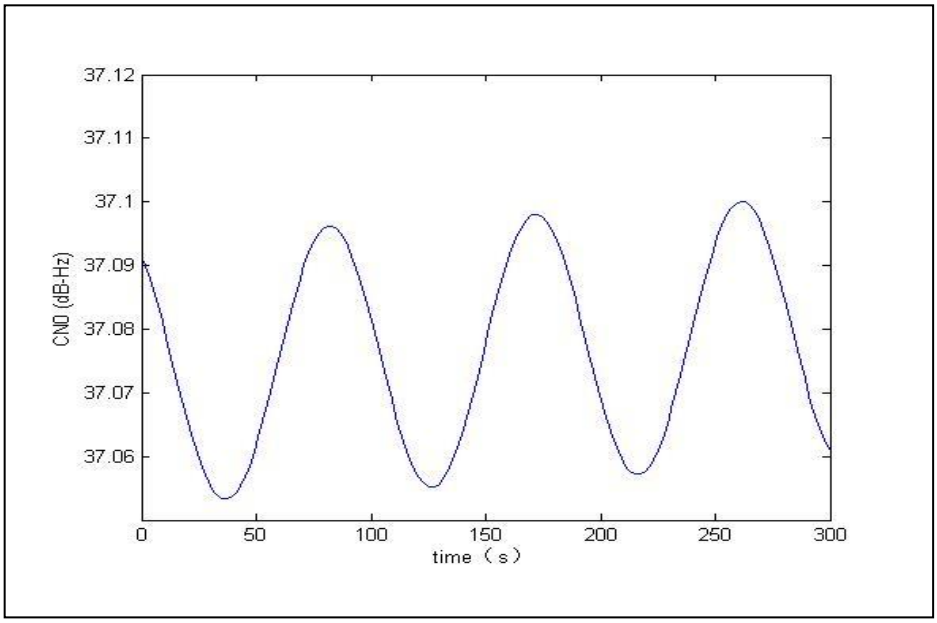


Figure 4-12. Calculated C/N_0 for PRN-14.

Table 4-3 shows the corresponding *J/S* calculations, assuming $(C/N_o)_{MIN}$ = 25 dB-Hz.

Table 4-3. J/S calculations for 25 dB-Hz tracking threshold.

Jamming	Q	R_c	$(C/N_o)_{threshold}$	C/N_o	J/S
NBJ	1	$1.023*10^6$	25 dB-Hz	37	34.82
SSJ	1.5	$1.023*10^6$	25 dB-Hz	37	36.58
WGJ	2	$1.023*10^6$	25 dB-Hz	37	37.83

Using these *J/S* values, the minimum range from a jamming source can be calculated from:

$$R_{min} = \frac{\lambda_j}{4\pi}\left(10^{\frac{ERP_{tj}-P_{rj}+G_{rj}-L_{rf}}{20}}\right) \quad (4.14)$$

where:

ERP_{tj} = Effective radiated power of the jammer (dBw);

λ_j = wavelength of jammer frequency (m);

P_{rj} = Received (incident) jamming power level at threshold = $J/S + P_{rs}$ (dBw);

P_{rs} = Minimum received (incident) signal power (dBw);

G_{rj} = GNSS antenna gain toward jammer (dBic);

L_{rf} = Jammer power attenuation due to receiver front-end filtering (dB).

4.3.4 Doppler Shift

Doppler shift is the change in frequency of the received signal that is experienced when the observer (aircraft) moves relative to the signal source (satellite). The magnitude of the frequency shift produced in the signal received from the nth satellite is a function of the relative velocity measured along the satellite-aircraft LOS. The Doppler shift of the nth satellite signal frequency is given by:

$$\Delta f_n = f\left(\frac{|\overrightarrow{v_n}| \mp |\overrightarrow{v_a}|}{c}\right) cos\chi_n \tag{6.28}$$

where:

$\overrightarrow{v_n}$ = nth satellite velocity component along the LOS;

$\overrightarrow{v_a}$ = aircraft velocity projection along the LOS;

c = speed of light [m s^{-1}];

f = GNSS signal frequency [Hz];

χ_n = angle between the aircraft velocity vector and the nth satellite LOS.

4.3.5 Multipath

Multipath is caused by the interference of multiple reflections (from the ground and the aircraft structure) with the direct signal transmitted by the satellite and represents a major source of error in GNSS observations. The level and characteristics of multipath depend on the geometry of the environment surrounding the antenna, the reflectivity of nearby objects/terrain and the satellite elevation angle. In order to build a reliable multipath model, a combination of SNR analysis

(comparison with the direct GNSS signal) and geometric ray-tracing methods is adopted. To start, we use the aircraft 3D CATIA model to identify the geometric characteristics of the multipath signal and study the SNR variations associated with multipath.

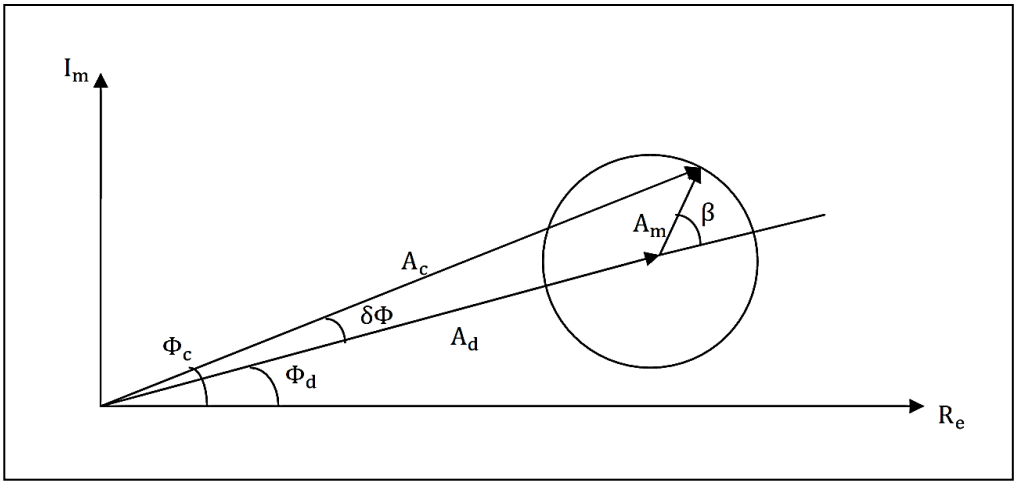


Figure 4-13. Phase of GNSS signal.

From Fig. 4-13, the SNR and phase error for a single reflection can be represented as a function of direct and multipath signal amplitudes and the multipath relative phase β (Ward, 1994):

$$SNR = A_c^2 = A_d^2 + A_m^2 + 2A_dA_m\cos\beta \tag{4.16}$$

$$\tan(\delta_\phi) = \frac{A_m\sin\beta}{A_d + A_m\cos\beta} \tag{4.17}$$

where A_d is the direct signal amplitude, A_m is multipath signal amplitude and β is the phase of the multipath. Fig. 4-14 shows that both the multipath phase β and the multipath amplitude affect the received signal. Therefore, we require a multipath model to simulate these two factors, considering the reflections from the airframe (wings and fuselage) and from the ground. In our research, we adopted the Aeronautical Multipath Channel (AMC) model developed during the ESA-SDS research (Steingass, 2004), (Steingass and Lehner, 2004).

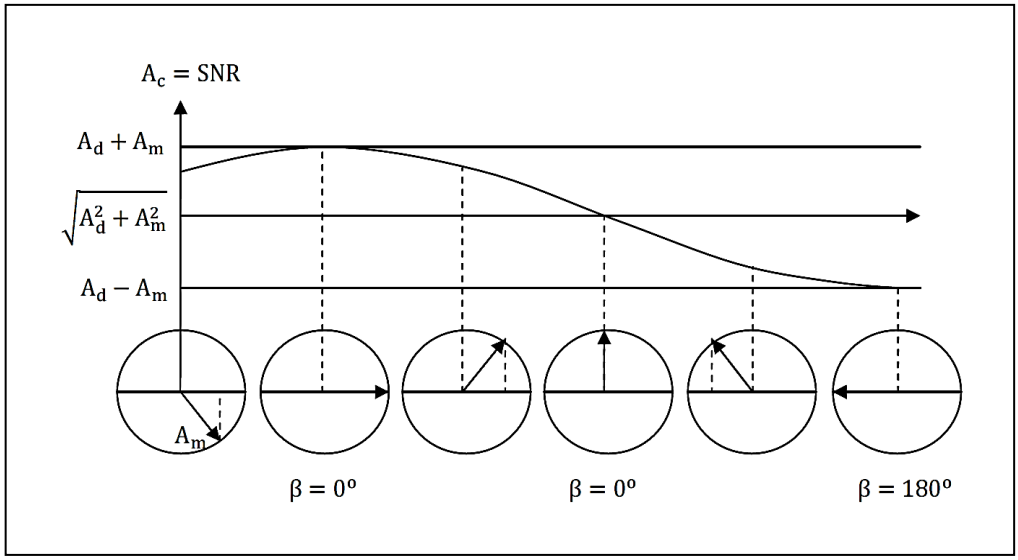


Figure 4-14. Variation of A_c as function of the angle β.

Fig. 4-15 illustrates the overall structure of the AMC model.

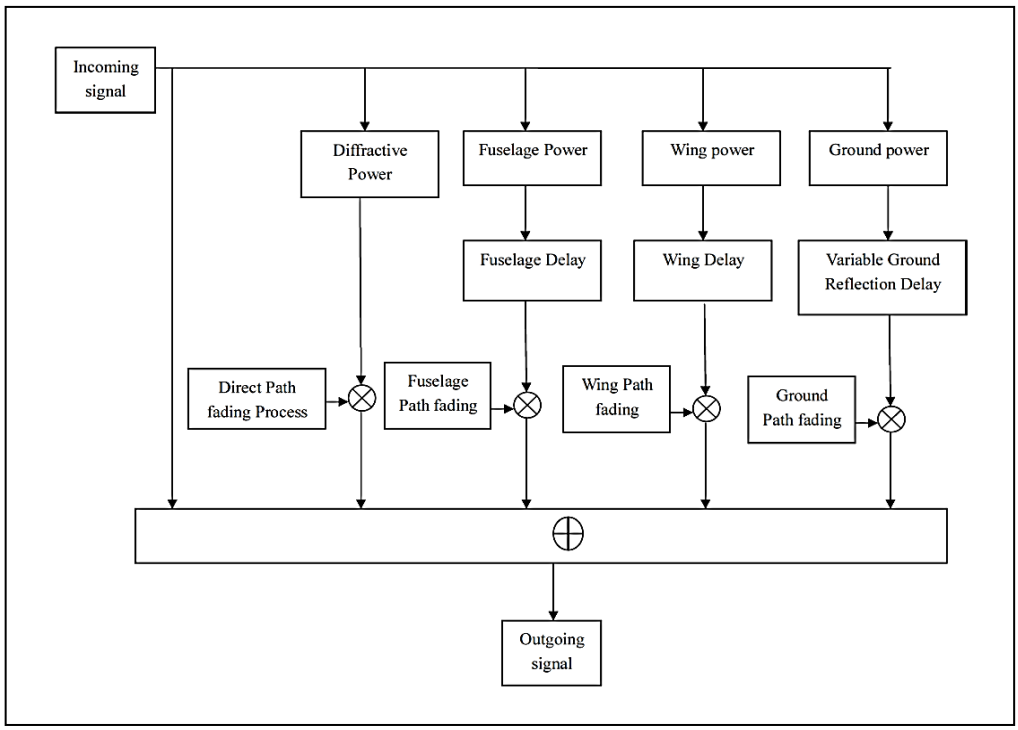


Figure 4-15. Multipath channel model. Adapted from Steingass (2004).

Let $h(t,\tau)$ be the impulse response of the multipath channel model. Then $h(t,\tau)$ is given by (Steingass, 2004):

$$h(t,\tau) = 1 + \sum_{i=1}^{3} \sqrt{P_i} * n_i(t) * \delta(t - \tau_i) \tag{4.18}$$

where P_i is the echo power of the i^{th} path. The signal $n_i(t)$ is a noise signal with power i, and a power spectral density $N(f)$:

$$N(f) = \begin{cases} 0 & f < -B/2 \\ \dfrac{1}{B} & -B/2 < f < B/2 \\ 0 & f > B/2 \end{cases} \tag{4.19}$$

where B is the noise bandwidth. From the multipath channel model in Fig. 4-15, the wing reflection, the fuselage reflection and the ground-echo are the main components of the multipath signal. Fig. 4-16 shows the geometric reflection model. The incoming wave is emitted from point T, the receiver is location at R, and the reflection point at S. Location V is a defined point on the reflecting surface and n stands for a unit vector normal to the surface.

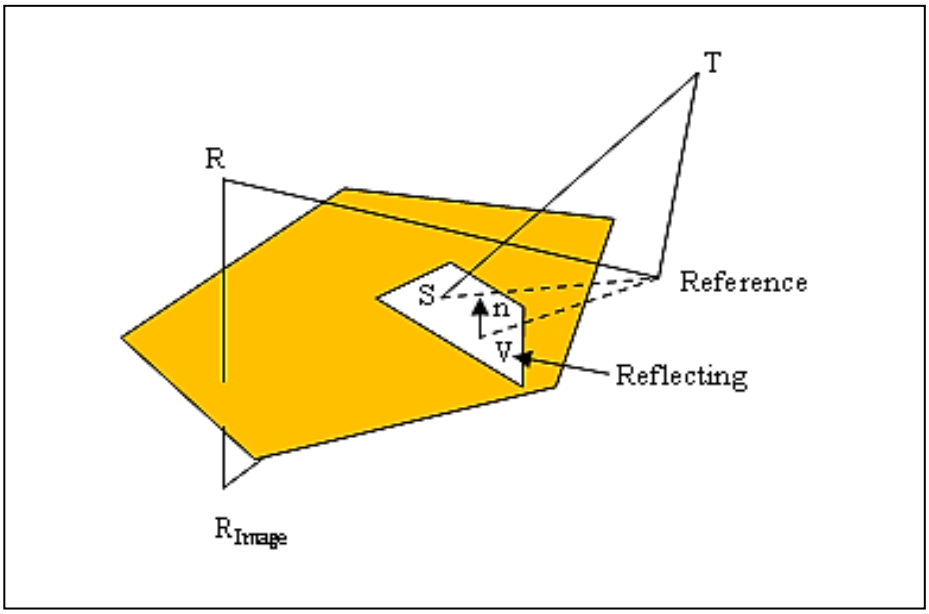


Figure 4-16. Geometric reflection model.

In ray-tracing theory, the reflection point S and the defined point V should satisfy the equation:

$$(S - V) \times n = 0 \tag{4.20}$$

and the line equation connecting T and R_{image}:

$$S = T + t \times (R_{image} - T) \tag{4.21}$$

where t is a parameter between 0 and 1. Combining the Eqs. (4-20) and (4-21):

$$S = T + \frac{n \times V - n \times T}{n \times (R_{image} - T)} (R_{image} - T) \tag{4.22}$$

The corresponding extra path length, L_{mS}, due to specular reflection, is then:

$$L_{mS} = |T - S| + |R - S| - |T - R| \tag{4.23}$$

In our wing reflection model, the wing is assumed to be flat. Applying Gaussian Doppler Spectrum (GDS) theory, the power of the wing echo spectrum is assumed to be [12, 14]:

$$P_{Gr(dB)} = 20 * \log_{10}\left(\frac{1}{\sqrt{2\pi\sigma^2}} * e^{-\frac{f^2}{2\sigma^2}}\right) \tag{4.24}$$

where the deviation σ=3.8 Hz. The wing reflection signal delay can be calculated from:

$$\tau_{wing}(t) = \frac{2 * L * \sin(E)}{C_0} \tag{4.25}$$

where L is the antenna height from the wing, E is the elevation angle [deg] and C_0 is the speed of light. In the our fuselage reflection model the fuselage is assumed to be a cylinder. The power of the fuselage echo spectrum is given by:

$$P_{proc}(dB) = 20 * \log_{10}\left[k_1 * e^{(k_2 * |f|)} - SNR - k_3\right] \tag{4.26}$$

where k_1 , k_2 and k_3 are the fuselage geometric coefficients described in (Steingass, 2004). Previous research (Steingass and Lehner, 2004), showed that the fuselage reflection characteristics change very little by increasing the fuselage radius. For easier implementation of the fuselage reflection model, a 2-dimensional polynomial function of 4th order was fitted to each parameter (mean, b_2, b_3). As an example, considering the TORNADO-IDS upper antenna located on the fuselage at a height of $L_{fuselage}$= 0.05 metres, the fuselage reflection time delay is $\tau_{fuselage} = 1.7 \times 10^{-10}$s. Ground reflection becomes important only during the landing phase, when the aircraft is in close proximity of the terrain. Like before, assuming a Gaussian distributed ground reflection amplitude with zero mean, the ground-echo power is given by:

$$P_{Gr(dB)} = 20 * \log_{10}\left(\frac{1}{\sqrt{2\pi\sigma^2}} * e^{-\frac{f^2}{2\sigma^2}}\right) \tag{4.27}$$

where, in this case, the deviation σ = 3.8 Hz. Assuming that the terrain is flat:

$$\tau_{ground}(t) = \frac{2 * h * \sin(E)}{C_0} \tag{4.28}$$

where h is the aircraft altitude and E is the elevation angle. Obviously, this basic ground-echo model can be expanded to take into account various terrain and man-made buildings geometries. As discussed in Parkinson and Spilker (1996), GPS receivers can effectively reject most of the multipath signal if the differential delay $\Delta\tau > 1.5$ μs for the C/A code and 0.15 μs for the P(Y) code. As a consequence, the region of potential ground-echo multipath problems for the C/A code is:

$$h * \sin(E) < (1.5\ \mu s) * C_0 = 448.5\ \text{m} \tag{4.29}$$

Above this threshold, simulation and flight test activities performed on various aircraft showed that the fuselage reflections are normally the main contributors to the airframe multipath. In most conditions, the effect of signals reflected from the aircraft wings are comparatively smaller (Steingass, 2004), (Steingass and Lehner, 2004). In particular, it was found that the airframe multipath ranging error budget

can be minimised by placing the GNSS antenna 5 (or more) centimetres above the highest point on the aircraft fuselage. Applying this criterion to the TORNADO-IDS GPS antenna installation, the airframe multipath error associated to each satellite pseudorange observation remained below 2 metres in all relevant flight conditions and aircraft-satellite relative geometries. However, when flying in the region of potential ground-echo multipath, the multipath error could be much more significant. In straight-and-level flight conditions, the fuselage and wing effectively impede ground-echo multipath signals from reaching the antenna. However, as the aircraft bank and pitch angles are increased due to manoeuvring, ground-multipath signals are more likely to reach the antenna. During TORNADO-IDS flight test activities performed with satellite elevation angles between 5 and 90 degrees and bank/pitch angles exceeding 45 degrees, it was observed that the no significant ground-echo multipath errors are present for altitudes above 500 feet AGL. As this value is much lower that the theoretical threshold established by Eq. (4.29), it was concluded that the signal attenuation due to ground reflection was responsible for the reduced sensitivity to ground-echo multipath. Nevertheless, reducing the aircraft altitude below 500 feet AGL and performing attitude manoeuvres exceeding 45 degrees, significant ground-echo multipath ranging errors were experienced. In particular, it was observed that the effect of ground-echo signals translate into a sudden increase of the multipath ranging error of up to two orders of magnitude with respect to the airframe multipath errors alone.

During a low-level TORNADO-IDS flight trial, it was found that the ground-multipath ranging error reached a value of about 140 metres when the aircraft was flying at an altitude of 300 feet AGL over flat terrain with a roll angle exceeding 45 degrees. It must be pointed out, however, that such particular flight conditions are only likely to be encountered in military aircraft and some UAVs. Due to the flight profile requirements and manoeuvring constraints of typical airliners, the ground multipath contributions can be normally neglected in these cases.

According to the Standard Multipath Error Model (SMEM) research (Murphy et al., 2004) and experimental validation activities performed in the United States on various types of civil airliners (Booth et al., 2000), the airframe multipath ranging

error $(\sigma_{multipath})$ associated to a satellite observation can be calculated directly as a function of the satellite elevation angle:

$$\sigma_{multipath} = 0.13 + 0.53e^{\left(-\frac{E}{10}\right)} \quad \text{(m)} \tag{4.30}$$

This model was endorsed by the ICAO GNSS panel (Booth et al., 2000) and included in the Minimum Operational Performance Standards (MOPS) for the Wide Area Augmentation System (RTCA, 2006-a) and for the MASPS/MOPS of the Local Area Augmentation System (RTCA, 2004), (RTCA, 2008-b). Further research is currently ongoing on other airframe types, including general aviation aircraft and various classes of UAVs. For small UAV platforms, multipath effects associated with low-level flight in urban environments is being also investigated. Preliminary results obtained with a small-size UAV show that multipath ranging errors in excess of 100 metres are possible when the vehicle flies in proximity of large buildings. Further research is needed to corroborate these initial findings and to obtain other useful experimental models applicable to the various classes of UAV platforms being considered for future ABIA system development.

4.4 CONCLUSION

Based on the experimental research and flight test activities conducted on GNSS and T-ABIA a more advanced ABIA system was developed. This system is suitable for manned and unmanned aircraft, including both military and civil safety-critical applications. This new ABIA system, can provide steering information to the pilot (as the T-ABIA system for flight test applications) and, additionally, electronic commands to the aircraft/UAV Flight Control System (FCS), allowing for real-time integrity monitoring, avoidance of mission/safety-critical flight conditions and fast recovery of the Required Navigation Performance (RNP) in case of GNSS data degradation or loss. In this chapter, we have presented the fundamental design features of this novel GNSS ABIA system. Additionally, the key mathematical models required for the ABIA integrity flags have been introduced (i.e., antenna obscuration, geometric accuracy degradations, SNR, multipath and Doppler shift).

The IFG detailed design (integrity flag thresholds criteria) and a detailed TORNADO-IDS simulation case study are presented in the next chapter.

4.5 REFERENCES

Aircraft Drawings (2012). Military and Commercial Aircraft Line Drawings. Available online at: http://www.aircraftdrawindsdownload.com. Accessed 15 June 2012.

Boithias, L. (1982). Radio Wave Propagation. McGraw Hill (New York).

Booth, J., Murphy, T. and Liu, F. (2000), "Validation of the Airframe Multipath Error Allocation for Local Area Differential GPS." In Proceedings of the IAIN World Congress in association with the ION 2000 Annual Meeting, San Diego, CA.

Braasch, M. S. (1992), "On the characterization of multipath errors in satellite-based precision approach and landing systems." PhD Thesis - College of Engineering and Technology, Ohio University. Available online at: http://etd.ohiolink.edu/view.cgi/Braasch%20Michael.pdf?ohiou1173748635. Accessed 10 May 2012.

Davenport, W. B. and Root, W. L. (1987), "An Introduction to the Theory of Random Signals and Noise." IEEE Press (New York).

Friis, H.T. (1944), "Noise Figures in Radio Receivers." Proceedings of the Institute of Radio Engineers, 32, 419-422.

Kaplan, E. D. and Hegarty, C. J. (2006), "Understanding GPS: Principles and Applications." Artech House. 2006.

Kintner, P. M., Ledvina, B. M. and de Paula, E. R. (2007), "GPS and ionospheric scintillations." Space Weather, Vol. 5, pp. 1-23.

Murphy, T., Friedman, R., Booth, J., Geren, P., Molloy, N., Clark, B. and Burns, J. (2004), "Program for the Investigation of Airborne Multipath Errors." Proceeding of the ION National Technical Meeting (NTM) 2004, San Diego, CA.

Ochieng, W. Y., Sauer, K., Walsh, D., Brodin, G., Griffin, S. and Denney, M. (2003). "GPS Integrity and Potential Impact on Aviation Safety." The Journal of Navigation, Vol. 56, pp. 51–65.

Parkinson, B. W., Spilker, J. J. Jr., Editors (1996), "Global Positiong System: Theory and Applications – Volume I." Progress in Astronautics and Aeronautics, Vol. 163. Published by the American Institute of Aeronautics and Astronautics.

RTCA (2004), "Minimum Aviation System Performance Standards (MASPS) for the Local Area Augmentation System (LAAS). Radio Technical Commission for

Aeronautics (RTCA) Inc., Special Committee No. 159. Document RTCA DO-245A. Washington DC (USA). 2004.

RTCA (2006-a), "Minimum Operational Performance Standards for Global Positioning System/Wide Area Augmentation Systems Airborne Equipmen." Radio Technical Commission for Aeronautics (RTCA) Inc., Special Committee No. 159. Document RTCA DO-229D. Washington DC (USA).

RTCA (2006-b). "Minimum Operational Performance Standards for GNSS Airborne Active Antenna for the L1 Frequency Band." Radio Technical Commission for Aeronautics (RTCA) Inc., Special Committee No. 159. Document RTCA DO-301. Washington DC (USA). 2006-b.

RTCA (2008-a), "Minimum Operational Performance Standards for GPS/GBAS Airborne Equipment." Radio Technical Commission for Aeronautics (RTCA) Inc., Special Committee No. 159. Document RTCA DO-253C. Washington DC (USA).

RTCA (2008-b), "GNSS-Based Precision Approach Local Area Augmentation System (LAAS) Signal-in-Space Interface Control Document (ICD)." Radio Technical Commission for Aeronautics (RTCA) Inc., Special Committee No. 159. Document RTCA DO-246D. Washington DC (USA).

Sabatini, R. and Palmerini, G. B.. (2008). "Differential Global Positioning System (DGPS) for Flight Testing." NATO Research and Technology Organization (RTO) Systems Concepts and Integration Panel (SCI) AGARDograph Series RTO-AG-160 Vol. 21.

Steingass, A. (2004). "The High Resolution Aeronautical Multipath Navigation Channel." German Aerospace Center DLR. Available online at: http://www.kn-s.dlr.de/satnav. Accessed on 14th May 2012.

Steinggass, A., Lehner, A. (2004). "Aeronautical Channel Model." German Aerospace Center DLR. Available online at: http://www.kn-s.dlr.de/satnav. Accessed on 14th May 2012.

Ward, P. W. (1994). "GPS Receiver RF Interference Monitoring, Mitigation, and Analysis Techniques." Navigation, Journal of the Institute of Navigation (USA), 41, pp. 367-391.

ITU (2013). "Ionospheric propagation data and prediction methods required for the design of satellite services and systems." International Telecommunication Union (ITU), Recommendation ITU-R P.531-12 (P Series – Radiowave propagation).

(This page is left black for the purpose of typesetting)

5

ABIA INTEGRITY FLAGS

5.1 INTRODUCTION

As discussed in the previous chapter, the ABIA system was developed to allow real-time avoidance of safety-critical flight conditions and fast recovery of the required navigation performance in case of GNSS data losses. In more detail, the ABIA system addresses all four cornerstones of GNSS integrity augmentation in mission-essential and safety-critical avionics applications: prediction (caution flags), avoidance (optimal flight path guidance), reaction (warning flags) and correction (recovery flight path guidance). The ABIA architecture and key mathematical models used to describe GNSS integrity threats were presented in the previous chapter. Based on these models, this chapter addresses the ABIA caution and warning integrity flags criteria and presents detailed results of simulation case-studies performed on various manned and unmanned aircraft for civil and military applications (i.e., TORNADO-IDS, A320 and AEROSONDE UAV).

5.2 IFG MODULE SIMULATOR

The ABIA IFG is designed to provide CIF and WIF alerts (i.e., in accordance with the specified TTC and TTW requirements) in all relevant flight phases. In order to evaluate the performance of the Masking, Multipath, C/N_0, J/S and Doppler analysis algorithms presented in Chapter 3, the IFG software was developed and

tested in MATLAB, together with a detailed Aircraft (A/C) Three Dimensional (3D) Model in CATIA (Computer Aided Three-dimensional Interactive Application), a 3D Terrain and Objects Database, a GNSS Constellation Simulator and a Navigation/Flight Dynamics Simulator. Fig. 5-1 shows the architecture adopted for the IFG module simulation. Another key feature of the IFG module presented in this second paper is a pre-defined set of CIF and WIF thresholds applicable to the specific A/C dynamic conditions and satellite constellations observed during the flight.

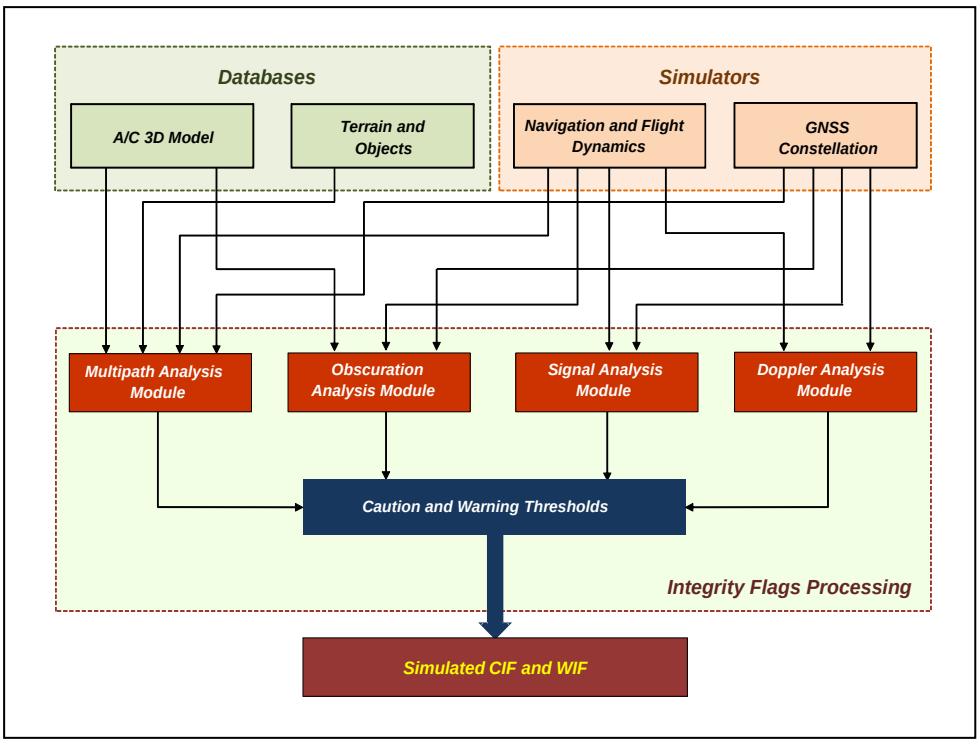


Figure 5-1. ABIA IFG module simulator.

A GNSS Constellation Simulator (GCS) was implemented to support GNSS satellite visibility, signal and geometry analysis. It calculated GNSS satellite position and velocity in the Earth-Centred Earth-Fixed (ECEF) reference frame and obtained satellite visibility data from any point along the A/C flight trajectory. The GCS was developed in MATLAB to simulate primarily GPS and GALILEO constellations. However, the GCS was conceived as a flexible tool capable to incorporate other current and likely future GNSS constellations (GLONASS, BDS, etc.), including space-based regional and global augmentation systems. The satellite position and

velocity were calculated from the Kepler's laws of orbital motion and, for the case of GPS satellites, using either the YUMA or SEM almanac data (Celestrak, 2012). An A/C Navigation/Dynamics Simulator (ADS) was also implemented to generate the nominal flight path trajectory and attitude (Euler) angles. The ADS employed a classical Three Degrees of Freedom (3DOF) point-and-variable mass model. Further details about 3DOF models are provided in Chapter 6 and in (Sabatini et al., 2012a). As described in Chapter 3, the ABIA IFG uses a set of predefined threshold parameters to trigger the generation of both caution and warning flags associated with antenna obscuration, Doppler shift, multipath, direct carrier/interference and satellite geometry degradations. More details about the simulation process are provided in the following paragraphs with a special focus on the CIF and WIF threshold setting criteria incorporated into the ABIA IFG module design.

5.3 INTEGRITY FLAG CRITERIA

The philosophy adopted to set-up thresholds for the ABIA CIF and WIF integrity flags is depicted in Fig. 5-2.

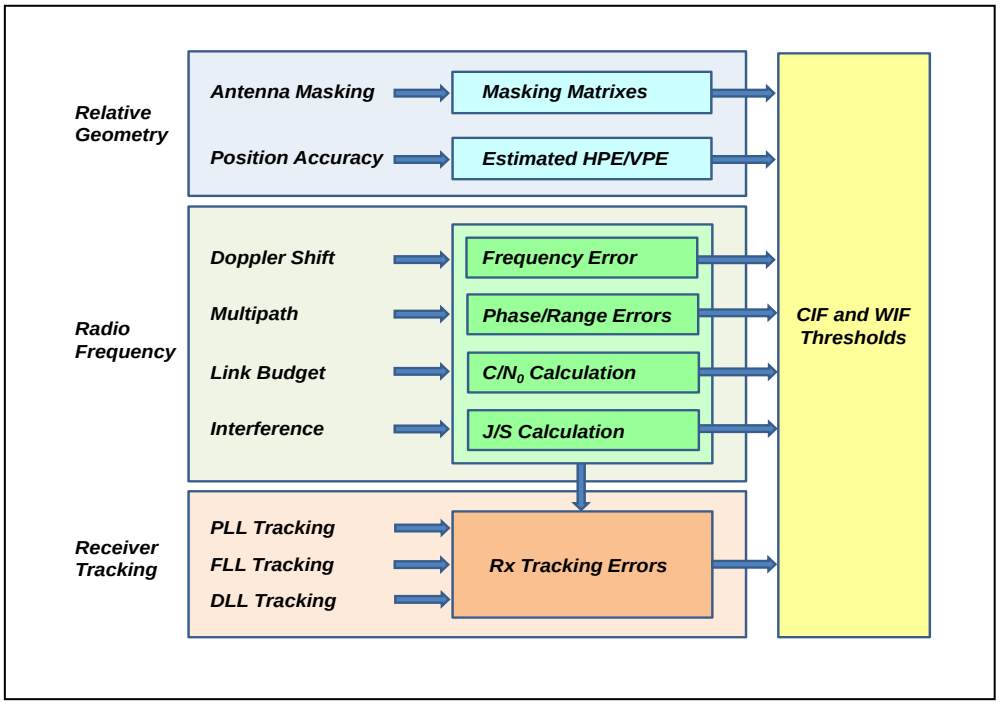


Figure 5-2. Integrity flag thresholds criteria.

Integrity flags are generated based on a dedicated error analysis addressing the following aspects of GNSS performance:

- Satellite-A/C (receiver) relative geometry and position errors;
- Radio frequency (RF) signal errors (i.e., Doppler, jamming and multipath);
- Receiver Tracking Errors (RTE).

In particular, the RTE models are used to support the development of robust criteria for the RF signal thresholds, in addition to the criteria based on experimental results (e.g., ground and flight test activities with GNSS). In the following, we present the detailed criteria adopted for setting the various CIF and WIF thresholds.

As a preliminary design target for the ABIA IFG, specific Service Level (SL) requirements were set for the CIF, with a target Detection Rate (DR) of 100% and a minimum TTC of 2 seconds (to be achieved in all flight phases). Based on the definition, the target TTW (WIF) is coincident with the TTA specified in ICAO standards for the various flight phases. However, the verification of this requirement (requiring hardware-in-the-loop and human-in-the-loop simulation, aircraft integration case studies and ground/flight test activities) was not an objective of this research project.

5.3.1 Relative Geometry and Obscuration

As described in (Sabatini et al., 2012), in order to generate CIF/WIF associated to critical antenna masking conditions, a dedicated analysis is required taking into account the variation of the attitude angles. Therefore, using the CATIA 3D model of the A/C, series of Antenna Obscuration Matrixes (AOMs) are collected with pitch angles varying between -90 degree and 90 degree and with roll angles varying between -90 degree and 90 degree. An example of the resulting Global Masking Profile (GMP) obtained for the TORNADO-IDS is shown in Fig. 5-3. In this figure, also the GPS satellite constellation is shown (from the GCS module).

The obscuration integrity flag criteria are the following:

- **When the current A/C manoeuvre will lead to less the 4 satellite in view, the CIF shall be generated.**
- **When less than 4 satellites are in view, the WIF shall be generated.**

Additionally, if only four satellites are in view:

- **When one (or more) satellite(s) elevation angle (antenna frame) is less than 10 degrees, the caution integrity flag shall be generated.**
- **When one (or more) satellite(s) elevation angle is less than 5 degrees, the warning integrity flag shall be generated.**

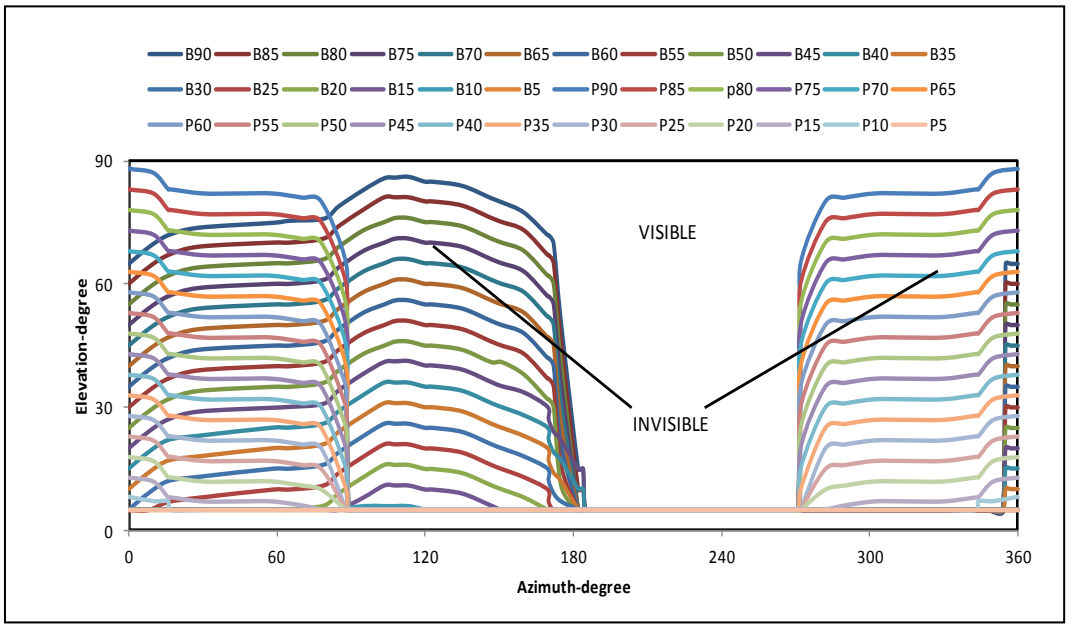


Figure 5-3. TORNADO-IDS global masking profile (B = bank, P = pitch, all in degrees).

5.3.2 Radio Frequency Link Errors

Multipath integrity flags were defined using the Early-Late Phase (ELP) observable and the range error. In a GPS receiver having three correlators (early, prompt and late), the phase of a correlator is given by (Mubarak et al., 2009):

$$\Phi_C(t) = \tan^{-1}\left(\frac{Q_C}{I_C}\right) \tag{5.11}$$

where the subscript *C* refers to early (E), prompt (P) and late (L) respectively.

The prompt phase is always kept close to zero by the carrier tracking loop. Early and late correlators are then placed on each side of the prompt, which means one of the phase of the correlator is positive and the other is negative. So, the phase difference between the two is increased in the presence of multipath. ELP is simply the phase difference between the early and late correlator outputs, where the phase of a correlator output is equal to the inverse tangent of the *Q(t)* channel output divided by the *I(t)* channel output. Mathematically, the ELP is calculated by (Mubarak and Dempster, 2009):

$$\mathrm{ELP}(t) = \tan^{-1}\left[\frac{Q_L(t)}{I_L(t)} - \frac{Q_E(t)}{I_E(t)}\right] \tag{5.12}$$

The probability of multipath detection is approximately 80% by setting the ELP threshold at 0.1 radians (Fig. 5-4).

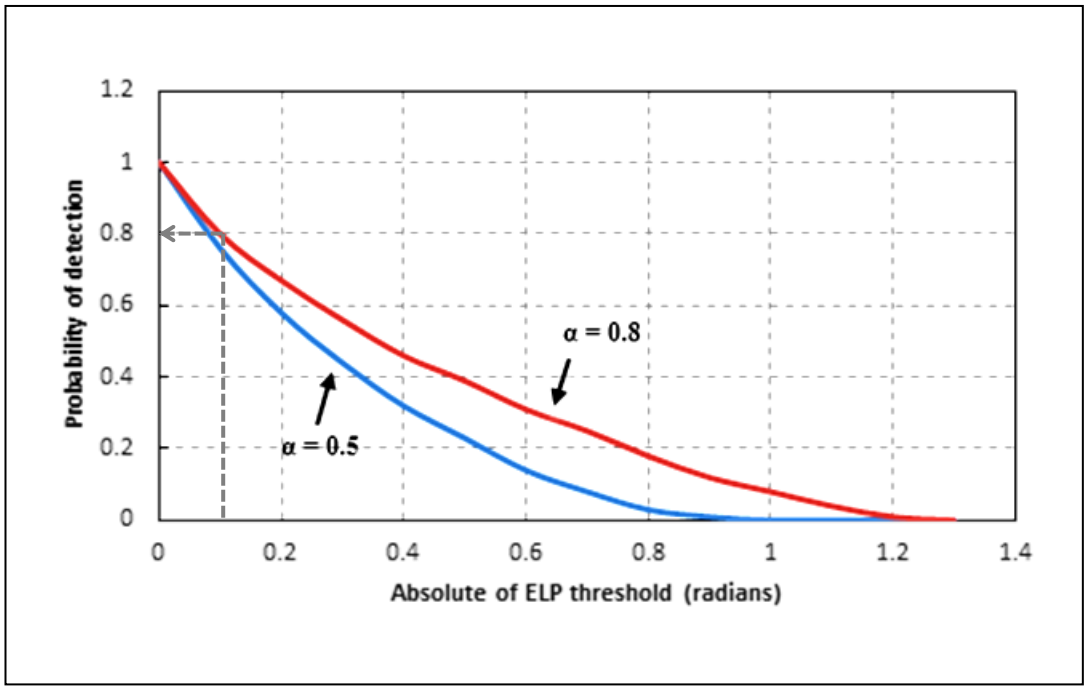


Figure 5-4. Probability of detecting multipath for varying ELP thresholds. The symbol α indicates the radio of multipath to direct signal amplitude (i.e., $\alpha = A_m/A_d$). Adapted from Mubarak et al. (2010).

Additionally, as shown in Fig. 5-5, with an ELP threshold of 0.1 radians, the Probability of False Alarm (PFA) is 0.3 when C/N_0 is 42 dB/Hz. This is an acceptable compromise for the ABIA caution flag implementation.

Multipath range error experimental results are also used to trigger the warning integrity flag associated to multipath. As discussed in (Sabatini et al., 2012), the effect of ground-echo signals translate into a sudden increase of the multipath ranging error of up to two orders of magnitude with respect to the airframe multipath errors alone. However, the region of potential ground-echo multipath for the L1 frequency only extends up to 448.5 metres AGL (theoretical value applicable to all A/C types).

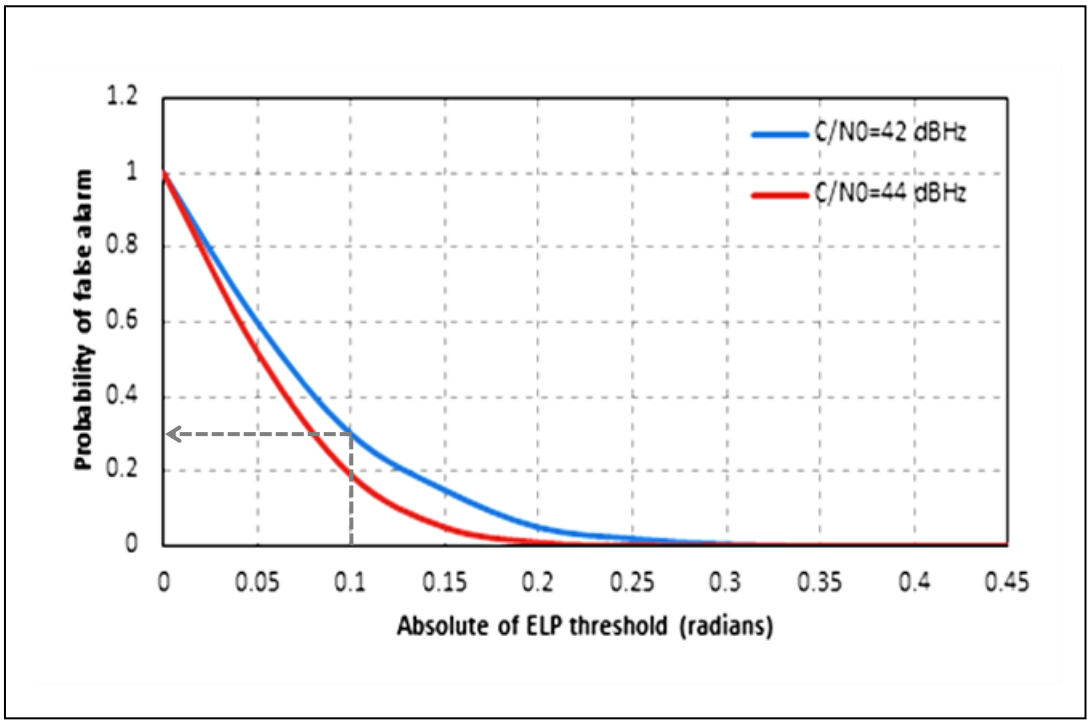


Figure 5-5. PFA for varying ELP threshold. Adapted from (Mubarak and Dempster, 2010).

As a result of our analysis, the multipath integrity flags criteria are the following:

- **When the ELP exceeds 0.1 radians, the caution integrity flag shall be generated.**

- **When the multipath ranging error shows a sudden increase with the A/C flying in proximity of the ground (below 448.5 metres), the warning integrity flag shall be generated.**

Based on results of the GPS-TSPI flight test activities (Sabatini and Palmerini, 2008), an additional (practical) criteria was developed for the TORNADO-IDS A/C. During TORNADO-IDS flight trials it was observed that flying above 500 ft AGL (even with pitch/bank angles exceeding 45 degrees), the ground-echo multipath was not a factor and the multipath range error (due to the airframe only) never exceeded 2 metres. Consequently, an additional criteria applicable to the TORNADO-IDS A/C is the following:

- **When the multipath ranging error exceeds 2 metres and the A/C flies in proximity of the ground (below 500 ft AGL), the warning integrity flag shall be generated.**

As discussed in Sabatini et al. (2012), avionics GNSS receivers are resistant to dynamic stress errors. A robust avionics GNSS receiver design typically employs an FLL as a backup to the PLL during initial loop closure and during high-dynamic stress with loss of phase lock, but will revert to pure PLL for the steady-state low to moderate dynamics in order to produce the highest carrier Doppler phase measurements. However, flight test activities performed with avionics GPS receivers showed that the reacquisition time after loss of one or more satellite signals could be up to 35 seconds, depending on flight conditions and satellite constellations (Sabatini et al., 2008). Fig. 5-6 shows the fitting functions and associated curves relative to the acquisition time experimental data presented in Chapter 3 (Fig. 3-44) and in (Sabatini et al., 2008). These functions can be used to estimate the TTSF of an avionics GNSS receiver based on satellite-A/C relative velocity (LOS component). It is evident that for C/N_0 below 28 dB-Hz the acquisition time exceeds 1 sec even in low dynamics conditions. Therefore, in these conditions, the required acquisition times might become unacceptable in case of satellite signal losses during certain mission-essential and safety-critical GNSS tasks (e.g., military weapon aiming, missile guidance, precision approach).

Consequently, the following criteria were defined for the Doppler integrity flags thresholds:

- **When the C/N_0 is below 28 dB-Hz and the signal is lost, the caution integrity flag shall be generated if the estimated acquisition time is less than the application-specific TTA requirements.**
- **When the C/N_0 is below 28 dB-Hz and the signal is lost, the warning integrity flag shall be generated if the estimated acquisition time exceeds the application-specific TTA requirements.**

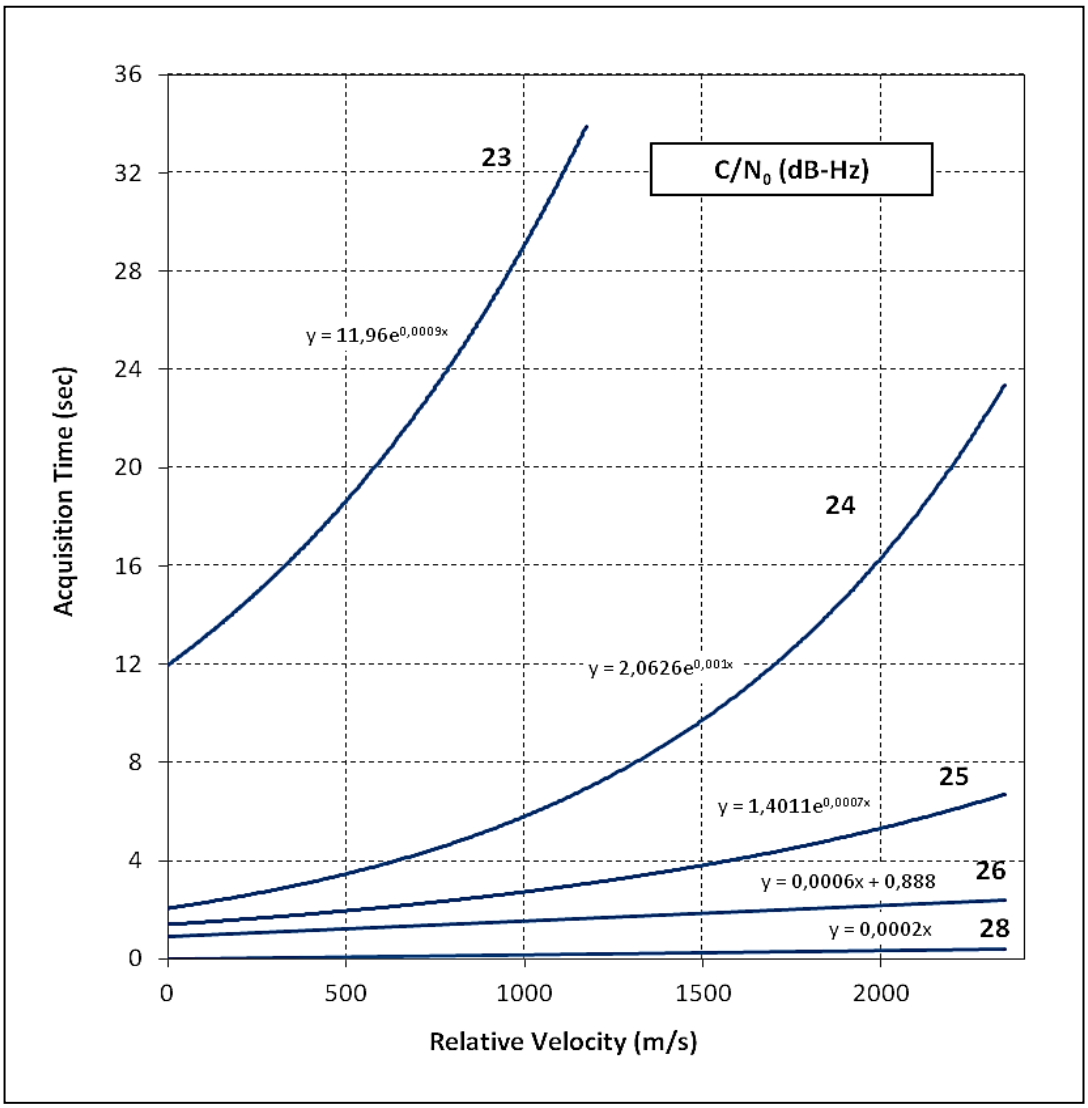


Figure 5-6. Doppler shift and signal acquisition in avionics GPS receivers.

5.3.3 Receiver Tracking Errors

As discussed before, in order to define additional robust criteria for the ABIA integrity thresholds associated with dynamic stress errors, signal fading (C/N_0 reduction) and interferences (J/S increase), a dedicated analysis of the GNSS receiver tracking performance was required. When the GNSS code and/or carrier tracking errors exceed certain thresholds, the receiver loses lock to the satellites. Since both the code and carrier tracking loops are nonlinear, especially near the threshold regions, only Monte Carlo simulations of the GNSS receiver in different dynamics and SNR conditions can determine the receiver tracking performance (Ward, 1997). Nevertheless, some conservative rule-of-thumbs approximating the measurement errors of the GNSS tracking loops were considered adequate for the ABIA conceptual design.

Numerous sources of measurement errors affect the Carrier Tracking Loops and Code Tracking Loops. However, for our purposes, it was sufficient to analyze the dominant error sources in each type of tracking loop. Considering a typical GNSS receiver employing a two-quadrant arctangent discriminator, the Phase Lock Loop (PLL) threshold is given by:

$$3\sigma_{PLL} = 3\sigma_j + \theta_e \leq 45^{\circ} \tag{5.13}$$

where:

σ_j = 1-sigma phase jitter from all sources except dynamic stress error;

θ_e = dynamic stress error in the PLL tracking loop.

Expanding Eq. (5.13), the 1-sigma threshold for the PLL tracking loop becomes (Kaplan and Hegarty, 2006):

$$\sigma_{PLL} = \sqrt{\sigma_{tPLL}^2 + \sigma_v^2 + \theta_A^2} + \frac{\theta_e}{3} \leq 15^{\circ} \tag{5.14}$$

where:

σ_{tPLL} = 1-sigma thermal noise;

σ_v = vibration-induced oscillator phase noise;

θ_A = Allan variance–induced oscillator jitter.

The PLL thermal noise is often thought to be the only carrier tracking error, since the other sources of PLL jitter may be either transient or negligible. The PLL thermal noise jitter is computed as follows:

$$\sigma_{tPLL} = \frac{360}{2\pi}\sqrt{\frac{B_n}{c/n_0}\left(1+\frac{1}{2T\ c/n_0}\right)} \quad [\text{deg}] \tag{5.15}$$

where:

B_n = carrier loop noise bandwidth [Hz];

c/n_0 = carrier to noise power ratio ($c/n_0 = 10^{(\mathrm{C/N_0})/10}$ with C/N_0 in dB-Hz);

T = predetection integration time (seconds).

$\mathrm{B_n}$ and $\mathrm{C/N_0}$ can be derived from the SNR model described before.

Determination of the vibration-induced oscillator phase noise is a complex analysis problem. In some cases, the expected vibration environment is so severe that the reference oscillator must be mounted using vibration isolators in order for the GPS receiver to successfully operate in PLL.

The equation for vibration induced oscillator jitter is:

$$\sigma_v = \frac{360 f_L}{2\pi}\sqrt{\int_{f_{min}}^{f_{max}} S_v^2(f_m)\frac{P(f_m)}{f_m^2}\,df_m} \quad [\text{deg}] \tag{5.16}$$

where:

f_L = L-band frequency [Hz];

$S_v(f_m)$ = oscillator vibration sensitivity of $\Delta f/f_L$ per g as a function of f_m;

f_m = random vibration modulation frequency [Hz];

$P(f_m)$ = power curve of the random vibration as a function of f_m [g^2/Hz];

g = gravity acceleration.

Usually the oscillator vibration sensitivity $S_v(f_m)$ is not variable over the range of the random vibration modulation frequency, so Eq. (5.16) can be simplified to:

$$\sigma_v = \frac{360 f_L S_v}{2\pi} \sqrt{\int_{f_{min}}^{f_{max}} \frac{P(f_m)}{f_m^2} df_m} \quad [\text{deg}] \tag{5.17}$$

The equations used to determine Allan deviation phase noise are empirical. They are stated in terms of what the requirements are for the short-term stability of the reference oscillator as determined by the Allan variance method of stability measurement. The equation for second-order loop short-term Allan deviation is:

$$\theta_{A2} = 144 \frac{\sigma_A(\tau) * f_L}{B_n} \quad [\text{rad}] \tag{5.18}$$

The equation for third–order loop short-term Allan deviation for PLL is:

$$\theta_{A3} = 160 \frac{\sigma_A(\tau) * f_L}{B_n} \quad [\text{rad}] \tag{5.19}$$

where:

$\sigma_A(\tau)$ = Allan deviation-induced jitter [deg];

f_L = L-band input frequency [Hz];

τ = short-term stability gate time for Allan variance (seconds);

B_n = noise bandwidth.

Usually $\sigma_A(\tau)$ can be determined for the oscillator and it changes very little with gate time τ. In our research, the loop filter is assumed as a third-order with a noise bandwidth B_n = 18 Hz and the gate time $\tau = 1/B_n = 56$ ms. The Allan deviation is specified to be $\sigma_A(\tau) = 10^{-10}$. The dynamic stress error depends on the loop bandwidth and order. In a third-order loop, the dynamic stress error is (Kaplan and Hegarty, 2006):

$$\theta_{e3} = \frac{d^3R/dt^3}{\omega_0^3} = \frac{d^3R/dt^3}{\left(\frac{B_n}{0.7845}\right)^3} = 0.4828 \frac{\frac{d^3R}{dt^3}}{B_n^3} \quad [\text{deg}] \tag{5.20}$$

where:

R = LOS range to the satellite;

d^2R/dt^2 = maximum LOS acceleration dynamics [deg/s^2];

ω_0 = loop filter natural radian frequency;

B_n = noise bandwidth.

For the L1 frequency we have: $d^3R/dt^3 = (98/\mathrm{s}^3) \times (360°/\mathrm{cycle}) \times (1575.42 \times 10^6\ \mathrm{cycles/s})/c = 185398°/\mathrm{s}^3$.

Frequency jitter due to thermal noise and dynamic stress error are the main errors in a GNSS receiver Frequency Lock Loop (FLL). The receiver tracking threshold is such that the 3-sigma jitter must not exceed one-fourth of the frequency pull-in range of the FLL discriminator. Therefore, the FLL tracking threshold is:

$$3\sigma_{FLL} = 3\sigma_{tFLL} + f_e \leq 1/4T \quad \text{[Hz]} \tag{5.21}$$

where:

$3\sigma_{tFLL}$ = 3-sigma thermal noise frequency jitter;

f_e = dynamic stress error in the FLL tracking loop.

Eq. (5.21) shows that the dynamic stress frequency error is a 3-sigma effect and is additive to the thermal noise frequency jitter. The reference oscillator vibration and Allan deviation–induced frequency jitter are small-order effects on the FLL and are considered negligible. The 1-sigma frequency jitter threshold is 1/(12T) = 0.0833/T Hz. The FLL tracking loop jitter due to thermal noise is:

$$\sigma_{tFLL} = \frac{1}{2\pi T}\sqrt{\frac{4FB_n}{c/n_0}\left[1 + \frac{1}{Tc/n_0}\right]} \quad \text{[Hz]} \tag{5.22}$$

where F is 1 at high C/N_0 and 2 near the threshold. σ_{tFLL} is independent of C/A or P(Y) code modulation and loop order. Since the FLL tracking loop involves one more integrator that the PLL tracking loop of the same order, the dynamic stress error is:

$$f_e = \frac{d}{dt}\left(\frac{1}{360\omega_0^n}\frac{d^nR}{dt^n}\right) = \frac{1}{360\omega_0^n}\frac{d^{n+1}R}{dt^{n+1}} \quad \text{[Hz]} \tag{5.23}$$

Regarding the code tracking loop, a conservative rule-of-thumb for the Delay Lock Loop (DLL) tracking threshold is that the 3-sigma value of the jitter due to all sources of loop stress must not exceed the correlator spacing (d), expressed in chips. Therefore:

$$3\sigma_{DLL} = 3\sigma_{tDLL} + R_e \leq d \quad [\text{chips}] \tag{5.24}$$

where:

σ_{tDLL} = 1-sigma thermal noise code tracking jitter;

R_e = dynamic stress error in the DLL tracking loop.

The DLL thermal noise code tracking jitter is given by:

$$\sigma_{tDLL} = \sqrt{\frac{4F_1 d^2 B_n}{c/n_0}\left[2(1-d) + \frac{4F_2 d}{Tc/n_0}\right]} \quad [\text{Hz}] \tag{5.25}$$

where:

F_1 = DLL discriminator correlator factor (1 for time shared tau-dithered early/late correlator and 0.5 for dedicated early and late correlators);

d = Correlator spacing between early, prompt and late;

B_n = Code loop noise bandwidth;

F_2 = DLL dicriminator type factor (1 for early/late type discriminator and 0.5 for dot product type discriminator).

The DLL tracking loop dynamic stress error is given by:

$$R_e = \frac{\frac{dR^n}{dt^n}}{\omega_0^n} \quad [\text{chips}] \tag{5.26}$$

where dR^n/dt^n is expressed in chips/sec^n. The PLL, FLL and DLL error equations described above allow to determine the C/N_0 corresponding to the tracking threshold of the receiver. A generic criteria applicable to the ABIA system is:

$$(C/N_0)_{Threshold} = \max[(C/N_0)_{PLL}, (C/N_0)_{FLL}, (C/N_0)_{DLL}] \tag{5.27}$$

where:

$(C/N_0)_{PLL}$= Minimum carrier-to-noise ratio for PLL carrier tracking;

$(C/N_0)_{FLL}$= Minimum carrier-to-noise ratio for FLL carrier tracking;
$(C/N_0)_{DLL}$= Minimum carrier-to-noise ratio for DLL code tracking.

Numerical solutions of Equations (5.13), (5.21) and (5.24) show that the weak link in unaided avionics GNSS receivers is the PLL due to its greater sensitivity to dynamics stress. Therefore, the $(C/N_0)_{PLL}$ threshold can be adopted in these cases. In general, when the PLL loop order is made higher, there is an improvement in dynamic stress performance. This is why third order PLL are widely adopted in avionics GNSS receivers (e.g., TORNADO-IDS). Assuming 15 to 18 Hz noise bandwidth and 5 to 20 msec predetection integration time (typical values for avionics receivers), the rule-of-thumb tracking threshold for the PLL gives 25 to 28 dB-Hz. Additionally, in aided avionics receiver applications, the PLL tracking threshold can be significantly reduced by using external velocity aiding in the carrier tracking loop. With this provision, a tracking threshold of approximately 15 to 18 dB-Hz can be achieved.

Using these theoretical and experimental threshold values, we can also calculate the receiver Jamming-to-Signal (J/S) performance for the various cases of practical interest, as described in (Sabatini et al., 2012). When available, flight test data collected in representative portions of the A/C operational flight envelope (or the results of Monte Carlo simulation) shall be used. Taking an additional 5% margin on the 3-sigma tracking thresholds for the CIF, the following additional criteria are introduced for the ABIA integrity thresholds:

- **When $42.25° \leq 3\sigma_{PLL} \leq 45^{\circ}$ or $0.2375T \leq 3\sigma_{FLL} \leq 0.25T$ or $0.05d \leq 3\sigma_{DLL}d$ the CIF shall be generated.**
- **When $3\sigma_{PLL} > 45^{\circ}$ or $3\sigma_{FLL} > 1/4T$ or $3\sigma_{DLL} > d$ the WIF shall be generated.**

Additionally, taking a 1 dB margin on the maximum receiver *J/S* performance to generate the CIF, the following criteria were adopted for the CIF and WIF flags associated to interference:

- **When the difference between the received (incident) jammer power (dBw) and the received (incident) signal power (dBw) is 1 dB below the**

***J/S* performance of the receiver at its tracking threshold, the CIF shall be generated.**

- **When the difference between the received (incident) jammer power (dBw) and the received (incident) signal power (dBw) is above the *J/S* performance of the receiver at its tracking threshold, the WIF shall be generated.**

During the GPS-TSPI flight test activities performed on TORNADO-IDS with unaided L1 C/A code avionics receivers (see Chapter 3 and reated appendixes), it was also found that, in all dynamics conditions explored, a C/N_0 of 25 dB-Hz was sufficient to keep tracking of the satellites (Sabatini et al., 2008). Consequently, taking the usual 1 dB margin for the CIF, the following additional criteria were adopted for the C/N_0 integrity flags:

- **When the C/N_0 is less than 26 dB-Hz the CIF shall be generated.**
- **When the C/N_0 is less than 25 dB-Hz the WIF shall be generated.**

5.3.4 EHE and EVE Integrity Flags

In the early stages of this research project, an investigation was carried out to assess the potential of introducing additional integrity flag criteria in the ABIA IFG based on UERE and DOP. Using the definitions of DOP factors introduced in Chapter 2, the 1-sigma $EPE_{3\text{-}D}$, $EHE_{2\text{-}D}$ and $EVE_{1\text{-}D}$ can be expressed as:

$$\sigma_{n-d} = DOP_{n-d} \times \sigma_{UERE} \tag{5.28}$$

where σ_{n-d} is the standard deviation of the n-dimensional positioning error component, DOP_{n-D} is the n-dimensional DOP factor and σ_{UERE} is the standard deviation of the satellite pseudorange measurement error. Considering the URE and UEE components of the UERE vector, we can write:

$$\sigma_{UERE} = \sqrt{\sigma_{URE}^2 + \sigma_{UEE}^2} \tag{5.29}$$

As discussed in Chapter 2, the URE is the largest error component and is dominated by atmospheric propagation; while the UEE is heavily dependent on GNSS receiver specifications (see Tables 2-2, 2-3 and 2-4). In order to generate CIFs and WIFs that are consistent with GNSS RNP, an attempt was made to directly use the EHE/EVE and the SIS protection requirements (HAL and VAL) applicable to the different flight phases (see Chapter 2, Table 2-7). Consequently, two additional integrity flags were defined as follows:

- **When the $EHE_{3\text{-}\sigma}$ exceeds the HAL or the $EVE_{3\text{-}\sigma}$ exceeds the VAL, the CIF shall be generated.**
- **When the $EHE_{2\text{-}\sigma}$ exceeds the HAL or the $EVE_{2\text{-}\sigma}$ exceeds the VAL, the WIF shall be generated.**

However, the impossibility of measuring the UERE in real-time led to the need of adopting conservative/inaccurate estimates for its receiver-dependent, SV-dependent and control segment-dependent components, such as those provided by GPS receiver manufacturers for the UEE and, in real-time applications, the relatively inaccurate URE estimates provided by the URA[1]. Based on this fact and considering the simulation results described in later sections of this chapter, this approach was successively discarded (see paragraph 5.4.4). It is in fact well known that, with current generation GPS satellites, the AOD varies significantly from SV to SV due to staggered upload operations (Di Esposti et al., 2003). The URE can vary significantly over time and between SVs due to differences or changes in AOD, uncertainty in SV dynamics, SV clock behaviour, geometry/observability, etc. The current URA index binning structure definition for civilian signals has insufficient resolution to adequately represent the current and projected decrease in SIS errors. Also, the current URA information is not updated frequently enough for aviation applications that require advanced RAIM features such as enhanced RAIM (eRAIM)

[1] The User Range Accuracy (URA) is a conservative representation of each satellite's expected rms URE performance based on historical data over the curve fit interval represented by the NAV data from which the URA is read. The URA is a coarse representation of the expected URE statistic, in that it is quantized to the levels represented by the URA index "N" as defined in IS-GPS-200.

and predictive RAIM (pRAIM) (Yang et al., 2013), (Volchansky, 2009). Further research is needed to

5.4 SIMULATION CASE STUDIES

In order to validate the design of the ABIA IFG module, some detailed simulation case-studies were performed on various representative military/civil manned and unmanned aircraft platforms. These platforms included:

- TORNADO Interdiction and Strike (IDS);
- Airbus 320 (A320) medium-range passenger transport aircraft;
- Boeing 747 (B747) long-range passenger transport aircraft;
- AEROSONDE UAV.

All simulated A/C trajectories included the following flight phases and flight legs:

- ***Takeoff:*** Straight Climb (SC) leg;
- ***Route Capture Insertion:*** Turning Climb (TC) leg;
- ***Cruise Phase:*** Straigh and Level (SL) and/or Level Turn (LT) legs;
- ***Initial Descent:*** Turning Descent (TD) and/or Straight Descent (SD) leg;
- ***Final Descent:*** Approach (AP) straight descent leg.

The duration of each flight leg was defined in accordance with the typical mission profiles of the designated aircraft types. The terrain profile was assumed to be flat and free from man-made features. No jamming sources were considered in the simulation case studies. For the avionics GPS receiver characteristics, we used a C/A code receiver with a flat random vibration power curve from 20Hz to 2000Hz with amplitude of $0.005\mathrm{g}^2/\mathrm{Hz}$ and the oscillator vibration sensitivity $S_v(f_m) = 1 \times 10^{-9}$ parts/g. Additionally, a third-order loop noise bandwidth of 18 Hz was considered and a maximum LOS jerk dynamic stress of $10\mathrm{g/s}=98\mathrm{m/s}^3$ was assumed. Finally, the following simplified antenna gain pattern was adopted:

$$G_R(dB) = 7.8659 * \sin E - 4.3659 \tag{5.30}$$

This resulting GPS antenna gain pattern is shown in Fig. 5-7.

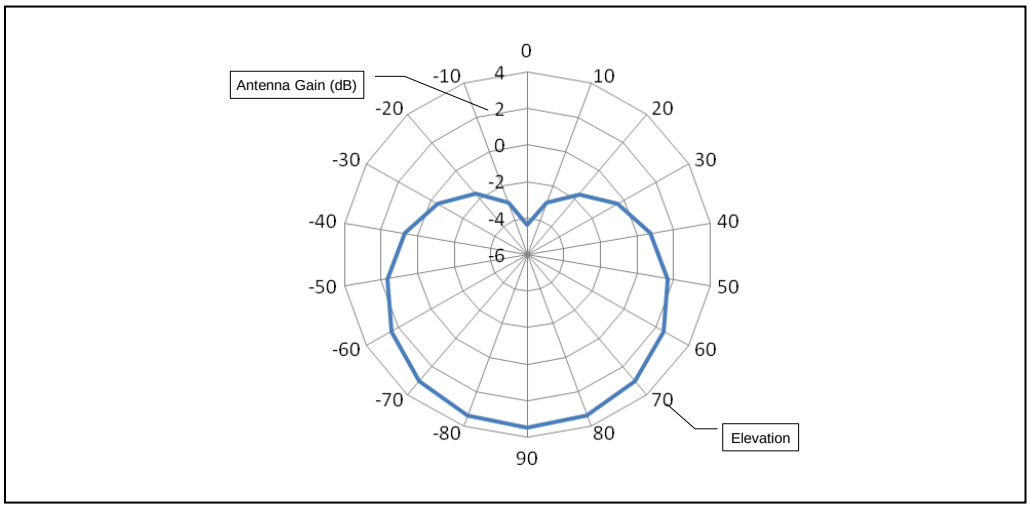


Figure 5-7. Simplified GPS antenna gain pattern.

The ground traces of GPS satellites are shown in Fig. 5-8.

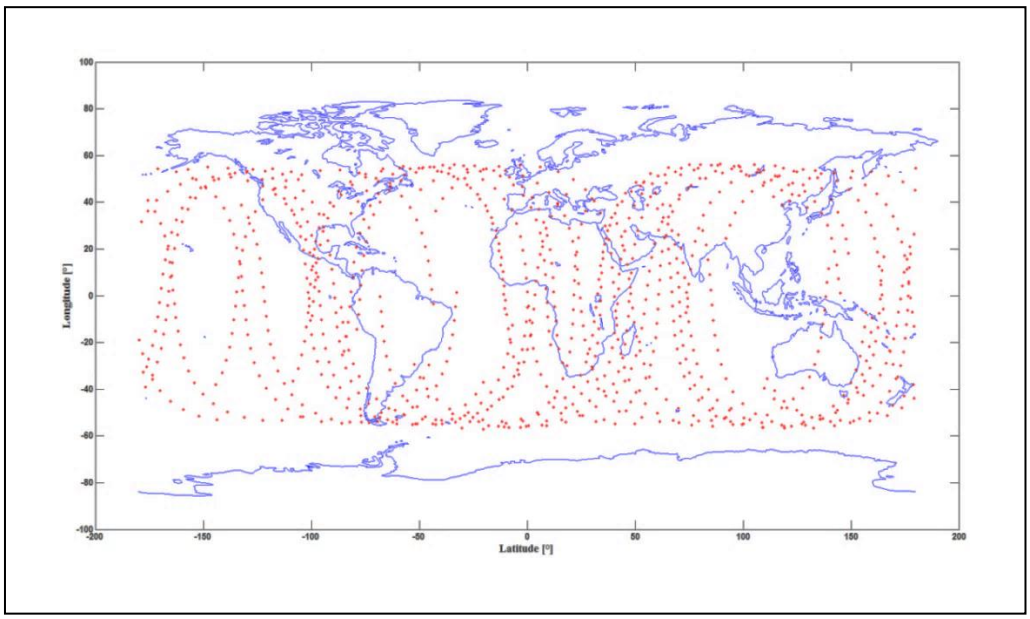


Figure 5-8. GPS satellites ground traces.

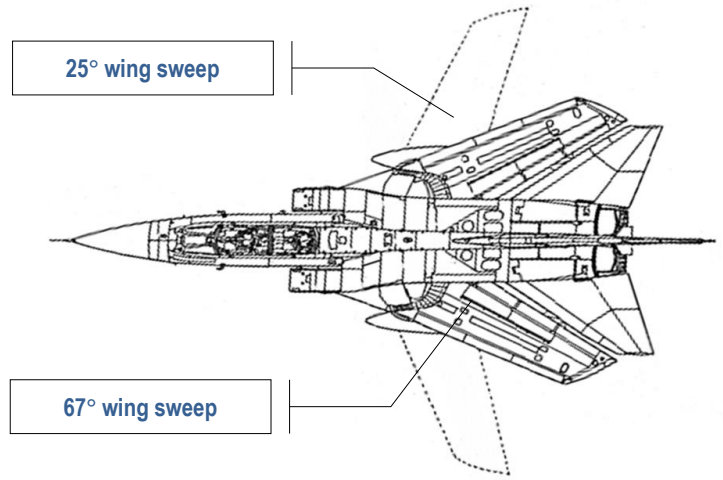
The initial point of the A/C trajectory was located at London Heathrow international airport (WGS coordinates: 51° 28′ 39″ N, 0° 27′ 41″ W) and the GPS constellation available on the 30th of July 2012 (starting at 10:00 a.m.) was simulated using the YUMA almanac data. The CIFs and WIFs relative to antenna masking, geometric

accuracy degradations, S/N, multipath and Doppler shift were generated. Details on these simulation case studies are provided in the following sub-paragraphs.

5.4.1 TORNADO-IDS Simulation

Various geometric parameters were required to develop a detailed CATIA model of the A/C. Some of the main parameters are listed in Table 5-1 (Aircraft Drawings, 2012). Further details are provided in Appendix C.

Table 5-1. TORNADO-IDS dimensions.



LENGTH	16.72 m (54 ft 10 in)
WINGSPAN	13.91 m at 25° wing sweep (45.6 ft) 8.60 m at 67° wing sweep (28.2 ft)
HEIGHT	5.95 m (19.5 ft)
WING AREA	26.6 m² (286 ft²)

The TORNADO-IDS 3-D CATIA model obtained is shown in Fig. 5-9. When calculating the AOM and the corresponding satellite visibility, the antenna location

must be included in the model. Military A/C typically have an Upper Antenna (UA) at the top of the fuselage and a Lower Antenna (LA) at the base of the fuselage. In our case, the upper antenna is assumed to be located 1.5 m behind the cockpit along the A/C centreline projection and 5 cm high on the A/C skin surface (Sabatini and Palmerini, 2008). The lower antenna is right below the upper antenna on the opposite side of the fuselage (Fig. 5-10). The line of sight (LOS) is measured in the antenna frame (i.e., origin at the antenna focal point) and the transformation from body-frame to antenna frame is obtained from:

$$F_{antenna} = F_{body} + T_{body}^{antenna} \text{ (m)} \tag{5.31}$$

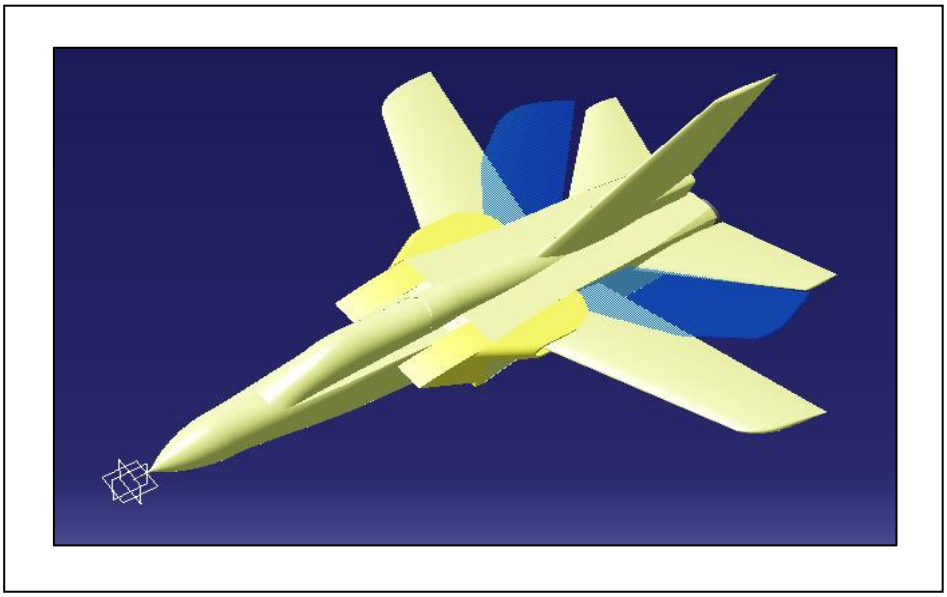


Figure 5-9. TORNADO-IDS 3-D CATIA model.

The transformation matrixes for the upper and lower antennae are:

$$T_{body}^{upper} = \begin{bmatrix} -0.88 \\ 0 \\ -0.74 \end{bmatrix} \text{ (m)} \tag{5.32}$$

$$T_{body}^{lower} = \begin{bmatrix} -0.88 \\ 0 \\ 2.13 \end{bmatrix} \text{ (m)} \tag{5.33}$$

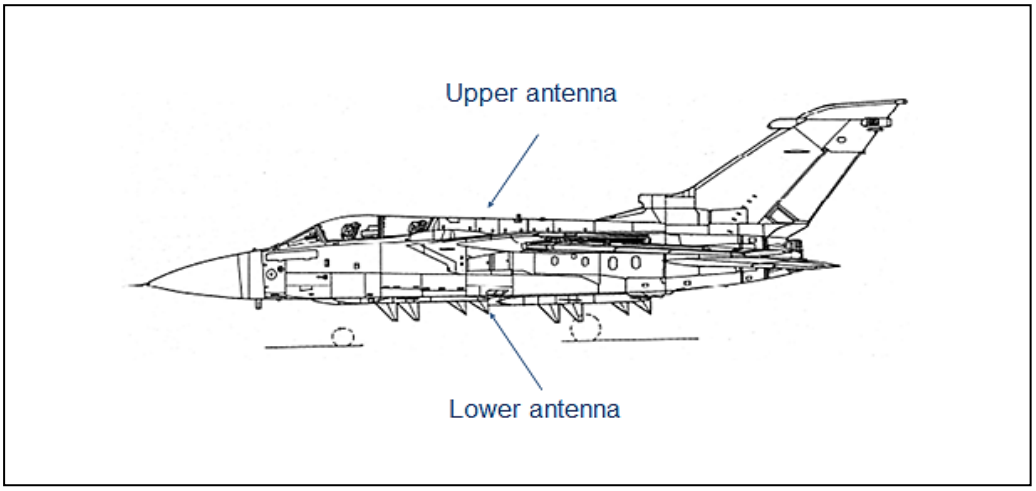


Figure 5-10. TORNADO-IDS antennae locations.

The specific flight profile simulated for the TORNADO-IDS case study is shown in Fig. 5-11. In this case, all flight legs last 300 seconds, except the AP leg lasting 200 seconds. The total flight duration is 2000 seconds.

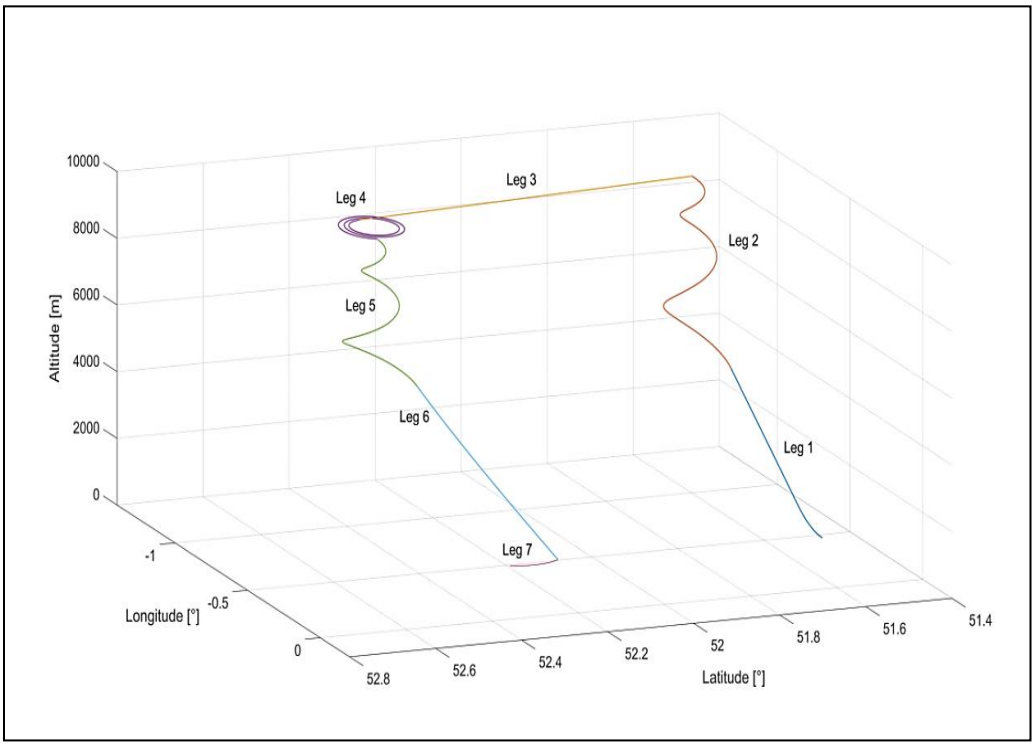


Figure 5-11. TORNADO-IDS flight profile.

The overall results of the IFG simulation (CIFs and WIFs generated during the flight) are shown in Table 5-2. Figure 5-12 shows in more details the specific causes of CIF and WIF events. It was observed that, in all cases, the CIFs were triggered at least 2 seconds before the successive WIF.

Table 5-2. Integrity flag time for TORNADO-IDS.

FLIGHT LEG	CIF Time	WIF Time
CLIMB	---	---
TURNING CLIMB	301 ~ 315 s, 417 ~ 474 s, 546 ~ 584 s	433 ~ 447 s, 557 ~ 566 s
CRUISE	---	---
LEVEL TURN	906 ~ 1012 s, 1023 ~ 1138 s, 1143 s ~ 1200 s	908 ~ 909 s, 927 ~ 984 s, 990 ~ 991 s, 1025 ~ 1028 s, 1049 ~ 1107 s, 1114 ~ 1115 s, 1152 ~ 1156 s, 1173 ~ 1177 s, 1187 ~ 1200 s
TURNING DESCENT	1210 ~ 1249 s, 1321 ~ 1338 s, 1348 ~ 1379 s, 1489 ~ 1500 s	1230 ~ 1249 s, 1350 ~ 1379 s
STRAIGHT DESCENT	1501 ~ 1800 s	1790 ~ 1800 s
APPROACH	1800 ~ 2000 s	1800 ~ 2000 s

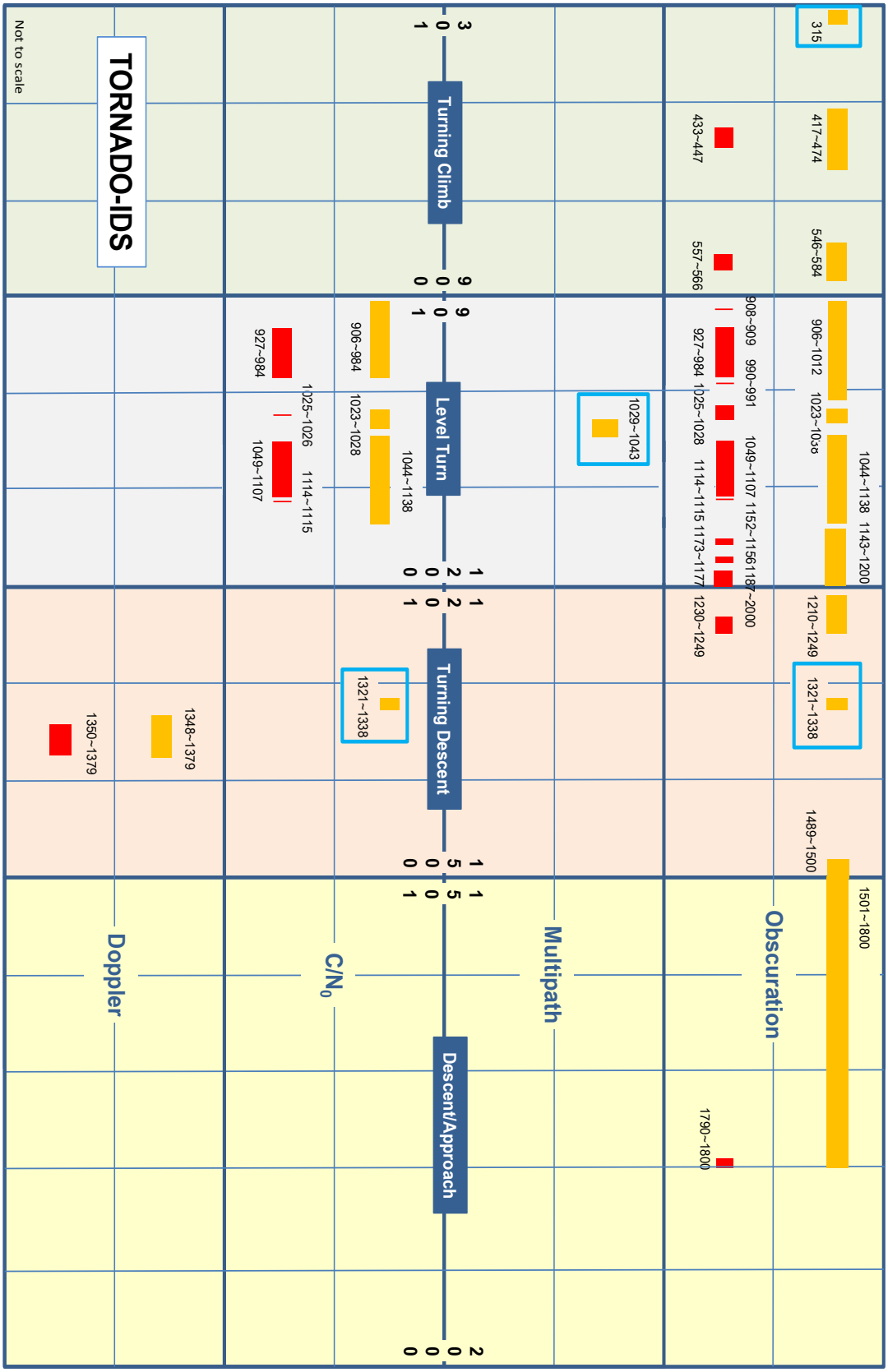


Figure 5-12. Detailed causes of CIFs and WIFs (TORNADO-IDS).

Focussing on the CIF early detection capability, we can compute the IFG Detection Rate (DR) as follows:

$$DR_{CIF} = \frac{Number\ of\ WIF\ following\ a\ CIF}{Total\ Number\ of\ WIF} \times 100 \tag{5.34}$$

As all CIFs were followed by WIFs we obtain DR_{CIF}=100%.

Classifying a CIF not followed by a WIF as a False Alarm (light blue boxes in Fig. 5-12), the FA Rate (FAR) of the IFG can be calculated as follows:

$$FAR_{CIF} = \frac{Total\ Number\ of\ false\ CIF}{Total\ Number\ of\ CIF} \times 100 \tag{5.35}$$

A total of 17 CIFs were generated and 4 were not associate to a WIF. Therefore, the False Alarm Rate (FAR) was FAR_{CIF}=23.5%.

5.4.2 A320 SIMULATION

A320 is a medium-range aircraft globally employed by major airlines and low-cost carrier mostly for passenger regional flights. This aircraft was selected for the IFG simulation due to its widespread use in the civil aviation community and its representative size/geometry and flight dynamics characteristics well documented in the literature. The main dimensions of the A320 aircraft and the GPS antenna location are presented in Fig. 5-13. The antenna transformation matrix is:

$$T_{body} = \begin{bmatrix} -10.63 \\ 0 \\ -3.4 \end{bmatrix} \text{(m)} \tag{5.36}$$

The A320 3-D CATIA model is shown in Figure 5-14.

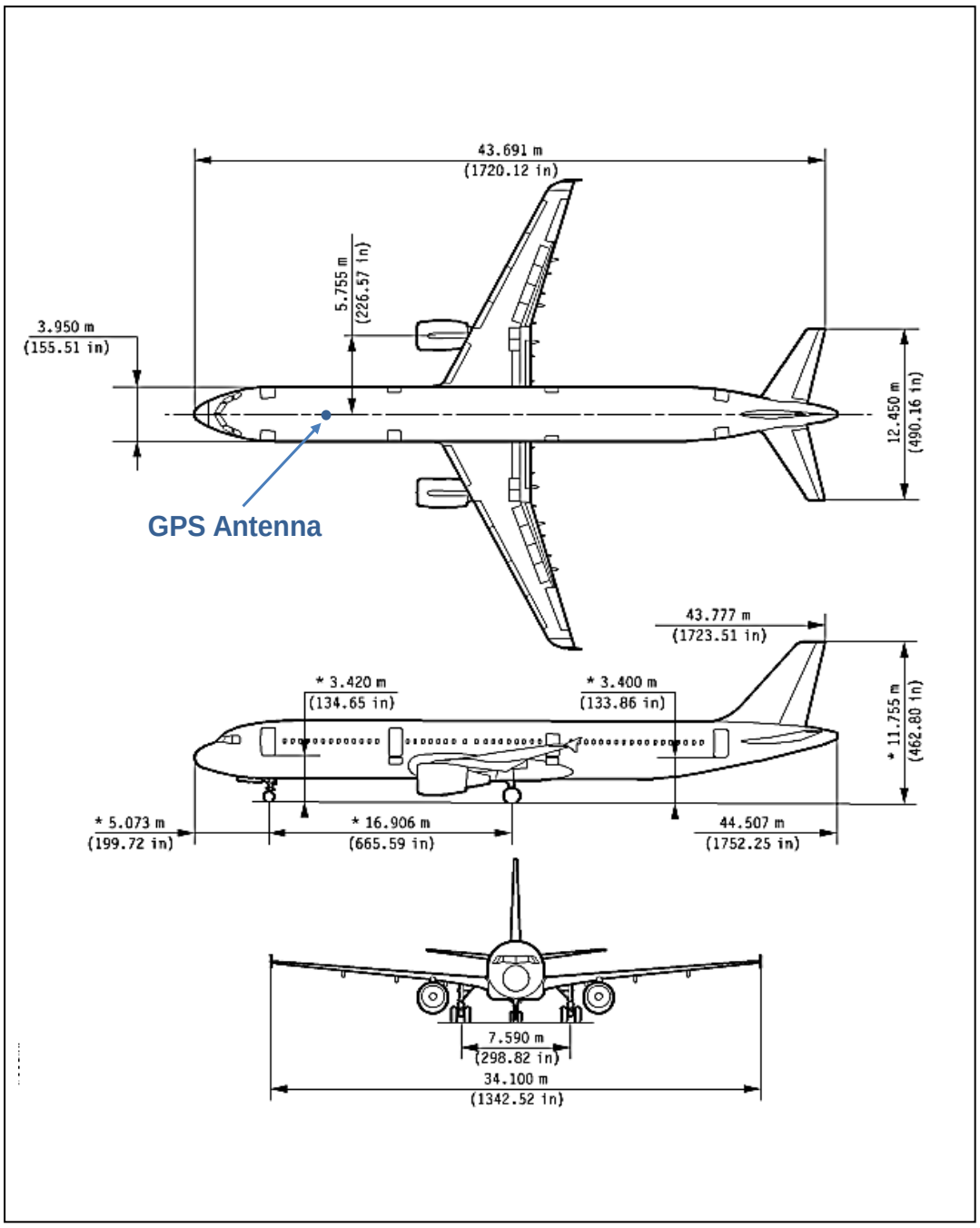


Figure 5-13. A320 dimensions and GPS antenna location (Aircraft Drawings, 2012).

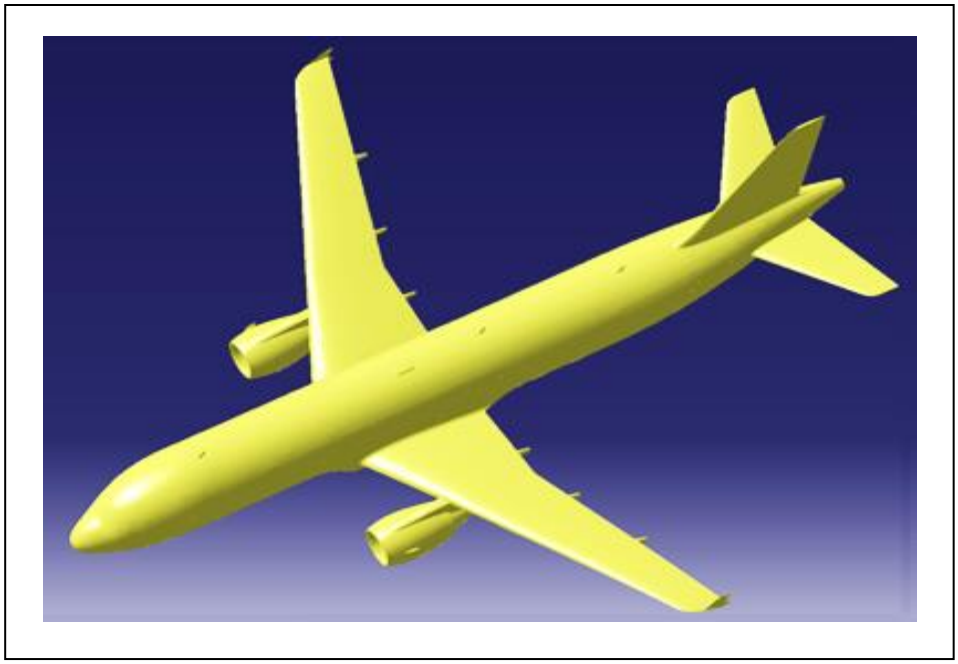


Figure 5-14. CATIA models of A320.

The simulated A320 flight profile is shown in Fig. 5-15. The A320 flight was from London Heathrow to Paris Charles De Gaulle international airport and its total duration was 2980 seconds (SC = 600 s, TC = 300 s, SL = 1000 s, LT = 30 s, SD = 700 s and AP = 350s).

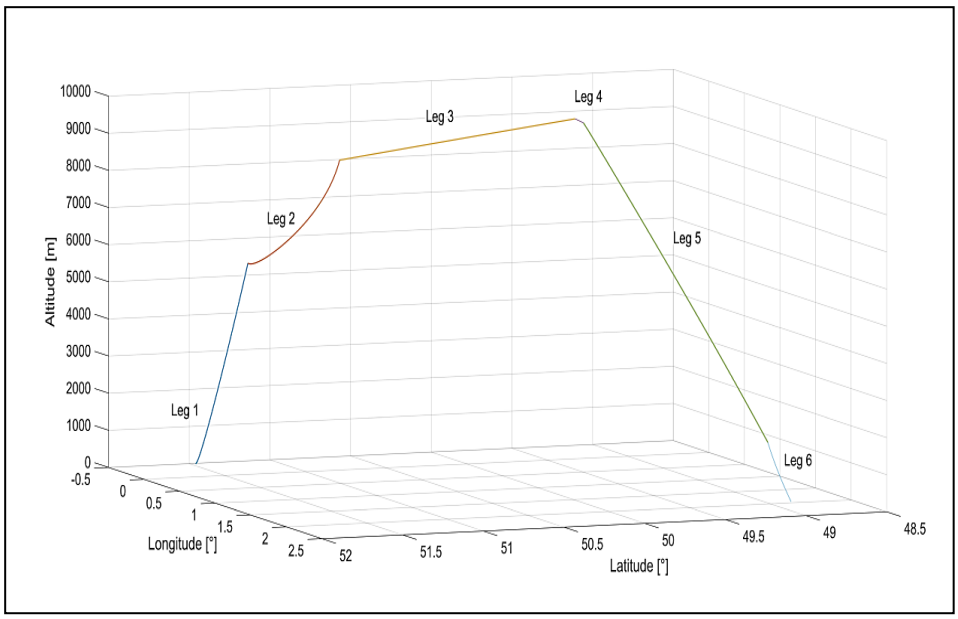


Figure 5-15. A320 flight profiles.

The overall results of the A320 IFG simulation (CIFs and WIFs generated during the flight) are shown in the Tables 5-3. Fig. 5-16 lists the specific causes of CIF and WIF events recorded during the A320 flight.

Table 5-3. Integrity flag time for A320.

FLIGHT LEG	CIF Tine	WIF Time
CLIMB	---	---
TURNING CLIMB	601 ~ 900 s	---
CRUISE	---	---
LEVEL TURN	---	---
STRAIGHT DESCENT	2383 ~ 2418 s	---
APPROACH	2634 ~ 2980 s	2636 ~ 2642 s

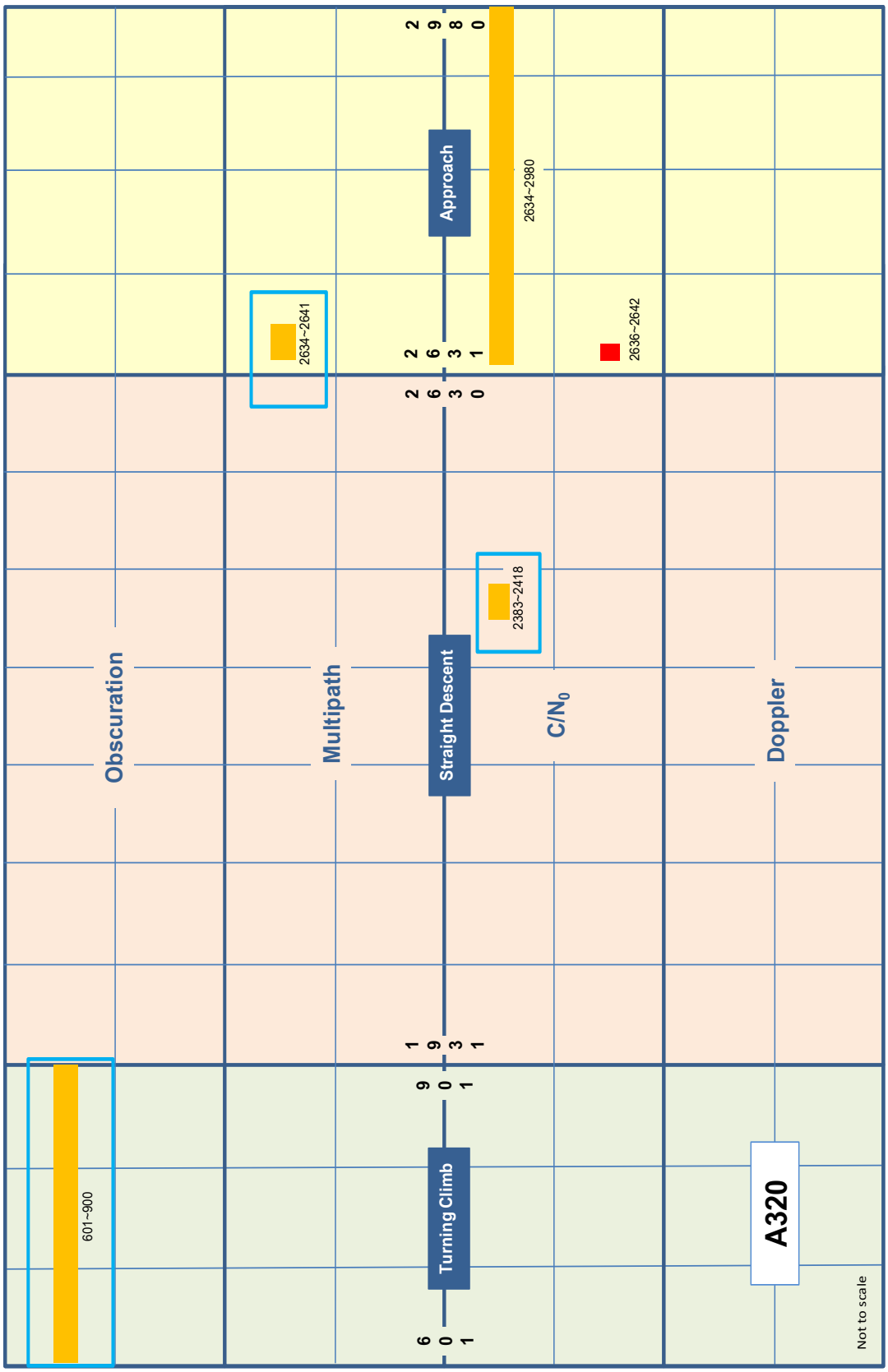


Figure 5-16. Detailed causes of CIFs and WIFs (A320).

The relatively more benign flight dynamics of A320 led to a reduced number of CIF and even less WIF events compared to the TORNADO-IDS case study. However, as in the TONADO-IDS IFG simulation, it was observed that the CIF was always triggered at least 2 seconds before the successive WIF. As the single WIF generated was associated to a CIF, DR_{CIF}=100%. A total of 4 CIFs were generated and 3 were not associated to a WIF. Therefore, the False Alarm Rate (FAR) was FAR_{CIF}=75%. This relatively high FAR value is probably a consequence of the fact that the ABIA IFG thresholds are largely based on experimental flight test activities performed on relatively small size and high-performance military platforms, whose geometric layout and dynamic characteristics are dissimilar from large commercial transport aircraft. This suggests that different CIF thresholds might be required for large commercial transport aircraft. Further research is needed to confirm this hypothesis.

5.4.3 AEROSONDE UAV SIMULATION

The AEROSONDE "Laima" geometric parameters were extracted from the literature to draw a detailed 3-D model of the aircraft (Holland et al., 2001), (Burston et al., 2014), (Aircraft Drawings, 2012). The AEROSONDE 3-D CATIA model obtained is shown in Fig. 5-17.

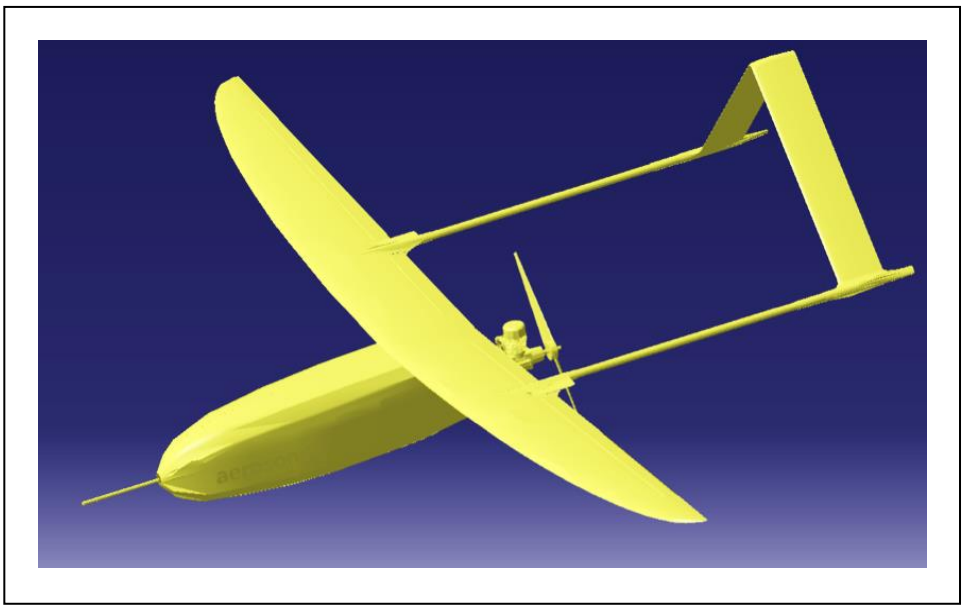


Figure 5-17. AEROSONDE 3-D CATIA model.

The aircraft has a wing span of 2.9 m, a length of 2.2 m, a wing area of 0.55 m² and a Propeller Radius of 0.25 m. The AEROSONDE version considered is equipped with a 24cc fuel injected premium unleaded gasoline engine and its overall weight is 13 - 15 kg (29-33 lbs.) depending on payload, fuel tank and battery configurations. The payload is up to 2 kg (4.4 lbs.) with full fuel load (5 kg). The UAV can reach a speed of 80-150 km/hr (50-93 miles/hour) in cruise and 9 km/hour (6 miles/hr) in climb. The operational range is greater than 3,000 km with an endurance of 30 hours at 0.1 – 6 km altitude (depending on payload). Communication tasks are accomplished by V/UHF radio and/or LEO satellites. The location of the AEROSONDE GPS antenna is shown in Fig. 5-18.

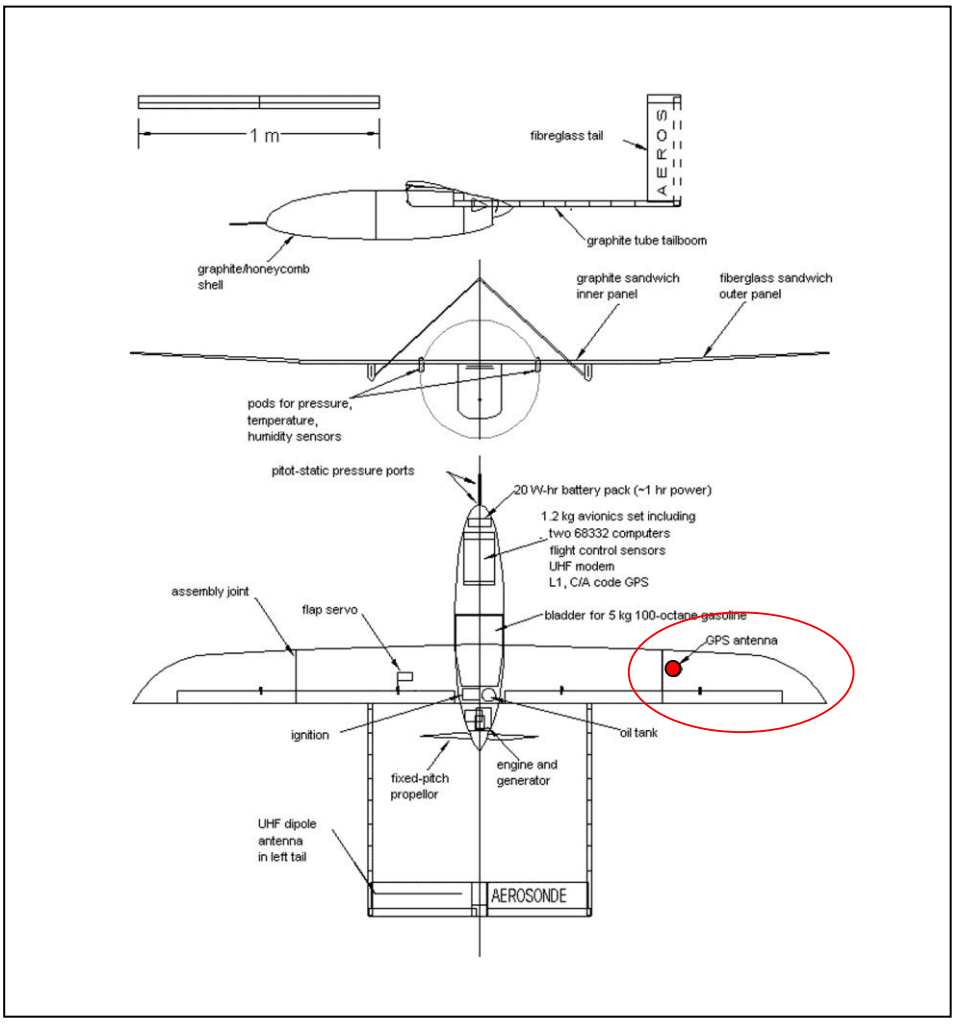


Figure 5-18. AEROSONDE UAV antenna location. Adapted from (Maslanik, 2002).

For the AEROSONDE UAV, the antenna transformation matrix is:

$$T_{body} = \begin{bmatrix} 0.34 \\ 1.69 \\ 0.43 \end{bmatrix} \text{ (m)} \tag{5.37}$$

Unlike the other simulated platforms, the AEROSONDE GPS antenna is not located in correspondence of the aircraft longitudinal axis, leading to a very complex and non-symmetric masking envelope. Therefore, to speed-up and automate the process of AMM generation, an Automatic Masking Profile Computation (AMPC) software was developed (Fig. 5-19).

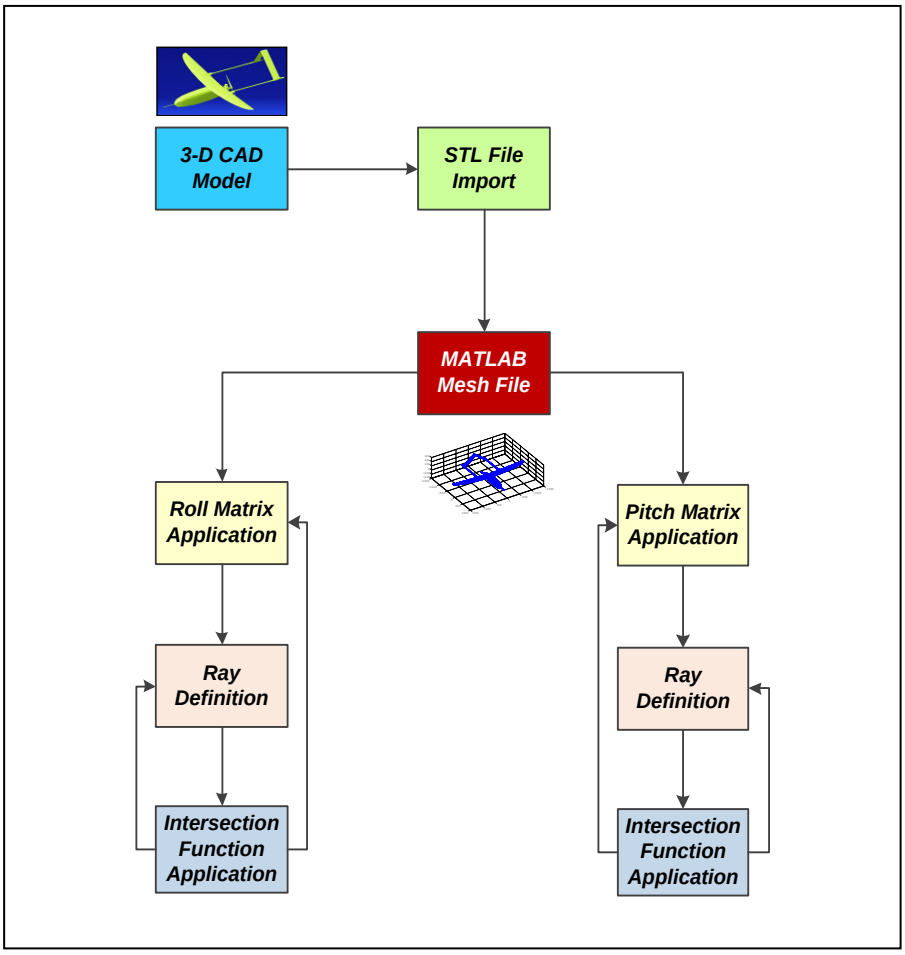


Figure 5-19. AMPC logic diagram.

The AMPC software populates a database (look up tables) containing the obscuration information of GNSS satellite signals for different aircraft roll and pitch angles. This is accomplished by implementing two different modules in the AMPC: the first is

used to transform the aircrafts CAD model in a mesh of small triangular surfaces that allows straightforward computations of line/surface intersections in a MATLAB™ environment; the second is used to rotate the aircraft in pitch and roll (bank), and to calculate the intersections between the aircraft structure (i.e., fuselage, wings and tail) and the line-of-sight (LOS) to all satellites in view as illustrated in Fig. 5-18. After creating the 3-D aircraft surface model, the corresponding CAD file was transformed in a Stereolithography (STL) file format. An STL file is a convenient representation of a complex 3D surface geometry, made by a number of oriented triangles (mesh). Each of these triangles is described by two elements: the first is a unit normal vector to the facet; the second element is a set of three points (listed in counter clockwise order) representing the vertices of the triangle. This representation is ideally suited for the ABIA simulation environment. An example of AEROSONDE mesh imported and plotted in MATLAB™ is illustrated in Fig. 5-20.

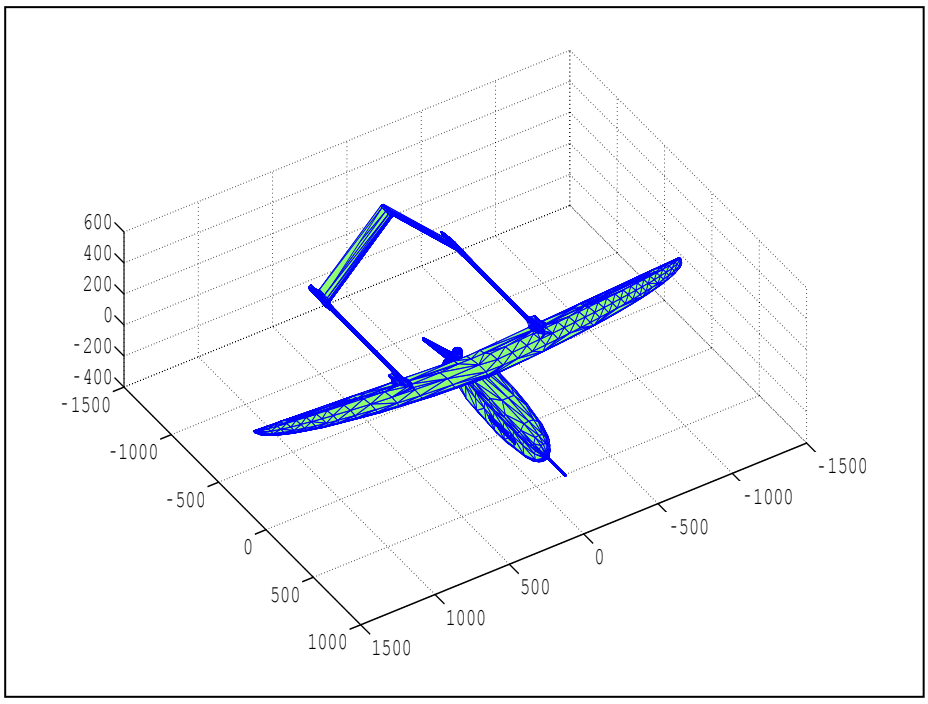


Figure 5-20. AEROSONDE mesh in MATLAB™.

Using this representation, the AMMs are generated calculating all possible intersections of the aircraft body (all triangular surfaces) with the LOS antenna-satellites during pitch and roll motion (Fig. 5-21).

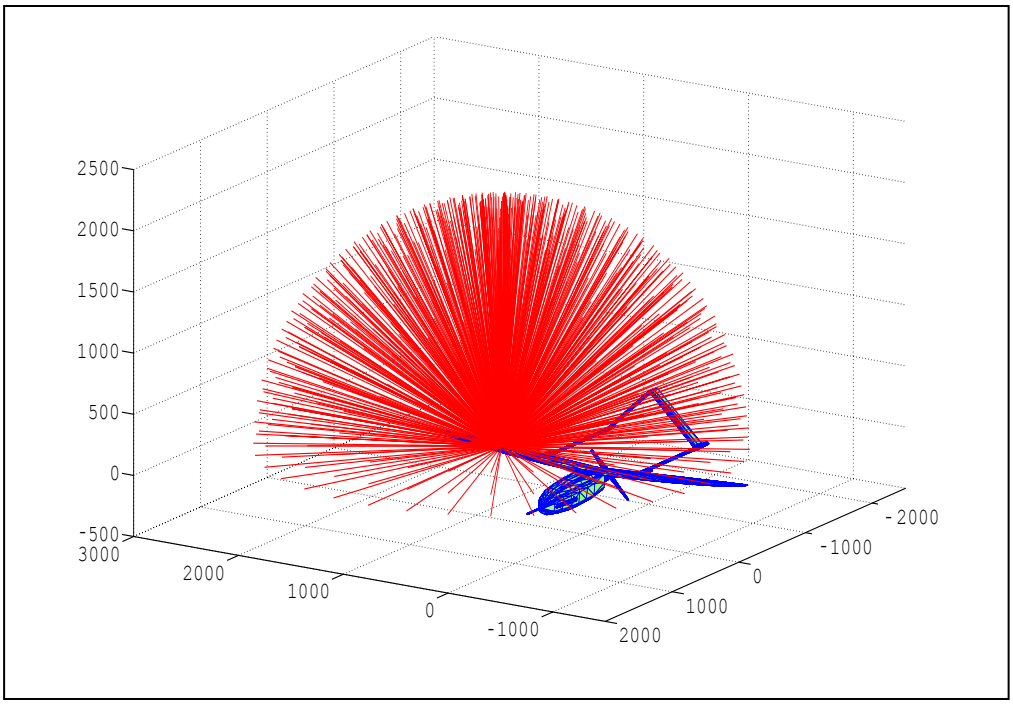


Figure 5-21. AEROSONDE masking profile simulation.

The simulated AEROSONDE UAV trajectory is shown in Fig. 5-22. It included the seven flight legs (SC = 450 s, TC = 450 s, SL = 1300 s, LT = 450 s, TD = 450 s, SD = 200 s and A = 100 s), for a total of 3400 seconds.

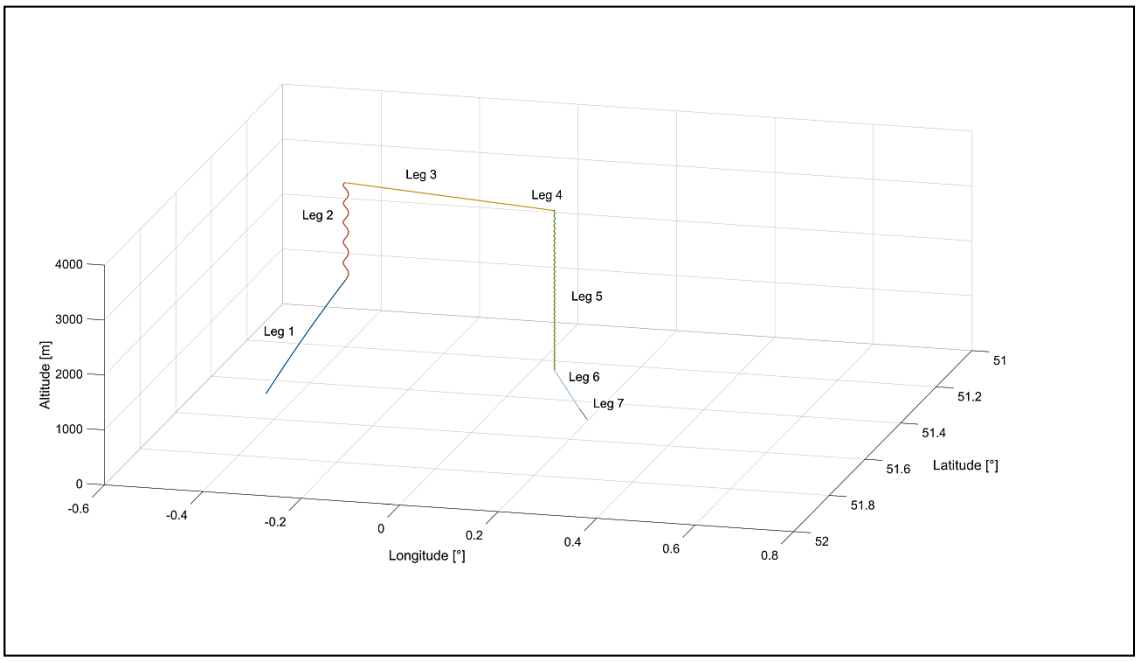


Figure 5-22. AEROSONDE UAV simulated trajectory.

The overall results of the AEROSONDE IFG simulation are listed in Table 5-4.

Table 5-4. Integrity Flags for AEROSONDE.

FLIGHT LEG	CIF Time	WIF Time
CLIMB	---	---
TURNING CLIMB	---	---
CRUISE	---	---
LEVEL TURN	2241 ~ 2311 s, 2413 ~ 2485 s, 2491 ~ 2650 s	2259 ~ 2263 s, 2273 ~ 2283 s, 2432 ~ 2436 s, 2446 ~ 2485 s, 2609 ~ 2612 s, 2621 ~ 2630 s
TURNING DESCENT	2688 ~ 2752 s, 2811 ~ 2881 s, 2944 ~ 3012 s, 3079 ~ 3100 s	2690 ~ 2739 s, 2814 ~ 2869 s, 2946 ~ 3003 s, 3081 ~ 3100 s
STRAIGHT DESCENT	---	---
FINAL APPROACH	3301 ~ 3400 s	3303 ~ 3400 s

The specific causes of CIF and WIF events are shown in Figure 5-23.

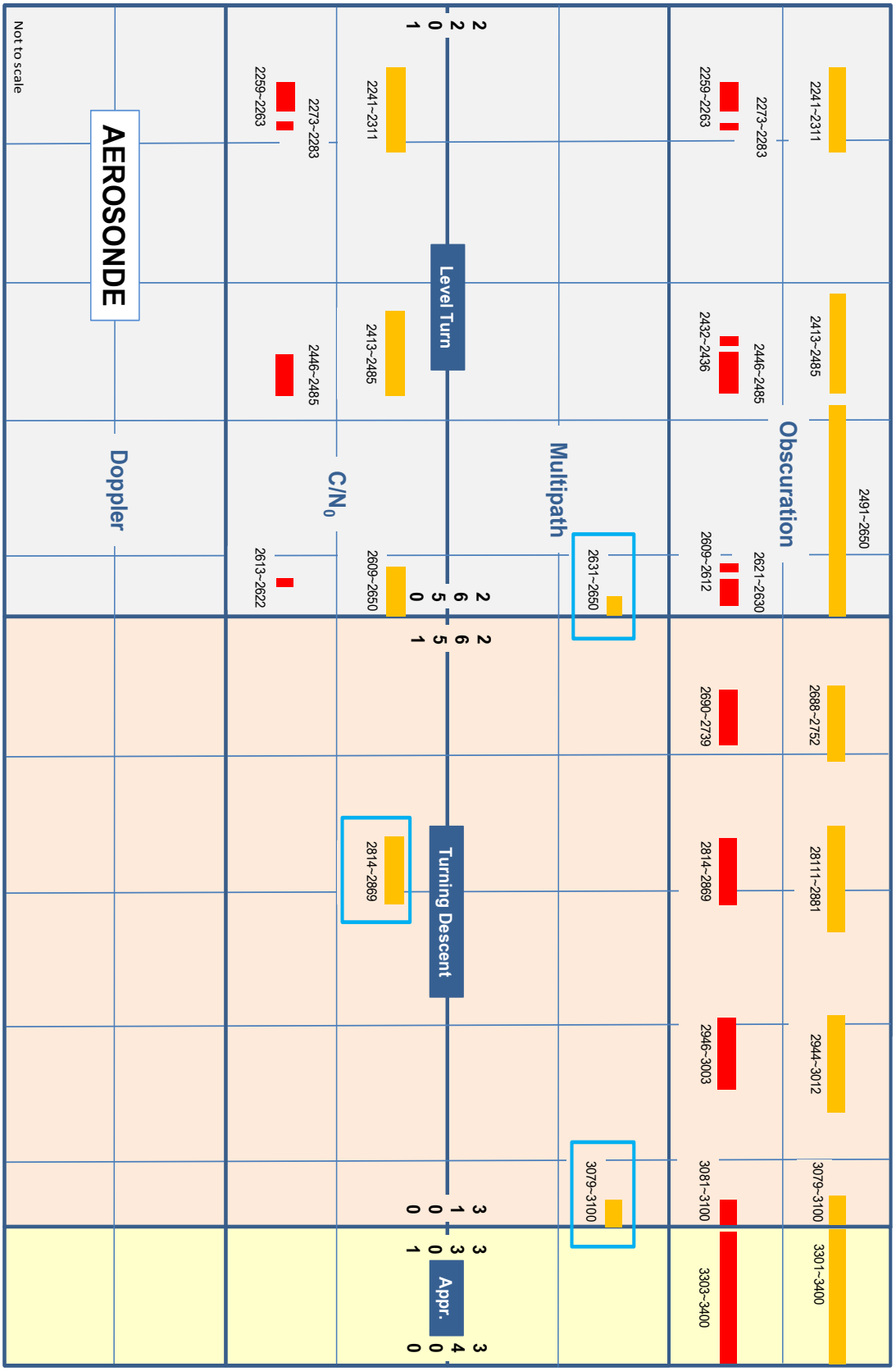


Figure 5-23. Detailed causes of CIFs and WIFs (AEROSONDE).

Also in the case of AEROSONDE, the CIFs were always triggered at least 2 seconds before the successive WIFs. All CIFs were followed by WIFs leading to DR_{CIF} of 100%. Additionally, all CIFs were followed by a WIF, A total of 13 CIFs were generated and 3 were not associated to WIFs. Therefore, the False Alarm Rate (FAR) was FAR_{CIF}=23%. These results are consistent with the other simulation case studies and corroborate the general validity of the models developed for the CIF/WIF thresholds.

5.4.4 EHE and EVE INTEGRITY FLAGS

As discussed in paragraph 5.3.4, a preliminary investigation was also accomplished to assess the potential of introducing additional integrity flag criteria based on UERE and DOP values. The EHE and EVE 2-σ and 3-σ values were estimated using Eq. (5.28) and typical UEE/URE values from Tables 2.3 and 2.4 (see Chapter 2). In particular the UERE 95% was obtained by combining the URE maximum average value during normal operations over all AODs (i.e., URE = 7.8 m 95%) and the UEE for a modern L1 code-range receiver (i.e., UEE = 4.5 m 95%). The resulting CIFs and WIFs are shown in Figures 5-24, 5-25 and 5-26, together with all other CIFs/WIFs recorded in each simulated flight. As displayed in these figues, EHE/EVE flags were generated only during precision approach phases when the estimated horizontal and/or vertical errors exceeded the prescribed HAL and VAL thresholds. Despite considering 3-σ errors for the CIF and 2-σ errors for the WIF, the predictive behaviour of the CIF was observed only for AVP-2 (TORNADO and AEROSONDE cases). It is therefore concluded that using conservative estimates of the URE/UEE budgets from the literature while accounting for HDOP/VDOP variations only, is not an adequate approach for a possible ABIA IFG implementation. Possible real-time applications with current generation GPS receivers would have to utilise the relatively inaccurate information provided by the URA to obtain URE estimates and, even assuming good UEE estaimtes from the GNSS receiver manufacturer, this would not lead to much better results. Based on theses considerations, the EHE/EVE integrity flags were not utilised in the

successive phases of the ABIA research documented in this thesis. Instead, since SBAS and GBAS systems are already operational and can provide EHE/EVE integrity flags usable by manned/unmanned aircraft in all flight phases, the synergies of these systems with ABIA are investigated in Chapter 7.

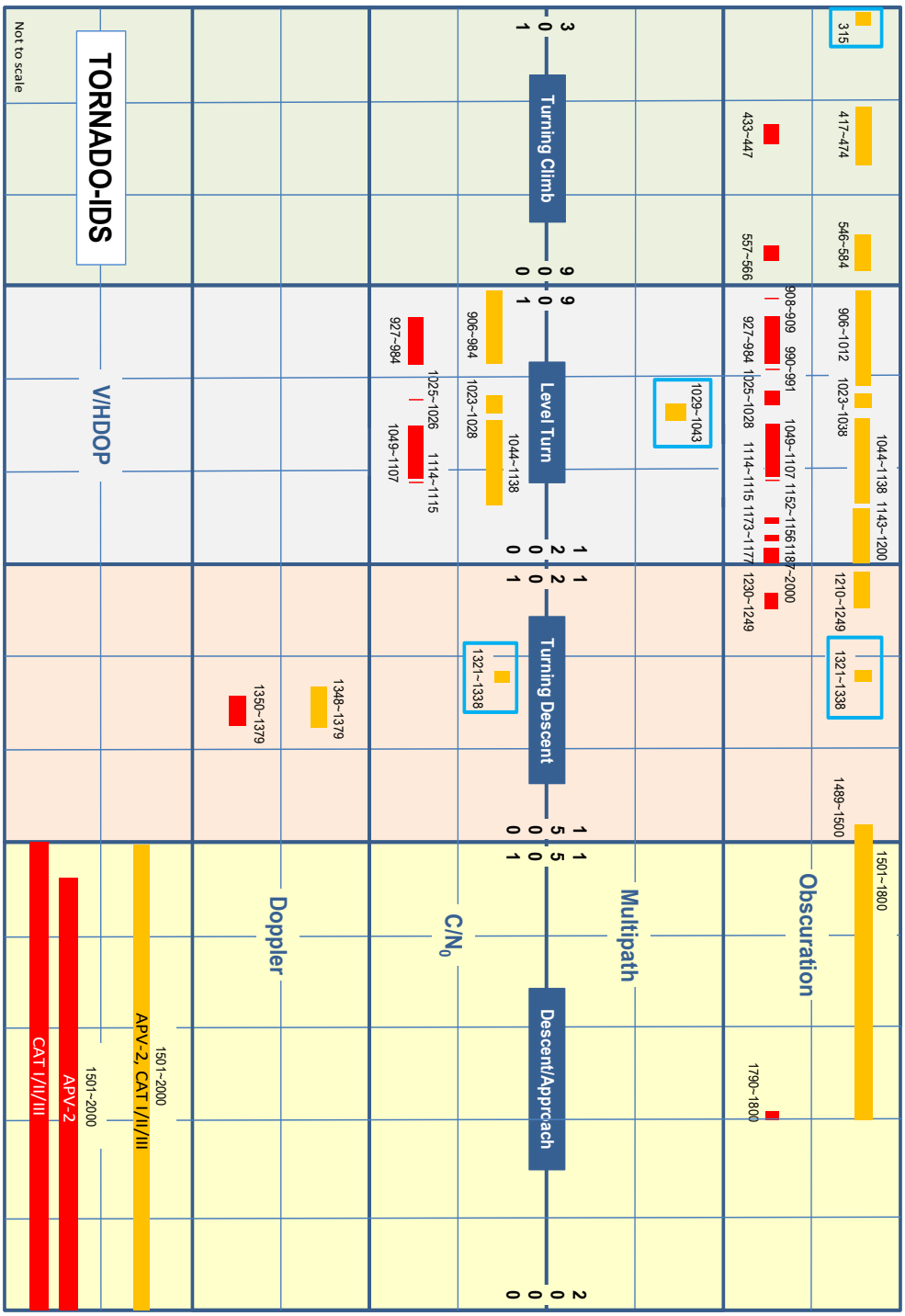


Figure 5-24. CIFs and WIFs with EHE/EVE flags (TORNADO-IDS).

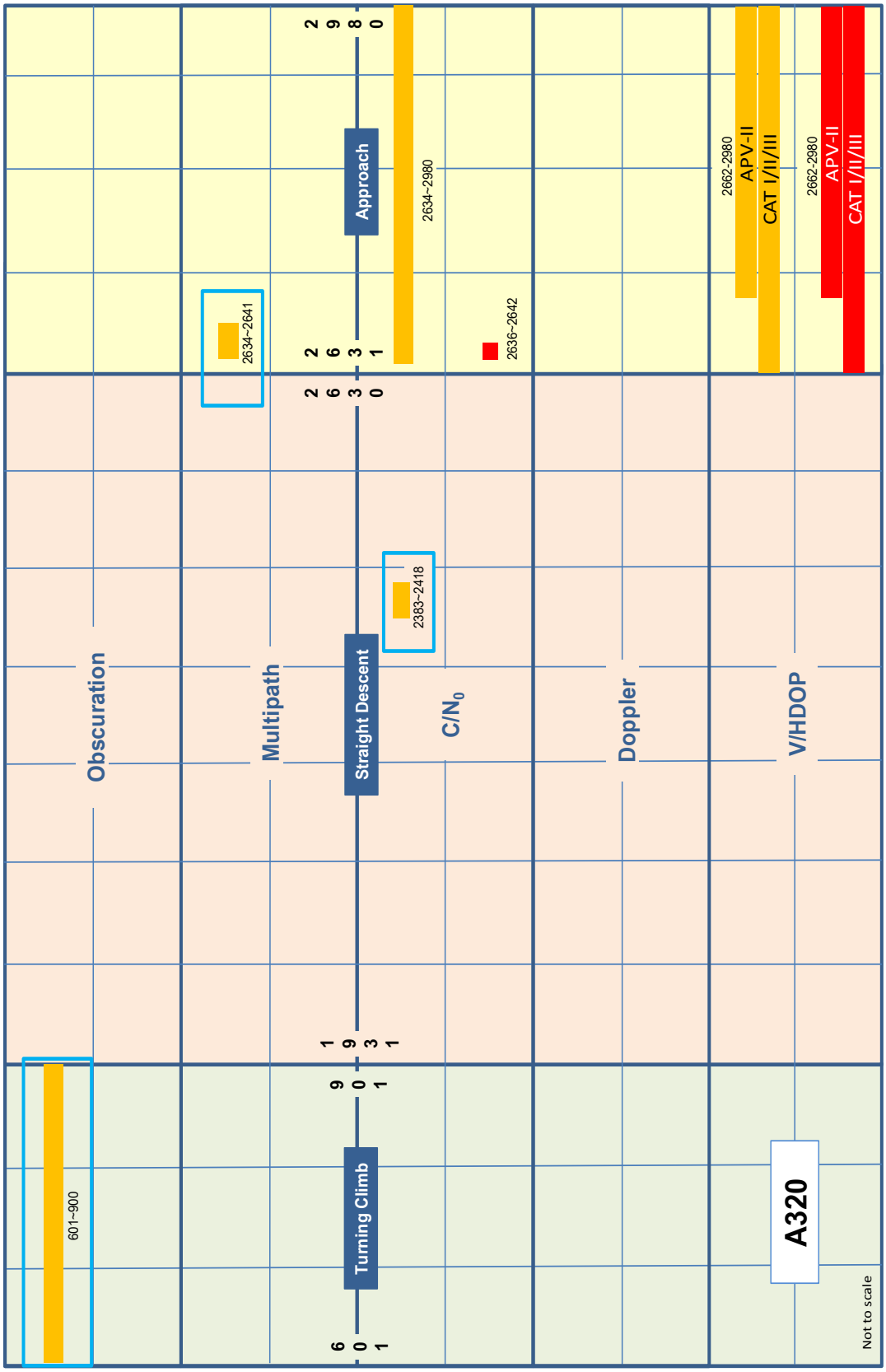


Figure 5-25. CIFs and WIFs with EHE/EVE flags (A320).

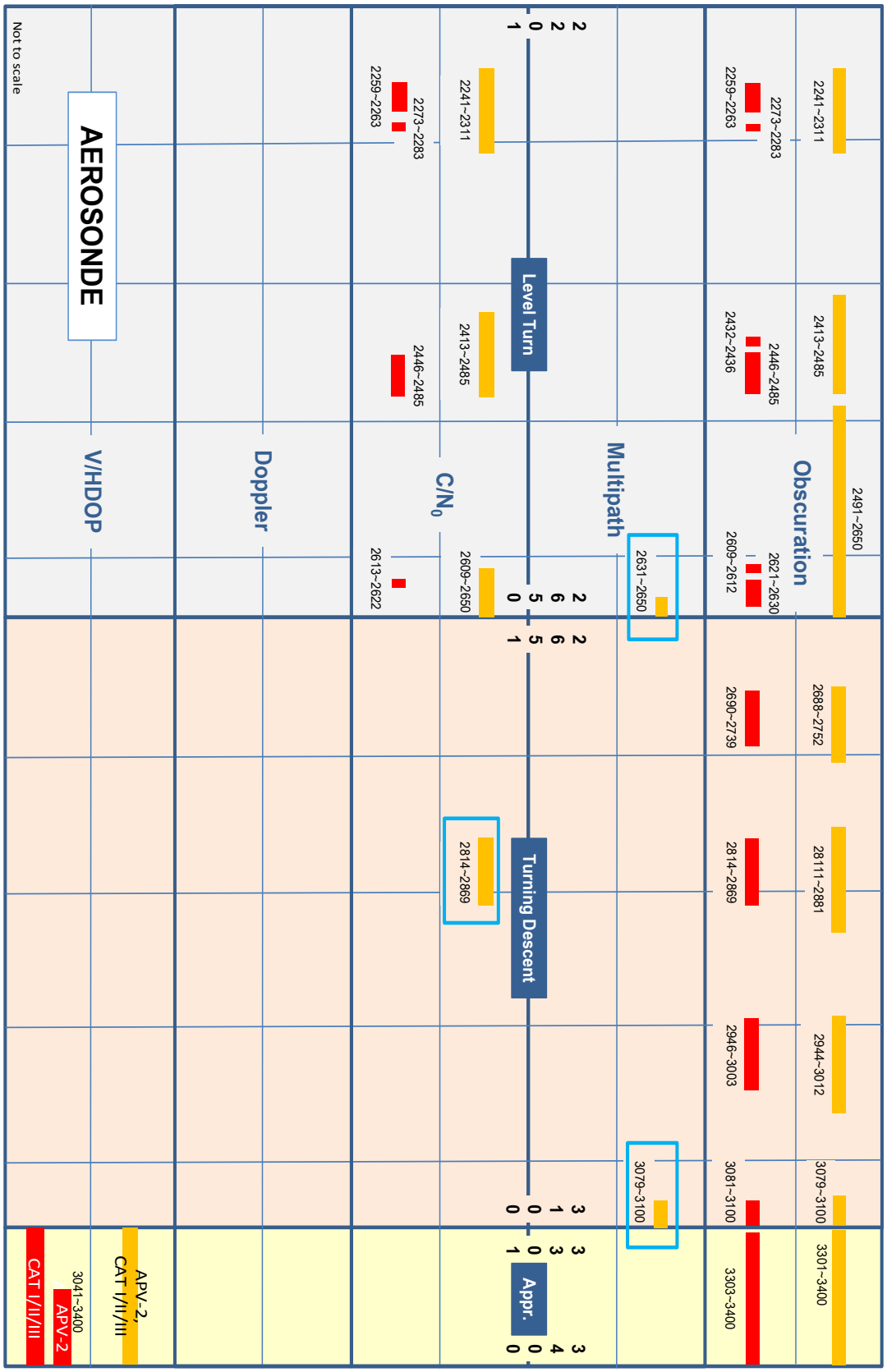


Figure 5-26. CIFs and WIFs with EHE/EVE flags (AEROSONDE).

Modernised GPS, GALILEO and other GNSS constellations will provide enhanced accuracy and integrity relative to the current GPS system. Timely update of broadcast ephemeris and clock parameters would reduce AOD and ranging error associated with SV orbital and clock state prediction. Up-to-date, reliable statistical accuracy information in the form of broadcast URA and User Range Rate Accuracy (URRA) would enhance the availability of accuracy and integrity for aviation operations. This would provide greater resolution in URE estimates to more closely reflect the observed SIS accuracy, allowing user equipment to reliably implement weighted LOS measurement error processing to optimize PVT solutions and to increase integrity (Di Esposti et al., 2003). Therefore, in future research, the original idea of producing UERE driven CIFs/WIFs will be further investigated. Additionally, the potential of ABIA and SBAS/GBAS to assist eRAIM and pRAIM operations will be assessed.

5.5 DISCUSSION

The conventional integrity performance metrics (i.e., AL, TTA, IR, PL) are still applicable to ABIA but, as discussed, some additional metrics are needed (TTC and TTW). ABIA is an autonomous aircraft-based integrity augmentation system exploiting on-board avionics to generate both predictive integrity flags (CIFs) and reactive integrity flags (WIFs). As detailed in this chapter, integrity thresholds were established for ABIA based on the existing literature and experimental flight test activities on GNSS/DGNSS, with a focus on signal degradations/losses caused by the aircraft dynamics (and satellite-aircraft relative dynamics). Based on the literature review and experimental data gathered on the various causes of signal degradation or loss (ground and flight test activities performed on GNSS/DGNSS), it was possible to empirically define thresholds for aircraft-satellite relative geometry (masking matrixes and antenna performance), radio frequency link (Doppler, multipath, C/N_0 and J/S) and receiver tracking (PLL, FLL and DLL). However, in the absence of adequate experimental data it was impossible to obtain error statistics and to study the possible correlations between the various sources of GNSS data error/loss.

Therefore, these sources of where treated independently and separated integrity flag thresholds were defined for each of them (using ad-hoc margins between the CIF and the corresponding WIF). This approach is different from that generally used in GBAS/SBAS and RAIM, where errors are cumulated in a RSS sense and confidence levels (inflations) are applied to the overall error statistics. Another clear difference (and advantage) of ABIA over LAAS/WAAS/RAIM, is that ABIA considers the aircraft dynamics in the computation of the various integrity flags, while LAAS/WAAS/RAIM do not.

In order to correctly define the CIF-WIF separation margins, the ABIA performance requirements were defined in terms of target TTC (TTC $\geq$ 2 seconds) and DR (DR=100%). Imposing these targets in the IFG module design allowed and initial assessment of the achievable ABIA performance. TTW and FAR targets were not specified at the present stage of ABIA research as a proper verification of TTW and FAR can only be accomplished by performing integration case studies, hardware-in-the-loop and human-in-the-loop simulations, as well as suitable ground/flight test activities. These activities are recommended for future research.

Clearly, there is also a need for a statistical definition of the ABIA performance in terms of conventional AL/PL and further research is recommended in this field. This will allow a direct comparison of ABIA with other augmentation systems (SBAS, GABS and RAIM) and a more detailed identification of the synergies attainable in various manned and unmanned aircraft applications. For the time being, and until further research is carried out (addressing hardware/human-in-the-loop simulations, aircraft integration studies and ground/flight test activities) to produce statistically representative data samples, the IR associated to the ABIA was evaluated by targeting a DR of 100%. As this choice has a negative impact on the FAR (as demonstrated by the simulation case studies), future research will concentrate on finding optimal trade-offs between DR and FAR in all required flight phases and in a variety of operational tasks. As statistical data analysis will progress, it will also be possible to introduce Detection Probability (DP) and False Alarm Probability (FAP) metrics to better describe the ABIA performance.

5.6 CONCLUSION

In this chapter we presented the criteria used for generation of CIFs and WIFs in the ABIA IFG. These criteria are associated to a variety of events including antenna obscuration, geometric accuracy degradations, SNR, multipath and Doppler shift. Detailed simulation case studies were performed on TORNADO-IDS, A320 and AEROSONDE aircraft. Relevant flight manoeuvres/phases were considered in these simulations, including straight climb, level/turning cruise, turning climb/descent and straight descent. From the results of these simulation activities, the following conclusions are drawn:

- In the limited but representative range dynamic conditions explored, data analysis showed that the ABIA Integrity Flag Generator (IFG) is capable of providing useful integrity flags when GNSS signals are degraded or lost.
- The target SL requirements set for the CIF (DR=100% and TTC<2 seconds) were achieved in the selected manned/unmanned platform implementations and in all operational conditions tested (a limited but representative cross-section of the aircraft operational flight envelopes).
- After the integrity caution flag is generated, the time available for the pilot/autopilot to react (i.e., at least 2 seconds), would be adequate to support aviation safety-critical tasks including GLS precision approach and automatic landing applications.

A verification of the target TTW (corresponding to the TTA specified in ICAO standards for the various flight phases) was not possible within the scope of the simulation case studies described in this chapter. Future research will address this gap, including integration case studies, hardware-in-the-loop and human-in-the-loop simulations, as well as experimental ground and flight test activities.

In conclusion, the simulation results presented in this chapter confirm the suitability of the models developed for the ABIA CIF/WIF thresholds. It is evident that the availability of a usable CIF (i.e., at least 2 seconds predictive) represents a significant progress in this research. In fact, the availability of a usable CIF allows the

implementation of an early correction loop, with the potential for both manned A/C and UAVs to avoid flight conditions potentially leading to unacceptable GNSS data degradations or losses. Therefore, it is envisaged that a properly designed ABIA Flight Path Guidance (FPG) module could take full advantage of this predictive behaviour, allowing an A/C or UAV to correct its flight trajectory/attitude in order to avoid the occurrence of GNSS data degradations/losses.

It is important to mention that the analytical and semi-empirical models used in thesis to describe GNSS signal degradations (i.e., masking, multipath, C/N, J/S and Doppler) and receiver tracking thresholds are only valid under specific assumptions, limiting the range of possible applications to the specific conditions in which the models were developed and validated. Where applicable, these limitations have been explicitly mentioned. However, a refinement of these models (also based on future ABIA experimental activities and addressing the evolutions being experienced by GNSS technologies) is an important target for future research.

5.7 REFERENCES

Aircraft Drawings (2012). Military and Commercial Aircraft Line Drawings. Online database. http://www.aircraftdrawindsdownload.com. Accessed 15 June 2011.

Burston, M. T., Sabatini, R., Clothier, R., Gardi, A. and Ramasamy S. (2014), "Reverse Engineering of a Fixed Wing Unmanned Aircraft 6DOF Model for Navigation and Guidance Applications." Applied Mechanics and Materials, Vol. 629, pp. 164-169, 2014.

CAA (2003). GPS Integrity and Potential Impact on Aviation Safety. CAA Safety Regulation Group Paper 2003/09.

Celestrak (2012). SEM Almanacs. http://www.celestrak.com/GPS/almanac/SEM/ definition.asp. Accessed 15 June 2012.

Celestrak (2012). YUMA Almanacs. http://www.celestrak.com/GPS/almanac/ Yuma/ definition.asp. Accessed 15 June 2011.

Holland, G. J., Webster, P. J., Curry, J. A., Tyrell, G., Gauntlett, D., Brett, G., Becker, J., Hoag, R. and Vaglienti, W. (2001), "The Aerosonde robotic aircraft: A new paradigm for environmental observations." Bulletin of the American Meteorological Society, Vol. 82, Issue 5, pp. 889-901.

ICAO (2006). Annex 10 to the Convention on International Civil Aviation. Aeronautical Telecommunications - Volume 1: Radio Navigation Aids. Edition 6.

Kaplan, E. D. and Hegarty, C. J. (2006). Understanding GPS: Principles and Applications. Second Edition. Artech House (London).

Maslanik, J. (2002), "Polar remote sensing using an unpiloted aerial vehicle." Seminar held at Colorado Center for Astrodynamics Research (CCAR), University of Colorado at Boulder. Available online at: http://www2.hawaii.edu/~jmaurer/uav/#specifications (overview and editing by Maurer J.). Webpage visited in May 2012.

Mubarak, O. M. and Dempster, A. G. (2009). Statistical Analysis of Early Late Phase for Multipath Detection. IGNSS Symposium 2009. Gold Coast, Australia.

Mubarak, O. M. and Dempster, A. G. (2010). Analysis of early late phase in single and dual frequency GPS receivers for multipath detection. The University of New South Wales (Australia) online paper. http://www.gmat.unsw.edu.au/snap/staff/omer_mubarak.htm. Accessed May 2011.

Parkinson, B. W. and Spilker, J. J. (1996). Global Positioning System: Theory and Applications - Volume I. AIAA - Progress in Astronautics and Aeronautics.

RTCA (2004). DO-245A: Minimum Aviation System Performance Standards for Local Area Augmentation System (LAAS).

Sabatini, R., Moore, T. and Hill, C. (2013-a), "A New Avionics Based GNSS Integrity Augmentation System: Part 1 – Fundamentals." Journal of Navigation, Vol. 66, No. 3, pp. 363-383.

Sabatini, R., Moore, T. and Hill, C. (2013-b), "A New Avionics Based GNSS Integrity Augmentation System: Part 2 – Integrity Flags." Journal of Navigation, Vol. 66, No. 4, pp. 511-522. June 2013.

Sabatini, R. and Palmerini, G. (2008), "Differential Global Positioning System (DGPS) for Flight Testing." NATO Research and Technology Organization (RTO) Systems Concepts and Integration Panel (SCI) AGARDograph Series RTO-AG-160, Vol. 21.

Ward, P. W. (1997). Using a GPS Receiver Monte Carlo Simulator to Predict RF Interference Performance. In Proceedings of the 10th International Technical Meeting of The Satellite Division of The Institute of Navigation, Kansas City, MO.

(This page is left black for the purpose of typesetting)

6

ABIA FLIGHT PATH GUIDANCE MODULE

6.1 INTRODUCTION

The main task of the ABIA FPG module is to generate a flyable A/C trajectory that avoids unacceptable GNSS integrity degradations. This requires that the aircrew (or the A/C automatic flight control systems) be provided with the guidance information necessary to avoid a WIF after the onset of a CIF. Based on the definitions provided in Chapter 3, this corresponds to the implementation of an early correction loop. The problem is approached as a standard trajectory optimisation problem that can be efficiently solved using optimal control techniques. This chapter addresses the different components of the optimization problem (i.e., dynamic constraints, path constraints, boundary conditions and cost functional) and presents some simulation case studies carried out to corroborate the validity of the trajectory optimisation algorithms proposed for integration into the FPG module.

6.2 TRAJECTORY OPTIMISATION

Optimising the A/C trajectory subject dynamic, geometric and operational constraints is a well-known optimal control problem that can be solved using a variety of direct or indirect methods. All the standard components of an optimization problem are present (Fig. 6-1): the A/C Dynamics Model (ADM) gives the dynamic constraints (allowing the generation of a flyable trajectory); the CIF thresholds and

the current GNSS parameters define a certain number of path constraints ensuring that WIF thresholds are not exceeded on the whole trajectory; the boundary conditions include minimum, maximum, initial and final values for the various state and command variables involved in the computation (these are given by the on-board A/C sensors and by the Flight Management System (FMS), which stores the information relative to the initial flight plan).

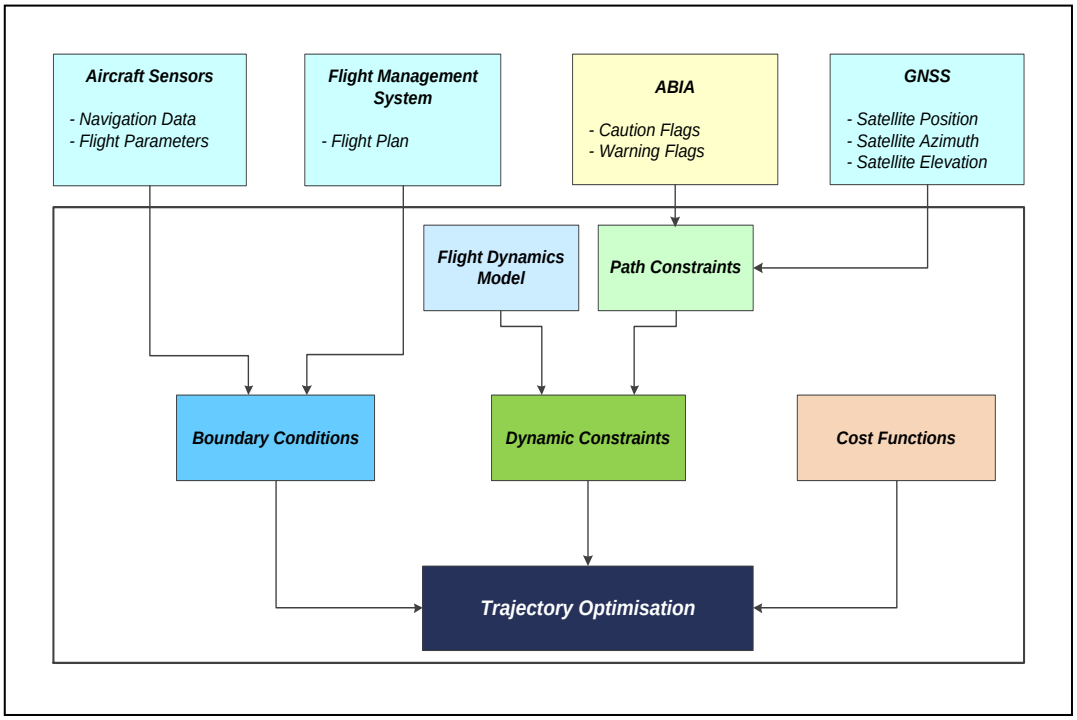


Figure 6-1. Trajectory optimization problem.

A cost function is implemented to address the minimisation of certain performance criteria. In safety-critical GNSS applications (e.g., curved/segmented precision approaches), all the necessary constraints associated to integrity degradations are included in the path constraints and the trajectory is optimised for minimum time to destination waypoint. However, more complex criteria can be set based on the actual A/C performance parameters (e.g., minimum fuel consumption) or on the characteristics of the mission (i.e., to maximise distance from another A/C, to minimise the distance from the initial waypoint, etc.). Later sections will address these options in more detail.

6.3 FLIGHT DYNAMICS MODELS

As the concept of flight trajectory is deeply related to the dynamics of the body in aerial motion, flight dynamics model implementations are discussed beforehand. The focus of this research is on fixed-wing civil/military A/C; hence the Six Degree of Freedom (6DOF) and 3 Degree of Freedom (3DOF) models introduced here are specifically tailored to this category of flying platforms. A detailed discussion on the derivation of flight dynamics equations from first principles is beyond the scope of this thesis and the reader may refer to (Hull, 2010), (Zipfel, 2007), (Pamadi, 2004), (Steven et al., 2003), (Phillips, 2010), (Imado et al., 2011) for more information.

Assuming the A/C to be a rigid body with a static mass distribution, a rather accurate model of its flight dynamics can be introduced, which is derived from the equilibrium of forces and momentums along the coordinate axes of a suitable Cartesian reference frame with origin in the centre of mass of the A/C (i.e., body frame). This model involves a high number of parameters to define the properties of inertia, aerodynamic stability and control forces. Adequate experimental and numerical investigations are typically required in order to define the parameters with good precision. For implementation in avionics guidance and control systems (e.g., fly-by-wire flight control systems) and for other applications including flight simulation and trajectory estimation/route planning, A/C flight dynamics are typically described by a set of Differential Algebraic Equations (DAE). A discussion of the analytical derivation may be found in (Hull, 2019) and (Zipfel, 2007). Typical avionics implementations are described in (Pamadi, 204) and Stevens et al., 2003). The set of DAE and complementary kinematic relations defining the 6DOF rigid body dynamics of a fixed-wing A/C are (Phillips, 2010):

$$\begin{bmatrix} \dot{u} \\ \dot{v} \\ \dot{w} \end{bmatrix} = \frac{g}{W} \begin{bmatrix} F_{X_b} \\ F_{Y_b} \\ F_{Z_b} \end{bmatrix} + g \begin{bmatrix} -s\theta \\ s\phi\, c\theta \\ c\phi\, c\theta \end{bmatrix} + \begin{bmatrix} rv - qw \\ pw - ru \\ qu - pv \end{bmatrix} \tag{6.1}$$

$$\begin{bmatrix}\dot{p}\\ \dot{q}\\ \dot{r}\end{bmatrix}=\begin{bmatrix} I_{XX_b} & 0 & -I_{XZ_b}\\ 0 & I_{YY_b} & 0\\ -I_{ZX_b} & 0 & I_{ZZ_b}\end{bmatrix}^{-1}\begin{bmatrix} M_{X_b}+\left(I_{YY_b}-I_{ZZ_b}\right)qr+I_{XZ_b}pq\\ M_{Y_b}+\left(I_{ZZ_b}-I_{XX_b}\right)pr+I_{XZ_b}(r^2-p^2)\\ M_{Z_b}+\left(I_{XX_b}-I_{YY_b}\right)pq-I_{XZ_b}qr\end{bmatrix} \quad (6.2)$$

$$\begin{bmatrix}x_f\\ y_f\\ z_f\end{bmatrix}=\begin{bmatrix} c\theta c\psi & s\phi s\theta c\psi-c\phi s\psi & c\phi s\theta c\psi+s\phi s\psi\\ c\theta s\psi & s\phi s\theta s\psi+c\phi c\psi & c\phi s\theta s\psi-s\phi c\psi\\ -s\theta & s\phi c\theta & c\phi c\theta\end{bmatrix}\begin{bmatrix}u\\ v\\ w\end{bmatrix}+\begin{bmatrix}v_{WX_f}\\ v_{WY_f}\\ v_{WZ_f}\end{bmatrix} \quad (6.3)$$

$$\begin{bmatrix}\phi\\ \theta\\ \psi\end{bmatrix}=\begin{bmatrix}1 & s\phi s\theta/c\theta & c\phi s\theta/c\theta\\ 0 & c\phi & -s\phi\\ 0 & s\phi/c\theta & c\phi/c\theta\end{bmatrix}\cdot\begin{bmatrix}p\\ q\\ r\end{bmatrix} \quad (6.4)$$

where:

$I_{XX_b}, I_{YY_b}, I_{ZZ_b}, I_{XZ_b}$ = non-null components of the inertia tensor [kg m^2];

$v_{WX_f}, v_{WY_f}, v_{WZ_f}$ = components of the wind vector along the three axes of the Earth-fixed reference frame [m s^{-1}];

$F_{X_b}, F_{Y_b}, F_{Z_b}$ = resultants of the aerodynamic and propulsive forces acting along the three axes of the body reference frame [N];

$M_{X_b}, M_{Y_b}, M_{Z_b}$ = resultants of the aerodynamic and propulsive moments acting around the three axes of the body reference frame [N m];

x_f, y_f, z_f = components of the relative position vector between the Earth-fixed reference frame and the body centre of mass [m];

ϕ, θ, ψ = Euler angles, respectively representing bank, pitch and heading rotations [rad];

u, v, w = translational velocity components along the three axes of the body reference frame [m s^{-1}];

p, q, r = rotational velocity components around the three axes of the body reference frame; respectively representing rolling, pitching and yawing rates [rad s^{-1}];

W, g = A/C weight [N] and gravity acceleration [m s^{-2}];

s, c = sine and cosine operators.

In particular, Eq. 6.1 represent the translational dynamics, Eq. 6.2 the rotational dynamics, Eq. 6.3 the kinematics and Eq. 6.4 the Euler rotations of the body frame with respect to the Earth-fixed reference frame.

An alternative approach adopted to derive a simplified set of equations for atmospheric flight is based on the approximation of the A/C as a point-mass object thereby neglecting the aspects associated to its rotational dynamics. The resulting 3DOF models are based on Newton's second law expressed along the coordinate axes of the body frame and on the motion of such frame with respect to an inertial reference frame of convenience. 3DOF models can involve either a constant mass or a variable mass. Models belonging to the first category are adopted when the analysed timeframe is relatively short (so that the fuel consumption may be neglected) or when no fuel is consumed, such as in the case of sailplanes or total engine failures. The 3DOF A/C dynamics model equations can be expressed as follows (Valenzuela and Rivas, 2011):

$$\frac{dV}{dt} = \frac{T\cos\alpha - D(V,h,L)}{m} - g\sin\gamma \tag{6.5}$$

$$\frac{d\gamma}{dt} = (T\sin\alpha + L)\frac{\cos\phi}{mV} - \frac{g\cos\gamma}{V} \tag{6.6}$$

$$\frac{d\psi}{dt} = (T\sin\alpha + L)\frac{\sin\phi}{mV\cos\gamma} \tag{6.7}$$

$$\frac{d\Phi}{dt} = \frac{V cos\gamma \cos\psi}{r_M + h} \tag{6.8}$$

$$\frac{d\Lambda}{dt} = \frac{V cos\gamma \sin\psi}{\cos\Phi\,(r_T + h)} \tag{6.9}$$

$$\frac{d\mathrm{h}}{dt} = V sin\gamma \tag{6.10}$$

$$\frac{dm}{dt} = -F_F = -c(V,h)T \tag{6.11}$$

where:

m = aircraft mass [kg];

V = longitudinal velocity [m s^{-1}];

T = thrust magnitude [N];

α = angle of attack [rad];

h = altitude [m];

L = lift magnitude [N];

D = drag magnitude [N];

g = gravity acceleration [m s^{-2}];

γ = flight path angle [rad];

ϕ = bank or roll angle [rad];

ψ = heading angle [rad];

c = specific fuel consumption [kg/sN];

F_F = fuel flow [l s^{-1}];

Φ = geodetic latitude [rad];

Λ = geodetic longitude [rad];

r_m = meridional radius of curvature [m];

r_t = transverse radius of curvature [m].

Key assumptions adopted in the 3DOF model formulation are:

- Earth's shape is approximated as an ellipsoid using WGS-84 parameters.
- The atmosphere is considered at rest relatively to the earth.
- A standard ISA atmospheric model is adopted to describe temperature, pressure and density variations as a function of altitude.
- The A/C is modelled as a rigid body with a vertical plane of symmetry.
- The A/C mass reduction in flight is due to fuel consumption only.
- Thrust, aerodynamic forces and weight act on the A/C Centre of Gravity (CG).
- All manoeuvres are well coordinated and no sideslip is present.
- The flight is subsonic and the thrust vector is aligned with the longitudinal axis of the aircraft (body frame).

The classical formulas for lift and drag are:

$$L = \frac{1}{2}\rho V^2 C_L \mathrm{S} \tag{6.12}$$

$$D = \frac{1}{2}\rho V^2 C_D S \tag{6.13}$$

where C_L is the lift coefficient, C_D is the drag coefficient, S is the wing area and ρ is the air density. Both C_L and C_D can be obtained from the aircraft polar curves when available (practical avionics implementations typically adopt lookup tables). Alternatively, the lift and drag coefficients are computed using the available derivatives. For the lift coefficient, the following equation is used:

$$C_L = C_{L0} + C_L^{\alpha}\alpha \tag{6.14}$$

where C_{L0} is the zero-alpha lift (i.e., the lift coefficient at zero angle of attack), and C_L^{α} is the alpha derivative (i.e., the first-order variation of C_L with respect to the angle of attack). For the drag coefficient a similar approach can be adopted and the following equation is used:

$$C_D = C_{D0} + \frac{\left(C_L - C_{Lmin_D}\right)^2 S}{\pi e_O b^2} \tag{6.15}$$

where C_{D0} is the minimum drag coefficient of the airplane, C_{Lmin_D} is the lift at minimum drag, which is usually but not necessarily equal to C_{L0}, b is the wing span and e_O is the Oswald efficiency factor (for conventional fixed-wing aircraft with moderate aspect ratio and sweep, e_O is typically between 0.7 and 0.85).

6DOF and 3DOF rigid-body models are normally unsuitable for the calculation of A/C trajectories over extended time periods and this is due to the complexity of the resulting trajectory estimation problem, accumulation of numerical errors, environmental perturbations and the presence of short period modes that are likely to generate instabilities (Imado et al., 2011). These models are nevertheless fundamental for the study of A/C manoeuvres and more in general for the analysis of A/C dynamic stability and control. Therefore, they can be successfully adopted in trajectory prediction/optimisation studies, especially in combination with a careful selection of engine models and path constraints.

6.4 FPG MODULE DYNAMICS MODEL IMPLEMENTATION

The ABIA FPG module employs the 3DOF point-and-variable mass model of Equations (6.5) to (6.11), subject to the following additional assumptions:

- The flight data available needed for trajectory computation are those typically provided by state-of-the-art A/C sensors and integrated avionic systems (GNSS, INS, air data computer, engine instruments, etc.).
- Since the load factor ($n = 1/\cos\mu = L/mg$) is accurately measured by the on-board avionics, we replace the lift force magnitude (L) in Equations (6.6) and (6.7) giving:

$$\frac{d\gamma}{dt} = \frac{1}{V}\left(\frac{T\sin\alpha}{nm} + g - g\cos\gamma\right) \tag{6.16}$$

$$\frac{d\psi}{dt} = (T\sin\alpha + nmg)\frac{\sin\mu}{mV\cos\gamma} \tag{6.17}$$

- As the angle of attack (α) and the pitch angle (θ) are measured by the on-board avionics, the flight path angle in Equations (6.5), (6.6), (6.7) and (6.10) is given by:

$$\gamma = \theta - \alpha \tag{6.18}$$

The thrust parameters needed are the thrust given by the engine T and the F_F (or the specific fuel consumption, s_{sfc} from which F_F can be calculated). Both are function of the current altitude, velocity and engine power settings. Different propulsive technologies are associated with largely dissimilar energy sources and consumption rates in a variety of aeronautical applications. This fact is increasingly evident with the advent of novel alternative propulsion systems for manned and unmanned A/C applications. Nevertheless, most of the currently operated transport A/C rely on air-breathing internal combustion engines of the turbofan or turboprop type (employing hydrocarbon fuels), which are an established technology with efficient and cost-effective production and supply chains. Therefore, we start this section with a brief outline of useful models for the estimation of fuel consumption and thrust in current

generation turbojet and turboprop engines. In the trajectory prediction/optimisation context, steady state empirical models are commonly employed to reproduce the dependencies of thrust and fuel flow on altitude (z), true airspeed (v_{TAS}), temperature and throttle (τ), which are the only parameters directly associated with the A/C trajectory. The following expressions were adopted in the development of Eurocontrol Base of Aircraft Data (BADA), to determine the maximum thrust (T_{max}) and the fuel flow (F_F) of a turbofan propelled A/C (Eurocontrol, 2014):

$$(T_{\max})_{ISA} = C_{T1}\left(1 - \frac{H_P}{C_{T2}} + C_{T3}H_P^2\right) \tag{6.19}$$

$$T_{max} = (T_{\max})_{ISA} \times [1 - C_{T5}(\Delta T - C_{T4})] \tag{6.20}$$

$$F_F = \max\left[T_{HR}\, C_{f1}\left(1 + \frac{v_{TAS}}{C_{f2}}\right),\ C_{f3}\left(1 - \frac{H_P}{C_{f4}}\right)\right] \tag{6.21}$$

where T_{HR} is the thrust acting parallel to the aircraft velocity vector, H_P is the geopotential pressure altitude in feet, ΔT is the deviation from the standard atmosphere temperature in kelvin, v_{TAS} is the true airspeed. $C_{T1} \dots C_{T5}$, $C_{f1} \dots C_{f4}$ are the empirical thrust and fuel flow coefficients, which are also supplied as part of BADA for a considerable number of currently operating A/C (Eurocontrol, 2014). Similarly, the following expressions were adopted in BADA to determine the maximum climb thrust and fuel flow of a turboprop propelled A/C:

$$(T_{\max})_{ISA} = \frac{C_{T1}}{v_{TAS}}\left(1 - \frac{H_P}{C_{T2}}\right) + C_{T3} \tag{6.22}$$

$$T_{max} = (T_{\max})_{ISA} \times [1 - C_{T5}(\Delta T - C_{T4})] \tag{6.23}$$

$$F_F = \max\begin{bmatrix} T_{HR}\, C_{f1}\left(1 - \frac{v_{TAS}}{C_{f2}}\right)\cdot\left(\frac{v_{TAS}}{1000}\right), \\ C_{f3}\left(1 - \frac{H_P}{C_{f4}}\right) \end{bmatrix} \tag{6.24}$$

where again $C_{T1} \dots C_{T3}$, $C_{f1} \dots C_{f4}$ are also supplied as part of BADA for a considerable number of currently operating A/C (Eurocontrol, 2014). In this

research, this approach was successfully employed for the A320 simulation case studies described in this thesis.

Unfortunately, no open source database is currently available for the variety of reciprocating engines (i.e., internal combustion piston engines) currently employed in the vast majority of small size UAV and general aviation light A/C. Therefore, we considering as an example one of the propulsive systems mounted on the AEROSONDE UAV, which employs a standard piston engine coupled to a fixed pitch propeller. For this system, the thrust force can be calculated as follows (Unmanned Dynamics, 2003):

$$T = \frac{4}{\pi^2}\rho R_p^4 \Omega^2 C_T \tag{6.25}$$

where Ω is the propeller rotation speed directly computed with the engine rotation speed and the gearbox ratio, R_P is the propeller radius and C_T is the thrust coefficient. The propeller moment is given by:

$$M_P = -\frac{4}{\pi^3}\rho R_p^5 \Omega^2 C_P \tag{6.26}$$

where C_P is the power coefficient. A convenient parameter is the advance ratio (J_{ar}), which is given by:

$$J_{ar} = \frac{\pi V}{\Omega R_p} \tag{6.27}$$

Fig. 6-2 and Fig. 6-3 show, respectively, the C_T and C_P variations as a function of J_{ar}. The second parameter to be computed is F_F, which depends of the engine rotation speed and of the Manifold Pressure (MAP). This is the pressure at which the fuel-air mixture is forced into cylinders of the engine and it is a function of throttle setting (i.e., pilot engine control) and atmospheric pressure.

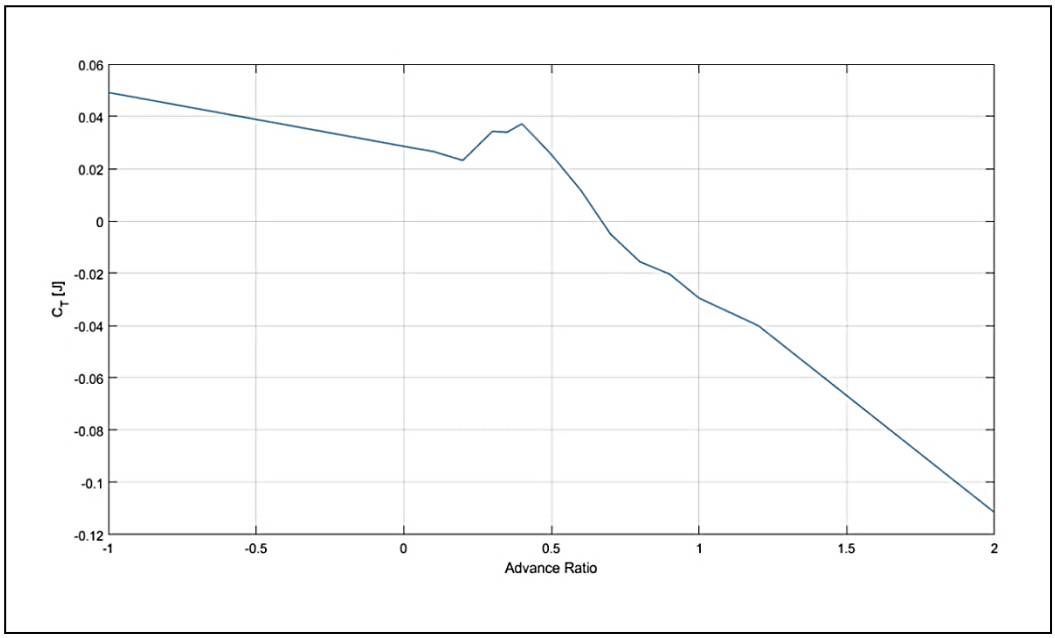


Figure 6-2. Thrust coefficient as a function of advance ratio (Unmanned Dynamics, 2012).

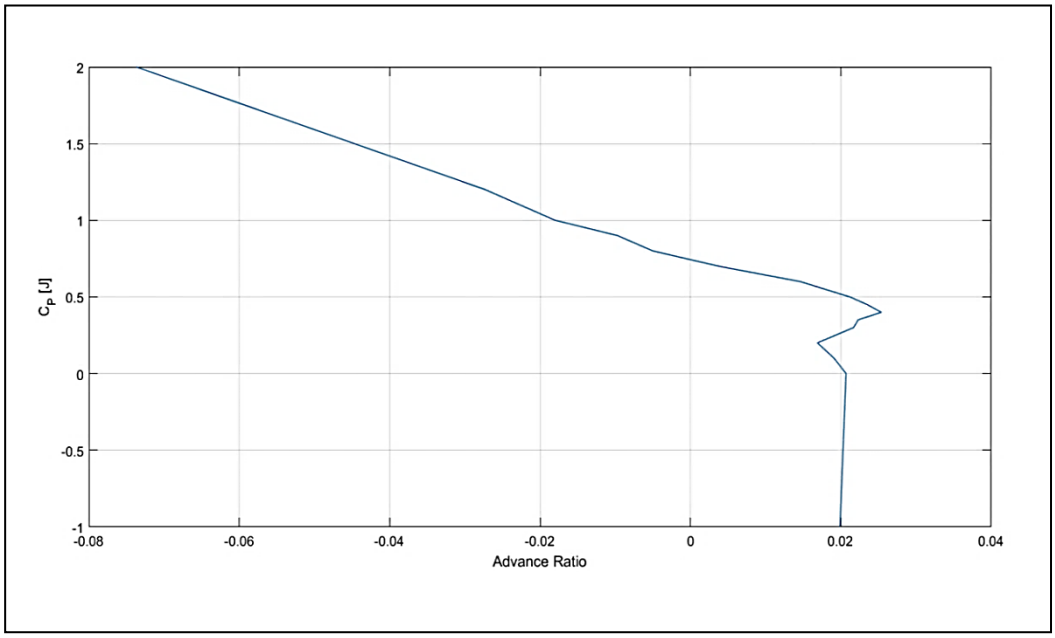


Figure 6-3. Power coefficient as a function of advance ratio (Unmanned Dynamics, 2012). .

The mapping of the fuel flow versus the engine Revolutions per Minute (RPM) and the MAP, is shown in Fig. 6-4. In our simulation case studies, we assume that the RPM always reaches the maximum point (i.e., the RPM value always gets the maximum power for a given throttle demand).

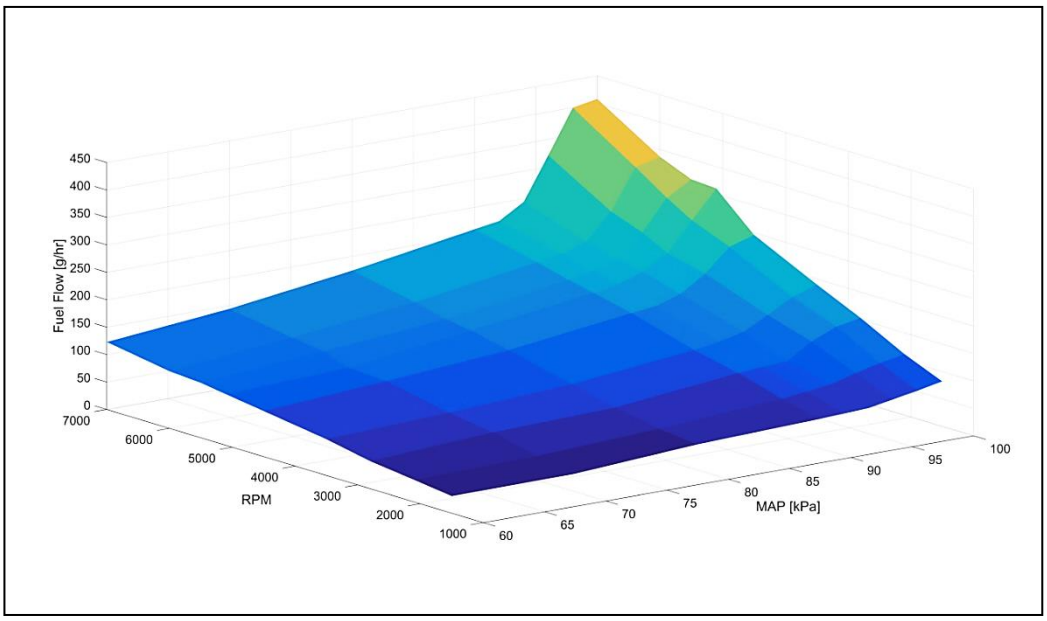


Figure 6-4. AEROSONDE fuel flow map (Unmanned Dynamics, 2012). .

If the availability of detailed data is limited for reciprocating engines, it is practically impossible to find detailed data in the public domain on military A/C propulsive systems performance. Based on the research and flight test activities performed in the initial phases of this research (T-ABIA), approximated A/C performance data were used for the TORNADO-IDS A/C. All relevant aerodynamic and propulsive parameters used for the TORNADO-IDS, A320 and AEROSONDE 3DOF practical implementations are presented in Appendix B.

6.5 PATH CONSTRAINTS AND BOUNDARY CONDITIONS

As discussed in Chapter 3, most GNSS integrity degradations depend on the relative positions of the GNSS receiver antenna and each satellite. The relative motion of the GNSS receiver antenna and the satellite is also crucial. Therefore degradations related to one satellite do not affect the system in the same manner as the others. The CIF/WIF thresholds defined in Chapter 4 for antenna obscuration, Doppler shift, multipath, carrier, interference and satellite geometry degradations are capable of detecting the adverse conditions leading to unacceptable degradations or complete losses of the satellite signals. An analysis of the different type of

degradations results in inferring that a common criterion based on satellite elevation variation in the body frame can be adopted as a geometric constrain in the trajectory optimisation process. This applies to all degradations except Doppler shift (so, for this phenomenon a separate analysis is required). The elevation and azimuth angles in body frame (blue) are depicted in Fig. 6-5 where P_S is the satellite position, P_{SXY} is the satellite position projected into the XY plane, R is the line of sight vector, E is the elevation angle and Az is the azimuth angle. The right-hand rule gives the direction of rotation of both elevation and azimuth angles. Considering the top view of the A/C, when the elevation angle increases in the positive direction (going up), the azimuth is rotating in a clockwise direction. The elevation angle in the body frame is computed using the simple trigonometry relation:

$$E = \sin^{-1}\left(\frac{R_z}{|R|}\right) \tag{6.28}$$

where R_z is the Z-axis component of the line of sight vector.

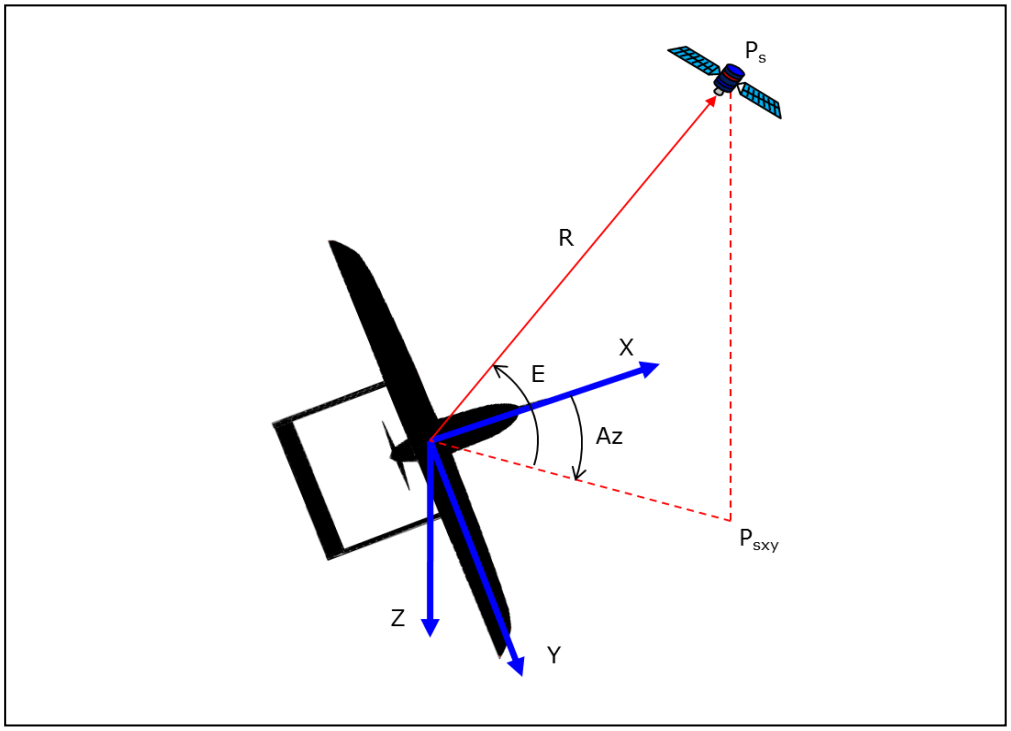


Figure 6-5. Elevation and azimuth in body frame.

In order to be used as a dynamic constraint for trajectory optimisation, the elevation angle to each satellite is associated to Euler angles by converting the LOS vector

from the ENU reference frame to the body frame. The positions of the A/C and satellite are given in the ENU frame, so the LOS vector is computed using:

$$\vec{R} = \vec{P_S} - \vec{P_R} \tag{6.29}$$

where P_R is the receiver position vector in the ENU frame. The conversion in body frame is obtained using the matrix:

$$C_{BODY}^{ENU} = \begin{bmatrix} C_\mu C_\psi + S_\mu S_\theta S_\psi & -C_\mu S_\psi + S_\mu S_\Gamma C_\psi & -S_\mu C_\theta \\ C_\theta S_\psi & C_\theta C_\psi & S_\theta \\ S_\mu C_\psi - C_\mu S_\theta S_\psi & -S_\mu S_\psi - C_\mu S_\theta C_\psi & C_\mu C_\theta \end{bmatrix} \tag{6.30}$$

where:

S_θ = sine of the pitch angle;

C_θ = cosine of the pitch angle;

S_μ = sine of the bank angle;

C_μ = cosine of the bank angle;

S_ψ = sine of the yaw angle;

C_ψ = cosine of the yaw angle.

As discussed in Chapter 4, the magnitude of the Doppler shift this can be calculated by:

$$\Delta f_n = f\left(\frac{|\vec{v_n}| \mp |\vec{v_a}|}{c}\right) cos\chi_n \tag{6.31}$$

where:

$\vec{v_n}$ = n^{th} satellite velocity component along the LOS;

$\vec{v_a}$ = aircraft velocity projection along the LOS;

c = speed of light [m s^{-1}];

f = GNSS signal frequency [Hz];

χ_n = angle between the aircraft velocity vector and the n^{th} satellite LOS.

When the Doppler CIF thresholds described in Chapter 5 are exceeded, the FPG module initiate an optimisation process aiming to avoid any further observed increase in Doppler shift. In particular, the implemented algorithm studies the variations of $\vec{v_n}$ and $\vec{v_a}$ for each tracked satellite and imposes geometric constraints

to the trajectory that are accounted for in the trajectory optimisation process. With reference to the geometry illustrated in Fig. 6-6, the following trigonometric relationship holds true:

$$(\vec{v}\cos\chi_n)\sin E_n = \vec{v}\cos\chi_n' \tag{6.32}$$

where:

$\vec{v}$ = aircraft velocity vector;

E_n = elevation angle of the nth satellite;

χ_n = relative bearing of the aircraft to the satellite;

χ_n' = azimuth of the LOS projection in the antenna plane.

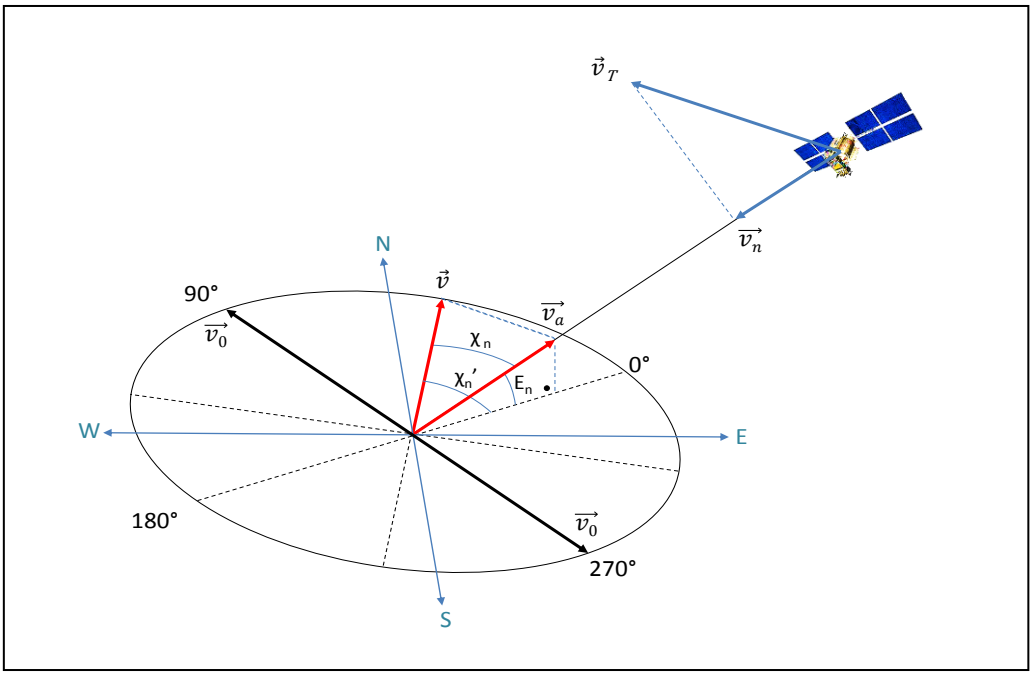


Figure 6-6. Reference geometry for Doppler shift analysis.

From Equations (6.31) and (6.32), we can determine the aircraft-satellite relative geometric conditions that maximise or minimise Doppler shift. In particular, combining the two equations we obtain:

$$\Delta f_n = f\left(\frac{|\vec{v_n}| \mp |\vec{v_a}|}{c}\right)\frac{\cos\chi_n'}{\sin E_n} \tag{6.33}$$

Eq. (6.33) shows that both the elevation angle of the satellite and the aircraft relative bearing to the satellite affect the magnitude of the Doppler shift. In particular, reductions of E_n lead to increases in Doppler shift, while $\chi_n{}'$ drives increments or decrements in Doppler shift depending on the size of the angle and the direction of the A/C velocity vector. By inspecting Fig. 6-6, it is evident that a relative bearing of 90° and 270° would lead to a null Doppler shift as in this case there is no component of the A/C velocity vector ($\overrightarrow{v_0}$ in this case) in the LOS to the satellite. However, in all other cases (i.e., $\vec{v} \neq \overrightarrow{v_0}$), such a component would be present and this would lead to increments or decrements in Doppler shift depending on the relative directions of the vectors $\vec{v}$ and $\overrightarrow{v_n}$. This fact is better shown in Fig. 6-7, where we assume steady flight without loss of generality.

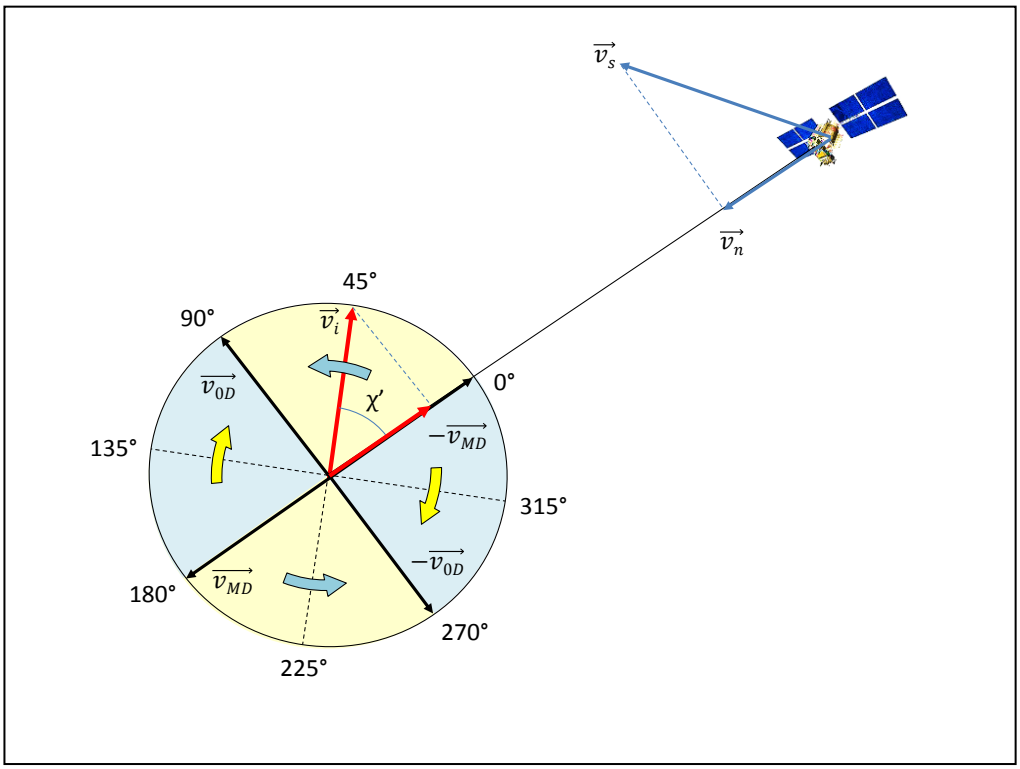


Figure 6-7. Reference geometry for Doppler shift manoeuvre corrections.

As the time required for typical A/C heading change manoeuvres is much shorter than the timeframe associate to significant satellite constellation changes, each satellite can be considered stationary in the body reference frame of the manoeuvring aircraft. Therefore, during manoeuvres leading to Doppler CIFs, we can consider an

initial aircraft velocity vector $\overrightarrow{v_i}$ and define path constraints that avoid the Doppler WIF. This can be done by imposing that the aircraft increases the heading rates towards the directions $\overrightarrow{v_0}$ or -$\overrightarrow{v_0}$ and minimises the heading rates towards the directions $\overrightarrow{v_M}$ and -$\overrightarrow{v_M}$. The choice of $\overrightarrow{v_0}$ or -$\overrightarrow{v_0}$ is based simply on the minimum required heading change (i.e., minimum required time to accomplish the correction). Regarding the elevation angle (*E*) dependency of Doppler shift, Eq. (6.33) shows that minimising the elevation angle becomes an objective also in terms of Doppler trajectory optimisation.

6.6 COST FUNCTIONS

The selection of the optimal trajectory is based on minimising a cost function of the form (Sabatini et al., 2014 c):

$$J = w_t \cdot \mathrm{t} + w_f \int [SFC \cdot T(t)]dt \tag{6.31}$$

where SFC $[kg\ N^{-1}s]$ is the specific fuel consumption, $T(t)$ is the thrust profile and $\{w_t\ , w_f\}$ are the weightings attributed to time and fuel minimisation objectives. In safety-critical UAS SAA applications, this cost function can be expanded to include other parameters such as the distance of the host aircraft from the avoidance volume associated with a ground obstacle or a conflicting air traffic (Sabatini et al., 2014 c):

$$J = w_t \cdot \mathrm{t}_{SAFE} + w_f \int [SFC \cdot T(t)]dt - \mathrm{w}_d \cdot D_{min} + \\ - w_{id} \cdot \int D(t)dt \tag{6.32}$$

where $\mathrm{D(t)}$ is the estimated distance of the generated avoidance trajectory points from the avoidance volume associated with the obstacle, $D_{min} = min[D(t)]$ is the estimated minimum distance of the avoidance trajectory from the avoidance volume, $t_{SAFE} = t|_{D_{min}}$ is the time at which the safe avoidance condition is successfully attained and $\{w_t\ , w_f, w_d, w_{id}\}$ are the weightings attributed to time, fuel, distance and integral distance respectively. In time-critical avoidance tasks appropriate higher

weightings are used for time and distance cost elements and an automated gain control function can be implemented taking into account the host aircraft-obstacle relative dynamics. Further information about possible UAS SAA implementations is provided in Chapter 8.

6.7 TRAJECTORY OPTIMISATION ALGORITHMS

As discussed above, the IFG outputs (CIFs and WIFs) are used in the FPG module. The key requirement of the FPG module is to generate guidance information that optimize the short-term Autopilot and Flight Director System (A&FDS) control parameters (e.g., attitude angles and airspeed), as well as the medium/long-term trajectory to be flown. The information update process starts from the current information stored in the Flight Management System (FMS) and produces a new set of geometric/dynamic constraints in all conditions where CIFs are raised (to avoid WIFs). A trajectory optimisation process is then initiated to meet the specified mission objectives and to comply with this new set of constraints. The results obtained from the computation of the optimal trajectory can be utilized as new inputs to the IFG software (both in real-time and mission planning implementations), so further updates can be performed when needed to prevent the triggering of CIFs and WIFs.

From a practical point of view, trajectory optimisation can be defined as the action of finding the inputs to a given system characterised by a set of equations of motion and dynamic constraints, which will maximise or minimise specific parameters (e.g., time, fuel consumption, distance from another aircraft, relative velocities). In most cases, optimisation problems cannot be solved analytically and, therefore, numerical iterative methods need to be used. One of the key challenges of the online trajectory optimisation task is to produce results in real-time (real-time here is intended for the specific application/scenario involved), since the mathematical algorithms and the associated numerical solvers have to be capable of producing accurate and usable outputs in a relatively short time.

Both offline and online aircraft trajectory optimisation tasks are typically formulated as Optimal Control Problems (OCP). This is because optimal control theory provides a well-established framework for the determination of dynamic systems optimal trajectories (in a mathematical sense). In the OCP formulation, the trajectory optimisation problem can be analytically stated as follows (Rao, 2010-a):

"*Determine the states* $x(t) \in \mathbb{R}^n$, *the controls* $u(t) \in \mathbb{R}^m$, *the parameters* $p \in \mathbb{R}^q$, *the initial time* $t_0 \in \mathbb{R}$ *and the final time* $t_f \in \mathbb{R} \mid t_f > t_0$, *that optimise the performance index:*

$$J = \Phi[x(t_f), u(t_f), p] + \int_{t_0}^{t_f} \Psi\,[x(t), u(t), p]\,dt \tag{6.33}$$

subject to the dynamic constraints:

$$\dot{x}(t) = f[x(t), u(t), t, p] \tag{6.34}$$

to the path constraints:

$$C_{min} \leq C[x(t), u(t), t; p] \leq C_{max} \tag{6.35}$$

and to the boundary conditions:

$$\mathcal{B}_{min} \leq \mathcal{B}[x(t_0), x(t_f), u(t_0), u(t_f); p] \leq \mathcal{B}_{max} \tag{6.36}$$

where Φ *is the Mayer term and* Ψ *is the Lagrange term of the cost function expressed in a Bolza form."*

OCP can be solved using various methods and the two main categories are: direct methods and indirect methods (Betts, 1998), (Rao, 2010-a), (Lewis et al., 2012), (Gardi et al., 2016). The indirect methods are based on calculus of variation. The problem needs to have maximum and minimum boundaries and an initial guess is made between the boundaries, followed by a computation of the different values of the outputs and constraints. The errors between the outputs and the terminal conditions are compared and if the errors are above the specified thresholds, the initial guess is modified accordingly and the process starts again until the errors reach values that meet the threshold conditions. Indirect methods for optimisation present several advantages since the base algorithm can be directly applied to a wide number of optimisation problems with a relatively small number of variables, so that

computational requirements are reduced. However, the Hamiltonian systems required by the calculus of variation are often unstable and the error with unknown initial conditions grows rapidly. If the initial conditions estimation differs widely from the actual conditions, the system will converge slowly or even diverge in some cases. Therefore, in the case of complex problems (e.g., high dynamics conditions) a more appropriate method must be employed.

In the case of the direct methods, the aircraft dynamics (continuous) variables are translated into a number of discretised state and command parameters. The problem is then transformed into a finite-dimensional non-linear optimisation problem and the states are implicitly integrated with a quadrature method for a subset of points (nodes) chosen in the main interval defined by the maximum and minimum boundaries. These quadrature methods can be one of the Euler methods, midpoint method, implicit Runge-Kutta method, etc. Direct methods are further divided into direct shooting and collocation methods. Direct shooting methods employ user defined analytical functions to parameterise the states and controls for the entire OCP domain, while collocation methods adopt piecewise polynomial functions to parameterise states and control. The most computationally efficient class of collocation methods adopts linearly independent polynomial functions and is called pseudo-spectral (the spectral decomposition is not performed in the frequency domain but in the time domain, hence the “pseudo” prefix). The main drawbacks of direct methods are a strong accuracy dependency on the selected discretisation functions and the large number of variables introduced by the parameterisation of states and controls, as well as by the implicit integration of subintervals. Therefore, the computational power required for direct methods can be significant. This problem has often being solved considering that the Jacobian and Hessian of the constraints comprise a majority of null derivatives. The direct methods present advantages in terms of the radii of divergence, which is large; this means that the convergence to the optimal solution is fast even with a poor estimation of initial conditions. The number of iterations and the convergence time depend entirely on the definition of the problem and how well the states and variables are parameterised; hence, there is a direct impact on the control time. Compared with indirect methods,

in the direct methods there are no means to know how close a given solution is to the optimal solution, which instead is possible in the case of indirect computation.

Planning or optimising a new trajectory for an aircraft is subject to numerous objectives and constraints. Those can be derived from Air Traffic Management (ATM) imposed requirements, flight plan/mission objectives, Separation Maintenance/Collision Avoidance (SM/CA), and environmental requirements. Thus, the optimisation process needs to find the best trade-off between all objectives subject to the dynamics/operational constraints associated with the platform, the planned mission and the current flight profile/phase. Clearly, different sets of data (from widely differing sources) and significantly different objectives/constraints can be used at the mission planning stage and in real-time flight trajectory optimisation tasks. ABIA offers the advantage of meeting the requirements of strategic and tactical air operation tasks, with a possibility to also enhance the performance of SM/CA systems that rely on GNSS as the primary source of navigation data. These include modern cooperative SM/CA systems (e.g., ADS-B) or non-cooperative sensors integrated with GNSS-driven Navigation, Guidance and Control (NGC) systems.

For a practical implementation, some additional considerations have to be made. The new trajectory determined by the FPG module has to be completely flyable by the aircraft and the mission (defined in the FMS flight plan) shall not be compromised by the new trajectory. Additionally, the new trajectory shall not lead to other hazards like terrain, traffic or weather. As a consequence, the FPG module has to be designed to allow the dynamic setting of boundary conditions for the entire set of variables involved. From the discussion above the following key requirements are derived:

1. The FPG module shall react to any CIF/WIF triggering as follows:
    a. Initiating an early-correction loop that prevents the occurrence of a WIF, as soon as CIF is generated.
    b. Initiating an immediate (emergency) correction in the unlikely event of a WIF not preceded by a CIF.

2. As soon as activated, the FPG module shall set dynamic constraints that allow the computation of an optimal flight trajectory that prevents the triggering of new CIFs/WIFs and that minimises the deviations from the original aircraft trajectory (e.g., FMS flight plan).

6.7.1 Mission Planning and ATM Applications

Based on the literature review (Betts et al, 1995), (Betts, 1998), (Rao, 2010-a), (Von Stryk et al., 1992), (Zhou et al., 1996), (Rao, 2010-b), (Lewis et al., 2012), (Gardi et al., 2016), the Radau pseudospectral method was selected for the ABIA mission planning implementation (offline IFG and FPG modules). This widely used method employs orthogonal collocation Gaussian quadrature implicit integration, where collocation is performed at the Legendre-Gauss-Radau points. The Generalised Pseudospectral Optimal Control Software, version 2 (GPOPS-II) was chosen for ABIA due to its availability in the public domain and its documented suitability for aerospace applications (Rao et al., 2010). GPOPS-II is implemented as a MATLAB toolbox were the user defines the dynamics/path constraints, the boundary conditions and the cost functions that apply to a specific OCP. The user can also define a number of parameters used in the optimisation process, including the quadrature mesh characteristics, the maximum number of iterations and the numerical differentiation method. Further details about GPOPS-II and some examples of aerospace OCPs can be found in (Patterson et al., 2014). The suitability of these techniques for ATM and Air Traffic Flow Management (ATFM) offline and online operations has been demonstrated in recent research (Gardi et al, 2016).

6.7.2 Real-time Applications

For the real-time FPG module implementation, a suitable Direct Constrained Optimisation (DCO) method is implemented. In this method the aircraft dynamics model is used to generate a number of feasible flight trajectories that also satisfy the GNSS constraints. The feasible trajectories are calculated by initialising the aircraft dynamics model with a Manoeuvre Identification Algorithm (MIA). The MIA

allows identifying a sub-set of ADM equations (and the associated boundary conditions of states and controls) that must be integrated to predict future states and to determine the optimal controls that minimise the cost functions. A schematic representation of the FPG module DCO implementation is shown in Fig. 6-8.

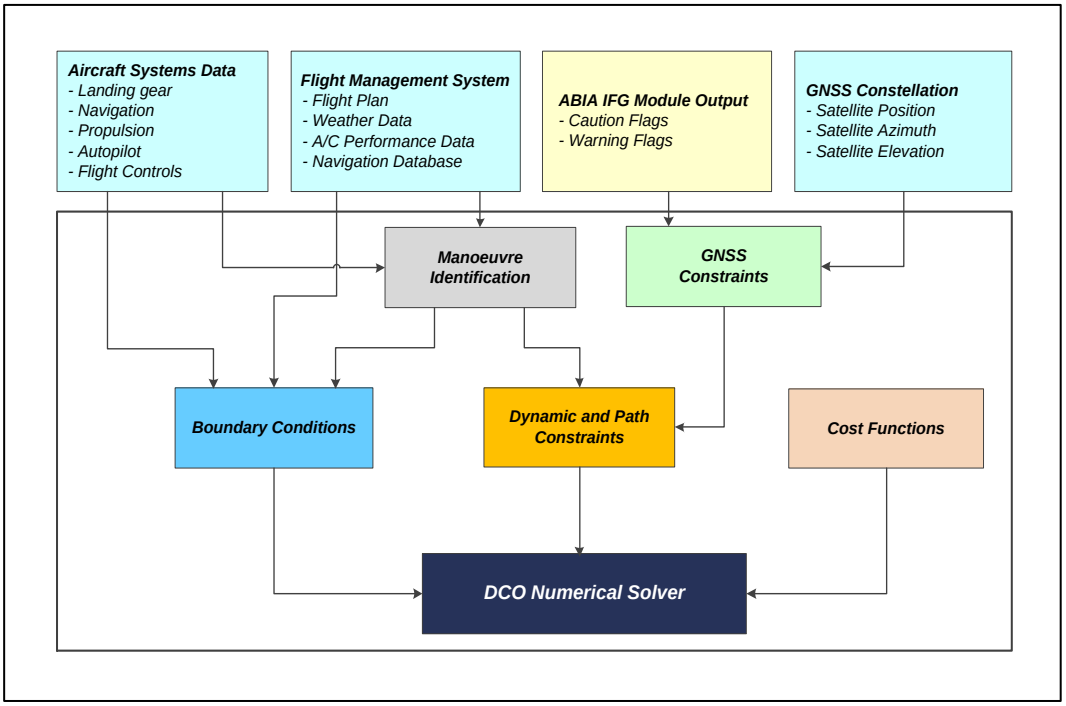


Figure 6-8. DCO implementation scheme.

Although this method does not implement an iterative algorithm that converges to the mathematical optimum, it is preferred for real-time safety-critical applications due to its robustness, much reduced complexity and faster convergence rate. Additionally, the DCO prevents problems of non-convergence or divergence frequently experienced in OCPs for highly non-linear dynamic systems. In the ABIA FPG implementation, the DCO algorithm is designed so that the deviations from the pre-planned flight trajectory (e.g., FMS flight plan) are minimised. This is achieved by introducing additional geometric (path) constraints in the process and implementing a Bézier approximation curve algorithm to guarantee smoothness of the resulting aircraft trajectory (Delahaye et al., 2014). Further details about the criteria adopted for manoeuvre identification and how these are used to set dynamic/path constraints in the DCO process are described in Appendix C.

6.7.3 Optimisation Criteria

In both real-time and mission planning implementations, the flight trajectory optimisation algorithm is initiated when integrity degradations are predicted (CIF generated) by the IFG module. The optimisation criteria adopted in the FPG module are the following:

a) With 5 satellites in view, the value of E_n for each satellite tracked shall be 5 degrees greater than the threshold value causing the activation of any CIF.

b) With 4 satellites in view, the value of E_n for each satellite tracked shall be 10 degrees greater than the threshold value causing the activation of any CIF.

c) If the CIF is not due to Doppler shift, the minimum elevation limit is set to 5 degrees above the current SV elevation angle.

d) If the CIF is due to Doppler shift, the aircraft heading rates are increased towards the directions $\overrightarrow{v_0}$ or $-\overrightarrow{v_0}$ and reduced in the directions $\overrightarrow{v_M}$ and $-\overrightarrow{v_M}$. The choice of $\overrightarrow{v_0}$ or $-\overrightarrow{v_0}$ is based on the minimum required heading change.

e) Constrained Geometric Optimisation (CGO) or Pseudospectral Multi-Objective (PMO) Trajectory Optimisation Techniques are used for real-time FPG implementations and for offline mission planning applications respectively.

The boundary values of each parameter involved in the trajectory optimisation process are obtained from the following sources:

a) Navigation Data and Flight Parameters at CIF (NFC), which define the initial conditions when the optimization process in started (i.e., at CIF generation time step).

b) Planned Flight Trajectory (PFT), which define the final condition of the optimization problem. The final condition gives the point when the A/C will go back on the initially planned trajectory (e.g., the trajectory stored in the FMS).

c) A/C Dynamic Constraints (ADC), which define the minimum and maximum values of the state and control variables.

d) Satellite Constellation Data (SCD), which provide the azimuth and elevation boundaries for the path constraints.

6.8 SIMULATION CASE STUDIES

Simulation case studies were carried out on the AEROSONDE UAV to validate the FPG module mission planning and real-time functionalities. The representative flight profile shown in Fig. 6-9 (e.g., a typical UAV flight plan) was used as a reference to test both the PMO and CGO trajectory optimisation capabilities.

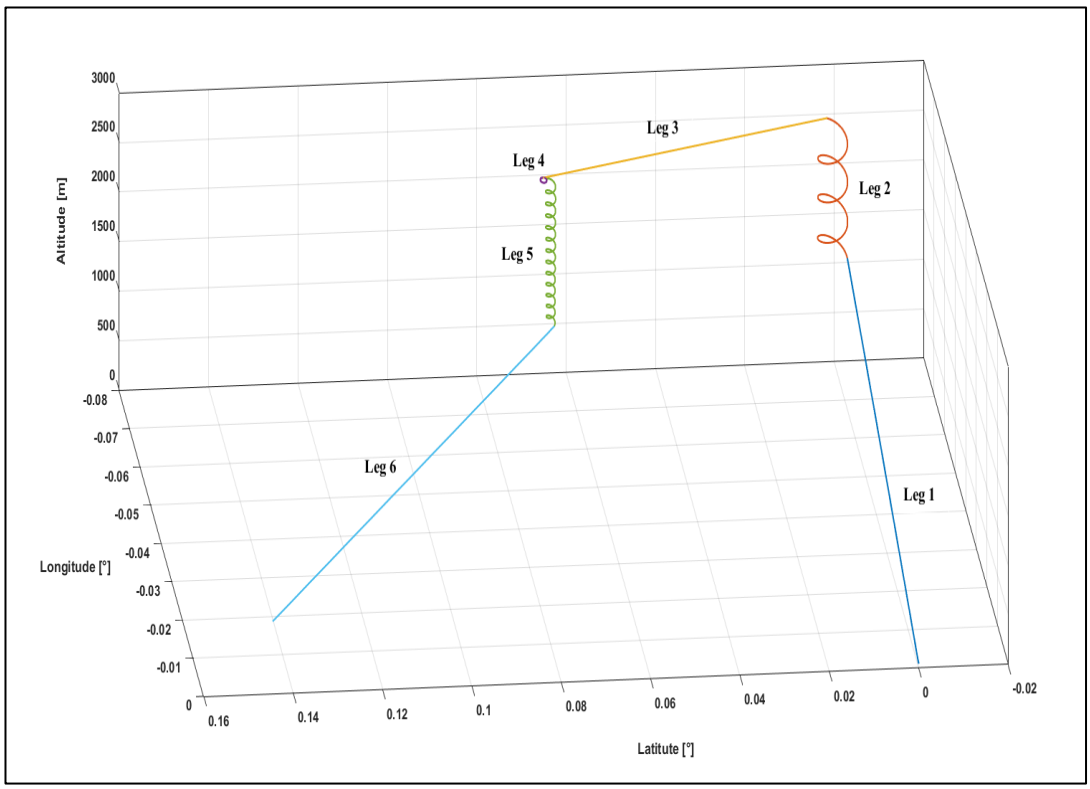


Figure 6-9. Reference AEROSONDE flight profile.

This reference flight profile contains the following 6 successive legs lasting 300 seconds each:

1. Straight climb with a constant pitch angle;

2. Turning climb phase with constant pitch and constant bank angle;
3. Constant speed straight-and-level cruise phase;
4. Level turn phase with constant bank angle;
5. Turning descent phase with constant pitch and bank angle;
6. Straight descent with a constant pitch.

The IFG is simulated as described in Chapter 3 with the AEROSONDE FMS flight profile as the initial flight trajectory to be optimised (i.e., preventing WIFs after CIFs onsets). The satellites data used are based on the GPS almanac data extracted from YUMA between 10:00am and 10:05am on the 30th July, 2012 (i.e., 5 minutes flight duration). The IFG simulation results are shown in Fig. 6-10. A number of CIF and WIF flags are triggered during the level turn and the turning descent flight phases. This can be observed in more details in Fig. 6-11 (and Fig. 6-12.

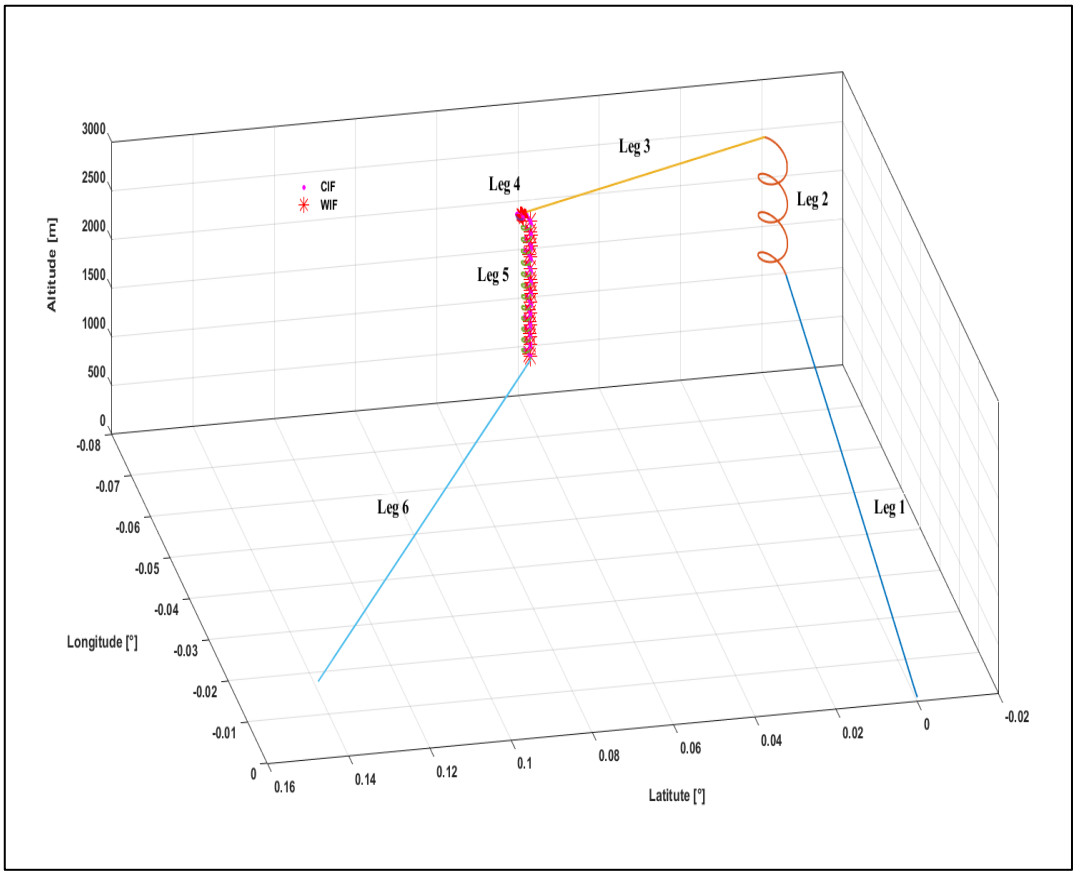


Figure 6-10. CIFs and WIFs generated by the IFG module.

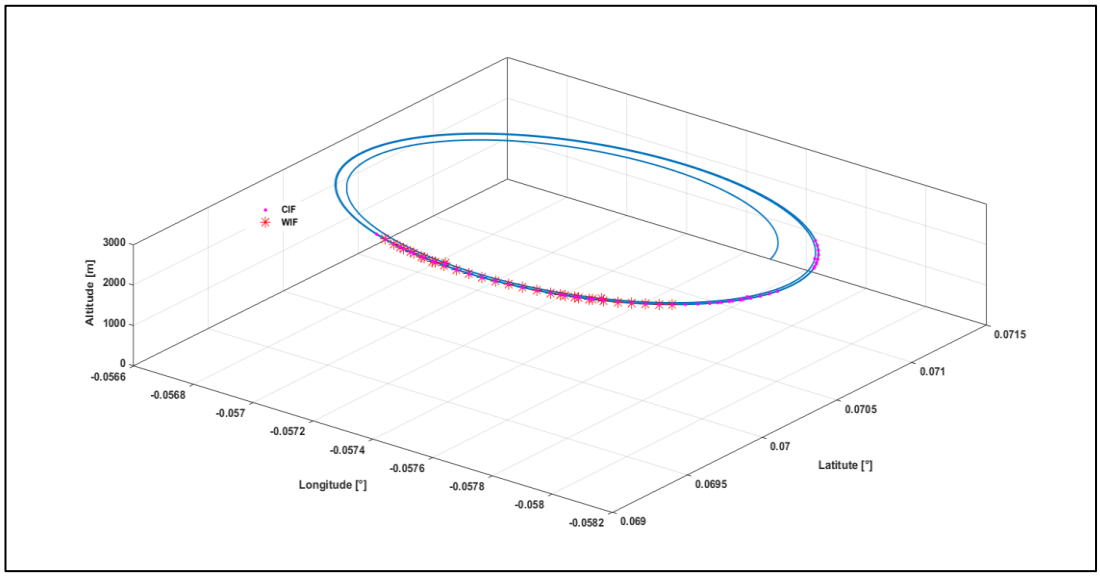


Figure 6-11. CIFs and WIFs generated during level turn.

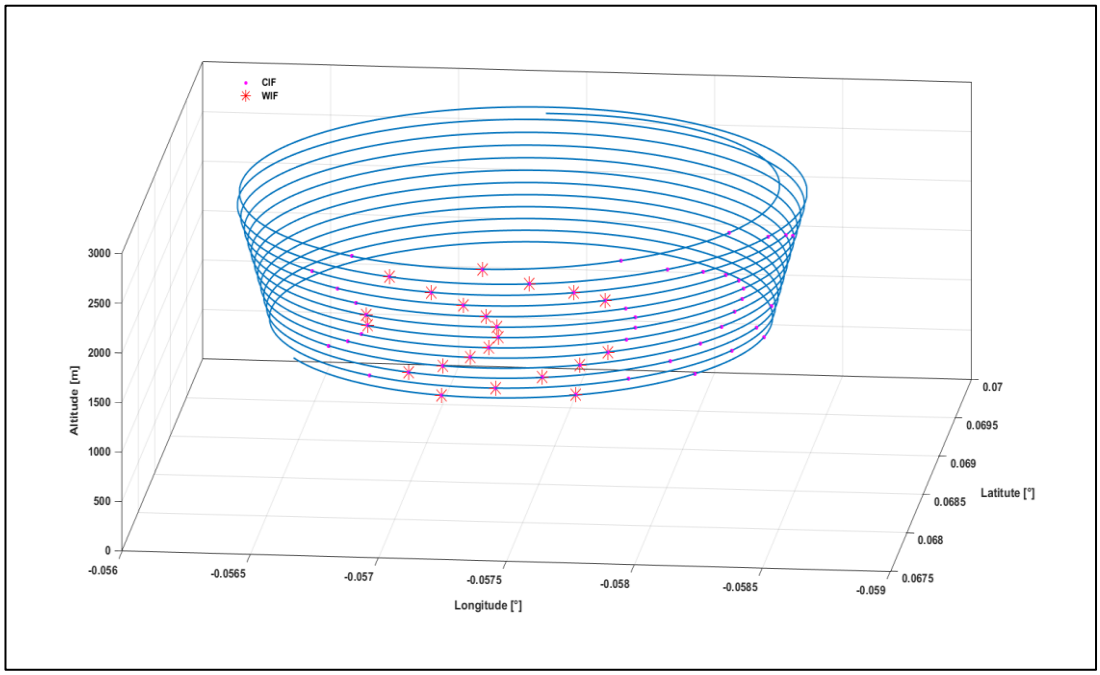


Figure 6-12. CIFs and WIFs generated during turning descent.

To test the FPG module ability to optimise the aircraft flight trajectories in mission planning and real-time ABIA implementations, a flight segment was extracted from leg 5 and used to test the PMO and CGO flight path optimisation techniques. This flight segment is shown in Fig. 6-13.

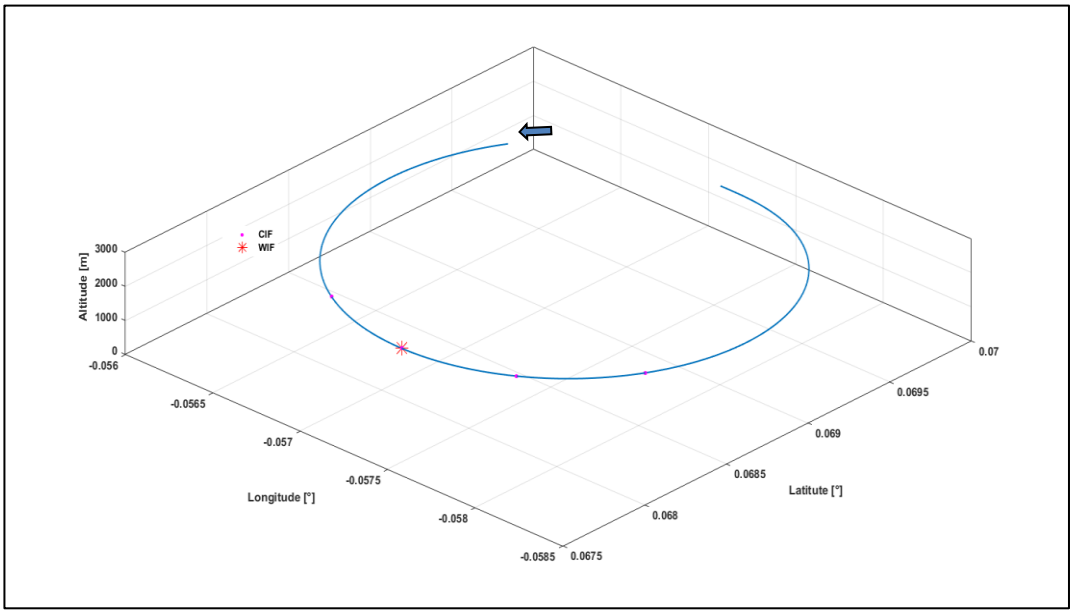


Figure 6-13. Turning descent segment with CIF and WIF.

Fig. 6-14 shows the results obtained implementing the PMO technique. In this case, the trajectory optimisation loop took 8.12 seconds to complete in a standard PC equipped with an Intel i7 quad-core processor and 8 GB RAM.

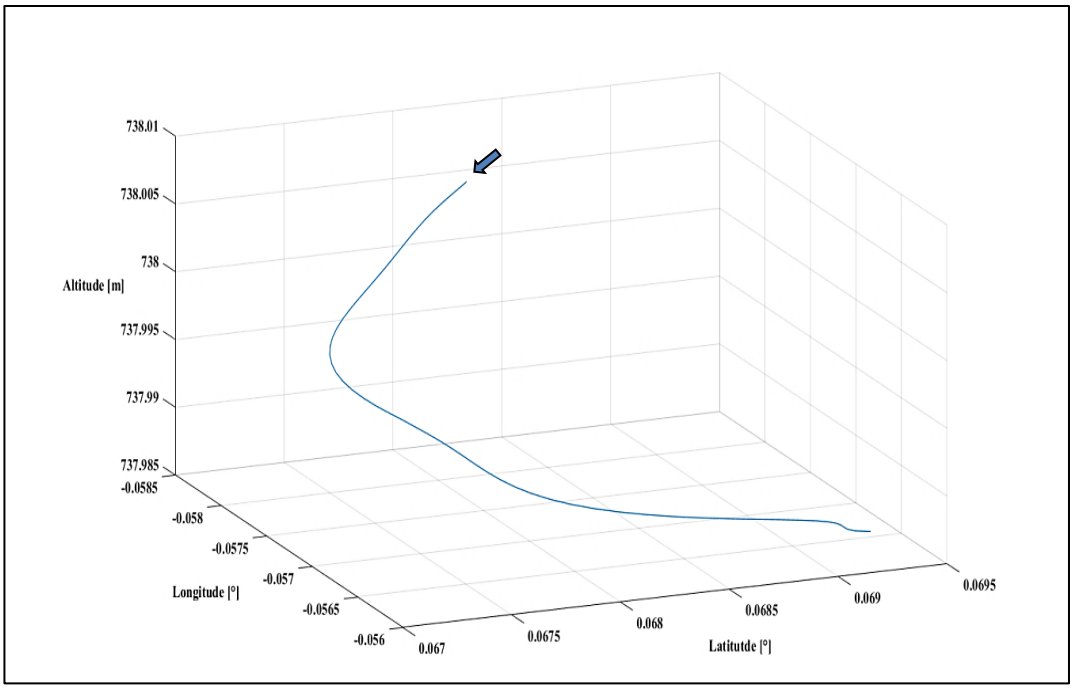


Figure 6-14. Turning descent segment optimised with PMO.

The trajectory obtained with the CGO technique is shown in Fig. 6-15. In this case, the trajectory optimisation loop took 0.42 seconds to complete in a standard PC equipped with an Intel i7 quad-core processor and 8 GB RAM.

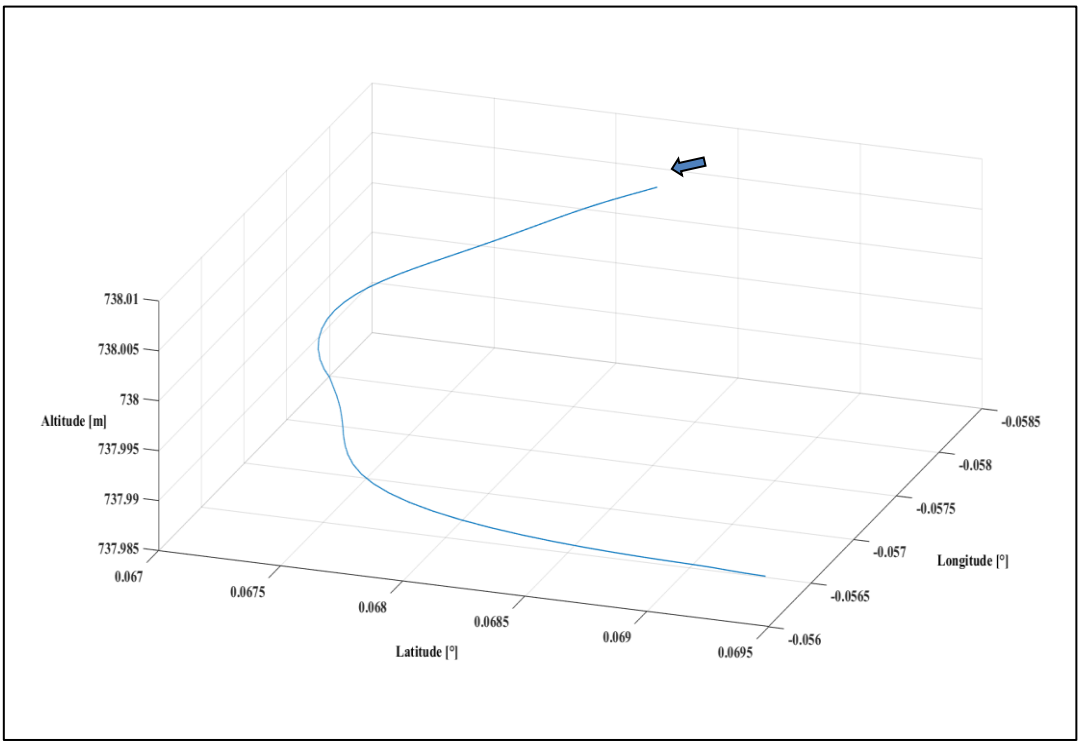


Figure 6-15. Turning descent segment optimised with CGO.

Further AEROSONDE simulations showed that, based on flight path length and aircraft dynamics (initial conditions), the time required for flight path optimisation varied between 5 and 220 seconds for the PMO and between 0.3 and 0.9 seconds for the CGO. Based on these results, it is evident that the PMO algorithms cannot be directly employed in real-time ABIA applications. This is because, even with the reatively benign flight dynamics of a small UAV like the AEROSONDE, the time required to perform trajectory optimisation is too long for real-time path following tasks in Automatic Flight Control System (AFCS). As already mentioned, the PMO technique is capable of generating a mathematical optimum and is better suited for ABIA mission planning/ATM applications (i.e., ground-based and avionics mission planning tools).

6.9 CONCLUSION

In this chapter we have addressed the design and testing requirements of the ABIA FPG module. The purpose of this module is to exploit the ABIA predictive features (CIFs generated at least 2 seconds before the WIFs), allowing the aircraft to correct its flight trajectory/attitude and to avoid the occurrence of the critical GNSS data losses. Analysing the various causes of GNSS data degradation or loss, geometric/mission optimisation criteria were introduced in terms of satellite elevation angle and heading rates. Adopting these criteria and an adequate form of the aircraft dynamics model (3DOF with variable mass and constraints/initial conditions set by a manoeuvre recognition algorithms), two different approaches were introduced to solve the guidance problem (i.e., generation of optimal flight trajectories) both in mission planning and real-time ABIA applications. The approach proposed for mission planning employs a classical Pseudospectral Multi-Objective (PMO) technique and the real-time optimisation is accomplished by a Constrained Geometric Optimisation (CGO) method. Simulation case studies were accomplished on the AEROSONDE UAV to verify the suitability of the proposed techniques in a realistic operational scenario (including complex flight manoeuvres and GLS precision approach legs). The PMO technique converged to a mathematical optimum within 5 - 220 seconds depending on the length and complexity of the flight path to be optimised, while the CGO technique was able to generate trajectories free from GNSS data degradations/losses within 0.3 - 0.9 seconds. It is therefore concluded that the adoption of PMO/CGO techniques in the ABIA FPG module would allow an efficient exploitation of the IFG module predictive features both in mission planning and real-time trajectory optimisation problems, potentially meeting GNSS integrity requirements for ATM online operations and AFCS/ABIA integration for GLS down to CAT III. Further research is needed to corroborate these initial findings, including detailed integration case studies, hardware-in-the-loop and human-in-the-loop simulations, as well as suitable ground/flight test activities.

6.10 REFERENCES

Airbus (2015), "A320 Specifications". Aircraft dimensions and key data webpage. Available online at: http://www.airbus.com/aircraftfamilies/passengeraircraft/a320family/a320/specifications/ (Accessed 2nd May, 2013).

Benson, D. A., Huntington, G. T., Thorvaldsen, T.P. and Rao, A.V. (2006), "Direct Trajectory Optimization and Costate Estimation via an Orthogonal Collocation Method." Journal of Guidance, Control, and Dynamics, vol. 29, pp. 1435– 1440.

Benson, D. A., Huntington, G. T., Thorvaldsen, T. P. and Rao, A. V. (2006), "Direct Trajectory Optimization and Costate Estimation via an Orthogonal Collocation Method." Journal of Guidance, Control, and Dynamics, vol. 29, pp. 1435–1440.

Betts, J. T. (1998), "Survey of numerical methods for trajectory optimization", Journal of Guidance, Control, and Dynamics, vol. 21, pp. 193-207.

Betts, J. T. and Cramer, E. J. (1995), "Application of direct transcription to commercial aircraft trajectory optimization", Journal of Guidance, Control, and Dynamics, vol. 18, pp. 151-159.

Chircop, K., Zammit-Mangion, D. and Sabatini, R. (2012), "Bi-Objective Pseudospectral Optimal Control Techniques for Aircraft Trajectory Optimization." 28th International Congress of the Aeronautical Sciences (ICAS).

Delahaye, D., Puechmorel, S., Tsiotras, P. and Feron, E. (2014), "Mathematical Models for Aircraft Trajectory Design: A Survey." Lecture Notes in Electrical Engineering, Vol. 290, *Air Traffic management and Systems*, pp. 205-247.

Eurocontrol (2008), "Initial 4D Trajectory Data Link (4DTRAD) Concept of Operations." European Organisation for the Safety of Air Navigation (Eurocontrol). Brussels (Belgium).

Eurocontrol (2014), "USER Manual for the Base of Aircraft Data (BADA)." Revisiom 3.12. The European Organisation for the Safety of Air Navigation (Eurocontrol) Experimental Centre (EEC). Technical/Scientific Report No. 14/04/24-44.

Gardi, A., Sabatini, R. and Ramasamy, S. (2016), "Multi-Objecive Four Dimesional Trajectory Optimisation in the ATM Context." Progress in the Aerospace Sciences (in press). Published online in April 2016 (DOI: 10.1016/j.paerosci.2015.11.006)

Garg, D., Hager, W. W., and Rao, A. V. (2011), "Pseudospectral Methods for Solving Infinite-Horizon Optimal Control Problems." Automatica, vol. 47, pp. 829–837.

Garg, D., Hager, W. W. and Rao, A. V. (2011), "Pseudospectral Methods for Solving Infinite-Horizon Optimal Control Problems." Automatica, Vol. 47, pp. 829–837.

Garg, D., Patterson, M. A., Darby, C. L., Francolin, C., Huntington, G. T., Hager, W. W. and Rao, A. V. (2011), "Direct Trajectory Optimization and Costate Estimation of Finite-Horizon and Infinite-Horizon Optimal Control Problems Using a Radau Pseudospectral Method." Computational Optimization and Applications, vol. 49, pp. 335–358.

Garg, D., Patterson, M. A., Hager, W. W., Rao, A. V., Benson, D. A. and Huntington, G. T. (2010), "A Unified Framework for the Numerical Solution of Optimal Control Problems Using Pseudospectral Methods." Automatica, vol. 46, pp. 1843–1851.

Garg, D., Patterson, M. A., Darby, C. L., Francolin C., Huntington G. T., Hager W. W. and Rao A. V. (2011), "Direct Trajectory Optimization and Costate Estimation of Finite-Horizon and Infinite-Horizon Optimal Control Problems Using a Radau Pseudospectral Method." Computational Optimization and Applications, Vol. 49, pp. 335–358.

Garg, D., Patterson, M. A., Hager, W. W., Rao, A. V., Benson, D. A. and Huntington, G. T. (2010), "A Unified Framework for the Numerical Solution of Optimal Control Problems Using Pseudospectral Methods." Automatica,, vol. 46, pp. 1843–1851.

Hull, D. G. (2007), "Fundamentals of Airplane Flight Mechanics." Springe-Verlag, Berlin - Heidelberg (Germany).

ICAO, Doc 9613 - Performance-Based Navigation (PBN) Manual, third ed., 2008.

Lewis, F. L., Vrabie, D. and Syrmos, V. L. (2012), "Optimal Control, Technology and Engineering", Third Edition. John Wiley & Sons, New York City, NY (USA).

Optimal (2005), "OPTIMAL - Optimised Procedures and Techniques for the Improvement of Approach and Landing." Report No. D1.2 (Operational Concept). Available online at: http://www.optimal.isdefe.es/ (visited in June 2013).

Rao, A. V. (2010-a), "Survey of Numerical Methods for Optimal Control", Advances in the Astronautical Sciences, vol. 135, pp. 497-528.

Rao, A. V. (2010-b), "Trajectory Optimization." In Encyclopedia of Aerospace Engineering, John Wiley & Sons Ltd.

Rao, A. V., Benson, D. A., Darby, C. L., Patterson, M. A., Francolin, C., Sanders, I. and Huntington, G. T. (2010), "Algorithm 902: GPOPS, A MATLAB Software for Solving Multiple-Phase Optimal Control Problems Using the Gauss Pseudospectral Method." ACM Transactions on Mathematical Software, vol. 37, p. 39-48.

Rodrıguez, J. M., Deniz, L. G., Herrero, L. G., Portas, J. B. and Corredera, J. B. (2008), "A 4D Trajectory Negotiation Protocol for Arrival and Approach Sequencing." Integrated Communications, Navigation and Surveillance Conference (ICNS).

Sabatini, R. (2008), "Differential Global Positioning System (DGPS) for Flight Testing." NATO Research and Technology Organization (RTO) – Systems Concepts and Integration Panel (SCI). AGARDograph Series RTO-AG-160 Vol. 21.

Sabatini, R., Moore, T. and Hill C. (2013-a), "A New Avionics Based GNSS Integrity Augmentation System: Part 1 – Fundamentals." Journal of Navigation, Vol. 66, No. 3, pp. 363-383.

Sabatini, R., Moore, T. and Hill C. (2013-b), "A New Avionics Based GNSS Integrity Augmentation System: Part 2 – Integrity Flags." Journal of Navigation, Vol. 66, No. 4, pp. 511-522.

SESAR (2012), "SESAR Release." No. 2 (March 2012). Single European Sky ATM Research (SESAR) Joint Undertaking.

Unmanned Dynamics (2003). "Aerosim Blockset User's Guide." Version 1.01. Unmanned Dynamics LLC, Hood River, OR (USA). Document available online at: https://people.rit.edu/pnveme/EMEM682n/Matlab_682/aerosim_ug.pdf (accessed 3rd June 2012).

Von Stryk, O. and Bulirsch, R. (1992), "Direct and indirect methods for trajectory optimization", Annals of Operations Research, vol. 37, pp. 357-373.

Whidborne, J. (2010), "AVMS - The Aerosonde model." Tutorial for the Department of Aerospace Engineering, Cranfield University (UK).

Zhou K., Doyle J. C. and Glover K. (1996), "Robust and optimal control", Prentice Hall, Upper Saddle River, NJ (USA).

(This page is left black for the purpose of typesetting)

7

ABIA SYNERGY WITH SBAS AND GBAS

7.1 INTRODUCTION

This chapter presents some simulation case studies performed to investigate the synergies attainable from the integration of ABIA with SBAS and GBAS. The ABIA IFG performances determined in Chapter 5 are compared here with the SBAS/GBAS integrity flag generation capability using the same manned/unmanned platforms (i.e., TORNADO-IDS, A320 and AEROSNDE UAV) and the same flight trajectories. The chapter opens with a brief descrption of the SBAS and GBAS integrity models implemented in the simulation, with an identification of the SBAS and GBAS integrity algorithms used in the simulation case studies aligned with the applicable standards (RTCA, 2004), (RTCA, 2006), (RTCA, 2008-a), (RTCA, 2008-b). Successive sections present the results of the simulation case studies, providing insights on possible mutual benefits attainable by integrating ABIA with SBAS and GBAS systems.

7.2 SBAS AND GBAS INTEGRITY MODELS

The aim of the SBAS and GBAS integrity models is to introduce the system functionslities required to compute the Vertical and Horizontal Protection Levels (VPL and HVL) and to compare them with the designated Vertical and Horizontal Alert Limits (VAL and HAL). As discussed, only the LAAS MOPS (RTCA, 2008-a) introduces the concept of predictive integrity flags, which are called Predictive

Vertical Protection Limit (PVPL) and Predicted Horizontal Protection Limit (PLPL). However, the standard does not provide detailed guidance on how these features can be implemented in practice to exploit potential synergies with ABAS. Additionally, PVAL/PLPL features are not present in the WAAS MOPS (RTCA, 2006-a). Fig. 7-1 shows the integrity flag generation algorithm implemented in the SBAS simulator. These algorithms are used to evaluate the SBAS integrity in line with the current WAAS MOPS (RTCA, 2006-a). Therefore, only WIF (reactive) alerts are generated when the HPL/VPL exceed the HAL/VAL.

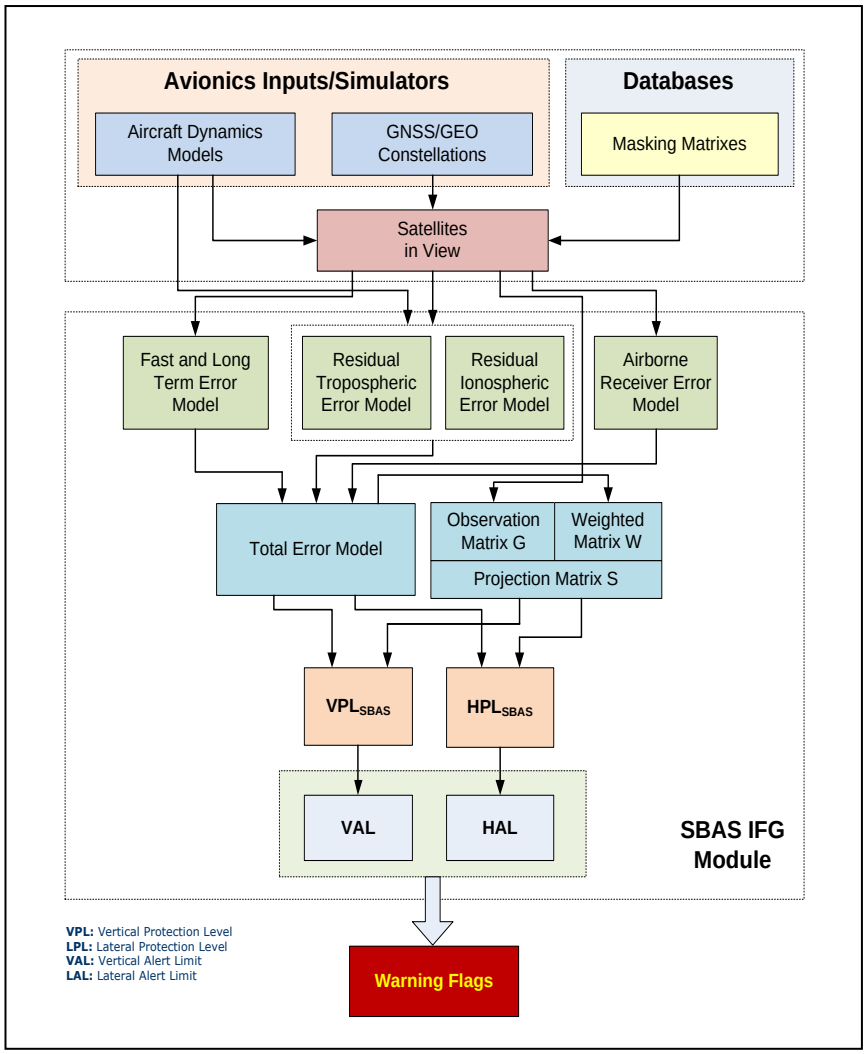


Figure 7-1. SBAS integrity algorithm.

The GCS simulator (GPS/GALILEO) described in Chapter 4 is expanded to include GEO satellites from WAAS and EGNOS. The simulator computes the real-time

position of all satellites in the ECEF coordinate system. The GEO pseudorange measurement equation and range error sources are the same as GPS pseudorange measurement. The aircraft dynamics models and masking matrixs used here are the same already introduced in the GBAS IFG simulator (Chapters 3 and 4).

The VAL and HAL limits defined in the WAAS MOPS are listed in Table 7-1.

Table 7-1. SBAS Vertical Alert Limit and Horizontal Alert Limit (RTCA, 2006).

NAVIGATION MODE	VERTICAL ALERT LIMIT (VAL)	HORIZONTAL ALERT LIMIT (HAL)
Oceanic/Remote	NA	7408 m
En Route	NA	3704 m
Terminal	NA	1852 m
LNAV or LNAV/VNAV Approach	NA	556 m
LNAV/VNAV Approach (after FAWP)	50 m	556 m
LPV or LP Approach	50 m	40 m
LPV II	35 m	40 m

The SBAS VAL is the threshold used to generate integrity flags based on the SBAS VPL. For oceanic, en route, terminal, or Lateral Navigation/Vertical Navigation (LNAV/VNAV) approaches, the VAL is not defined by the WAAS MOPS and ICAO SARPs (RTCA, 2006), (ICAO, 2006). LNAV/VNAV approaches use lateral guidance (556 m lateral limit) from GNSS and/or GBAS and vertical guidance provided by either barometric altimeter or GBAS. Aircraft that do not use GBAS for the vertical guidance portion must have VNAV-capable altimeters, which are typically integrated with modern Flight Directors and/or Flight Management Systems (FMS). Localizer Performance with Vertical Guidance (LPV) enables the aircraft descent to 200-250 feet above the runway and can only be flown with a WAAS/EGNOS receiver. LPV approaches are operationally equivalent to the legacy ILS but are more economical because no navigation infrastructure has to be installed in proximity of the runway. Localizer Performance (LP) is a Non-Precision Approach (NPA) procedure that uses the high precision of LPV for lateral guidance

and barometric altimeter for vertical guidance. LP approaches can only be flown by aircraft equipped with WAAS/EGNOS receivers. The minimum descent altitude for the LP approach is expected to be approximately 300 feet above the runway.

The fast corrections and long term corrections are two important messages transmitted by SBAS. The long term corrections contain information on the slowly varying satellite orbit and clock errors. The fast corrections provide additional information on the fast varying clock errors. Long term corrections consist of position and clock offset values only (EGNOS) or they also contain velocity and clock drift corrections (WAAS). The User Differential Range Error (UDRE) message provides information that allows the user to derive a bound on the projection of the satellite orbit and satellite clock errors onto the line of sight of the worst case user. The UDRE is transmitted as an indicator (UDREI). The coversions of UDREI into $UDRE_i$ and $\sigma^2_{i,UDRE}$ is provoded in Table 7-2.

Table 7-2. $UDREI_i$ and $UDRE_i$ (RTCA, 2006-a).

$UDREI_i$	$UDRE_i$ meters	$\sigma^2{}_{i,UDRE}$ meters^2
0	0.75	0.0520
1	1.0	0.0924
2	1.25	0.1444
3	1.75	0.2830
4	2.25	0.4678
5	3.0	0.8315
6	3.75	1.2992
7	4.5	1.8709
8	5.25	2.5465
9	6.0	3.3260
10	7.5	5.1968
11	15.0	20.7870
12	50.0	230.9661
13	150.0	2078.695
14	Not Monitored	Not Monitored
15	Do Not Use	Do Not Use

In our simulation, the δUDRE is calculated based on Message Type 28 data (Todd, 2001), (RTCA, 2006-b). It is assumed that fast and long term corrections are applied to the satellites but the correction degradation model is not used (i.e., an active type 7 or 10 message data is not available). In these conditions, the residual fast and long term error is defined as (RTCA, 2006-a):

$$\sigma_{i,flt}^2 = [(\sigma_{i,UDRE}) \cdot (\delta UDRE) + 8]^2 \quad [\text{m}] \tag{7-1}$$

The residual tropospheric error is denoted as $\sigma_{i,tropo}$. It is modelled as a random parameter with a standard deviation of $\sigma_{i,tropo}$ as specified in the MOPS (RTCA, 2006-a). Fig. 7-2 shows the residual tropospheric error curve used in our simulation.

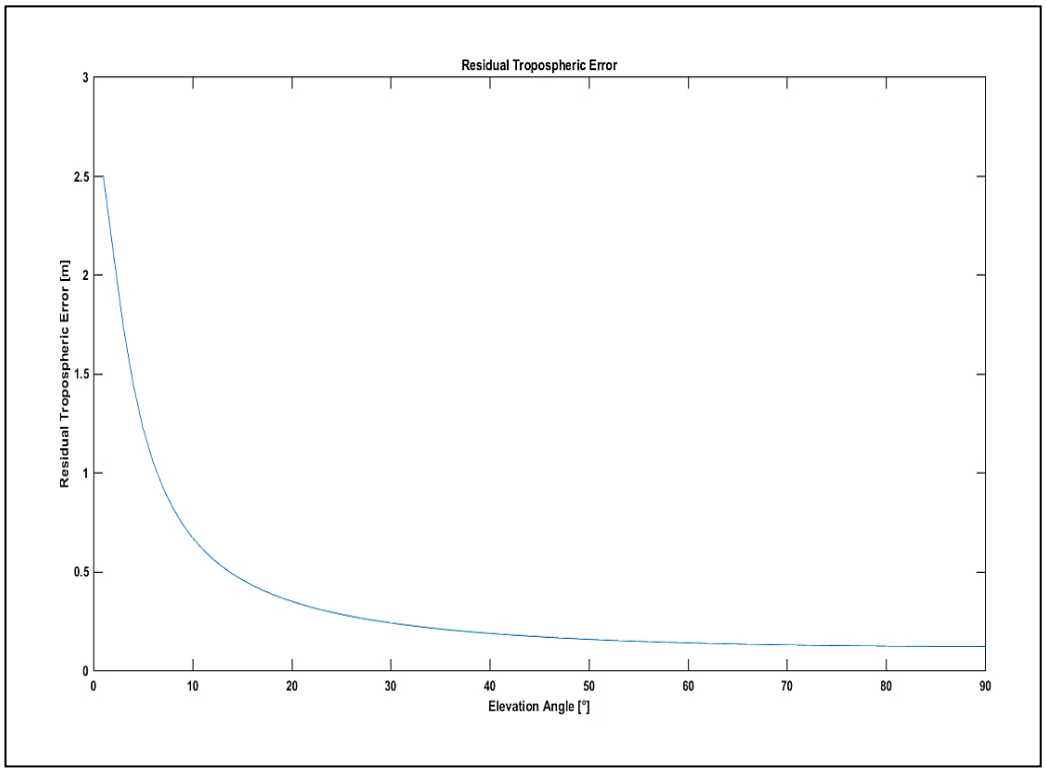


Figure 7-2. Residual tropospheric error from the WAAS MOPS.

This error curve was obtained from:

$$\sigma_{i,tropo} = [\sigma_{TVE} \cdot m(\theta_i)] \quad [\text{m}] \tag{7-2}$$

where the tropospheric vertical error is $\sigma_{TVE} = 0.12$ m and the shaping function is:

$$m(\theta_i) = \frac{1.001}{\sqrt{0.002001 + sin^2(\theta_i)}} \tag{7-3}$$

where θ_i is the satellite elevation angle in degrees.

The residual ionospheric error ($\sigma^2_{i,UIRE}$) was defined in Eq. (2-54) of Chapter 2. Real-time data from can be obtained from the FAA website for WAAS (FAA, 2014-a) and from the ESA website for EGNOS (ESA, 2015). The FAA also created a comprehensive portal containing real-time data on other GBAS systems including not only WAAS and EGNOS, but also MSAS and GAGAN (FAA, 2014-b). The airborne receiver error is denoted as $\sigma_{i,air}$. This error is defined in the WAAS MOPS based on the equipment operation classes. There are four operation classes defined in the WAAS MOPS (RTCA, 2006). A description of these classes is provided in Table 7-3.

Table 7-3. SBAS Operational Classes (RTCA, 2006).

CLASS	DESCRIPTION
Class 1	Equipment that supports oceanic and domestic en route, terminal, approach (LANV), and departure operation. When in oceanic and domestic en route, terminal, LNAV, and departure operations, this class of equipment can apply the long-term and fast SBAS differential corrections when they are available.
Class 2	Equipment that supports oceanic and domestic en route, terminal, approach (LANV, LNAV/VNAV), and departure operation. When in LNAV/VNAV, this class of equipment applies the long-term, fast and ionospheric corrections. When in oceanic and domestic en route, terminal, approach (LNAV), and departure operations, this class of equipment can apply the long-term and fast SBAS differential corrections when they are available.
Class 3	Equipment that supports oceanic and domestic en route, terminal, approach (LANV, LNAV/VNAV, LP, LPV), and departure operation. When in LPV, LP, or LNAV/VNAV, this class of equipment applies the long-term, fast and ionospheric corrections. When in oceanic and domestic en route, terminal, approach (LNAV), and departure operations, this class of equipment can apply the long-term and fast SBAS differential corrections when they are available.
Class 4	Equipment that supports only the final approach segment operation. This class of equipment is intended to serve as an ILS alternative that supports LP and LPV operation with degradation (fail-down) from LPC to lateral only (LNAV). Class 4 equipment is only applicable to functional Class Delta, and equipment that meets Class Delta-4 is also likely to meet the requirements for Class Beta-1, 2, or -3.

For Class 1 equipment:

$$\sigma_{i,air}^2 = 25m^2 \tag{7-4}$$

For Class 2, 3 and 4 equipment:

$$\sigma_{i,air} = (\sigma_{noise,GNSS}^2[i] + \sigma_{multipath}^2[i] + \sigma_{divg}^2[i])^{1/2} \tag{7-5}$$

The multipath error for the airborne equipment is described by the distribution $N(0, \sigma_{multipath}^2)$ where:

$$\sigma_{multipath}[i] = 0.13 + 0.53e^{(-\theta_i/10deg)} \text{ [m]} \tag{7-7}$$

where, as before, θ_i is the satellite elevation angle in degree.

The steady-state value of $(\sigma_{noise,GNSS}^2[i] + \sigma_{divg}^2[i])^{1/2}$ at the minimum and maximum signal levels shall be as follows (RTCA, 2006).

Minimum signal level from GNSS core satellite:

$(\sigma_{noise,GNSS}^2[i] + \sigma_{divg}^2[i])^{1/2} \leq 0.36$ metres for airborne Accuracy Designator A

$(\sigma_{noise,GNSS}^2[i] + \sigma_{divg}^2[i])^{1/2} \leq 0.15$ meters for airborne Accuracy Designator B

Maximum signal level from GNSS core satellite:

$(\sigma_{noise,GPS}^2[i] + \sigma_{divg}^2[i])^{1/2} \leq 0.15$ meters for airborne Accuracy Designator A

$(\sigma_{noise,GPS}^2[i] + \sigma_{divg}^2[i])^{1/2} \leq 0.11$ meters for airborne Accuracy Designator B

SBAS satellite minimum signal level:

$$(\sigma_{noise,GPS}^2[i] + \sigma_{divg}^2[i])^{1/2} \leq 1.8 \text{ meters}$$

SBAS satellite maximum signal level:

$$(\sigma_{noise,GPS}^2[i] + \sigma_{divg}^2[i])^{1/2} \leq 1.0 \text{ meters}$$

The total error σ_i^2 is given by (RTCA, 2006):

$$\sigma_i^2 = \sigma_{i,flt}^2 + \sigma_{i,UIRE}^2 + \sigma_{i,air}^2 + \sigma_{i,tropo}^2 \tag{7-8}$$

The projection matrix (**S**) is defined as (RTCA, 2006):

$$\mathbf{S} = \begin{bmatrix} s_{east,1} & s_{east,2} & \cdots & s_{east,N} \\ s_{north,1} & s_{north,2} & \cdots & s_{norht,N} \\ s_{U,1} & s_{U,2} & \cdots & s_{U,N} \\ s_{t,1} & s_{t,2} & \cdots & s_{t,N} \end{bmatrix} = (\mathbf{G}^{\mathrm{T}} \cdot \mathbf{W} \cdot \mathbf{G})^{-1} \cdot \mathbf{G}^{\mathrm{T}} \cdot \mathbf{W} \tag{7-9}$$

where:

G = observation matrix;

W = weighted matrix;

$s_{east,i}$ = partial derivative of position error in the east direction with respect to the pseudorange error on the i[th] satellite;

$s_{north,i}$ = partial derivative of position error in the north direction with respect to the pseudorange error on the i[th] satellite;

$s_{U,i}$ = partial derivative of position error in the vertical direction with respect to the pseudorange error on the i[th] satellite;

$s_{U,i}$ = is the partial derivative of time error with respect to pseudorange error on the i[th] satellite.

The weighted matrix **W** is defined as:

$$\mathbf{W} = \begin{bmatrix} w_1 & 0 & \cdots & 0 \\ 0 & w_2 & \cdots & 0 \\ \vdots & \vdots & \ddots & \vdots \\ 0 & 0 & \cdots & w_N \end{bmatrix} \tag{7-10}$$

$$w_i = 1/\sigma_i^2 \tag{7-11}$$

and the observation matrix **G** consists of N rows of LOS vectors from each satellite augmented by a "1" for the clock. Thus, the i[th] row corresponds to the i[th] satellites in

view and can be written in terms of the azimuth angle Az_i and elevation angle θ_i. The i[th] row of the **G** matrix is:

$$\mathbf{G_i} = [-\cos\theta_i \sin Az_i \quad -\cos\theta_i \cos Az_i \quad -\sin\theta_i \quad 1] \tag{7-12}$$

The SBAS Vertical Protection Level (VPL_{SBAS}) is calculated using the equation:

$$VPL_{SBAS} = K_V d_U \tag{7-6}$$

where:

$$d_U^2 = \sum_{i=0}^{N} s_{U,i}^2 \sigma_i^2 \tag{7-14}$$

The value of K_V used for computing VPL is: K_V=5.33.

The SBAS Horizontal Protection Level (HPL_{SBAS}) is calculated using the equations:

$$HPL_{SBAS} = \begin{cases} K_{H,NPA} \cdot d_{major}, & \text{for en route through LNAV} \\ K_{H,PA} \cdot d_{major}, & \text{for LNAV/VNAV, LP, LPV approach} \end{cases} \tag{7-15}$$

where:

$$d_{major} \equiv \sqrt{\frac{d_{east}^2 + d_{north}^2}{2} + \sqrt{(\frac{d_{east}^2 - d_{north}^2}{2})^2 + d_{EN}^2}} \tag{7-16}$$

$$d_{east}^2 = \sum_{i=0}^{N} s_{east,i}^2 \sigma_i^2 \tag{7-7}$$

$$d_{north}^2 = \sum_{i=0}^{N} s_{norht,i}^2 \sigma_i^2 \tag{7-18}$$

$$d_{EN}^2 = \sum_{i=0}^{N} s_{east,i} s_{north,i} \sigma_i^2 \tag{7-19}$$

The values $K_{H,NPA}$ is 6.18 for en route through LNAV and 6.0 for LNAV/VNAV, LP, LPV.

Fig. 7-3 shows the GBAS integrity algorithm implemented in the simulator. This algorithm is based on the applicable RTCA standards (RTCA, 2008-a), (RTCA-2008-b) and, in addition to the VPL and LPL required for all GLS classes, also PVPL and PLPL features for high performance GLS are implemented (as described below). If the VPL or LPL exceeds the threshold (i.e., VAL or LAL respectively), a WIF is generated. If one of the PVPL and PLPL exceeds the threshold, the CIF is generated.

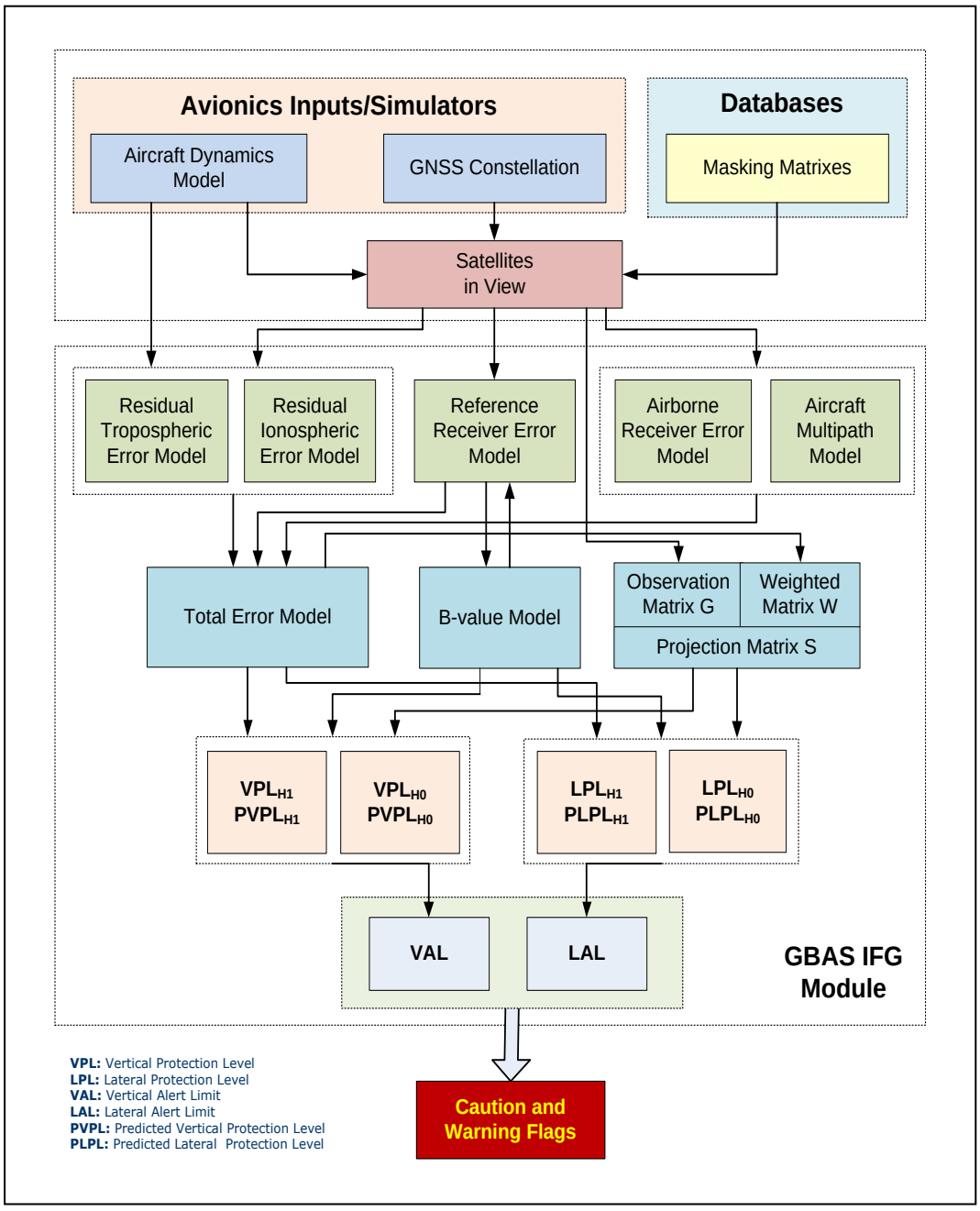


Figure 7-3. GBAS integrity algorithm.

As showed in the Fig. 7-3, there are two conditions in the protection level calculations. One is the H_0 hypothesis, the other is H_1 hypothesis. The H_0 hypothesis refers to no faults are present in the range measurements (including both the signal and the receiver measurements) used in the ground station to compute the differential corrections. The H_1 hypothesis refers to the presence of a fault in one or more range measurements that is caused by one of the reference receivers used in the ground station.

The residual tropospheric and ionospheric errors are due to the position difference of reference receiver and aircraft. According to he LAAS MASPS, the tropospheric error is defined as (RTCA, 2004):

$$\sigma_{tropo}(\theta) = \sigma_N h_0 \frac{10^{-6}}{\sqrt{0.002 + sin^2(\theta)}}\left(1 - e^{-\frac{\Delta h}{h_0}}\right) \tag{7-8}$$

where:

σ_N = troposphere refractivity uncertainty transmitted in the GBAS Message Type 2;

θ = elevation angle for the ith ranging source. It is expressed in the ENU frame;

Δh = difference in altitude between airborne and ground subsystems (reference receivers), in meters;

h_0 = tropospheric scale height (transmitted in GBAS Message Type 2).

The residual ionospheric error is defined as (RTCA, 2004):

$$\sigma_{iono} = F_{pp}\sigma_{vert_iono_gradient}(x_{air} + 2\tau v_{air}) \tag{7-21}$$

where F_{pp} is the obliquity defined in Eq. (2-55).

The reference receiver error model is used to generate the total error which contributing the corrected pseudorange for a GPS satellite caused by the reference receiver noise.

The standard deviation of the reference receiver error is (RTCA, 2004):

$$\sigma_{pr_gnd,GPS}(\theta_i) = \sqrt{\frac{(a_0 + a_1 e^{-\theta_i/\theta_0})^2}{M} + (a_2)^2} \tag{7-9}$$

where:

M = number of ground reference receiver subsystems;

θ_i = elevation angle for the ith ranging source.

and the accuracy parameter a_0, a_1, a_2 and θ_0 are defined in Table 7-4 for various Ground Accuracy Designators (GAD).

Table 7-4. GAD and Accuracy Requirements (RTCA, 2004).

Ground Accuracy Designator	θ_i [deg]	a_0 (m)	a_1 (m)	θ_0 [deg]	a_2 (m)
A	>5	0.5	1.65	14.3	0.08
B	>5	0.16	1.07	15.5	0.08
C	>35	0.15	0.84	15.5	0.04
	≤35	0.24	0	-	0.04

The airborne receiver error is a function of the satellite elevation angle above the local level plane. It is defined as (RTCA, 2004):

$$\sigma_{receiver}(\theta_i) = a_0 + a_1 e^{-(\theta_i/\theta_0)} \tag{7-10}$$

where θ_i is the elevation angle for the ith ranging source and the parameters a_0, a_1 and θ_0 are defined in Table 7-5 for various Airborne Accuracy Designators (AAD). Also the aircraft multipath error is a function of the satellite elevation angle. The Airframe Multipath Designator (AMD) is a letter that indicates the airframe multipath error contribution to the corrected pseudorange for a GPS satellite.

Table 7-5. AAD and Accuracy Requirement (RTCA, 2004).

Airborne Accuracy Designator	θ_0 [deg]	a_0 (m)	a_1 (m)
A	6.9	0.15	0.43
B	4	0.11	0.13

There are two types of AMD in the LAAS MASPS, denoted as A and B (RTCA, 2004). The aircraft multipath error for AMD type A is:

$$\sigma^{A}_{multipath}[\mathrm{i}] = (0.13 + 0.53e^{(-\theta_i/10)}) \quad [\mathrm{m}] \tag{7-24}$$

For AMD type B:

$$\sigma^{B}_{multipath}[\mathrm{i}] = (0.13 + 0.53e^{(-\theta_i/10)})/2 \quad [\mathrm{m}] \tag{7-25}$$

The multipath model for AMD type A ($\sigma^{A}_{multipath}$) was obtained during an FAA sponsored research program, which was aimed at investigating and quantifying the total effect of multipath from the airframe and from ground multipath during approach and landing operations (Murphy et al., 2004). Fig. 7-4 illustrates the procedure used to estimate the multipath error. The FAA sponsored program included the development of an electromagnetic modelling capability to predict amplitude, time delay and phase characteristic of airframe multipath. The final empirical model is the result of extensive flight test data analysis conducted with large commercial airliner platforms (i.e., B777-300ER and B737-NG) as described in (Murphy et al. 2005-a) and (Murphy et al., 2005-b). As stated in the LAAS MASPS (RTCA, 2004), the multipath model for AMD type B ($\sigma^{B}_{\mathrm{multipath}}$) is still under development. Therefore, in our research, we will only use $\sigma^{A}_{\mathrm{multipath}}$ both for large commercial aircraft and for military/unmanned aircraft cathegories. Since $\sigma^{A}_{multipath}$ is expected to produce conservative multipath error estimations in these cases, this is acceptable until more reliable $\sigma^{B}_{multipath}$ models are developed.

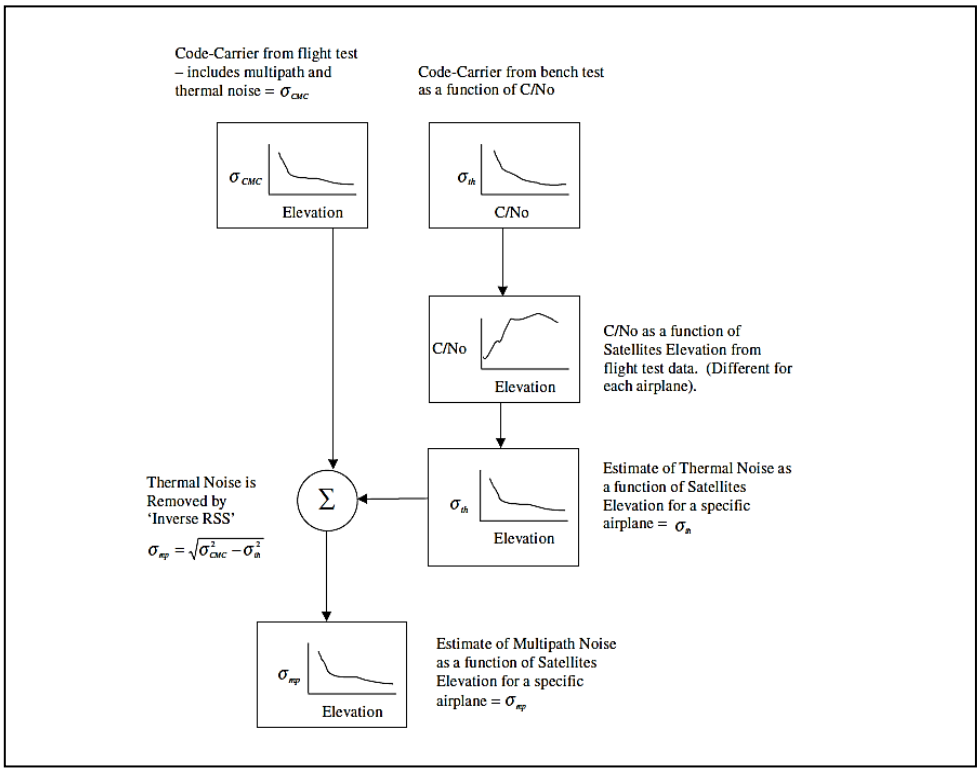


Figure 7-4. Flight test data analysis procedure (Murphy et al., 2004).

Fig. 7-5 shows the relationship between multipath error and satellite elevation angle for AMD type A.

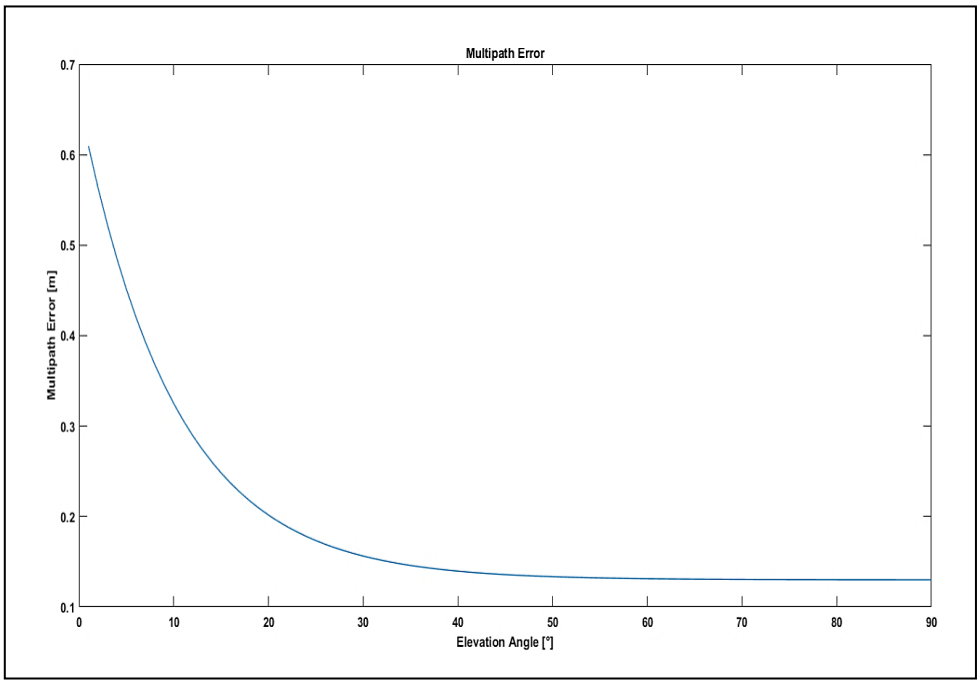


Figure 7-5. Multipath error for AMD type A.

From the figure, it is observed that the multipath error decreases very quickly as the elevation angle increases from 5 degree to 20 degree. Decreases less from 20 to 40 degrees and remains almost unchanged (below 0.15 m) when the elevation is greater than 40 degrees.

The B-value is used to detect and exclude the faults in the pseudorange corrections before they are transmitted to airborne users. It is transmitted in the GBAS Message Type 1. The B-value is calculated from (RTCA, 2008-a):

$$\sigma_B{}^i = \frac{1}{\sqrt{M_i - 1}} \sigma_{pr_{gnd},GNSS}(\theta_i) \tag{7-26}$$

where:

θ_i = elevation angle for the ith ranging source;

M_i = reference receiver number used to generate the $\sigma_{pr_{gnd},GNSS}(\theta_i)$.

B-value thresholds (T_B) are used to verify if all pseudorange corrections produced by the reference receivers are consistent with each other. If one measurement is faulty, it is excluded from the composite pseudorange correction calculatins (i.e., if one of the B-values for the ith satellite exceeds the threshold, that measurement will be excluded).

Vraious researchers have developed useful models to calculate T_B (Liu, 1998), (Xie, 2001). Based on this work, the B-value threshold used in our GBAS simulator is:

$$T_B^i = 5.6\sigma_B^i \tag{7-27}$$

The H_0 Hypothesis total error model is (RTCA, 2004):

$$\sigma_i^2 = \sigma_{pr_{gnd},i}^2 + \sigma_{tropo,i}^2 + \sigma_{air,i}^2 + \sigma_{iono,i}^2 \tag{7-28}$$

where $\sigma_{air,i}^2$ is the total aircraft contribution to the corrected pseudorange error for the ith satellite. This is defined as:

$$\sigma_{air,i}^2 = \sigma_{receiver}^2(\theta_i) + \sigma_{multipath}^2(\theta_i) \tag{7-29}$$

The H_1 hypothesis total error model is (RTCA, 2004):

$$\sigma_{i,H1}^2 = \frac{M_i}{M_i - 1}\sigma_{pr_{gnd},i}^2 + \sigma_{tropo,i}^2 + \sigma_{air,i}^2 + \sigma_{iono,i}^2 \tag{7-30}$$

where M_i is the number of reference receivers used to compute the pseudorange corrections for the i[th] satellite.

As in the case of SBAS, the GBAS projection matrix (**S)** matrix is obtained from the observation matrix (**G**) and weighted matrix (**W**), and its elements determine the protection levels of GBAS. As before, the **S** matrix is defined as:

$$\mathbf{S} = (\mathbf{G}^{\mathrm{T}} \cdot \mathbf{W} \cdot \mathbf{G})^{-1} \cdot \mathbf{G}^{\mathrm{T}} \cdot \mathbf{W} \tag{7-31}$$

where the GBAS observation matrix (**G**) and weight matrix (**W**) have the same formats already defined for SBAS.

The fault-free vertical protection level (VPL_{H0}) can be calculated using the equation (RTCA, 2004):

$$VPL_{H0} = K_{ffmd}\sqrt{\sum_{i=1}^{N} s^2{}_{Apr_vert,i}\,\sigma_i{}^2} \tag{7-32}$$

where $s_{Apr_vert,i}$ is the projection of the vertical component and translation of the along track errors into the vertical for the i[th] satellite. This is given by:

$$s_{Apr_vert,i} = s_{v,i} + s_{x,i} * \tan\theta_{GS} \tag{7-33}$$

where:

θ_{GS} = glidepath angle for the final approach path.

N = number of ranging sources used in the position solution.

The vertical faut-free missed detection multipliers (K_{ffmd}) are listed in Table 7-6.

Table 7-6. Vertical Missed Detection Multipliers (RTCA, 2004).

GSL	K_{ffmd}			K_{md}		
	M_m=2	M_m=3	M_m=4	M_m=2	M_m=3	M_m=4
A,B,C	5.762	5.810	5.847	2.935	2.898	2.878
D	6.8	6.9	6.9	3.8	3.7	3.7
E	6.8	6.9	6.9	3.8	3.7	3.7
F	6.8	6.9	6.9	3.8	3.7	3.7

The H_1 hypothesis vertical protection level (VPL_{H1}) can be calculated using the equations:

$$VPL_{H1} = MAX\{VPL_j\} \tag{7-34}$$

$$VPL_j = \left|B_{j,vert}\right| + K_{md}\sigma_{vert,H1} \tag{7-35}$$

where j is the ground reference receiver index, K_{md} is found in Table 7-9 and the other terms are:

$$\mathrm{B}_{j,vert} = \sum_{i=1}^{N} s_{vert,i} B_{i,j} \tag{7-36}$$

$$\sigma^2_{vert,H1} = \sum_{i=1}^{N} s^2_{vert,i}\sigma^2_{i,H1} \tag{7-37}$$

The fault-free lateral protection level (LPL_{H0}) is calculated using the equation (RTCA, 2004):

$$LPL_{H0} = K_{ffmd}\sqrt{\sum_{i=1}^{N} s^2{}_{Apr_lat,i}\sigma_i{}^2} \tag{7-38}$$

where $s_{Apr_lat,i}$ is the projection of the vertical component and translation of the along track errors into the vertical for i^{th} satellite (also denoted $s_{lat,i}$) and the multiplier K_{ffmd} can be found in Table 7-7.

Table 7-7. Lateral Missed Detection Multipliers (RTCA, 2004).

GSL	K_{ffmd}			K_{md}		
	M_m=2	M_m=3	M_m=4	M_m=2	M_m=3	M_m=4
A,B,C	5.762	5.810	5.847	2.935	2.898	2.878
D	6.9	7.0	7.0	3.9	3.9	3.9
E	6.9	7.0	7.0	3.9	3.9	3.9
F	6.9	7.0	7.0	3.9	3.9	3.9

The H_1 hypothesis lateral protection level (LPL_{H1}) can be calculated using the following equations from the LAAS MASPS (RTCA, 2004):

$$LPL_{H1} = MAX\{LPL_j\} \tag{7-39}$$

$$LPL_j = \left|B_{j,lat}\right| + K_{md}\sigma_{lat,H1} \tag{7-40}$$

where:

$$\mathrm{B}_{j,lat} = \sum_{i=1}^{N} s_{lat,i} B_{i,j} \tag{7-41}$$

$$\sigma^2_{lat,H1} = \sum_{i=1}^{N} s^2_{lat,i}\sigma^2_{i,H1} \tag{7-42}$$

The subscript j is the ground subsystem reference receiver index and the multiplier K_{md} can be found in 7-10. If the GBAS provides GSL E or F services, then the predicted protection level must be calculated to enable continuity of the GBAS signal-in-space. The Predicted Vertical Protection Level (PVPL) and Predicted Lateral Protection Level (PLPL) are defined in MASPS as (RTCA, 2004):

$$\mathrm{PVPL} = MAX\{PVPL_{H0}, PVPL_{H1}\} \tag{7-43}$$

$$\mathrm{PLPL} = MAX\{PLPL_{H0}, PLPL_{H1}\} \tag{7-44}$$

$$PVPL_{H0} = K_{ffmd}\sqrt{\sum_{i=1}^{N} s^2{}_{vert,i}\sigma_i{}^2} \tag{7-45}$$

$$PVPL_{H1} = K_{ffd}\sigma_{B,vert} + K_{md}\sigma_{vert,H1} \tag{7-46}$$

$$PLPL_{H0} = K_{ffmd}\sqrt{\sum_{i=1}^{N} s^2{}_{lat,i}\sigma_i{}^2} \tag{7-47}$$

$$PLPL_{H1} = K_{ffd}\sigma_{B,lat} + K_{md}\sigma_{lat,H1} \tag{7-48}$$

where K_{ffd} is the multiplier which determines the probability of fault-free detection given M reference receivers. Table 7-8 lists the fault-free detection multipliers.

Table 7-8. Fault-Free Detection Multipliers (RTCA, 2004).

GSL	K_{ffd}		
	M_m=2	M_m=3	M_m=4
E	5.5	5.5	5.6
F	5.6 (vertical) / 5.9 (lateral)	5.7(vertical) / 5.9 (lateral)	5.7 (vertical) / 6.0 (lateral)

$$\sigma^2_{B,vert} = \sum_{i=1}^{N} s^2_{vert,i}\frac{\sigma^2_{pr_gnd,i}}{(M_i - 1)} \tag{7-49}$$

$$\sigma^2_{B,lat} = \sum_{i=1}^{N} s^2_{lat,i}\frac{\sigma^2_{pr_gnd,i}}{(M_i - 1)} \tag{7-50}$$

The VAL defines the threshold values of VPL and PVPL (i.e, the GBAS signal is not to be used to navigate the aircraft when the VPL exceeds the VAL/PVAL). The VAL values are listed in Table 7-9.

Table 7-9. Vertical Alert Limit (RTCA, 2004).

Intended GSL	Height above LTP/FTP (feet)	Alert Limit (meters)
A	---	FASVAL
B	---	FASVAL
C	H≤200	FASVAL
	200<H≤1340	0.02925*H(ft)+ FASVAL-5.85
	H>1340	FASVAL+33.35
D,E,F	H≤100	FASVAL
	100<H≤200	FASVAL
	200<H≤1340	0.02925*H(ft)+ FASVAL-5.85
	H>1340	FASVAL+33.35

Sinilarily, the Lateral Alert Limit (LAL) defines the threshold values of LPL and PLPL. The LAL values are listed in Table 7-10.

Table 7-10. Lateral Alert Limit (RTCA, 2004).

Intended GSL	Distance from LTP/FTP (meters)	Alert Limit (meters)
A,B	---	FASLAL
C	Along the runway and for D≤873	FASLAL
	873<D≤7500	0.0044*D(m)+ FASLAL-3.85
	D>7500	FASLAL+29.15
D,E,F	Along the runway and for D≤291	FASLAL
	291<D≤873	0.03952*D(m)+ FASLAL-11.5
	873<D≤7500	0.0044*D(m)+ FASLAL+19.15
	D>7500	FASLAL+52.15

The Final Approach Segment Vertical and Lateral Alert Limits (FASVAL and FASLAL) are listed in Table 7-11. In the simulation case studies described in this chapter, a FASVAL of 5.3 metres and a FASLAL of 15.5 metres are adopted.

Table 7-11. FASVAL and FASLAL **Error! Reference source not found.**

GSL	FASVAL	FASLAL
A,B,C	≤10 m	≤40 m
A,B,C,D	≤10 m	≤17 m
A,B,C,D,E	≤10 m	≤17 m
A,B,C,D,E,F	≤10 m	≤17 m

7.3 SIMULATION CASE STUDIES

Simulation case studies were performed on the A320 performing the same flight profile described in Chapter 4. To reflect the typical operational employment of SBAS and GBAS, SBAS was simulated in all flight phases (like ABIA) and GBAS was simulated during the approach phases, including both iniatil descent (TD/SD segments) and FA segments. The results of the SBAS/GBAS simulation were then compared with the ABIA IFG simulation results described in Chapter 5 to identify potential synergies between the three augmentation techniques. To facilitate the comparison, the aircraft trajectories and GNSS data were the same already utilised in the IFG simulation cases described in Chapter 5. The following assuptions were adopted in the simulation case studies:

- The SBAS equipment is class 3 and is used for LNAV/VNAV and LVP 1/LPV2 operations.
- The AMD type A is used for all aircraft.
- The number of GBAS reference receivers is 4.
- The GBAS service coverage is 23 NM from the LTP.
- GSL=F, AAD=B, GAD=B.

The criteria for producing SBAS/GBAS CIFs and WIFs are listed below:

- **When VPL_{SBAS} exceeds VAL or HPL_{SBAS} exceeds HAL, the WIF is be**

generated.

- **When $PVPL_{GBAS}$ exceeds VAL or $PLPL_{GBAS}$ exceeds LAL, the CIF is generated.**
- **When VPL_{GBAS} exceeds VAL or HPL_{GBAS} exceeds HAL, the WIF is generated.**

Fig. 7-6 shows the TORNADO-IDS flight trajectory and illustrates the portion of the TMA where GBAS is available. Since a standard definition for this airspace region is not available at present, we call this area the GNSS Coverage Area (GCA). The point of entry in the GCA is highlighted in Fig. 7-6. In this case, GBAS provides information when the TORNADO-IDS is flying leg number 6 (SD) and leg number 7 (FA). The GBAS coverage starts 1689 seconds from take-off and 311 seconds before landing (end of the simulation).

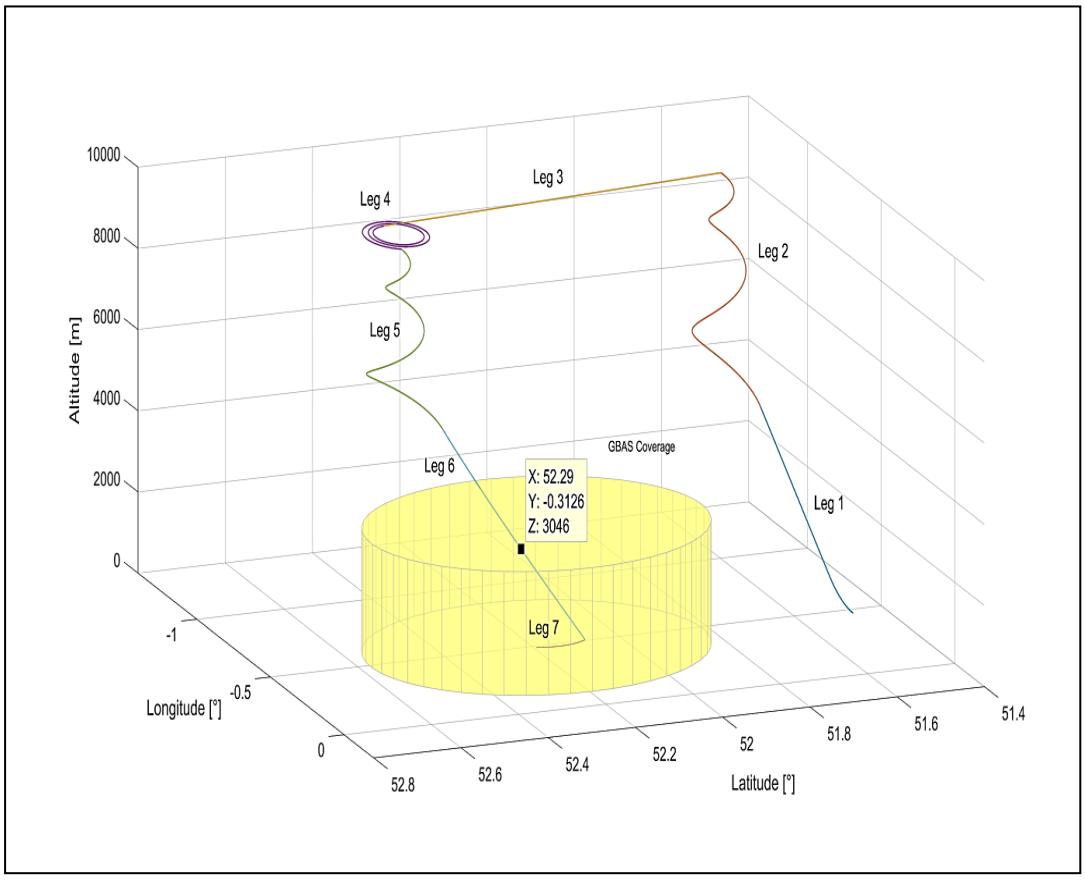


Figure 7-6. TORNADO-IDS flight trajectory and GCA.

The SBAS WIFs generated during the flight are listed in Table 7-12. SBAS where produced during the TC, LT and TD flight legs. No integrity flags where observed during the SD and FA flight legs.

Table 7-12. WIFs for SBAS (TORNADO-IDS).

FLIGHT LEG		WIF
CLIMB		---
TURNING CLIMB		310 ~ 330 s, 366 ~ 374 s, 424 ~ 490 s, 546 ~ 595 s
CRUISE		---
LEVEL TURN		906 ~ 912 s, 1023 ~ 1026 s, 1028 ~ 1100s
TURNING DESCENT		1210 ~ 1219 s, 1234 ~ 1240 s, 1241 s, 1245 ~ 1257 s, 1265 s, 1269 ~ 1281 s, 1293 ~ 1305 s, 1317 ~ 1329 s, 1341 ~ 1354 s, 1361 s, 1363 ~ 1377 s, 1387 ~ 1401 s, 1402 s, 1407 ~ 1408 s, 1410 ~ 1414 s, 1434 ~ 1447 s, 1457 ~ 1470 s, 1480 ~ 1493 s
STRAIGHT DESCENT		1501 ~ 1712 s
APPROACH	LNAV/VNAV	---
	LPV 1	1800 ~ 2000 s
	LPV 2	

WIFs are geerated during the TC, LT, TD and FA flight legs. The causes of these WIF flags are listed in Table 7-13.

Table 7-13. SBAS CIFs and WIFs causes (TORNADO-IDS).

FLAG	TC	LT	TD	SD	AP
HPL WIF	310 ~ 330 s, 366 ~ 374 s	906 ~ 912 s, 1023 ~ 1026 s, 1028 ~ 1100s	1210 ~ 1219 s, 1234 ~ 1240 s, 1241 s, 1245 ~ 1257 s, 1265 s, 1269 ~ 1281 s, 1293 ~ 1305 s, 1317 ~ 1329 s, 1341 ~ 1354 s, 1361 s, 1363 ~ 1377 s, 1387 ~ 1401 s, 1402 s, 1407 ~ 1408 s, 1410 ~ 1414 s, 1434 ~ 1447 s, 1457 ~ 1470 s, 1480 ~ 1493 s	1501 ~ 1712 s	1800 ~ 2000 s
VPL WIF	424 ~ 490 s, 546 ~ 595 s	---	1210 ~ 1219 s, 1234 ~ 1240 s, 1241 s, 1245 ~ 1257 s, 1265 s, 1269 ~ 1281 s, 1293 ~ 1305 s, 1317 ~ 1329 s, 1341 ~ 1354 s, 1361 s, 1363 ~ 1377 s, 1387 ~ 1401 s, 1402 s, 1407 ~ 1408 s, 1410 ~ 1414 s, 1434 ~ 1447 s, 1457 ~ 1470 s, 1480 ~ 1493 s	1501 ~ 1712 s	1800 ~ 2000 s

Both the HAL and VHL thresholds were exceeded by the HPLs and VPLs in the TC, TD and FA flight legs. During the LT flight leg, the HPL WIF was genaerated but this was not coupled with a VPL WIF.

The GBAS integrity flags generated during the TORNADO-IDS simulated flight are listed in Table 7-14. In this case, in addition to WIFs, CIF flags were also generated when the PVPL/PHPL exceeded the VAL/HAL thresholds. The CIF was generated 6 seconds before the first WIF. Clearly, this is a desirable behaviour for the SBAS CIF.

Table 7-14. CIFs and WIFs for GBAS (TORNADO-IDS).

FLIGHT LEG		CIF	WIF
GBAS APPROACH	CAT I	1784 ~ 2000 s	1790 ~ 1800 s 1992 ~ 2000 s
	CAT II		
	CAT III		

The causes of CIF and WIF flags are listed in Table 7-15. It is shown that the HAL thresholds were exceeded by the PHPL/HPL but the VAL thresholds were not exceeded by the PVPL/VPL.

Table 7-15. Causes of CIFs and WIFs for GBAS (TORNADO-IDS).

PHASE	INITIAL DESCENT	FINAL APPROACH
PHPL CIF	1784 ~ 1800 s	1801 ~ 2000 s
HPL WIF	1790 ~ 1800 s	1992 ~ 2000 s
PVPL CIF	---	---
VPL WIF	---	---

Table 7-16 lists the full set of CIFs and WIFs generated by ABIA, SBAS and GBAS during the first five flight legs (i.e., before SD and FA). It is evident that some of the CIFs and WIFs generated by ABIA are paralleled by SBAS WIFs. In some cases, the ABIA CIF is in fact generated a few seconds before the corresponding SBAS WIF (as well as at least 2 seconds before the ABIA WIF). Clearly, this is a desirable behaviour and it shows that some potential synergies between ABIA and SBAS are in fact present.

Table 7-16. CIFs and WIFs for ABIA/SBAS/GBAS (TORNADO-IDS) from climb to descent.

FLIGHT LEG	CIF	WIF
CLIMB	---	---
TURNING CLIMB	**ABIA** 301 ~ 315 s, 417 ~ 474 s, 546 ~ 584 s	**ABIA** 433 ~ 447 s, 557 ~ 566 s
		SBAS 310 ~ 330 s, 366 ~ 374 s, 424 ~ 490 s, 546 ~ 595 s
CRUISE	---	---
LEVEL TURN	**ABIA** 906 ~ 1012 s, 1023 ~ 1138 s, 1143 s ~ 1200 s	**ABIA** 908 ~ 909 s, 927 ~ 984 s, 990 ~ 991 s, 1025 ~ 1028 s, 1049 ~ 1107 s, 1114 ~ 1115 s, 1152 ~ 1156 s, 1173 ~ 1177 s, 1187 ~ 1200 s
		SBAS 906 ~ 912 s, 1023 ~ 1026 s, 1028 ~ 1100s
TURNING DESCENT	**ABIA** 1210 ~ 1249 s, 1321 ~ 1338 s, 1348 ~ 1379 s, 1489 ~ 1500 s	**ABIA** 1230 ~ 1249 s, 1350 ~ 1379 s
		SBAS 1210 ~ 1219 s, 1234 ~ 1240 s, 1241 s, 1245 ~ 1257 s, 1265 s, 1269 ~ 1281 s, 1293 ~ 1305 s, 1317 ~ 1329 s, 1341 ~ 1354 s, 1361 s, 1363 ~ 1377 s, 1387 ~ 1401 s, 1402 s, 1407 ~ 1408 s, 1410 ~ 1414 s, 1434 ~ 1447 s, 1457 ~ 1470 s, 1480 ~ 1493 s

Table 7-17 lists the complete set of CIFs and WIFs generated by ABIA/SBAS in all flight phases and by GBAS during the initial descent and final approach phases. Also in this case, some potential synergies can be identified as the first ABIA CIF is generated exactly at the same time as the SBAS WIF and the GBAS CIF is produced 6 seconds before the ABIA WIF.

Table 7-17. CIFs and WIFs for ABIA/SBAS/GBAS (TORNADO-IDS) in descent and approach.

FLIGHT LEG		CIF	WIF
DESCENT AND APPROACH	LNAV/VNAV	**ABIA** 1501 ~ 1800 s **GBAS** 1784 ~ 2000 s	**SBAS** 1501 ~ 1712 s 1800 ~ 2000 s (LPV)
	LPV 1/2		
	CAT I/III		**ABIA** 1790 ~ 2000 s **GBAS** 1790 ~ 1800 s 1992 ~ 2000 s

Based on these results, it is evident that the performance of SBAS and GBAS can be enhanced by adding ABIA models to the existing standards (RTCA, 2004), (RTCA, 2006), (RTCA, 2008-a), (RTCA, 2008-b). As both SBAS and GBAS use redundant GNSS satellite observations to support Fault Detection and Exclusion (FDE) within the GNSS receiver (i.e., implementing a form of RAIM), some additional integrity falg criteria can be introduced. Based on FAA technical standard orders TSO-C145C (FAA, 2008-a) and TSO-C146C (FAA, 2008-b), a current generation WAAS-enabled GNSS receiver uses RAIM for instances when the augmentation signl becomes unavailable. In this WAAS/RAIM integration scheme, the minimum number of satellites required for FDE is 6. At present, no information is available regarding the provision of RAIM features within LAAS-enabled GNSS receivers. Therefore, we can assume the inclusion of a basic form of RAIM within suach receiver (i.e., at least 5 satellites are required for FDE). Based on these assumptions, the number of satellites in view can be used to set additional integrity thresholds for SBAS and GBAS:

- **When the number of satellites in view is less than 6, the GBAS CIF is generated.**
- **When the number of satellites in view is less than 5, the GBAS WIF is generated.**

- **When the number of satellites in view is less than 7, the SBAS CIF is generated.**
- **When the number of satellites in view is less than 6, the SBAS WIF is generated.**

These new thresholds are well suited for implementation into the ABIA IFG. Table 7-18 lists the CIFs and WIFs generated by ABIA to support SBAS operations by introducing the new criteria listed above.

Table 7-18. CIFs and WIFs for SBAS Obscuration (TORNADO-IDS).

FLIGHT LEG		CIF	WIF
CLIMB		---	---
TURNING CLIMB		301 ~ 600 s	---
CRUISE		---	---
LEVEL TURN		900 ~ 1200 s	---
TURNING DESCENT		1201 ~ 1500 s	---
DESCENT AND APPROACH	LNAV/VNAV	1501 ~ 1800 s	---
	LPV 1/2		

The GBAS integrity flags generated during the approach phase applying the GBAS-related obscuration criteria, are listed in Table 7-19.

Table 7-19. CIFs and WIFs for GBAS Obscuration (TORNADO-IDS).

FLIGHT LEG		CIF	WIF
APPROACH	LPV ½	---	---
	CAT I/III	1689 ~ 2000 s	1689 ~ 1800 s, 1992 ~ 2000 s

Tables 7-20 provides a summary view of all CIFs and WIFs generated by the SBAS, GBAS and ABIA systems in all flight phases, including the newly introduced CIF criteria for satellite obscuration applicable to SBAS and GBAS.

Table 7-20. CIFs and WIFs for ABIA/SBAS/GBAS (TORNADO-IDS) from climb to descent.

FLIGHT LEG		CIF	WIF
TURNING CLIMB		**ABIA** 301 ~ 315 s, 417 ~ 474 s, 546 ~ 584 s	**ABIA** 433 ~ 447 s, 557 ~ 566 s
		SBAS 301 ~ 600 s	**SBAS** 301 ~ 340 s, 368 ~ 374 s, 410 ~ 490 s, 512 ~ 515 s, 542 ~ 595 s
LEVEL TURN		**ABIA** 906 ~ 1012 s, 1023 ~ 1138 s, 1143 s ~ 1200 s	**ABIA** 908 ~ 909 s, 927 ~ 984 s, 990 ~ 991 s, 1025 ~ 1028 s, 1044 ~ 1107 s, 1114 ~ 1115 s, 1152 ~ 1156 s, 1173 ~ 1177 s, 1187 ~ 1200 s
		SBAS 901 ~ 1200 s	**SBAS** 901 ~ 1200 s
DESCENT (>23NM)		**ABIA** 1210 ~ 1249 s, 1321 ~ 1338 s, 1348 ~ 1379 s, 1489 ~ 1500 s	**ABIA** 1230 ~ 1249 s, 1350 ~ 1379 s
		SBAS 1201 ~ 1500 s	**SBAS** 1210 ~ 1219 s, 1234 ~ 1240 s, 1241 s, 1245 ~ 1257 s, 1265 s, 1269 ~ 1281 s, 1293 ~ 1305 s, 1317 ~ 1329 s, 1341 ~ 1354 s, 1361 s, 1363 ~ 1377 s, 1387 ~ 1401 s, 1402 s, 1407 ~ 1408 s, 1410 ~ 1414 s, 1434 ~ 1447 s, 1457 ~ 1470 s, 1480 ~ 1493 s
APPROACH (DESC. 1 & 2)	L/VNAV	**ABIA** 1501 ~ 2000 s	**ABIA** 1790 ~ 2000 s **SBAS** 1501 ~ 1712 s, 1800 ~ 2000 s
	LPV 1		
	LPV 2		
	CAT-I/III	**ABIA** 1689 ~ 2000 s **GBAS** 1689 ~ 2000 s	**ABIA** 1790 ~ 2000 s **GBAS** 1790 ~ 1800 s 1992 ~ 2000 s

Based on the results of this simulation case study, it is evident that integration of ABIA with SBAS and GBAS allows an extended TTC (predictive alert provided by the CIFs) in all conditions, while additional WIFs are generated by ABIA that the current SBAS/GBAS systems are not able to provide.

Fig. 7-7 shows the A320 flight trajectory and illustrates the portion of the TMA where GBAS is available. In this case, GBAS provides information when the A320 is flying leg number 5 (SD) and leg number 7 (FA). The aircraft enters the GCA after 2521 seconds from take-off and 459 seconds before the end of the simulation.

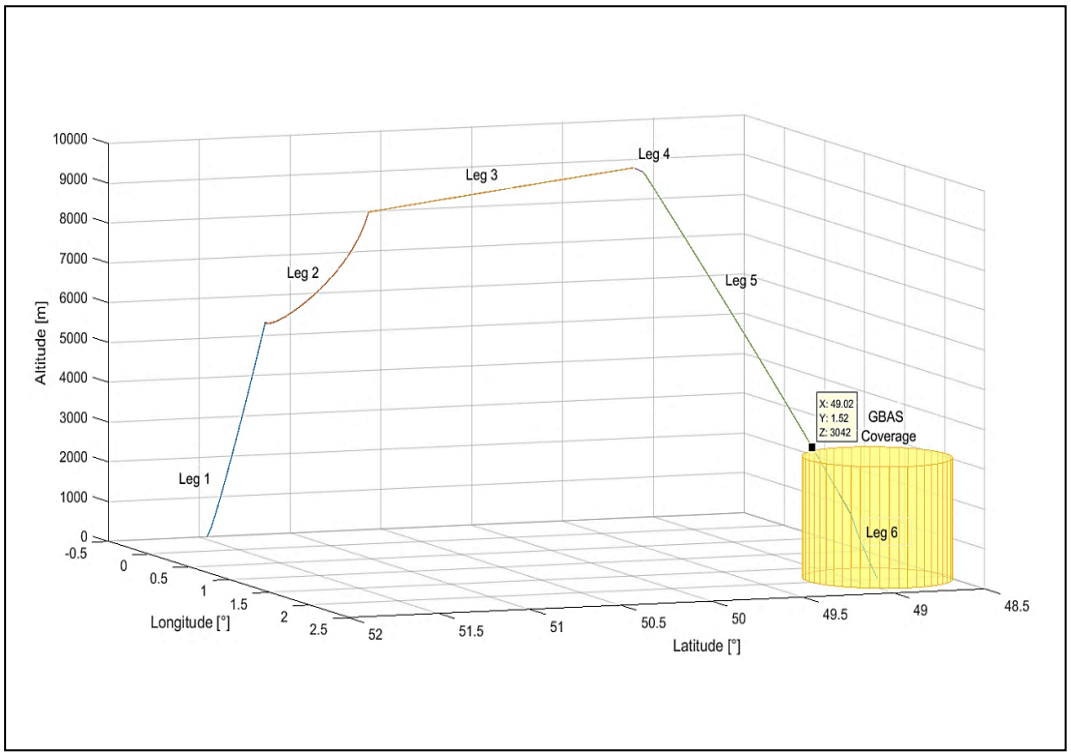


Figure 7-7. A320 flight trajectory and GCA.

Table 7-21 lists the CIFs and WIFs generated by SBAS adopting the full set of criteria listed above (i.e., SBAS H/VPL WIFs and satellite visibility CIF/WIFs).

Table 7-21. CIFs and WIFs for SBAS (A320).

FLIGHT LEG		CIF	WIF
CLIMB		---	---
TURNING CLIMB		601 ~ 900 s	---
CRUISE		---	---
LEVEL TURN		---	---
STRAIGHT DESCENT		1931 ~ 2630 s	---
DESCENT	L/VNAV	2631 ~ 2980 s	2636 ~ 2638 s
	LPV 1		
	LPV 2		

The causes of individual flags are listed in Table 7-22. No WIFs were generated by stand-alone SBAS but both CIFs and WIFs were generated by the ABIA augmented IFG simulator (i.e., based on the additional obscuration criteria).

Table 7-22. SBAS CIF and WIF causes (A320).

PHASE	SC	TC	SL	LT	SD	AP
Satellite Visibility CIF	No Flag 0 ~ 600 s SV 11 lost	601 ~ 900 s SV 3, 4, 9, 16, 25, 27, 28, 30, 31	No Flag 901 ~ 1900 s SV 11, 31 lost	---	1931 ~ 2630 s SV 4, 7, 9, 16, 27, 30	2631 ~ 2980 s SV 4, 7, 9, 16, 27, 30, 31
Satellite Visibility WIF	---	601 ~ 900 s SV 31	901 ~ 1900 s SV 11, 31	---	1931 ~ 2630 s SV 27	2631 ~ 2980 s SV 4, 7, 9, 16, 27, 30, 31
HPL WIF	---	---	---	---	---	---
VPL WIF	---	---	---	---	---	---

The GBAS integrity flags generated during the A320 flight are listed in Table 7-23.

Table 7-23. CIFs and WIFs for GBAS (A320).

FLIGHT LEG		CIF	WIF
STRAIGHT DESCENT		1931 ~ 2630 s	1931 ~ 2630 s
APPROACH	LPV 1	---	---
	LPV 2	---	---
	CAT I	2632 ~ 2980 s	2636 ~ 2980 s
	CAT II		
	CAT III		

The causes of CIF and WIF flags are listed in Table 7-24. In this case, GBAS alone was only able to generate a PHPL CIF (4 second predictive), followed by the HPL WIF. The introduction of additional obscuration criteria led to a much extended TTC, which is obviously desiable for safety-critical operations such as precision approach.

Table 7-24. GBAS CIF and WIF causes (A320).

PHASE	STRAIGHT DESCENT	APPROACH
Satellite Visibility CIF	1931 ~ 2630 s SV 4, 7, 9, 16, 27, 30	2631 ~ 2980 s SV 4, 7, 9, 16, 27, 30, 31
Satellite Visibility WIF	1931 ~ 2630 s SV 4, 7, 9, 16, 27, 30	2631 ~ 2980 s SV 4, 7, 9, 16, 27, 30, 31
PHPL CIF	---	2632 ~ 2980 s
HPL WIF	---	2636 ~ 2980 s
PVPL CIF	---	---
VPL WIF	---	---

Table 7-25 lists all CIFs and WIFs generated by SBAS, GBAS and ABIA in the various flight phases. Also in this case, the synergies between ABIA and SBAB/GBAS are evident.

Table 7-25. Combined CIFs and WIFs for ABIA/SBAS/GBAS (A320).

FLIGHT LEG		CIF	WIF
CLIMB		---	---
TURNING CLIMB		**ABIA** 601 ~ 900 s **SBAS Obscuration** 601 ~ 900 s	---
CRUISE		---	---
LEVEL TURN		---	---
STRAIGHT DESCENT		**ABIA** 2383 ~ 2418 s **SBAS** 1931 ~ 2630 s	---
DESCENT	L/VNAV	**ABIA** 2634 ~ 2980 s **SBAS** 2631 ~ 2980 s	**ABIA** 2636 ~ 2942 s **SBAS** 2631 ~ 2980 s
	LPV 1		
	LPV 2		
	CAT I	**ABIA** 2634 ~ 2980 s **GBAS** 2632 ~ 2980 s	**ABIA** 2636 ~ 2942 s **GBAS** 2636 ~ 2980 s
	CAT II		
	CAT III		

Fig. 7-8 shows the AEROSONDE UAV flight trajectory and illustrates the portion of the TMA where GBAS is available. In this case, GBAS provides information when the AEROSONDE is flying the legs number 5 (TD), 6 (SD) and 7 (FA). The aircraft enters the GCA during the TD leg after 2745 seconds from take-off and 205 seconds before landing (end of the simulation). Use of SBAS/GBAS approach modes is assumed in legs 6 (SD) and 7 (FA).

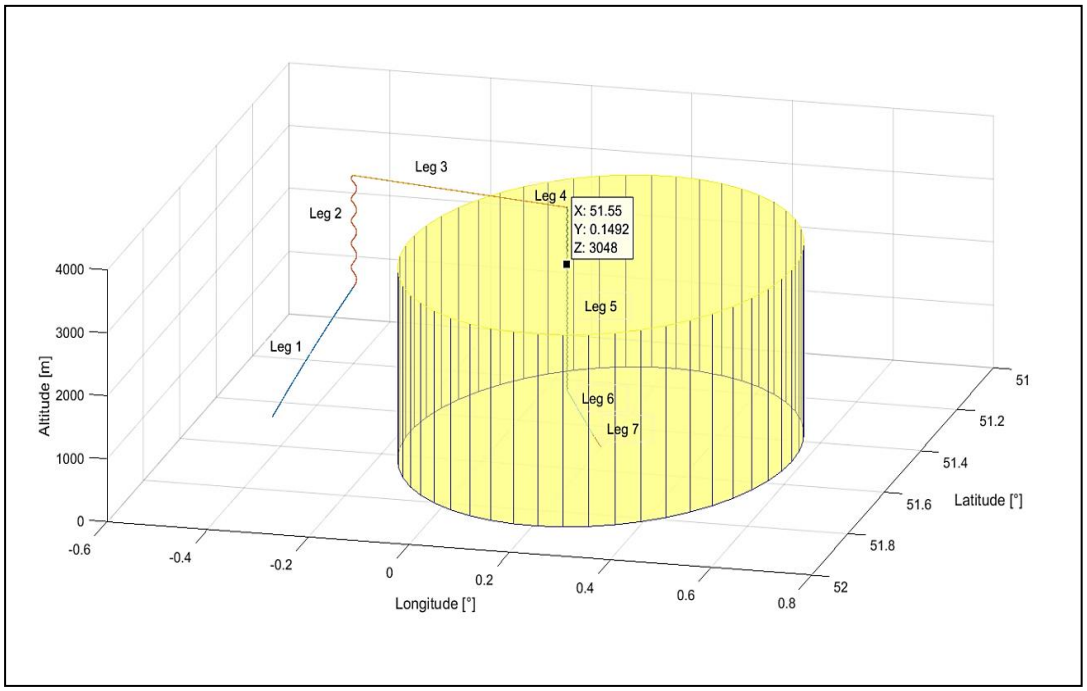


Figure 7-8. AEROSONDE UAV simulated trajectory.

The SBAS WIFs and CIFs recorded during the AEROSONDE flight are listed in Table 7-26.

Table 7-26. CIF and WIF for SBAS (AEROSONDE).

FLIGHT LEG		CIF	WIF
CLIMB		---	---
TURNING CLIMB		---	---
CRUISE		---	---
LEVEL TURN		2201 ~ 2650 s	2296 ~ 2358 s, 2445 ~ 2448 s, 2453 ~ 2650 s
TURNING DESCENT		2651 ~ 3100 s	2701 ~ 2739 s, 2832 ~ 2869 s, 3081 ~ 3093 s
SD and FA	L/VNAV	---	---
	LPV 1	---	3161 ~ 3400 s
	LPV 2	---	3161 ~ 3400 s

The causes of CIF and WIF flags are listed in Table 7-27.

Table 7-27. SBAS CIF and WIF causes (AEROSONDE).

PHASE	TC	LT	TD	SD	AP
Obscuration CIF	No Flag 451 ~ 900 s SV 3, 8 lost	2201 ~ 2650 s SV 3, 4, 8, 11, 16, 25, 28, 30	2651 ~ 3100 s SV 6, 7, 8, 9, 27, 31	No Flag 3101 ~ 3300 s SV 16 lost	3301 ~ 3400 s SV 6, 7, 8, 9, 25, 27, 31
Obscuration WIF	No Flag 451 ~ 900 s SV 3, 8 lost	2201 ~ 2650 s SV 3, 4, 8, 11, 16, 25, 28, 30	2651 ~ 3100 s SV 6, 7, 8, 9, 27, 31	No Flag 3101 ~ 3300 s SV 16 lost	3301 ~ 3400 s SV 6, 7, 8, 9, 25, 27, 31
HPL WIF	---	2296 ~ 2358 s, 2445 ~ 2448 s, 2453 ~ 2650 s	---	---	---
VPL WIF	---	---	2701 ~ 2739 s, 2832 ~ 2869 s, 3081 ~ 3093 s	3161 ~ 3300 s	3301 ~ 3400 s

The GBAS integrity flags generated during the the flight are listed in Table 7-28.

Table 7-28. CIF and WIF for GBAS (AEROSONDE).

FLIGHT LEG		CIF	WIF
DESCENT		2745 ~ 3100 s	3051 ~ 3100 s
FINAL APPROACH	**LPV 1**	---	---
	LPV 2	---	---
	CAT I	3301 ~ 3400 s	3301 ~ 3400 s
	CAT II		
	CAT III		

The causes of CIF and WIF flags are listed in Table 7-29.

Table 7-29. GBAS CIF and WIF causes (AEROSONDE).

PHASE	TD	SD	AP
Satellite Visibility CIF	2745 ~ 3100 s SV 6, 7, 8, 9, 27	No Flag 3101 ~ 3300 s SV 16 lost	3301 ~ 3400 s SV 6, 7, 8, 9, 25, 27, 31
Satellite Visibility WIF	3051 ~ 3100 s SV 6, 7, 8, 9, 27, 31	No Flag 3101 ~ 3300 s SV 16 lost	3301 ~ 3400 s SV 6, 7, 8, 9, 25, 27, 31
PHPL CIF	---	3101 ~ 3400 s	
HPL WIF	---	3101 ~ 3400 s	
PVPL CIF	---	3101 ~ 3400 s	
VPL WIF	---	3101 ~ 3400 s	

Table 7-30 lists all CIFs and WIFs generated by SBAS, GBAS and ABIA in the various flight phases. Also in this case, the synergies between ABIA and SBAB/GBAS are evident.

Table 7-30. Combined CIF and WIF flags for ABIA/SBAS/GBAS (AEROSONDE).

FLIGHT LEG		CIF	WIF
CLIMB		---	---
TURNING CLIMB		---	---
CRUISE		---	---
LEVEL TURN		**ABIA** 2241 ~ 2311 s, 2413 ~ 2485 s, 3491 ~ 2650 s	**ABIA** 2259 ~ 2263 s, 2273 ~ 2283 s, 2432 ~ 2436 s, 2446 ~ 2485 s, 2609 ~ 2612 s, 2621 ~ 2630 s
		SBAS 2201 ~ 2650 s	**SBAS** 2201 ~ 2650 s
TURNING DESCENT		**ABIA** 2688 ~ 2752 s, 2811 ~ 2881 s, 2944 ~ 3012 s, 3079 ~ 3100 s	**ABIA** 2690 ~ 2739 s, 2814 ~ 2869 s, 2946 ~ 3003 s, 3081 ~ 3100 s
		SBAS 2651 ~ 3100 s	**SBAS** 2651 ~ 3100 s
		GBAS 2745 ~ 3100 s	**GBAS** 3051 ~ 3100 s
APPROACH	L/VNAV	**ABIA** 3301 ~ 3400 s	**ABIA** 3303 ~ 3400 s
	LPV 1		**SBAS** 3161 ~ 3400 s
	LPV 2		
	CAT I	**ABIA** 3301 ~ 3400 s **GBAS** 3301 ~ 3400 s	**ABIA** 3303 ~ 3400 s **GBAS** 3301 ~ 3400 s
	CAT II		
	CAT III		

7.4 DISCUSSION

A clear advantage of ABIA over LAAS/WAAS, is that ABIA considers the aircraft dynamics in the computation of the various integrity flags, while LAAS and WAAS do not. This allows the implementation of model-predictive integrity flags (CIFs). As discussed in the thesis, the LAAS MOPS envisage the possibility of developing predictive aircraft-based integrity augmentation features (e.g., ABAS) but no information or guidance is provided in the standards on how to implement such predictive integrity features. ABIA is a possible answer to this important research gap. It is evident that the possibility of predicting additional integrity violations (due to dynamics) and extending the Time-to-React (TTR) by considering the aircraft-satellite relative motion represent a major advantage of ABIA in mission-essential an safety-critical GNSS applications. Based on the simulation case studies performed, ABIA provides predictive flags (CIFs) at least 2 seconds before the onset of an integrity event (TTC). This will allow:

- ***Supplementing SBAS:*** allowing improved performance in en-route, terminal and approach operations (e.g., route planning and real-time trajectory optimisation).
- ***Supplementing GBAS:*** in precision approach/autoland and surface operations: potentially allowing GNSS to meet CAT-III integrity requirements.

Based on the simulation case studies performed, it is evident that the ABIA predictive integrity features work synergically with the WAAS and LAAS integrity models. However, further research is needed to corroborate these preliminary findings and to investigate the synergies attainable in a wider range of manned and unmanned aircraft applications. Further research is also recommended to assess the synergies of ABIA with other forms of ABAS and with RAIM, including enhanced RAIM (eRAIM) and predictive RAIM (pRAIM), with a special focus on a multi-constellation GNSS environment. To fully assess the synergies of ABIA with other augmentation systems (SBAS/GBAS/RAIM and alternative forms of ABAS), future

research will include integration case studies, hardware-in-the-loop and human-in-the-loop simulations, as well as suitable ground/flight test activities.

7.5 CONCLUSION

In this chapter, the SBAS and GBAS integrity models were described (based on the applicable WAAS and LAAS standards) and some simulation case studies were performed to investigate the synergies attainable from the online integration of ABIA with SBAS and GBAS. The ABIA IFG performances studied in Chapter 5 were compared with the SBAS/GBAS CIF/WIF generation performances using the same manned/unmanned platforms and in the same flight phases. Based on all simulation case studies performed, it is concluded that the ABIA system works synergically with SBAS and GBAS, enhancing integrity levels in all flight phases, from initial climb to final approach. The ABIA algorithms are capable of generating suitable predictive and reactive flags (CIFs and WIFs) in the same flight phases where SBAS and GBAS are designed to operate. Therefore, the integration of ABIA with SBAS/GBAS is a clear opportunity for future research towards the development of a Space-Ground-Avionics Augmentation Network (SGAAN) suitable for manned and unmanned aircraft applications and for a variety of mission-essential and safety-critical aviation applications of GNSS, including flight test, precision approach and automatic landing.

7.5 REFERENCES

Di Esposti, R., Di Lellio, J., Galvin, D., Kelley, C. and Shih, J.M. (2003), "GPS III URA and URRA Information for Optimal User Performance." In Proceedings of the 2003 National Technical Meeting of The Institute of Navigation, Anaheim, CA (USA), pp. 504-512.

ESA (2014), “EGNOS Real time Performance.” European Space Agency Web Portal. Available at: http://www.egnos-pro.esa.int/IMAGEtech/imagetech_realtime_flash.html (visited in January 2014).

FAA (2008-a), "Airborne Navigation Sensors Using the Global Positioning System (GPS) Augmented by the Satellite Based Augmentation System." Federal Aviation Administration, Technical Standard Order (TSO) No. TSO-C145C.

FAA (2008-b), "Stand-Alone Airborne Navigation Equipment Using the Global Positioning System (GPS) Augmented by the Satellite Based Augmentation System." Federal Aviation Administration (FAA), Technical Standard Order (TSO) No. TSO-C146C.

FAA (2014-a), "Real-Time Service Monitoring Subsystem Display and User Manual." Federal Aviation Administartion (USA). Available at: http://www.nstb.tc.faa.gov/sms/ (downloaded 21st May 2016).

FAA (2014-b), "The William J. Hughes Technical Center WAAS Test - Team Interactive Web Application Portal." Federal Aviation Administartion (USA). Available at: http://www.nstb.tc.faa.gov/portal.htm (visitied in January 2014).

ICAO (2002), "Global Air Navigation Plan for CNS/ATM Systems." International Civil Aviation Organization. Document No. 9750 AN/963. Second Edition, 2002.

ICAO (2005), "Global Navigation Satellite System (GNSS) Manual." International Civil Aviation Organization. Document No. 9849 AN/457. First Edition.

ICAO (2006), "International Standards and Recommended Practices. Annex 10 to the Convention on International Civil Aviation." Aeronautical Telecommunications. Volume I: Radio Navigation Aids. Sixth Edition (Including Amendments 1-81).

ICAO (2006), "Standards and Recommended Practices (SAPRs) Volume 1 – Annex 10." Including Amendments 1-81, Issue 6.

ICAO (2010), "GBAS CAT II/III Development Baseline SARPs." Draft proposed changes to Annex 10, Volume I, as agreed at the 17 – 28 May 2010 meeting of the ICAO Navigation Systems Panel (NSP). Available online at: http://www.icao.int/safety/airnavigation/documents/ gnss_cat_ii_iii.pdf (downloaded 21st May 2013).

ICAO (2010), "GBAS CAT II/III Development Baseline SARPs." Draft proposed changes to Annex 10, Volume I, as agreed at the 17 – 28 May 2010 meeting of the ICAO Navigation Systems Panel (NSP). Available online at: http://www.icao.int/safety/airnavigation/documents/ gnss_cat_ii_iii.pdf (downloaded 21st May 2013).

Murphy, T., Friedman, R., Booth, J., Geren, P., Molloy, N., Clark, B. and Burns, J. (2004), "Program for the Investigation of Airborne Multipath Errors." In Proceedings of the 2004 National Technical Meeting of The Institute of Navigation, San Diego, CA (USA), pp. 781-792.

Murphy, T., Harris, M., Booth, J., Geren, P., Pankaskie, T., Clark, B., Burns, J. and Urda, T. (2005-a), "Results from the Program for the Investigation of Airborne

Multipath Errors." In Proceedings of the 2005 National Technical Meeting of The Institute of Navigation, San Diego, CA (USA), pp. 153-169.

Murphy, T., Harris, M., Geren, P., Pankaskie, T., Clark, B. and Burns, J. (2005-b), "Results from the Program for the Investigation of Airborne Multipath Errors." In Proceedings of the 18th International Technical Meeting of the Satellite Division of The Institute of Navigation (ION GNSS 2005), Long Beach, CA (USA), pp. 2670-2687.

Peck, S. and Tekawy, J. (1997), "User Differential Range Error Algorithms for the Wide Area Augmentation System." In Proceedings of the 53th Annual Meeting, Albuquerque. NM (USA).

RTCA (2004), "Minimum Aviation System Performance Standards (MASPS) for the Local Area Augmentation System (LAAS). Radio Technical Commission for Aeronautics (RTCA) Inc., Special Committee No. 159. Document RTCA DO-245A. Washington DC (USA). 2004.

RTCA (2006-a), "Minimum Operational Performance Standards for Global Positioning System/Wide Area Augmentation Systems Airborne Equipmen." Radio Technical Commission for Aeronautics (RTCA) Inc., Special Committee No. 159. Document RTCA DO-229D. Washington DC (USA).

RTCA (2006-b). "Minimum Operational Performance Standards for GNSS Airborne Active Antenna for the L1 Frequency Band." Radio Technical Commission for Aeronautics (RTCA) Inc., Special Committee No. 159. Document RTCA DO-301. Washington DC (USA).

RTCA (2008-a), "Minimum Operational Performance Standards for GPS/GBAS Airborne Equipment." Radio Technical Commission for Aeronautics (RTCA) Inc., Special Committee No. 159. Document RTCA DO-253C. Washington DC (USA).

RTCA (2008-b), "GNSS-Based Precision Approach Local Area Augmentation System (LAAS) Signal-in-Space Interface Control Document (ICD)." Radio Technical Commission for Aeronautics (RTCA) Inc., Special Committee No. 159. Document RTCA DO-246D. Washington DC (USA).

Volchansky, L. (2009), "Predictive RAIM for RNAV 1 and RNAV 2 Operations Using TSO-C129 GPS." ICAO SAM Implementation Group, AIR-130. Available online at: http://www.icao.int/SAM/Documents/2009/SAMIG4/presentation%20ICAO_SAM_IG_RAIM_Volchansky_v4.pdf (Visited on 23th March 2015).

Walter, T., Hansen, A. and Enge, P. (2001), "Message Type 28." In Proceedings of the 2001 National Technical Meeting of the Institute of Navigation, Long Beach, CA (USA), pp. 522-532.

Xie, G., Pullen, S., Luo, M., Normark, P., Akos, D., Lee, J., Enge, P. and Pervan, B. (2001), "Integrity Design and Updated Test Results for the Stanford LAAS Integrity

Monitor Testbed." In Proceedings of the 57th Annual Meeting of the Institute of Navigation, Albuquerque, NM (USA), pp. 681-693.

Yang, L., Zhang, Y. and Gao Y. (2013), "Enhanced RAIM Based on Weighted and Subset Schemes for GNSS Receiver." In Proceedings of the ION 2013 Pacific PNT Meeting, Honolulu, Hawaii (USA), pp. 661-666.

8

ABIA SYNERGY WITH UAS SENSE-AND-AVOID

8.1 INTRODUCTION

In modern Unmanned Aircraft System (UAS) applications, GNSS can support the development of low-cost and high performance (and relatively low cost and low-volume/weight) navigation and guidance systems. Additionally, when used in conjunction with suitable data link technologies, GNSS-based navigation systems facilitate the provision of Automated Dependent Surveillance (ADS) functionalities for cooperative UAS Sense-and-Avoid (SAA). In non-cooperative SAA, the adoption of GNSS can also provide the key positioning and, in some cases, attitude data (using multiple antennas) required for automated collision avoidance. A key limitation of GNSS for both cooperative (ADS) and non-cooperative applications is represented by the achievable levels of integrity. Therefore, the implantation of ABIA functionalities could support the development of an Integrity-Augmented SAA (IAS) system suitable for both cooperative and non-cooperative scenarios. A possible IAS architecture is presented in this chapter and its performances are evaluated in representative simulation case studies.

8.2 ABIA SYSTEM FOR UAS

One of the key challenges encountered by the aviation community for integration of UAS into non-segregated airspace is the provision of a Sense-and-Avoid (SAA) capability meeting the stringent integrity requirements set by international standards and national certification authorities. As discussed in previous chapters, the ABIA research demonstrated the potential of this new technology to enhance GNSS integrity performance in a variety of mission-essential and safety-critical applications including experimental flight test/flight inspection, precision approach and automatic landing (also in synergy with GBAS and SBAS). Therefore, an ABIA system was developed for UAS applications (Fig. 8-1).

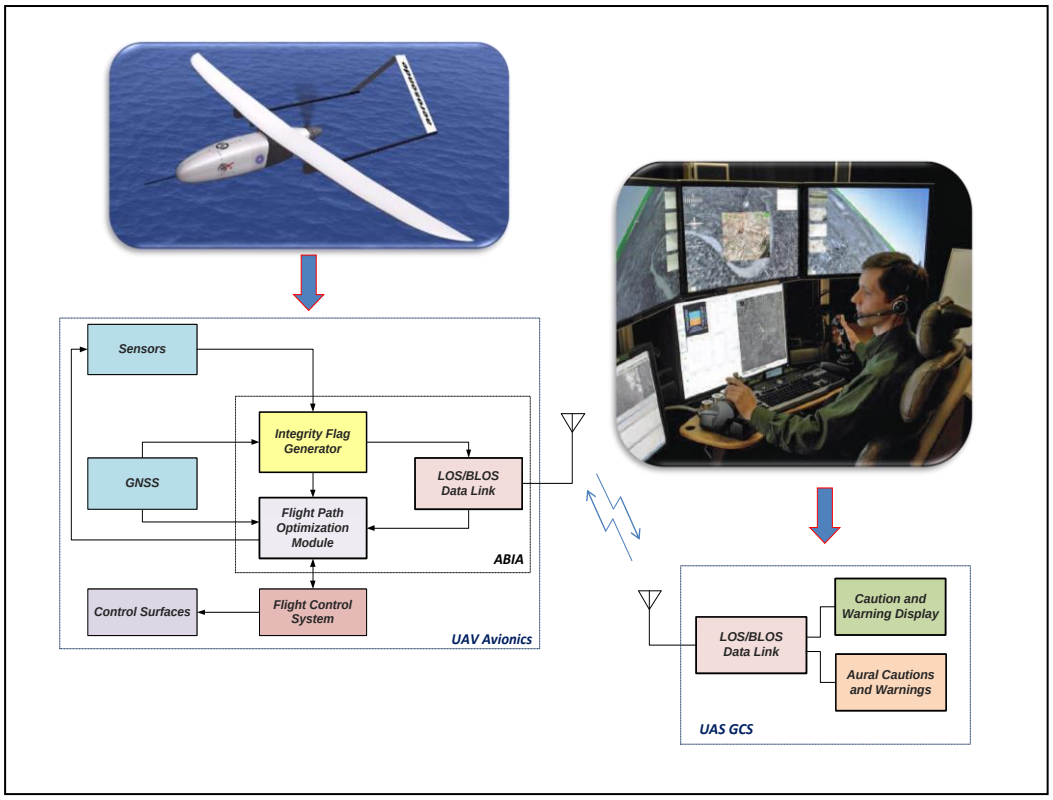


Figure 8-1. ABIA system architecture for UAS applications.

As in the manned aircraft version, this system performs a continuous monitoring of GNSS integrity levels in flight by analysing the relationships between aircraft manoeuvres and GNSS accuracy degradations or signal losses (Doppler shift, multipath, antenna obscuration, signal-to-noise ratio, jamming, etc.). In case of any

detected or predicted integrity threshold violation, the ABIA system provides suitable warning or caution signals to the UAV AFCS and to the remote Ground Control Station (GCS), thereby allowing timely correction manoeuvres to be performed. This increased level of integrity could provide a pathway to support unrestricted access of UAS to all classes of airspace.

8.3 SENSE-AND-AVOID

Cooperative and non-cooperative SAA are implemented to address UAS safe integration into the non-segregated airspace. The SAA capability can be defined as the automatic detection of possible conflicts (i.e., collision threats) by the UAV platform and the implementation of avoidance manoeuvres to prevent the identified collision threats. As part of our research, the possible synergies attainable with the adoption of different detection, tracking and trajectory generation algorithms were studied. Additionally, the error propagation from different sources and the impacts of host and intruders dynamics on the ultimate SAA solution were investigated. The system detection range and Filed-of-View/Field-of-Regard (FOV/FOR) have to be adequate to ensure separation from the intruder to prevent a probable near mid-air collision. This criterion is also naturally applicable in the case of small UAV since the vast majority of mid-air collision events occur below 3000 ft (Rodriguez et al, 2013). A number of cooperative and non-cooperative sensors/systems have been studied recently. Cooperative systems typically include Traffic Collision Avoidance System (TCAS)/Airborne Collision Avoidance System (ACAS) and Automatic Dependent Surveillance Broadcast (ADS-B). The inclusion of ADS-B in association with GNSS-based navigation systems redefines the paradigm of Cooperative SAA (C-SAA) in the CNS/ATM context by allowing the share of accurate GNSS trajectory information. Optical, thermal, LIDAR, MMW Radar and acoustic sensors can be used as part of Non-Cooperative SAA (NC-SAA) architectures. As an example, a combined C-SAA/NC-SAA architecture is depicted in Fig. 8-2 with an identification of primary (solid line) and auxiliary sensors (dashed line) for cooperative and non-cooperative SAA tasks. Additionally, ATM primary surveillance radar and Air Traffic Controller (ATCo) digital instructions using

Controller to Pilot Data Link Communications (CPDLC) are considered. The sequential steps involved in the SAA process for executing an efficient Tracking, Deciding and Avoiding (TDA) loop are also illustrated in Fig. 8-2. Criticality analysis is carried out to prioritize (i.e., to determine if a collision risk threshold is exceeded for all tracked intruders) and to determine the action commands. If an avoidance action is required, the SAA system generates an optimal avoidance trajectory using a fast-converging guidance algorithm such as differential geometry (Rodriguez et al., 2013), (Ramasamy et al., 2014). PMO techniques would have the benefit of providing a mathematical optimum. However, they can be used instead of DCO only if the SAA time horizon allows (i.e., only if the time to conflict is much greater than the computational time required to obtain an optimal trajectory). This could be the case, for example, in properly developed air traffic separation maintenance systems.

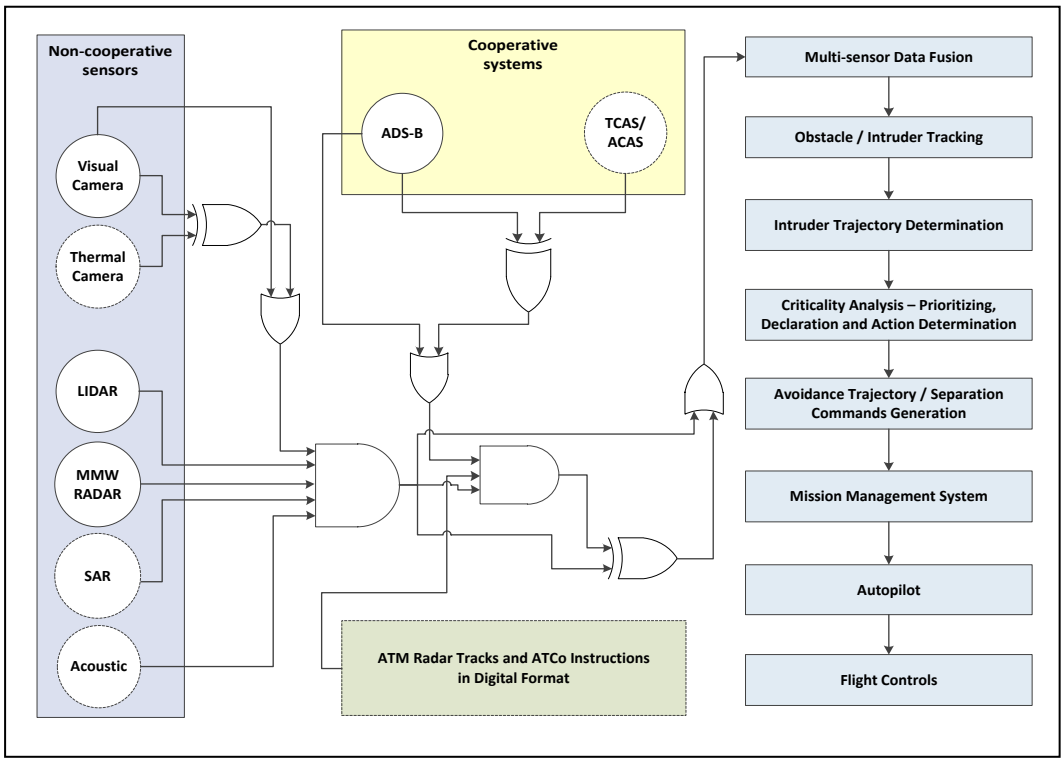


Figure 8-2. SAA system architecture. Adapted from (Ramasamy et. al., 2015).

Error analysis is performed to determine the overall uncertainty volume in the airspace surrounding the intruder tracks based on the cooperative/non-cooperative

unified method described in Ramasamy et al. (2015). This is accomplished by considering both the navigation and the tracking errors affecting the measurements and translating them to unified range and bearing uncertainty descriptors (Sabatini et al., 2014-a).

8.4 ABIA/SAA SYSTEMS INTEGRATION

A generic ABIA/SAA integration architecture is illustrated in Fig. 8-3. Position, Velocity, and Attitude/Rates (PVA) measurements are obtained by using the various navigation sesosrs/systems on-board the aircraft (i.e., implementing multi-sensor data fusion techniques).

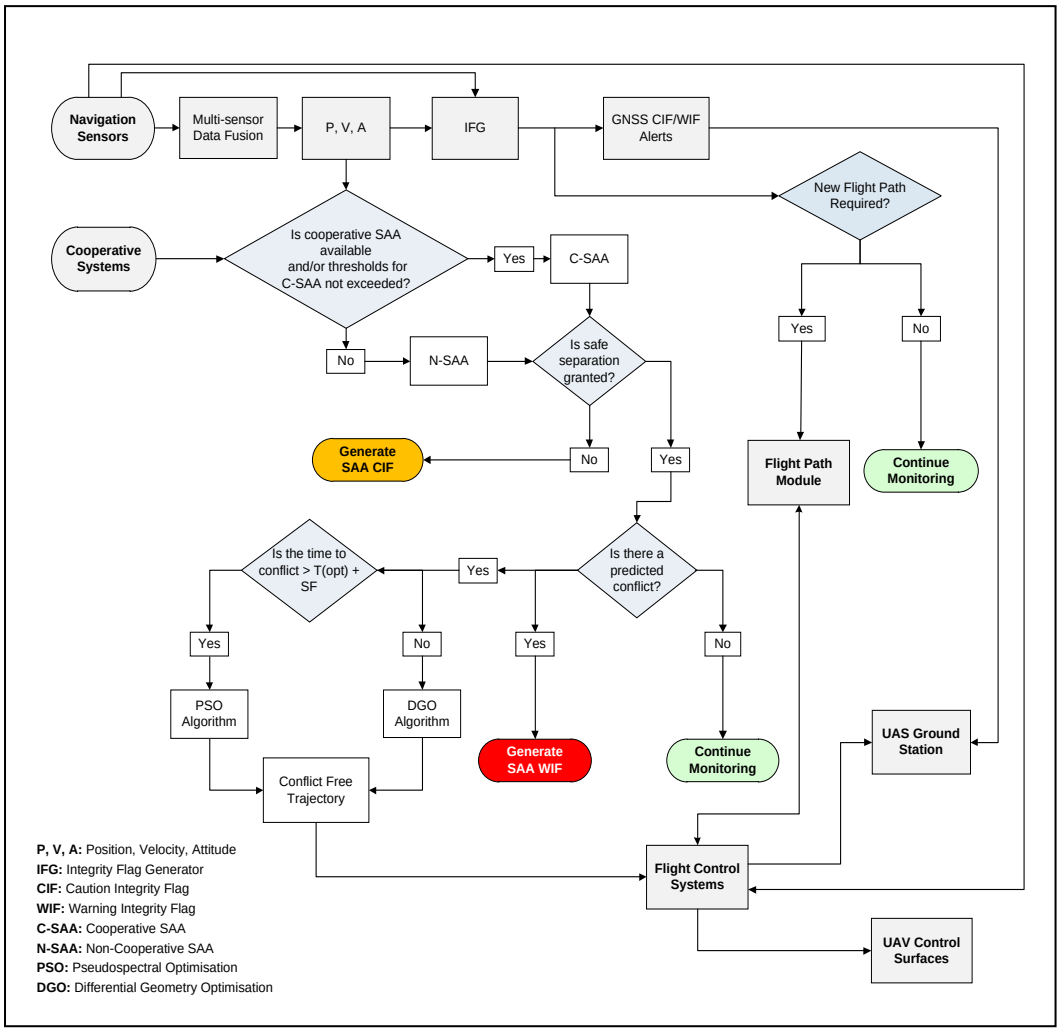


Figure 8-3. ABIA/SAA integrated architecture.

The current aircraft flight trajectory is estimated feeding these data to the aircraft dynamics model. The ABIA IFG module is run on this trajectory. Based on the Boolean decision logic that sorts sensors/systems data based on estimated performance parameters, the C-SAA or non-cooperative SAA sensors/systems are used for safe-separation. If both the safe-separation thresholds are violated, a mid-air collision threat is detected and the SAA WIF is generated. To prevent any WIF, the flight path optimization process starts when the first CIF is generated. PMO and DCO techniques are used to generate a new optimised trajectory free of any integrity degradations. Depending on the relationship between the available time-to-collision and the computation time required to generate the optimal trajectory, PMO or DCO solutions are applied. The optimised trajectory data are sent to the AFCS (and to the ground pilot) for execution of the avoidance manoeuvres. In the trajectory optimisation process the aircraft 3DOF/6DOF model defines the dynamics constraints, while the satellite elevations and the aircraft heading rates are used as path constraints. Additionally, the implemented guidance algorithm is based on minimisation of the following cost functional (Sabatini et al, 2014-b):

$$J = w_t \cdot \mathrm{t}_{SAFE} + w_f \int [SFC \cdot T(t)]dt - \mathrm{w}_d \cdot D_{min} + - w_{id} \cdot \int D(t)dt \qquad (8.1)$$

where $\mathrm{D(t)}$ is the estimated distance of the generated avoidance trajectory points from the avoidance volume associated with the obstacle, $D_{min} = min[D(t)]$ is the estimated minimum distance of the avoidance trajectory from the avoidance volume, $t_{SAFE} = t|_{D_{min}}$ is the time at which the safe avoidance condition is successfully attained, $SFC\ \left[\frac{\mathrm{kg}}{\mathrm{N}} \cdot \mathrm{s}\right]$ is the specific fuel consumption, $T(t)$ is the thrust profile and $\{w_t, w_f, w_d, w_{id}\}$ are the weightings attributed to time, fuel, distance and integral distance respectively. In time-critical avoidance applications (i.e., closing-up obstacles with high relative velocities) appropriate higher weightings are used for the time and distance cost elements.

8.5 SIMULATION

Some simulation case studies were performed to evaluate the performance of the ABIA/SAA integrated architecture. The following test platforms were used in the simulations:

- AEROSONDE UAV (ABIA host platform);
- AIRBUS 320 (A320) and AEROSONDE UAV intruders.

For these platforms, 3DOF aircraft dynamics models were implemented, together with typical navigation/tracking error figures available in the literature (Sabatini et al., 2013-a), (Sabatini et al., 2013-b). In all scenarios, an avoidance volume (accounting for navigation and tracking errors) was generated by the SAA system. PMO or DCO techniques were used to generate the new trajectory based on the available time to conflict (i.e., host entering the avoidance volume). The avoidance trajectory was initiated by the SAA system when the probability of collision exceeded the required threshold value. Minimum time was used as the only criteria in the cost functional for both PMO and DCO techniques. The boundary conditions were set from the value of the flight parameters at CIF time steps and a collision avoidance trajectory free of GNSS integrity degradation was generated. In all test cases, an avoidance volume (sum of navigation and tracking errors) was generated by the SAA system (Ramasamy et al., 2014-b), (Sabatini et al., 2015). PMO or DCO techniques were used to generate the new (optimal) trajectory based on the available time to conflict (i.e., host entering the avoidance volume). The avoidance trajectory was initiated by the SAA system when the probability of collision exceeded the required threshold value. Time, fuel, distance and integral distance were used in the cost functional, the UAV 3DOF dynamic model was used as dynamic constraint, and the minimum elevation criteria as path constraint for both PMO and DCO techniques. Boundary conditions were set from the values of the flight parameters at the first CIF epoch. Fig. 8-4 illustrates the C-SAA test scenario where two AEROSONDE UAVs (1 ABIA host platform and 1 intruder) are 90° off track at the same Flight Level (FL). The risk of collision is detected and resolved by the host UAV platform. This platform is equipped with the integrated ABIA/SAA system

described above and is therefore able to generate an avoidance trajectory which is free from CIF/WIF occurrences. As depicted in Fig. 8-4, the host UAV SAA (only) avoidance trajectory and the ABIA/SAA avoidance trajectory have a different rejoin point on the original track. For convenience, the binding sphere containing the 3-sigma uncertainty envelope at the predicted point of collision is shown in the figure and three points are highlighted on the host platform trajectory (Sabatini et al., 2014):

- ***SAA Break-off Point:*** Corresponding to the point where the host UA initiates the avoidance trajectory (commanded by the SAA system). The cost function criteria adopted in this case is minimum time.
- ***SAA Safe Manoeuvring Point:*** Corresponding to the point where the host UAV can manoeuvre safely (any manoeuvre within its operational flight envelope) has 0 ROC. From this point onwards the SAA cost function criteria switches to minimum time and minimum fuel to get back on the original (desired) track.
- ***ABIA Re-join Point:*** Corresponding to the point where the host UAV re-joins the original (desired) track without GNSS data degradations.

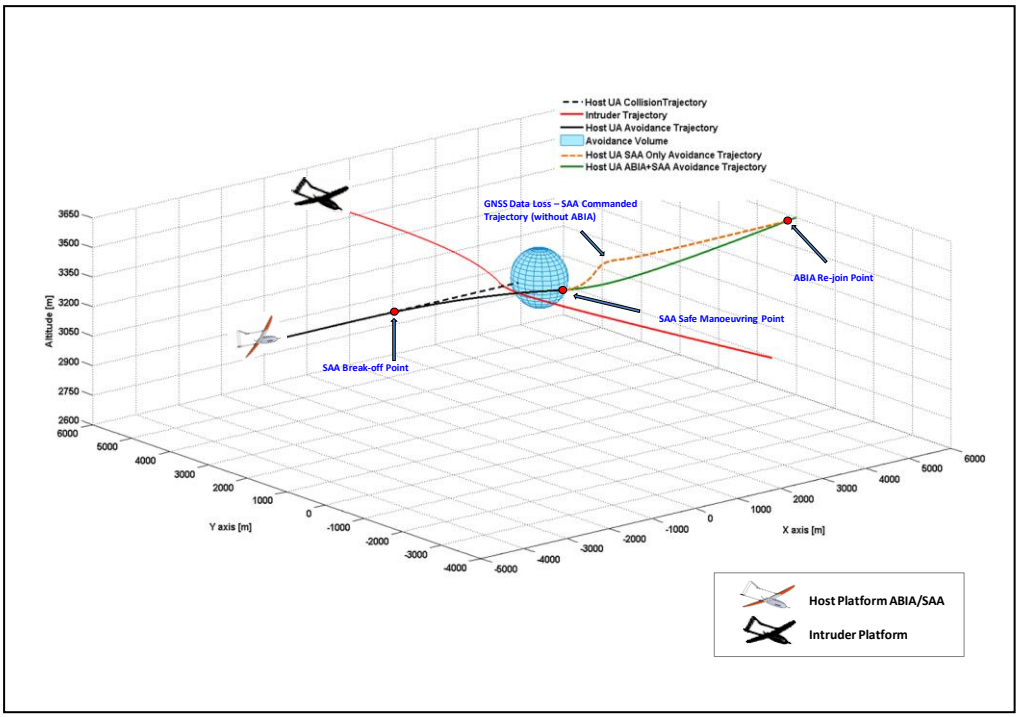


Figure 8-4. 2 UAV 90° collision C-SAA scenario.

The horizontal separation and predicted conflict probability in this case are shown in Fig. 8-5 and 8-6 respectively.

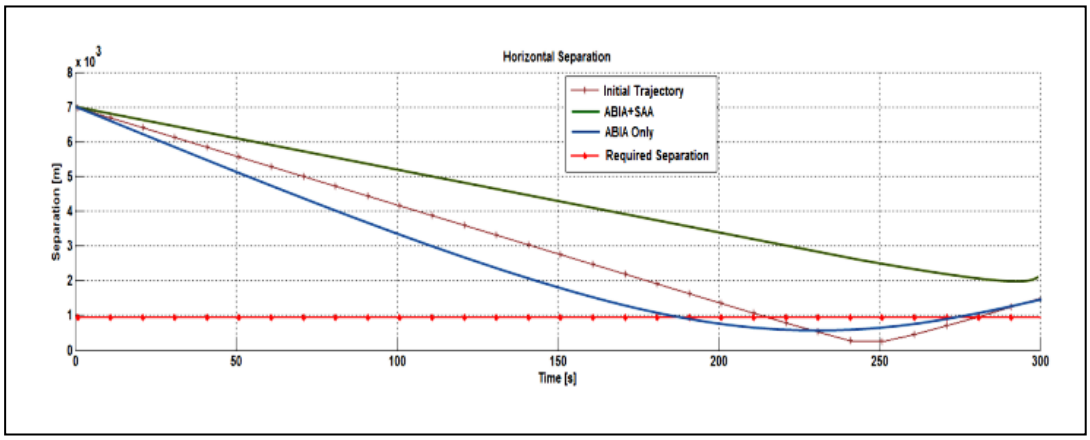


Figure 8-5. Achieved horizontal separation.

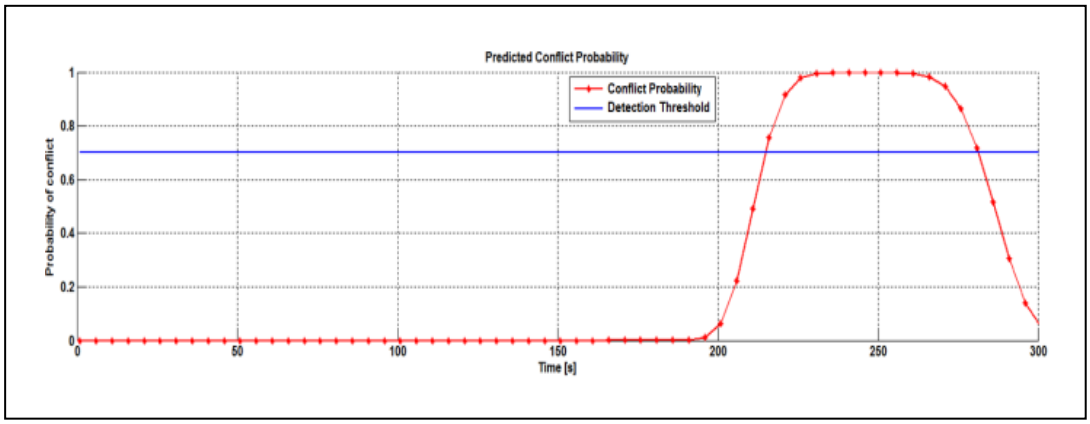


Figure 8-6. Predicted conflict probability.

Fig. 8-7 illustrates the NC-SAA test scenario where the AEROSONDE UAV (ABIA/SAA host platform) and an A320 are flying on the same FL but 90° off track to each other.

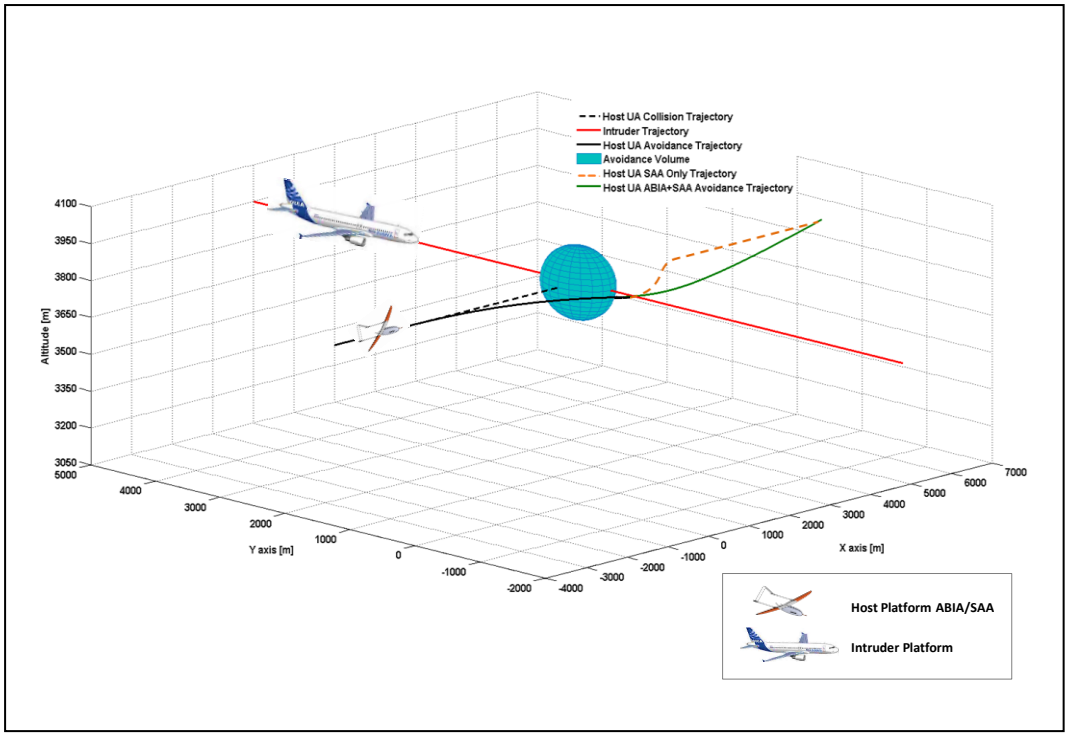


Figure 8-7. UAV 90° collision NC-SAA scenario.

The horizontal and vertical separation obtained is illustrated in Fig. 8-8.

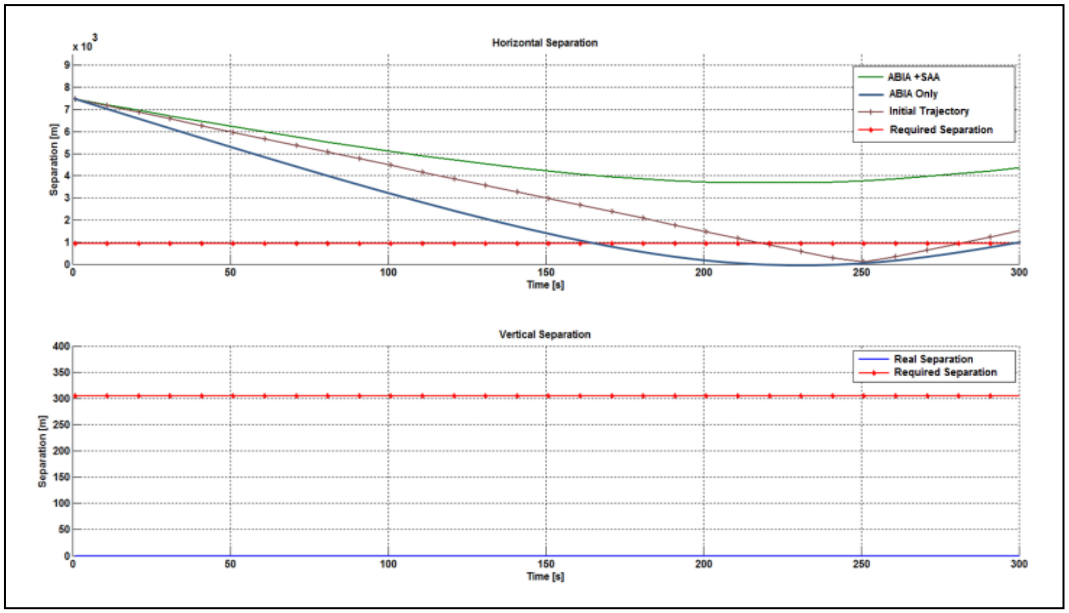


Figure 8-8. Horizontal and vertical separation.

Fig. 8-9 illustrates an additional C-SAA test scenario where the ABIA host platform (AEROSONDE UAV) and two intruders (two other AEROSONDE UAVs) are at the same FL.

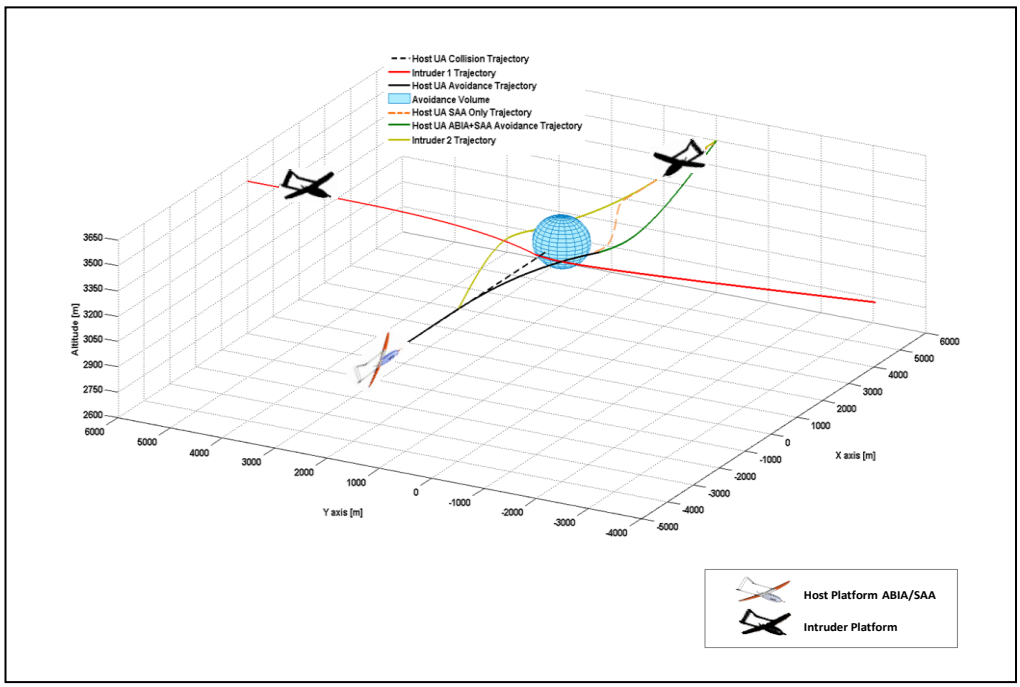


Figure 8-9. 3 UAV collision C-SAA scenario.

Intruder No. 1 is 90° off track and intruder No. 2 is following an head-on path with the host UAV. The horizontal and vertical separation obtained with respect to intruder No. 1 and No. 2 are illustrated in the Figures 8-10 and 8-11 respectively.

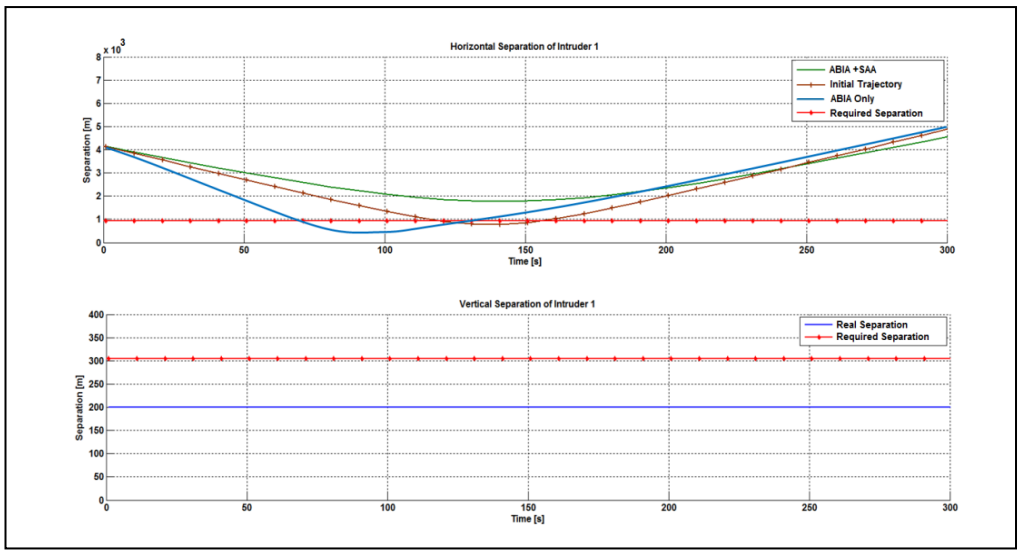


Figure 8-10. Horizontal and vertical separation of intruder No. 1.

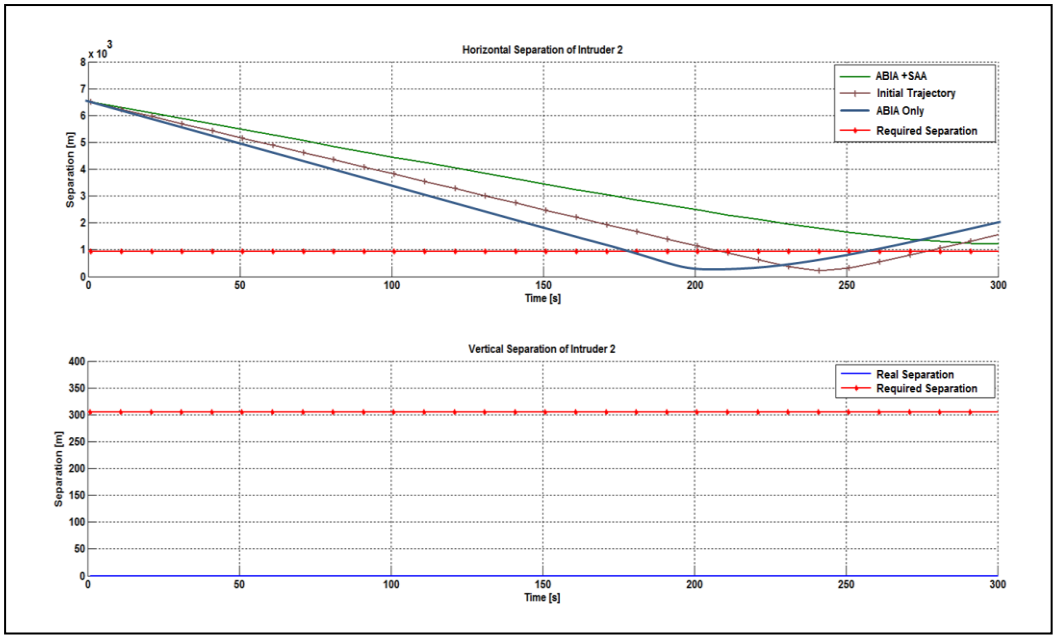


Figure 8-11. Horizontal and vertical separation of intruder No. 2.

In the C-SAA and NC-SAA scenarios investigated and in the dynamic conditions explored, all near mid-air collision threats were successfully avoided by implementing adequate trajectory optimisation algorithms. Both PMO and DCO algorithms proved successful in C-SAA and NC-SAA scenarios depending on the available time for the optimisation loops (distance host-intruders and relative dynamics). Based on the navigation error of the host aircraft and on the tracking error of the intruder, an optimised avoidance trajectory without GNSS data losses is constructed around the computed uncertainty envelope.

A simulation was performed in the presence of a low-power omnidirectional GNSS personal jammer as shown in Fig. 8-12. In case of jamming, the overall avoidance volume is obtained by combining the tracking error of the jamming signal radiation pattern (main lobe in the case of a directional jammer) and the navigation error of the host platform. The optimised avoidance trajectory is constructed tangential to the radiation pattern of the jammer by taking into account the position uncertainty of the host platform (blue spherical sector in Fig. 8-12).

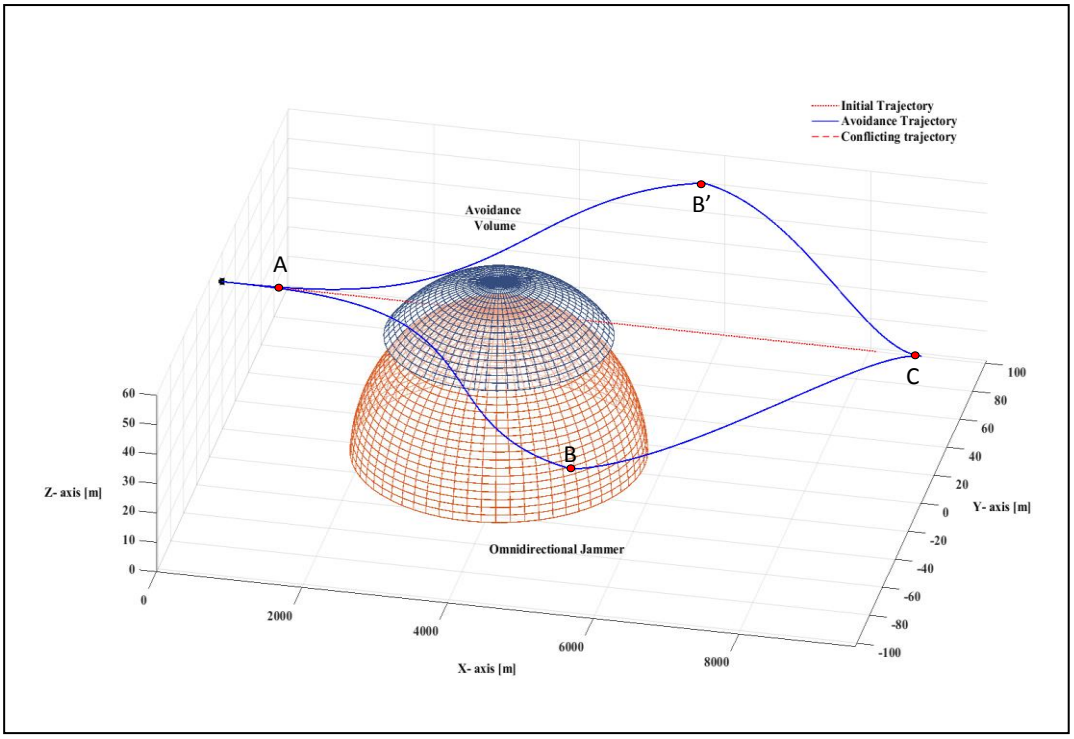


Figure 8-12. Avoidance trajectory for an omnidirectional jammer. (Sabatini et al., 2014).

In Fig. 8-12, after the omnidirectional jammer was identified and located, two symmetric optimal avoidance trajectories (ABC and AB'C) were generated based on the cost function approach defined earlier, with weights set to $w_t = 50\%, w_f = 20\%, w_d = 15\%, w_{id} = 15\%$. In this simulation, the constraints imposed by ABIA in terms of UAV platform dynamics and GNSS satellite elevation angles were considered to generate the optimised avoidance trajectories, thus preventing degradation or losses of navigation data during the whole jammer avoidance manoeuvre.

8.6 CONCLUSION

The synergies between a GNSS ABIA system and an existing UAS SAA architecture for cooperative and non-cooperative applications were explored in this chapter. The integration of ABIA in UAS cooperative and non-cooperative SAA architectures leads to an Integrity Augmented SAA (IAS) solution that is well suited

for a variety of mission-essential and safety-critical applications. Simulation case studies were performed on the IAS integrated system in various representative scenarios, including C-SAA, NC-SAA and in the presence of jamming. These results confirm that the proposed IAS system is capable of performing high-integrity conflict detection and resolution when GNSS is used as the primary source of navigation data, both in cooperative and non-cooperative SAA scenarios.

8.7 REFERENCES

Ramasamy, S., Sabatini, R. and Gardi, A. (2015), "Unifying Cooperative and Non-Cooperative RPAS Detect-and-Avoid." SAE AeroTech Congress 2015. Technical Paper 2015-01-2470.

Ramasamy, S., Sabatini R. and Gardi A. (2014), "Avionics Sensor Fusion for Small Size Unmanned Aircraft Sense-and-Avoid." Paper presented at IEEE Workshop on Metrology for Aerospace, pp. 271-276, Benevento (Italy).

Rodriguez, L., Sabatini, R., Gardi, A. and Ramasamy, S. (2013), "A Novel System for Non-Cooperative UAV Sense-and-Avoid." Paper presented at European Navigation Conference 2013, Vienna (Austria).

Sabatini, R., Moore, T. and Hill, C. (2014-a), "Avionics-Based GNSS Integrity Augmentation for Unmanned Aerial Systems Sense-and-Avoid." In Proceedings of the 27th International Technical Meeting of the Satellite Division of the Institute of Navigation: ION GNSS+ 2014. Tampa, FL (USA).

Sabatini, R., Gardi, A.and Ramasamy, S. (2014-b), "A Laser Obstacle Detection and Avoidance System for Unmanned Aircraft Sense-and-Avoid." Applied Mechanics and Materials, Vol. 629, Trans Tech Publications, Switzerland, pp. 355-360.

Sabatini, R., Ramasamy, S., Gardi A. and Salazar, L .R. (2013-a), "Low-cost Sensors Data Fusion for Small Size Unmanned Aerial Vehicles Navigation and Guidance." International Journal of Unmanned Systems Engineering, Vol. 1, No. 3, pp. 16-47.

Sabatini, R., Richardson, M. A., Bartel, C., Kaharkar, A., Shaid, T., Rodriguez, L. and Ramasamy S. (2013-b), "A Low-cost Vision Based Navigation System for Small Size Unmanned Aerial Vehicle Applications." Journal of Aeronautics and Aerospace Engineering, Vol. 2, No. 3.

9

CONCLUSIONS AND FUTURE RESEARCH

9.1 CONCLUSIONS

In this research, we developed an ABIA system specifically targeting GNSS integrity augmentation for manned aircraft and Unmanned Aircraft Systems (UAS) applications. Although current SBAS/GBAS augmentation systems can provide significant improvement of GNSS navigation performance, a properly designed and flight certified ABIA system could play a key role in GNSS augmentation for mission-essential and safety-critical applications such as aircraft precision approach, autolanding and UAS Sense-and-Avoid (SAA). Furthermore, using suitable data link and data processing technologies, a certified ABIA capability could be a core element of a future GNSS Space-Ground-Avionics Augmentation Network (SGAAN). The conclusions of this research project are summarised below in terms of achieved research objectives:

- **Perform a detailed review of GNSS aviation applications with a focus on integrity augmentation systems.**

  In recent years, various strategies have been developed to increase the levels of integrity of GNSS based navigation and landing systems. In addition to Space Based Augmentation Systems (SBAS) and Ground Based Augmentation Systems (GBAS), GNSS augmentation may also take the form of additional information being provided by other avionics systems. As the additional avionics systems operate via separate principles than the GNSS,

they are not subject to the same sources of error or interference. A system such as this is referred to as an Aircraft Based Augmentation System (ABAS). ABAS is different from RAIM (Receiver Autonomous Integrity Monitoring), in which the aircraft characteristics (flight dynamics, body shape, antenna location, EMC/EMI, etc.) are typically not considered and various consistency checks are accomplished using the GNSS signals in order to detect and exclude faulty/unreliable satellites. Unlike SBAS and GBAS technology, previous research on ABAS mainly concentrates on additional information being blended into the position calculation to increase accuracy and/or continuity of the integrated navigation solutions. Additionally, no significant attempts have been made of developing ABAS architectures capable of generating integrity signals suitable for mission-essential and safety-critical GNSS applications (e.g., aircraft precision approach and landing) and no commercial ABAS products are available at present.

- **Investigate GNSS and DGNSS performance in TSPI applications.**

  During flight test activities with GNSS and DGNSS TSPI systems, it was observed that one or more of the following conditions was prone to cause positioning data degradations or losses:

  - The aircraft reaching the CAA associated with a particular aircraft configuration;
  - Bad satellite geometries and low satellite C/N_0 values;
  - Aircraft DGNSS data link antennae coverage limitations;
  - Interference caused by the DGNSS data link or other RF signals;
  - Multipath caused by GNSS signals reflected by the Earth or the aircraft body surfaces.

  The last two problems could be mitigated by existing technology solutions (i.e., choosing a VHF data link, filtering the radio frequency signals reaching the GNSS antenna, identifying suitable locations for the GNSS antenna and providing adequate shielded of the antenna itself, either by physical devices

or via dedicated software masks, etc.). However, there was little to nothing one could do in order to prevent critical GNSS data losses during realistic test/training manoeuvres and particular approach procedures (e.g., curved and segmented approaches) performed with high performance military aircraft. Furthermore, although in some cases a careful mission planning could significantly reduce the number of GNSS outages, the adoption of specific aircraft piloting strategies (using the information currently available in the aircraft cockpits) could not effectively avoid the occurrence of these events.

- **Develop a TSPI ABIA system suitable for flight test, flight inspection and training applications.**

  A case study was undertaken in order to identify an integrity augmentation method/technique suitable for GNSS-TSPI. This method was originally intended for adoption in a dedicated ground-based simulation tool for mission planning and post-mission data analysis purposes. However, the concept successively evolved into a real-time T-ABIA system suitable for integration in the aircraft avionics and FTI systems; thus effectively providing augmentation of GNSS integrity in flight. Simulation and flight test activities were performed to corroborate the validity of the mathematical models for T-ABIA and the system was successfully integrated into a TORNADO-IDS test-bed aircraft to generate pilot alerts (within the specified maximum TTA) when the critical conditions for GNSS signal losses were likely to occur. Additionally, the T-ABIA system was able to provide some basic guidance information to prevent the aircraft reaching critical conditions for GNSS data degradations or losses.

- **Define the functional architecture of an ABIA system suitable for manned and unmanned aircraft applications.**

  Based on the experimental research and flight test activities conducted on GNSS and T-ABIA a more advanced ABIA system was developed. This system is suitable for manned and unmanned aircraft, including both military

and civil safety-critical applications. This new ABIA system, can provide steering information to the pilot (as the T-ABIA system for flight test applications) and, additionally, electronic commands to the aircraft/UAV Automatic Flight Control System (AFCS), allowing for real-time integrity monitoring, avoidance of mission/safety-critical flight conditions and fast recovery of the Required Navigation Performance (RNP) in case of GNSS data degradation or loss. The functional architecture and key design features of this novel GNSS ABIA system were defined.

- **Develop suitable models and algorithms to generate ABIA alerts, including caution (predictive) and warning (reactive) integrity flags.**

  The mathematical models and algorithms required for the ABIA Integrity Flag generator (IFG) module implementation were developed. The models address the main sources of GNSS data degradation or loss in flight including: antenna obscuration, geometric accuracy degradations, SNR, multipath and Doppler shift. Additionally, based on a detailed review of the available literature and flight test data analysis, suitable thresholds were identified used for generation of Caution Integrity Flags (CIFs) and Warning Integrity Flags (WIFs) in the ABIA IFG module.

- **Perform simulation case studies to verify the technical suitability of the models and algorithms developed for the ABIA caution and warning integrity flags.**

  Detailed simulation case studies were performed on TORNADO-IDS, A320 and AEROSONDE aircraft. Relevant flight manoeuvres/phases were considered in these simulations, including straight climb, level/turning cruise, turning climb/descent and straight descent. From the results of these simulation activities, the following conclusions are drawn:

  - In the limited but representative range dynamic conditions explored, data analysis showed that the ABIA Integrity Flag Generator (IFG) is capable of providing useful integrity flags when GNSS signals are

degraded or lost.

- The target SL requirements set for the CIF (DR=100% and TTC<2 seconds) were achieved in the selected manned/unmanned platform implementations and in all operational conditions tested (a limited but representative cross-section of the aircraft operational flight envelopes).
- After the integrity caution flag is generated, the time available for the pilot/autopilot to react (i.e., at least 2 seconds), would be adequate to support aviation safety-critical tasks including GLS precision approach and automatic landing applications.

These simulation results corroborate the validity of the models developed for the ABIA IFG module. The availability of a usable CIF (i.e., at least 2 seconds predictive) allows the implementation of early correction loops in both manned A/C and UAVs to avoid flight conditions potentially leading to unacceptable GNSS data degradations or losses.

- **Develop suitable mathematical models for flight path guidance, allowing avoidance of (or fast recovery from) mission/safety-critical flight conditions.**

  Mathematical models were developed for incorporation into the ABIA FPG module and their validity was tested in a simulation environment. The purpose of the FPG module is to exploit the ABIA predictive integrity flags (CIFs), allowing the aircraft to correct its flight trajectory/attitude and to avoid the occurrence of the critical GNSS data losses. Analysing the various causes of GNSS data degradation or loss, geometric/mission optimisation criteria were introduced in terms of satellite elevation angle and heading rates. Adopting these criteria and an adequate form of the aircraft dynamics model (3DOF with variable mass and constraints/initial conditions set by a manoeuvre recognition algorithms), two different approaches were introduced to solve the guidance problem (i.e., generation of optimal flight trajectories) both in mission-planning and real-time ABIA applications. The approach proposed for mission planning employs a classical Pseudospectral

Multi-Objective (PMO) technique and the real-time optimisation is accomplished by a Constrained Geometric Optimisation (CGO) method. Simulation case studies were accomplished on the AEROSONDE UAV to verify the suitability of the proposed techniques in a realistic operational scenario (including complex flight manoeuvres and GLS precision approach legs). The PMO technique converged to a mathematical optimum within 5 - 220 seconds depending on the length and complexity of the flight path to be optimised, while the CGO technique was able to generate trajectories free from GNSS data degradations/losses within 0.3 - 0.9 seconds. It is therefore concluded that the adoption of PMO/CGO techniques in the ABIA FPG module would allow an efficient exploitation of the IFG predictive features both in mission planning and real-time trajectory optimisation problems, potentially meeting GNSS integrity requirements for ATM online operations and allowing an effective AFCS/ABIA integration for GLS down to CAT III.

- **Start Investigating the potential of ABIA techniques to supplement SBAS/GBAS technology for en-route, terminal and approach operations.**

  SBAS and GBAS integrity models were analysed (based on the applicable WAAS and LAAS standards) and some simulation case studies were performed to investigate the synergies attainable from the online integration of ABIA with SBAS and GBAS. The ABIA IFG performances were compared with the SBAS/GBAS integrity flag generation performances using the same manned/unmanned platforms and in the same flight phases. Based on the simulation case studies performed, it is concluded that the ABIA system works synergically with SBAS and GBAS, enhancing integrity levels in all flight phases, from initial climb to final approach. The ABIA algorithms are capable of generating suitable integrity flags in the same flight phases where SBAS and GBAS are designed to operate. However, unlike SBAS and GBAS, ABIA considers the A/C-satellites relative dynamics producing predictive (as well as reactive) integrity flags (CIFs). Therefore, the integration of ABIA with SBAS/GBAS is a clear opportunity for future

research towards the development of a Space-Ground-Avionics Augmentation Network (SGAAN) suitable for manned and unmanned aircraft applications and for a variety of mission-essential and safety-critical aviation applications, including flight test, precision approach and automatic landing.

- **Start investigating the potential of ABIA techniques to enhance the performance of cooperative and non-cooperative UAS Sense-and-Avoid (SSA) in the Communication, Navigation and Surveillance/Air Traffic Management (CNS/ATM) and Avionics (CNS+A) context.**

  The synergies between a GNSS ABIA system and an existing UAS SAA architecture for cooperative and non-cooperative applications were explored. The integration of ABIA in UAS cooperative and non-cooperative SAA architectures leads to an Integrity Augmented SAA (IAS) solution that is well suited for a variety of mission-essential and safety-critical applications. Simulation case studies were performed in various representative scenarios, including Cooperative SAA (C-SAA), Non-Cooperative SAA (NC-SAA) and in the presence of jamming. These results confirm that the proposed IAS solution is capable of performing high-integrity conflict detection and resolution when GNSS is used as the primary source of navigation data. Further research is needed to develop a system that extends the ABIA concept to the various communication, navigation and surveillance systems required for trusted autonomous operations.

9.2 FUTURE RESEARCH

It is recommended that further research is carried out concentrating on the following main areas:

- Extend the ABIA concept to other navigation, communication and surveillance applications in the CNS+A context. This will require the

development of suitable mathematical models describing CNS/ATM and avionics systems operational and integrity performance.

- Investigate the potential of ABIA to enhance the performance of Next Generation Flight Management Systems (NG-FMSs) for manned and unmanned aircraft. This will require an evolution of current FMS architectures introducing suitable integrity monitoring and augmentation functionalities for 4-Dimensional Trajectory (4DT) planning and update throughout all flight phases.
- Evaluate the potential of ABIA techniques to enhance the performance of next generation CNS/ATM decision support tools for Performance/Intent Based Operations (PBO/IBO) and 4DT management.
- Assess the potential synergies between ABIA with other forms of ABAS and with RAIM techniques, including eRAIM and pRAIM in a multi-constellation GNSS environment.
- Refine the analytical and empirical models used to describe GNSS signal degradations (i.e., masking, multipath, C/N, J/S and Doppler) and receiver tracking performance based on future ABIA experimental activities (ground and flight testing), also addressing the significant evolutions being experienced by GNSS technologies.
- As GNSS technology progresses, assess the potential of introducing additional integrity flag criteria in the ABIA IFG based on UERE and DOP measurements. In particular, further research is needed for an accurate real-time determination of EHE/EVE in ABIA allowing a direct comparison with the SIS protection requirements (HAL and VAL) applicable to the different flight phases.
- Perform hardware-in-the-loop and human-in-the-loop simulations, aircraft integration studies and ground/flight test activities towards introducing a statistical definition of ABIA performance in terms of conventional Alert Limits (ALs) and Protection Levels (PLs). This will allow a direct comparison of ABIA with other augmentation systems (SBAS, GABS, RAIM

and other forms of ABAS) and a more detailed identification of the synergies attainable in various manned and unmanned aircraft applications.

- Define optimal trade-offs between Detection Rate (DR) and False Alarm Rate (FAR) in all required flight phases and in a variety of manned/unmanned aircraft operational tasks. As statistical data analysis will progress, it will also be possible to introduce Detection Probability (DP) and False Alarm Probability (FAP) metrics to better describe the ABIA performance.
- Perform hardware-in-the-loop and human-in-the-loop simulations, aircraft integration studies and ground/flight test activities to verify the ABIA IFG performance in terms of TTW (WIF) against the TTA requirements currently specified in ICAO standards for the various flight phases, as well as introducing new performance targets (as appropriate) based on the ABIA IFG predictive capability, the FPG module delay time and the pilot/AFCS response times associated to specific aircraft integration schemes.
- Evaluate the potential of introducing ionospheric scintillation models in the ABIA system implementation. In particular, future research will focus on possible mission planning implementations useful when flying over regions affected by intense scintillation and/or in times of predicted high scintillation.
- Further investigate the potential of ABIA techniques to support UAV SAA applications in the CNS+A context.
- Investigate the potential of ABAS/ABIA techniques to enhance GNSS integrity in aircraft surface operations.

Further research is also needed to investigate the synergies of ABIA with SBAS/GBAS/RAIM and other forms of ABAS in a wider range of manned and unmanned aircraft applications. Such applications and the potential benefits introduced by ABIA may include:

- ***UAS multi-sensor navigation and guidance systems:*** providing a mechanism for autonomous selection/de-selection of GNSS based on predicted performance. An extension of the ABIA concept is possible to other

navigation sensors/systems beyond GNSS, allowing a continuous performance monitoring of multiple sources of navigation data.

- ***Flight inspection and flight testing:*** speeding up the flight activities and allowing significant cost saving by avoiding the repetition of specific flight legs or entire flight sorties.
- ***PPP aviation applications in remote areas:*** potentially providing a new aircraft-autonomous integrity augmentation tool independent of ground networks.
- ***UAS precision agriculture and photogrammetry:*** speedup and cost saving of activities, allowing optimising the aircraft trajectories based on both mission requirements and GNSS performance requirements for autonomous operations.
- ***UAS Traffic Management (UTM):*** providing a possible aircraft-based technique to predict CNS performance degradations in complex urban environments, including the effects of multipath and obscuration in urban canyons.
- ***UAS Sense-and-Avoid (SAA):*** supporting avoidance volume calculations for cooperative and non-cooperative SAA cases and trajectory planning/replanning based on observed CNS performance parameters.
- ***Trusted autonomous operations:*** providing a mechanism to establish the level of trust that can be placed in avionics GNSS systems (and potentially in other CNS systems) based on both platform-satellite relative dynamics and external radiofrequency interference (both intentional and unintentional), facilitating Command and Control (C2) functions and single/multi-platform coordination in congested (and contested) airspace environments.

APPENDIXES

A

TORNADO-IDS EMC/EMI INVESTIGATION

A.1 GENERAL

Before installing the ASHTECH GNSS receiver in the TORNADO-IDS experimental aircraft, some ground tests were performed to investigate EMC/EMI aspects. In fact, due to the need of using an L-band telemetry data link for the TORNADO flight trails (including safety-critical test points and requiring real-time data analysis at a remote ground station), the EMC/EMI aspects of the GNSS and data link coexisting installations into the aircraft had to be deeply analysed. This was necessary because the GNSS and upper data link antennas, respectively receiving and transmitting in the same spectral band, were relatively close one to the other, and because possible interference problems degrading reception/reacquisition of GNSS signals at the airborne GNSS antenna location could seriously affect the validity of the flight trials (Sabatini et al., 2008).

A.2 TELEMETRY LINK INSTALLATION

As discussed, a telemetry link was installed on the TORNADO-IDS aircraft in order to allow exchange of FTI/GNSS and other avionics data between the aircraft and the ground (flight test control station). The telemetry assigned frequencies are 1442.5 MHz, 1436 MHz, and 1460 MHz. The main lobe of the data link carrier frequency has a main-lobe (600-700 KHz band) whose transmission level is 40 dBm (dB referred to 1 mW), and side-lobes with -50 dBm levels with respect to the main-

lobe. The power spectrum of the telemetry carrier signal at 1460 MHz received from the telemetry antenna directly connected to a spectrum analyser is shown in Fig. A-1.

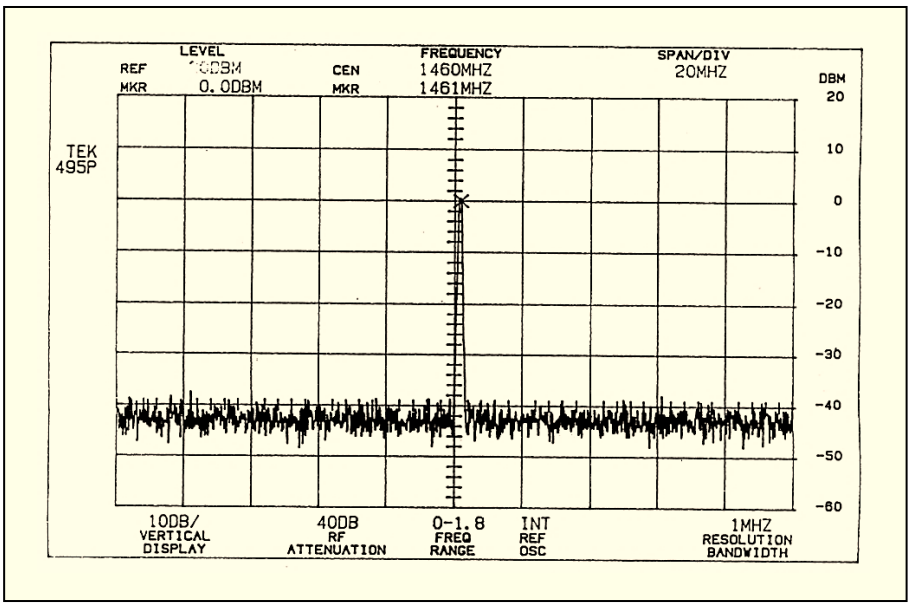


Figure A-1. Power spectrum of the 1460 MHz telemetry carrier.

A further spectrogram is shown in Fig. A-2. In this case, the spectrum analyser reference level was modified in order to detect spurious signals.

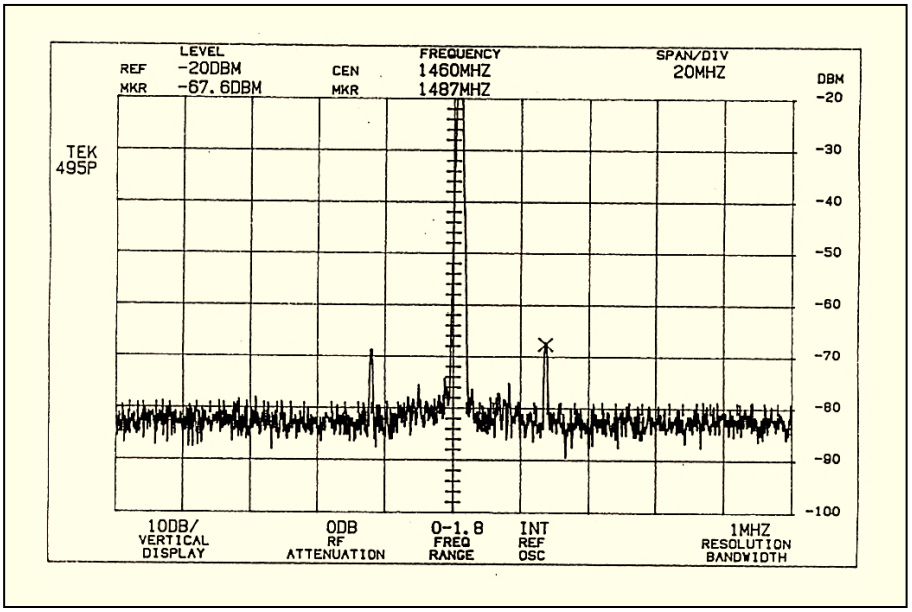


Figure A-2. Power spectrum of the 1460 MHz telemetry carrier (enlarged).

A.3 EXPERIMENTAL SETUP

The ASHTECH GNSS antenna and two telemetry antennas were installed on an aluminium-alloy plate. The telemetry antennas were placed at distances of 70 cm and 27 cm respectively from the GNSS antenna, in order to investigate the effect of distance on telemetry-GNSS interference. The Spectrum Analyser TEKTRONIX 495P (input impedance = 50 Ω, frequency interval = 100 Hz ÷1.8 GHz, maximum signal level = 30 dBm) was used for these tests. During the tests, two different telemetry transmitters were used:

- MICROCON T-710 model, high quality (very narrow-band) transmitter with carrier frequency of 1460 MHz;
- SOUTHERN CALIFORNIA MICROWAVE TTX 13L-10A model, medium quality transmitter with selectable carrier frequencies (interval 1435.5 MHz ÷ 1540.5 MHz).

For the ground test, the Spectrum Analyser was connected to the exit of the GNSS antenna pre-amplifier. This pre-amplifier had a gain of 48 ± 4 dB, an input voltage of 9.5 ± 2V, and an input current 80 ± 10 mA. The GNSS antenna pre-amplifier response to an input signal at –80 dBm is shown in Fig. A-3.

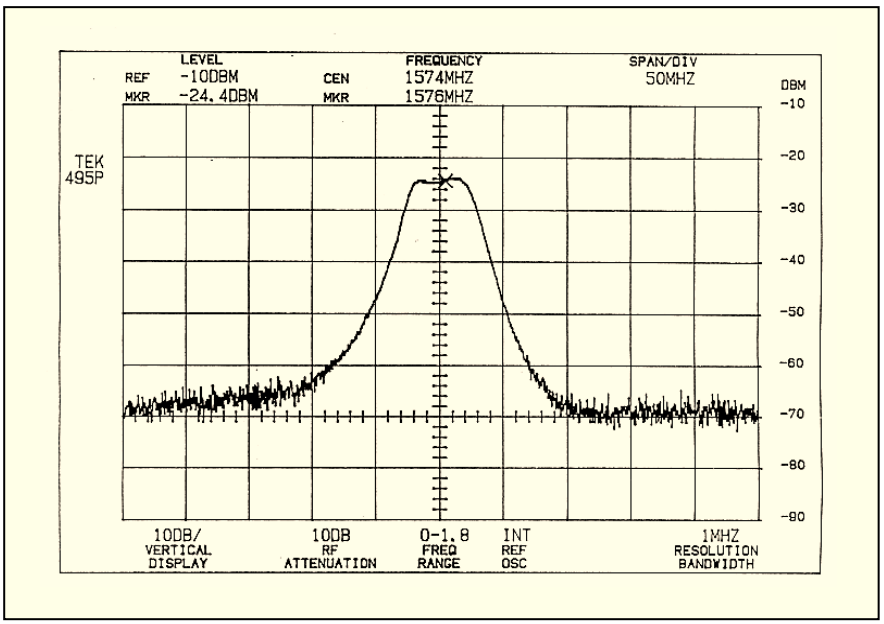


Figure A-3. GNSS antenna pre-amplifier response.

The instrumentation setup used for the measurements is shown in Fig. A-4.

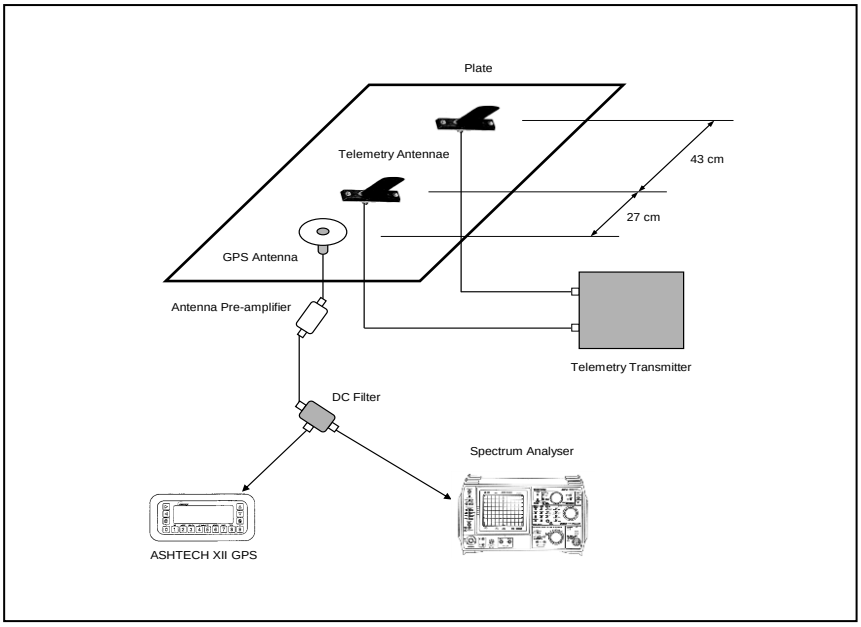


Figure A-4. Interference measurements setup.

With this experimental setup, the GNSS signal power spectrum in the absence of telemetry signal (Telemetry Transmitter off) could be displayed on the Spectrum Analyser (Fig. A-5).

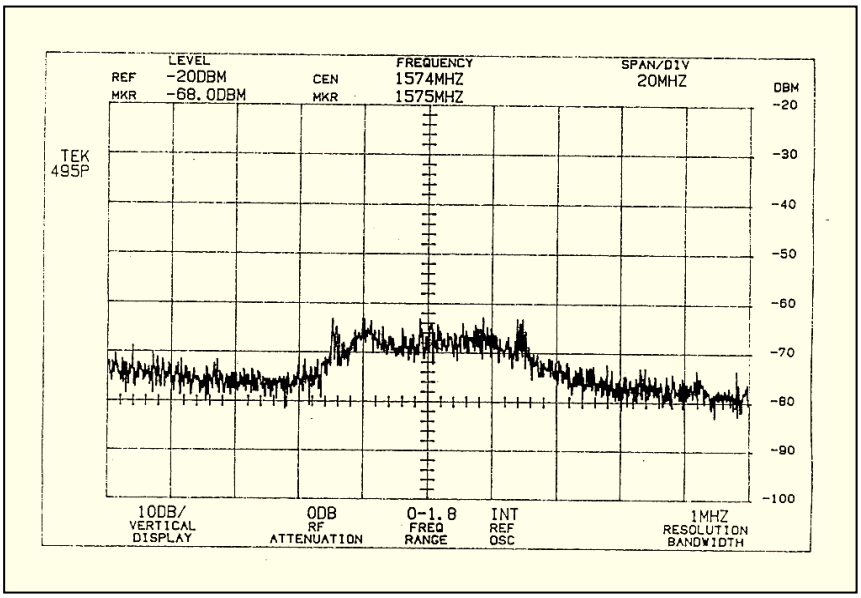


Figure A-5. GNSS signal power spectrum.

Successively, the Telemetry Transmitter was turned on. The resulting power spectrum in the GNSS signal band is shown in Fig. A-6.

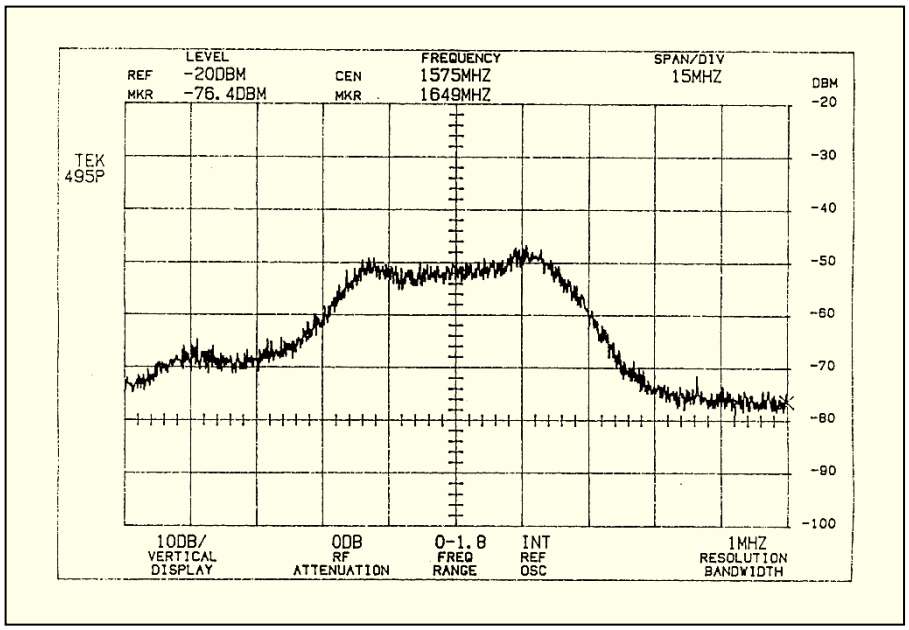


Figure A-6. GNSS/telemetry power spectrum in the GNSS signal band.

The complete spectrogram showing both the GNSS signal and the telemetry signal (carrier and spurious signals) is shown in Fig. A-7.

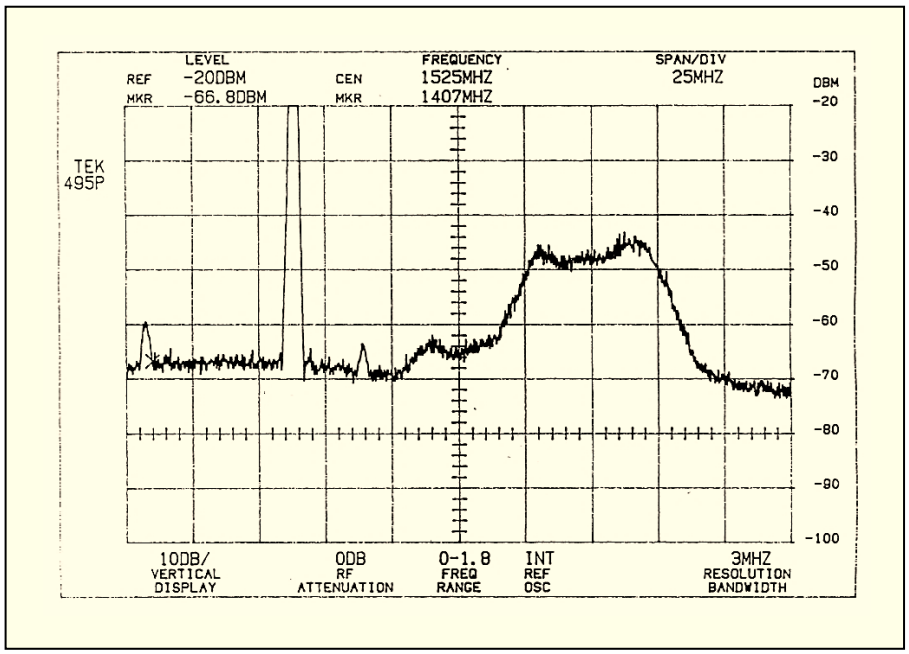


Figure A-7. Overall GNSS/telemetry signal power spectrum.

In order to verify the effects of this significant telemetry interference on the GNSS receiver, we looked at one of the GNSS display menus called "signal-health". This particular menu shows the tracked satellites numbers (**sv**) and some information regarding the signals received from the satellites, like the signal-to-noise ratio (**SNR**) and the satellite tracking parameter (**cnt**). An example is shown in Fig. A-8.

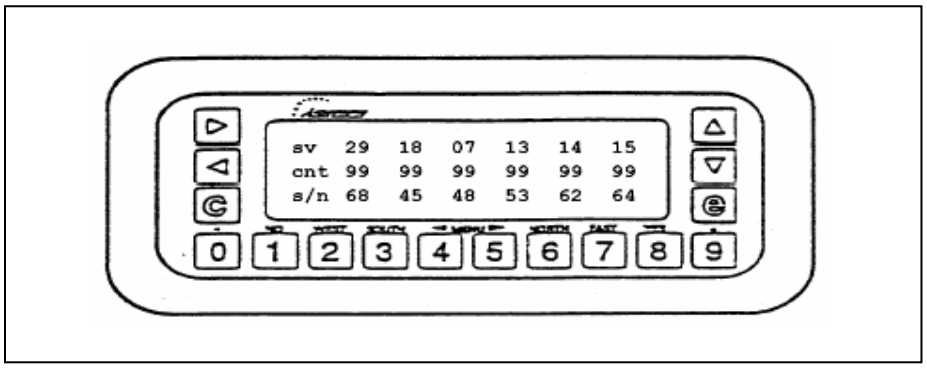


Figure A-8. ASHTECH Z12 signal-health display format.

Regarding the signal-to-noise ratio, a "week" signal has a **SNR** of less than 30 dB, while a "strong" signal has a **SNR** greater than 50 dB. The **cnt** parameter relative to a particular satellite goes to 00 when the receiver lose track to the satellite, and it is normally at a value of 99 when the satellite is being tacked. Fig. A-9 shows two signal-health formats relative to tracking (a) and loss of tracking (b) of the GNSS satellites due to telemetry transmission.

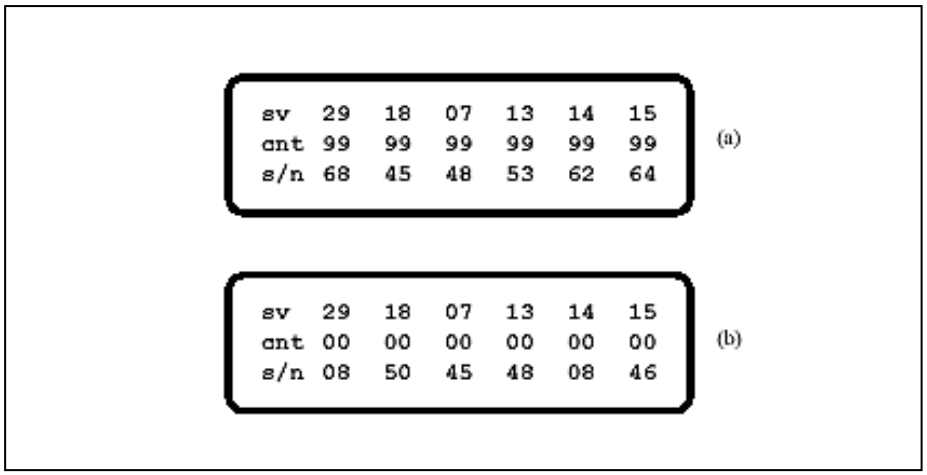


Figure A-9. Signal-health display formats before and during interference.

It was observed that the **SNR** parameters immediately decreased down to certain minimum values and then "froze" when the satellite signals were lost due to telemetry interference. No significant difference in the GNSS tracking behaviour was observed transmitting at all assigned telemetry frequencies (1442.5 MHz, 1436 MHz, and 1460 MHz), and using alternatively the two telemetry antennae installed on the plate (27 cm and 70 cm from the GNSS antenna).

A.4 FILTERING

Since the L-band telemetry transmission caused such a severe interference that prevented the GNSS receiver satellite signal tracking, an L-band filter was identified (MU-DEL ELECTRONICS MCP1478-110-9BB model), whose characteristics were deemed suitable for insertion between the Telemetry Transmitter and the antennae. The L-band filter characteristics are listed in Table A-1.

Table A-1. L-band filter characteristics.

Characteristics	Lower Rejection Point	Lower 1 dB Point	Centre Frequency	Upper 1 dB Point	Upper Rejection Point
	1239.9	1430	1478	1526	1563.1
Attenuation (spec.)	50 dB	2.0 dB	1.0 dB	2.0 dB	50 dB
Attenuation (meas.)	> 50 dB	< 2.0 dB	< 2.0 dB	< 2.0 dB	> 50 dB
VSWR (specs)	N/A	< 1.5 : 1	< 1.5 : 1	< 1.5 : 1	N/A
VSWR (meas.)	N/A	< 1.5 : 1	< 1.5 : 1	< 1.5 : 1	N/A

The L-band filter transfer function is shown in Fig. A-10. The filter attenuates the telemetry signal of about - 2 dBm, but it guarantees, based on its specifications, an attenuation of 50 dBm at frequencies greater than 1563.1 MHz. Therefore, in principle, this filter could avoid interference at 1575.42 MHz (GNSS L1 frequency). After installing the L-band filter between the Telemetry Transmitter and the antennae, further ground tests were performed.

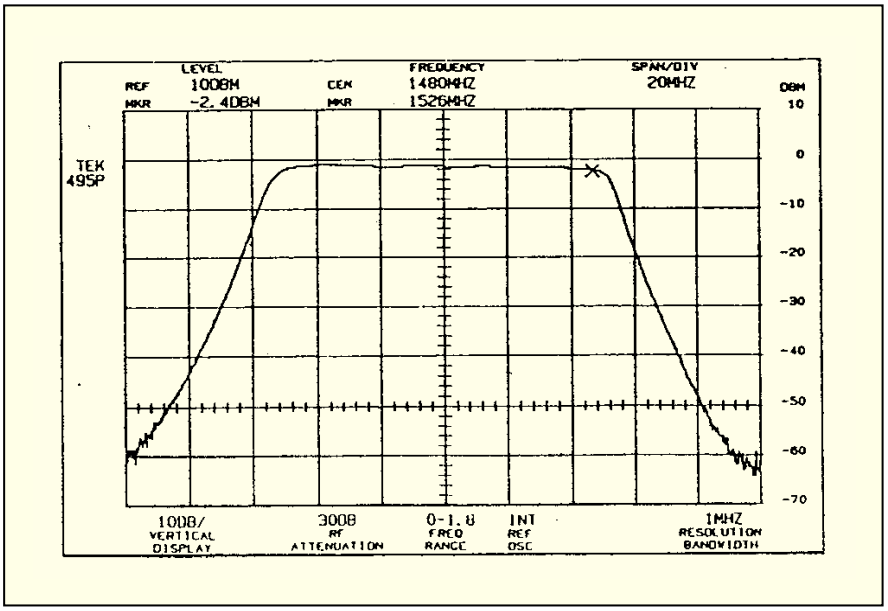


Figure A-10. L-band filter transfer function.

Two GNSS receiver signal-health formats recorded before (a) and after (b) activating the telemetry transmitter, are shown in Fig. A-11.

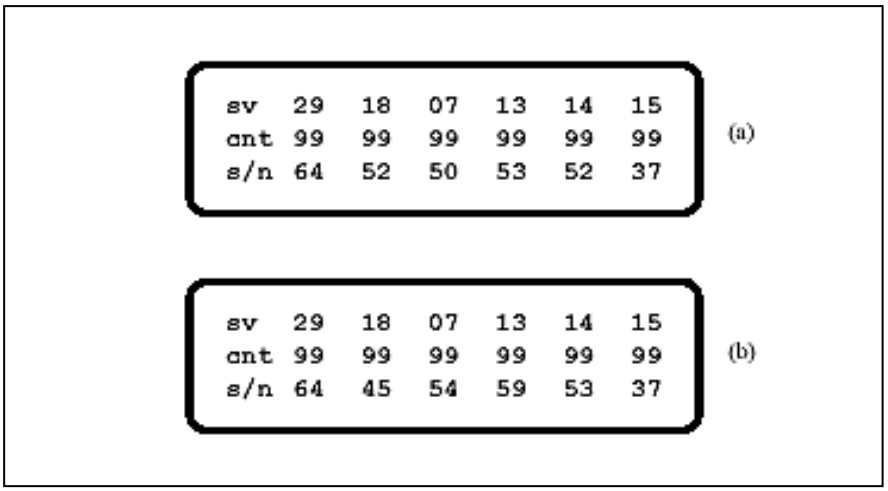


Figure A-11. Signal-health display formats with L-band filter.

It is evident that, from a practical point of view, the L-band filter significantly improved the GNSS receiver performance, avoiding the interference problems previously found. In order to further investigate the effects of the L-band filter insertion on the L1 GNSS signals tracked by the ASHTECH receiver, we also

measured the signal received by the GNSS antenna. The results of these measures are shown in Fig. A-12 and A-13.

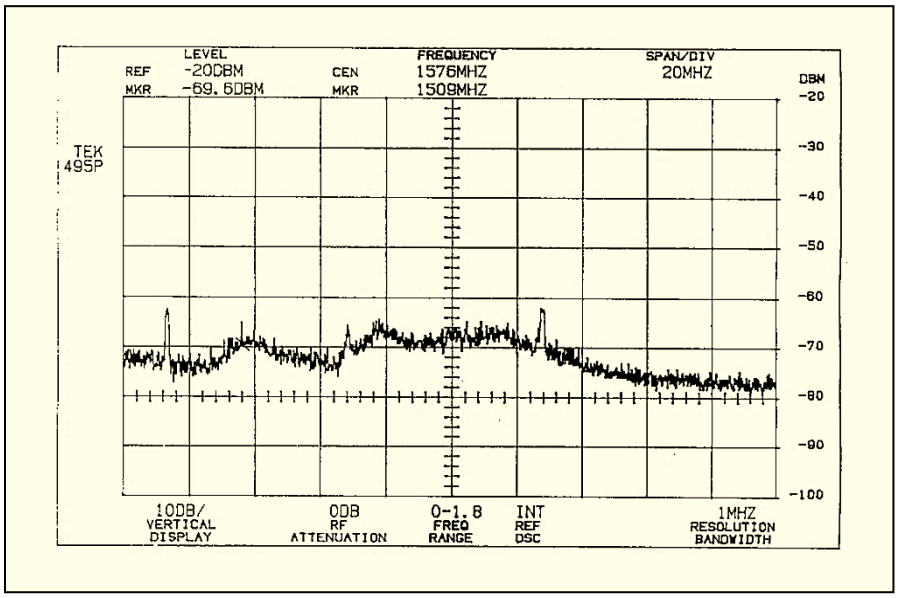


Figure A-12. GNSS/telemetry signal spectrum in the GNSS signal band (with filter).

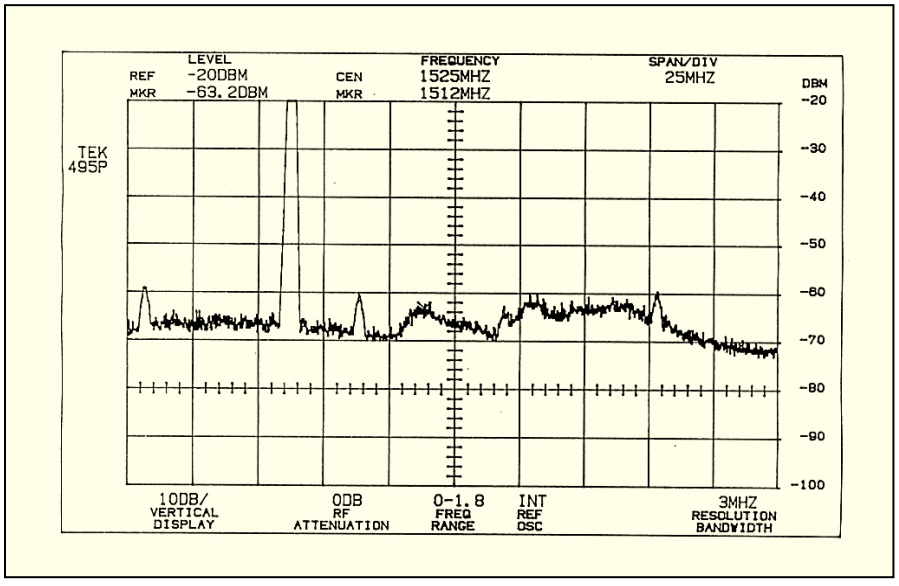


Figure A-13. Overall GNSS/telemetry signal spectrum (with filter).

Both the GNSS signal and the telemetry signal received by the GNSS antenna did not show significant changes. The irregularity of the spectrum and the presence of picks are probably due to signal distortions, which may be caused, for instance, by the GNSS antenna pre-amplifier. Unfortunately, the instrumentation available was not sufficient to test this hypothesis, since the level of the disturbance was comparable to the background noise. The telemetry signal spectrum with the L-band filter is almost unchanged, as shown in Fig. A-14.

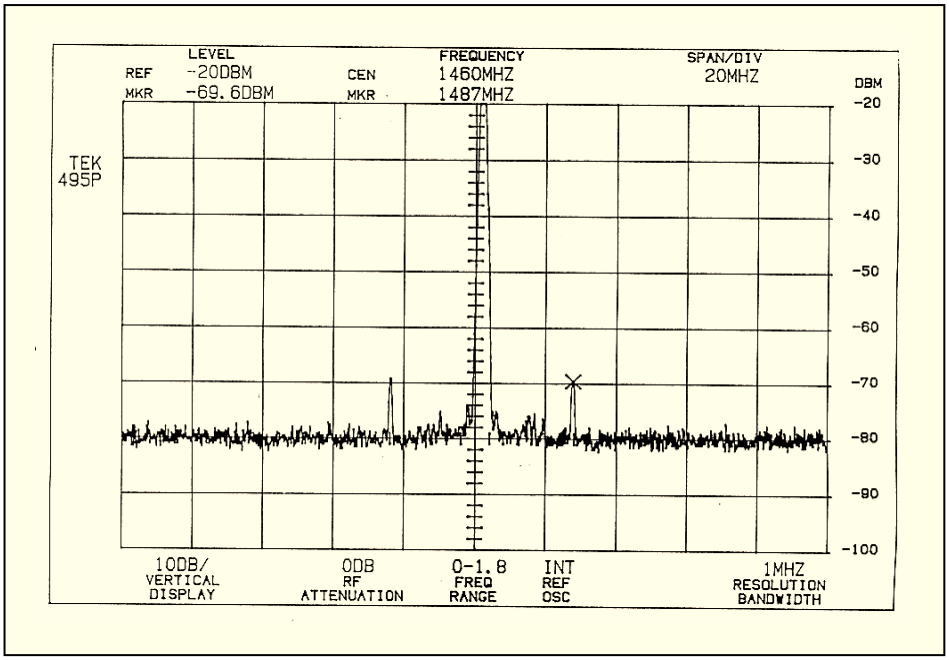


Figure A-14. Telemetry spectrum with L-band filter.

Finally, disconnecting the GNSS antenna pre-amplifier and connecting the GNSS antenna directly to the Spectrum Analyser, no significant changes were observed between the telemetry signal spectrum without the L-band filter (Fig. A-15) and with the L-band filter (Fig. A-16).

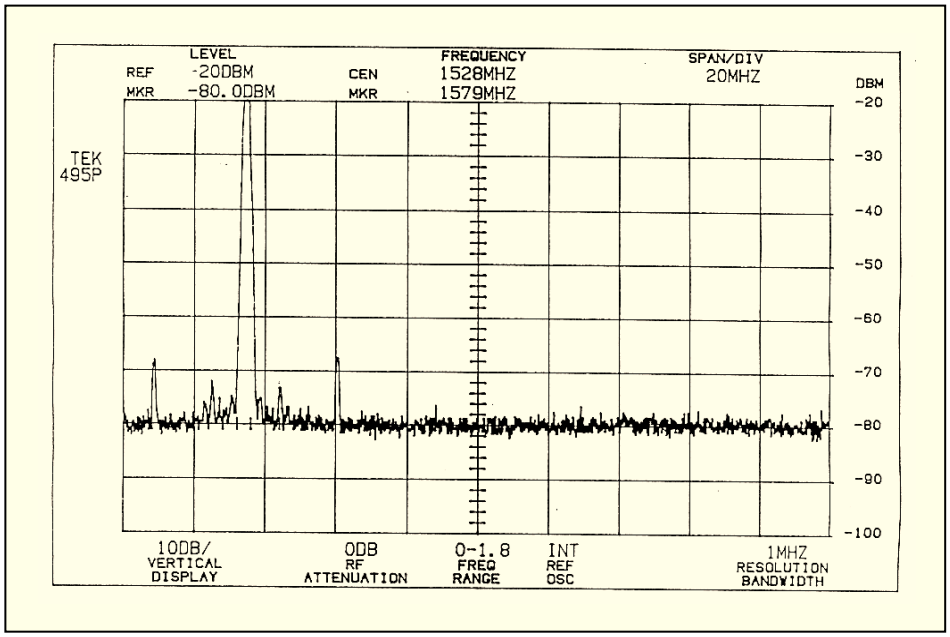


Figure A-15. Telemetry spectrum without L-band filter (no pre-amplifier).

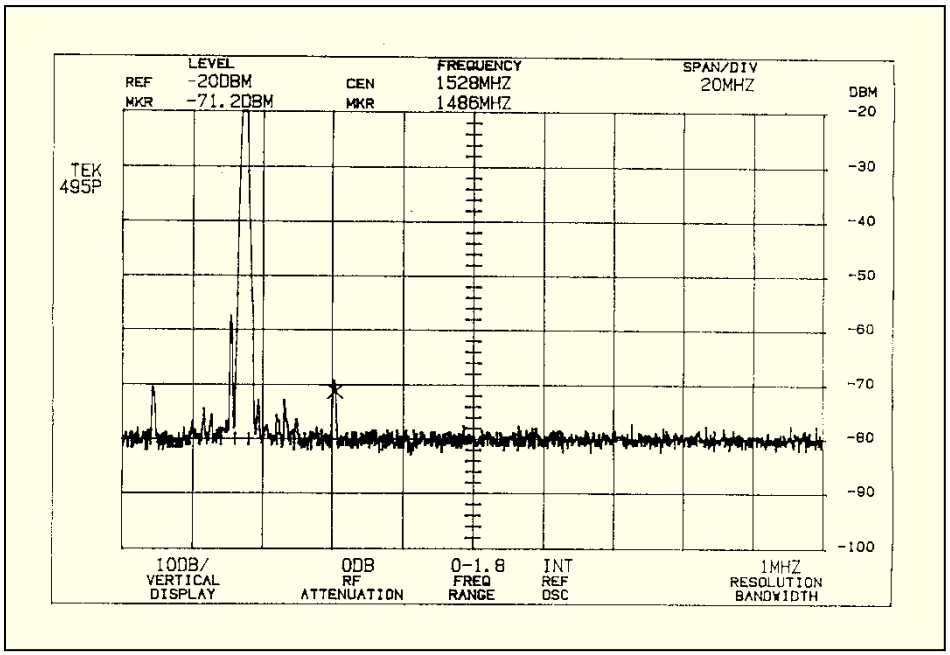


Figure A-16. Telemetry spectrum with L-band filter (no pre-amplifier).

Due to the positive results of the ground tests performed with the L-band filter MU-DEL ELECTRONICS mod. MCP1478-110-9BB, this filter was finally selected for installation in the TORNADO-IDS FTI system.

B.4 REFERENCES

Sabatini, R. and Palmerini, G. B. (2008), "Differential Global Positioning System (DGPS) for Flight Testing." NATO Research and Technology Organization (RTO) – Systems Concepts and Integration Panel (SCI). AGARDograph Series RTO-AG-160, Vol. 21.

B

3DOF ADM PRACTICAL IMPLEMENTATION

B.1 3DOF MODEL TAILORING

The 3DOF model presented in Chapter 6 (Equations 6-5 to 6-11), includes seven state variables $(V, \psi, \gamma, m, \Phi, \Lambda, h)$ and three control variables (T, α, ϕ). Hence, for it to be solved, at least three flight constraints must be specified for each flight segment.

In Straight, Level and Steady Flight (SLSF), the following constraints are applied:

- Constant altitude: $h = h_C$
- Constant Mach or CAS: $V = V_C(h_C)$
- Constant heading: $\psi = \psi_C$

Since the flight is horizontal, we also have:

- The lift is equal to the weight: $L = mg$
- $\phi = 0$
- $\theta = \alpha$

Hence, the 3DOF system of equations reduces to:

$$\frac{dm}{dt} = -c(V_C, h_C)T(V_C, m) \tag{B-1}$$

$$\frac{d\Phi}{dt} = \frac{V_C \cos\psi_C}{r_M + h_C} \tag{B-2}$$

$$\frac{d\Lambda}{dt} = \frac{V_C \sin\psi_C}{\cos(\Phi)\,(r_T + h_C)} \tag{B-3}$$

where:

$$T = \frac{1}{2}\rho {V_C}^2 S C_D(V_C, C_L) \tag{B-4}$$

$$C_L = \frac{2mg}{\rho {V_C}^2 S} \tag{B-5}$$

The relation linking C_D and C_L is given by the polar curves of a specific aircraft. These curves are determined performing experiments in wind tunnels and/or analysing data from flight tests.

In Straight, Level and Unsteady Flight (SLUF), the constraints are:

- Constant altitude: $h = h_C$
- Assuming that the engine ratings of the aircraft are known:
  - In case of Cruise: $T = T_{Maximum\ Cruise}(M, h_C)$
  - In Idle: $T = T_{IDLE}(M, h_C)$
- Constant heading: $\psi = \psi_C$

Since the flight is horizontal, we also have:

- The lift is equal to the weight: $L = mg$
- $\phi = 0$
- $\theta = \alpha$

Hence, the 3DOF takes the form:

$$m\frac{dV}{dt} = T(M, h_C)\cos\alpha - \frac{1}{2}\rho_A V^2 S C_D(M, C_L) \tag{B-6}$$

$$\frac{dm}{dt} = -c(V, h_C)T(M, h_C) \tag{B-7}$$

$$\frac{d\Phi}{dt} = \frac{V\cos\psi_C}{r_M + h_C} \tag{B-8}$$

$$\frac{d\Lambda}{dt} = \frac{V\sin\psi_C}{\cos(\Phi)\,(r_T + h_C)} \tag{B-9}$$

For the case of Steady Straight Descent/Climb (SSD/SSC), the constraints are:

- Constant Mach or CAS: $V(h)$
- Idle engine rating: $T = T_{IDLE}(M, h)$
- Constant heading: $\psi = \psi_C$
- Constant bank: $\phi = 0$

In this case, we also have:

- $\theta = \alpha + \gamma$ with $\gamma = \arcsin\left(\frac{d\mathrm{h}}{dt}\frac{1}{V(h)}\right)$

Hence, the 3DOF model reduces to:

$$mV(h)\frac{d\gamma}{dt} = T(M,h)\sin\alpha + L(m,h,\gamma) - mg\cos\gamma \tag{B-10}$$

$$\frac{dm}{dt} = -c(M,h)T(M,h) \tag{B-11}$$

$$\frac{d\Phi}{dt} = \frac{V(h)\cos\gamma\cos\psi_C}{r_M + h_C} \tag{B-12}$$

$$\frac{d\Lambda}{dt} = \frac{V(h)\cos\gamma\sin\psi_C}{(r_T + h_C)} \tag{B-13}$$

$$\frac{d\mathrm{h}}{dt} = V(h)\sin\gamma \tag{B-14}$$

where the lift is defined as:

$$L = \frac{1}{2}\rho V^2(h) S C_L(m,h,\gamma) \tag{B-15}$$

and the lift coefficient C_L is the solution of:

$$\frac{1}{2}\rho V^2(h)SC_{D}(M,C_L) = T(M,h)) - mgsin\gamma - mV(h)\frac{dV}{dh}sin\gamma \qquad \text{(B-16)}$$

During SD flight phases (e.g., approach glide path), the following constraints can be applied:

- Constant CAS, typically the approach speed $V(h) = CAS_{APP}$
- Constant heading: $\psi = \psi_C$
- Constant flight path angle, in practice defined by the ILS/GLS for suitably equipped aircraft: $\gamma = \gamma_C$

Since the flight is straight and the path angle is constant, we also have:

- $\phi = 0$
- $L = mg\cos(\gamma_C)$

Hence, the 3DOF equations reduce to:

$$\frac{dm}{dt} = -c(M,h)T(M,h) \qquad \text{(B-17)}$$

$$\frac{d\Phi}{dt} = \frac{V(h)\cos\gamma_C\cos\psi_C}{r_M + h_C} \qquad \text{(B-18)}$$

$$\frac{d\Lambda}{dt} = \frac{V(h)\cos\gamma_C\sin\psi_C}{(r_T + h_C)} \qquad \text{(B-19)}$$

$$\frac{d\mathrm{h}}{dt} = V(h)\sin\gamma_C \qquad \text{(B-20)}$$

where the thrust T can be expressed as:

$$T = \frac{1}{2}\rho\, V^2(h)SC_D(M,C_L) + mgsin\gamma_C + mV^2(h)\frac{dV_C}{dh}\sin\gamma_C \qquad \text{(B-21)}$$

with:

$$C_L = \frac{2mgcos\gamma_C}{\rho\, V^2(h)S} \qquad \text{(B-22)}$$

During steady LT flight, the constraints are:

- Constant altitude: $h = h_C$
- Constant Mach or CAS: $V(h)$
- Constant bank angle: $\phi = \phi_C$

The turn is assumed to be properly coordinated and, since the flight is horizontal, we also have:

- $\gamma = 0$ (i.e., $\theta = \alpha$)
- $L = \frac{mg}{\cos(\phi_C)}$

Hence, the 3DOF model reduces to:

$$\frac{dm}{dt} = -c(M,h)T(M,h) \tag{B-23}$$

$$mV\frac{d\psi}{dt} = (Tsin\alpha + L)sin\phi \tag{B-24}$$

$$\frac{d\Phi}{dt} = \frac{V\cos\psi}{r_M + h} \tag{B-25}$$

$$\frac{d\Lambda}{dt} = \frac{V\sin\psi}{\cos\phi\,(r_T + h)} \tag{B-26}$$

where the thrust T is given by Eq. (6-40) and the lift is:

$$C_L = \frac{2mg}{\rho\, V^2(h) S\cos(\phi_C)} \tag{B-27}$$

In the case of Level Unsteady Turn (LUT), the constraints are:

- Constant altitude: $h = h_C$
- Assuming that the engine ratings of the aircraft are known:
  - In case of Cruise: $T = T_{Maximum\ Cruise}(M, h_C)$
  - In Idle: $T = T_{IDLE}(M, h_C)$

- Constant bank angle: $\phi = \phi_C$

Since the flight is horizontal and the turn is coordinated we also have:

- $\gamma = 0$
- $L = \frac{mg}{\cos(\phi_C)}$

Hence, the 3DOF reduces to:

$$\frac{dm}{dt} = -c(M,h)T(M,h) \tag{B-28}$$

$$m\frac{dV}{dt} = T(M,h)cos\alpha - \frac{1}{2}\rho V^2 S C_D(V, C_L) \tag{B-29}$$

$$mV\frac{d\psi}{dt} = [T(M,h)sin\alpha + L(m)]sin\phi \tag{B-30}$$

$$\frac{d\Phi}{dt} = \frac{V\cos\psi}{r_M + h} \tag{B-31}$$

$$\frac{d\Lambda}{dt} = \frac{V\sin\psi}{\cos\Phi\,(r_T + h)} \tag{B-32}$$

where the lift coefficient C_L is given by Eq. (B-27).

For steady TC or TD (Fig. B-1), the constraints are:

- Constant Mach or CAS: $V_C(h)$
- Assuming that the engine ratings of the aircraft are known:
  - In case of Climb: $T = T_{Maximum\ Climb}(M,h)$
  - In case of Descent: $T = T_{IDLE}(M,h)$
- Constant bank angle: $\phi = \phi_C$

Additionally, we have:

- $\theta = \acute{a} + \gamma$ with $\gamma = \arcsin\left(\frac{dh}{dt}\frac{1}{V_C}\right)$

Hence, all 3DOF model equations are used in this case:

$$mV\frac{d\gamma}{dt} = [T(M,h)\sin\alpha + L(m,h,\gamma)]\cos\phi_C - mg\cos\gamma \tag{B-33}$$

$$mV\frac{d\psi}{dt} = [T(M,h)sin\alpha + L(m,h,\gamma)]\frac{sin\phi_C}{\cos\gamma} \tag{B-34}$$

$$\frac{dm}{dt} = -c(V_C,h)T(M,h) \tag{B-35}$$

$$\frac{d\Phi}{dt} = \frac{V_C cos\gamma\cos\psi}{r_M + h} \tag{B-36}$$

$$\frac{d\Lambda}{dt} = \frac{V_C cos\gamma\sin\psi}{\cos\Phi\,(r_T + h)} \tag{B-37}$$

$$\frac{d\mathrm{h}}{dt} = V_C sin\gamma \tag{B-38}$$

where $L(m,h,\gamma)$ is defined by Eq. (B-15) and the lift coefficient C_L is given by Eq. (B-27).

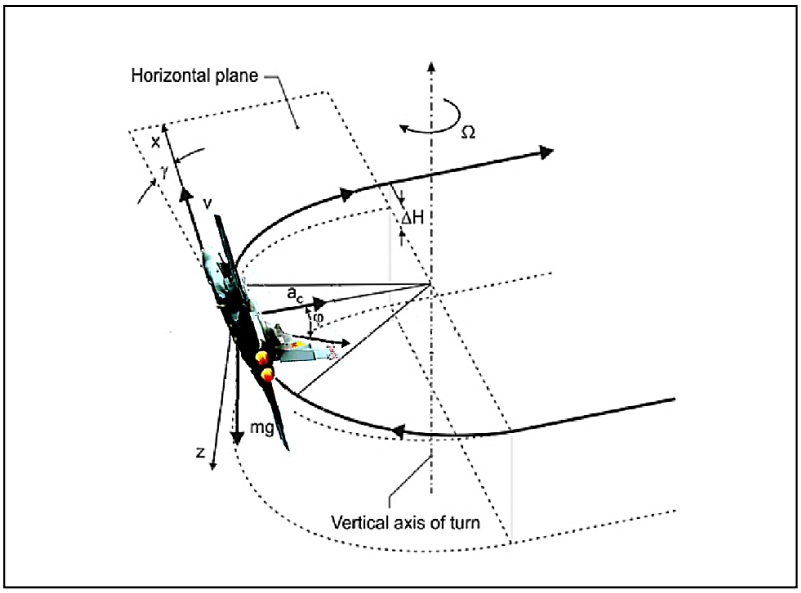


Figure B-1. Aircraft TC/TD manoeuvres.

Similarly, for unsteady TC and TD flight, the full set of equations is used and specific constraints are defined in terms of pitch angle and/or rate of descent to replace the constant Mach/CAS constraint.

B.2 MANOEUVRE IDENTIFICATION ALGORITHM

The IFG Manoeuvre Identification Algorithm (MIA) determines the type of manoeuvre an aircraft is flying based on observation of the data available in the Aircraft Data Network (ADN) and comparing these data with a pre-defined set of criteria for manoeuvre identification. The criteria adopted in the MIA are listed in Table B-1.

Table B-1. ADN manoeuvre Identification criteria.

MANOEUVRE/FLIGHT PHASE		IDENTIFICATION CRITERIA
GROUND OPERATIONS (GO)		Weight on Wheels (WOW)
STRAIGHT CLIMB (SC)	TAKE OFF	Pitch Up, Altitude Increase, No Bank, Flaps Down and/or Landing Gear Down
	STRAIGHT CLIMB	Pitch Up, Altitude Increase, No Bank
TURNING CLIMB (TC)		Pitch up, Altitude increase, Bank, Heading Variation
STRAIGHT AND LEVEL (SL)		No pitch, Constant Altitude, No Bank, Constant Heading angle
LEVEL TURN (LT)		No Pitch, Constant Altitude, No Bank, Heading Variation
TURNING DESCENT (TD)	CURVED/SEGMENTED APPROACH	Pitch down, Altitude decrease, Bank, Heading Variation, Flaps Down/Landing Gear Down
	TURNING DESCENT	Pitch down, Altitude decrease, Bank, Heading Variation
STRAIGHT DESCENT (SD)	STRAIGHT APP./GLIDE PATH	Pitch Down and/or Negative, Constant Flight Path Angle, Altitude decrease, No Bank, Constant Heading, Flaps Down/Landing Gear Down
	STRAIGHT DESCENT	Pitch Down and/or Negative Flight Path Angle, Altitude decrease, No Bank, Constant Heading

The inputs needed to perform this analysis are attitude angles (and associated rates), altitude, flaps position and landing-gear states. Attitude angles and angular rates are typically provided by an INS, altitude is provided by barometric and/or radio-altimeters and data flaps/landing-gear positions are provided from their respective actuators. Additionally, steady (i.e., constant velocity) or unsteady flight conditions can be detected simply observing the CAS/Mach variations over time. Another criterion used to strengthen this first set of conditions is the use of manoeuvre transition probabilities. This criterion is based on assessing the probabilities associated to two types of manoeuvres being performed sequentially. An example is shown in Fig. B-2 where specific probability levels (denoted by arrows) are associated to each type of transition. Green arrows indicate high probability, orange medium and red low probability. The absence of arrow between to manoeuvres indicates a null probability (i.e., a transition that is not possible). The transition probability levels can be defined by performing fight simulations and/or extracting data from flight tests.

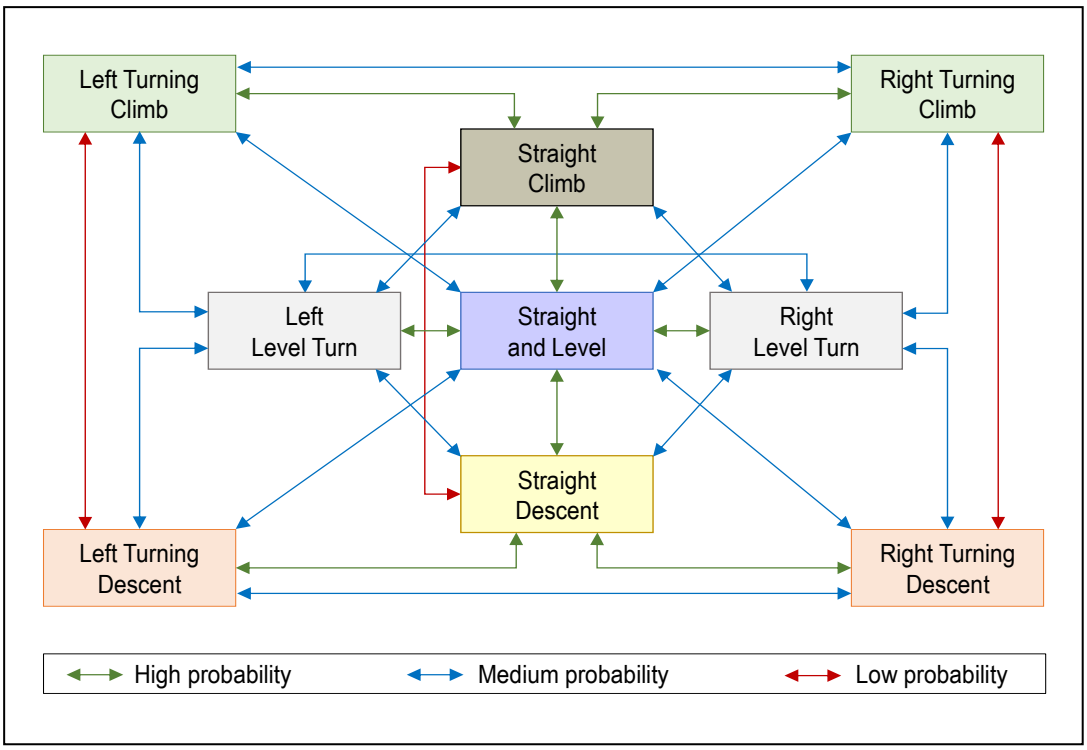


Figure B-2. Manoeuvre transition probability chart (example).

As an example, the TORNADO-IDS transition manoeuvre probability levels based on flight test data are listed in Table B-2.

Table B-2. Transition Probabilities for TORNADO-IDS.

Transition	Probability Level
Between SL and SC/SD	High
Between SL and LT	High
Between SC and TC	High
Between SD and TD	High
Between SL and TC/TD	Medium
Between SC/SD and LT	Medium
Between TC/TD and LT	Low
Between TC and TD	Low
Between SC/SD to LT	Low

It should be noted that these probability levels are relative to a TORNADO-IDS flying a predefined (non-aerobatics and non-tactical) mission profile by a crew with high level of skills (experimental test pilot/navigator). Hence, the transitions between turning modes are associated with low probabilities of occurrence since they are typically used to compensate for piloting/navigation errors (e.g., altitude or heading errors). Hence, these probabilities apply to relatively benign flight conditions and could be extended to other civil/military aircraft as well. However, they would not be representative of manned/unmanned aircraft performing acrobatics or tactical/dogfight manoeuvres. If the detailed mission profile is already known (e.g., FMS data), an additional criterion can be included to account for the transition time. This would require comparing the current time with the theoretical transition time registered in the FMS database. However, a detailed mission plan is typically employed for scheduled commercial and military flights; less frequently for general aviation and small UAV flights.

B.3 3DOF AIRCRAFT DATA

The aircraft data used in the practical 3DOF implementations are presented here. For the TORNADO-IDS aircraft, the accurate performance data could not be disclosed. Therefore, some approximated lookup tables are presented here based on the aircraft polar curves and thrust curves. Only dry thrust data were used in the simulations and are listed here. The A320 and AEROSONDE UAV data were sourced from the available open literature.

B.3.1 TORNADO-IDS Data

Table B-3. TORNADO-IDS characteristics (Fredriksen, 2000), (Richardson, 1986).

Characteristic	Description
Crew	2
Length	16.72 m (54 ft 10 in)
Wingspan	13.91 m (45.6 ft) at 25° wing sweep 8.60 m (28.2 ft) at 67° wing sweep
Height	5.95 m (19.5 ft)
Wing area	26.6 m² (286 ft²)
Empty Weight	13,890 kg (31,620 lb)
Max. Take-off Weight	28,000 kg (61,700 lb)
Power Plant	2 Turbo-Union RB199-34R Mk 103 afterburning turbofan engines
Dry Thrust	43.8 kN (9,850 lbf) each
Thrust with Afterburner	76.8 kN (17,270 lbf) each
Maximum Speed	Mach 2.2 (2,400 km/h, 1,490 mph) at 9,000 m / 30,000 ft altitude 800 knots, 1,482 km/h, 921 mph indicated airspeed near sea level
Range	1,390 km (750 NM) typical combat
Ferry Range	3,890 km (2,100 NM) with four external drop tanks
Service Ceiling	15,240 m (50,000 ft)
Rate of Climb	76.7 m/s (15,100 ft/min)
Thrust/weight	0.55

Table B-4. Configuration A – C_L and C_D for M = 0.4.

C_L	C_D
0	0.031
0.1	0.034
0.2	0.038
0.3	0.042
0.4	0.047
0.5	0.056
0.6	0.065
0.7	0.072
0.8	0.087
0.9	0.109
1.0	0.131
1.1	0.172
1.2	0.237
1.3	0.391
1.37	0.507

Table B-5. Configuration A – C_L and C_D for M = 0.8

C_L	C_D
0	0.034
0.1	0.036
0.2	0.039
0.3	0.042
0.4	0.049
0.5	0.061
0.6	0.077
0.7	0.110
0.8	0.145
0.9	0.183
1.0	0.225
1.1	0.267
1.2	0.330
1.3	0.390
1.4	0.440
1.42	0.480

Table B-6. Configuration B – C_L and C_D for M = 0.4.

C_L	C_D
0	0.032
0.163	0.037
0.344	0.044
0.524	0.059
0.688	0.081
0.852	0.111
1.008	0.192
1.131	0.266
1.237	0.248
1.352	0.433
1.467	0.529

Table B-7. Configuration B – C_L and C_D for M = 0.8.

C_L	C_D
0	0.055
0.163	0.062
0.344	0.071
0.524	0.089
0.688	0.119
0.852	0.167
1.008	0.231
1.131	0.297
1.237	0.366
1.352	0.452
1.467	0.551

Table B-8. Configuration B – C_L and C_D for M = 1.0.

C_L	C_D
0	0.068
0.1426	0.070
0.36	0.085
0.573	0.118
0.77	0.162
0.95	0.225
1.114	0.296
1.213	0.372
1.36	0.466
1.467	0.559
1.557	0.651

Table B-9. Configuration B – C_L and C_D for M = 1.4.

C_L	C_D
0	0.085
0.131	0.090
0.278	0.103
0.393	0.125
0.524	0.163
0.655	0.209
0.770	0.270
0.885	0.329
1.024	0.407
1.155	0.481
1.245	0.551

Table B-10. Configuration C – C_L and C_D for M = 0.2.

C_L	C_D
0	0.023
0.091	0.026
0.200	0.031
0.290	0.038
0.480	0.056
0.660	0.080
0.790	0.104
0.087	0.125
1.030	0.173

Table B-11. Configuration C – C_L and C_D for M = 0.8.

C_L	C_D
0	0.032
0.091	0.035
0.200	0.039
0.290	0.044
0.480	0.062
0.660	0.082
0.770	0.101
0.870	0.123
0.980	0.167

Table B-12. Configuration C – C_L and C_D for M = 0.9.

C_L	C_D
0	0.0275
0.190	0.0300
0.400	0.0400
0.593	0.0710
0.760	0.1190
0.960	0.1930

Table B-13. Configuration C – C_L and C_D for M = 1.0.

C_L	C_D
0	0.039
0.11	0.040
0.19	0.042
0.33	0.047
0.5	0.060
0.69	0.089
0.88	0.134
1.10	0.184

Table B-14. Configuration C – C_L and C_D for M = 1.4.

C_L	C_D
0	0.037
0.12	0.038
0.19	0.040
0.34	0.049
0.48	0.071
0.65	0.118
0.84	0.191

Table B-15. Configuration C – C_L and C_D for M = 1.6.

C_L	C_D
0	0.0360
0.1	0.0384
0.2	0.0420
0.3	0.0480
0.4	0.0580
0.5	0.0710
0.7	0.1060

Table B-16. Configuration C – C_L and C_D for M = 2.0.

C_L	C_D
0	0.035
0.1	0.037
0.2	0.043
0.3	0.053
0.4	0.070
0.5	0.087

Table B-17. Tornado Dry Thrust for Z = 0 m MSL.

M	T_D [kg]
0.271	8465
0.410	8605.9
0.554	9239.7
0.703	10014.4
0.847	10648.2
1.152	10929.9
1.296	10155.2
1.457	8746.7
1.601	7380.5
1.745	6281.8
1.894	5225.5
1.955	4802.9

Table B-18. Tornado Dry Thrust for Z = 5000 m MSL.

M	T_D [kg]
0.503	5745.3
0.673	6341.4
0.843	6932.4
1.007	7336.89
1.183	7487.6
1.353	7323.3
1.517	6916.3
1.687	6343.5
1.857	5797.7
2.027	5366.65

Table B-19. Tornado Dry Thrust for Z = 10000 m MSL.

M	T_D [kg]
0.5030	2521.10
0.6730	2760.60
0.8437	3183.10
1.0070	3676.10
1.1830	4211.38
1.3530	4802.90
1.5170	5507.20
1.6870	6183.28
1.8570	6281.80
2.0270	6000.10
2.1970	5394.50

B.3.2 A320 Data

Table B-20. A320 characteristics (Airbus, 2016).

Characteristic	Description
Overall Length	37.57 m
Cabin Length	27.51 m
Fuselage Width	3.95 m
Max Cabin Width	3.70 m
Wing Span: (Geometric)	34.10 m
Wing Area	122.6 m²
Height	11 m
Track	7.59 m
Wheelbase	12.64 m
Typical Seating	150 (2-class), Max 180
Range	6150 km with shark lets
Maximum Take-off Weight	73.5 (78.0) tonnes
Maximum Landing Weight	64.5 (66.0) tonnes
Maximum Zero Fuel Weight	61.0 (62.5) tonnes
Maximum Fuel Capacity	up to 24 210 (30 190) litres
Engines	2 × V2500-A5 or 2 × CFM56-5B
Thrust Range	98 (120) kN

Table B-21. A320 derivatives used in the 3-DOF Model (Eurocontrol, 2014).

Derivative	Value	Units
$C_{D0,CR}$	0.026659	[-]
$C_{D2,CR}$	0.038726	[-]
$C_{TC,1}$	142310	[N]
$C_{TC,2}$	51680	[ft]
$C_{TC,3}$	0.56809×10^{-10}	[1/ft^2]
$C_{TC,4}$	10.138	[K]
$C_{TC,5}$	0.008871	[1/K]
C_{TCcr}	0.95	[-]
$C_{TC,h}$	0.13603	[-]
$C_{TC,l}$	0.10847	[-]
$h_{p,d}$	29831	[ft]
C_{f1}	0.75882	[kg/min·kN]
C_{f2}	2938.5	[kts]
C_{f3}	8.9418	[kg/min]
C_{f4}	93865	[feet]
C_{fcr}	0.96358	[-]

B.3.3 AEROSONDE UAV Data

Table B-22. AEROSONDE UAV characteristics (Maslanik, 2002).

Characteristic	Description
Wingspan	2.9 m
Wing Area	0.55 m^2
Weight	13-15 kg (29-33 lbs.)
Engine	24cc fuel injected, premium unleaded gasoline
Battery	20 W-hr
Fuel tank	5 kg when full
Speed	80-150 km/hr (50-93 miles/hour) cruise, 9 km/hour (6 miles/hr) climb
Range	> 3,000 km distance, > 30 hours, 0.1-6 km altitude (depending on payload)
Payload	up to 2 kg (4.4 lbs.) with full fuel load
Navigation	GPS
Communications	UHF radio or LEO satellite
Material	Carbon fibre
Propeller	Real propeller, allows for atmospheric measurements before air is disturbed by propeller
Propeller Radius	0.25 m

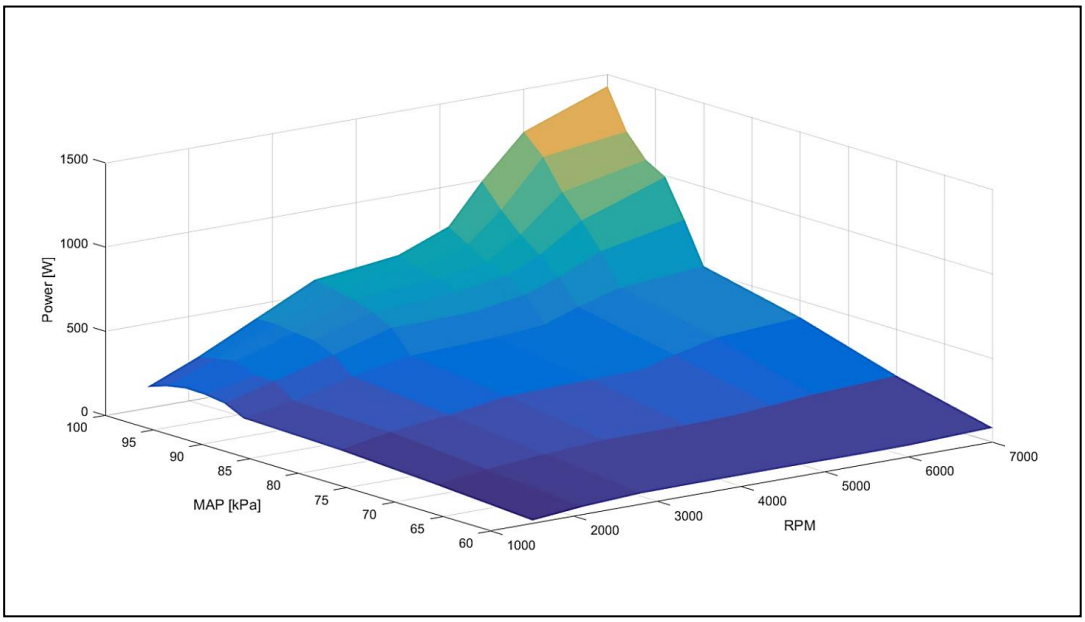


Figure B-3. Power vs. MAP vs. RPM (Unmanned Dynamics, 2012).

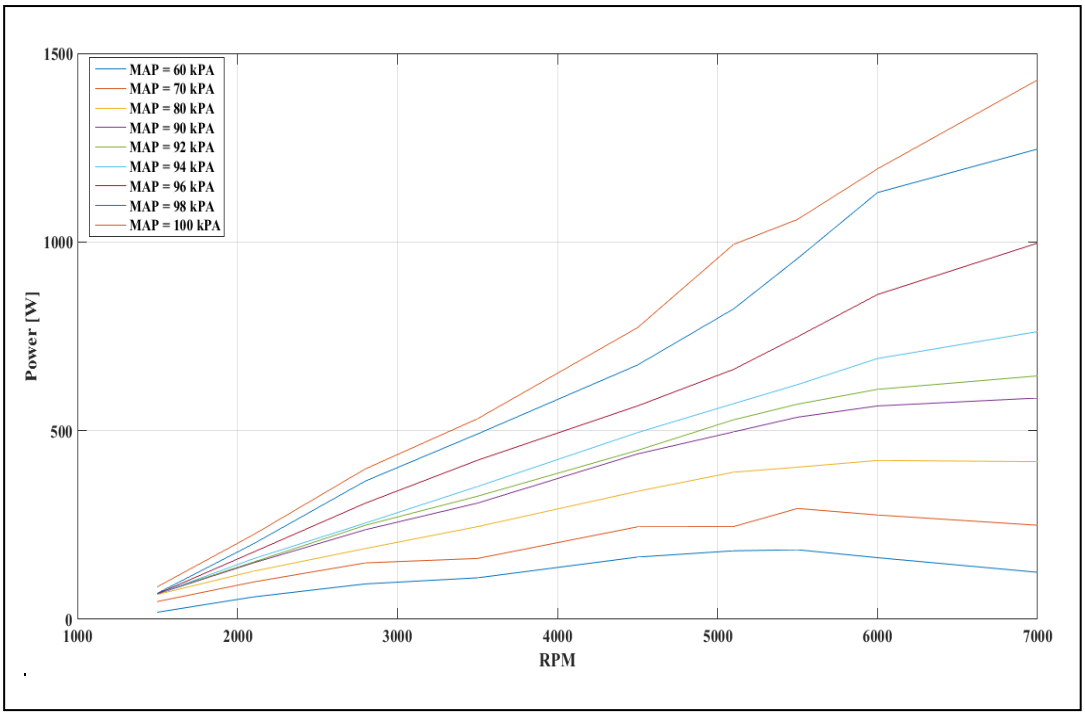


Figure B-4. AEROSONDE power curves (Unmanned Dynamics, 2012).

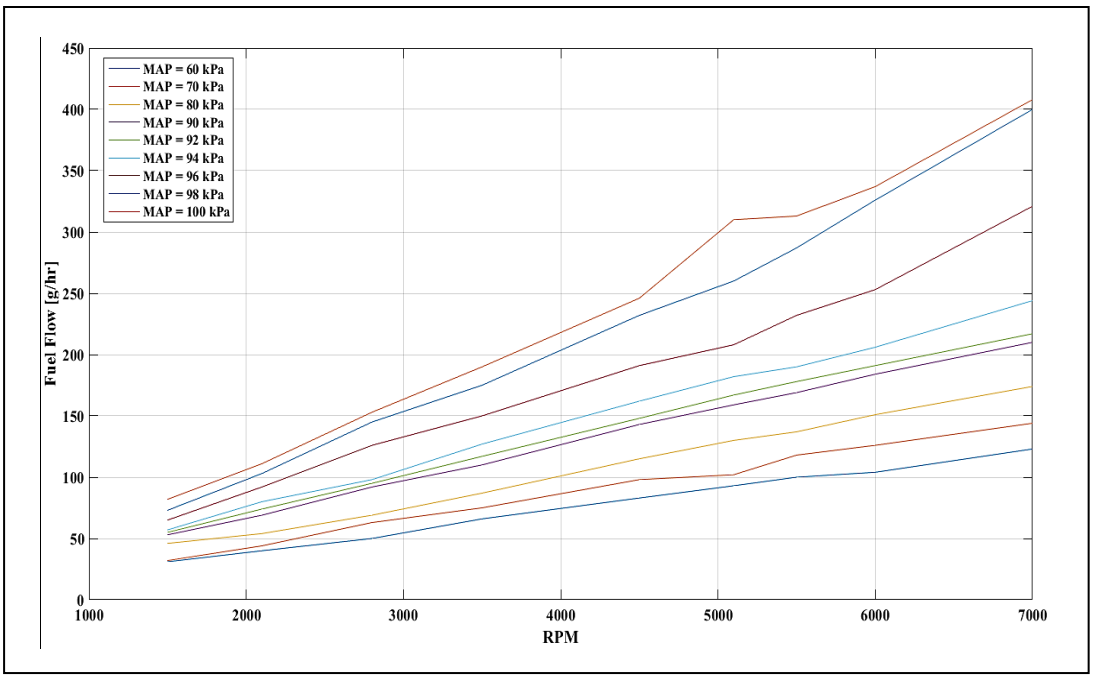


Figure B-5. AEROSONDE fuel flow curves (Unmanned Dynamics, 2012).

Table B-23. AEROSONDE 3-DOF derivatives model (Unmanned Dynamics, 2012).

Derivative	Value	Units
C_{L0}	0.23	[-]
$C_{L\alpha}$	5.6106	[-]
C_{D0}	0.0434	[-]
C_{LminD}	0.23	[-]

B.5 REFERENCES

Airbus (2015), "A320 Specifications." Aircraft dimensions and key data webpage. Available online at: http://www.airbus.com/aircraftfamilies/passengeraircraft/a320family/a320/specifications/ (Accessed 2nd May, 2013).

Unmanned Dynamics (2003). "AEROSIM Blockset User's Guide." Version 1.01. Unmanned Dynamics LLC, Hood River, OR (USA). Document available online at: https://people.rit.edu/pnveme/EMEM682n/Matlab_682/aerosim_ug.pdf (accessed 3rd June 2012).

Unmanned Dynamics (2012). "AEROSIM Matlab Toolbox." Version 1.2. Unmanned Dynamics LLC, Hood River, OR (USA). Available online at: http://www.u-dynamics.com/aerosim/default.htm (accessed 25th May 2013).

Maslanik, J. (2002), "Polar remote sensing using an unpiloted aerial vehicle." Seminar held at Colorado Center for Astrodynamics Research (CCAR), University of Colorado at Boulder. Available online at: http://www2.hawaii.edu/~jmaurer/uav/#specifications (overview and editing by Maurer J.). Webpage visited on 22nd May 2012.

Eurocontrol (2014), "USER Manual for the Base of Aircraft Data (BADA)." Revisiom 3.12. The European Organisation for the Safety of Air Navigation (Eurocontrol) Experimental Centre (EEC). Technical/Scientific Report No. 14/04/24-44.

Eurocontrol (2013), "Base of Aircraft Data (BADA)." Family 3, Vers. 3.9. The European Organisation for the Safety of Air Navigation (Eurocontrol). Software licencing instructions are available at: http://www.eurocontrol.int/services/bada (Software license obtained in February 2013)

Fredriksen, J. C. (2000), " Warbirds: An Illustrated Guide to World Military Aircraft, 1914–2000." ABC-CLIO Ltd. ISBN-10: 1576073645 / ISBN-13: 9781576073643, pp. 255-256.

Richardson, D. (1986), "TORNADO, Modern Fighting Aircraft (Aviation fact file)." Salamander Books Ltd. (UK). ISBN-10: 0861012011 / ISBN-13: 9780861012015, pp. 30-31.